Transactions of the ASME® Journal of Heat Transfer

HEAT TRANSFER DIVISION
Chair, **Y. JALURIA**
Vice Chair, **Y. BAYAZITOGLU**
Past Chair, **J. H. KIM**
Secretary, **M. K. JENSEN**
Treasurer, **R. W. DOUGLASS**
Member, **R. D. SKOCYPEC**

Editor, **V. DHIR** (2005)

Associate Editors,
C. AMON (2004)
P. AYYASWAMY (2004)
K. BALL (2004)
H. H. BAU (2003)
V. P. CAREY (2003)
G. CHEN (2005)
J. CHUNG (2005)
G. DULIKRAVISH (2004)
A. EMERY (2005)
M. FAGHRI (2003)
J. G. GEORGIADIS (2003)
M. JENSEN (2004)
D. B. R. KENNING (2004)
K. KIHM (2005)
H. LEE (2004)
G. P. PETERSON (2003)
V. PRASAD (2005)
R. D. SKOCYPEC (2003)
S. THYNELL (2005)
P. VANKA (2005)

BOARD ON COMMUNICATIONS
Chair and Vice President
OZDEN OCHOA

OFFICERS OF THE ASME
President, **SUSAN H. SKEMP**
Executive Director,
VIRGIL R. CARTER
Treasurer,
R. E. NICKELL

PUBLISHING STAFF
Managing Director, Engineering
THOMAS G. LOUGHLIN

Director, Technical Publishing
PHILIP DI VIETRO

Managing Editor, Technical Publishing
CYNTHIA B. CLARK

Production Coordinator
COLIN McATEER

Production Assistant
MARISOL ANDINO

Transactions of the ASME, Journal of Heat Transfer (ISSN 0022-1481) is published bi-monthly (Feb., Apr., June, Aug., Oct., Dec.) by The American Society of Mechanical Engineers, Three Park Avenue, New York, NY 10016. Periodicals postage paid at New York, NY and additional mailing offices. POSTMASTER: Send address changes to Transactions of the ASME, Journal of Heat Transfer, c/o THE AMERICAN SOCIETY OF MECHANICAL ENGINEERS, 22 Law Drive, Box 2300, Fairfield, NJ 07007-2300. **CHANGES OF ADDRESS** must be received at Society headquarters seven weeks before they are to be effective. Please send old label and new address. **STATEMENT from By-Laws.** The Society shall not be responsible for statements or opinions advanced in papers or ... printed in its publications (B7.1, Para. 3), **COPYRIGHT © 2002** by The American Society of Mechanical Engineers. For authorization to photocopy material for internal or personal use under those circumstances not falling within the fair use provisions of the Copyright Act, contact the Copyright Clearance Center (CCC), 222 Rosewood Drive, Danvers, MA 01923, tel: 978-750-8400, *www.copyright.com*. Request for special permission or bulk copying should be addressed to Reprints/Permission Department. **INDEXED** by Applied Mechanics Reviews and Engineering Information, Inc. Canadian Goods & Services Tax Registration #126148048.

Published Bimonthly by The American Society of Mechanical Engineers

VOLUME 124 • NUMBER 4 • AUGUST 2002

HEAT TRANSFER PHOTOGALLERY

TECHNICAL PAPERS

Conduction

Forced Convection

Natural and Mixed Convection

(Contents continued on inside back cover)

This journal is printed on acid-free paper, which exceeds the ANSI Z39.48-1992 specification for permanence of paper and library materials. ∞™
♲ 85% recycled content, including 10% post-consumer fibers.

Downloaded 04 Feb 2011 to 194.85.80.107. Redistribution subject to ASME license or copyright; see http://www.asme.org/terms/Terms_Use.cfm

(**Contents continued**)

Journal of Heat Transfer **Volume 124, Number 4** **AUGUST 2002**

Radiative Heat Transfer

Evaporation, Boiling, and Condensation

Porous Media

Heat Transfer Enhancement

Combustion and Reactive Flows

ANNOUNCEMENTS

Journal of
Heat Transfer

Heat Transfer Photogallery

The sixth ‘‘Heat Transfer Photogallery’’ was sponsored by the K-22 Heat Transfer Visualization Committee for the 2001 International Mechanical Engineering Congress and Exhibition in New York last November. Seven entries were selected for publication in this special section of the ASME JOURNAL OF HEAT TRANSFER.

The purpose of publishing these photographs is to draw attention to the innovative features of optical diagnostic techniques and aesthetic qualities of thermal processes. To focus on visualization, the text is kept to a minimum and further details should be found through the listed references or directly from the authors. The photographs include: (1) thermal tuft visualization of surface-coated thermochromic liquid crystals (TLC) for detecting flow direction, (2) surface-coated TLC visualization of heat transfer augmentation by perforated fin surfaces [1], (3) two-color laser induced fluorescence (LIF) visualization for micro-scale temperature field mapping of stratified thermal layers [2], (4) nano-scale thermal writing/erasing using a heated atomic force microscope cantilever [3], (5) Mach-Zehnder interferometric imaging of the free convection around a heated louvered blind near a vertical isothermal plate [4,5], (6) IR thermal imaging of thermocapillary driven flow by the laser heating of an acoustically levitated and flattened glycerin drop [6], and (7) Coherent Gradient Sensing Interferometry [7], visualization of iso-gradient contours in convective/diffusive glycerin-water mixtures.

I wish that the journal readers enjoy viewing these collections, acquire knowledge of the state-of-the-art features potentially applicable for their own research, and promote their participation in 2002-IMECE Photogallery session presentation (refer to the Call for Photogallery for 2002-IMECE announced in this volume).

References

[1] Wang, Z., Ireland, P. T., and Jones, T. V., 1993, ‘‘An Advanced Method of Processing Liquid Crystal Colour Change Images From Transient Heat Transfer Experiments Using an Intensity History Method,’’ ASME Paper 93-GT-283.

[2] Kim, H. J., and Kihm, K. D., 2001, ‘‘Application of Two-Color Laser Induced Fluorescence (LIF) Technique for Temperature Mapping,’’ 2001 ASME IMECE, Paper No. IMECE 2001/HTD-24411.

[3] King, W. P., Kenny, T. W., Goodson, K. E., Cross, G. L. W., Despont, M., Durig, U., Rothuizen, H., Binnig, G., and Vettiger, P., 2001, ‘‘Atomic Force Microscope Cantilevers for Combined Thermomechanical Data Writing and Reading,’’ Appl. Phys. Lett., **78**, pp. 1300–1302.

[4] Naylor, D., Duarte, N., Petryk, J., and Machin, A. D., 2000, ‘‘Flow- and Temperature-Field Visualization of a Window with a Heated Louvered Blind,’’ Journal of Flow Visualization and Image Processing, **7**(3), pp. 243–253.

[5] Phillips, J., Naylor, D., Harrison, S. J., and Oosthuizen, P. H., 2001, ‘‘Numerical Study of Convective and Radiative Heat Transfer from a Window Glazing with a Venetian Blind,’’ International Journal of HVAC&R Research, **7**(4), pp. 383–402.

[6] Sadhal, S. S., Trinh, E. H., and Wagner, P., 1997, ‘‘Unsteady Spot Heating of a Drop in a Microgravity Environment,’’ Microgravity Sci. Technol., **9**, pp. 80–85.

[7] Tippur, H. V., 1992, ‘‘Coherent Gradient Sensing: A Fourier Optic Analysis and Applications to Fracture,’’ Appl. Opt., **31**, pp. 4428–4438.

K. D. Kihm
Department of Mechanical Engineering,
Texas A&M University,
College Station, TX 77843-3123

Fig. 1: Validation of Technique A comparison was made between the results provided by a traditional tuft (made from audiotape) with the results provided by the "cool" thermal tuft for flow over a backward-facing step (step height = 25mm). This flow condition was chosen because of the well-documented features of the separated flow region downstream of the step.

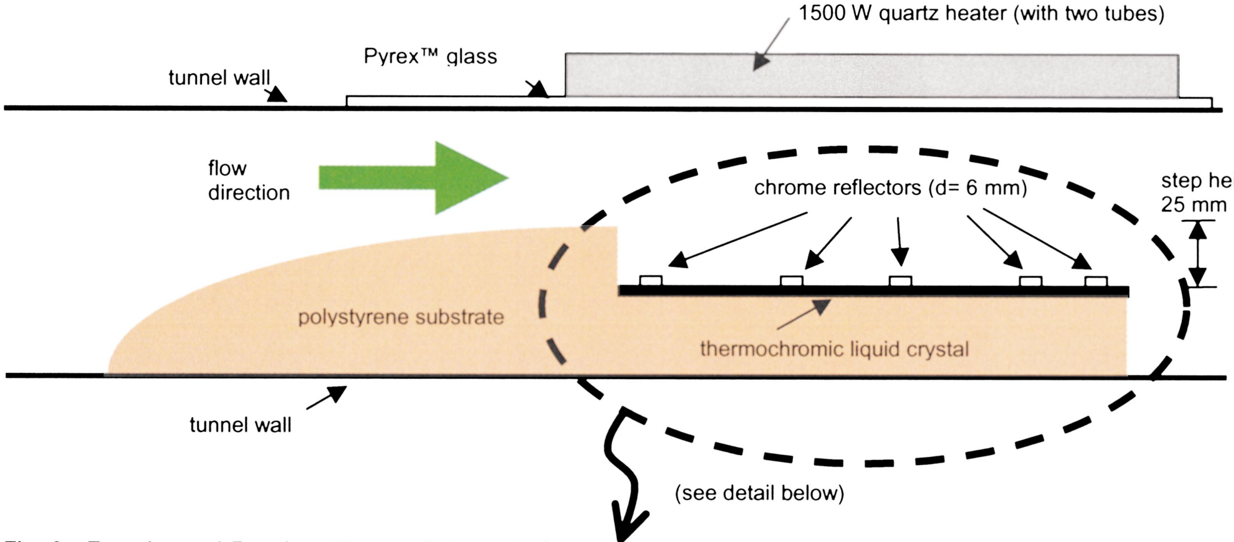

Fig. 2: Experimental Results The "cool" thermal tuft captured the presence of the important flow features including the weak counter-rotating vortex, the reverse flow region, the reattachment point, and the region of attached flow. These features were also captured with both smoke flow visualization and with traditional tufts made from audiotape as shown below. The results also agreed well with published results.

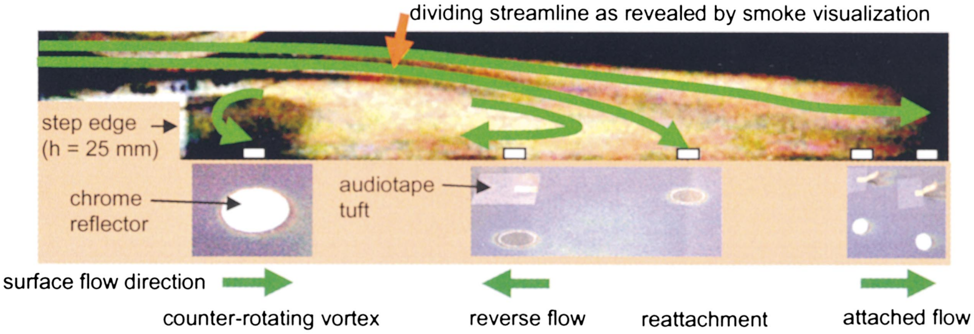

Summary

An optical flow diagnostic technique was developed to detect surface flow direction in weakly separated flows. The technique makes use of thermochromic liquid crystals applied to a surface that is first coated with flat-black paint. A thin reflective material is affixed to the test surface. The surface is heated uniformly from above with infrared heaters. The reflective surface remains cool relative to the nearby black surface. A thermal tuft of relatively cool air (having just passed over the reflector) is advected in the direction of the surface flow thereby creating a "comet tail" of liquid crystal color response. The "comet tail" points in the direction of the surface flow.

The "cool" thermal tuft successfully provides a means for detecting surface flow direction. The advantages of this method are the following: it is sensitive enough to detect the presence of weakly separated flows; it is non-obtrusive; it is reversible so does not require clean-up between runs; and it can be applied to vertical surfaces because there is nothing to drip.

Fig. 3: Close-up of "cool" thermal tuft

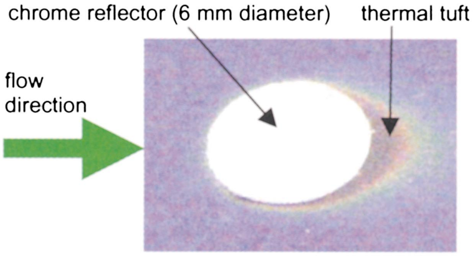

A "Cool" Thermal Tuft for Detecting Surface Flow Direction

A.R. Byerley
Dept. of Aeronautics
USAF Academy, CO

O. Störmer
BWB
Ingolstadt, Germany

J. W. Baughn
U.C. Davis
Davis, CA

T.W. Simon
Univ. of Minnesota
Minneapolis, MN

K. Van Treuren
Baylor University
Waco, TX

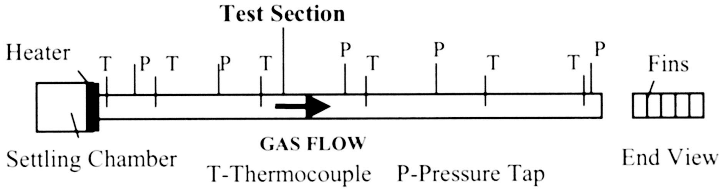

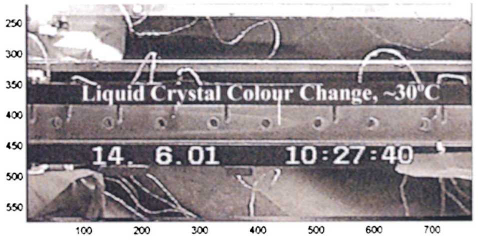

Raw Data – Single Frame, CCD

Perforated Fin Results

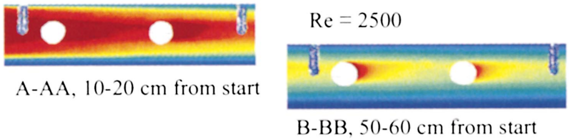

A-AA, 10-20 cm from start

B-BB, 50-60 cm from start

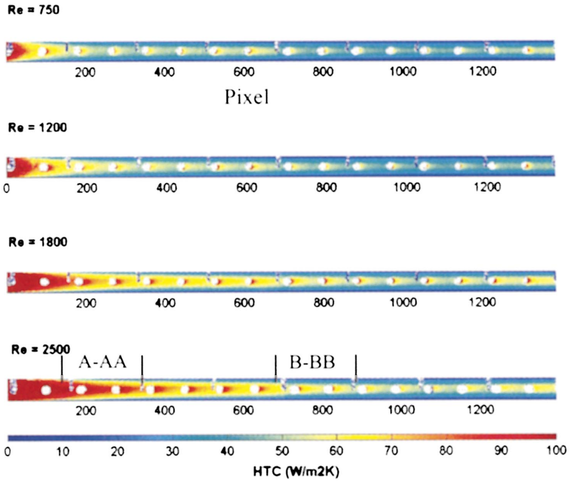

Plain Fin Results

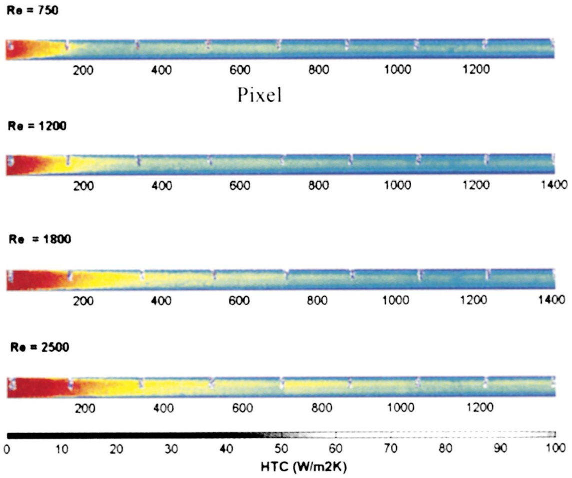

Photographs on the Effect of Perforations on the Heat Transfer due to Laminar Flow over an Extended Surface

M. Cerza
Mechanical Engineering Department
US Naval Academy
Annapolis, MD USA 21402

J. C. Adams and P. T. Ireland
Department of Engineering Science
The University of Oxford
Oxford, UK OX1 3PJ

J. Oswald
Rolls Royce plc, Ansty
Coventry, UK CV7 9JR

ABSTRACT

In the past it has not been resolved as to whether perforated surfaces on a fin enhance heat transfer. In this photographic study which utilizes liquid crystal thermography, the evidence suggests that there is an increase in the local heat transfer coefficient in the vicinity of the downstream side of the perforations. The perforations appear to partially disrupt the thermal boundary layer and they appear to allow a partial restart of the boundary layer on the backside of the hole. For these series of photographs, a transient heating technique is employed. Helium at approximately 70°C is allowed to flow through 5 perspex channels separated by 1 mm thick perforated fins. The channel cross sectional areas are 33 mm high by 13.1 mm wide. The channel length is 1 m. The initial temperature of the channels was 24°C. A one degree, narrow band, liquid crystal (30°C colour change temperature) was painted over the black painted centre channel fin. The time history of the colour change of the painted fin was recorded on a standard CCD video camera. The peak intensity-time relationships were obtained from image processing the recorded video and the heat transfer coefficients were evaluated using a transient thin fin heat transfer model. The helium temperature was measured at 5 locations along the channel. As can be seen, there appears to be a local heat transfer enhancement near the backside of the perforations. Comparisons are made to non-perforated fins in the channel Reynolds number range of 750-2500.

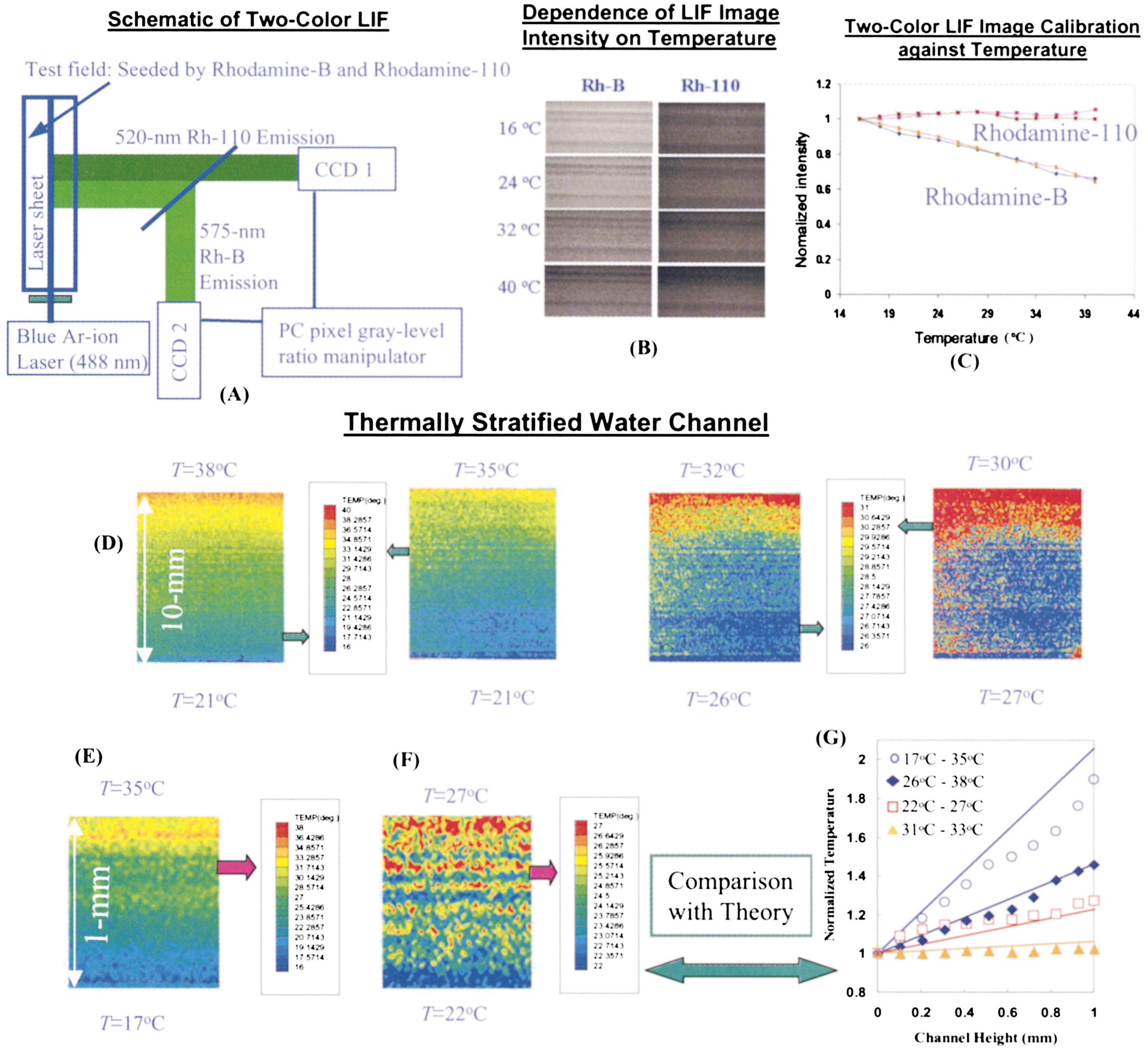

TWO-COLOR (Rh-B & Rh-110) LASER INDUCED FLUORESCENCE (LIF) THERMOMETRY WITH SUB-MILLIMETER MEASUREMENT RESOLUTION

H. J. Kim and K. D. Kihm
Texas A&M University, College Station, Texas

Two-color laser induced fluorescence (LIF) technique (**Inset A**) uses two fluorescence dyes with different emission characteristics – one is the temperature sensitive dye (Rhodamine-B) and the other is the temperature insensitive dye (Rhodamine-110). The ratio of the two fluorescence emission intensities, therefore, provides a calibrated correlation with temperature that does not depend on the laser illumination intensity variation and is free from the possible bias occurring from background noise (**Insets B & C**). The developed technique measures thermally stratified water layers with known linear temperature distributions. The **Inset D** shows "false-color" images of the intensity ratios measured for 10-mm cuvette, and the **Insets E** and **F**, for 1-mm cuvette. The temperature data, converted from these images (**E, F**) using the calibration (**C**), shows fairly accurate comparison with the theory (**Inset G**). The minimal spatial resolution is estimated to 10 μm and the maximum data uncertainty for a spatial resolution of 300μm by 200μm is estimated to be ±1.45 °C with a 95% confidence interval.

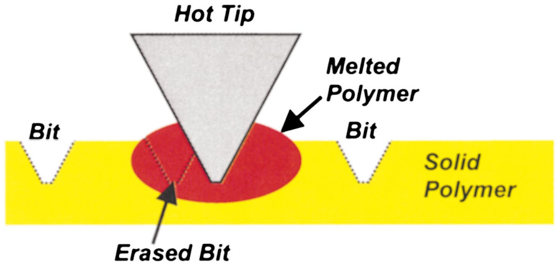

Figure 1: Thermal writing and erasing. Heat and force from the cantilever tip cause the polymer to soften and flow, forming an indentation data bit. Erasing or modifying previously written indentations is possible by melting the region near a previously formed structure.

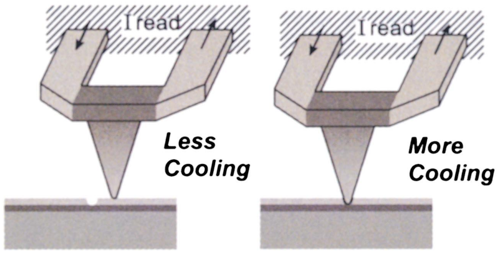

Figure 2: Thermal nanoimaging is accomplished by measuring the cantilever response to short ($\sim$10 μs) electrical pulses. The thermal resistance between the cantilever and the substrate varies as the cantilever tip follows the contours of previously written structures, producing a measurable change in the cantilever heating temperature.

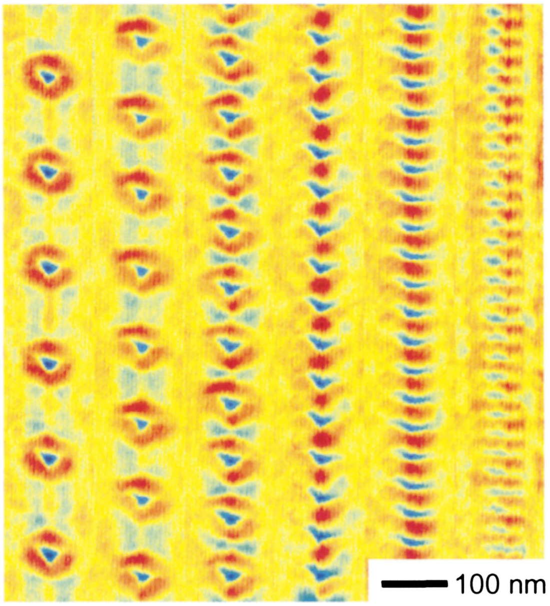

Figure 3: Tracks of thermally written indentations in a thin polymer layer. Color corresponds to the vertical, out-of-plane dimension. As the indentation periodicity increases, heat diffusion and melted polymer flow influences neighbor indentations. The maximum data density demonstrated here is 0.9 Tbit in^{-2}.

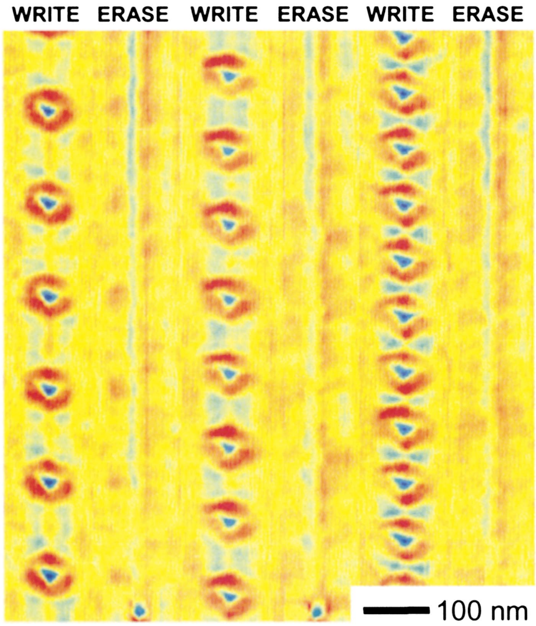

Figure 4: Tracks of thermally written and thermally erased indentations. Since erasing requires writing, each block of erased bits requires one 'erase' bit at the end of the track.

THERMAL WRITING AND NANOIMAGING WITH A HEATED ATOMIC FORCE MICROSCOPE CANTILEVER

William P. King and Kenneth E. Goodson
Department of Mechanical Engineering, Stanford University, Stanford, CA 94305-3030

In thermal writing for surface modification or data storage, a heated atomic force microscope cantilever (AFM) tip is in contact with and scans over a thin polymer film, as shown in Fig. 1. Heat conduction along the cantilever tip induces thermomechanical formation of nanometer-sized indentations in the polymer. Erasing or modifying previously written structures is possible by writing such that heat from the tip and flow of the polymer influence nearby structures, also shown in Fig. 1. A thermal nanoimaging technique measures vertical feature sizes by monitoring changes in the thermal impedance across the cantilever-polymer gap as the cantilever tip follows the contours of the written structures, shown in Fig. 2.

Indentations written with varying periodicity in Figure 3 show that heat transfer and polymer flow near the tip limit the packing density of indentations, corresponding to a data storage density limit of 0.9 Tbit in^{-2}. Figure 4 shows indentations written and then erased. Figures 3 and 4 are made with the thermal nanoimaging technique at 3 KHz and a lateral pixel spacing of 3 nm. The $\Delta R/R$ reading sensitivity is 0.02 per vertical nanometer.

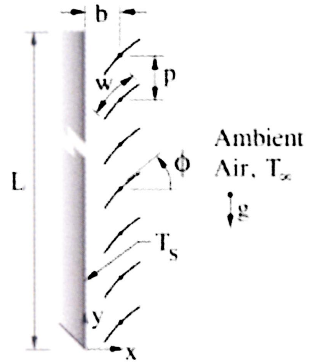

Fig. 1: Sketch of the experimental geometry.

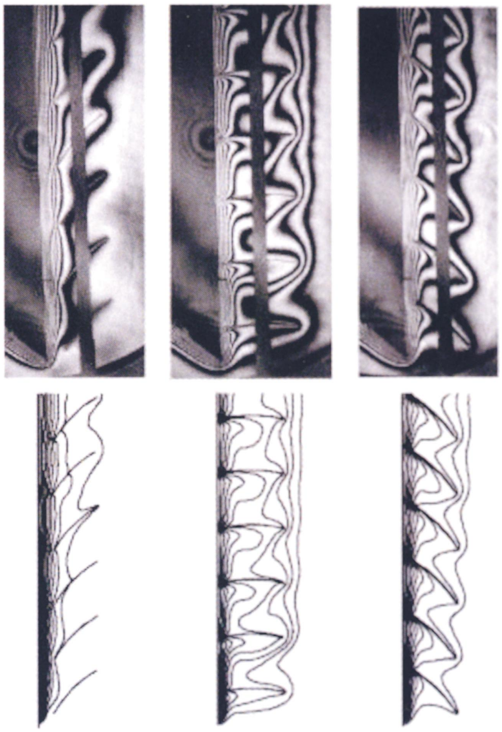

Fig. 2: Comparison of infinite fringe interferograms with numerical isotherms for blind slat angles of ϕ=45°, ϕ=0° and ϕ=-45° (T_S-T_∞=20°C, q=0 W/m^2, b=14.5mm, p=22.2mm).

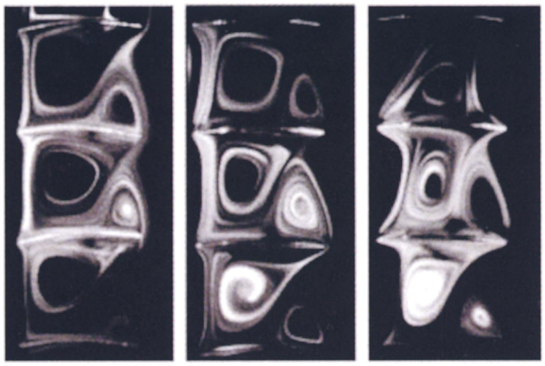

q=0 W/m^2 q=117 W/m^2 q=233 W/m^2

Fig. 3: Flow visualization showing the effect of solar heat flux (q) on the flow between the slats (T_S-T_∞=20°C, ϕ=0°, b=14.5 mm, p=22.2mm)

no blind q=0 W/m^2 q=117 W/m^2 q=233 W/m^2

Fig. 4: Infinite fringe interferograms showing the effect of solar heat flux (q) on the temperature field (T_S-T_∞=20°C, ϕ=0°, b=14.5 mm, p=22.2mm).

VISUALIZATION OF CONVECTION AT AN INDOOR WINDOW GLAZING WITH A VENETIAN BLIND

D. Naylor, N. Duarte, A.D. Machin and J. Phillips
Ryerson University, Toronto, Ontario, Canada

P.H. Oosthuizen and S.J. Harrison
Queen's University, Kingston, Ontario, Canada

Flow and temperature field visualization photographs have been obtained of the free convection about a heated louvered blind adjacent to an isothermal vertical plate. This configuration, shown in Fig. 1, is an approximate model of an indoor window glazing with a venetian blind that is heated by absorbed solar radiation. The absorbed solar heat flux (q) was simulated by heating the blind slats using thin foil electric heaters. Flow visualization photographs were taken using a sheet of laser light and cigarette smoke. Full-field temperature visualization and local heat transfer measurements were obtained using a Mach-Zehnder interferometer.

These images were obtained as part of an ongoing project that examines the effect of shading devices on the thermal performance of windows. The results are being used to develop numerical models of the complex thermal interaction between the blind and window.

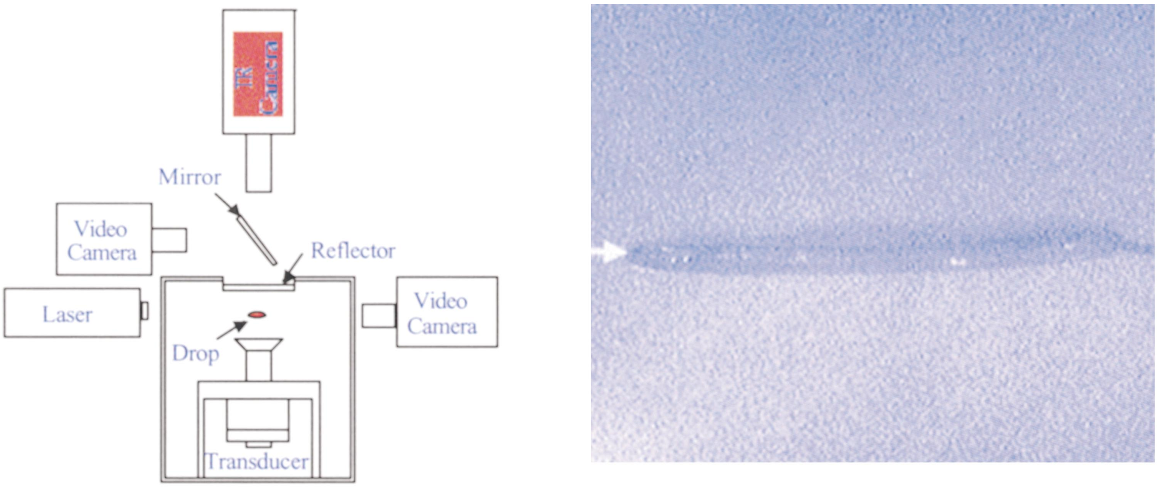

Fig. 1(a) Apparatus

(b) Side View

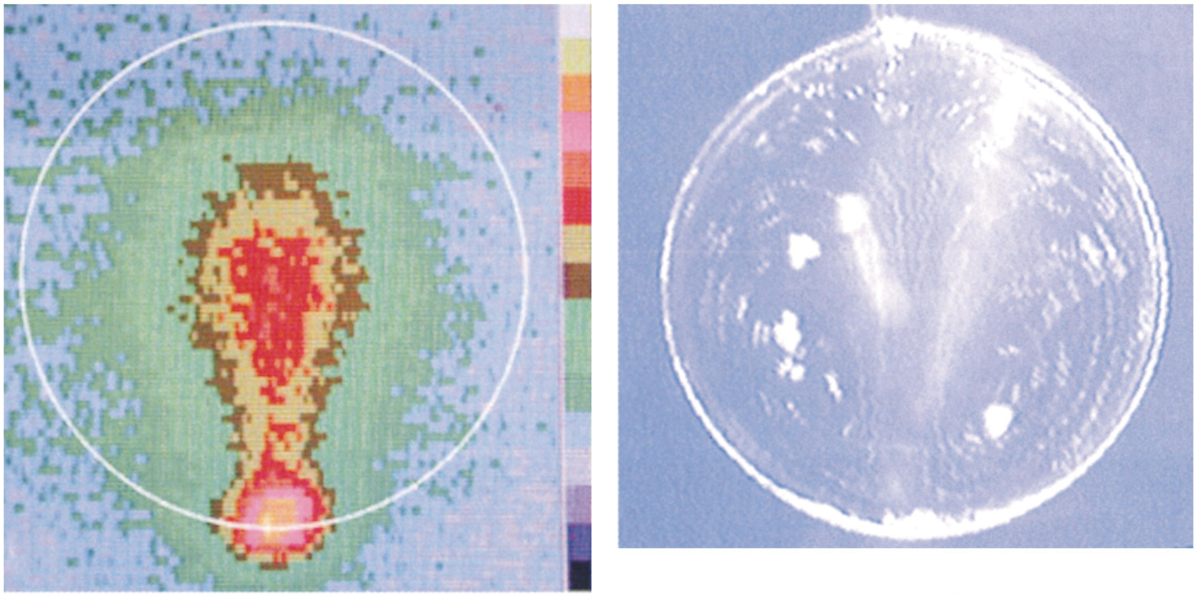

(c) Thermal Image

(d) Top View

THERMOCAPILLARY FLOW INDUCED BY LASER HEATING OF AN ACOUSTICALLY LEVITATED AND FLATTENED GLYCERIN DROP

K. Ohsaka, S. S. Sadhal, and A. Rednikov, Aerospace and Mechanical Engineering, University of Southern California, Los Angeles, California

A glycerin drop is acoustically levitated and flattened using an acoustic apparatus schematically shown in Fig. 1(a). Fig. 1(b) shows a side view of the levitated drop that is lightly touched by a non-conductive needle at the corner to prevent undesirable spinning. The flattened drop is approximately 7 mm in diameter and 0.5 mm thick. The drop is then locally heated by a CO_2 laser beam, approximately 2 mm in diameter, at the edge from the left-hand side, as shown by the arrow in Fig 1 (b). Fig. 1(c) shows a steady state thermal image of the top surface of the drop taken by an IR camera. The white circle indicates the physical position of the drop. The laser beam hits at the bottom corner. Heat conduction and convection inside of the drop and strong convective heat loss at the edge of the drop due to acoustic streaming create the temperature distribution so that the isotherms take the shape of an exclamation mark. Thermocapillary flow associated with this temperature distribution is visualized in Fig. 1(d), where the flows start from the heated spot (lowest position in the picture), move along the diameter of symmetry, split right and left, and return along the edge. A stagnation point exists at the top of the drop.

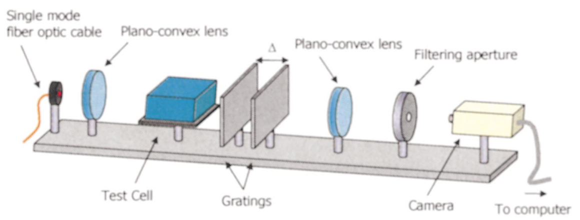

Schematic of the gradient sensing interferometer.

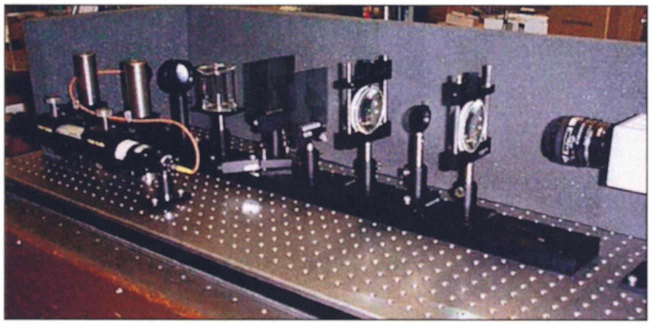

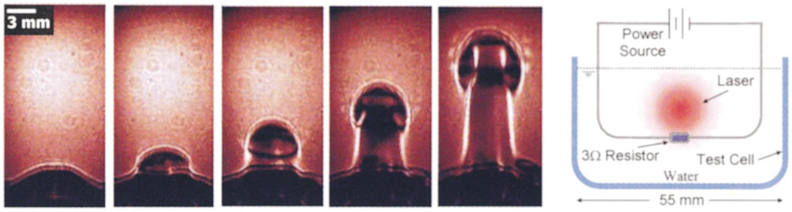

Thermal gradient field of a rising "mushroom shaped" plume in water. The images shown are taken at 200 ms interval.

Variation in concentration gradient due to the diffusion of glycerin-water mixture (1:3) in water. The images are at 100 ms, 220 ms, 880 ms and 2880 ms with respect to the left most image.

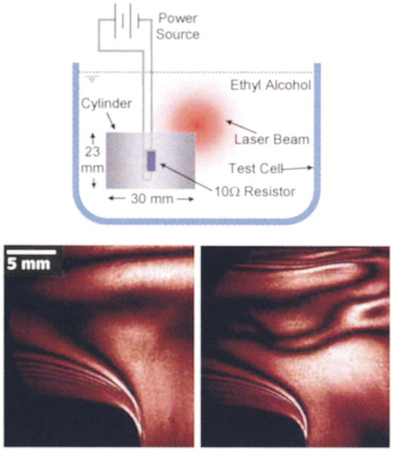

Laminar and oscillatory convection in the presence of a heated block using ethyl alcohol as the fluid medium.

Visualization of Iso-Gradient Lines in Convective and Diffusive Systems using Gradient-Sensing Interferometry

S.L. Wong, D. Mishra, J.P. Longtin, R. Singh and V. Prasad
Department of Mechanical Engineering
State University of New York at Stony Brook, Stony Brook, NY, 11794

Three-dimensional flow visualization using optical techniques remains one of the most challenging obstacles in understanding and interpreting complex fluid-thermal flows. Over the years, many diverse techniques have been developed for this purpose, including a broad class of interferometric techniques. Most interferometers for convective flow visualizations use a dual-beam configuration that is very delicate, e.g., the Mach-Zhender interferometer. These instruments are extremely sensitive to vibrations and require high-quality optics, while their sensitivity is limited by the wavelength of the light source. In this study an alternative interferometric technique, the *coherent gradient sensing interferometer* (CGSI) is employed for flow visualization. This interferometer senses gradients in the refractive index field and eliminates the need for a separate reference beam to create the interference pattern. It is insensitive to vibrations, has no reference beam, and does not require high-quality optics for accurate measurements. The sensitivity of the interferometer can also be easily varied.

The CGSI technique uses two diffraction gratings to create primary and secondary diffraction patterns. These diffracted rays then interfere to create interference patterns. Using a filtering lens, different diffraction-order spots can be separated. First order spots are lines of constant gradient in the refractive index field scanned by the beam prior to its interaction with the first of the two gratings. Gradients perpendicular to the grating directions are visible as fringes. The sensitivity of the interferometer can be easily adjusted by varying the distance between the gratings. Also by changing the grating directions, gradients in any direction can be visualized.

Funding for this work was provided by NSF through Grant No. CTS-0079494

An Inverse Method for Simultaneous Estimation of the Center and Surface Thermal Behavior of a Heated Cylinder Normal to a Turbulent Air Stream

Jiin-Hong Lin

Cha'o-Kuang Chen
e-mail: ckchen@mail.ncku.edu.tw

Yue-Tzu Yang

Department of Mechanical Engineering,
National Cheng Kung University,
Tainan, Taiwan 70101,
Republic of China

A two-dimensional inverse analysis utilizes a different perspective to simultaneously estimate the center and surface thermal behavior of a heated cylinder normal to a turbulent air stream. A finite-difference method is used to discretize the governing equations and then a linear inverse model is constructed to identify the unknown boundary conditions. The present approach is to rearrange the matrix forms of the governing differential equations and estimate the unknown boundary conditions of the heated cylinder. Then, the linear least-squares-error method is adopted to find the solutions. The results show that only a few measuring points inside the cylinder are needed to estimate the unknown quantities of the thermal boundary behavior, even when measurement errors are considered. In contrast to the traditional approach, the advantages of this method are that no prior information is needed on the functional form of the unknown quantities, no initial guesses are required, no iterations in the calculating process are necessary, and the inverse problem can be solved in a linear domain. Furthermore, the existence and uniqueness of the solutions can easily be identified. [DOI: 10.1115/1.1473140]

Keywords: Conduction, Convection, Cylinder, Heat Transfer, Inverse, Numerical Methods, Turbulent

1 Introduction

In recent years, much effort has been devoted to studying the inverse analysis in many design and manufacturing problems especially when direct measurements of surface conditions are not possible. It is difficult to install thermocouples on the surface of heated objects, and they are easily burned out. Therefore, if the temperature is measured at one or more interior locations of the objects and is then used to predict the surface thermal behavior of the objects, the difficulties encountered by Tseng et al. [1] with the surface mounting of thermocouples can be avoided. There have been numerous applications of inverse heat conduction problems (IHCP) in various branches of science and engineering, such as the prediction of the inner wall temperature of a reactor, the determination of the heat transfer coefficients and the outer surface conditions of a space vehicle, and the prediction of temperature or heat flux at the tool-workpiece interface of machine cutting.

The estimation for the boundary conditions in inverse heat conduction problems has received a great deal of attention in recent years (e.g., [2–7]). All inverse problems are ill-posed, and a small measurement error will induce a large estimated error (e.g., [8–21]). Hence, the solution may not be unique. Various methods, including analytical or numerical approaches, have been developed to solve the inverse heat conduction and convection problems. Traditionally, the inverse problem includes two phases: the process of analysis and the process of optimization. In the analysis process, the unknown conditions are assumed and then the results of the problem are solved directly through the numerical methods such as finite-difference methods and finite-element methods (e.g., [3–4]). The solutions from the above process are used to integrate with data measured at the interior points of the solid. Thus, a nonlinear problem is constructed for the optimization process. In the optimization process, an optimizer, such as the conjugated gradient method or the steepest decent method, is used to guide the exploring points systematically to search for a new set of guess conditions, which is then substituted for the unknown conditions in the analysis process. However, there are a few drawbacks in the traditional approaches expressed above. One is that the iterative process in the computation cannot be avoided. The other is that the inverse problem can only be solved in a nonlinear domain.

In order to remedy the drawbacks in the traditional approaches, this work continues the study of a recently presented and innovative methodology [13] for solving IHCP. The present approach is to rearrange the matrix forms of the governing differential equations such that the unknown boundary conditions can be represented explicitly. The linear least-squares-error method is then adopted to find the solutions for the unknown boundary conditions. In the inverse analysis, the simulated temperatures are taken at a few interior points of the cylinder. The unknown thermal boundary conditions such as surface temperatures, local Nusselt numbers, local heat flux, and even the unknown temperature of the hot wire will be obtained simultaneously through this proposed inverse method. In addition, no explicit functional form is assumed for the undetermined thermal boundary conditions, whereas in other methods polynomial or series forms are employed.

The advantages of this inverse method are that no prior information is needed on the functional form of the unknown quantities, no initial guesses are required, and no iterations in the calculating process are necessary and that the inverse problem can be solved in a linear domain. Furthermore, the existence and uniqueness of the solutions can be easily identified. However, the accuracy of the estimated thermal boundary conditions is sensitive to

---

Contributed by the Heat Transfer Division for publication in the JOURNAL OF HEAT TRANSFER. Manuscript received by the Heat Transfer Division June 7, 1999; revision received February 27, 2002. Associate Editor: S. S. Sadhal.

the errors of temperature measurement within the cylinder. In this work, the validity and robustness of the proposed methodology are presented and compared with the results of Giedt [14].

2 Physical Model

Consider the problem of a cylinder with surface temperature $T(\theta)$ placed in a uniform air stream of temperature, T_∞ and velocity, U_∞. Figure 1 gives a general illustration of the convectively cooled cylinder in cross-flow. According to the symmetric characteristics, only a half domain of the cylinder is considered. The detailed geometry, computational grid and the four types of measuring locations of the cylinder are shown in Fig. 2. The cylinder is considered to be long enough so that end effects can be neglected and accordingly the flow is assumed two-dimensional. For simplification, the embedded hot wire, at the center of the heated cylinder, is assumed to be a point source and is maintained at constant temperature, T_w. In addition, the effect of temperature variation on fluid and cylinder properties is assumed negligible and the fluid is incompressible.

The governing equation for the temperature field of the cylinder can be expressed as

$$\frac{\partial^2 T(r,\theta)}{\partial r^2}+\frac{1}{r}\frac{\partial T(r,\theta)}{\partial r}+\frac{1}{r^2}\frac{\partial^2 T(r,\theta)}{\partial \theta^2}=0$$

$$0 \leqslant r \leqslant 0.05 \text{ (m)}$$

$$0 \leqslant \theta \leqslant \pi \text{ (rad)} \tag{1}$$

where $T(r,\theta)$ is the temperature at each grid point (r,θ).

The appropriate boundary conditions are

$$\frac{\partial T(r,\theta)}{\partial \theta}=0 \qquad \theta=0 \tag{2a}$$

$$\frac{\partial T(r,\theta)}{\partial \theta}=0 \qquad \theta=\pi \tag{2b}$$

$$T(r,\theta)=T_w \qquad r=0 \tag{2c}$$

$$q(\theta)=-k_c\frac{\partial T(r,\theta)}{\partial r}=h(\theta)[T(r,\theta)-T_\infty] \quad r=R \tag{2d}$$

where, $q(\theta)$ is the local heat flux at the interface between the cylinder and the flow around the cylinder, k_c is the thermal conductivity of the cylinder, $h(\theta)$ is the local heat transfer coefficient, and T_∞ is the temperature of the uniform air stream.

The following constant parameters are used: the radius of the cylinder $R=0.05$ m, the thermal conductivity of the cylinder $k_c=14$ W/m·K (nichrome), the external air temperature $T_\infty=300$ K, and the thermal conductivity of the air stream $k_\infty=0.0263$ W/m·K. Moreover, the hot wire temperature is $T_w=473$ K, which is used to heat the cylinder.

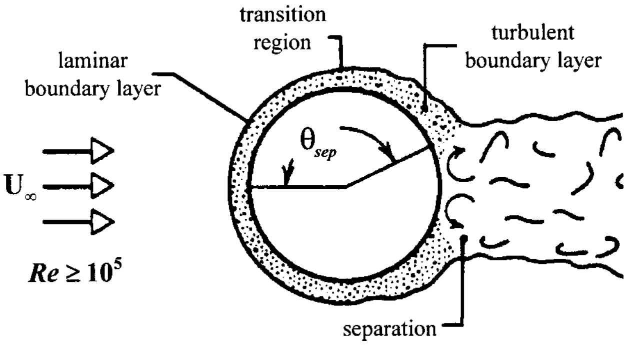

Fig. 1 General illustration of the cylinder system

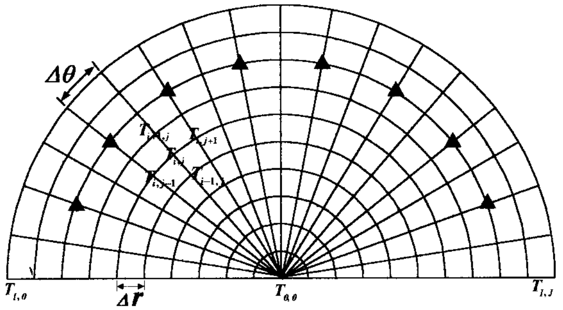

(*a*) Type 1

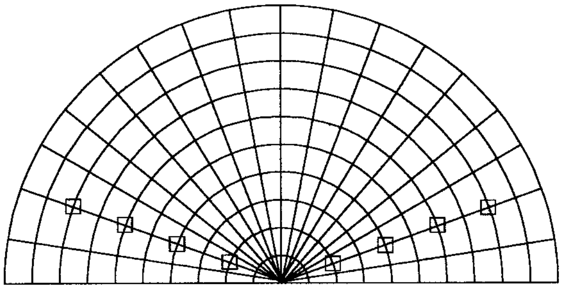

(*b*) Type 2

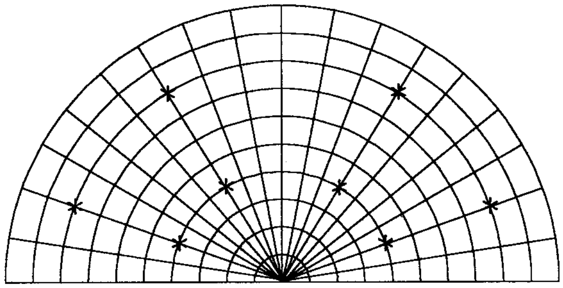

(*c*) Type 3

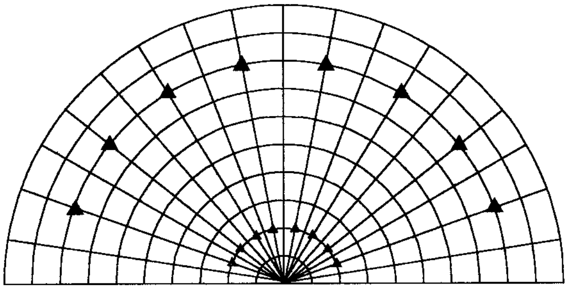

(*d*) Type 4

Fig. 2 Detail geometry and computational grid of a half domain of the cylinder with four types of measuring locations: (*a*) Type 1; (*b*) Type 2; (*c*) Type 3; and (*d*) Type 4

3 Numerical Method

3.1 The Direct Problem. The finite-difference method is employed in the analysis process. After discretization, the governing equation, Eq. (1), and the boundary conditions, Eqs. (2*a*)–(2*d*), can be expressed in the following recursive forms:

$$\frac{1}{(\Delta r)^2}(T_{i+1,j}-2T_{i,j}+T_{i-1,j})+\frac{1}{r_i}\frac{1}{2\Delta r}(T_{i+1,j}-T_{i-1,j})$$

$$+\frac{1}{r_i^2}\frac{1}{(\Delta \theta)^2}(T_{i,j+1}-2T_{i,j}+T_{i,j-1})=0 \tag{3}$$

$$\frac{T_{i,1}-T_{i,0}}{\Delta\theta}=0 \qquad \theta=0 \tag{4a}$$

$$\frac{T_{i,J}-T_{i,J-1}}{\Delta\theta}=0 \qquad \theta=\pi \tag{4b}$$

$$T_{0,j}=T_w \qquad r=0 \tag{4c}$$

$$q_{s,j}=-k_c\frac{T_{s,j}-T_{s-1,j}}{\Delta r}=h_{s,j}(T_{s,j}-T_\infty) \qquad r=R \tag{4d}$$

where Δr and $\Delta\theta$ are the increments in the spatial coordinates, $T_{i,j}$ is the temperature at the grid (i,j), the subscript i is the i^{th} grid along the r coordinate, the subscript j is the j^{th} grid along the θ coordinate, the subscript J represents the grid on the boundary $\theta=\pi$, and the subscript s represents the grid on the cylindrical surface $r=0.05$ m.

In regard to the treatment of the boundary condition, Eq. (4d), the segments used on the boundary are as many as there are nodes. Thus, the values of the heat transfer coefficients $h_{s,j}$ and the temperatures $T_{s,j}$ at different nodes on the boundary are treated as distinct.

Using the recursive forms an equivalent matrix equation for the direct analysis can be expressed as

$$\mathbf{A}_{n\times n}\mathbf{T}_{n\times 1}=\mathbf{D}_{n\times 1} \tag{5}$$

where, matrix **A** is a constant matrix, which is constructed from the thermal properties and the spatial coordinates. The components of vector **T** are the temperatures at discrete points, and the components of matrix **D** are the function of the boundary conditions. The direct analysis is to determine the temperatures at the nodes when all the boundary conditions and thermal properties are known. The direct problem expressed in Eq. (5) can then be solved using the Gauss elimination method.

In this study, the temperature data obtained from the direct problem is used to simulate the measurements of the interior points of the cylinder in the inverse problem, and the local heat transfer coefficient $h(\theta)$ required to solve the direct problem is given in the work of Giedt [14].

3.2 The Inverse Problem. This inverse problem is to identify the unknown thermal boundary behavior from the temperature measurements taken within the cylinder. By substituting Eqs. (4a)–(4d) into Eq. (3) and rearranging the recursive forms consisting of the governing equation and the boundary conditions, we have a linear inverse model that can be expressed as:

$$\mathbf{A}_{n\times n}\mathbf{T}_{n\times 1}=\mathbf{B}_{n\times m}\mathbf{C}_{m\times 1} \tag{6}$$

For the inverse model, matrix **A** can be constructed according to numerical methods and the known physical models, that is, the governing equation. Vector **T** is composed of the temperatures measured at several different locations within the cylinder by the thermocouples. **B** is the coefficient matrix of **C**, and **C** is the vector of the unknown boundary conditions, such as the temperature of the hot wire, the Nusselt numbers, heat flux and temperatures at discrete grid points on the cylindrical surface.

The purpose of this research is to propose an approach to replace the nonlinear least-squares methods [15–17] so that the iterative calculations in the analysis and optimization phases can be eliminated in the inverse heat conduction problems. In the proposed method, the linear inverse model, Eq. (6), is constructed to represent the undetermined thermal boundary conditions explicitly. Note that in the process of constructing the linear inverse model, no explicit functional form is assumed for the undetermined thermal quantities. In other words, the inverse analysis involves the determination of unknown thermal boundary conditions at discrete grid points with no prior knowledge of the functional form of these unknown quantities. Finally, the measurements are substituted into the inverse model. As a result, the inverse model becomes a linear combination of the unknown thermal boundary conditions, and the inverse problems in Eq. (6) can then be solved through the linear least-squares-error method.

Assuming that the estimated conditions of $\mathbf{C}_{\text{estimated}}$ can be obtained by means of the given estimated temperature $\mathbf{T}_{\text{estimated}}$, that is,

$$\mathbf{A}\mathbf{T}_{\text{estimated}}=\mathbf{B}\mathbf{C}_{\text{estimated}} \tag{7a}$$

$$\mathbf{T}_{\text{estimated}}=\mathbf{A}^{-1}\mathbf{B}\mathbf{C}_{\text{estimated}}=\mathbf{E}\mathbf{C}_{\text{estimated}} \tag{7b}$$

where, $\mathbf{E}=\mathbf{A}^{-1}\mathbf{B}$.

Comparing the estimated temperature $\mathbf{T}_{\text{estimated}}$ with the measured temperature $\mathbf{T}_{\text{measured}}$, the error function **F** can be represented as

$$\mathbf{F}=(\mathbf{T}_{\text{estimated}}-\mathbf{T}_{\text{measured}})^T(\mathbf{T}_{\text{estimated}}-\mathbf{T}_{\text{measured}}) \tag{8}$$

Substituting Eq. (7b) into Eq. (8), we can rewrite the error function **F** as the following matrix equation:

$$\begin{aligned}\mathbf{F}&=(\mathbf{E}\mathbf{C}_{\text{estimated}}-\mathbf{T}_{\text{measured}})^T(\mathbf{E}\mathbf{C}_{\text{estimated}}-\mathbf{T}_{\text{measured}})\\&=(\mathbf{C}^T_{\text{estimated}}\mathbf{E}^T-\mathbf{T}^T_{\text{measured}})(\mathbf{E}\mathbf{C}_{\text{estimated}}-\mathbf{T}_{\text{measured}})\\&=\mathbf{C}^T_{\text{estimated}}\mathbf{E}^T\mathbf{E}\mathbf{C}_{\text{estimated}}-\mathbf{T}^T_{\text{measured}}\mathbf{E}\mathbf{C}_{\text{estimated}}\\&\quad-\mathbf{C}^T_{\text{estimated}}\mathbf{E}^T\mathbf{T}_{\text{measured}}+\mathbf{T}^T_{\text{measured}}\mathbf{T}_{\text{measured}}\end{aligned} \tag{9}$$

Then, the error function **F** can be minimized by differentiating **F** with respect to $\mathbf{C}_{\text{estimated}}$ as

$$\frac{\partial\mathbf{F}}{\partial\mathbf{C}_{\text{estimated}}}=0 \tag{10}$$

Inserting Eq. (9) into Eq. (10), we have the following:

$$\mathbf{E}^T\mathbf{E}\mathbf{C}_{\text{estimated}}+\mathbf{E}^T\mathbf{E}\mathbf{C}_{\text{estimated}}-\mathbf{E}^T\mathbf{T}_{\text{measured}}-\mathbf{E}^T\mathbf{T}_{\text{measured}}=0$$

$$\mathbf{E}^T\mathbf{E}\mathbf{C}_{\text{estimated}}=\mathbf{E}^T\mathbf{T}_{\text{measured}} \tag{11}$$

Thus, vector $\mathbf{C}_{\text{estimated}}$ can then be solved as follows:

$$\mathbf{C}_{\text{estimated}}=(\mathbf{E}^T\mathbf{E})^{-1}\mathbf{E}^T\mathbf{T}_{\text{measured}}=\mathbf{R}\mathbf{T}_{\text{measured}} \tag{12}$$

where, $(\mathbf{E}^T\mathbf{E})^{-1}\mathbf{E}^T$ is the reverse matrix of the inverse problem and is denoted by $\mathbf{R}_{m\times n}$. The expressed process is derived by the linear least-squares-error method.

By estimating vector **C**, the thermal boundary behavior such as the temperatures of the surface and the hot wire, the local Nusselt numbers $\text{Nu}(\theta)$ and the local heat flux $q(\theta)$ on the cylindrical surface can be obtained simultaneously.

In Eq. (12), the inverse problem is solved by the linear least-squares-error method. As such, a special feature of this approach is that the iteration in the calculating process can be avoided, and the problem can be solved in a linear domain. Furthermore, it can be verified that the final solution, that is, Eq. (12), from the proposed method is the necessary condition of the optimum from the traditional nonlinear least-squares approach [18].

In the inverse problem, it is important to investigate the stability of the estimation. Usually, a small measurement error will induce a large estimated error in the ill-posed inverse problem. The methods of future time and regularization have been widely used to stabilize the results of the inverse estimation [8,11]. Those methods impose the physical condition onto the problem and increase the computational load in the estimated process. Consequently, the stability of the problem can be increased, while the computational load of the problem is also increased. In the present research, it is possible to stabilize the estimated results through a smoothing process [19]. This method computes a moving average of the estimation. The result of data is the average of the N-point around the current point. In this process, N must be an odd number. Then, the stability of the estimation can be increased.

In most cases, not all of the points need to be measured. The realistic experimental approach is to measure only a few points in the problems. Therefore, in Eq. (12), only parts of matrix $\mathbf{R}_{m\times n}$ and vector $\mathbf{T}_{n\times 1}$ corresponding to the measurement locations need to be constructed to estimate the unknown boundary conditions of the inverse problem. Consequently, the sizes of matrix $\mathbf{R}_{m\times n}$ and vector $\mathbf{T}_{n\times 1}$ will reduce to $\mathbf{R}_{m\times n'}$ and $\mathbf{T}_{n'\times 1}$ respectively, where $n'<n$ and that the number $(n)'$ of elements of vector $\mathbf{T}_{n'\times 1}$ is equal to the number $(n)'$ of measurements we have taken. In other words, the size of matrix $\mathbf{R}_{m\times n'}$ will vary with the size of vector $\mathbf{T}_{n'\times 1}$, that is, the order of the matrices is affected by the number of discrete measurements. However, in solving Eq. (12), the number of measurements needs to be sufficient so that the rank of the reverse matrix $\mathbf{R}$ is equal to the number of undetermined elements of vector $\mathbf{C}$. Otherwise, Eq. (12) will be underdetermined, and the problem cannot be solved through the proposed method. In general, when a large number of the measurements are selected, the costs for computation and experiment increase. However, the accuracy of the estimated results increases as well.

According to the described derivation, it is possible to identify the existence and uniqueness of the solution. The method by which to identify the properties of the solutions is based on the theory of linear algebra. If the rank of reverse matrix $\mathbf{R}$ is less than the number of undetermined elements of vector $\mathbf{C}$, the number of measurements needs to be increased. Furthermore, if the rank of the reverse matrix $\mathbf{R}$ is equal to the number of undetermined elements of vector $\mathbf{C}$, the perpendicular distance from vector $\mathbf{C}$ to the column space of matrix $\mathbf{E}$ needs to be checked. If the distance vanishes and the matrix equation, Eq. (12), is consistent (i.e., the measurement errors are not considered), the solution exists and is unique. If the matrix equation is inconsistent, a unique least-squares solution can be approximated [20].

4 Results and Discussion

This paper analyzes the IHCP of the cylinder normal to a turbulent air stream. Using the direct method mentioned previously combined with the boundary conditions given by Giedt [14], the Reynolds number effects on the isothermal patterns are studied, as shown in Fig. 3. Because the hot wire is imbedded in the center of the cylinder, the heat emission from the cylindrical surface is totally caused by the forced convection of air stream. Results show that the isothermal lines near the center of the cylinder $(r=0)$ are closer than those which are far from the center. It can also be seen in Fig. 3 that the temperature gradient tends to increase with increasing Reynolds number of the air stream.

To discuss the correlation between the measuring locations and the accuracy of the results, we take four types of measuring locations, as marked in Fig. 2, in the present example. The sensors of thermocouples are located at the marked grid points, and the temperature data at these points are obtained from Fig. 3, which are calculated by the direct method, to simulate the measurements. The simulated temperature measurements used in the inverse problem are considered to include measurement errors. In other words, the random errors of simulated measurements are added to the exact temperatures computed from the solutions of the direct problem. Thus, the measured temperature $\mathbf{T}_{\text{measured}}$ can be expressed as

$$\mathbf{T}_{\text{measured}}=\mathbf{T}_{\text{exact}}(1+\omega\sigma) \tag{13}$$

where, $\mathbf{T}_{\text{exact}}$ is the exact temperature, ω is the random variable generated by subroutine DRNNOR of the IMSL [21], and σ is the standard deviation of the measurement error. For normally distributed random errors, the probability of a random value, ω, lying in the range $-2.576<\omega<2.576$ is 99 percent [22].

Figure 4 shows the hot wire temperatures obtained by the inverse matrix method for Re=140,000, 170,000, and 219,000. Results show that even the measurement error ($\sigma=5$ percent) is considered, the actual hot wire temperature can be predicted precisely by the proposed inverse method.

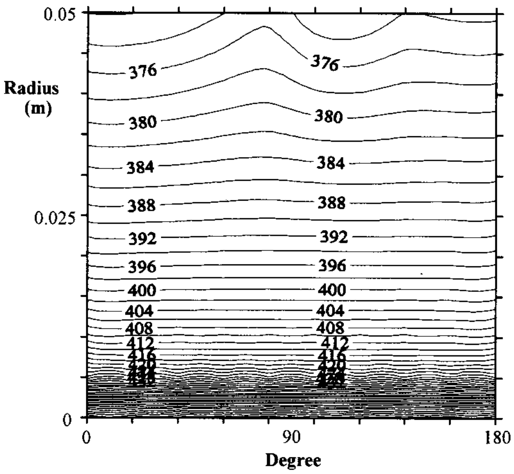

(a) Re=140000

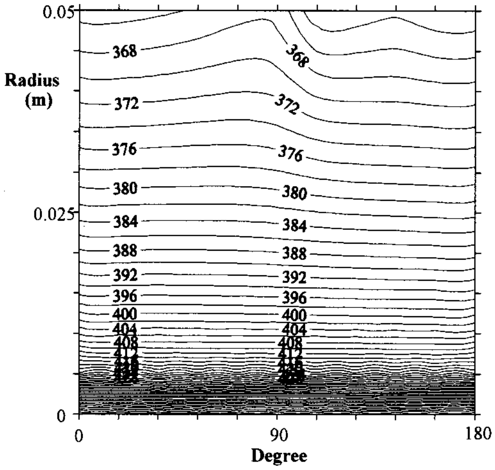

(b) Re=170000

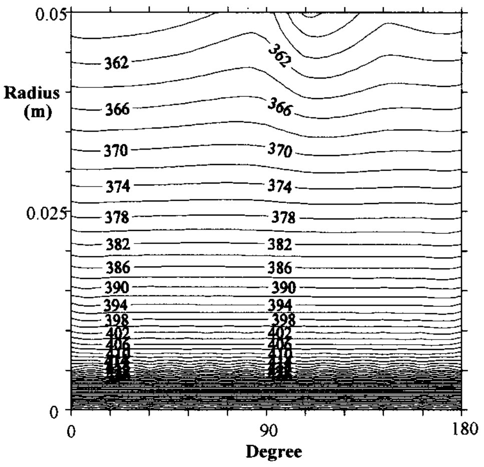

(c) Re=219000

Fig. 3 The isothermal patterns inside the heated cylinder: (*a*) Re=140,000; (*b*) Re=170,000; and (*c*) Re=219,000

Figure 5 illustrates the estimated results of the surface temperature $T(\theta)$ when the measurement error is not considered $(\sigma=0)$. From Fig. 5, we can see that the estimated results are in

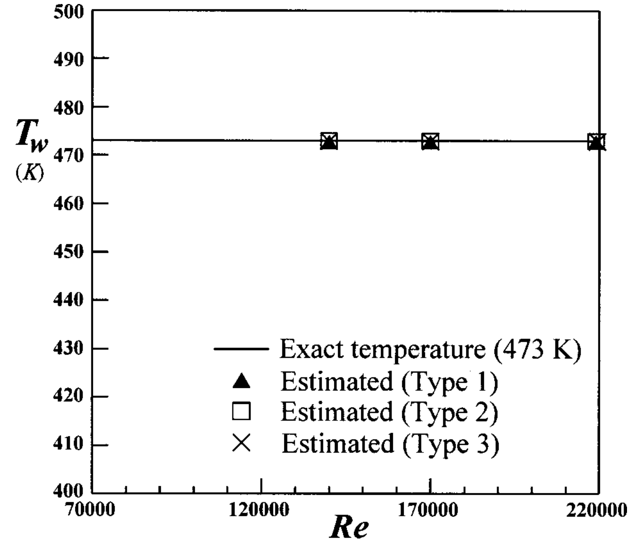

Fig. 4 The estimated hot wire temperature for different values of Reynolds number with the measurement error $\sigma = 5$ percent is considered and different types of measuring locations and adopted

very good agreement with the exact temperatures regardless of whether the type of measuring locations is Type 1, Type 2, or Type 3. With increasing Reynolds number of the air stream, the laminar boundary layer of the cylinder undergoes a transition to a turbulent boundary layer. When transition occurs, the point of separation is suddenly set back to a position farther on the downstream surface of the cylinder because of the interaction between the inertia force in the flow field, the inverse pressure gradient and the viscous effect on the cylinder surface. However, the location where the separation occurs depends upon the value of Reynolds number. Results show that the distributions of temperature along the cylinder surface are strongly influenced by the effects of the stagnation point, the transition from laminar to turbulent flow, the separation point and the tail vortexes behind the cylinder. As θ is increased from the forward stagnation point ($\theta = 0$ deg), the effect of heat transfer along the surface becomes weaker because of the developing of the laminar boundary layer. Thus, the surface temperature increases from the forward stagnation point, reaching a maximum and then reducing gradually at the transition region. It is due to the fact that the capability of heat transfer becomes better during the transition from laminar to turbulent flow. After this region, as a result of the effect of flow separation, the effect of heat transfer is weak again and the temperature increases. Then, the temperature decreases slightly at the region of tail vortexes behind the cylinder with the superior property of heat transfer.

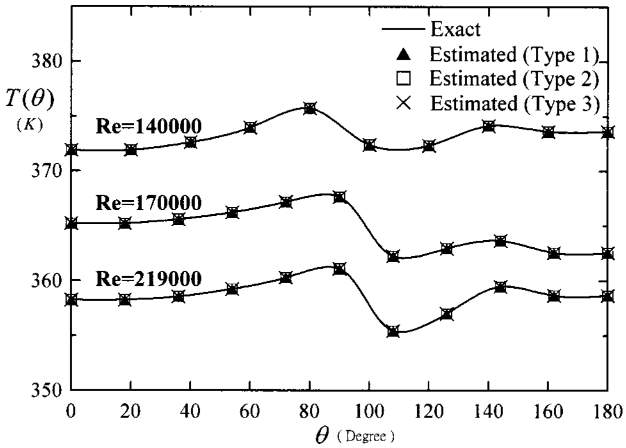

Fig. 5 The estimated surface temperature for different types of measuring locations without considering measurement error ($\sigma = 0$)

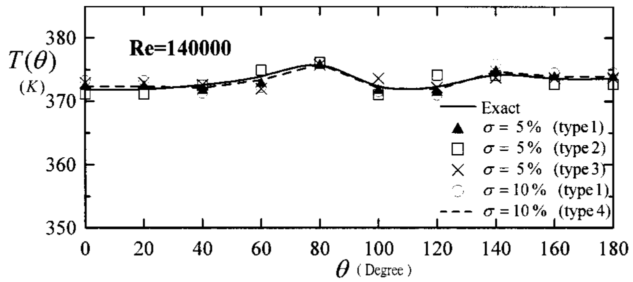

(*a*) Re = 140000

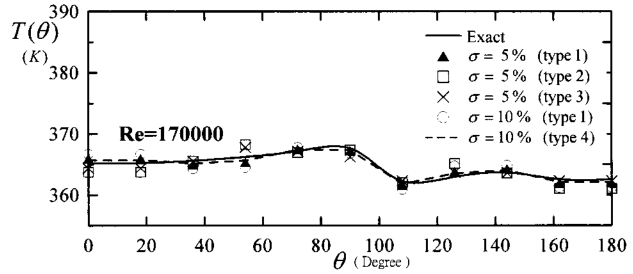

(*b*) Re = 170000

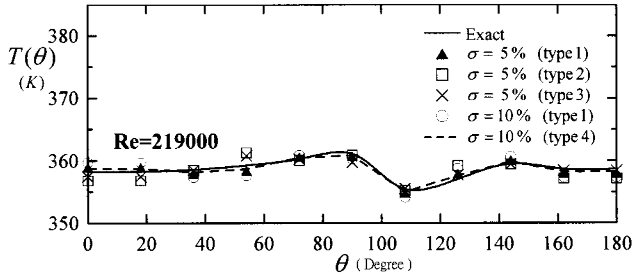

(*c*) Re = 219000

Fig. 6 The estimated surface temperature for different types of measuring locations with measurement errors $\sigma = 5$ percent and $\sigma = 10$ percent are considered: (*a*) Re=140,000; (*b*) Re =170,000; and (*c*) Re=219,000

With considering the measurement errors, the estimated and exact surface temperatures for Re=140,000, 170,000 and 219,000 with different types of measuring locations are shown in Fig. 6 for comparison. It is obvious that the estimated surface temperatures, with measurement error ($\sigma = 5$ percent), are in good agreement with the exact profiles when the measuring location, Type 1, is taken. However, when measuring locations Type 2 and Type 3 are adopted, slight discrepancies between the estimated and exact temperatures are generated. But the results are still satisfactory. It implies that for more accurate estimation of surface conditions, the locations of the sensors are preferred closer to the cylindrical surface. In IHCP, the precision of the estimations depends strongly on the accuracy of the measurements. As will be seen in the figures for the measuring locations Type 1, although the estimated values are good approximations whether measurement error $\sigma = 5$ percent or $\sigma = 10$ percent is adopted, the estimated solutions with measurement error $\sigma = 5$ percent are still more precise than the solutions with measurement error $\sigma = 10$ percent. In other words, it is clear that large measurement errors make the estimated results deviate from the exact values in the inverse analysis. Furthermore, the effect of the number of points at which

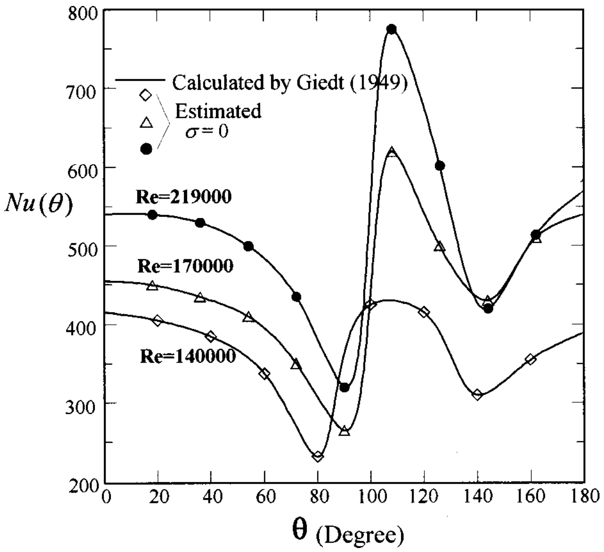

Fig. 7 The estimated distribution of local Nusselt number along the heated cylinder surface without measurement error ($\sigma=0$)

the temperature is measured on the accuracy of the results is also important. Figure 6 reveal that the estimated results with measuring location Type 1 (eight measuring points) are less accurate than those with measuring location Type 4 (sixteen measuring points) when measurement error $\sigma=10$ percent is considered. Briefly, from the figures we see that greater measurement error requires more measuring points to increase the accuracy of the inverse solutions.

When the measuring location Type 1 is adopted without considering measurement errors ($\sigma=0$), the estimated values of local Nusselt numbers Nu(θ) and local heat flux $q(\theta)$ along the heated cylindrical surface obtained from the inverse method are plotted against θ in Fig. 7 and Fig. 8 respectively for the different values of Reynolds number. Figure 7 shows a comparison of the estimated distributions of local Nusselt numbers via the proposed method with those calculated by Giedt [14]. It reveals that the estimated and calculated local Nusselt numbers are in a very good agreement. Furthermore, Fig. 7 and Fig. 8 illustrate that the estimated distributions of local heat flux are approximative to the distributions of local Nusselt numbers. It is in virtue of the fact that the quantities of heat flux are greatly influenced by the values of Nusselt numbers, which are related to the capabilities of heat transfer. From the figures, it has been found that the values of local Nusselt numbers Nu(θ) and local heat flux $q(\theta)$ for a cylinder losing heat to a normal air stream depend on the Reynolds number of the flow and on the location along the cylinder circumference. The heat transfer rate increases with increasing Reynolds number. The estimated local Nusselt numbers and local heat flux show a maximum between $\theta=100$ deg and $\theta=120$ deg, which is attributed to the high heat transfer rate at the transition region. In addition, there are two distinct minimum values of Nu(θ) and $q(\theta)$ occur. The lower of the two is between $\theta=80$ deg and $\theta=93$ deg on the front half of the cylinder since the effect of heat transfer is weak here during the developing of the laminar boundary layer. The location of this minimum moves back along the

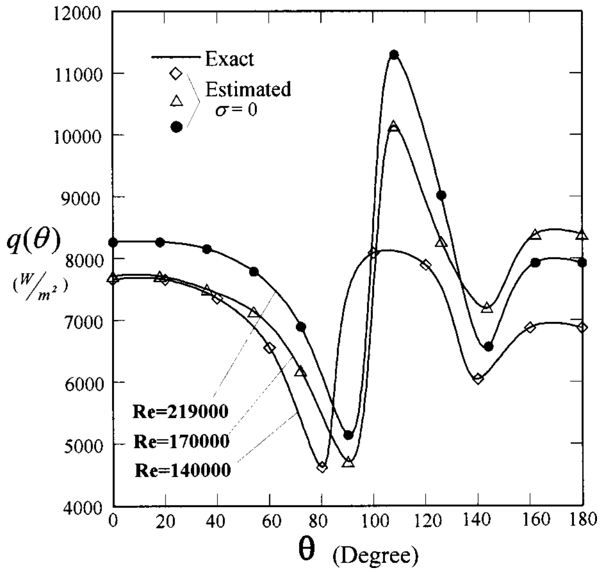

Fig. 8 The estimated distribution of local heat flux along the heated cylinder surface without measurement error ($\sigma=0$)

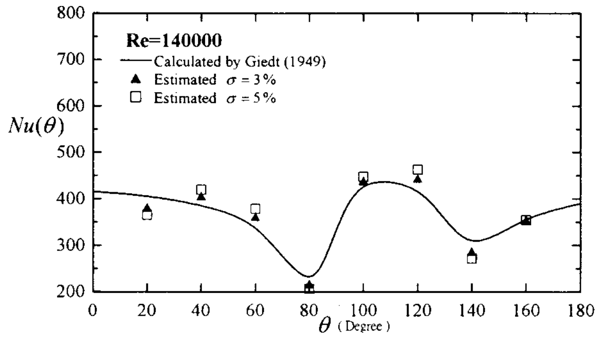

(a) Re = 140000

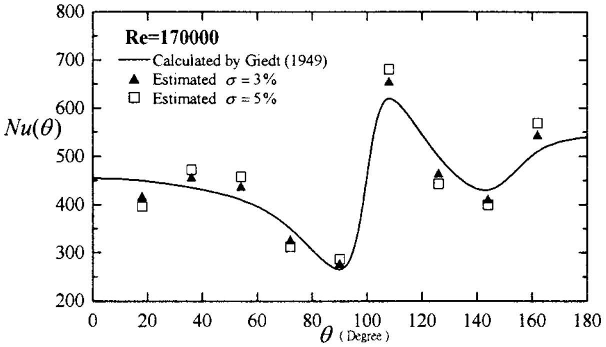

(b) Re = 170000

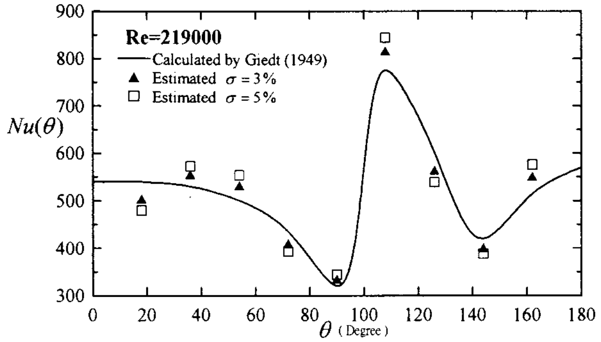

(c) Re = 219000

Fig. 9 The estimated distribution of local Nusselt number along the heated cylinder surface with measurement errors ($\sigma=3$ percent and $\sigma=5$): (a) Re=140,000; (b) Re=170,000; and (c) Re=219,000

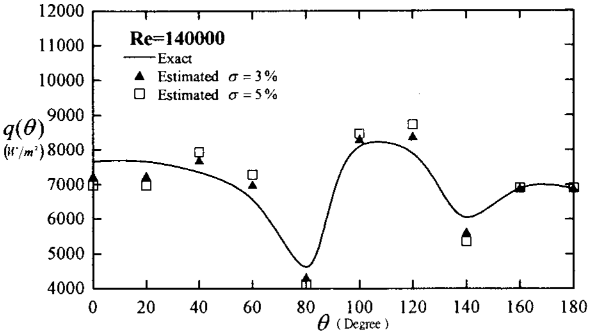

(*a*) Re = 140000

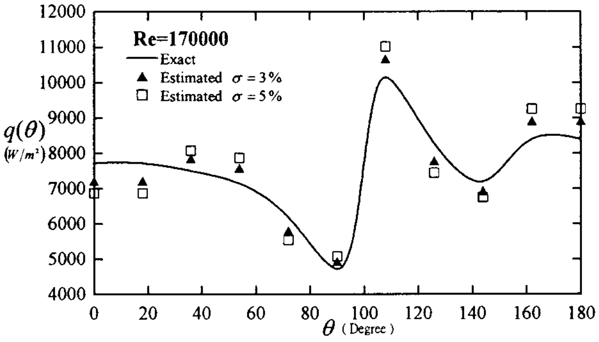

(*b*) Re = 170000

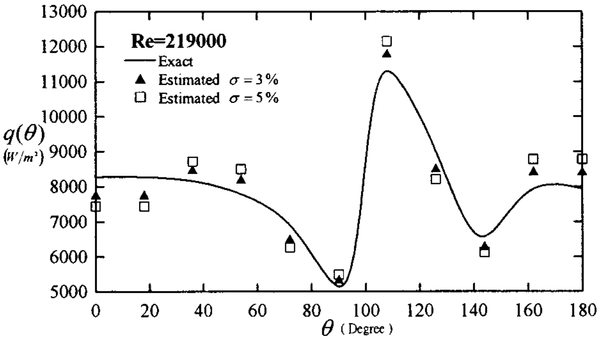

(*c*) Re = 219000

Fig. 10 The estimated distribution of local heat flux along the heated cylinder surface with measurement errors ($\sigma = 3$ percent and $\sigma = 5$): (*a*) Re=140,000; (*b*) Re=170,000; and (*c*) Re=219,000

cylinder circumference with increasing Reynolds number. Moreover, the second of the two minimum values is between $\theta = 140$ deg and $\theta = 150$ deg on the back half of the cylinder. The minimum value is due to the low heat transfer rate at this region, which is verified by the fact that at this region ($\theta = 140$ deg ~ 150 deg) the flow separated from the surface of the cylinder. After the separation point, the values of Nu(θ) and $q(\theta)$ increase at the rear of the cylinder ($\theta = 150 \sim 80$ deg) owing to the mixing effect caused by flow vortexes.

The estimated distributions of local Nusselt number Nu(θ) with measurement errors $\sigma = 3$ percent and $\sigma = 5$ percent for $Re = 140{,}000$, 170,000, and 219,000 are shown in Fig. 9 for comparison, when the measuring location Type 1 is adopted. The results show that the estimated distributions with measurement error $\sigma = 3$ percent have good agreement with the results of Giedt [14]. However, the estimated values are still good approximations even when measurement error $\sigma = 5$ percent is adopted. It indicates that the proposed method can predict this phenomenon effectively.

In Fig. 10, when the measuring location Type 1 is adopted, a comparison between the estimated local heat flux $q(\theta)$ and the exact ones for various values of Re=140,000, 170,000, and 219,000 are shown with considering and measurement errors $\sigma = 3$ percent and $\sigma = 5$ percent. It demonstrates that an increase of Reynolds number increases the heat flux on the heated cylindrical surface. Further, it is also obvious that the estimated results are accurate and robust when measurement error $\sigma = 3$ percent is included. When measurement error is $\sigma = 5$ percent, the results are still satisfactory. Consequently, as shown in the figures, the proposed method is applicable and effective to deal with the IHCP in this study.

5 Conclusions

An inverse method has been successfully introduced for estimating the unknown boundary conditions such as the surface thermal behavior of the cylinder and the temperature of the hot wire imbedded in the center of the cylinder. Using the reverse matrix, the proposed inverse model is reconstructed from the available temperature measurements and the discrete forms of the differential heat conduction equation. This inverse model can represent the unknown conditions explicitly. The results can be solved without iteration by a linear least-squares-error method. Furthermore, the special feature of the proposed method is that the uniqueness of the solution can be easily identified. The present study of the heated cylinder normal to a turbulent air stream has been used to evaluate the accuracy and the robustness of the proposed method. From the results, it appears that by using the proposed method, without measurement error, the exact solution can be found even with only a few measuring points. When measurement errors are considered, more measuring points at locations inside the cylinder are needed in order to enhance stability and accuracy. In addition, results also show that this method is robust no matter the thermocouples are distributed in the radial or angular direction.

In contrast to the traditional approach, this proposed inverse analytic method requires no prior information on the functional form of the unknown quantities, no initial guesses, and no iterations in the calculating process. Furthermore, the advantage of this method is that the unknown quantities of the thermal boundary behavior can be estimated directly and the inverse problem can be solved in a linear domain. It is different from the traditional method using nonlinear least-squares formulation, which requires numerous iterations in the process and needs to perform its calculation in the nonlinear domain. This implies that the present model offers a great deal of flexibility. Through the proposed method, the center and surface thermal behavior can be obtained merely by the inexpensive measurement such as infrared measuring devices or thermocouples. Thus, expensive sensors for the direct measurement are not needed any more and the difficulties encountered in the measuring processes can be avoided. Consequently, the results show that the proposed method is an accurate, robust and efficient inverse technique. It is evident that the proposed inverse method in this study has the potential to be implemented in the field of two-dimensional inverse heat conduction problems.

Acknowledgments

We would like to thank the National Science Council of the Republic of China for supporting this work under contract no. NSC-87-2218-E-006-013.

Nomenclature

$\mathbf{A}$ = constant matrix constructed from thermal properties and spatial coordinates
$\mathbf{B}$ = coefficient matrix of $\mathbf{C}$
$\mathbf{C}$ = vector constructed from the unknown boundary conditions
$\mathbf{D}$ = matrix constructed from the functions of the boundary conditions

$\mathbf{E}$ = product of $\mathbf{A}^{-1}$ and $\mathbf{B}$
$\mathbf{F}$ = error function
$h(\theta)$ = function of the unknown local heat transfer coefficients
k = thermal conductivity
$\mathrm{Nu}(\theta)$ = function of the unknown local Nusselt numbers
$q(\theta)$ = function of the unknown local heat flux
$\mathbf{R}$ = reverse matrix
R = radius of the cylinder
(r,θ) = cylindrical coordinate
T = temperature
$T(\theta)$ = function of the unknown surface temperature
$T(r,\theta)$ = temperature at each grid point (r,θ)
$\mathbf{T}$ = temperature vector
U = velocity

Greek Symbols

Δr = increment of radial coordinate
$\Delta \theta$ = increment of angular coordinate
ω = random variable
σ = standard deviation of the measurement error

Subscripts

c = cylinder
estimated = estimated data
exact = exact data
i = index of radial coordinate
j = index of angular coordinate
J = index of angular coordinate at boundary
measured = measured data
s = surface
w = hot wire
∞ = uniform air stream

References

[1] Tseng, A. A., Lin, F. H., Gunderia, A. S., and Ni, D. S., 1989, ‘‘Roll Cooling and Its Relationship to Roll Life,’’ Metall. Trans. A, **20**(11), pp. 2305–2320.
[2] Stolz, Jr., G., 1960, ‘‘Numerical Solutions to an Inverse Problem of Heat Conduction for Simple Shapes,’’ ASME J. Heat Transfer, **82**, pp. 20–26.
[3] Bass, B. R., 1980, ‘‘Application of the Finite Element Method to the Nonlinear Inverse Heat Conduction Problem Using Beck’s Second Method,’’ ASME J. Eng. Ind., **102**(2), pp. 168–176.
[4] Beck, J. V., Litkouhi, B., and St. Clair, C. R., 1982, ‘‘Efficient Sequential Solution of Nonlinear Inverse Heat Conduction Problem,’’ Numer. Heat Transfer, **5**(3), pp. 275–286.
[5] Jarny, Y., Ozisik, M. N., and Bardon, J. P., 1991, ‘‘General Optimization Method Using Adjoint Equation for Solving Multidimensional Inverse Heat Conduction,’’ Int. J. Heat Mass Transf., **34**(11), pp. 2911–2919.
[6] Hsu, T. R., Sun, N. S., Chen, G. G., and Gong, Z. L., 1992, ‘‘Finite Element Formulation for Two-Dimensional Inverse Heat Conduction Analysis,’’ ASME J. Heat Transfer, **114**, pp. 553–557.
[7] Yang, Y. T., Hsu, P. T., and Chen, C. K., 1997, ‘‘A Three-Dimensional Inverse Heat Conduction Problem Approach for Estimating the Heat Flux and Surface Temperature of a Hollow Cylinder,’’ J. Appl. Phys., J. Phys. D, **30**, pp. 1326–1333.
[8] Beck, J. V., Blackwell, B., and St. Clair, C. R., 1985, *Inverse Heat Conduction—Ill-Posed Problem*, Wiley, New York.
[9] Morozov, V. A., and Stressin, M., 1993, *Regularization Method for Ill-Posed Problems*, CRC Press, Boca Raton, FL.
[10] Murio, D. A., 1993, *The Mollification Method and the Numerical Solution of Ill-Posed Problems*, Wiley, New York.
[11] Tikhnov, A. N., and Arsenin, V. Y., 1997, *Solution of Ill-Posed Problems*, Winston and Sons, Washington, D.C.
[12] Lin, J. H., Chen, C. K., and Yang, Y. T., 2001, ‘‘Inverse Method for Estimating Thermal Conductivity in One-Dimensional Heat Conduction Problems,’’ AIAA Journal of Thermophysics and Heat Transfer, **15**(1), pp. 34–41.
[13] Yang, C. Y., and Chen, C. K., 1996, ‘‘The Boundary Estimation in Two-Dimensional Inverse Heat Conduction Problems,’’ J. Appl. Phys., J. Phys. D, **29**(2), pp. 333–339.
[14] Giedt, W. H., 1949, ‘‘Investigation of Variation of Point Unit-Heat-Transfer Coefficient Around a Cylinder Normal to an Air Stream,’’ Trans. ASME, **71**, pp. 375–381.
[15] Kalman, R. E., 1960, ‘‘A New Approach to Linear Filtering and Prediction Problems,’’ *Trans. ASME*, **82D**, pp. 35–45.
[16] Pfahl, Jr., R. C., 1966, ‘‘Nonlinear Least-Squares: A Method for Simultaneous Thermal Property Determination in Ablating Polymeric Materials,’’ J. Appl. Polym. Sci., **10**(8), pp. 1111–1119.
[17] Sorenson, H. W., 1980, Parameter Estimation: Principles and Problems, Marcel Dekker, New York.
[18] Yang, C. Y., 1997, ‘‘Noniterative Solution of Inverse Heat Conduction Problems in One Dimension,’’ Communications in Numerical Methods in Engineering, **13**(6), pp. 419–427.
[19] *KaleidaGraph Reference Guide Version 3.05*, 1994, Abelbeck Software, pp. 174.
[20] Friedberg, S. H., Insel, A. J., and Spence L. E., 1992, *Linear Algebra*, 2nd ed, Prentice Hall, Singapore, pp. 147–167.
[21] IMSL User’s Manual, 1985, Math Library Version 1.0, IMSL Library Edition 10.0, IMSL, Houston, TX.
[22] Silva Neto, A. J., and Ozisik, M. N., 1993, ‘‘Inverse Problem of Simultaneously Estimating the Timewise Varying Strength of Two-Plane Heat Source,’’ J. Appl. Phys., **73**, pp. 2132–2137.

Fang Yan

Bakhtier Farouk
e-mail: bfarouk@coe.drexel.edu

Department of Mechanical Engineering
and Mechanics,
Drexel University,
Philadelphia, PA 19104

Computations of Low Pressure Fluid Flow and Heat Transfer in Ducts Using the Direct Simulation Monte Carlo Method

High Knudsen number (Kn) gas flows are found in vacuum and micro-scale systems. Such flows are usually in the slip or transition regimes. In this paper, the direct simulation Monte Carlo (DSMC) method has been applied to compute low pressure, high Kn flow fields in partially heated channels. Computations were carried out for nitrogen, argon, hydrogen, oxygen and noble gas mixtures. Variation of the Kn is obtained by reducing the pressure while keeping the channel width constant. Nonlinear pressure profiles along the channel centerline are observed. Heat transfer from the channel walls is also calculated and compared with the classical Graetz solution. The effects of varying pressure, inlet flow and gas transport properties (Kn, Reynolds number, Re and the Prandtl number, Pr respectively) on the wall heat transfer (Nusselt number, Nu) were examined. A simplified correlation for predicting $\overline{Nu}$ as a function of the Peclet number, $\overline{Pe}$ and $\overline{Kn}$ is presented. [DOI: 10.1115/1.1458018]

Introduction

Heat transfer in developing flows in channels and tubes has been intensely studied in the past [1] due to their practical use as well as their theoretical importance. In the combined entrance region, simultaneous development of the hydrodynamic and thermal boundary layers have to be considered. Most of the past studies considered continuum formulations, which is valid for low Knudsen numbers, Kn$<$0.01. Due to a variety of novel applications viz. micro-electromechanical systems (MEMS), low-pressure chemical vapor deposition (CVD) reactors, etc., the transport problem in the non-continuum (Kn$>$0.01) regime has generated renewed interests in the above problem [2,3]. There are two distinct classes of high Knudsen number non-continuum flow problems—one due to micro length-scale and the other due to large mean free path (very low pressure) of the gas molecules. Both classes of problems offer unique challenges in obtaining their solutions. Though approximate techniques have been attempted, particle methods such as molecular dynamics (MD), particle-in-cell (PIC) and the direct simulation Monte Carlo (DSMC) are attractive tools for the study of such flows.

Traditional continuum computational fluid dynamic (CFD) techniques are often invalid for analyzing flows in MEMS or in low-pressure devices. This inaccuracy stems from their calculation of molecular transport effects such as viscous dissipation and thermal conduction from bulk flow quantities such as mean velocity and temperature. This approximation of continuum phenomena fails as the characteristic length of the flow gradients (L) approaches the average distance traveled by molecules between collisions (mean free path, λ). The Knudsen domain ($0<\mathrm{Kn}<\infty$) is often divided into four regimes. When Kn$<$0.01, the flow is considered to be continuum; for 0.01$<$Kn$<$0.1, it is in the slip-flow regime, for 0.1$<$Kn$<$3, it is called the transition-flow regime. When Kn$>$3, the flow is considered to be free molecular and is sufficiently rarefied to allow molecular collisions to be completely neglected in analysis. The collisionless Boltzmann equation is therefore applicable for such flows. Though approximate techniques have been attempted, the kinetic theory approach makes sense for the low-pressure problems as found in low-pressure CVD reactors.

The direct simulation Monte Carlo (DSMC) method is a well-established approach that has been used widely and successfully to simulate high Kn number gas flow problems [4]. Several numerical studies using the DSMC method [2,5–7] have been reported. In this paper, we investigate the fluid flow and heat transfer for high Kn in a partially heated duct using DSMC. The objective of the simulation is to study the effect of Kn, Re, and Pr on heat transfer from the heated walls under the rarefied flow conditions. Specifically, subsonic pressure-driven flows are considered. The predicted heat flux results are compared with the Graetz solution with uniform flow inlet. A large number of cases are calculated with varying inlet Kn, Re, and Pr from the slip-flow regime to the transition-flow regime. Based upon these simulations, a simple correlation connecting $\overline{\mathrm{Nu}}$ with $\overline{\mathrm{Pe}}$ and $\overline{\mathrm{Kn}}$ is developed.

Problem Description

We consider rarefied subsonic gas flows between parallel plates (60 cm long and 10 cm apart) as shown in Fig. 1. Molecules come in from the left side and go out through the right side. A portion of the plates (20 cm) at the entrance region is unheated, so that the flow can develop. In the next portion, the walls are heated and held at constant temperature. Also, this configuration resembles that of the classical Graetz problem. The flow fields are computed for specified values of pressure at the inlet and the outlet. The inlet velocity is determined according to the information from the calculated domain rather than being specified. The inlet temperature is 300 K for all cases. The temperature of the heated walls is held at 600 K.

Computations were carried out for nitrogen, argon, hydrogen, oxygen and noble gas mixture flows. Results were obtained for a relatively wide range of $\overline{\mathrm{Re}}$, $\overline{\mathrm{Kn}}$, and $\overline{\mathrm{Pr}}$. It is interesting to note here that for the highly rarefied conditions and the non-isothermal flow fields considered, the parameters, Kn, and Re vary substantially along the flow directions. For reporting the results, we con sider axially averaged values, $\overline{\mathrm{Re}}$, and $\overline{\mathrm{Kn}}$. The values of Pr (for the cases reported here) do not vary appreciably along the length of channels.

Contributed by the Heat Transfer Division for publication in the JOURNAL OF HEAT TRANSFER. Manuscript received by the Heat Transfer Division August 12, 1999; revision received April 25, 2001. Associate Editor: R. L. Mahajan.

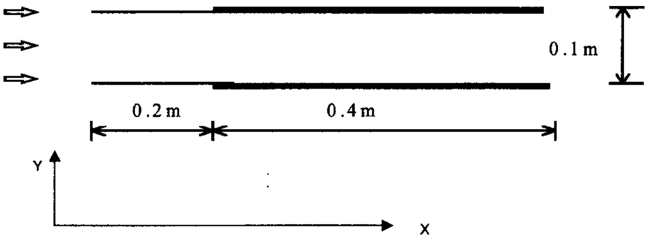

Fig. 1 Schematic of the problem geometry

The thermal boundary conditions were chosen following the Graetz problem [8]. Unlike the Graetz solution, we consider developing flows. However, due to the other similarities, we compared the present heat transfer predictions with those obtained from the Graetz solution with either parabolic and uniform velocity profiles. It has been shown that molecular gas flow characteristics in the channel are essentially the same when inlet Kn is the same and the boundaries are geometrically similar [9]. It means that the characteristic properties of flow are independent of the size of channel if the same inlet Kn and boundary conditions are maintained. We considered a fairly large cross section ($O[10^{-1}]$m) channel but at lower inlet pressures (about 7 Pa) instead of the atmospheric pressure and micron-sized cross sections found in microchannels.

Model Description

The direct simulation Monte Carlo (DSMC) method was used to obtain the density, pressure, velocity and the temperature fields in the channels. The DSMC method retains its validity at high Kn because no continuum assumptions are made. In the DSMC method, a real gas is simulated by thousands or millions of simulated particles. The positions, velocities and initial states of these simulated particles are stored and modified in time in the process of particles moving, colliding among themselves, and interacting with boundaries in the simulated physical space. Each simulated particle represents a very large number of physical molecules. In this fashion, the number of molecular trajectories and molecular collisions that must be calculated is substantially reduced, while the physical velocities, molecular size and internal energies are preserved in the simulation. Further, the DSMC method uncouples the analysis of the molecular motion from that of the molecular collisions by use of a time step smaller than the real physical collision time. Continuous improvement in the efficiency and accuracy of the DSMC method have been accomplished by Bird [4] over the last several decades. His method and some other advanced DSMC techniques have been implemented for the practical analysis of both low pressure flows [10] and MEMS flows [2,5,9]. The well-known DSMC code from Bird [4] with modification on the boundary conditions [11] is used to generate the present results.

In Bird's [4] DSMC procedure, four steps are implemented: cycling the movement of particles, indexing particles into cells, selecting collision pairs, and calculating post-collision properties. The computational domain is divided into a certain number of cells. The physical space is used to facilitate the choice of molecules for collisions and for sampling the macroscopic flow quantities such as pressure, temperature etc. The DSMC method applied to low-pressure fluid flow simulation is intuitively attractive because it is valid for all flow regimes. Generally, in the DSMC framework, the flows with high velocities are much easier to compute than flows with low velocity because of the statistical scatter [4]. In DSMC, the computational time step must be less than the mean collision time. Another condition that must be satisfied during a DSMC procedure is that the smallest dimensions of the computational cells must not be greater than one-third of the mean-free path. In addition, the importance of statistical scatter caused by small perturbation increases as the flow velocity becomes smaller. For the present problem, the thermal speed is approximately 500 m/s. For the flow speeds considered here (10 m/s~100 m/s), the statistical noise is thus significant. However, as the sample sizes from the ensemble or time average increase, the correct result will in principle emerge. The statistical fluctuations decrease with the square root of the sample size. The sample sizes used in the present study is of the order of 10^6. The accuracy of the calculation presented is thus acceptable [4] for the large sample size considered.

Boundary Conditions. Two dimensional subsonic flow simulations (considered in the present study) by the direct simulation Monte Carlo technique in the slip and transitional regimes are rare [3]. One of the difficulties lies in specifying the outlet boundary conditions where particles may move upstream and reenter the flow domain. In hypersonic flows or free molecular flows, we can neglect the particles re-entering from the outlet boundary. In subsonic flows in the transitional regime, we cannot neglect particles, which go out of the boundary and may reenter. Nanbu [3] applied a porous wall at the inlet of a duct to prevent molecules from going upstream. Another difficulty in two dimensional subsonic-flow particle simulations in transitional regime is in controlling the flow velocity inside the domain. If particles do not re-enter from the exit (assuming expansion to vacuum), they are accelerated to the exit and velocities inside the domain do not stay uniform.

In the present calculations, the inlet and outlet boundary conditions were formulated following the procedure outlined by Piekos and Breuer [6,11]. The inlet and outlet pressures are considered to be specified. This pressure drop drives the gas flow through the channel. At the inlet boundary, temperature is kept constant (300 K), and the density is specified (via ideal-gas law) according to the given inlet pressure. The transverse velocity of flow is set to zero. At the outlet, pressure is specified and zero gradient boundary conditions are considered for temperature, transverse velocity and streamwise velocity. Only the number density is calculated according to the given outlet pressure. It has been shown [12] that using mean velocity of inflow and outflow is not accurate enough in the DSMC simulation. However the velocities we are using to implement the boundary conditions are the local velocities at each inlet and outlet cell.

DSMC Code Validations. Two independent comparisons are carried out to validate our DSMC results. First, we compare the DSMC result with an analytical solution [13] for a long channel without any heated section. Then, we compare our DSMC results obtained for the schematic described in Fig. 1 with the analytic Graetz solution (presented in the next section).

For the first comparison, we consider a pressure driven flow in which the channel length, L, is long enough, i.e., $L/d \gg 1$ and isothermal as well as steady-flow are assumed. The Navier-Stokes equations can be simplified and solved analytically with a velocity-slip boundary condition. The solution [13] gives a pressure profile, which is uniform across the channel and changes along the channel according to

$$P^*(x^*) = -6\frac{2-\alpha}{\alpha}\mathrm{Kn}_o + \sqrt{\left(6\frac{2-\alpha}{\alpha}\mathrm{Kn}_o\right)^2 + \Bigl(P_i^{*2} + 12\frac{2-\alpha}{\alpha}\mathrm{Kn}_o P_i^*(1-x^*) + \left(1+12\frac{2-\alpha}{\alpha}\mathrm{Kn}_o\right)x^*}, \qquad (1)$$

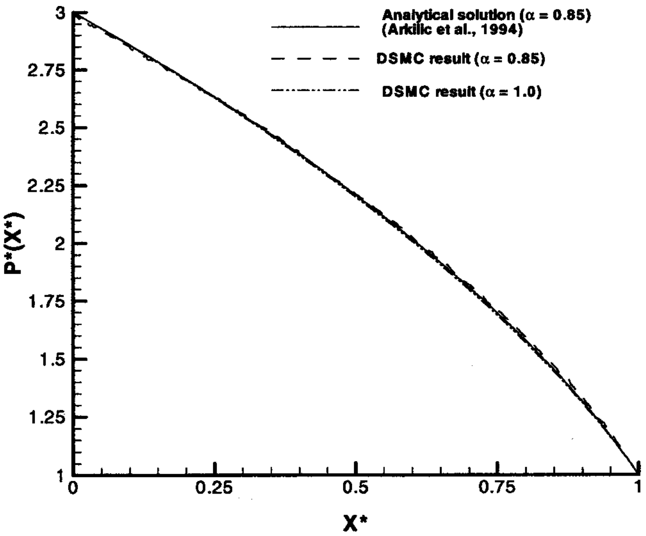

Fig. 2 Comparison of axial pressure distribution for channel flow (with slip-walls)

where $P^*(x^*)$ and P_i^* are the local pressure along the channel and inlet pressure, both normalized by the outlet pressure, Kn_o is the outlet Knudsen number, x^* is the streamwise coordinate normalized by L and α is the accommodation coefficient.

The channel length is chosen to be 2.4 m and the width is 0.05 m to make the aspect ratio equal to 48. The flow domain is divided into 28000 cells (350×80) and initially 50 stationary particles per cell are set at random position. Every cell is subdivided into two sub-cells in each direction. The sub-cell is introduced to cause all collisions to occur between particles in neighboring cells. As the simulation starts, the gas particles are accelerated and eventually when the temporal variation of the outlet velocity profile is small enough, (the maximum changes of the outlet velocity at all exit locations less than 1 percent), we assume the flow to have reached the steady state condition. The time step used is less than one-third of the typical particle mean collision time [4]. The typical molecular displacement in each direction during a time step is thus less than one third of the cell size. The "variable hard sphere" (VHS) model is used to account for the collisions [4] since VHS model has been widely used in both slip flow and transition flow simulation [2,9,11]. The gas properties used in the calculation such as molecular diameter, molecular mass, viscosity-temperature index and reference temperature can be obtained according to Bird [4]. The inlet pressure is 6.7 Pa while the outlet pressure is 2.23 Pa. Temperature is 300 K everywhere and the outlet Kn_o is about 0.048. The accommodation coefficient α is set to be 0.85. It can be seen from Fig. 2 that the agreement between the DSMC result and the analytical solution is excellent.

Results and Discussion

In this section, we present results for the low-pressure subsonic flows in a partially heated duct, as shown schematically in Fig. 1. A range of $\overline{\mathrm{Kn}}$ (from 0.01 to 3.0) was considered for the simulations. The variation of inlet Kn was implemented by the change of the inflow number density. In addition to nitrogen, argon, hydrogen and oxygen, different noble gas mixtures are used for the simulations. Since mixing helium with other noble gases can change the mixture Pr significantly, we carried out simulations with such gas mixtures. The mixtures considered are He-Xe (62 percent/38 percent), He-Kr (60 percent/40 percent), He-Ar (58 percent/42 percent) with Pr 0.18, 0.23, and 0.39 respectively [14]. The plates are considered as diffuse reflectors with full thermal and momentum accommodation. Experiments with "engineering" surfaces in contact with gases at normal temperatures indicate that the reflection process approximates diffuse reflection with complete thermal accommodation [4].

Viscosity and thermal conductivity of the gases at low pressure are calculated using the kinetic theory [15] for pure gases. Viscosity and thermal conductivity—both increase as temperature increases while the specific heat changes negligibly with the variation of temperature for the cases considered. The Prandtl number Pr, thus is found to be almost independent of temperature for the cases studied here. For noble gas mixtures, the above properties are calculated following Giacobbe [16].

Calculations were carried out for a large number of cases. The $\overline{\mathrm{Re}}$, $\overline{\mathrm{Kn}}$, and $\overline{\mathrm{Pr}}$ were systematically varied to obtain detailed information about the flow fields and to estimate the $\overline{\mathrm{Nu}}$. Tables 1, 2, and 3 list the cases considered in the study. Table 1 lists the cases studied with inlet pressure of 6.7 Pa and outlet pressure of 5.3 Pa. Tables 2 and 3 list cases studied with inlet pressures of 0.67 and 0.067 Pa and outlet pressures of 0.53 and 0.053 Pa, respectively. In addition to the parameters of the cases, the tables also contain the computed values of $\overline{\mathrm{Re}}$, $\overline{\mathrm{Kn}}$, and $\overline{\mathrm{Nu}}$. In the problem formulation, the coordinate origin was set at the transition point between the unheated section and the heated section. That is, for $x<0$, the wall temperature is 300 K, and for $x \geqslant 0$, the wall temperature is 600 K. Hence $\overline{\mathrm{Nu}}$, $\overline{\mathrm{Re}}$, and $\overline{\mathrm{Kn}}$ are the average values obtained from the heated section since the fluid flow and heat transfer in this section are of most interest.

The $\overline{\mathrm{Kn}}$ in the tables ranges from 0.01 to 3.0 to cover both slip-flow and transitional flow regime for all gases and gas-mixtures studied. The computed $\overline{\mathrm{Re}}$ is found to decrease with the increase of the $\overline{\mathrm{Kn}}$ number. This is an expected result. Also under the conditions of same inlet and outlet pressure, the $\overline{\mathrm{Kn}}$ decreases for molecules with lager diameters.

The simulations were done for nitrogen, argon, hydrogen, oxygen and noble gas mixtures, where the inlet Kn was varied systematically over two orders of magnitude. In case 1 (the base case), we consider a slip flow regime with nitrogen. The calculations in this study were carried out with a mesh size that met the general requirement that were discussed by Bird [4]. As described earlier, every cell is subdivided into two sub-cells in each direc-

Table 1 Values of $\overline{\mathrm{Nu}}$ versus $\overline{\mathrm{Re}}$, $\overline{\mathrm{Kn}}$, and $\overline{\mathrm{Pr}}$ for $P_{\mathrm{in}}=6.7$ Pa and $P_{\mathrm{out}}=5.3$ Pa

Case	Gas	Molecular $D \times 10^{10}$ m	Pr	$\mathrm{Kn}_{\mathrm{in}}$	$\overline{\mathrm{Re}}$	$\overline{\mathrm{Kn}}$	$\overline{\mathrm{Nu}}$
1	N_2	4.17	0.68	0.008	11.22	0.016	4.646
2	Ar	4.17	0.667	0.008	17.26	0.016	4.977
3	H_2	2.92	0.70	0.0163	2.536	0.037	2.623
4	O_2	4.07	0.65	0.0084	9.483	0.018	3.012
5	He-Xe(68%–32%)	3.42	0.18	0.0119	15.83	0.024	2.843
6	He-Kr(60%–40%)	3.30	0.23	0.0128	10.02	0.029	2.080
7	He-Ar(58%–42%)	3.10	0.39	0.0145	6.484	0.033	2.610

Table 2 Values of $\overline{Nu}$ versus $\overline{Re}$, $\overline{Kn}$ and Pr for $P_{in}=0.67$ Pa and $P_{out}=0.53$ Pa

Case	Gas	Molecular $D\times10^{10}$ m	Pr	Kn_{in}	$\overline{Re}$	$\overline{Kn}$	$\overline{Nu}$
8	N_2	4.17	0.68	0.08	0.614	0.178	0.822
9	Ar	4.17	0.667	0.08	0.974	0.177	1.029
10	H_2	2.92	0.70	0.163	0.191	0.358	0.575
11	O_2	4.07	0.65	0.084	0.524	0.195	0.882
12	He-Xe(68%–32%)	3.42	0.18	0.119	0.947	0.241	0.521
13	He-Kr(60%–40%)	3.30	0.23	0.128	0.620	0.293	0.433
14	He-Ar(58%–42%)	3.10	0.39	0.145	0.426	0.332	0.432

Table 3 Values of $\overline{Nu}$ versus $\overline{Re}$, $\overline{Kn}$ and Pr for $P_{in}=0.067$ Pa and $P_{out}=0.053$ Pa

Case	Gas	Molecular $D\times10^{10}$ m	Pr	Kn_{in}	$\overline{Re}$	$\overline{Kn}$	$\overline{Nu}$
15	N_2	4.17	0.68	0.8	0.067	1.619	0.112
16	Ar	4.17	0.667	0.8	0.105	1.606	0.139
17	H_2	2.92	0.70	1.63	0.027	3.276	0.052
18	O_2	4.07	0.65	0.84	0.061	1.789	0.091
19	He-Xe(68%–32%)	3.42	0.18	1.19	0.098	2.288	0.076
20	He-Kr(60%–40%)	3.30	0.23	1.28	0.069	2.729	0.065
21	He-Ar(58%–42%)	3.10	0.39	1.45	0.050	3.069	0.062

tion. When the temporal variation of the outlet velocity profile is small enough, (the maximum changes of the outlet velocity at all exit locations less than 1 percent), we assume the flow to have reached the steady-state condition. The time step used is less than one-third of the typical particle mean collision time [4]. The "variable hard sphere" (VHS) model is used to account for the collisions [4].

The calculations for the base case were repeated with different mesh size to establish the grid independency of the results presented. First, computations were made with 420×100 cells. Computations were then carried out with 350×80 and 200×60 mesh sizes. A comparison of the temperature profiles across the duct at point $x=0$ (the transition point from the unheated section to the heated section) and at point $x=0.4$ are shown in Figs. 3(*a*) and 3(*b*), respectively, for the three mesh sizes considered. There was no significant change in the results for the mesh sizes 420×100 and 350×80. The mesh size (350×80) was considered adequate for the simulations as case 1 gives the highest $\overline{Re}$.

The effect of the initial "particle numbers per cell" on the simulation results was also investigated. Figure 4 shows the temperature profiles obtained with different particle numbers for the base case with a mesh size of 350×80. Results were obtained with 60, 50, and 40 particles per cell. The variation in the predicted temperature profiles was small. We use 50 particles per cell for the cases studied. All computations were performed on an IBM-RISC-6000 (Model 360) workstation. Typical computation time ranged from 20 to 30 hours for a case.

Figure 5 shows the temperature contours in the flow domain for the base case. In some regions of the unheated section, temperature is a little higher than 300 K due to molecular diffusion. In the heated section, temperature gradually increases due to the heating and the exit gas temperature is almost equal to the wall temperature. Figure 6 shows the velocity vectors for the base case. Since the $\overline{Kn}$ is fairly low for this case, the velocity profiles are parabolic as expected. However, slight slip can be observed in the present results. The slip magnitude of velocity is about 7 m/s at the inlet and 23 m/s at the outlet. The Mach number at the outlet for this case is 0.2.

In addition to using the VHS model, the base case calculations

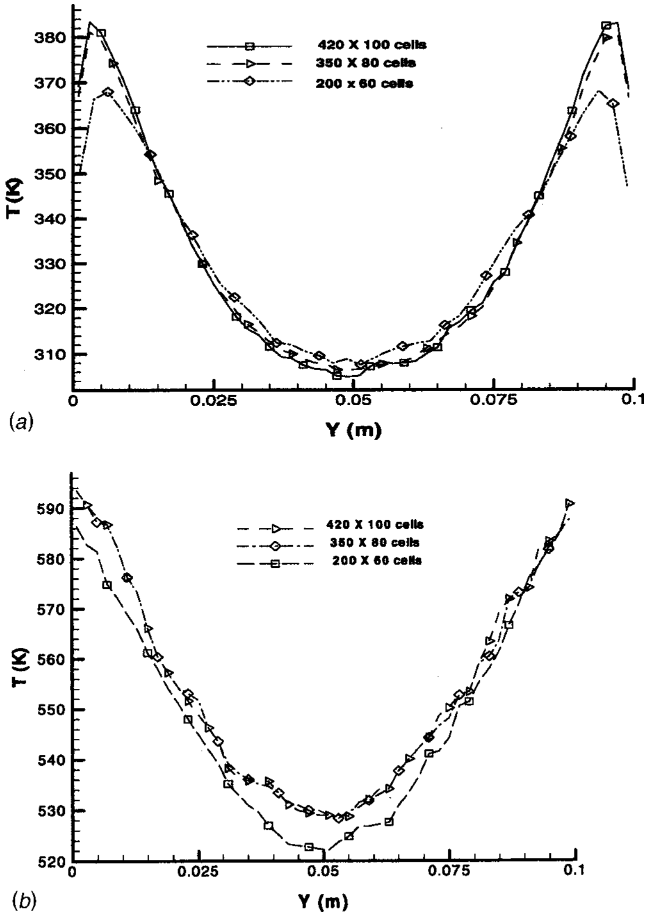

Fig. 3 (*a*) **The effect of cell size on temperature profile at $x=0$ m (50 particles/cell); and** (*b*) **the effect of cell size on temperature profile at $x=0.4$ m (50 particles/cell)**

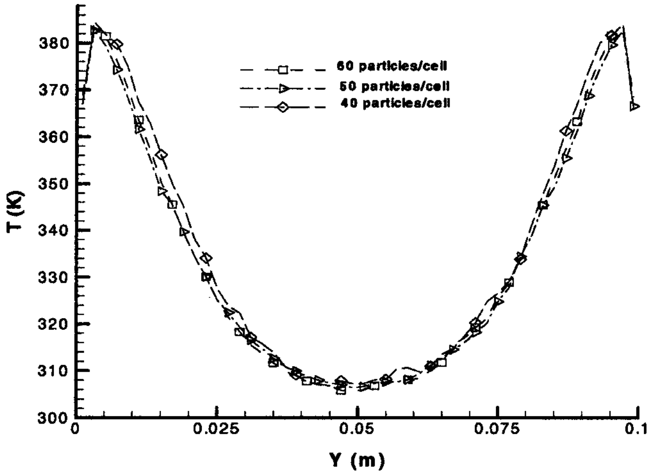

Fig. 4 The effect of particle number on temperature profile at $x=0$ (350×80 cells)

were repeated with the VSS (variable soft sphere) model. The variation of pressure along the axis (transversely averaged) is shown in Fig. 7 for both the VHS and VSS models. The difference between the predictions is very small. We note a significant nonlinear characteristic in the predicted pressure distribution. It is interesting to note that the slope of the pressure distribution increases at $x=0.0$. This is caused by the introduction of the heated section in the channel. It is well known that pressure is proportional to temperature and number density. The number density decreases along the channel while temperature increases for $x>0$.

Heat flux results from the DSMC simulation (for the base case) are next compared with the well-known Graetz solution [8] with both "parabolic flow" and "uniform flow" conditions. Wall heat fluxes are calculated from the differences between the energies of the impinging particles and the reflected particles. Figure 8 shows the heat flux variation along the flow direction. The results from the DSMC simulation and Graetz solution agree qualitatively in the heated region. Negative heat fluxes (heat transfer from the gas to the wall) are predicted for some portion of the unheated walls. This shows heat conduction due to molecular diffusion is not negligible and the unheated sections of the walls cool the heated particles. Additional differences between the DSMC results and the Graetz solution exist. These differences are expected as the Graetz solution is valid for fully developed incompressible continuum flows whereas rarefied developing flow conditions are considered in the present case. Although the velocity at the heated section is more parabolic than uniform (see Fig. 6), the Graetz solution for heat flux with "uniform velocity" agrees better with the DSMC results than the Graetz solution with "parabolic velocity". This is because of the presence of slip in the DSMC results. It is well known that slip at the wall can enhance the heat transfer. The Graetz solutions do not provide exact validation because the DSMC computations cannot be performed under identical conditions to those assumed in deriving the analytic solution.

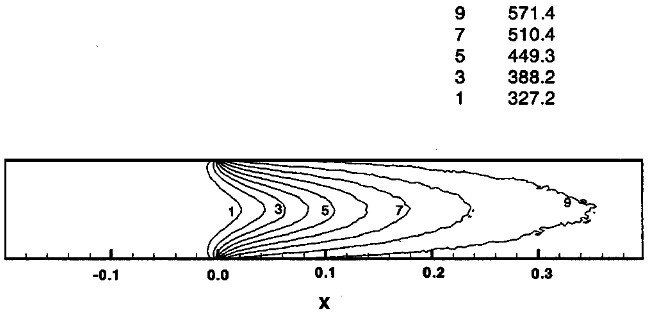

Fig. 5 Temperature contour for the base case

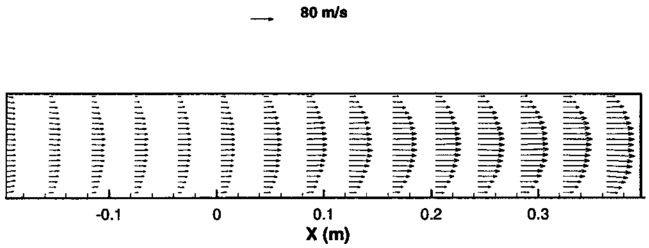

Fig. 6 Velocity vectors for the base case

The heat transfer coefficient $h(x)$ is calculated as

$$h(x)=\frac{|q_{\text{wall}}|}{|T_w(x)-T_b(x)|},$$

where $T_w(x)$ and $T_b(x)$ are the local wall and bulk-mean temperatures respectively. Figure 9 shows the variation of local

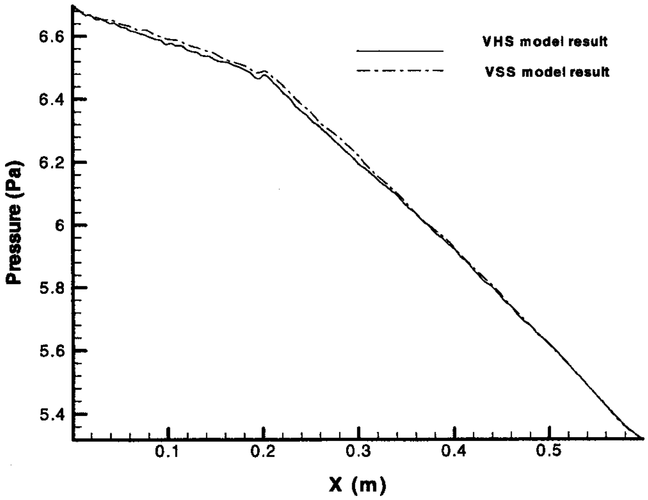

Fig. 7 Pressure distribution along centerline for the base case

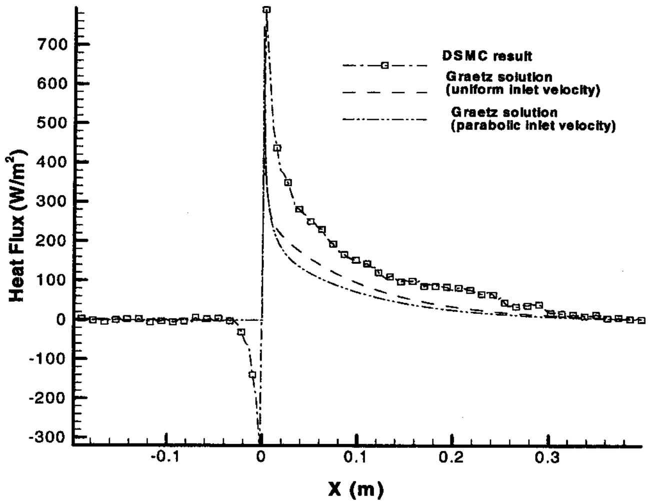

Fig. 8 Heat flux along the plate for the base case

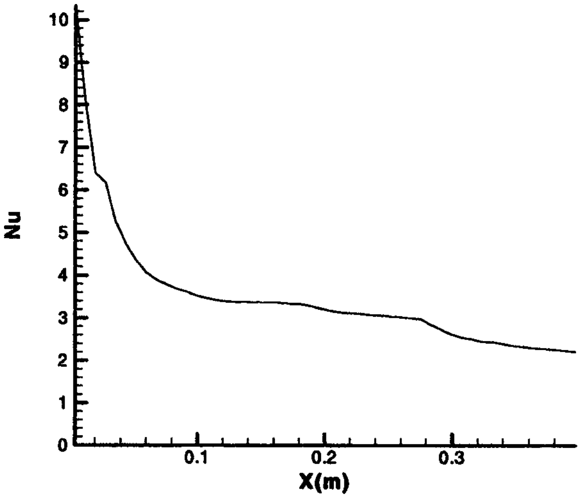

Fig. 9 Mean Nu as a function of position along the plate for the base case

$\mathrm{Nu}(x)[=h(x)d/\kappa(x)]$ along the axial direction for the heated portion of the walls. Nu varies significantly in the heated section of the flow. Since the temperature increases along the channel, thermal conductivity increases accordingly. Thus the variation of $\mathrm{Nu}(x)$ is due to both the heat flux and thermal conductivity variation along the flow direction.

Significant variations are also observed in the variation of local (transversely averaged) Kn(x) and Re(x). The axial variation of Kn(x) and Re(x) for the base case are shown in Figs. 10(a) and 10(b) respectively. Due to the sharp drop of density in the axial direction, Kn increases rapidly in the heated section while Re decreases on the other hand. It is seen from Fig. 10(a) that most of the flow is in the slip-flow regime. Although velocity and viscosity increase along the channel, the rapid decrease of density causes the Re to drop along the channel.

We now present results of nitrogen flow in the transition flow regime (case 8 in Table 2). The inlet pressure here is 0.67 Pa, and the outlet pressure is 0.53 Pa to give a pressure ratio of 1.27. For this high Kn flow (inlet Kn=0.08, outlet Kn=0.22), diffusion is much more pronounced. This can be seen clearly from the temperature contours (Fig. 11). Figure 12 shows the velocity vectors as predicted by DSMC calculations for case 8. The velocity gradient across the channel width is smaller. The amount of velocity slip at the wall is about 13 m/s near the inlet and 30 m/s at the outlet, which are large, compared to those for the base case. Because of the very low density, the Re is extremely low. In the transition area between the unheated and the heated regions, a strong nonlinear pressure distribution is again observed (Fig. 13). It can be seen from Fig. 13 that the pressure rises to a local maximum near $x=0$ due to the rapid increase of temperature. This is because the diffusion effect is more pronounced here compared to the base case.

The heat flux along the length for case 8 is shown in Fig. 14. The predictions are also compared with the Graetz solution with "parabolic velocity." The heat transfer is highest at the channel transition region where the temperature difference is the largest. Compared to the base case, the heat flux values along the wall are considerably smaller for case 8. The Graetz solution is again found to qualitatively compare with the DSMC prediction of the heat flux. The variation of the local Nu along the axis for case 8 is shown in Fig. 15. Compared with the former slip flow case (base case), the variation of Nu near the origin is relatively smaller in the transitional flow case. It shows that molecular diffusion in transition flow is dominant.

Figure 16(a) shows the variation of Kn along the axial direction for case 8 for the heated section. Changes in both pressure and

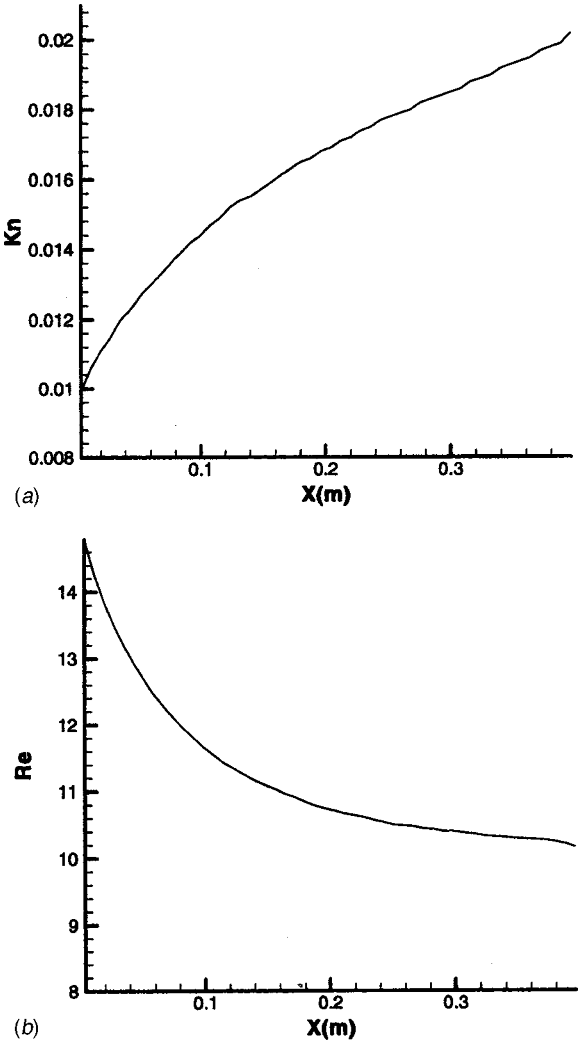

Fig. 10 (*a*) Kn as the function of position along the plate for the base case; and (*b*) Re as the function of position along the plate for the base case

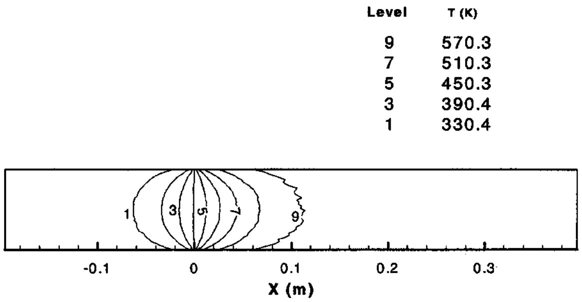

Fig. 11 Temperature contours for transition flow (case 8)

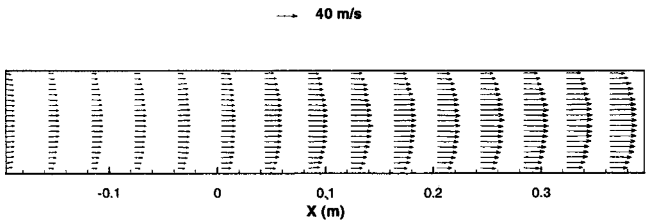

Fig. 12 Velocity vectors for transitional flow (case 8)

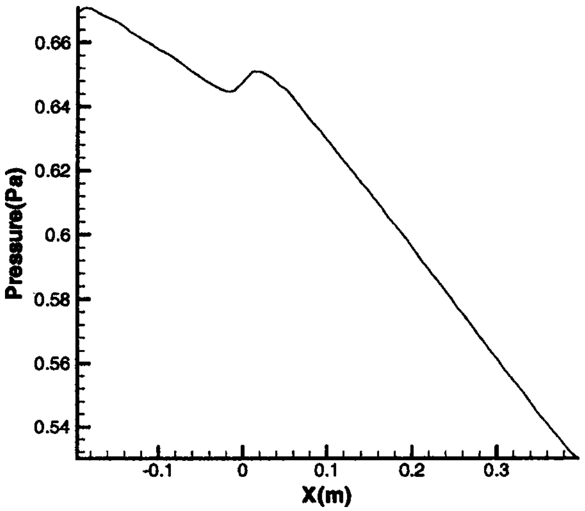

Fig. 13 Pressure distribution along the centerline for transitional flow (case 8)

temperature contribute to the increase of velocity in the axial direction. Figure 16(*b*) shows the axial variation of Re along the axis. In this case, towards the end of the channel, the temperature of the fluid approaches the wall temperature. The statistical scatter of temperature thus becomes more pronounced. The temperature fluctuation induces the fluctuation shown in Re in Fig. 16(*b*).

The effect of diffusion is found to be even stronger in case 15. Simulations for similar conditions (Cases 1, 8, and 15) were repeated for different gases such as argon, hydrogen, oxygen and noble gas mixtures, as shown in Tables 1, 2, and 3. Comparing the results for cases 1, 2, 3, and 4 (Table 1, we see that for similar values of $\overline{\mathrm{Kn}}$, the diatomic gases (nitrogen, oxygen and hydrogen) have lower values of $\overline{\mathrm{Nu}}$ compared to that of Ar. $\overline{\mathrm{Nu}}$ again decreases with increasing $\overline{\mathrm{Kn}}$ for all gases considered.

Noble gas mixtures were used in order to study the effect of Pr on heat transfer for the channel flows in low pressure. The Pr is 0.67 for all noble gases (at the reference temperature of 293 K). However, certain properties of the gaseous mixtures are not necessarily functions that vary linearly with subcomponent mole fractions. For example, the viscosities of some binary mixtures vary oddly with mixture composition. A variety of intermolecular attractive and repulsive forces that exist between real gas molecules must be considered. The Pr of gas mixtures were calculated following Giacobbe [16]. For the noble gas mixtures considered, the

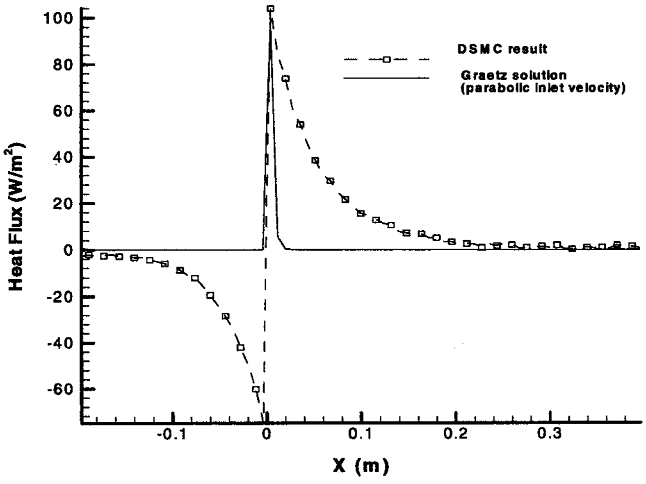

Fig. 14 Heat flux along the plate for transition flow (case 8)

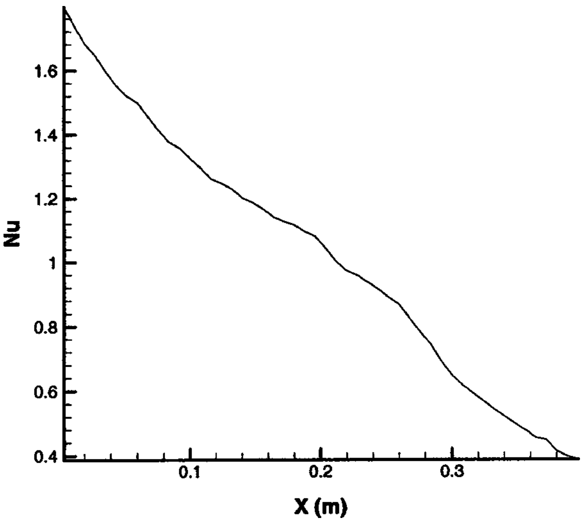

Fig. 15 Local Nu as a function of position along the plate for transitional flow (case 8)

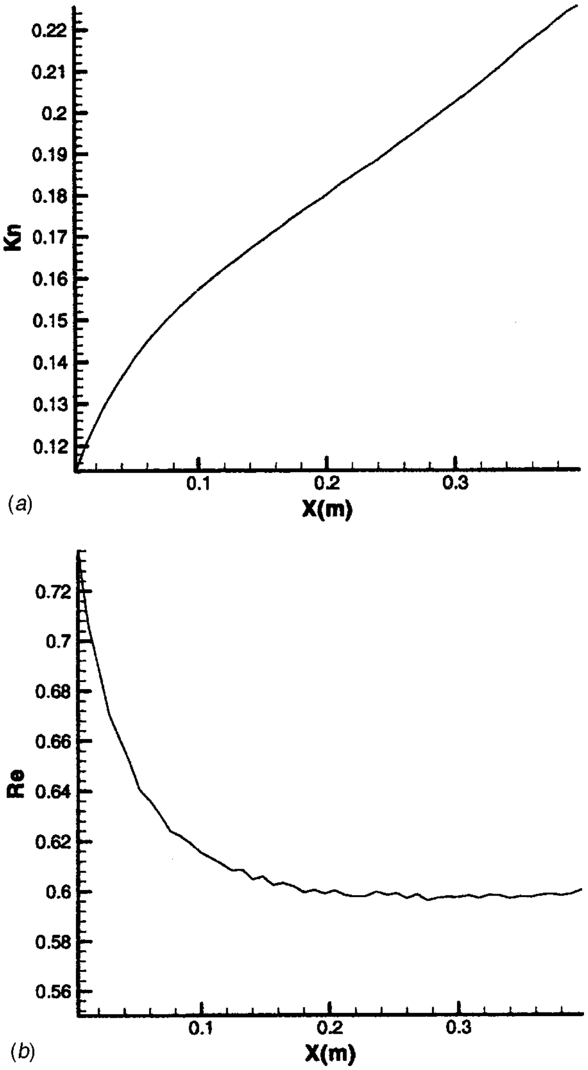

Fig. 16 (*a*) Kn as the function of position along the axis for transitional flow (case 8); (*b*) Re as a function of position along the plate for transitional flow (case 8)

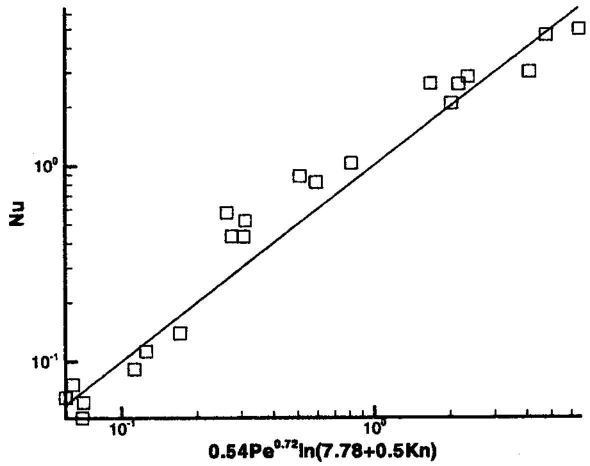

Fig. 17 Parity plot showing correlation of computed data

Pr varied from 0.18 to 0.39 (see Tables 1, 2, and 3). Compared with the values of $\overline{\mathrm{Nu}}$ predicted for Argon, the $\overline{\mathrm{Nu}}$ values for noble gas mixtures are found to be smaller. Low Pr of the noble gas mixtures thus reduces the values of $\overline{\mathrm{Nu}}$.

A simplified expression for predicting $\overline{\mathrm{Nu}}$ as a function of $\overline{\mathrm{Pe}}$, and $\overline{\mathrm{Kn}}$ was obtained following the correlations given by Graetz where Peclet number, Pe=Re.Pr. Using a linear regression technique, the following form is obtained from the data shown in Tables 1, 2, and 3:

$$\overline{\mathrm{Nu}} = 0.54\ \overline{\mathrm{Pe}}^{0.72}\ln(7.78+0.5\ \overline{\mathrm{Kn}}).$$

A parity plot showing the degree of correlation of the computed data is shown in Fig. 17 with a confidence level of 85 percent.

The coefficient of $\overline{\mathrm{Kn}}$ is positive which indicates that for a given $\overline{\mathrm{Pe}}$, $\overline{\mathrm{Nu}}$ increases as the $\overline{\mathrm{Kn}}$ increases. However, it must be pointed out that for most gases, $\overline{\mathrm{Pe}}$ usually decreases as $\overline{\mathrm{Kn}}$ is increased. Since the additive constant in the above correlation is large (7.78), the effect of $\overline{\mathrm{Kn}}$ is rather weak on $\overline{\mathrm{Nu}}$. Since the correlation is based on a data set that only contains low values of $\overline{\mathrm{Re}}$, the continuum correlation given by Graetz for uniform inlet flow is not recovered by setting $\overline{\mathrm{Kn}}\rightarrow 0$. Comparing the present correlation with that for Graetz [1], the exponential coefficient (0.72) of $\overline{\mathrm{Pe}}$ is found to be larger than its continuum counterpart (0.33). Hence, for low-pressure flow the effect of $\overline{\mathrm{Pe}}$ on convection heat transfer becomes more pronounced.

Conclusions

High $\overline{\mathrm{Kn}}$ number low speed flows through partially heated parallel plates are studied using the DSMC technique. Diatomic and monatomic gases as well as noble gas mixtures were considered. Heat fluxes along the plates are calculated and compared with the Graetz analytical solution (with uniform inlet flow). Heat fluxes predicted by the DSMC method agree qualitatively with the Graetz solution in the heated region. However, significant differences exist because of the rarefied flows considered. Molecular diffusion dominates at large $\overline{\mathrm{Kn}}$. Nonlinear pressure distribution was observed along the channel. As the $\overline{\mathrm{Kn}}$ number increases, the heat flux decreases monotonically along the channel wall. Future calculations are planned for high (atmospheric) pressure slip and transitional flows (high Kn) through smaller size (micro) channels by the DSMC method.

Nomenclature

c_p = specific heat
d = channel width
D = molecular diameter
h = heat transfer coefficient
L = channel length; also, characteristic length of flow gradients
Kn = Knudsen number, $\mathrm{Kn}=\lambda/d$
$\overline{\mathrm{Kn}}$ = average Knudsen number for the heated section
Nu = Nusselt number, $\mathrm{Nu}=hd/\kappa$
$\overline{\mathrm{Nu}}$ = average Nusselt number for the heated section
P = pressure
P^* = Normalized pressure, $P^*=P/P_{\mathrm{out}}$
Pe = Peclet number, Pe=Re.Pr
Pr = Prandtl number, $\mathrm{Pr}=\nu/\kappa$
Re = Reynolds number, $\mathrm{Re}=\overline{U}d/\nu$
$\overline{\mathrm{Re}}$ = average Reynolds number for the heated section
T = temperature
$\overline{U}(x)$ = average streamwise velocity
x = coordinate along channel length
x^* = normalized x coordinate $x^*=x/L$
y = coordinate along channel width

Greek Symbols

α = accommodation coefficient
λ = mean free path
ν = kinematic viscosity
κ = thermal conductivity

References

[1] Kakac, S., and Ozgu, M. R., 1969, "Analysis of Laminar Flow Forced Convection Heat Transfer in the Entrance Region of a Circular Pipe," Waerme-Stoffuebertrag., **2**, pp. 240–245.

[2] Oh, C. K., Oran, E. S., and Sincovits, R. S., 1997, "Computations of High-Speed, High Knudsen Number Microchannel Flows," J. Thermophys. Heat Transfer, **11**, No. 4, pp. 497–505.

[3] Nanbu, K., Igarashi, and Mitamura, 1991, "Molecular Simulation of a Gas-Phase Reaction in a Low Pressure CVD Reactor," Reports of the Institute of Fluid Science, Tohoku University, Sendai, Japan, Vol. 3, pp. 35–51.

[4] Bird, G. A., 1994, *Molecular Gas Dynamics and The Direct Simulation of Gas Flow*, Oxford Engineering Science, Oxford University Press, New York, NY.

[5] Beskok, A., and Karniadakis, G., 1994, "Simulation of Heat Momentum Transfer in Complex Microgeometries," J. Thermophys. Heat Transfer, **8**, No. 4, pp. 647–655.

[6] Piekos, E. S., and Breuer, K. S., 1996, "Numerical Modeling of Micromechanical Devices Using the Direct Simulation Monte Carlo Method," ASME J. Fluids Eng., **118**, pp. 464–469.

[7] Oran, E. S., Oh, C. K., and Cybyk, B. Z., 1998, "Direct Simulation Monte Carlo: Recent Advances and Applications," Annu. Rev. Fluid Mech., **30**, pp. 403–442.

[8] Graetz, L., 1883, "Uber die Warmeleitungs Fahigkeit von Flussigkeiten," Annalen der Physic und Chemie, **18**, pp. 79–84.

[9] Mavriplis, C., Ahn, J. C., and Goulard, R., 1997, "Heat Transfer and Flowfields in Short Microchannels Using Direct Simulation Monte Carlo," J. Thermophys. Heat Transfer, **11**, No. 4, pp. 489–496.

[10] Nagayama, K., and Farouk, B., 1998, "Heat Transfer in Low Pressure Developing Flows Through Parallel Plates," *Int. Heat Transfer Conference*, Kyongju, Korea, Vol. 3, pp. 127–132.

[11] Piekos, E. S., and Breuer, K. S., 1995, "DSMC Modeling of Microchannel Devices," AIAA Paper 95-2089.

[12] Cai, C., Boyd, I. D., Fan, J., and Candler, G. V., 2000, "Direct Simulation Methods for Low-Speed Microchannel Flows," J. Thermophys. Heat Transfer, **14**, No. 3, pp. 368–378.

[13] Arkilic, E. B., Breuer, K. S., and Schmidt, M. A., 1994, "Gaseous Flow in Microchannels," *Application of Microfabrication to Fluid Mechanics*, ASME, FED-Vol. 197, pp. 57–66.

[14] Wetzel, M., and Herman, C., 1997, "Design Optimizing of Thermoacoustic Refrigerators," Int. J. Refrig., **20**, No. 1, pp. 3–21.

[15] Vincenti, W. G., and Kruger, C. H., 1965, *Introduction to Physical Gas Dynamics*, John Wiley and Sons Inc., New York, NY.

[16] Giacobbe, F. W., 1994, "Estimation of Prandtl Numbers in Binary Mixtures of Helium and Other Noble Gases," Acoustical Society of America, **96**, No. 6, pp. 3568–3580.

Heat Transfer in Rotating Rectangular Cooling Channels (AR=4) With Angled Ribs

Todd S. Griffith
e-mail: ddot1976@yahoo.com
Research Assistant

Luai Al-Hadhrami
Research Assistant

Je-Chin Han
M.C. Easterling Endowed Chair

Turbine Heat Transfer Laboratory,
Department of Mechanical Engineering,
Texas A&M University,
College Station, TX 77843-3123

An investigation into determining the effect of rotation on heat transfer in a rib-roughened rectangular channel with aspect ratio of 4:1 is detailed in this paper. A broad range of flow parameters have been selected including Reynolds number (Re=5000–40000), rotation number (Ro=0.04–0.3) and coolant to wall density ratio at the inlet $(\Delta\rho/\rho)_i = 0.122$*. The rib turbulators, attached to the leading and trailing surface, are oriented at an angle* (α=45 deg) *to the direction of flow. The effect of channel orientations of* β=90 *deg and 135 deg with respect to the plane of rotation is also investigated. Results show that the narrow rectangular passage exhibits a much higher heat transfer enhancement for the ribbed surface than the square and 2:1 duct previously investigated. Also, duct orientation significantly affects the leading and side surfaces, yet does not have much affect on the trailing surfaces for both smooth and ribbed surfaces. Furthermore, spanwise heat transfer distributions exist across the leading and trailing surfaces and are accentuated by the use of angled ribs. The smooth and ribbed case trailing surfaces and smooth case side surfaces exhibited a strong dependence on rotation number.*

[DOI: 10.1115/1.1471525]

Keywords: *Enhancement, Heat transfer, Rotating, Roughness, Turbines*

Introduction

As the world becomes exceedingly industrialized, there develops an ever-increasing demand for energy. Extensive research efforts have recently focused on methods for reducing the consumption of energy. One area focused on improvements in efficiency is the turbomachinery industry. There is a constant drive to decrease the cost associated with repairing a gas turbine as well as increasing the fuel efficiency. With the wide spread application of turbines from power generation to aircraft propulsion, the cost saving can be enormous. One method of increasing the efficiency of a turbine as well as the thrust of an aero-turbine is by increasing the combustion temperature. This poses a major problem in the hastened degradation of temperature sensitive components of the turbine, principally the turbine blades. To counter the high turbine inlet temperatures (1600–1800 K), the physics of turbulent heat transfer are investigated in a cooling model. Turbine blades incorporate internal cooling passages to extract the thermal energy absorbed from the hot combustion gases. This prolongs the life of the blade as well as allowing for increased combustion temperatures, which ultimately increases performance of the turbine.

A small amount of pressurized air is extracted from the compressor and injected into the turbine blades via the cooling air bypass. This relatively low enthalpy gas is forced through the internal cooling passages of the turbine blades, convectively extracting heat from the internal walls. For further thermal protection of the blade, a portion of the internal cooling air is ejected through tiny holes in the walls and tip of the blade, creating a cool film thermal boundary.

When considering the effects of rotation, certain flow phenomena are exhibited that are not observable in the stationary reference frame. Forces are generated under a rotational reference frame, principally the Coriolis and buoyancy forces. These forces generate secondary flows in the plane orthogonal to the mean flow direction. For radial outward flow, the Coriolis and buoyancy forces combine to shift the velocity profile toward the trailing surface. The coolant flow migrates along with the heat transfer augmentation toward the trailing surface. This rotationally induced migration of the cooler core flow results in the advantageous enhancement of heat transfer at the trailing surface, but it is typically balanced by the disadvantageous reduction in heat transfer from the leading surface. As with most temperature sensitive components, thermal failure in an isolated region is oftentimes just as problematic as failure of the entire component. This is why it is important to analyze the heat transfer phenomenon segment by segment along the length of the blade.

The aspect ratio of the channel also has a profound impact on the effect of rotation. Moving from the mid-chord to the trailing edge of the blade, the channels must become more rectangular as the blade becomes thinner. The orientation of a 4:1 aspect ratio cooling channel in a gas turbine blade is shown in Fig. 1. This thinning of the channel changes the effective secondary flow pattern from that of a square duct. For this reason, one cannot simply apply the knowledge of the rotationally induced flow patterns in a square channel to that of a rectangular channel. Therefore, an investigation of the rectangular channel is necessary to further understand the heat transfer characteristics of the internal cooling channels in a gas turbine blade.

To promote heat transfer in the internal cooling passage, various types of turbulators are used to trip the boundary layer. The onset of turbulence results in higher heat transfer by promoting mixing of the cooler core jet gases with the hot boundary layer at the walls. The most common and effective type of turbulator is referred to as the ‘‘rib’’ or ‘‘trip-strip.’’ These ribs appear as small rectangular surface protrusions, and are typically oriented at 45 deg to the direction of flow on the internal leading and trailing surfaces of the blade. When combining the effects of tripping the boundary layer (ribbed-turbulator) and rotational forces (Coriolis and buoyancy), entirely different turbulence and flow phenomenan are achieved. Combining into this equation the various shapes and sizes of internal cooling channels, it is clear that there is no one single solution that can be applied universally in the field of turbine heat transfer. For this reason, an experimental investigation into each combination of the previously mentioned parameters is necessary. Until now, published literature concerning the rotational effect on the regionally averaged heat transfer characteristics has not existed for the 4:1 aspect ratio duct.

Contributed by the Heat Transfer Division for publication in the JOURNAL OF HEAT TRANSFER. Manuscript received by the Heat Transfer Division August 14, 2001; revision received February 14, 2002. Associate Editor; H. S. Lee.

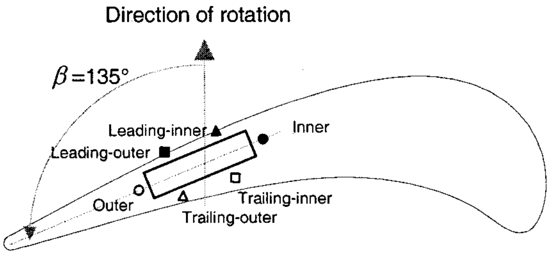

Fig. 1 Sketch illustrating orientation of a 4:1 aspect ratio channel in a gas turbine blade

There are numerous past studies on turbulent flow and heat transfer in the cooling channels of a gas turbine blade. Han and Park [1] published experimental investigations of the heat transfer phenomenon in a stationary rib roughened rectangular channel. Han et al. [2] performed a study of the effect of the rib angle on heat transfer distributions and pressure drop in a stationary square channel with two opposite in-line ribbed walls. These studies showed that the 60 deg and 45 deg V-shaped rib performs better than the 60 deg and 45 deg parallel rib. It was also concluded that the V-shaped rib out-performs 60 deg and 45 deg crossed ribs as well as the 90 deg rib. Wagner et al. [3,4] conducted detailed experimental investigation to determine the effects of rotation, or more specifically the effects of Coriolis and buoyancy forces on the regionally averaged heat transfer distribution of a serpentine square channel with smooth walls. This study determined that in the first pass, the effect of rotation created a thinner boundary layer on the trailing surface and a thicker boundary layer on the leading surface.

Parsons et al. [5] and Johnson et al. [6] studied the effects of channel orientation and wall heating condition on the regionally averaged heat transfer coefficients in a rotating two-pass square channel with ribbed walls. Parsons et al. [5] discovered that the heat transfer enhancement for the constant wall heat flux boundary condition was more pronounced when the duct is twisted 45 deg to the plane of rotation when compared to a channel oriented orthogonal to the plane of rotation. Johnson et al. [6] determined that the model orientation with respect to the rotation plane greatly affected the heat transfer distribution.

Dutta and Han [7] investigated the regionally averaged heat transfer coefficients in a rotating two-pass square channel with three different model orientations. They found that the orientation of the channel with respect to the plane of rotation affected the heat transfer distribution. More specifically, they determined that orienting the channel at an angle with respect to the plane of rotation reduced the effect of rotation when compared to the orthogonal channel orientation.

Until recently, most of the experimental studies have explored only square ducts. However, it is quite common to find rectangular cooling passages, particularly toward the trailing edge of a gas turbine blade. Since the profile of a turbine blade is curved, the exclusive use of square channels is not practical. Past research focused mainly on the square channel; therefore, published data for a rectangular cooling channel is rare. Al-Qahtani et al. [8] published a numerical prediction of the flow behavior and heat transfer in a rib-roughened, rotating, two pass rectangular channel of aspect ratio 2:1. An interesting description of the flow physics associated with rib flow is included in their investigation. Taslim et al. [9,10] investigated the heat transfer distribution in square and rectangular rib-roughened channels under rotation. They applied the liquid crystal technique to study the effect of rotation on wall heat transfer. It was discovered that the effects of rotation were more apparent in rib-roughened channels with a larger channel aspect ratio and a lower rib blockage ratio. This investigation studied only the heat transfer distribution in an orthogonal rotating channel.

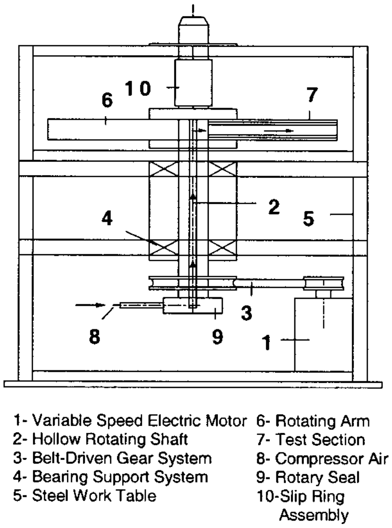

Fig. 2 Schematic of experimental rotating test rig

Willett and Bergles [11] performed a detailed investigation of the heat transfer in a narrow, 10:1 smooth rectangular channel oriented at 60 deg to the r-z plane. Most of their focus dealt with exploring the contribution of buoyancy forces under rotation. They found that the duct orientation induced a significant variation in the heat transfer coefficient in the spanwise direction. It was also found that the normalized Nusselt number at the far-aft-end of the trailing side (or the trailing-outer equivalent in this paper) is a strong function of rotation number and buoyancy number. However, they did not perform tests at an angle normal to the plane of rotation in order to determine how changing the duct orientation affects the heat transfer distribution within the rectangular channel, nor did they consider the effect of varying the surface configuration, such as the common ribbed surface. Also, most of their study presented data in streamwise averaged format, even though the data was taken at localized points. For a more comprehensive compilation of turbine heat transfer research, please see the book by Han et al. [12], the review paper by Han and Dutta [13], and the review paper by Dutta and Han [14].

Therefore, it is of interest to experimentally investigate the regionally averaged heat transfer distribution in a rotating, rectangular channel of aspect ratio 4:1. The fact that no such literature exists today on this subject raises the following questions:

1. How does the spanwise heat transfer distribution vary within a smooth and ribbed rectangular channel, and is it significant enough to require consideration when designing the cooling channels of a turbine blade?
2. Does the surface configuration and orientation of the rotating rectangular channel significantly affect the heat transfer distribution?
3. Do the narrow aspect ratio ducts exhibit different heat transfer distributions when compared to the square and rectangular channels of lower aspect ratio?

Answers to these questions are pursued in this paper.

Experimental Facility

The experimental test rig previously used by Dutta and Han [7] is utilized in this investigation (see Fig. 2). A variable frequency motor is connected via a gear-and-belt mesh to a hollow, rotating shaft. This shaft runs from the base of the test rig to the work platform and is attached orthogonal to the hollow, rotating arm. The test section is inserted inside the hollow rotating arm, which rotates in a plane orthogonal to the rotating shaft. A hand held optical tachometer is used to determine the rotational velocity of

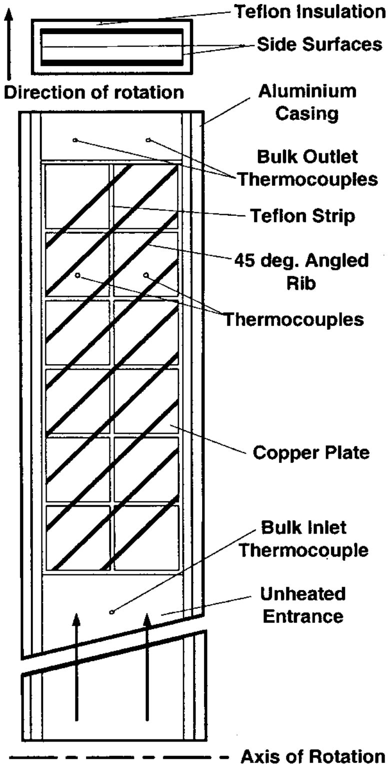

Fig. 3 Schematic of 4:1 test section

the arm. Thermocouple and heater wires are connected to a 100-channel slip-ring assembly mounted to the rotating shaft. The output of the thermocouples is transferred to a data logger. Fuse-protected power input to the heaters from the variac transformers is also transmitted through the slip ring assembly. Cooling air is pumped from a steady flow compressor, through an ASME orifice flow meter, then through the hollow rotating shaft, turning 90 deg and passing into the rotating arm, then through the test section and is finally expelled into the atmosphere.

The test section is a 0.5 in. by 2 in. by 6 in. long ($1.27\times5.08\times15.24$ cm) one-pass rectangular channel of aspect ratio 4:1 with a hydraulic diameter of $D=0.8$ in. The ratio of mean rotating radius to hydraulic diameter is $R/D=33$. The direction of airflow is radially outward from the axis of rotation. Two rows of copper plates are installed on both the leading and trailing surface to provide a grid for analysis of the spanwise variation in the regionally averaged heat transfer coefficient.

Figure 3 shows a detailed top view of the test section. The test section is divided into six cross-sections, each with six copper plates: two for the leading, two for the trailing, one for the outer and one for the inner surface. Moving along the direction of the flow (radially outward), there are six streamwise segments for a total of 36 copper plates in the entire test section. The channel length-to-hydraulic diameter ratio (L/D) is 7.5 with a ratio of 1.25 for each of the six cross-section segments. Each plate is separated by a 0.0626 in. (0.159 cm) thin strip of nylon to prevent heat conduction between plates. This is important since the objective is to study the spatial distribution of heat transfer.

The copper plates are mounted in a nylon substrate, which comprises the bulk of the test section. Pre-fabricated flexible heaters are installed beneath the leading and trailing surfaces, two to each surface. The outer and inner walls (or side walls) are each heated by a wire-wound resistance heater, which is also installed beneath the copper plates. All heaters supply steady, uniform heat flux to the copper plates. Sufficient power is supplied in order to maintain a maximum wall temperature of nearly 340 K for the corresponding section. This corresponds to an inlet coolant-to-wall density (temperature) ratio $(\Delta\rho/\rho)_i$ of 0.122 for every test. Thermal conducting paste is applied between the heater and copper plates to promote heat transfer from the heater to the plate. Each 1/8 in. (0.318 cm) thick plate has a 1/16 in. (0.159 cm) deep blind hole drilled in the backside in which a copper-constantan thermocouple is installed 1/16 in. (0.159 cm) from the plate surface with thermal conducting glue.

Two different surface configurations (smooth and 45 deg ribs) are studied as well as two different channel orientations with respect to the direction of rotation ($\beta=90$ deg and 135 deg). Figure 3 shows the ribbed surface configuration. The channel is rib-roughened on two opposite walls with 45 deg in-line ribs. The parallel rib configuration was chosen due to the widespread use of 45 deg parallel ribs in turbine blade cooling channels. The ribs are made of brass and are glued to the leading and trailing surfaces of the channel, resulting in a rib height-to-hydraulic diameter ratio (e/D) of 0.078 and a pitch-to-rib height (P/e) ratio of 10. The rib flow-attack angle, defined as the angle between the mean flow direction and the rib angle orientation (α), is maintained at 45 deg. The experiments were conducted for Reynolds numbers of 5000, 10,000, 20,000 and 40,000. The test section rotates at a speed of 550 rpm, resulting in a range of rotation number (Ro) from approximately 0.04–0.3.

Data Reduction

This investigation focuses on detailing the regionally averaged heat transfer coefficient at various locations within the internal cooling channel. This heat transfer coefficient is determined by the net heat flux from the heated plate to the cooling air, the surface area of the plate (A_p), the regionally averaged temperature of the plate, and the local bulk mean air temperature by the following:

$$h=q''_{\text{net}}/(T_w-T_{b,x}) \tag{1}$$

The net heat flux is calculated using the measured voltage and current supplied to the heater multiplied by the area fraction exposed to the respective plate minus the previously determined amount of heat losses due to external conduction, convection, and radiation energy escaping from the test section. This heat loss calibration is performed for both stationary and rotation experiments with a piece of insulation inserted inside the test section to inhibit natural convection. For this calibration, by knowing the amount of power supplied to the heater and measuring the temperature of the plate, it is possible to determine how much the heat is being lost into the environment using the conservation of energy principle. Equation (1) is used throughout the experiment, neglecting the change of area effect with the addition of ribs. That is, the heat transfer coefficient is calculated based on the projected area, neglecting the 28 percent increase in area due to the addition of ribs.

The regionally averaged wall temperature (T_w) is measured directly by the thermocouple installed in the blind hole on the back of each plate. The local bulk mean air temperature ($T_{b,x}$) is determined by a linear interpolation between the measured bulk air inlet and the average of two outlet temperatures (each installed at the midpoint of the two spanwise sections) due to the applicable constant heat flux assumption. Another method used to check the interpolation values is by performing an energy balance. It is reassuring to note that performing an energy balance to calculate the expected outlet temperature resulted in a close match to that of the average measured exit temperature value, typically to within 5 percent. Therefore the linear interpolation method is validated and is the method used in the calculation of the results presented in this paper. The energy balance equation is:

$$T_{b,i}=T_{\text{in}}+\sum_i (q-q_{\text{loss}})/\dot{m}c_p, \quad i=1,2\ldots6 \tag{2}$$

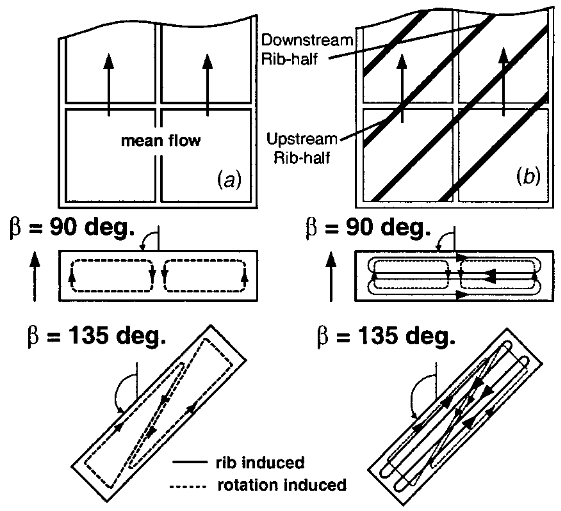

Fig. 4 Outward flow rectangular test section with: (*a*) smooth walls; and (*b*) 45 deg parallel ribs on leading and trailing surfaces.

To provide a common reference for each analysis, a correlation is used comparing the Nusselt number for the specific duct case to that of fully developed flow through a smooth stationary circular pipe at the same Reynolds number. For this investigation, the Dittus-Boelter correlation for heating ($T_w > T_{bx}$) is used:

$$\frac{\mathrm{Nu}}{\mathrm{Nu}_o} = \frac{hD}{k_{\mathrm{air}}} \frac{1}{(0.023\,\mathrm{Re}^{0.8}\mathrm{Pr}^{0.4})} \tag{3}$$

All air properties are taken based on the mean bulk air temperature with a Prandtl number (Pr) for air as 0.71.

Overall uncertainty for the regionally averaged heat transfer is predominantly dependent upon the difference between the wall temperature and the bulk air temperature, the net heat flux input and the ability to maintain a steady mass flow rate. As with most experiments, the uncertainty for this investigation decreases with the increasing magnitude of input parameters. For higher Reynolds numbers, the uncertainty has been determined to be nearly 7 percent. However, for lower Reynolds numbers ($\mathrm{Re}=5000$), the uncertainty could be as much as 20 percent. The uncertainty analysis was performed using the Kline and McClintock [15] uncertainty analysis procedure.

Results And Discussion

Before any discussion of the physics associated with the thin rectangular duct proceeds, it is important to set up a labeling scheme for the various surfaces in the duct. This labeling scheme, seen in Fig. 1, will be used throughout this paper. The inner and outer surface side walls are named according to their location in the turbine blade. That is, the inner surface is closer to the mid-chord position of the blade (a relatively internal position), and the outer surface is closer to the trailing edge of the blade, and thus is closer to an external surface of the blade. The leading and trailing surfaces of the blade follow the conventional definitions of these surfaces, however each surface is subdivided into two surfaces in order to investigate the span-wise distribution of heat transfer along the major surfaces (leading and trailing). Therefore we have a total of six surfaces: leading-outer, leading-inner, trailing-outer, trailing-inner, outer, and inner. Because of the many intrinsic differences between square and rectangular ducts, a brief discussion on the secondary flow patterns generated by rotation and the ribs in a thin rectangular duct follows.

Secondary Flow Behavior. Figure 4 shows a conceptualization of the secondary flow patterns of a smooth and ribbed rotating duct. The smooth duct seen in Fig. 4(*a*) shows how the rotational forces (dotted line) induce a migration of the cooler core flow toward the trailing surface in radially outward flow with the channel oriented at $\beta = 90$ deg to the plane of rotation. This results in an increase of the heat transfer from the trailing surface, although it typically results in a decrease in heat transfer at the leading surface.

Tilting the smooth duct to $\beta = 135$ deg causes the Coriolis forces to shift the secondary flow pattern from the case of $\beta = 90$ deg. Now the secondary flow due to rotation travels along the line from the leading most corner of the duct to the trailing most corner of the duct. This results in a significant increase in heat transfer at the outer surface as well as a moderate increase for the entire leading and trailing surfaces. When ribs are installed as seen in Fig. 4(*b*), the combination of secondary flows produces a flow behavior that is entirely different from the smooth surface. The ribs induce a flow pattern parallel to the ribs at the wall, traveling from the upstream rib-half surface (from the outer surface in this case) to the downstream rib-half surface (toward the inner surface in this case). This rib configuration was chosen because when the channel is tilted to $\beta = 135$ deg, the rib-induced secondary flow constructively combines with the rotation induced secondary flows. Past literature has paid little attention to the constructive and destructive combinations of rib and rotation-induced secondary flows. At $\beta = 90$ deg, the rib-induced secondary flow constructively combines with the rotation-induced secondary flows at the leading-outer and trailing-inner surfaces, while the two secondary flows destructively combine at the trailing-outer and leading-inner surfaces. It is impossible to achieve completely constructive rib- and rotation-induced secondary flows in a channel of $\beta = 90$ deg when using continuous ribs. If the ribs had been oriented with the upstream rib-half attached from the inner surface and the downstream rib-half following toward the outer surface, then a completely destructive combination of the rib and rotation-induced secondary flows would have resulted across the entire leading and trailing surfaces at the $\beta = 135$ deg orientation. While it would be interesting to investigate such behavior, this analysis was limited to only the smooth and 45 deg rib orientation that produces constructive combinations of secondary flow.

Smooth Channel Results. Figures 5–7 contain the smooth duct data for three different channel configurations: stationary, rotation with $\beta = 90$ deg and rotation with $\beta = 135$ deg. Each case is subdivided into four experiments: (*a*) $\mathrm{Re}=5000$, (*b*) $\mathrm{Re}=10000$, (*c*) $\mathrm{Re}=20000$, and (*d*) $\mathrm{Re}=40000$. The corresponding rotation numbers for these cases are 0.305, 0.151, 0.075, and 0.038, respectively. Please reference Figure 1 for the data legend and surface locations within the channel. Figure 5 contains data for the stationary cases. The higher than asymptotic values in the normalized Nusselt number plots are attributable to the entrance effect in thermally developing flow. The plots all approach a horizontal asymptote as the flow approached the thermally fully developed state.

Figure 6 shows the results for the rotation cases where the duct is oriented at $\beta = 90$ deg, that is, orthogonal to the plane of rotation. As was expected, the trailing surfaces exhibit higher heat transfer enhancement than the leading surfaces due to the migration of the colder core fluid toward the trailing surface caused by the Coriolis rotational forces. At a duct angle of $\beta = 90$ deg, the channel can be assumed to hold symmetry about the plane of rotation. This means that both of the leading surfaces (leading-outer and leading-inner) should have identical Nu plots, the trailing surfaces should exhibit identical behavior, and the two side surfaces should be equal. This is validated relatively well as seen in the figures, with a slight bias between the two trailing surfaces. An increase in the Reynolds number tends to suppress the effect of rotation. All six surfaces show very little streamwise variation in the Nu number plots. Both of the side surfaces (inner and outer) have a heat transfer enhancement nearly equal to the value of the two trailing surfaces.

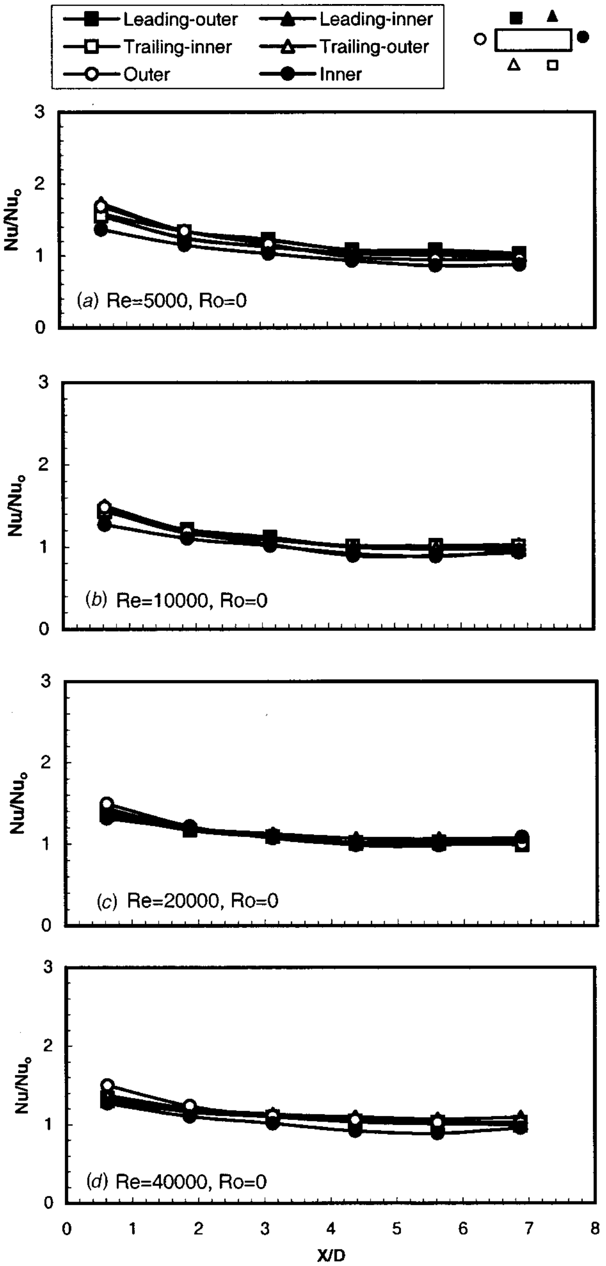

Fig. 5 Nusselt number ratio for stationary smooth case

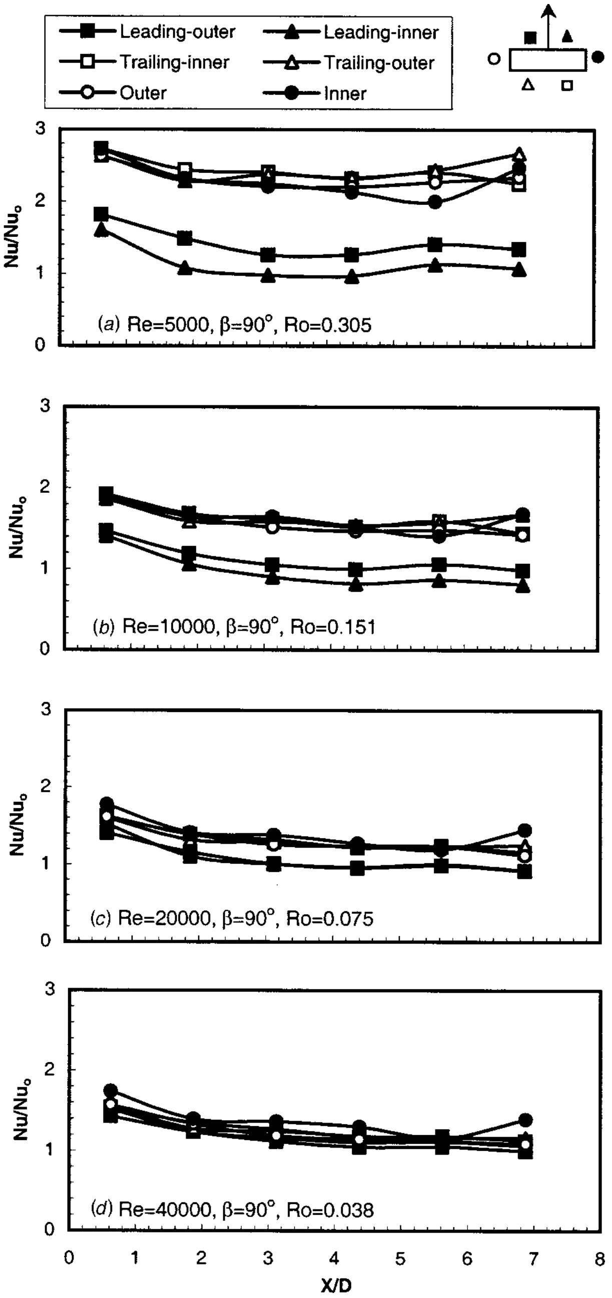

Fig. 6 Nusselt number ratio for rotation smooth case with $\beta=90$ deg

Figure 7 presents the results of the smooth rotation case with the channel oriented at $\beta=135$ deg with respect to the plane of rotation. Figure 7(*a*) shows that at a low Reynolds number (high rotation number), there are distinguishable differences in the heat transfer trends among the various surfaces. It can be seen that the trailing-outer and outer surface exhibit the highest heat transfer enhancement of all of the surfaces in the duct. This is attributed to the fact that these two surfaces are the primary recipients of the shifting of the cooler core flow under rotation. This phenomenon is illustrated in Fig. 4 of the preceding section. After the flow impinges on the trailing-outer and outer surfaces, it passes along the leading and trailing surfaces to the inner surface, where the heat transfer coefficient is the lowest, and the secondary flow slows down dramatically. Then the flow cycles again, passing from the leading most corner diagonally across the channel toward the trailing most corner. At a high rotation number, the inner surface heat transfer follows a trend quite similar to the stationary cases. It appears that this inner surface is barely affected by rotation. Both of the trailing surfaces have higher heat transfer coefficients than the leading surfaces. A new and interesting finding is the substantial difference in the heat transfer coefficient between the two trailing surfaces. Furthermore, this span-wise difference does not come into effect until nearly half-way through the channel for high rotation numbers (Ro$=0.305$). It is also shown that the leading surface heat transfer increased when compared to the orthogonal channel. The overall increase in heat transfer from nearly all surfaces can be attributed to the fact that twisting the channel greatly increased the linear distance along which the main Coriolis force is directed (from leading most to trailing most corner) and provides an overall better mixing than the $\beta=90$ deg. In the $\beta=90$ deg case, the principal Coriolis vector in the core region of the flow acts across only a short distance (the short width of the channel) and does not serve to mix the flow as well as the twisted channel.

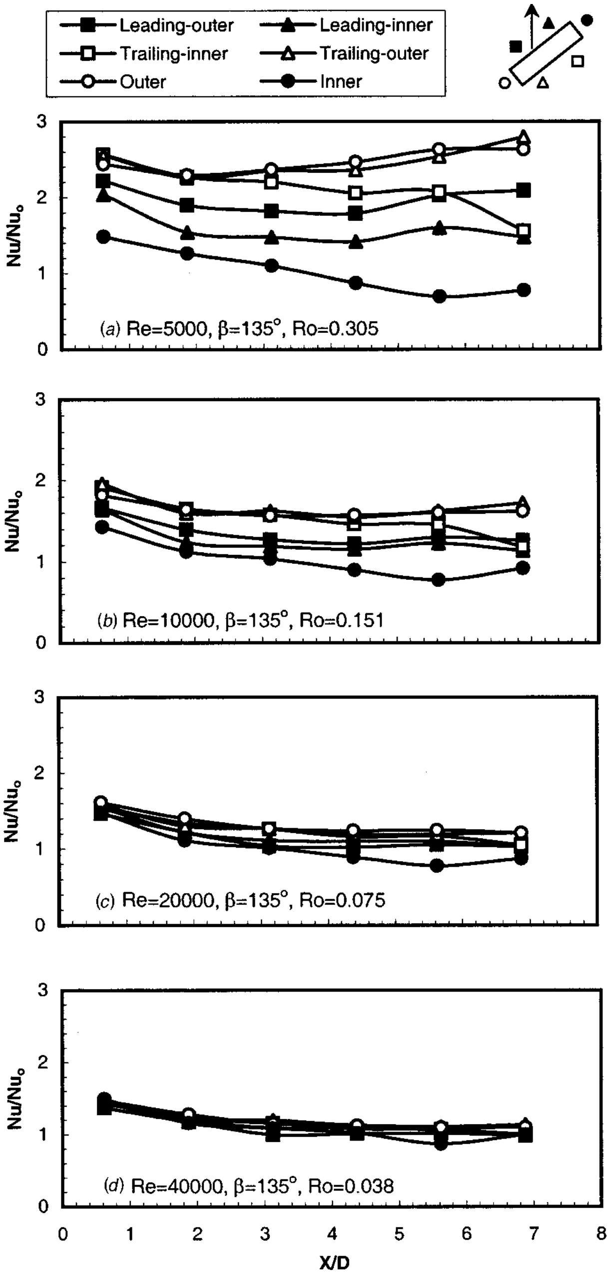

Fig. 7 Nusselt number ratio for rotation smooth case with $\beta = 135$ deg

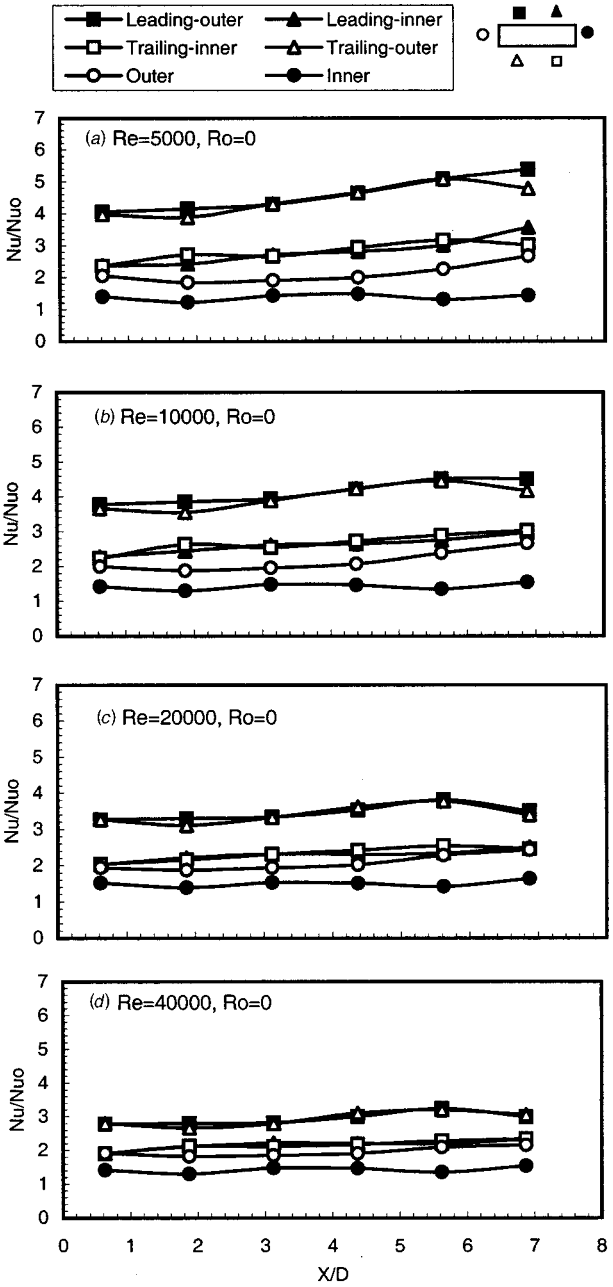

Fig. 8 Nusselt number ratio for stationary ribbed case

One evident contrast of the results of the $\beta = 135$ deg case (Fig. 7) compared to the $\beta = 90$ deg (Fig. 6) case is apparent in the side surfaces. For the twisted channel, the trend of the outer surface increases while the inner surface trend decreases with X/D. Furthermore, the inner surface decreases in a similar way as seen in the stationary case. The outer surface, which trails the inner surface, experiences a heat transfer enhancement of as much as three times that of the inner surface for the $\beta = 135$ deg case. This is due to the shift of the primary Coriolis induced flow vector from the center of the trailing surface in the $\beta = 90$ deg case to the trailing most corner in the $\beta = 135$ deg case. This trailing most corner is adjacent to the outer surface, and therefore the outer surface benefits greatly in heat transfer enhancement due to the twisting of the duct. This is desirable since the outer surface of the $\beta = 135$ deg case is closer to the trailing edge of the turbine blade, and thus is likely to experience a higher external heat flux than the inner surface. The inner surface interfaces with the side surface of the adjacent cooling passage, and therefore is less likely to be considered a critical surface.

Ribbed Channel Results. The data plots for the ribbed channel cases are presented in Figs. 8–10. Figure 8 shows the stationary ribbed channel data. It can be seen that the thermal entrance effect (decreasing to horizontal asymptote) that occurred in the smooth duct does not apply to the ribbed duct. This is due to the fact that the flow is no longer hydrodynamically fully developed immediately after the beginning of the test section, as was the case with the smooth duct. The ribs at the test section inlet trip the hydrodynamic boundary layer, and the flow is now considered not only thermally developing at the inlet, but also hydrodynamically developing at the inlet to the test section. In fact, the data curves tend to increase for the ribbed stationary case, whereas the plots decrease for the smooth stationary case.

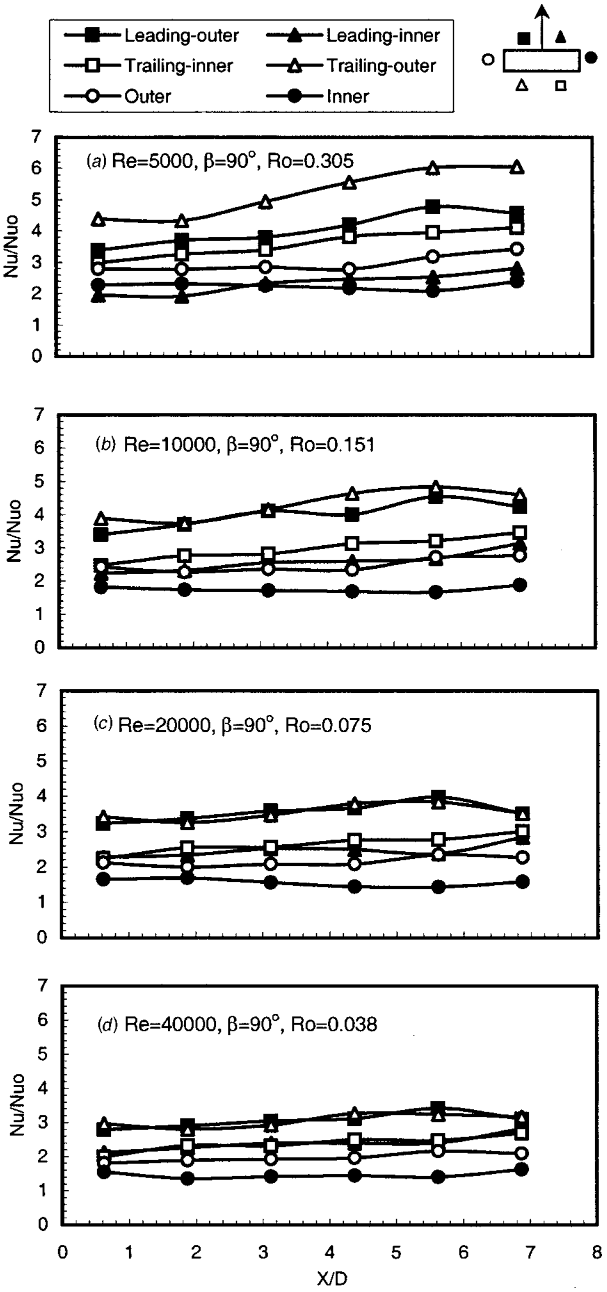

Fig. 9 Nusselt number ratio for rotation ribbed case with β=90 deg

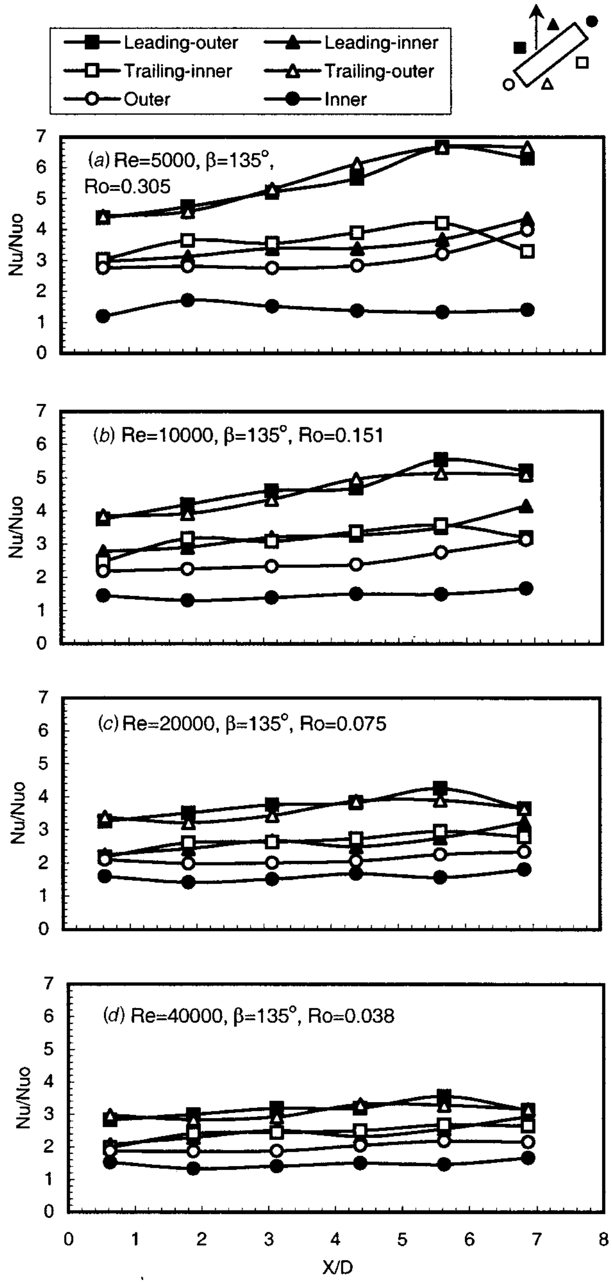

Fig. 10 Nusselt number ratio for rotation ribbed case with β=135 deg

An extremely important observation of this case is to note that the leading-outer and trailing-outer surfaces experience a significantly higher heat transfer enhancement than the leading-inner and trailing-inner surfaces. This is attributable to the orientation of the ribs. The ribs are attached such that the flow first meets the rib at the leading-outer and trailing-outer surfaces, which are the "upstream rib-half" surfaces (see Fig. 4). The second half of the rib, or "downstream rib-half" surface, follows as the rib extends toward the inner surface. Therefore, the ribs can be described as running from the outer surface to the inner surface at 45 deg to the main flow. As the flow first meets the rib at the upstream rib-half surface, the hydrodynamic boundary layer is tripped first at this point. The fluid at the ribbed wall is then channeled between the two ribs, flowing parallel to the ribs. The rib-induced secondary flow is fastest at the upstream rib-half surface, and slowing as it passes along the downstream rib-half surface toward the inner surface, which acts as a stagnation surface. The primary rib-half surface is able to convect more heat as the fluid passes quickly across the surface. When the flow slows along the downstream rib-half surface, less heat is convected away by the downstream rib-half surface. This explains why the leading-outer and trailing-outer (upstream rib-half) surfaces experience higher heat transfer than the leading-inner and trailing-inner (downstream rib-half) surfaces. Also, the outer surface has a higher heat transfer enhancement than the inner surface because it is peripherally affected by this faster, cooler, upstream rib-half tripped flow. In contrast, the inner surface experiences the heat transfer diminishing effects of flow stagnation.

The stationary rib cases show dependence on Reynolds number for the leading and trailing surfaces, however, the inner and outer surface exhibit nearly no dependence on Reynolds number. This is because as the Reynolds number increases, the rib is less effective at enhancing the heat transfer of the rectangular duct when compared with the stationary smooth circular duct correlation (i.e., normalized Nu decreases). Since the ribs are attached to the leading and trailing surfaces, they experience much more of the enhancing effects of the ribs, and conversely, are affected more by a reduced enhancement of heat transfer at higher Reynolds numbers.

Figure 9 shows the data plots for the ribbed duct under rotation with an orientation orthogonal to the plane of rotation ($\beta = 90$ deg). Looking to Fig. 9(*a*), we can see that at higher rotation numbers, there is clearly a higher heat transfer from the trailing-outer surface, and an increasing trend with X/D. Also, the trend is similar to that of the stationary case. For this reason, the rib-induced flow is observed to dominate the rotation induced secondary flow. Another important observation is that the leading-inner surface exhibits nearly the lowest heat transfer enhancement at the highest rotation number.

Figure 10 presents the plots for the ribbed, $\beta = 135$ deg twisted channel rotation experiments. We immediately can see that by twisting the channel, the leading-outer surface curve rises to meet the trailing-outer surface curve, with the trailing-outer surface maintaining nearly the same trend as seen in the $\beta = 90$ deg case. Even the trailing-outer surface trend increases slightly over that of the $\beta = 90$ deg case. From this behavior, it seems as though the effects of rotation for the twisted channel serve to better mix the flow than the orthogonal channel, and most of the surfaces benefit from the entirely constructive combining of rib and rotation-induced secondary flows for the $\beta = 135$ deg case. That is, all surfaces benefit except the inner surface, which is the only surface in the twisted channel to exhibit a lower heat transfer when compared with the orthogonal channel. This is expected because the heat transfer at the inner surface is now mitigated by not only its position as the leading most surface, but also by being situated at the end of the downstream rib-half. Since the inner surface is likely to be the surface exposed to the side wall of an adjacent cooling passage, a low heat transfer is not foreseen to be a significant problem. Therefore, we can say that the attachment scheme for continuous ribs chosen in this investigation will likely provide the most effective heat transfer augmentation at the necessary surfaces.

Streamwise Averaged Nusselt Number Ratio. An overall heat transfer coefficient for each surface is determined by averaging the streamwise data and then plotting the data as a function of rotation number. Figure 11 shows the streamwise averaged data for the smooth duct. Figure 11(*a*) ($\beta = 90$ deg) shows that the heat transfer at the trailing surfaces, the inner surface and the outer surface, is a strong function of rotation number. All four of these surfaces exhibit an increasing trend with increasing rotation number. The two leading surfaces show very little dependence on rotation number. Figure 11(*b*) ($\beta = 135$ deg) shows that the trailing surfaces are strongly dependent on rotation number. The inner surface is the only surface that shows virtually no dependence on rotation number for this case. A comparison of Figs. 11(*a*) and 11(*b*) reveals that the two leading surfaces for the $\beta = 135$ deg case are more dependent on rotation number than for the $\beta = 90$ deg case. These results are different than the results of the square channel of Dutta and Han [7] and the 2:1 rectangular channel investigated by Azad et al. [16]. A comparison of the 4:1 duct with the square and the 2:1 duct reveals that the aspect ratio significantly affects the rotational dependence on heat transfer, particularly for the leading surface. The square duct shows a decreasing trend, the 2:1 duct approaches a nearly horizontal trend, while the 4:1 duct shows an increasing trend. Therefore, as the channel becomes narrower, the heat transfer enhancement at the leading surfaces becomes more positive. It is now conclusive that the aspect ratio significantly affects the heat transfer distribution in the channel.

Figure 12 shows the streamwise averaged heat transfer enhancement for the ribbed duct. For the orthogonal channel of Fig. 12(*a*), the trailing surfaces and outer surface show an increasing trend with increasing rotation number. The trailing-outer surface exhibits the greatest dependence on rotation number, which is a result of the combination of rib and rotation-induced heat transfer enhancement. The leading surfaces exhibit little dependence on rotation number. Figure 12(*b*) shows that all surfaces are a function of rotation number except the inner surface. Furthermore, the twisted channel produces a nearly identical trend for the two up-

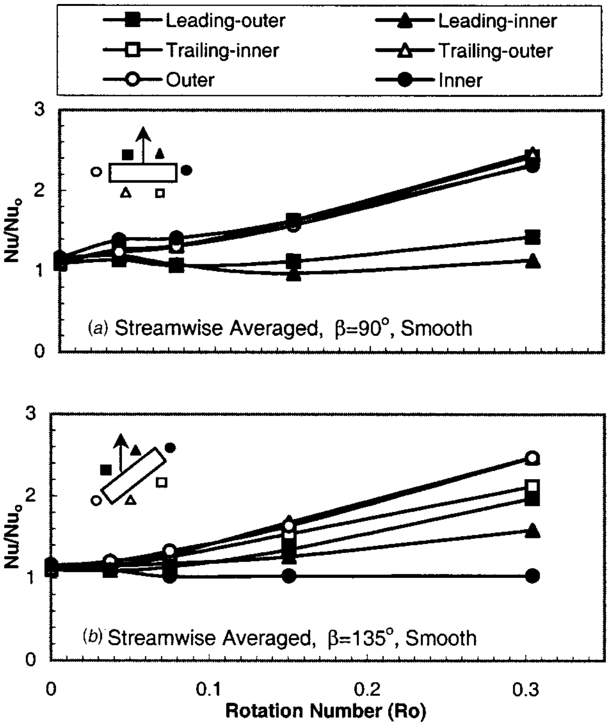

Fig. 11 Streamwise averaged Nusselt number ratio for smooth channel

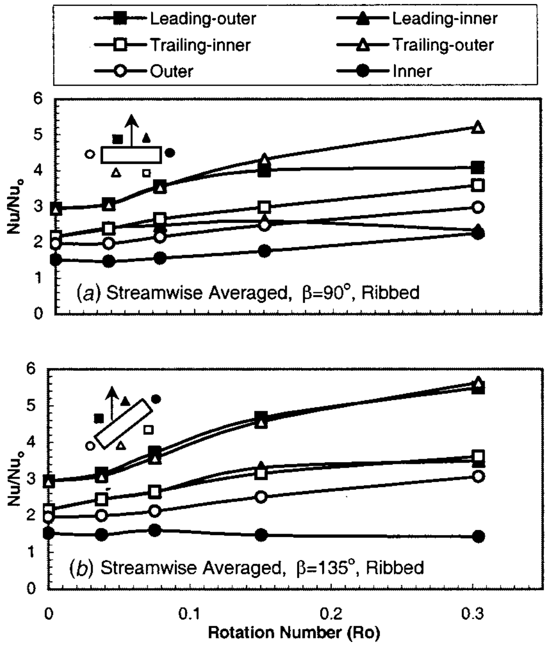

Fig. 12 Streamwise averaged Nusselt number ratio for ribbed channel

stream rib-half surfaces (leading-outer and trailing-outer). Also, the downstream rib-half surfaces (leading-inner and trailing-inner) show very similar trends. A comparison of Figs. 12(*a*) and 12(*b*) shows that the leading surfaces and the inner surface are positively affected by the channel orientation. The trailing surfaces and the outer surface appear to be unaffected by the channel orientation.

Conclusions

This investigation revealed that spanwise heat transfer differences of up to 25 percent for the smooth tilted channel and 50–75 percent for the ribbed channel exist across the leading and trailing surfaces. This observation should be addressed when designing the cooling channels of a gas turbine blade. In addition, the duct orientation significantly affects the leading, the inner, and the outer surfaces, yet does not have much effect on the trailing surfaces for both the smooth and ribbed cases. Furthermore, the smooth and ribbed case trailing surfaces and the smooth case side surfaces show a strong dependence on rotation number. Finally, the aspect ratio was determined to affect the leading surface heat transfer enhancement, where the enhancement increases as the channel becomes narrower. Therefore, this investigation has determined that spanwise variations in the heat transfer distribution of rectangular cooling passages exist and that the enhancement is a function of channel orientation, surface configuration, and aspect ratio.

Acknowledgments

The Advanced Gas Turbine Systems Research (AGTSR) program (project number SR-082) funded this experimental investigation under the supervision of the United States Department of Energy (DOE). The authors greatly appreciate the support of the AGTSR program and the DOE. Without such support, this research would not have been possible.

Nomenclature

A_p = surface area of copper plate (m^2)
D = hydraulic diameter (m)
e = rib height (m)
h = heat transfer coefficient (W/m^2 K)
k = thermal conductivity of coolant (W/mK)
L = length of duct (m)
Nu = regionally averaged Nusselt number, hD/k
Nu_o = Nusselt number in fully developed turbulent non-rotating tube flow without ribs
P = rib pitch (m)
Pr = Prandtl number
Q = heat transfer (W)
q''_{net} = net heat flux at wall (W/m^2)
R = mean rotating radius (m)
Re = Reynolds number, $\rho VD/\mu$
R_o = rotation number, $\Omega D/V$
T_{bx} = local coolant bulk temperature (K)
T_w = wall temperature (K)
V = bulk velocity in streamwise direction (m/s)
β = angle of channel orientation
Ω = rotational speed (rad/s)
α = rib angle
ρ = density of coolant (kg/m^3)
$(\Delta\rho/\rho)_i$ = coolant-to-wall density ratio at the inlet, $(\rho_w-\rho_{bi})/\rho_w=(T_w-T_{bi})/T_w$

References

[1] Han, J. C., and Park, J. S., 1988, ‘‘Developing Heat Transfer in Rectangular Channel With Rib Turbulators,’’ Int. J. Heat Mass Transf., **31**(1), pp. 183–195.
[2] Han, J. C., Zhang, Y. M., and Lee, C. P., 1991, ‘‘Augmented Heat Transfer in Square Channels With Parallel, Crossed, and V-Shaped Angled Ribs,’’ ASME J. Heat Transfer, **113**, pp. 590–596.
[3] Wagner, J. H., Johnson, B. V., and Hajek, T. J., 1991, ‘‘Heat Transfer in Rotating Passage With Smooth Walls and Radial Outward Flow,’’ ASME J. Turbomach., **113**, pp. 42–51.
[4] Wagner, J. H., Johnson, B. V., and Kooper, F. C., 1991, ‘‘Heat Transfer in Rotating Serpentine Passage With Smooth Walls,’’ ASME J. Turbomach., **113**(3), pp. 321–330.
[5] Parsons, J. A., Han, J. C., and Zhang, Y. M., 1995, ‘‘Effects of Model Orientation and Wall Heating Condition on Local Heat Transfer in a Rotating Two-Pass Square Channel With Rib Turbulators,’’ Int. J. Heat Mass Transf., **38**(7), pp. 1151–1159.
[6] Johnson, B. V., Wagner, J. H., Steuber, G. D., and Yeh, F. C., 1994, ‘‘Heat Transfer in Rotating Serpentine Passage With Selected Model Orientations for Smooth or Skewed Trip Walls,’’ ASME J. Turbomach., **116**, pp. 738–744.
[7] Dutta, S., and Han, J. C., 1996, ‘‘Local Heat Transfer in Rotating Smooth and Ribbed Two-Pass Square Channels with Three Channel Orientations,’’ ASME J. Heat Transfer, **118**, pp. 578–584.
[8] Al-Qahtani, M., Jang, Y., Chen, H. C., and Han, J. C., 2001, ‘‘Prediction of Flow and Heat Transfer in Rotating Two-Pass Rectangular Channels with 45 deg Rib Turbulators,’’ ASME Paper No. 2001-GT-0187.
[9] Taslim, M. E., Rahman, A., and Spring, S. D., 1991, ‘‘An Experimental Investigation of Heat Transfer Coefficients in a Spanwise Rotating Channel With Two Opposite Rib-Roughened Walls,’’ ASME J. Turbomach., **113**, pp. 75–82.
[10] Taslim, M. E., Bondi, L. A., and Kercher, D. M., 1991, ‘‘An Experimental Investigation of Heat Transfer in an Orthogonally Rotating Channel Roughened With 45 deg Criss-Cross Ribs on Two Opposite Walls,’’ ASME J. Turbomach., **113**, pp. 346–353.
[11] Willett, F. T., and Bergles, A. E., 2000, ‘‘Heat Transfer in Rotating Narrow Rectangular Ducts with Heated Sides Oriented at 60 deg to the R-Z Plane,’’ ASME Paper No. 2000-GT-224.
[12] Han, J. C., Dutta, S., and Ekkad, S. V., 2000, *Gas Turbine Heat Transfer and Cooling Technology*, Taylor and Francis, New York.
[13] Han, J. C., and Dutta, S., 2001, ‘‘Recent Developments in Turbine Blade Internal Cooling,’’ in *Heat Transfer in Gas Turbine Systems*, R. J. Goldstein, ed., Ann. N.Y. Acad. Sci., **934**, pp. 162–178.
[14] Dutta, S., and Han, J. C., 1998, ‘‘Rotational Effects on the Turbine Blade Coolant Passage Heat Transfer,’’ Annu. Rev. Heat Transfer, **9**, pp. 268–314.
[15] Kline, S. J., and McClintock, F. A., 1953, ‘‘Describing Uncertainties in Single-Sample Experiments,’’ Mech. Eng. (Am. Soc. Mech. Eng.), **75**, pp. 3–8.
[16] Azad, G. S., Uddin, J. M., Han, J. C., Moon, H. K., and Glezer, B., 2001, ‘‘Heat Transfer in a Two-Pass Rectangular Rotating Channel with 45 deg Angled Rib Turbulators,’’ ASME Paper No. 2001-GT-0186.

B. Weigand
Universität Stuttgart,
Institut für Thermodynamik der Luft- und Raumfahrt,
Pfaffenwaldring 31,
70569 Stuttgart, Germany

T. Schwartzkopff
Universität Stuttgart,
Institut für Aerodynamik und Gasdynamik,
Pfaffenwaldring 21,
70569 Stuttgart, Germany

T. P. Sommer
ALSTOM Power Generation Ltd,
5401 Baden, Switzerland

A Numerical Investigation of the Heat Transfer in a Parallel Plate Channel With Piecewise Constant Wall Temperature Boundary Conditions

For turbulent flows in ducts, streamwise heat conduction effects within the flow can be important for low Prandtl number fluids (liquid metals). The paper presents a numerical investigation of the influence of axial heat conduction within the flow on the heat transfer for hydrodynamically fully developed flow. The calculations have been carried out for a semi-infinite heated section as well as for a heated section of finite length. Additionally, by considering different models for calculating the turbulent heat flux, the normally used assumption that the eddy diffusivity in axial and normal direction are the same was investigated. [DOI: 10.1115/1.1482085]

Keywords: *Channel Flow, Forced Convection, Heat Transfer, Liquid Metals, Turbulence*

1 Introduction

Heat transfer for hydrodynamically fully developed channel flows is of theoretical interest and of technical importance. Normally, the effect of streamwise conduction within the flow on the heat transfer to a fluid flowing inside a duct can be neglected. The classical Graetz problem deals with heat transfer in the thermally developing region under such conditions [6,7,14].

However, for flows with small Péclet numbers, streamwise heat conduction effects in the fluid become increasingly important as Pe_D decreases. This is the case, for example, in compact heat exchangers where liquid metals are used as working fluids. Additionally, the effect of streamwise heat conduction within the flow might be important if the heated section is small in size compared to the hydrodynamic diameter [23].

In the past, many analytical and numerical investigations have been carried out which deal with the solution of the extended Graetz problem (considering axial heat conduction in the fluid) for thermally developing laminar flows in ducts. Extensive literature reviews on this subject can be found in [17,16,8]. Numerical investigations which deal with the extended Graetz problem for laminar flow in a pipe or a parallel plate channel are given for example in [8,13].

Although axial heat conduction can be ignored for turbulent convection in ordinary fluids and gases, with liquid metals this is not always be justified for small Reynolds number flows. In fact because of the very low Prandtl numbers for liquid metals ($0.001<\mathrm{Pr}<0.06$) the Péclet number can be smaller than ten in turbulent duct flows. A literature review about the convective heat transfer in liquid metals can be found in [16]. Lee [12], for example, studied the extended Graetz problem in turbulent pipe flow. He found that for Péclet numbers below 100, axial heat conduction in the fluid becomes important in the thermal entrance region. For a turbulent flow inside a parallel plate channel, the effect of axial heat conduction within the fluid was analyzed by Faggiani and Gori [3]. They solved numerically the energy equation for a constant heat flux boundary condition. Weigand [20] studied analytically the effect of axial heat conduction in a parallel plate channel and in a circular pipe for laminar and turbulent flows for the case of a constant wall temperature. For a finite heated section, Weigand et al. [23] obtained an analytical solution for the temperature field and the Nusselt number for a duct with piecewise constant heat flux at the wall. This investigation showed that axial heat conduction effects can also be important for larger Péclet numbers if the heated section is relatively short in length.

All the papers mentioned above used the fundamental assumption that gradient transport of the form $\overline{u_i'\Theta'}\sim\partial\Theta/\partial x_i$ holds and that the eddy diffusivities in the radial and axial directions are the same. Additionally, all papers used the concept of a turbulent Prandtl number to obtain the turbulent thermal diffusivity from the eddy viscosity as $\alpha_t=\nu_t'/\mathrm{Pr}_t$. As a direct consequence of these assumptions, the streamwise turbulent heat flux is only a function of the streamwise temperature gradient. Very small or zero streamwise turbulent heat fluxes will always be predicted if the streamwise temperature gradient is small or zero, respectively. As far back as 1949 Batchelor [1] suggested that the streamwise component of the turbulent heat flux should also be a function of the cross-stream temperature gradient and vice versa. Evidence of this effect has been obtained by direct numerical simulation, DNS, results which show significant values for the streamwise turbulent heat flux even though the streamwise temperature gradient is negligible compared to the cross-stream gradient [11].

Having observed that axial heat conduction effects can be important for low Péclet numbers as well as for the combination of moderate Péclet numbers and a short heated section, the proper modeling of the axial turbulent heat flux can be important. Algebraic models for the turbulent heat fluxes such as proposed, for example, by Gibson and Launder [5] improve the prediction of the axial turbulent heat flux. However, even if they are simplified using the assumption of equilibrium turbulence, they still require the solution of a linear system of equations for the turbulent heat fluxes. In solving this system of equations, a situation can occur where the system of equations becomes singular for certain combinations of the Reynolds stresses and mean temperature gradients, similar to the singularity noted by Gatski and Speziale [4] for algebraic Reynolds stress models. More recently, models based on a more general gradient transport type of the form proposed by

---

Contributed by the Heat Transfer Division for publication in the JOURNAL OF HEAT TRANSFER. Manuscript received by the Heat Transfer Division July 10, 2001; revision received March 14, 2002. Associate Editor: K. S. Ball.

Batchelor have been developed [18,24]. These models provide the advantages of algebraic models while remaining relatively simple and robust. Furthermore such models are more tractable for analytical work.

Using such a model for the turbulent heat flux, the present paper investigates the effect of axial heat conduction and particularly of the axial turbulent heat flux. The energy equation for hydrodynamically fully developed duct flow and a heated section is solved numerically using different models for the turbulent heat fluxes.

Additionally, the paper presents the effect of a finite heated section with a constant wall temperature. To the best knowledge of the authors of the present paper, both above mentioned topics have not been considered in literature before.

2 Analysis

Figure 1 shows the geometrical configuration and the coordinate system. The flow enters the duct with a hydrodynamically fully developed laminar or turbulent velocity profile and with a uniform temperature distribution T_0 for $x \to -\infty$. For $-\Delta x_{\mathrm{heat}}/2 < x < \Delta x_{\mathrm{heat}}/2$ the channel is uniformly heated by applying a constant wall temperature. A second case with constant wall temperature at $0 < x < +\infty$ is also considered. The characteristic length h denotes half of the channel height. The physical properties (c_p, ρ, k) of the fluid are considered to be constant.

2.1 Energy Equation. The energy equation for a hydrodynamically fully developed flow is given by

$$\rho c_p \left(u \frac{\partial T}{\partial x} \right) = \frac{\partial}{\partial x}\left(k \frac{\partial T}{\partial x} - \rho c_p \overline{u'T'} \right) + \frac{\partial}{\partial y}\left(k \frac{\partial T}{\partial y} - \rho c_p \overline{v'T'} \right). \tag{1}$$

The boundary conditions for Eq. (1) are as follows:

$$\begin{gathered} y=0 : \partial T/\partial y = 0 \\ y=h : x < -\Delta x_{\mathrm{heat}}/2,\ \Delta x_{\mathrm{heat}}/2 < x \quad T = T_0 \\ -\Delta x_{\mathrm{heat}}/2 < x < \Delta x_{heat}/2 \quad T = T_w \\ \lim_{x \to -\infty} T = T_0 \end{gathered} \tag{2}$$

After introducing the following nondimensional quantities into Eqs. (1)–(2)

$$\tilde{x} = \frac{x}{h}, \quad \tilde{y} = \frac{y}{h}, \quad \tilde{u} = \frac{u}{\overline{u}_0}, \quad \Theta = \frac{T - T_0}{T_w - T_0},$$
$$\overline{\tilde{u}'\Theta'} = \frac{\overline{u'T'}}{\overline{u}_0 (T_w - T_0)}, \quad \overline{\tilde{v}'\Theta'} = \frac{\overline{v'T'}}{\overline{u}_0 (T_w - T_0)}, \quad a = \frac{k}{\rho c_p},$$
$$\mathrm{Pe}_h = \frac{\overline{u}_0 h}{a} \tag{3}$$

the energy equation and the relating boundary conditions can be written as

$$\tilde{u}\mathrm{Pe}_h \frac{\partial \Theta}{\partial \tilde{x}} = \frac{\partial}{\partial \tilde{x}}\left(\frac{\partial \Theta}{\partial \tilde{x}} - \mathrm{Pe}_h \overline{\tilde{u}'\Theta'} \right) + \frac{\partial}{\partial \tilde{y}}\left(\frac{\partial \Theta}{\partial \tilde{y}} - \mathrm{Pe}_h \overline{\tilde{v}'\Theta'} \right). \tag{4}$$

$$\begin{gathered} \tilde{y}=0 : \partial \Theta/\partial \tilde{y} = 0 \\ \tilde{y}=1 : \tilde{x} < -\tilde{x}_{\mathrm{heat}}/2, \tilde{x}_{\mathrm{heat}}/2 < \tilde{x} \quad \Theta = 0 \\ -\tilde{x}_{\mathrm{heat}}/2 < \tilde{x} < \tilde{x}_{\mathrm{heat}}/2 \quad \Theta = 1 \\ \lim_{\tilde{x} \to -\infty} \Theta = 0 \end{gathered} \tag{5}$$

The turbulent heat fluxes $\overline{\tilde{u}'\Theta'}$ and $\overline{\tilde{v}'\Theta'}$ appearing in Eq. (4) have to be calculated from the mean quantities of the flow. Batchelor [1] proposed a turbulent eddy diffusion tensor. Thus, the turbulent heat fluxes can be calculated from

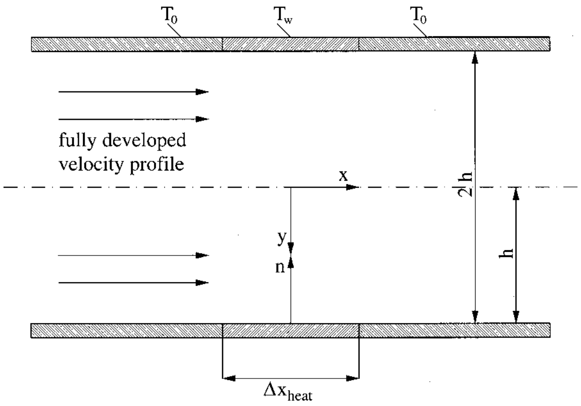

Fig. 1 Geometry and coordinate system

$$\begin{pmatrix} -\overline{\tilde{u}'\Theta'} \\ -\overline{\tilde{v}'\Theta'} \end{pmatrix} = \begin{pmatrix} D_{11} & D_{12} \\ D_{21} & D_{22} \end{pmatrix} \cdot \begin{pmatrix} \dfrac{\partial \Theta}{\partial \tilde{x}} \\ \dfrac{\partial \Theta}{\partial \tilde{y}} \end{pmatrix} \tag{6}$$

All models considered in the present study can be written in this form. Introducing Eq. (6) into Eq. (4), the energy equation obtains the following form

$$\tilde{u}\mathrm{Pe}_h \frac{\partial \Theta}{\partial \tilde{x}} = \frac{\partial}{\partial \tilde{x}}\left[(1 + \mathrm{Pe}_h D_{11}) \frac{\partial \Theta}{\partial \tilde{x}} \right] + \frac{\partial}{\partial \tilde{x}}\left[\mathrm{Pe}_h D_{12} \frac{\partial \Theta}{\partial \tilde{y}} \right] + \frac{\partial}{\partial \tilde{y}}\left[(1 + \mathrm{Pe}_h D_{22}) \frac{\partial \Theta}{\partial \tilde{y}} \right] + \frac{\partial}{\partial \tilde{y}}\left[\mathrm{Pe}_h D_{21} \frac{\partial \Theta}{\partial \tilde{x}} \right]. \tag{7}$$

As one can see from Eq. (7), the "ansatz" by Eq. (6) results in mixed second derivatives in the energy equation. This fact will be discussed later in more detail. For a hydrodynamically fully developed flow and the turbulent heat flux models in the herein discussed form, the D_{ij} are only depending on $\tilde{y}$. Therefore, one can simplify Eq. (7) to

$$\left[\tilde{u}\mathrm{Pe}_h - \mathrm{Pe}_h \frac{\partial D_{21}}{\partial \tilde{y}} \right] \frac{\partial \Theta}{\partial \tilde{x}} = \frac{\partial}{\partial \tilde{x}}\left[(1 + \mathrm{Pe}_h D_{11}) \frac{\partial \Theta}{\partial \tilde{x}} \right] + \frac{\partial}{\partial \tilde{y}}\left[(1 + \mathrm{Pe}_h D_{22}) \frac{\partial \Theta}{\partial \tilde{y}} \right] + \mathrm{Pe}_h [D_{12} + D_{21}] \frac{\partial^2 \Theta}{\partial \tilde{x} \partial \tilde{y}}. \tag{8}$$

2.2 Turbulent Heat Flux Models. In the present study two different models have been used in order to calculate the eddy diffusion tensor D_{ij} in Eq. (6). The first model is based on the simple gradient transport model with a scalar eddy diffusivity for which $D_{ij} = \tilde{\alpha}_t \delta_{ij}$ where a turbulent Prandtl number is used to calculate $\tilde{\alpha}_t$.

The second model is a simplified form of the explicit algebraic heat-flux model (EAHF) model by So and Sommer [18]. Here each element of D_{ij} is a function of the mean flow field and in general D_{ij} is fully occupied and non-symmetric. This more general model generates a turbulent heat flux in *x*-direction $\overline{u'\Theta'}$ even when the temperature gradient in *x*-direction is zero. Evidence for this effect has been obtained by DNS calculations. Note that the simple formulation is a special case combined in this.

2.2.1 The Isotropic Turbulent Heat Flux Model. Using the concept of the turbulent Prandtl number, the turbulent heat fluxes can be calculated by

$$\begin{pmatrix} -\overline{\tilde{u}'\Theta'} \\ -\overline{\tilde{v}'\Theta'} \end{pmatrix} = \begin{pmatrix} -\dfrac{\mathrm{Pr}}{\mathrm{Pr}_t}\tilde{\epsilon}_m\dfrac{\epsilon_{hx}}{\epsilon_{hn}} & 0 \\ 0 & -\dfrac{\mathrm{Pr}}{\mathrm{Pr}_t}\tilde{\epsilon}_m \end{pmatrix} \cdot \begin{pmatrix} \dfrac{\partial\Theta}{\partial\tilde{x}} \\ \dfrac{\partial\Theta}{\partial\tilde{y}} \end{pmatrix} \tag{9}$$

where D_{12} and D_{21} are identically zero for this simple model. For calculating the turbulent Prandtl number Pr_t the model of Kays and Crawford as given by Weigand et al. [22] has been used.

$$\mathrm{Pr}_t = \frac{1}{\dfrac{1}{2\mathrm{Pr}_{t\infty}} + C\mathrm{Pe}_t\sqrt{\dfrac{1}{\mathrm{Pr}_{t\infty}}} - (C\mathrm{Pe}_t)^2\left[1-\exp\left(-\dfrac{1}{C\mathrm{Pe}\sqrt{\mathrm{Pr}_{t\infty}}}\right)\right]} \tag{10}$$

$$\text{with}\quad \mathrm{Pe}_t = \mathrm{Pr}\,\frac{\epsilon_m}{\nu} \tag{11}$$

$$\mathrm{Pr}_{t\infty} = 0.85 + \frac{D}{\mathrm{Pr}\;\mathrm{Re}_D^{0.888}} \tag{12}$$

$$\text{and}\quad D = 100,\quad C = 0.3 \tag{13}$$

The eddy viscosity ϵ_m has been calculated using the Nikuradse mixing length distribution with the van Driest damping factor [10].

$$\epsilon_m = l^2\left|\frac{\partial u}{\partial y}\right| \tag{14}$$

$$l = h\left[0.14 - 0.08\left(\frac{y}{h}\right)^2 - 0.06\left(\frac{y}{h}\right)^4\right] \tag{15}$$

The relation $\epsilon_{hx}/\epsilon_{hn}$ specifies the ratio of axial to normal thermal diffusivity. This ratio has been set to one. This is a commonly used assumption (see for example [12,2]). Note that $\overline{u'\Theta'} = 0$ when $\partial\Theta/\partial\tilde{x} = 0$.

2.2.2 The Explicit Algebraic Heat-Flux (EAHF) Model. The model is given in [18,19]. It can be applied for a wide range of molecular Prandtl numbers. The general form of the EAHF model is given by:

$$-\overline{\tilde{u}_i'\theta'} = \tilde{\alpha}_t\frac{\partial\Theta}{\partial\tilde{x}_i} - \frac{1}{C_{1\theta}}\sqrt{\frac{k}{\epsilon}\frac{\overline{\theta^2}}{\epsilon_\theta}}\left[(2\tilde{\epsilon}_m + (1-C_{2\theta})\tilde{\alpha}_t)\overline{S}_{ik} + (1-C_{2\theta})\tilde{\alpha}_t\overline{\omega}_{ik}\right]\frac{\partial\Theta}{\partial\tilde{x}_k}. \tag{16}$$

with

$$\overline{S}_{ij} = \frac{1}{2}\left(\frac{\partial\tilde{u}_i}{\partial\tilde{x}_j} + \frac{\partial\tilde{u}_j}{\partial\tilde{x}_i}\right) \tag{17}$$

$$\overline{\omega}_{ij} = \frac{1}{2}\left(\frac{\partial\tilde{u}_i}{\partial\tilde{x}_j} - \frac{\partial\tilde{u}_j}{\partial\tilde{x}_i}\right). \tag{18}$$

For a hydrodynamic fully developed two dimensional flow these tensors become:

$$\overline{S} = \frac{1}{2}\begin{bmatrix} 0 & \partial\tilde{u}/\partial\tilde{y} \\ \partial\tilde{u}/\partial\tilde{y} & 0 \end{bmatrix} \tag{19}$$

$$\overline{\omega} = \frac{1}{2}\begin{bmatrix} 0 & \partial\tilde{u}/\partial\tilde{y} \\ -\partial\tilde{u}/\partial\tilde{y} & 0 \end{bmatrix}. \tag{20}$$

Now one can calculate the turbulent heat fluxes $\overline{\tilde{v}'\theta'}$ and $\overline{\tilde{u}'\theta'}$ as

$$\begin{pmatrix} -\overline{\tilde{u}'\Theta'} \\ -\overline{\tilde{v}'\Theta'} \end{pmatrix} = \begin{pmatrix} \tilde{\alpha}_t - \dfrac{1}{C_{1\theta}}\sqrt{\dfrac{k}{\epsilon}\dfrac{\overline{\theta^2}}{\epsilon_\theta}}\left((\tilde{\epsilon}_m + (1-C_{2\theta})\tilde{\alpha}_t)\dfrac{\partial\tilde{u}}{\partial\tilde{y}}\right) \\ -\dfrac{1}{C_{1\theta}}\sqrt{\dfrac{k}{\epsilon}\dfrac{\overline{\theta^2}}{\epsilon_\theta}}\left(\tilde{\epsilon}_m\dfrac{\partial\tilde{u}}{\partial\tilde{y}}\right) \quad \tilde{\alpha}_t \end{pmatrix} \cdot \begin{pmatrix} \dfrac{\partial\Theta}{\partial\tilde{x}} \\ \dfrac{\partial\Theta}{\partial\tilde{y}} \end{pmatrix} \tag{21}$$

where the following abbreviations have been used:

$$\tilde{\alpha}_t = c_\lambda f_\lambda k\sqrt{\frac{k}{\epsilon}\frac{\overline{\partial^2}}{\epsilon_\theta}} \tag{22}$$

$$\tilde{\epsilon}_m = c_\mu f_\mu\frac{k^2}{\epsilon}. \tag{23}$$

with

$$f_\lambda = (1-f_{\lambda l})\frac{C_{\lambda l}}{\mathrm{Re}_t^{1/4}} + f_{\lambda l}, \quad f_{\lambda l} = (1-e^{-n^+/A^+})^2,$$

$$f_\mu = \left(1 + \frac{3.45}{\sqrt{\mathrm{Re}_t}}\right)\cdot\tanh\left(\frac{n^+}{115}\right) \tag{24}$$

$$C_{\lambda l} = \begin{cases} \dfrac{0.4}{\mathrm{Pr}^{1/4}} & \text{for } \mathrm{Pr} < 0.1 \\ \dfrac{0.7}{\mathrm{Pr}} & \text{for } \mathrm{Pr} \geqslant 0.1 \end{cases} \tag{25}$$

$$A+ = \begin{cases} \dfrac{10}{\mathrm{Pr}} & \text{for } \mathrm{Pr} < 0.25 \\ \dfrac{39}{\mathrm{Pr}^{1/16}} & \text{for } \mathrm{Pr} \geqslant 0.25 \end{cases} \tag{26}$$

$$\mathrm{Re}_t = \frac{k^2}{\nu\epsilon} \tag{27}$$

and with the constants

$$c_\mu = 0.096,\quad c_\lambda = 0.095,\quad C_{1\theta} = 3.28,\quad C_{2\theta} = 0.4$$

In the original formulation of the model, one has to solve two additional partial differential equations for $(\overline{\theta^2}, \epsilon_\theta)$. However, this approach can be simplified. Therefore, one defines the following function R

$$R = \frac{\overline{\theta^2}/\epsilon_\theta}{k/\epsilon}. \tag{28}$$

The turbulent Prandtl number relates the eddy viscosity to the turbulent heat diffusion and can be written in the following form by using the Eqs. (22)–(23)

$$\mathrm{Pr}_t = C_\star R^{-1/2} \tag{29}$$

$$\text{with}\quad C_\star = \frac{c_\mu f_\mu}{c_\lambda f_\lambda}. \tag{30}$$

For the calculation of the turbulent Prandtl number the model of [22] has been used.

The equations $\overline{\theta^2}$ and α_t can now be obtained by

$$\frac{\overline{\theta^2}}{\epsilon_\theta} = \frac{C_\star^2}{\mathrm{Pr}_t^2}\frac{k}{\epsilon} \tag{31}$$

Table 1 Comparison of Nu_∞ for laminar flow with the predictions of [13,21]

Pe_D	Nu_∞			Error compared to [21]
	Analytical		Numerical	$((Nu_\infty)_N-(Nu_\infty)_A)/(Nu_\infty)_A$
	Nguyen [13]	Weigand [21]	Present calc.	[%]
1	8.0054	8.0058	8.0046	-0.0150
2	7.9165	7.9164	7.9114	-0.0632
5	7.7471	7.7468	7.7390	-0.1007
10	7.6306	7.6306	7.6201	-0.1376
20	7.5693	7.5692	7.5564	-0.1691
50	7.5457	7.5456	7.5347	-0.1445
100	7.5419	7.5407	7.5312	-0.1260
1000	7.5407	7.5407	7.5300	-0.1419

$$\tilde{\alpha}_t=c_\lambda f_\lambda \frac{k^2}{\epsilon}\frac{C_\star}{\mathrm{Pr}_t}. \tag{32}$$

3 Results and Discussion

3.1 Numerical Scheme. The energy Eq. (8) is a linear partial differential equation which has been solved by a relaxation scheme with a typical relaxation parameter of 0.7–0.9, depending on the used Pe_D number. The equation is solved by Brandt's FAS multi-grid method which is described in detail in the Numerical Recipes [15]. The computational domain is discretised using a Cartesian grid. The grid is refined by an analytical stretching function at the wall boundaries and around the temperature discontinuities. All derivatives are discretised by using central finite differences. Typical grid sizes range from 257×65 to 2049×513, depending on the Pe_D number used. The boundary conditions are directly applied to the equation, so no wall functions have to be used.

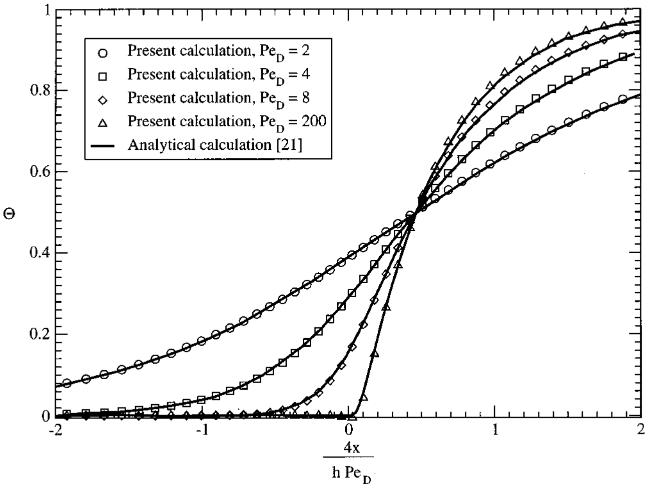

Fig. 2 Comparison of the numerically obtained fluid temperature at $\tilde{y}=0$ with the analytical solution for a laminar flow. Grid: 257×65 points. Heating: half infinite.

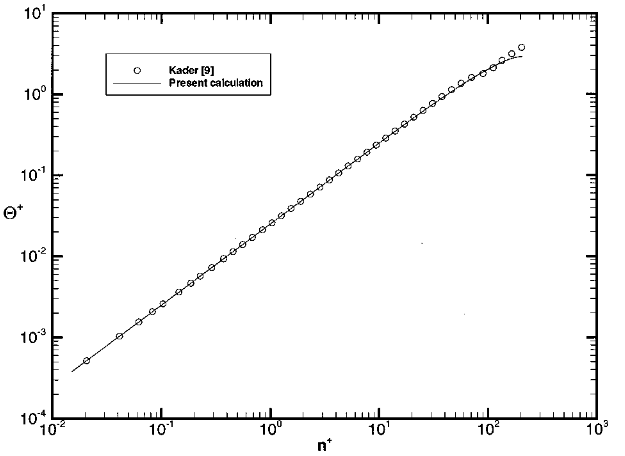

Fig. 3 Comparison of the numerically obtained fluid temperature $\Theta^+(y^+)$ with the formula given by Kader [9] for $Re_D=13000$, Pr=0.025 and $Re_\tau=206.8$. Resolution of the grid used in the computation 2049×257.

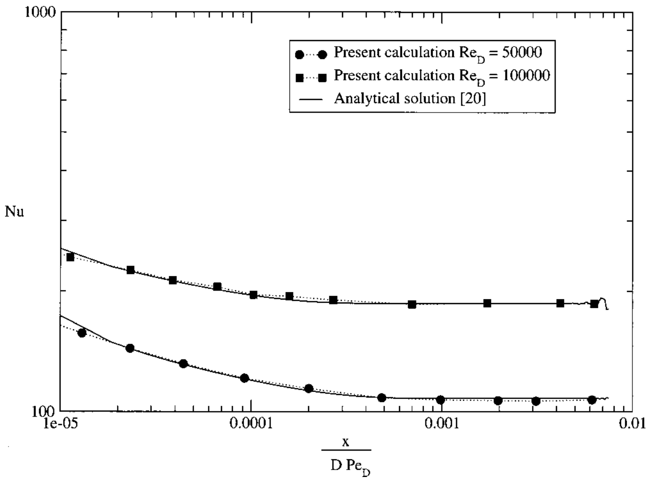

Fig. 4 Comparison of numerically calculated and analytical Nusselt number for turbulent flow. Constant Prandtl number Pr=0.72. Grid 513×65. Heating: half infinite.

3.2 Accuracy and Validation. For the validation of the numerical scheme and the grids used in the calculations, comparisons have been made between the present calculations and data available in the literature. Most of the results presented in the literature are given for laminar flows. To the knowledge of the authors of the present paper, there is only one paper dealing with turbulent duct flow with Dirichlet wall boundary conditions and axial heat conduction effects [20]. Furthermore, these results are available for a half infinite heated section.

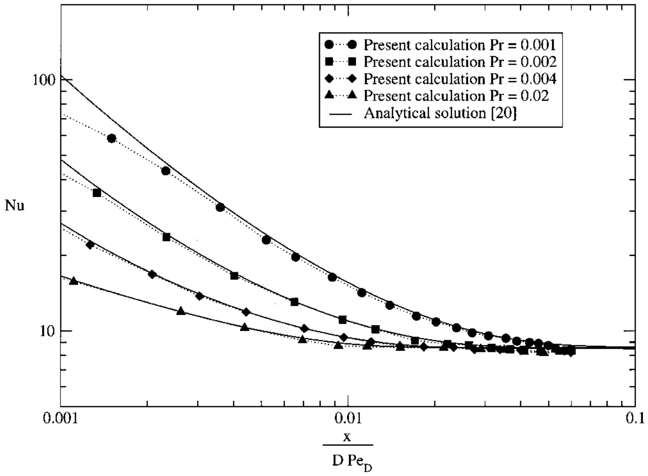

Fig. 5 Comparison of numerically calculated and analytical Nusselt number for turbulent flow. Constant Reynolds number $Re_D=5000$. Grid 513×65. Heating: half infinite.

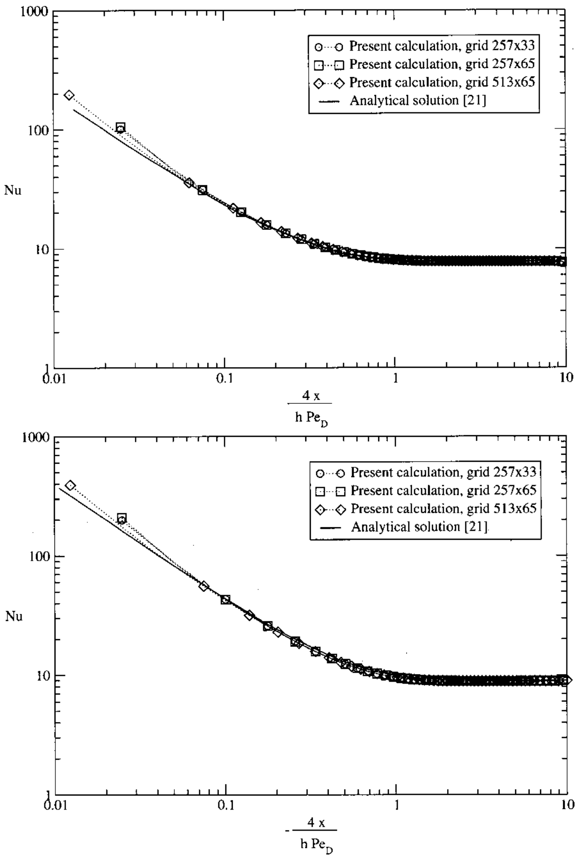

Fig. 6 Comparison of a numerical calculated local Nusselt number for laminar flow on different grids with an analytical solution at $x/(h\mathrm{Pe}_h)>0$ (top) and $x/(h\mathrm{Pe}_h)<0$ (bottom) for $\mathrm{Pe}_D=4$. Heating: half infinite.

3.2.1 Comparison of Nu_∞ Values for Laminar Flow. The validation has been started by a comparison of some analytically obtained Nu_∞ numbers [13,21]. The definition of the Nusselt number is given by

$$\mathrm{Nu}=\frac{-4\left.\frac{\partial\Theta}{\partial\tilde{y}}\right|_w}{\Theta_m-\Theta_w} \tag{33}$$

For thermally fully developed flow the numerator and denominator of Eq. (33) tend to zero, leading to a finite value of the Nusselt number. The prediction of Nu_∞ by numerical methods for constant wall temperature boundary conditions is a useful testcase because of this behavior in equation (33). In order to predict Nu_∞ accurately 6000 steps on a single-grid solver have been calculated after the solution on the multi-grid solver has been converged. The residual was then of the order of $\mathcal{O}(10^{-8})$. In Table 1 a comparison of the numerically obtained values compared to the values given in literature is given. As one can see, the numerically obtained values are in excellent agreement with the analytical values and the difference is always smaller than 0.2 percent.

3.2.2 Comparison of Temperature Profiles for Laminar Flow. In a next step some analytically obtained laminar temperature profiles [21] have been compared with numerical calculations. In Fig. 2 the temperature profiles at the middle of the channel ($\tilde{y}=0$) are shown for different Péclet numbers. The numerical predicted profiles are compared with analytical predictions. As it can be seen from Fig. 2 the numerical predictions are in excellent agreement with the analytical solution. Furthermore one can see how the influence of axial heat conduction decreases as the Péclet number increases.

3.2.3 Comparison of Temperature Profiles for Turbulent Flow. In [9] Kader gives an semiempirical formula for the dimensionless temperature profiles $\theta^+(n^+)$ in tube or channel flows which holds for Pr numbers from 6×10^{-3} to 40×10^3 and which was validated against numerous experimental data. As test case a flow with $\mathrm{Re}_D=13000$, $\mathrm{Pr}=0.0025$ and $\mathrm{Re}_\tau=206.8$ is used. In Fig. 3 the numerical results are plotted against the semiempirical correlation. As it can be seen, the numerical results are in excellent agreement with the given formula and thus with experimental data.

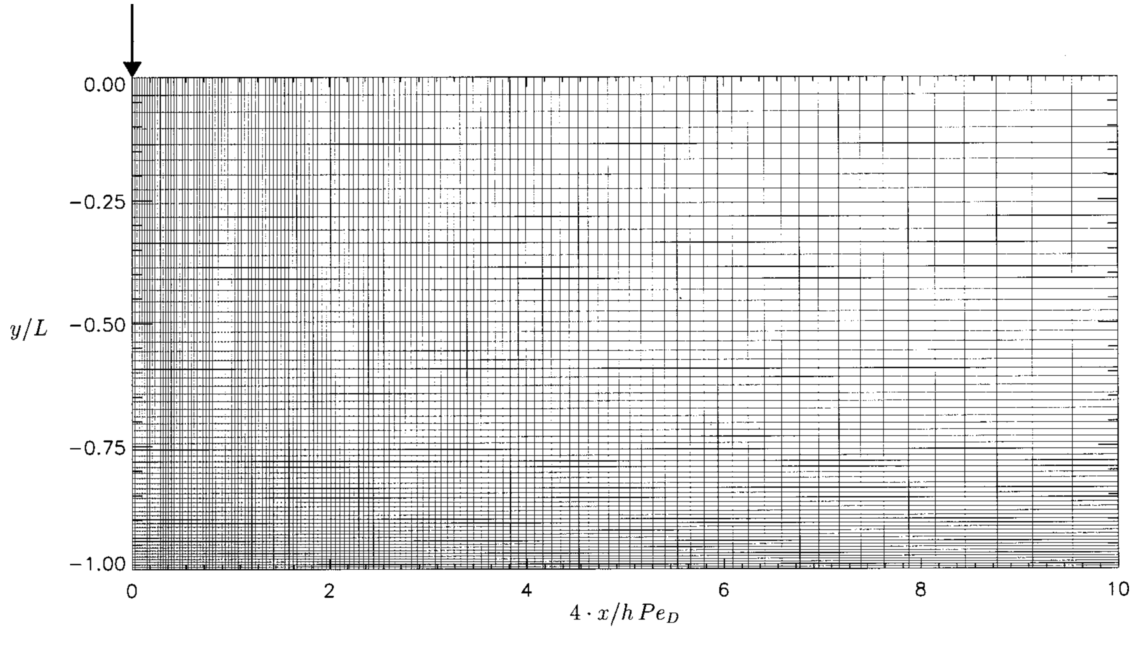

Fig. 7 Example of a grid used for the computation for a half infinite heated zone. Temperature jump at $\tilde{x}=0.0$. Resolution: 257×65 points.

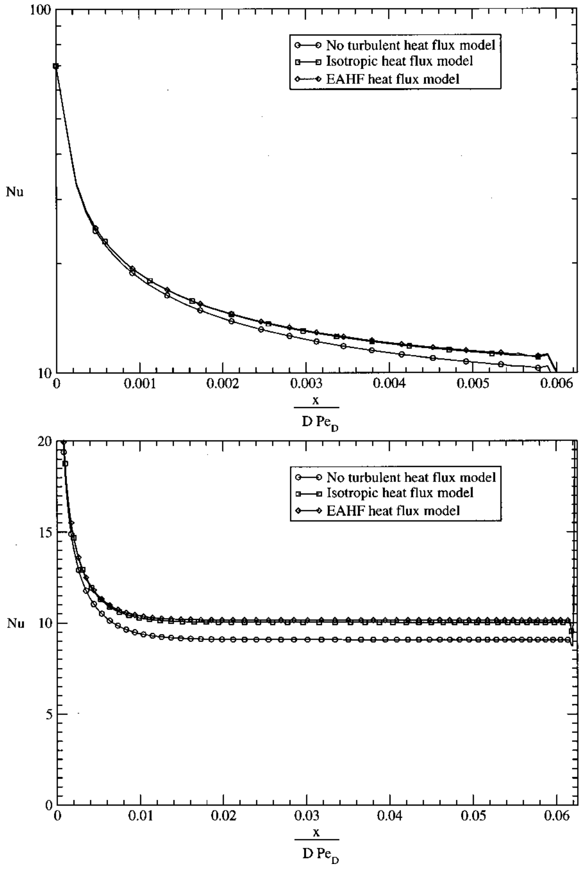

Fig. 8 Influence of the length of the heated zone on the Nusselt Number. $\mathrm{Pe}_D=400$, $\mathrm{Pr}=0.01$, grid 1025×129. Top: $\Delta x_{\mathrm{heat}}/D\mathrm{Pe}_D=0.00625$, bottom: $\Delta x_{\mathrm{heat}}/D\mathrm{Pe}_D=0.0625$.

3.2.4 Comparison of the Nusselt Number for Turbulent Flow. Weigand [20] gives an analytical solution of the extended turbulent Graetz problem. The calculations presented in [20] have been compared with experimental data and other calculations from literature and good agreement has been found. The analytical solution used the isotropic turbulent heat flux model presented in section 2.2.1. Two different cases are presented in [20]: The first case is a variation of the Reynolds number for a constant Prandtl number ($\mathrm{Pr}=0.72$) and the second case is a variation of the Prandtl number for a constant Reynolds number. Figures 4 and 5 show direct comparisons of the analytically and the numerically predicted Nusselt numbers. Again one sees that the numerical prediction is in very good agreement with the analytical solution. Figure 7 shows a typical grid used for the calculations described above.

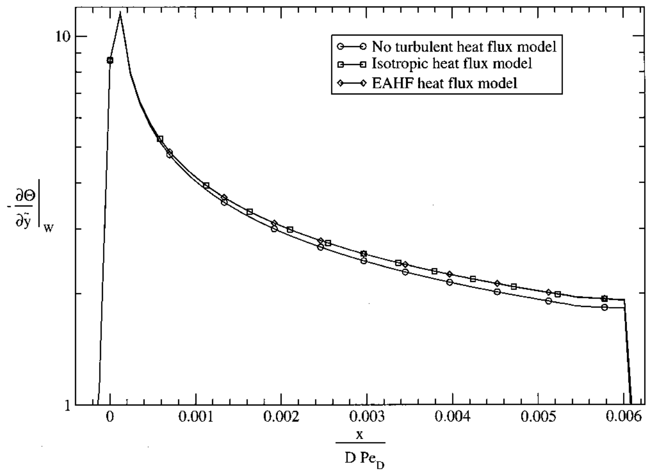

Fig. 9 Dimensionless temperature gradient at the wall for $\Delta x_{\mathrm{heat}}/D\mathrm{Pe}_D=0.00625$, $\mathrm{Pe}_D=400$, $\mathrm{Pr}=0.01$ and a grid 1025 ×129.

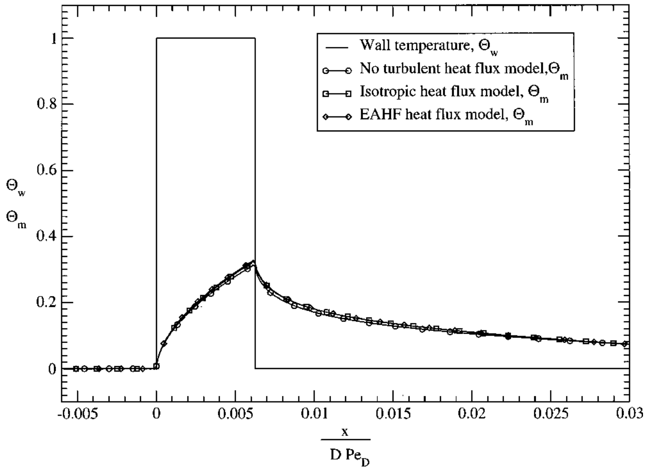

Fig. 10 Dimensionless wall temperature Θ_w and bulk temperature Θ_m for $\Delta x_{\mathrm{heat}}/D\mathrm{Pe}_D=0.00625$, $\mathrm{Pe}_D=400$, $\mathrm{Pr}=0.01$ and a grid 1025×129.

3.2.5 Grid Independence Studies for the Numerical Solution. One important criterion for the quality of the numerical solution is that the solution is independent of the grid. This means that the solution only varies slightly as the grid is changed. In Figure 6 the

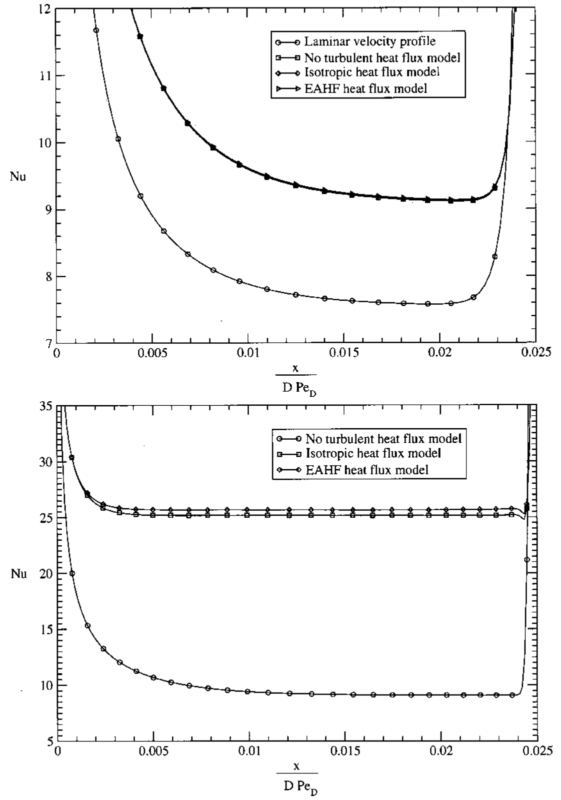

Fig. 11 Influence of the Pe number on the Nu number for a heated duct with a finite heated zone. $\mathrm{Re}_D=40000$, grid 1025 ×129 $(\Delta x_{\mathrm{heat}}/D\mathrm{Pe}_D)=0.025$. Top: $\mathrm{Pe}_D=40$, bottom: $\mathrm{Pe}_D=4000$.

distribution of the Nusselt number is shown for different grids versus an analytical solution [21] for laminar flow. As it can be seen a very good agreement between the numerical solution and the analytical solution can be noticed. Small differences in the numerical solution occur only very close to $x=0$ where the heating section begins.

3.3 Comparison of the Results of the Turbulent Heat Flux Models. After validating the present numerical solution technique for several cases, as discussed in the previous chapter, the present chapter focuses mainly on the results for a heated zone of finite length. These results have been obtained for the two different turbulent heat flux models which have been discussed in chapter 2.2. The case of a heated zone with a finite length has to the best knowledge of the present authors, not been investigated before for turbulent duct flows with piecewise uniform wall temperature. Therefore, the influence of a varying length of the heated zone and the influence of the Péclet and Prandtl number on the heat transfer will be discussed in detail.

The influence of the length of the heated zone on the heat transfer characteristics has been investigated for a given value of the Péclet number ($\mathrm{Pe}_D=400$) and a fixed value of the Prandtl number ($\mathrm{Pr}=0.01$). Five different values of the non-dimensional length of the heated zone have been computed ($x/(D\ \mathrm{Pe}_D)=6.25\cdot 10^{-3}$, $1.25\cdot 10^{-2}$, $2.5\cdot 10^{-2}$, $5\cdot 10^{-2}$, and $6.25\cdot 10^{-2}$). The distribution of the resulting Nusselt number in the heated zone for the two cases $x/(D\ \mathrm{Pe}_D)=6.25\cdot 10^{-3}$ and 0.0625 are shown in Fig. 8. For the small value of the nondimensional heated zone of $x/(D\ \mathrm{Pe}_D)=6.25\cdot 10^{-3}$ the Nusselt number can not reach a fully developed value within the heated zone. Figure 9 and 10 show the distribution of the temperature gradient at the wall ($\partial\Theta/\partial\tilde{y}|_w$) and the dimensionless temperatures Θ_w and Θ_m for the case discussed in Fig. 8. The figures show how axial heat conduction effects influence the temperature gradient at the wall and the bulk temperature near the start and the end of the heated zone. For the larger value of $x/(D\ \mathrm{Pe}_D)$ the influence of the axial heat conduction effects within the heated section vanishes and the Nusselt number attains the fully developed value within the heated section. Figure 8 shows also the difference in Nusselt number for the different turbulent heat flux models investigated. It can be seen that both models give nearly the same results. For a better comparison also a calculation for zero turbulent heat fluxes ($D_{ij}=1\cdot\delta_{ij}$, $i,j=1,2$) has been included. It can be seen that for the here discussed case of low Péclet numbers the effect of the turbulent heat flux for liquid metal flows is weak. Figure 11 shows the effect of a varying Péclet number for a given length of the heated zone of $x/(D\cdot\mathrm{Pe}_D)=0.025$ and a fixed value of the Reynolds number of 40,000. For the low value of the Péclet number of 40 the distribution of the Nusselt number shows that the whole region is strongly influenced by axial heat conduction effects. The value of the Nusselt number near the end of the heated zone is influenced by axial heat conduction effects within the heated zone. The effect of axial heat conduction near the end of the heated zone tends to decrease the temperature difference between the wall and the bulk-temperature, resulting in an increasing value of the Nusselt number at the end of the heated zone. Similar results have been observed by Hennecke [8] and Weigand [23] for the case of a constant heat flux at the wall. Additionally it can be noticed that the two different turbulent heat flux models result in nearly the same Nusselt number distribution. Furthermore, the obtained Nusselt number values are nearly identical to the ones calculated for zero turbulent heat flux. This shows that for this case the effect of the turbulent heat flux could be ignored. Of course, the effect of the higher gradients near the wall of the turbulent velocity profile result also in a higher Nusselt number. This effect has to be taken into account as it can be seen from the additional curve included in Fig. 11(*a*). For the higher Péclet number of 4000, Fig. 11(*b*) shows clearly the importance of the turbulent heat flux for this case. Also it can be seen that the effect of axial heat conduction is small. The two different turbulent heat flux models under investigation result only in small differences near the entrance of the heated zone. It can be seen that the simple isotropic model seems to be a very good approximation of the reality for the cases investigated herein.

By using more sophisticated models for the calculation of the turbulent heat flux, according to Eq. (6), mixed second derivatives of the temperature $\partial^2\Theta/(\partial\tilde{x}\cdot\partial\tilde{y})$ were introduced into the energy equation. This suggests that mathematically the type of the energy equation might change from elliptic to hyperbolic. This could happen in areas or the complete flow domain. Figure 12 shows a typical example for Re_D=40000 for all $\tilde{x}$. It can be seen that for different values of the Péclet number the energy equation attains a hyperbolic character for varying sizes of the domain. The abrupt change at $\mathrm{Pe}_D=4000$ is due to the discontinuity of $C_{\lambda l}$ in Eq. (25) for $\mathrm{Pr}=0.1$. A very similar result can be obtained also for the turbulent heat flux model of Younis et al. [24]. If one would accept the hypothesis that the energy equation should not change its character, this result could be used for determining the constants given in the turbulent heat flux model.

4 Conclusions

The present investigation has shown numerical calculations for the heat transfer inside a duct with a heated zone of finite length.

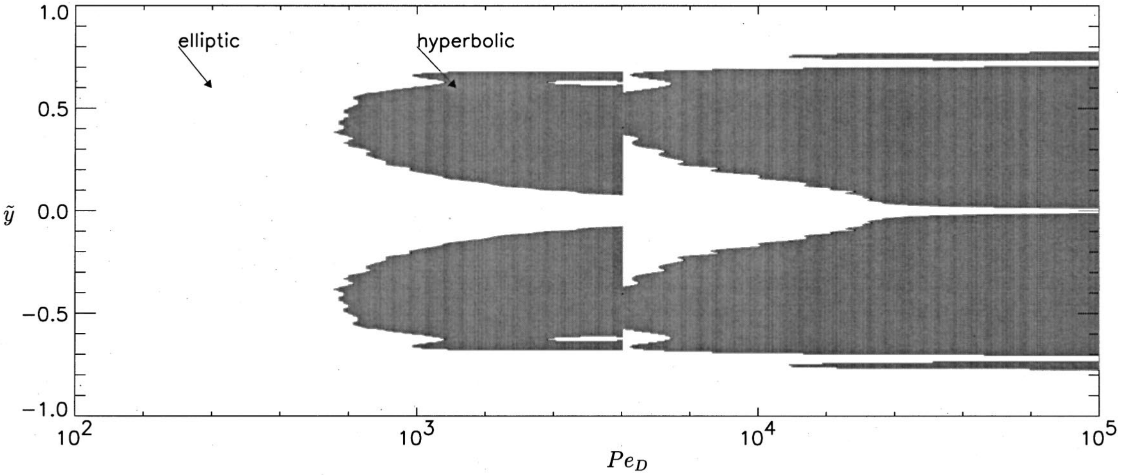

Fig. 12 Region where the flow is hyperbolic as a function of Pe_D for the EAHF model. Re_D=40000, $j_{\max}$=513.

It has been shown that the effect of axial heat conduction within the flow will influence the heat transfer for very short heated zones and will have a strong influence for decreasing values of the Péclet number. By using different turbulent heat flux models it could be shown that for the present case the effect of anisotropy of the turbulent heat flux on the heat transfer is small. Furthermore it could be shown that the more sophisticated models for calculating the turbulent heat flux might change the character of the energy equation. It is not yet clear if this result can be used as a constraint for evaluating the constants for such models.

Acknowledgment

The authors would like to take the opportunity to thank B. Younis, City University, UK for several detailed and helpful discussions.

Nomenclature

a = thermal diffusivity, $a=k/(\rho c_p)$, m^2/s
c_p = specific heat at constant pressure, J/(kg K)
D = hydraulic diameter, $D=4h$, m
$D_{i,j}$ = i, j component of turbulent eddy diffusion tensor, m^2/s
h = distance between centerline and the wall, m
k = heat conductivity, W/(Km)
k = turbulent kinetic energy, m^2/s^2
k^+ = normalized turbulent kinetic energy, $k^+=k/u_\tau^2$
l = mixing length, m
n = wall coordinate, $n=h-y$, m
n^+ = dimensionless wall coordinate, $n^+=nu_\tau/v$
Nu = Nusselt number, $\mathrm{Nu}=-4(\partial\Theta/\partial y)|_w/(\Theta_m-\Theta_w)$
Pe_D = Péclet number, $\mathrm{Pe}_D=\mathrm{Re}_D\mathrm{Pr}$
Pe_t = turbulent Péclet number, $\mathrm{Pe}_t=\mathrm{Pr}\epsilon_m/v$
Pr = Prandtl number, $\mathrm{Pr}=v/a$
Pr_t = turbulent Prandtl number, $\mathrm{Pr}_t=\epsilon_m/\epsilon_{hn}$
$\dot{q}_W$ = wall heat flux, $-k(dT/dy)|_w$, W/m^2
Re_D = Reynolds number, $\mathrm{Re}_D=(\overline{u_0}D)/v$
Re_t = turbulent Reynolds number, $\mathrm{Re}_t=k^2/(v\epsilon)$
Re_τ = friction Reynolds number, based on u_τ, $\mathrm{Re}_\tau=(u_\tau h)/v$
$\overline{S}_{ik}$ = mean strain rate tensor, $\overline{S}_{ik}=(1/2)\times(\partial\tilde{u}_i/\partial\tilde{x}_j+\partial\tilde{u}_j/\partial\tilde{x}_i)$
T = temperature, K
T_w = temperature of the heated wall, K
T_τ = friction Temperature, $q_w/(\rho c_p u_\tau)$, K
u = velocity in x-direction, m/s
$\tilde{u}$ = nondimensional velocity, $\tilde{u}=u/\overline{u_0}$
u^+ = velocity, normalized with u_τ, $u^+=u/u_\tau$
u_τ = friction velocity, $u_\tau=\sqrt{\tau_{nx_w}/\rho}$, m/s
$\overline{u_0}$ = mean velocity in x-direction, m/s
$\overline{u'u'}$, $\overline{u'v'}$, $\overline{v'v'}$ = Reynolds stress components, m^2/s^2
$\overline{u'u'}^+$, $\overline{u'v'}^+$, $\overline{v'v'}^+$ = normalized Reynolds stress components, $\overline{u_i'u_j'}^+=\overline{u_i'u_j'}/u_\tau^2$
$\overline{u'T'}$, $\overline{v'T'}$ = turbulent heat flux, (m K)/s
$\overline{\tilde{u}'\Theta'}$, $\overline{\tilde{v}'\Theta'}$ = nondimensional turbulent heat flux
v = velocity in y-direction, m/s
x,y = coordinates, m
$\tilde{x},\tilde{y}$ = nondimensional coordinates, $\tilde{x}=x/(\mathrm{Pe}_h h)$, $\tilde{y}=y/h$

Greek Symbols

α_t = eddy diffusivity, m^2/s
$\tilde{\alpha}_t$ = nondimensional eddy diffusivity
Δx_{heat} = length of heated section, m
ϵ = dissipation rate, m^2/s^2
ϵ^+ = normalized dissipation rate, $\epsilon^+=\epsilon\nu/u_\tau^4$
ϵ_{hx} = eddy diffusivity in axial direction, m^2/s
ϵ_{hn} = eddy diffusivity in normal direction to the flow, m^2/s
ϵ_m = eddy viscosity, m^2/s
$\tilde{\epsilon}_m$ = nondimensional eddy viscosity, $\tilde{\epsilon}_m=\epsilon_m/\nu$
ϵ_θ = dissipation rate of temperature variance $\epsilon_\theta=a\overline{(\partial\theta/\partial x_k)(\partial\theta/\partial x_k)}$, m^2/s
ν = kinematic viscosity, m^2/s
μ = dynamic viscosity, kg/(m s)
ρ = density, kg/m^3
Θ = nondimensional temperature, $(T-T_0)/(T_F-T_0)$
Θ_0 = nondimensional temperature of the unheated liquid
Θ_m = bulk temperature, $\Theta_m=\int u\Theta dy/\int u dy$
Θ_w = wall temperature
Θ^+ = nondimensional temperature, $(T_w-T)/T_\tau$
$\overline{\theta^2}$ = temperature variance
$\overline{\theta^2}^+$ = normalized temperature variance
τ_{nx} = shear stress, kg/(m s^2)
τ_{nx_w} = wall shear stress, kg/(m s^2)
$\overline{\omega}_{ik}$ = mean rot. rate tensor, $\overline{\omega}_{ik}=(1/2)(\partial\tilde{u}_i/\partial\tilde{x}_j-\partial\tilde{u}_j/\partial\tilde{x}_i)$
ξ,η = coordinates in transformed space

References

[1] Batchelor, G. K., 1949, ‘‘Diffusion in a Field of Homogeneous Turbulence,’’ Austral. J. Sci. Res., **A2**, pp. 437–450.

[2] Chieng, C. C., and Launder, B. E., 1980, ‘‘On the Calculation of Turbulent Heat Transfer Downstream From an Abrupt Pipe Expansion,’’ Numer. Heat Transfer, **3**, pp. 189–207.

[3] Faggiani, S., and Gori, F., 1980, ‘‘Influence of Streamwise Molecular Heat Conduction on the Heat Transfer for Liquid Metals in Turbulent Flow Between Parallel Plates,’’ ASME J. Heat Transfer, **102**, pp. 292–296.

[4] Gatski, T. B., and Speziale, C. G., 1993, ‘‘On Explicit Algebraic Stress Models for Complex Turbulent Flows,’’ J. Fluid Mech., **254**, pp. 59–78.

[5] Gibson, M. M., and Launder, B. E., 1976, ‘‘On the Calculation of Horizontal Turbulent Free Shear Flows Under Gravitational Influence,’’ ASME J. Heat Transfer, **98**, pp. 81–97.

[6] Graetz, L., 1883, ‘‘Uber die Wärmeleitungsfähigkeit von Flüssigkeiten,’’ Ann. Phys. Chem., **1**(18), pp. 79–94.

[7] Graetz, L., 1885, ‘‘Über die Wärmeleitfähigkeit von Flüssigkeiten,’’ Ann. Phys. Chem, **2**(25), pp. 337–357.

[8] Hennecke, D. K., 1968, ‘‘Heat Transfer by Hagen-Poiseuille Flow in the Thermal Development Region With Axial Conduction,’’ Waerme-und Stoffuebertrag., **1**, pp. 177–184.

[9] Kader, B. A., 1981, ‘‘Temperature and Concentration Profiles in Fully Turbulent Boundary Layers,’’ Int. J. Heat Mass Transf., **24**(9), pp. 1541–1544.

[10] Kays, W. M., and Crawford, M. E., 1993, *Convective Heat and Mass Transfer*, Mc Graw-Hill, New York.

[11] Kim, J., and Moin, P., 1989, ‘‘Transport of Passive Scalars in Turbulent Channel Flow,’’ in *Turbulent Shear Flows*, **6**, Springer-Verlag, Berlin, pp. 85–96.

[12] Lee, S. L., 1982, ‘‘Forced Convection Heat Transfer in Low Prandtl Number Turbulent Flows: Influence of Axial Conduction,’’ Can. J. Chem. Eng., **60**, pp. 482–486.

[13] Nguyen, T. V., 1992, ‘‘Laminar Heat Transfer for Thermally Developing Flow in Ducts,’’ Int. J. Heat Mass Transf., **35**(7), pp. 1733–1741.

[14] Nusselt, W., 1910, ‘‘Die Abhängigkeit der Wärmeübergangszahl von der Rohrlänge,’’ VDI Zeitschrift, **54**, pp. 1154–1158.

[15] Press, W. H., Teukolsky, S. A., Vetterling, W. T., and Flannery, B. P., *Numerical Recipes in Fortran77*, **1**, 2nd ed., Cambridge University Press.

[16] Reed, C. B., 1987, ‘‘Convective Heat Transfer in Liquid Metals,’’ in S. Kakac, R. K. Shah, and W. Aung, eds., *Handbook of Single-Phase Convective Heat Transfer*, Wiley, New York, Chap 8.

[17] Shah, R. K., and London, A. L., 1978, *Laminar Flow Forced Convection in Ducts*, Academic Press, New York, Chap. V and VI.

[18] So, R. M. C., and Sommer, T. P., 1996, ‘‘An Explicit Algebraic Heat-Flux Model for the Temperature Field,’’ Int. J. Heat Mass Transf., **39**(3), pp. 455–465.

[19] Sommer, T. P., 1994, ''Near-Wall Modeling of Turbulent Heat Transport in Non-Buoyant and Buoyant Flows,'' Ph.D. thesis, Arizona State University, Tempe, AZ.
[20] Weigand, B., 1996, ''An Exact Analytical Solution for the Extended Turbulent Graetz Problem With Dirichlet Wall Boundary Conditions for Pipe and Channel Flows,'' Int. J. Heat Mass Transf., **39**(8), pp. 1625–1637.
[21] Weigand, B., 1997, *Ausgewählte analytische Lösungsmethoden für komplexe, knovektive Wärmeübertragungsprobleme*, Dr. Hänsel-Hohenhausen Verlag der Deutschen Hochschulschriften, ISBN3-8267-2624-3.
[22] Weigand, B., Ferguson, J. R., and Crawford, M. E., 1997, ''An Extended Kays and Crawford Turbulent Prandtl Number Model,'' Int. J. Heat Mass Transf., **40**(17), pp. 4191–4196.
[23] Weigand, B., Kanzamar, M., and Beer, H., 2001, ''The Extended Graetz Problem With Piecewise Constant Wall Heat Flux for Pipe and Channel Flows,'' Int. J. Heat Mass Transf., **44**(20), pp. 3941–3952.
[24] Younis, B. A., Speziale, C. G., and Clark, T. T., 1996, ''A Non-Linear Algebraic Model for the Turbulent Scalar Flux,'' *International Conference on Turbulent Heat Transfer*, March 1996.

Transition in Convective Flows Heated Internally

Masato Nagata
Department of Aeronautics and Astronautics,
Graduate School of Engineering,
Kyoto University,
Japan

Sotos Generalis
School of Engineering and Applied Sciences,
Division of Chemical Engineering and Applied Chemistry,
Aston University, U.K.
e-mail: s.c.generalis@aston.ac.uk

The stability of internally heated convective flows in a vertical channel under the influence of a pressure gradient and in the limit of small Prandtl number is examined numerically. In each of the cases studied the basic flow, which can have two inflection points, loses stability at the critical point identified by the corresponding linear analysis to two-dimensional states in a Hopf bifurcation. These marginal points determine the linear stability curve that identifies the minimum Grashof number (based on the strength of the homogeneous heat source), at which the two-dimensional periodic flow can bifurcate. The range of stability of the finite amplitude secondary flow is determined by its (linear) stability against three-dimensional infinitesimal disturbances. By first examining the behavior of the eigenvalues as functions of the Floquet parameters in the streamwise and spanwise directions we show that the secondary flow loses stability also in a Hopf bifurcation as the Grashof number increases, indicating that the tertiary flow is quasi-periodic. Secondly the Eckhaus marginal stability curve, that bounds the domain of stable transverse vortices towards smaller and larger wavenumbers, but does not cause a transition as the Grashof number increases, is also given for the cases studied in this work. [DOI: 10.1115/1.1470169]

Keywords: Channel Flow, Convection, Heat Transfer, Shear Flows, Stability

1 Introduction

We consider an incompressible viscous flow in a vertical channel under the influence of a vertical pressure gradient with a homogeneously distributed heat source. There are several ways in which such a heat source may be produced. Heat released in chemical reactions taking place in the fluid, by currents through electrically conducting fluid solutions (Wilkie and Fisher [1]) and radioactive decay, are some examples. The case studied here has applications in industrial processes where liquid is carried through ducts while simultaneously undergoing convection. In particular, the case studied here is a simple model of a cooling mechanism in the nuclear fusion industry where liquid sodium is used to cool the hot plasma. The limit of vanishing Prandtl number is assumed in this work. The effects of temperature fluctuations have been studied, however, in a separate work, where the effects of the angle of inclination on the stability of the flow are also discussed (Generalis and Nagata [2]).

This system also poses an interesting problem from a mathematical viewpoint. The basic velocity profile has two inflection points if the Reynolds number R satisfies $-\mathrm{Gr}/2 \leqslant R \leqslant 0$, where Gr is the Grishof number (Gr gives the strength of the internal heating and R measures the magnitude of the external pressure gradient) and so we can expect the steady basic state to be linearly unstable, although the Rayleigh instability criteria is applicable only to inviscid cases. In fact, we find that this steady basic state loses stability in a Hopf bifurcation. We calculate the two-dimensional nonlinear wavelike equilibrium states, which are created at this Hopf bifurcation, and investigate the stability of this secondary flow to three-dimensional perturbations. We find that the secondary flow also loses stability via a Hopf bifurcation, indicating that the tertiary flow is quasi-periodic.

The technique adopted in this study is a variation of the one that was pioneered by Busse [3] and by Clever and Busse [4] sometime ago, in conjunction with Rayleigh-Bénard convection, (see also Clever and Busse [5]). A similar approach has already been used to analyze convective inclined channel flow heated from above and cooled from below (Nagata and Busse [6]).

It is known that in a narrow vertical enclosure heated from the side and for large values of the Rayleigh number (Ra=Pr Gr in our formulation) a stable vertical temperature gradient develops (Bergholz [7]) and stability characteristics strongly depend on the value of the control parameters. The numerical work of the linear analysis showed that if the vertical stratification exceeds a certain value and the Prandtl number is moderate (0→12.7) transition takes place in the form of traveling waves ([7] and references therein). In the experiments of [1] a uniform vertical temperature gradient was also assumed throughout the homogeneously heated fluid. The effects of temperature fluctuations are not taken into account in the present work, but are examined in [2]. Our results, based on a symmetric basic velocity profile, can also be contrasted with the results of the non-linear analysis of the plane Poiseuille flow by Ehrenstein and Koch [8], where it was found that the three-dimensional flow bifurcating from the lower branch is phase locked with the secondary flow. As our studies showed that our tertiary flow is not phase locked with the secondary flow, the problem studied in this paper is distinctive from previous non-linear analyses. In the following section we formulate our problem, and in Section 3 we investigate the linear stability of our basic steady state numerically within the framework of the Chebyshev collocation point method analogous to the one used in Wall and Nagata [9]. The marginal stability curve is examined against a range of (fixed) values of the Reynolds number (R measures the magnitude of the external vertical pressure gradient). Two distinct cases of R are selected for our nonlinear studies and in Section 4, we determine the two-dimensional wavelike equilibrium states which bifurcate from the corresponding basic state through a Hopf bifurcation, while in Section 5 we investigate the linear stability of this secondary periodic flows against three-dimensional perturbations. In Section 6, we discuss the conclusions of this work.

2 Formulation of the Problem

We consider an incompressible fluid in a vertical channel with infinite extent and of width $2h$. We apply the Boussinesq approximation to obtain the equations

$$\partial \mathbf{u}/\partial t + \mathbf{u}\cdot\nabla\mathbf{u} = -1/\rho\nabla\pi + g\alpha T\mathbf{i} + \nu\nabla^2\mathbf{u}, \tag{2.1}$$

$$\partial T/\partial t + \mathbf{u}\cdot\nabla T = \kappa\nabla^2 T + q, \tag{2.2}$$

Contributed by the Heat Transfer Division for publication in the JOURNAL OF HEAT TRANSFER. Manuscript received by the Heat Transfer Division July 13, 2001; revision received November 21, 2001. Associate Editor: P. S. Ayyaswamy.

$$\nabla \cdot \mathbf{u} = 0, \tag{2.3}$$

for the velocity vector $\mathbf{u}$, pressure π, density ρ and temperature variation from the environment T, where q is the volume strength of the heat source that generates the basic flow, κ is the thermal conductivity, α is the coefficient of thermal expansion, υ is the viscosity and g is the acceleration due to gravity. We adopt a reference frame with the origin of the position vector $\mathbf{r}$ fixed at the mid-channel and take (x,y,z) as Cartesian coordinates in the streamwise, spanwise and normal directions respectively, with corresponding unit vectors $\mathbf{i}$, $\mathbf{j}$, $\mathbf{k}$. The boundary conditions are

$$\mathbf{u} = 0, \quad T = 0, \quad \text{at} \quad z = \pm h \tag{2.4}$$

Using h, h^2/ν and $qh^2/(2\kappa \mathrm{Gr})$, where $\mathrm{Gr} = (g\alpha q h^5)/(2\nu^2\kappa)$ is the Grashof number, as the units of length, time and temperature, and choosing a constant vertical pressure gradient $\partial \pi/\partial x = -(2\rho\nu U_{\max})/h^2$ (where $U_{\max}$ is the maximum laminar velocity at midchannel for pure Poiseuille flow), we obtain from Eqs. (2.1–2.3) the following non-dimensional equations (the two infinite boundaries are kept at the same reference temperature, which is assumed equal to zero) for the governing Navier-Stokes, heat equation and incompressibility equations:

$$\partial \hat{\mathbf{u}}/\partial t + \mathbf{u}_0 \cdot \nabla \hat{\mathbf{u}} + \hat{\mathbf{u}} \cdot \nabla \mathbf{u}_0 + \hat{\mathbf{u}} \cdot \nabla \hat{\mathbf{u}} = -\nabla \hat{\pi} - \mathrm{Gr}(\mathbf{r}\cdot\mathbf{k})^2 \mathbf{i} + \theta \mathbf{i} + \nabla^2 \mathbf{u}, \tag{2.5}$$

$$\partial \theta/\partial t + \mathbf{u}_0 \cdot \nabla \theta + \hat{\mathbf{u}} \cdot \nabla \theta - 2\mathrm{Gr}(\mathbf{r}\cdot\mathbf{k})(\hat{\mathbf{u}}\cdot\mathbf{k}) = \mathrm{Pr}^{-1}(\nabla^2(T_0 + \theta) + 2\mathrm{Gr}), \tag{2.6}$$

$$\nabla \cdot \hat{\mathbf{u}} = 0, \tag{2.7}$$

where we substituted

$$\mathbf{u} = \mathbf{u}_0 + \hat{\mathbf{u}}, \tag{2.8}$$

$$T = T_0 + \theta, \tag{2.9}$$

with $\hat{\pi}$ the pressure deviation from π, $\mathrm{Pr} = \upsilon/\kappa$ is the Prandtl number and $R = (U_{\max} h)/\upsilon = -h^3 \nabla \pi / 2\upsilon^2$ is the Reynolds number. Terms that can be written as gradients have been combined into the expression for $\nabla \hat{\pi}$. In Eq. (2.8) the basic state is given by the basic velocity profile $\mathbf{u}_0 = iU_0(z)$ and in Eq. (2.9) $T_0(z)$ represents the basic temperature distribution. In Eqs. (2.8–2.9), $\hat{\mathbf{u}}$, θ represent the velocity and temperature fluctuations. The basic velocity and temperature contributions are obtained from Eqs. (2.5–2.6) when the deviations are ignored and are of the form

$$U_0 = (\mathrm{Gr}/12)(z^4 - 6z^2 + 5) + \mathrm{R}(1 - z^2) \tag{2.10}$$

$$T_0 = \mathrm{Gr}(1 - z^2) \tag{2.11}$$

The boundary conditions for the deviations are the homogeneous conditions described in Eq. (2.4)

$$\hat{\mathbf{u}} = 0, \quad \theta = 0, \quad \text{at} \quad \mathbf{z} = \pm 1. \tag{2.12}$$

By assuming the limit of vanishing Prandtl number ($\mathrm{Pr} \to 0$) the fixed temperature condition $\theta = 0$ at the boundaries ($z = \pm 1$), yields $\theta = 0$, so that the instability mechanism becomes purely hydrodynamic. The temperature deviation equation is ignored for the remainder of this work, but is discussed elsewhere [2]. In this work, therefore, the competing thermal instability is ignored and attention is restricted to the hydrodynamic case governed by the following set of equations:

$$\partial \hat{\mathbf{u}}/\partial t + \mathbf{u}_0 \cdot \nabla \hat{\mathbf{u}} + \hat{\mathbf{u}} \cdot \nabla \mathbf{u}_0 + \hat{\mathbf{u}} \cdot \nabla \hat{\mathbf{u}} = -\nabla \hat{\pi} + \nabla^2 \hat{\mathbf{u}}. \tag{2.13}$$

$$\nabla \cdot \hat{\mathbf{u}} = 0 \tag{2.14}$$

Note that the steady velocity profile U_0, given by Eq. (2.10), has inflection points in $-1 \leqslant z \leqslant 1$ when $-\mathrm{Gr}/2 \leqslant R \leqslant 0$ (for $\mathrm{Gr} > 0$). For $R > 0$ these inflection points lie outside the channel width, and for $R < -\mathrm{Gr}/2$, there are no inflection points. Note that $R < 0$ corresponds to a pressure gradient which, in the absence of heating, drives the fluid vertically downwards. Also, $\mathrm{Gr} < 0$ corresponds to heat being removed from the system. Eqs. (2.13) were also derived by Gershuni and Zhukhovitskii [10], who subsequently investigated the linear stability of the basic flow

$$U_0 = (\mathrm{Gr}/60)(5z^4 - 6z^2 + 1). \tag{2.15}$$

This basic steady state is derived by assuming that the total mass flux vanishes across any lateral cross-section of the channel. In comparison and for this work, we have not made the assumption that the remote ends of the channel are closed (as in [10]) and therefore our calculations assume the presence of a constant vertical pressure gradient.

Following [6] we separate the velocity field variations into an average part (over x and y-coordinates) $\breve{U}$, and a fluctuating part $\breve{\mathbf{u}}$,

$$\hat{\mathbf{u}} = \breve{U}\mathbf{i} + \breve{\mathbf{u}} \tag{2.16}$$

where

$$\breve{\mathbf{u}} = \delta\phi + \varepsilon\psi, \tag{2.17}$$

and we define the total mean flow as

$$\hat{U} = U_0 + \breve{U}. \tag{2.18}$$

In Eqs. (2.17) φ, ψ refers to the poloidal and toroidal part of the velocity fluctuations respectively, (see Chandrasekhar[11] and [4]), satisfying $\overline{\varphi} = \overline{\psi} = 0$, with the overbar denoting an average in the x, y directions. For a recent mathematical proof see Schmitt and von Wahl [12]. The operators $\boldsymbol{\delta}, \boldsymbol{\varepsilon}$ are of the form, (see [4]),

$$\delta_i = \lambda_j \partial_i \partial_j - \lambda_i \Delta, \tag{2.19}$$

$$\varepsilon_i = \varepsilon_{ijk} \lambda_k \partial_j, \tag{2.20}$$

with $\Delta = \nabla^2$ the Laplacian and $\boldsymbol{\lambda} = (0,0,1)$. It is worth pointing out that the incompressibility condition is satisfied automatically for such a decomposition of the velocity field and can therefore be eliminated from the rest of the analysis. By applying the operators $\boldsymbol{\delta}\cdot, \boldsymbol{\varepsilon}\cdot$ we obtain the following set of equations for the poloidal and toroidal part of Eq. (2.13):

$$\frac{\partial}{\partial t} \nabla^2 \Delta_2 \varphi - \nabla^4 \Delta_2 \varphi + \hat{U} \partial_x \nabla^2 \Delta_2 \varphi = \partial_z^2 \hat{U} \Delta_2 \partial_x \varphi - \boldsymbol{\delta} \cdot \{(\boldsymbol{\delta}\phi + \varepsilon\psi) \cdot \nabla(\boldsymbol{\delta}\phi + \varepsilon\psi)\}, \tag{2.21}$$

$$\frac{\partial}{\partial t} \Delta_2 \psi - \nabla^2 \Delta_2 \psi = \partial_z \hat{U} \Delta_2 \partial_y \varphi - \hat{U} \partial_x \Delta_2 \psi - \boldsymbol{\varepsilon} \cdot \{(\boldsymbol{\delta}\phi + \varepsilon\psi) \cdot \nabla(\boldsymbol{\delta}\phi + \boldsymbol{\varepsilon}\psi)\}, \tag{2.22}$$

where Δ_2 is the planform Laplacian. The mean flow contribution is given by

$$\partial_z^2 \breve{U} + \partial_z \overline{\Delta_2 \phi(\partial_x \partial_z \phi + \partial_y \psi)} = \partial_t \breve{U} \tag{2.23}$$

by applying the fixed pressure condition $\overline{\partial_x \hat{\pi}} = 0$. The overbar denotes the x-y average and is obtained by applying the operator $((\alpha\beta/4\pi^2)\int_0^{2\pi/\alpha}\int_0^{2\pi/\beta} dx dy \cdot)$ on the x-component of Eq. (2.13). We note that Eqs. (2.21–2.23) combined with the assumption of constant vertical pressure gradient are subject to the homogenous boundary conditions

$$\phi = \partial\phi/\partial z = \breve{U} = \psi = 0 \quad \text{at} \quad z = \pm 1 \tag{2.24}$$

In the following section the flow with various different values of the Reynolds number will be analyzed.

3 Linear Analysis

Squire's theorem is applicable in the present problem and subsequently for a linear stability analysis of the basic state (2.10) we neglect the toroidal part ($\psi = 0$) and we set $\partial y = 0$. By additionally neglecting the nonlinear terms of Eq. (2.21) and the mean flow contribution (2.23) we obtain for the poloidal part

$$\frac{\partial}{\partial t}\nabla^2\Delta_2\varphi=\nabla^4\Delta_2\varphi-U_0\partial_x\nabla^2\Delta_2\varphi+\partial_z^2U_0\Delta_2\partial_x\varphi. \tag{3.1}$$

Setting

$$\phi=\Phi(z)\exp\{i\alpha(x-ct)\}, \tag{3.2}$$

with α real, we employ the Chebyshev collocation point method and in order to take into account the boundary conditions of Eq. (2.24) we substitute

$$\Phi(z)=\sum_{n=0}^{N}(1-z^2)^2a_nT_n(z), \tag{3.3}$$

where T_n is the nth order Chebyshev polynomial. Equation (3.1) is then evaluated at the $N+1$ collocation points

$$z_i=\cos((i+1)\pi/(N+2)), \quad i=0,\ldots,N.$$

The resulting amplitude equations define an algebraic eigenvalue problem

$$A\mathbf{x}=\sigma B\mathbf{x} \tag{3.4}$$

in the unknown complex variables a_n, with A and B, $(N+1)\times(N+1)$ complex matrices. The *QZ* method was utilized to solve the eigenvalue problem of Eq. (3.4). The real part of σ, σ_r, defines the rate of damping or amplification of the disturbances. The imaginary part of σ, σ_i, defines the phase velocity c of the propagating disturbances in the flow, with $c=-\sigma_i/\alpha$. In order to achieve numerical accuracy of the results a high enough truncation number N must be chosen. It was found that N had to be chosen such that the condition $N\geqslant 39$ was satisfied. This value was chosen for all subsequent calculations in this paper and for consistency with the secondary stability problem, to be addressed in Section 4. Figure 1 shows the neutral curves in the (Gr,α) plane for various fixed values of the Reynolds number R, while in Fig. 2 the values of the corresponding phase velocities are provided. The corresponding critical Grashof number is the highest value allowed by the linear analysis for the basic flow to retain its laminar form. While for $R=-1000,-700,-500,\ldots,4000,5772,\ldots$, the basic state is stable for points below the appropriate neutral curve, and unstable for points above the neutral curve, for $R=-5772$ (an example of heat being removed from the system as Gr<0), the basic state is unstable below the neutral curve and stable above. It is interesting to note that for $R=5772$ the neutral curve touches Gr=0, in agreement with the standard result of Poiseuille flow (see for example [8]). Note that the critical Grashof and wavenumbers for $R=0$ are given by, $(\mathrm{Gr}_c,\alpha_c)=(2906.3637,1.247)$ and for $R=-500$ they are $(\mathrm{Gr}_c,\alpha_c)=(1449.3198,1.83)$. Each neutral curve in Fig. 1 almost always corresponds to a Hopf bifurcation.

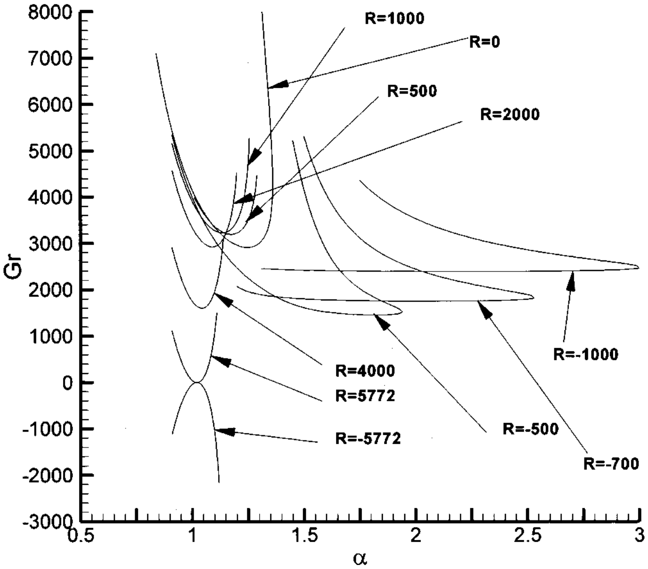

Fig. 1 Linear stability curves in the Gr, α plane for various values of *R*, as indicated

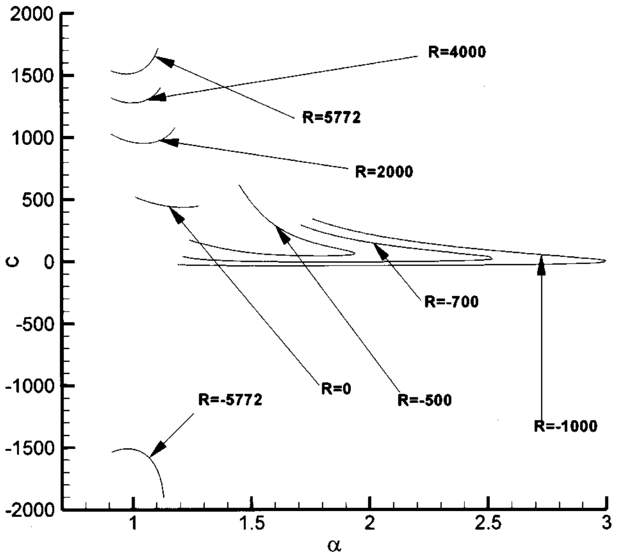

Fig. 2 Phase velocity curves as functions of the wavenumber α for various values of *R*, as indicated

4 Secondary Equilibrium States

4.1 Numerical Method. In this section we calculate the nonlinear equilibrium solutions that are created at the Hopf bifurcation points of the stability curves as predicted by the linear analysis discussed in the previous section, due to two-dimensional disturbances (Squire's Theorem). Two different cases were considered in this and the subsequent sections, those for $R=0$ and $R=-500$. Here we ignore the equation for the toroidal part (Eq. (2.22)) and the spanwise direction and therefore assume that $\psi=\partial_y=0$, retaining however Eq. (2.21) for the poloidal part and Eq. (2.23) that provides the average (mean) flow contribution

$$\frac{\partial}{\partial t}\nabla^2\Delta_2\varphi-\nabla^4\Delta_2\varphi+\hat{U}\partial_x\nabla^2\Delta_2\varphi$$
$$=\partial_z^2\hat{U}\Delta_2\partial_x\varphi-\boldsymbol{\delta}\cdot\{(\boldsymbol{\delta}\phi+\boldsymbol{\varepsilon}\psi)\cdot\nabla(\boldsymbol{\delta}\phi+\boldsymbol{\varepsilon}\psi)\}, \tag{4.1}$$

$$\partial_z^2\breve{U}+\partial_z\overline{\Delta_2\phi(\partial_x\partial_z\phi+\partial_y\psi)}=\partial_t\breve{U} \tag{4.2}$$

We note that Eqs. (4.1–4.2) combined with the assumption of constant vertical pressure gradient are subject to the homogeneous boundary conditions

$$\phi=\partial\phi/\partial z=\breve{U}=0 \quad \text{at} \quad z=\pm 1 \tag{4.3}$$

The nonlinear secondary equilibrium solutions are obtained with the aid of the Chebyshev collocation point method, as in the case of the linear stability analysis of the previous section. We briefly outline the method here. We expand ϕ in terms of the set of orthogonal functions T_n:

$$\phi=\sum_{m=-\infty,m\neq 0}^{\infty}\sum_{n=0}^{\infty}\exp\{im\alpha(x-ct)\}(1-z^2)^2a_{mn}T_n(z), \tag{4.4}$$

Table 1 Values of the l_2-norm for the poloidal part of the velocity field for a sample of the integer range *M*, *N* and for α=1.247, Gr=3500. The total number of the complex coefficients α_{mn} in the Fourier expansion of the poloidal part of the velocity fluctuations is also given.

l_2 - norm ($\times 10^2$)	M	N	a_{mn}
0.86858044	3	37	266
0.86857981	3	39	280
0.87483385	4	39	360
0.87832114	5	29	330
0.87952273	5	31	352
0.87904204	5	33	372
0.87915113	5	35	396
0.87914524	5	37	418
0.87914445	5	39	440

while we write

$$\breve{U}=\sum_{\substack{n=\text{even}\\n=0}}^{\infty}C_n(1-z^2)T_n(z), \tag{4.5}$$

for the mean flow distortions, with T_n the nth order Chebyshev polynomial. For ϕ to be real the following conditions must be satisfied by the complex coefficients a_{mn} of Eq. (4.4):

$$a_{-mn}=a^*_{mn} \tag{4.6}$$

where * denotes complex conjugate. The symmetry of the problem allows the imposition of the additional constraints on the coefficients a_{mn}:

$$a_{mn}=0 \quad m+n=\text{even} \tag{4.7}$$

When Eqs. (4.4–4.5) are substituted in Eqs. (4.1–4.2), and the resulting equations are multiplied by $((\alpha/2\pi)\int_0^{2\pi/\alpha}dx\exp(i\gamma\alpha x))$ and evaluated at $z_i=\cos((i+1)\pi/(N+2))$, $i=0,\ldots,N$, while at the same time are transformed into a moving frame of reference $\{\tilde{x},\tilde{z},\tilde{t}\}$ moving with speed c in the x-direction, such that $\{\tilde{x}=x-ct,\tilde{z}=z,\tilde{t}=t\}$ (and dropping the tilde hereafter), the following system of $(N+1)(2M+1)$ nonlinear algebraic equations is obtained:

$$A_{ij}x_j+B_{ijk}x_jx_k=0, \tag{4.8}$$

where the matrix A_{ij} and the tensor B_{ijk} are functions of α, Gr, R, and the vector x_i has as elements the unknown amplitudes $\{a_{mn},c,C_n\}$. The operation of transforming into a moving frame of reference introduces the team $c\partial_x\nabla^2\Delta_2\phi$ into the system of equations. Care therefore has to be exercised in dealing with the phase velocity. In our numerical work c has been allocated a position in x_i that is not reserved for a_{mn}, for some m,n, say $m=2$ and $n=1$. This is achieved by introducing t such that $\mathrm{Im}(a_{21}\exp(-i2act))=0$ and redefining the coefficients $\hat{a}_{mn}=a_{mn}\exp(-imact)$ (dropping the hat hereafter). As mentioned above we proceed to evaluate the system of Eqs. (4.1–4.2) at the $N+1$ Chebyshev collocation points given by

$$z_i=\cos((i+1)\pi/(N+2)), \quad i=0,\ldots,N.$$

The Newton-Raphson iterative method is employed in order to obtain solutions to the resulting finite system of equations. Steady solutions have been obtained for a variety of values of the Grashof, Reynolds and wave numbers.

4.2 Results. In order to establish the required truncation level consistent with well converged solutions in our analysis we have used for the secondary equilibrium solutions the vector l_2-norm, which for the complex coefficients a_{mn} is defined as:

$$|l_2|=\left\{\sum_{n=0}^{N}\sum_{m=-M,m\neq 0}^{M}a_{mn}a^*_{mn}\right\}^{1/2} \tag{4.9}$$

We present in Table 1 the vector l_2-norm of Eq. (4.9) for various

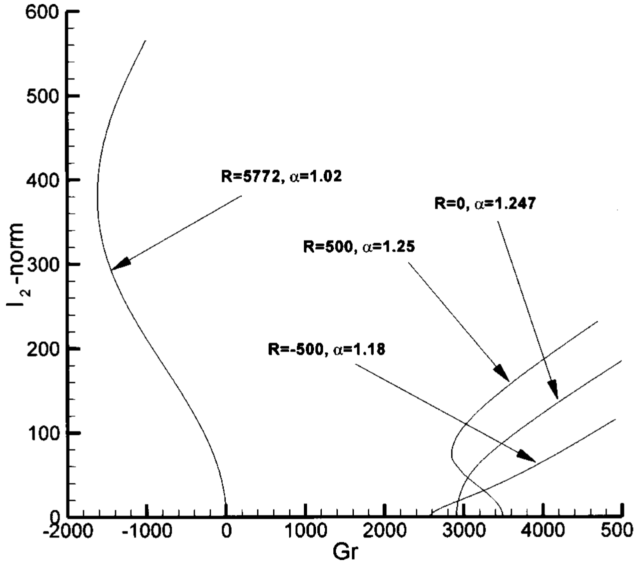

Fig. 3 L_2-norm curves as functions of Gr for various values of *R* and the wavenumber α, as indicated

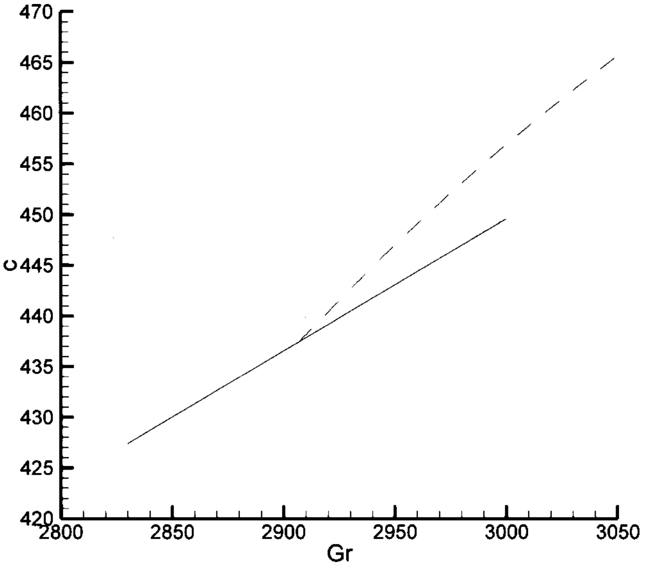

Fig. 4 Phase velocity curves as functions of Gr for $\alpha=1.247$, $R=0$. Linear analysis predictions are given by the solid line, while the dashed curve represents the phase velocity values for the nonlinear periodic equilibrium state bifurcating from the laminar state at $\mathrm{Gr}_c=2906.3637$.

values of m, n for the complex coefficients a_{mn}. The corresponding number of unknown coefficients are also presented there. We note that the corresponding wave number is fixed at $a=1.247$ with Gr=3500. Well converged secondary solutions have been obtained for $N=39$, $M=5$. These two parameter values were therefore retained for this work (and for consistency with the linear case).

In Fig. 3 we present the l_2-norm as a function of Gr for various different values of R: -500, 0, 500, 5772. While the latter two bifurcate subcritically the former two correspond to supercritical Hopf bifurcations. We also present in Fig. 4 the phase velocity as a function of the Grashof number for $R=0$, $\alpha=1.247$, and show the deviations from the values predicted by the linear theory, due to nonlinear effects. In order to visualize the nature of the steady solutions the total flow, disturbance and fluctuating stream functions are shown in Fig. 5, for the nonlinear state $\alpha=1.247$, Gr $=7000$. From Fig. 5(a) the flow is seen to be characterized by a sequence of transverse vortices aligned along the vertical axis. The addition of the disturbance $\int\check{U}dz$ to the fluctuating stream function creates a "snake"-like wavy motion, oscillating between positive and negative values of the horizontal coordinate z, as can be seen in Fig. 5(b). This meandering effect is present in Fig. 5(c), where the total flow contribution is depicted. Similar effects for the total flow contribution were observed in [8] in the case of Poiseuille flow. It is worth mentioning that in the zero mass flux basic state case of [10], primary instabilities only were considered. Consequently they were only able to predict the shape of the pattern produced by the two-dimensional (secondary) flow presented here. The finite value Prandtl number case has been considered by the authors recently in a separate work [2]. In Fig. 6 we show the total mean supercritical flow, an important quantity for comparisons with laboratory work, plotted against the channel width, for the nonlinear equilibrium state characterized by $\alpha=1.62$ and for various values of Gr.

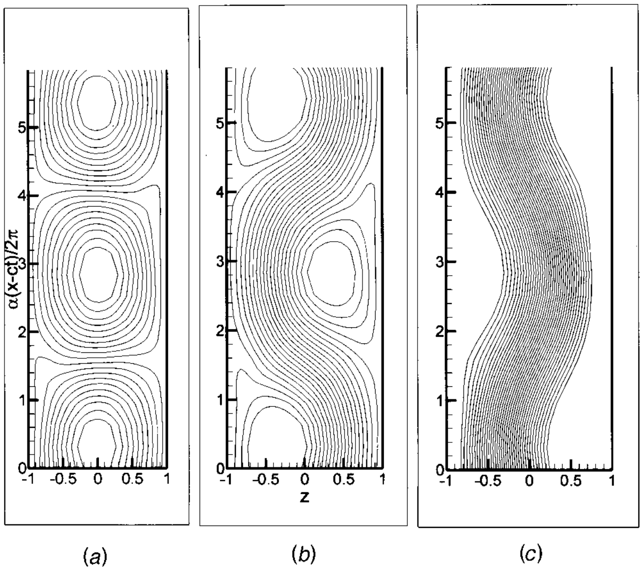

(a) (b) (c)

Fig. 5 The stream function of (a) the velocity fluctuations $\partial\phi/\partial x$, (b) the disturbance $\partial\phi/\partial x+\int_{-1}^{z}\check{U}dz$, and ($c$) the total flow, $\partial\phi/\partial x+\int_{-1}^{z}\hat{U}dz$, for the secondary state $\alpha=1.247$, Gr $=7000$, $R=0$

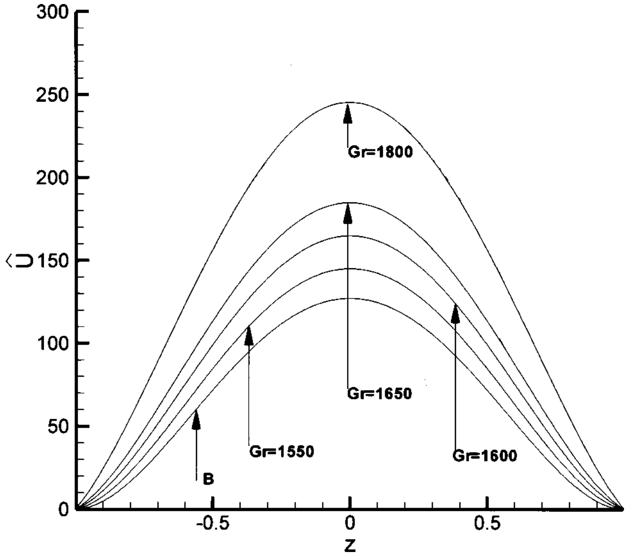

Fig. 6 Total mean flow ($\hat{U}$) profile for various Grashof numbers and for a fixed wavenumber $\alpha=1.62$ and Reynolds number $R=-500$, Gr=1550, 1600, 1650, and 1800, as indicated. B represents the basic flow contribution.

5 Instabilities of the Secondary Flow

We now study the linear stability of the secondary flow, in order to identify possible bifurcation points for the tertiary flow. In this section we have restricted ourselves to examining the stability of the flow with two values for the Reynolds number, $R=0$, -500. As Squire's theorem is not applicable in this case we cannot restrict ourselves to two dimensions and therefore we superimpose three-dimensional (solenoidal) infinitesimal disturbances on the secondary flow $\hat{U}\mathbf{i}+\check{\mathbf{u}}$ in the form

$$\tilde{\mathbf{u}}=\delta\tilde{\phi}+\varepsilon\tilde{\psi} \tag{5.1}$$

and we seek to numerically evaluate their corresponding growth rates σ. Disturbances with $\sigma_r<0$ will indicate a stable solution, while for $\sigma_r=0$ we have neutral stability and possibility of bifurcation for the tertiary flow. As there is no explicit dependence on y,t and the dependence on x is periodic we assume a periodic dependence on the first two coordinates. Three-dimensional solu-

Table 2 Values of the real, σ_{1r}, and imaginary, σ_{1i}, parts of the most dangerous eigenvalue σ_1, for a sample of the integer range $4 \leqslant M \leqslant 8$, $21 \leqslant N \leqslant 51$. Here $\alpha=1.25$, Gr=2910, Pr=$R=0$. The value of the parameters $\{d,b\}$ is fixed at $\{\alpha/4,1.0\}$, respectively. $\tilde{x}_i$ represents the number of the unknown (complex) perturbation coefficients.

$\tilde{x}_i$	N	M	σ_{1r}	σ_{1i}
308	21	3	4.8594122744	1.77233578302
396	21	4	4.87370354231	1.76854456194
660	21	7	4.8736823588	1.76855020079
748	21	8	4.87368235757	1.76855020038
816	23	8	-2.00251223878	3.68337061264
884	25	8	-1.97427450192	3.67830947034
1020	29	8	-2.00254877652	3.68677267093
576	31	4	-1.99699850387	3.68519277836
1088	31	8	-1.99699906625	3.68519293591
648	35	4	-2.00340703417	3.68711433805
1224	35	8	-2.00340843439	3.68711474207
880	39	5	-2.00407080983	3.68731499128
1360	39	8	-2.00407081905	3.68731499112
1056	47	5	-2.00407040272	3.68731486633
1632	47	8	-2.00407039951	3.68731487224
1144	51	5	-2.00407039685	3.68731485776
1768	51	8	-2.00407040048	3.68731487387

tions that bifurcate from the corresponding neutral stability points are computed via linear secondary stability theory, as described in the following section.

5.1 Numerical Method . We denote the complex disturbance on φ,ψ by $\tilde{\varphi},\tilde{\psi}$ respectively and we set:

$$\tilde{\phi}=\sum_{m=-\infty}^{\infty}\sum_{n=0}^{\infty}\exp\{im\alpha(x-ct)+id(x-ct)+iby+\sigma t\}\times(1-z^2)^2\tilde{a}_{mn}T_n(z), \tag{5.2}$$

$$\tilde{\psi}=\sum_{m=-\infty}^{\infty}\sum_{n=0}^{\infty}\exp\{im\alpha(x-ct)+id(x-ct)+iby+\sigma t\}\times(1-z^2)\tilde{b}_{mn}T_n(z), \tag{5.3}$$

with T_n the nth order Chebyshev polynomial and the boundary conditions:

$$\tilde{\phi}=\partial\tilde{\phi}/\partial z=\tilde{\psi}=0 \quad \text{at} \quad z=\pm 1. \tag{5.4}$$

In order to derive the corresponding equations for the disturbance field $\{\tilde{\Phi},\tilde{\Psi}\}$, we replace $\{\phi,\psi\}$, by $\{\phi+\tilde{\phi},\psi+\tilde{\psi}\}$ in Eqs. (2.21–2.22) and subtract the equations for the secondary solutions $\{\varphi,\psi\}$, while at the same time we ignore terms that are nonlinear in the disturbances, arriving at:

$$\begin{aligned}\frac{\partial}{\partial t}\nabla^2\Delta_2\tilde{\varphi}-\nabla^4\Delta_2\tilde{\varphi}+\hat{U}\partial_x\nabla^2\Delta_2\tilde{\varphi}&=\partial_z^2\hat{U}\Delta_2\partial_x\tilde{\varphi}+c\partial_x\nabla^2\Delta_2\tilde{\phi}-\boldsymbol{\delta}\cdot\{(\boldsymbol{\delta}\tilde{\phi}+\boldsymbol{\varepsilon}\tilde{\psi})\cdot\nabla(\boldsymbol{\delta}\phi)\\&\quad+(\boldsymbol{\delta}\phi)\cdot\nabla(\boldsymbol{\delta}\tilde{\phi}+\boldsymbol{\varepsilon}\tilde{\psi})\},\end{aligned} \tag{5.5}$$

$$\begin{aligned}\frac{\partial}{\partial t}\Delta_2\tilde{\psi}-\nabla^2\Delta_2\tilde{\psi}&=\partial_z\hat{U}\Delta_2\partial_y\tilde{\varphi}-\hat{U}\partial_x\Delta_2\tilde{\psi}+c\partial_x\Delta_2\tilde{\psi}\\&\quad-\boldsymbol{\varepsilon}\cdot\{(\boldsymbol{\delta}\tilde{\phi}+\boldsymbol{\varepsilon}\tilde{\psi})\cdot(\nabla(\boldsymbol{\delta}\phi)+(\boldsymbol{\delta}\phi)\cdot\nabla(\boldsymbol{\delta}\tilde{\phi}+\varepsilon\tilde{\psi})\}\end{aligned} \tag{5.6}$$

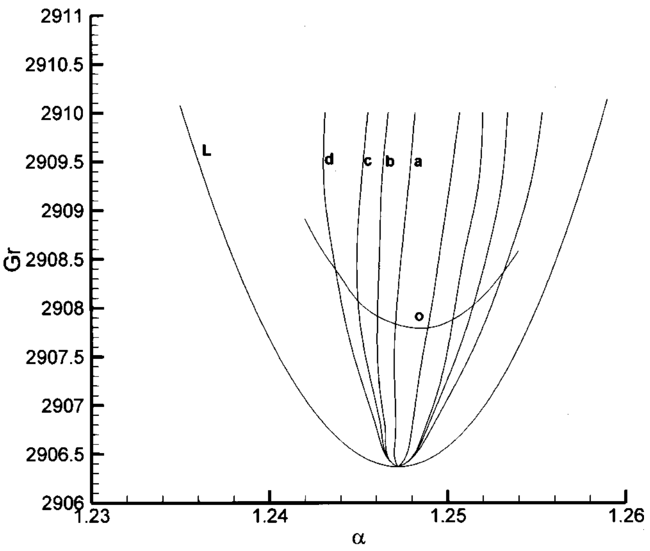

Fig. 7 Stability of transverse traveling waves for the case of *R*=0. The stable region is bounded by the Eckhaus and Hopf (labeled by *o* (Oscillatory)) curves. Various Eckhaus curves are presented depending on the maximum growth obtained for various values of the parameter *d*: (*a*) *d*=0.00001, (*b*) *d*=0.006, (*c*) *d*=0.01, and (*d*) *d*=0.02. *L* represents the linear stability curve.

As the value of d^2+b^2 will be assumed to be different from zero for the rest of the analysis, there are no contributions to the mean flow.

When we substitute Eqs. (5.2–5.3) into Eqs. (5.5–5.6), introduce the new coefficients $\tilde{\tilde{a}}_{mn}=\tilde{a}_{mn}\exp(-imact-icdt)$, $\tilde{\tilde{b}}_{mn}=\tilde{b}_{mn}\exp(-imact-icdt)$, (dropping the second ~ hereafter) and operate by $((\alpha b/4\pi^2)\int_0^{2\pi/a}dx\int_0^{2\pi/b}dy\exp(-\sigma t-iby-i(\gamma\alpha x+dx))\cdot)$ the following eigenvalue problem for the eigenvalue results:

$$Q_{ij}\tilde{x}_j=\sigma R_{ij}\tilde{x}_j\,, \tag{5.7}$$

in the unknown complex variables $\{\tilde{a}_{mn},\tilde{b}_{mn}\}$ represented by $\tilde{x}_i$. The real $2(2M+1)(N+1)$ matrices Q_{ij},R_{ij} are functions of the real parameters d,b, the wavenumber α, the parameter Gr and the amplitudes of the steady state solution $\{a_{mn},b_{mn},C_n\}$. We then proceed to evaluate Eq. (5.7) at the $N+1$ Chebyshev collocation points given by

$$z_i=\cos((i+1)\pi/(N+2)),\quad i=0,\ldots,N.$$

We have used here the same truncation level as that of the preceding section. Equations (5.7) are solved with the use of the NAG subroutine F02BJF. Typically the dimension of the vector $\tilde{x}_i$ is twice as large as the dimension of the vector x_i for the truncation level employed, as comparison between Tables 1 and 2 shows. In Table 2 the behavior of the leading eigenvalue σ_{1r} for a sample of the integer range $3\leqslant M\leqslant 8$, $21\leqslant N\leqslant 51$ and for the secondary state $\alpha=1.25$, Gr=2190, Pr=R=0 is also given. As can be verified from Table 2 low N is not sufficient to resolve the qualitative behavior of the eigenvalue problem and even the wrong sign can be obtained if the number of Chebyshev polynomials employed is not sufficiently large.

We note that in all cases examined the symmetry relations $\sigma_{1r}(b,d)=\sigma_{1r}(b,\pm d)$ (b fixed), $\sigma_{1r}(b,d)=\sigma_{1r}(\pm b,d)$ (d fixed), were always observed. Our results, described in some detail below, show that in all cases examined the most unstable mode always takes place at $d\neq\alpha$.

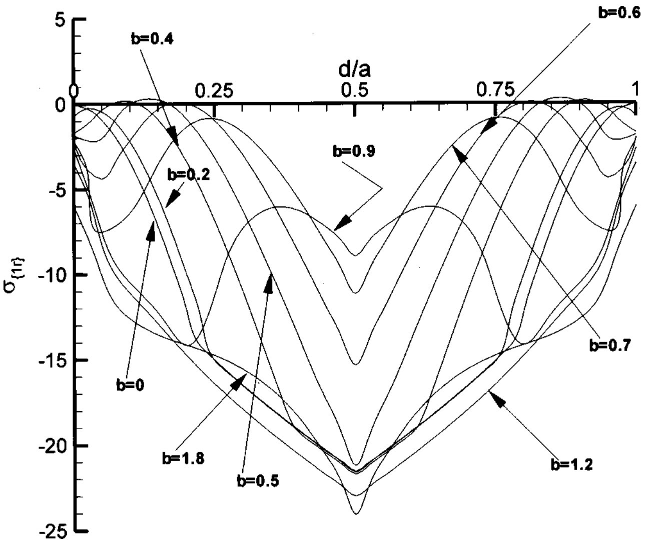

Fig. 8 Real part of the leading eigenvalue σ_{1r} as a function of *d* for α=1.247, Gr=2908, and for fixed values of the parameter *b* as indicated

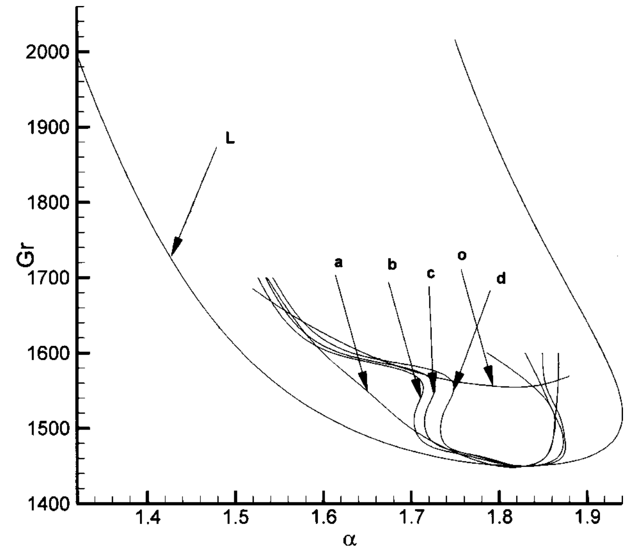

Fig. 9 Stability of transverse traveling waves for the case *R*=−500. The stable region is bounded by the Eckhaus and Hopf (labeled by *o* (Oscillatory)) curves. Various Eckhaus curves are presented depending on the maximum growth observed for various values of the parameter *d*: (*a*) *d*≈α/10, (*b*) *d*=0.1, (*c*) *d*=0.08, and (*d*) *d*=0.04. *L* represents the linear stability curve.

5.2 Results: *R*=0 Case. In Fig. 7 we present the stability range of transverse traveling vortices. It is bounded by the Eckhaus and Hopf bifurcation curves. For the Eckhaus curve, which bounds the area of the stable transverse traveling waves towards larger and lower wavenumbers, $b=0$. A number of Eckhaus curves are plotted, depending on the value of the parameter d. Several values of the Grashof number were studied and the maximum real part of the eigenvalue was evaluated. The value of Gr which determines the boundary of the curve was calculated by interpolation.

In order to determine such boundaries for a given value of the Grashof number that characterizes a secondary solution, we determine the eigenvalue σ of Eq. (5.7) as a function of the parameters b,d. We examined a variety of combinations of the relevant parameters, where a large number of eigenvalues was investigated for wavenumbers in the range $1.237\leqslant\alpha\leqslant 1.255$. In order to determine the value of b for which the maximum growth rate, σ_r, will occur, we fix the value of d to the one for which the maximum value of σ_r was observed for a given value of b, and we then examine σ_r as a function of b. A sample of the calculations is given in Fig. 8. Here we provide the real part of the leading eigenvalue σ_1, σ_{1r}, as a function of d for fixed values of b and for the case $\alpha=1.247$, Gr=2908. Even though a finite value for the parameters M, N has been assumed in this work, curves in Fig. 8 are symmetric.

Concentrating on the results presented in Fig. 8, we see that as the value of the parameter b varies the real part of σ_{1r} crosses the d/α axis. Because this eigenvalue has $\sigma_{1i}\neq 0$ at the zero growth rate point $\sigma_{1r}=0$ a Hopf bifurcation takes place. This occurrence combined with the underlying two-dimensional transverse traveling wave shows that a bifurcation to a spatially periodic flow with two frequencies in time appears. The three-dimensional flow is therefore quasi-periodic in time. Finally, as can be seen from Fig. 8, maximum growth rates were observed for $d\approx n\alpha/5$, $n=1,4$, for a fixed value of $0.4\approx b\approx 0.6$.

5.3 Results: $R=-500$ Case. In Fig. 9 we present the stability range of transverse traveling vortices. It is again bounded by the Eckhaus and Hopf bifurcation curves. For the Eckhaus curve, as before $b=0$. As in the case for $R=0$ a number of curves are plotted, depending on the value of d, for which maximum growth was observed.

In order to determine such boundaries for a given value of the Grashof number that characterizes a secondary solution, we determine the eigenvalue σ of Eq. (5.7) as a function of the parameters b,d. We examined a variety of combinations of the relevant parameters, where a large number of eigenvalues was investigated for wavenumbers in the range $1.5\leqslant\alpha\leqslant 1.9$. In order to determine the value of b for which the maximum growth rate, σ_r, will occur, we fix the value of d to the one for which the maximum value of σ_r was observed for a given value of b, and we then examine σ_r as a function of b. Maximum growth rates were observed for $d/\alpha\approx 1/4-0.3$, (with the symmetric peak at $d/\alpha\approx 0.7-3/4$) for a fixed value of $0.9\approx b\approx 1.2$. From our results presented we observed that as the value of the parameter b varies the real part of σ_{1r} crosses the d/α axis. Because this eigenvalue has $\sigma_{1i}\neq 0$ at the zero growth rate point $\sigma_{1r}=0$ a Hopf bifurcation to traveling wave solutions takes place, as in the case for $R=0$. The three-dimensional flow is therefore quasi-periodic in time in this case as well.

6 Conclusions

In this work we presented stability analysis of flows in a vertical channel uniformly heated and with (or without) the imposition of a constant pressure gradient. Squire's theorem is applicable in the standard linear analysis [10]. Linear stability analysis in the (Gr,α)-plane and for various values of the Reynolds number R showed that neutral curves almost always corresponded to a Hopf bifurcation.

Next, nonlinear secondary equilibrium states were obtained numerically with the aid of the Chebyshev collocation point method and the Newton-Raphson iterative method. We showed that the secondary equilibrium states bifurcate supercritically or subcritically from the neutral curve, depending on the value of R. Nonlinear properties of the secondary flow, such as the phase velocity and spatial structures of the transverse vortices, were analyzed in detail. Finally we studied the stability of the secondary flow, by applying the Floquet theory. We superimposed the general type of three-dimensional perturbations on the secondary equilibrium states for the cases $R=0$ and $R=-500$, where their primary bifurcation is supercritical. The stability ranges were found to be bounded by the Eckhaus and Hopf bifurcation curves. We observed that the Eckhaus curve bounded the range of stable secondary flow towards larger and smaller wavenumbers. Several (Eckhaus) stability curves were established depending on the value of d for the cases $R=0$ and $R=-500$. It was found that, in general, with increasing value of d, the sideband stability region was increased. The stability boundary of the secondary flow towards larger values of Gr was established via a Hopf bifurcation curve, indicating that the secondary flow is quasi-periodic. In the case of an inclined convective channel heated from above and cooled from below [6], the basic velocity profile is anti-symmetric about the mid-plane of the channel. The preferred three-dimensional flow in these cases is steady. When the basic velocity profile is symmetric, as the cases studied in this work, nonlinear analyses are currently available only for the case of Poiseuille flow, where it was found that the tertiary flow bifurcating from the lower branch is phase locked with the secondary flow [8]. The results obtained in this paper with the symmetric basic velocity profile are distinctive since we established that our tertiary flow is quasi-periodic. The extension of the current work to the more realistic case of finite Prandtl number, including comparisons with available experimental observations has been attempted and will be presented separately [2].

References

[1] Wilkie, D., and Fisher, S. A., 1961, ‘‘Natural Convection in a Liquid Containing a Distributed Heat Source,’’ *International Heat Transfer Conference*, Paper 119, University of Colorado, Boulder, CO, pp. 995–1002.

[2] Generalis, S., and Nagata, M., 2001, ‘‘Transition in Homogeneously Heated Inclined Convective Plane-Parallel Shear Flows,’’ in preparation.

[3] Busse, F. H., 1967, ‘‘On the Stability of Two-Dimensional Convection in a Layer Heated From Below,’’ J. Math. Phys., **46**, pp. 149–160.

[4] Clever, R. M., and Busse, F. H., 1975, ‘‘Transition to Time-Dependent Convection,’’ J. Fluid Mech., **65**, pp. 625–645.

[5] Clever, R. M., and Busse, F. H., 1995, ‘‘Tertiary and Quartenary Solutions for Convection in a Vertical Fluid Layer Heated From the Side,’’ Chaos, Solitons Fractals, **5**, pp. 1795–1803.

[6] Nagata, M., and Busse, F. H., 1983, ‘‘Three-Dimensional Tertiary Motions in a Plane Shear Layer,’’ J. Fluid Mech., **135**, pp. 1–26.

[7] Bergholz, R. F., 1977, ‘‘Instability of Steady Natural Convection in a Vertical Fluid Layer,’’ J. Fluid Mech., **84**, pp. 743–768.

[8] Ehrenstein, U., and Koch, W., 1991, ‘‘Three-Dimensional Wavelike Equilibrium States in Plane Poiseuille Flow,’’ J. Fluid Mech., **228**, pp. 111–148.

[9] Wall, D. P., and Nagata, M., 2000, ‘‘Nonlinear Equilibrium Solutions for the Channel Flow of Fluid With Temperature-Dependent Viscosity,’’ J. Fluid Mech., **406**, pp. 1–26.

[10] Gershuni, G. Z., and Zhukhovitskii, E. M., 1976, *Convective Stability of Incompressible Fluids*, Keterpress Enterprises, Jerusalem, translated from the Russian by D. Lowish.

[11] Chandrasekhar, S., 1961, *Hydrodynamic and Hydromagnetic Stability*, Dover Publications, New York.

[12] Schmitt, B. J., and Wahl, W. von, 1992, ‘‘Decomposition of Solenoidal Fluids into Poloidal Fields, Toroidal Fields and the Mean Flow. Applications to the Boussinesq-Equations,’’ in *The Navier-Stokes Equations II—Theory and Numerical Methods*, J. G. Heywood, K. Masuda, R. Rautmann, and S. A. Solonnikov, eds., Springer Lecture Notes in Mathematics, pp. 291–305.

Coupling of Buoyant Convections in Boron Oxide and a Molten Semiconductor in a Vertical Magnetic Field

Martin V. Farrell
Graduate Research Assistant
Department of Mechanical
and Aerospace Engineering,
North Carolina State University,
Campus Box 7910,
Raleigh, NC 27695

Nancy Ma
Assoc. Mem. ASME
e-mail: nancy_ma@ncsu.edu
Assistant Professor of Mechanical
and Aerospace Engineering,
Department of Mechanical
and Aerospace Engineering,
North Carolina State University,
Campus Box 7910,
Raleigh, NC 27695

This paper treats the buoyant convection in a layer of boron oxide, called a liquid encapsulant, which lies above a layer of a molten compound semiconductor (melt) between cold and hot vertical walls in a rectangular container with a steady vertical magnetic field B. The magnetic field provides an electromagnetic (EM) damping of the molten semiconductor which is an excellent electrical conductor but has no direct effect on the motion of the liquid encapsulant. The temperature gradient drives counter clockwise circulations in both the melt and encapsulant. These circulations alone would lead to positive and negative values of the horizontal velocity in the encapsulant and melt, respectively, near the interface. The competition between the two buoyant convections determines the direction of the horizontal velocity of the interface. For $B=5$ T, there is significant EM damping of the melt motion and the encapsulant drives a positive interfacial velocity and a small clockwise circulation in the melt. For a much weaker field $B=0.1$ T, the maximum velocity in the melt is hundreds of times larger than that of the encapsulant, thus causing nearly all the encapsulant to circulate in the clockwise direction. [DOI: 10.1115/1.1473141]

Keywords: Crystal Growth, Heat Transfer, Magnetohydrodynamics, Modeling

Introduction

There are many fluid flows that occur during semiconductor crystal growth. The physical understanding of these flows is key to the development of optimal crystal growth systems. Since molten semiconductors are excellent electrical conductors, a magnetic field can be used to control the melt motion in order to control the dopant distribution in the crystal, which depends on the convective and diffusive transport of the dopant in the melt. Electronic and optical devices are manufactured on single-crystal wafers sliced from ingots of semiconductors crystals. Since the performance of any device depends strongly on the uniformity of the local dopant concentration in the wafer on which it is produced, a major objective during the solidification of any semiconductor is to minimize dopant segregation in the crystal. With recent manufacturing advances, millions of devices are now produced on a single wafer, so that the need for a uniform dopant concentration in the wafer has dramatically increased. Hurle and Series [1], Walker [2], and Walker and Ma [3] reviewed the literature on the use of magnetic fields during the bulk growth of semiconductor crystals.

At each stage during the growth of a crystal by any process, there are infinitely many different ways to tailor the strength and configuration of the externally applied magnetic field, the rotation rates of the crystal and crucible, the distribution of the heat flux into the melt, the radiative and conductive heat losses from the melt, etc., so that process optimization through trial-and-error experimental crystal growth is not practical. Understanding of melt motion and development of models which accurately predict the dopant distribution in an entire crystal for any combination of process variables are needed to facilitate process optimization.

During the magnetic liquid encapsulated Czochralski (MLEC) growth of compound semiconductor crystals, such as indium-phosphide, phosphoric gas is bubbled at high pressure through an indium melt, and the indium and phosphorus fuse to form the compound InP. A layer of boron oxide (B_2O_3) encapsulates the melt to prevent escape of the volatile component (P). A single crystal seed is lowered through the encapsulant which initiates solidification and crystal growth begins in the presence of an externally-applied magnetic field. This is an extremely important process because it was the first to produce 8-cm diameter twin-free indium-phosphide crystals, and was accomplished by using magnetic stabilization [4,5]. Morton et al. [6] presented a model of dopant transport during the MLEC process. Previous researchers have investigated the effect of a steady magnetic field on buoyant convection in rectangular enclosures [7–9]. In particular, Alchaar et al. [7] and Garandet et al. [8] treated two-dimensional buoyant convection in a rectangular enclosure with a vertical magnetic field. Previous research which has treated systems that have liquid encapsulation have neglected any coupling between the buoyant convections in the molten semiconductor and in the liquid encapsulant and assumed that the liquid encapsulant is stagnant [10,11]. The steady magnetic field provides an electromagnetic damping of the molten semiconductor, which has a large electrical conductivity σ, but has no direct effect on the electrically-insulating boron oxide. The magnetic field has an indirect effect on the buoyant convection in the boron oxide through the coupling of its motion through the encapsulant-melt interface.

In the present paper, we treat a model problem which captures certain aspects of the coupling between the buoyant convections in the liquid encapsulant and in the molten semiconductor with a steady vertical magnetic field. Our model problem assumes that (1) the geometry is rectangular and not axisymmetric, (2) there is no solidification of the semiconductor crystal, and (3) the thermal boundary conditions are different from those in the liquid-encapsulated Czochralski process. Our model does include the essential physical phenomena that occurs in the coupling of the buoyant convections during MLEC crystal growth.

Problem Formulation

This paper treats the two-dimensional buoyant convection in two layers of fluid with a molten semiconductor (melt) encapsu-

---

Contributed by the Heat Transfer Division for publication in the JOURNAL OF HEAT TRANSFER. Manuscript received by the Heat Transfer Division July 7, 2001; revision received February 28, 2002. Associate Editor: K. S. Ball.

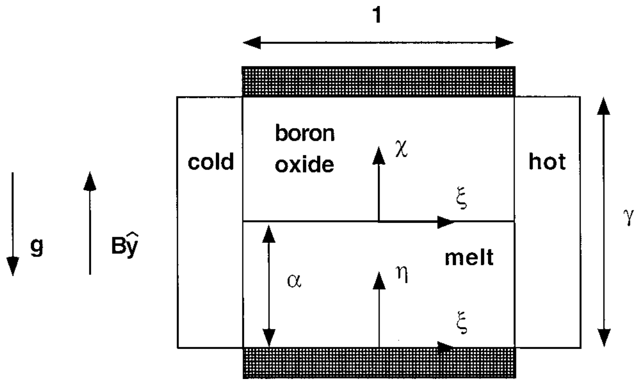

Fig. 1 Two-dimensional problem with a liquid encapsulant and molten semiconductor with a uniform, steady, vertical magnetic field $B\hat{y}$ and with coordinates normalized by the distance between the hot and cold vertical walls.

lated by a layer of boron oxide in a steady vertical magnetic field $B\hat{\mathbf{y}}$. Here, B is the magnetic flux density while $\hat{\mathbf{x}}$ and $\hat{\mathbf{y}}$ are the unit vectors for the Cartesian coordinate system. Our dimensionless problem is sketched in Fig. 1. The coordinates and lengths are normalized by the horizontal length of the melt or boron oxide L, so that α and $(\gamma\text{-}\alpha)$ are the dimensionless depths of the melt and boron oxide, respectively. Along $x=0$ and $x=1$, the liquids are maintained at temperatures T_c and T_h, respectively, where $T_h > T_c$. The boundaries at $y=0$ and $y=\gamma$ are thermal insulators. Here, the fluid flows are driven by the temperature difference so that the characteristic velocities for the buoyant convection in the melt [12] and in the encapsulant are

$$U=\frac{\rho g \beta(\Delta T)}{\sigma B^2}, \qquad (1a)$$

$$U_e=\frac{\rho_e g \beta_e(\Delta T)L^2}{\mu_e}, \qquad (1b)$$

respectively, where $(\Delta T)=T_h-T_c$ is the characteristic temperature difference, and g is gravitational acceleration. Here, ρ and β are the density and volumetric thermal expansion coefficient of the melt while ρ_e, β_e, and μ_e are the density, volumetric thermal expansion coefficient and dynamic viscosity of the encapsulant. With $(\Delta T)=50$ K and $L=5$ cm [13], the characteristic velocity in the encapsulant is $U_e=0.0141$ m/s while the characteristic velocity in the melt is $U=0.1571$, 0.006284 or 0.00006284 m/s for $B=0.1$, 0.5, or 5 T, respectively. The thermophysical properties of InP and B_2O_3 are provided in Table 1.

Table 1 Thermophysical properties of InP and B_2O_3

Property	InP	B_2O_3
Viscosity (Pa•s)	$8.19\text{x}10^{-4}$	10
Density (kg/m^3)	5050	1530
Specific heat (J/kg•K)	424	1864.3
Thermal conductivity (W/m•K)	22.8	2.0
Volumetric thermal expansion coefficient (K^{-1})	$4.44\text{x}10^{-4}$	$0.75\text{x}10^{-4}$
Electrical conductivity (S/m)	$7\text{x}10^{5}$	0

The electric current in the melt produces an induced magnetic field which is superimposed upon the applied magnetic field produced by the external magnet. The characteristic ratio of the induced to applied magnetic field strengths is the magnetic Reynolds number, $R_m=\mu_p \sigma U L$, where μ_p is the magnetic permeability of the melt. For all crystal-growth processes, $R_m \ll 1$ and the additional magnetic fields produced by the electric currents in the melt are negligible.

In the Navier-Stokes equation for the melt, the characteristic ratio of the electromagnetic (EM) body force term to the inertial terms is the interaction parameter, $N=\sigma B^2 L/\rho U$, which varies as B^4. In the energy equation, the characteristic ratio of the convective to conductive heat transfer is the thermal Péclet number, $\text{Pe}_t=\rho c_p U L/k$, where c_p and k are the specific heat and thermal conductivity of the melt, respectively. For a sufficiently strong magnetic field, N is large, and Pe_t is small, so that the inertial terms and the convective heat transfer terms are negligible. In a recent study, Ma and Walker [14] investigated the role of inertia and convective heat transfer on the buoyant convection during MLEC growth, and determined the errors associated with the neglect of inertial effects or of convective heat transfer for field strengths between 0.1 T and 0.9 T. For MLEC growth of indium phosphide, they found that inertia and convective heat transfer significantly affect the buoyant convection when $B=0.1\,T$ for which $N=1.037$ and $\text{Pe}_t=277.3$. As the magnetic field strength is increased from this value, the interaction parameter increases as B^4 and the thermal Péclet number decreases as B^{-2}, so that the ratios of the inertial force to the EM body force and of convective heat transfer to conductive heat transfer decrease. Ma and Walker [14] found that the error due to neglect of inertial effects is only 2.7 percent for $B=0.2\,T$ where $N=16.59$ and $\text{Pe}_t=69.33$, and is totally negligible for $B \geqslant 0.5\,T$, while the error due to neglect of convective heat transfer is less than 4 percent for $B \geqslant 0.43\,T$. Inclusion of inertia and convective heat transfer for weak magnetic field strengths is a straightforward extension of the present model, and will be included in future studies.

For the encapsulant, the characteristic ratio of the inertial force to the viscous force is the Reynolds number $\text{Re}=\rho_e U_e L/\mu_e$ and the characteristic ratio of the convective to conductive heat transfer is $\text{Pe}_{te}=\rho_e c_{pe} U_e L/k_e$, where c_{pe} and k_e are the specific heat and thermal conductivity of the encapsulant, respectively. For boron oxide, Re=0.108 so that inertial terms are negligible. For boron oxide, the thermal Péclet number based on our choice for the characteristic velocity U_e is $\text{Pe}_{te}=1003$. From our study, we find that the dimensionless velocities in the encapsulant are extremely small, i.e., they vary from roughly 10^{-7} to 10^{-5}, so that the effective thermal Péclet number is $\text{Pe}_{te,\text{effective}}=\text{Pe}_{te}\Psi_{e,\max}$. Since $\text{Pe}_{te,\text{effective}} \ll 1$, convective heat transfer in the encapsulant is negligible.

The steady-state solutions for pure conduction are

$$T(\xi,\eta)=T_e(\xi,\chi)=\tfrac{1}{2}(\xi+1), \qquad \text{for} \quad -1 \leqslant \xi \leqslant 1, \qquad (2a)$$

and

$$-1 \leqslant \eta \leqslant 1 \quad \text{or} \quad -1 \leqslant \chi \leqslant 1, \qquad (2b)$$

where T is the deviation of the dimensional temperature in the melt from T_c normalized by (ΔT), and T_e is the deviation of the dimensional temperature in the encapsulant from T_c normalized by (ΔT). Here, $\xi=2x-1$, $\eta=-1+2y/\alpha$ and $\chi=(2y-\gamma-\alpha)/(\gamma-\alpha)$ are rescaled coordinates so that $-1 \leqslant \xi \leqslant +1$, $-1 \leqslant \eta \leqslant +1$ and $-1 \leqslant \chi \leqslant +1$.

For the present plane recirculating flow in the melt, the condition of zero net electric current in the z direction implies that the electric field is zero [7]. The only non-zero component of the electric current density, normalized by σUB, is given by Ohm's law, $j_z = u$, where $\mathbf{v}(\xi,\eta) = u\hat{\mathbf{x}} + v\hat{\mathbf{y}}$ is the dimensionless velocity in the melt normalized by U.

For an inertialess flow, the buoyant convection in the molten semiconductor is governed by

$$\frac{\partial u}{\partial \xi} + \frac{1}{\alpha}\frac{\partial v}{\partial \eta} = 0, \tag{3a}$$

$$0 = -\frac{\partial p}{\partial \xi} - u + \frac{2}{\mathrm{Ha}^2}\left(\frac{\partial^2 u}{\partial \xi^2} + \frac{1}{\alpha^2}\frac{\partial^2 u}{\partial \eta^2}\right), \tag{3b}$$

$$0 = -\frac{1}{\alpha}\frac{\partial p}{\partial \eta} + T + \frac{2}{\mathrm{Ha}^2}\left(\frac{\partial^2 v}{\partial \xi^2} + \frac{1}{\alpha^2}\frac{\partial^2 v}{\partial \eta^2}\right), \tag{3c}$$

$$u = \frac{2}{\alpha}\frac{\partial \psi}{\partial \eta}, \quad v = -2\frac{\partial \psi}{\partial \xi}, \tag{3d}$$

where p is the deviation of the pressure from the hydrostatic pressure normalized by $\rho g \beta (\Delta T) L$, and ψ is the dimensionless streamfunction in the melt normalized by UL, T in the buoyancy term is given by Eq. (2*a*). The motion of the electrically-conducting melt and the externally applied magnetic field drives an induced electric current in the melt in the *z*-direction. This current in turn provides an electromagnetic body force $-u\hat{\mathbf{x}}$ which opposes the horizontal melt motion as reflected in Eq. (3*b*). Here, the Hartmann number $\mathrm{Ha} = BL(\sigma/\mu)^{1/2}$ is the square root of the ratio of the electromagnetic body force to the viscous force, where μ is the dynamic viscosity of the molten semiconductor.

For an inertialess flow, the buoyant convection in the encapsulant is governed by

$$\frac{\partial u_e}{\partial \xi} + \frac{1}{(\gamma-\alpha)}\frac{\partial v_e}{\partial \chi} = 0, \tag{4a}$$

$$0 = -\frac{\partial p_e}{\partial \xi} + \frac{2}{\mathrm{Ha}^2}\left[\frac{\partial^2 u_e}{\partial \xi^2} + \frac{1}{(\gamma-\alpha)^2}\frac{\partial^2 u_e}{\partial \chi^2}\right], \tag{4b}$$

$$0 = -\frac{1}{(\gamma-\alpha)}\frac{\partial p}{\partial \eta} + T_e + \frac{2}{\mathrm{Ha}^2}\left[\frac{\partial^2 v_e}{\partial \xi^2} + \frac{1}{(\gamma-\alpha)^2}\frac{\partial^2 v_e}{\partial \chi^2}\right], \tag{4c}$$

$$u_e = \frac{2}{(\gamma-\alpha)}\frac{\partial \psi_e}{\partial \chi}, \quad v_e = -2\frac{\partial \psi_e}{\partial \xi}, \tag{4d}$$

where $\mathbf{v}_e(\xi,\chi) = u_e\hat{\mathbf{x}} + v_e\hat{\mathbf{y}}$ is the dimensionless velocity in the encapsulant normalized by U_e, p_e, is the deviation of the pressure from the hydrostatic pressure normalized by $\mu_e U_e/L$, and ψ_e is the dimensionless streamfunction in the encapsulant normalized by $U_e L$, while T_e in the buoyancy term is given by Eq. (2*b*).

We apply the no-slip and no-penetration conditions along the walls at $\xi = -1$, $\xi = +1$, $\eta = -1$ and $\chi = +1$. For our flat interface, the no-slip and no-penetration conditions are

$$u(\xi,t) = \frac{\lambda_B}{\lambda_\mu}\mathrm{Ha}^2 u_e(\xi,-1), \qquad \text{for} \quad -1 \leqslant \xi \leqslant +1, \tag{5a}$$

$$v(\xi,+1) = 0, \qquad \text{for} \quad -1 \leqslant \xi \leqslant +1, \tag{5b}$$

$$v_e(\xi,-1) = 0, \qquad \text{for} \quad -1 \leqslant \xi \leqslant +1. \tag{5c}$$

Here, $\lambda_\beta = \rho_e \beta_e/(\rho\beta)$ and $\lambda_\mu = \mu_e/\mu$. With boron oxide and molten indium-phosphide, $\lambda_\beta = 0.10235$ and $\lambda_\mu = 12210$. The stress is continuous across the interface so that

$$\frac{\partial u}{\partial y}(\xi,+1) = \lambda_B \ \mathrm{Ha}^2\frac{\partial u_e}{\partial y}(\xi,-1), \qquad \text{for} \quad -1 \leqslant \xi \leqslant +1. \tag{6}$$

Here we neglect gradients of the interfacial tension due to gradients of the temperature or of dopant concentration along the encapsulant-melt interface. A measure of the effects of interfacial tension gradients is the Marangoni number for the encapsulant, $Ma_e = \rho_e(-d\Gamma/dT)(\Delta T)L/\mu_e^2$, where Γ is the interfacial tension of the encapsulant-melt interface. There is no published data on the tension of an interface between a liquid semiconductor and boron oxide. If we use the values of Γ for a liquid-silicon free surface, which are certainly much larger than those for an encapsulant-melt interface, we find that $Ma_e = 0.00516$ for our typical process.

A Chebyshev spectral collocation method was used to solve Eqs. (3)–(6) for ψ and ψ_e with Gauss-Lobatto collocation points in ξ, η and χ. In an asymptotic solution for $\mathrm{Ha} \gg 1$, the melt is divided into (1) an inviscid core, (2) parallel layers which have an $\Delta x = O(\mathrm{Ha}^{-1/2})$ thickness adjacent to the walls at $\xi = \pm 1$ and which carry an $O(\mathrm{Ha}^{1/2})$ flow, and (3) Hartmann layers which have an $\Delta y = O(\mathrm{Ha}^{-1})$ thickness and which carry an $O(\mathrm{Ha}^{-1})$ flow. We use a sufficient number of collocation points to resolve the large velocity gradients near $\xi = \pm 1$ and to resolve the Hartmann layers at $\eta = \pm 1$. The number of collocation points in each direction in both the melt and the encapsulant were increased until the results were independent of these numbers. The required number of collocation points increased as B was increased in order to resolve the gradients in the boundary layers. For example, for $B = 0.2\ T$ with $\alpha = 0.3$ and $\gamma = 0.5666$, the difference in the maximum values of the streamfunctions both in the melt and in the encapsulant are each less than 1 percent. Here, we compare the results for the numerical results with 71, 51, and 26 collocation points and with 36, 36, and 16 collocation points in the ξ, η, and χ directions, respectively. For $B = 0.5\ T$ with $\alpha = 0.3$, and $\gamma = 0.5666$, we used a larger number of collocation points, namely, 71, 81, and 31 in the ξ, η, and χ directions, respectively.

Results

Prior to solidification in the liquid-encapsulated Czochralski process, the axisymmetric melt is entirely encapsulated by the boron oxide. A single crystal seed is lowered to the surface of the melt which initiates solidification. The crystal grows into the melt until the desired diameter is reached, and the crystal has a flat top. When the desired diameter is reached, the crystal is pulled vertically upward through the layer of encapsulant. During this period of time, the encapsulant's depth increases because the growing crystal displaces the encapsulant that lies above it. Once the flat top of the crystal is pulled out of the encapsulant, the encapsulant's depth is constant and the melt's depth continues to decrease due to solidification. The purpose of the present paper is to illustrate the degree of coupling for various magnetic field strengths so we only present results for $\alpha = 0.3$ and $\gamma = 0.5666$.

With the cold and hot walls at the left and right, respectively, the temperature gradient drives counterclockwise circulations in both the melt and the encapsulant. These circulations alone would lead to positive and negative values of u in the encapsulant and

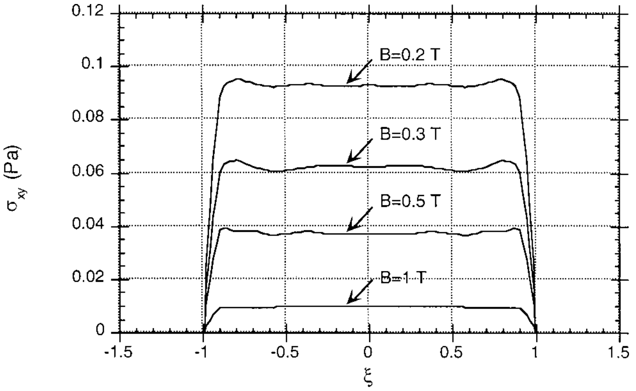

Fig. 2 Interfacial shear stress σ_{xy} versus ξ for $B = 0.2$, 0.3, 0.5, and 1 T

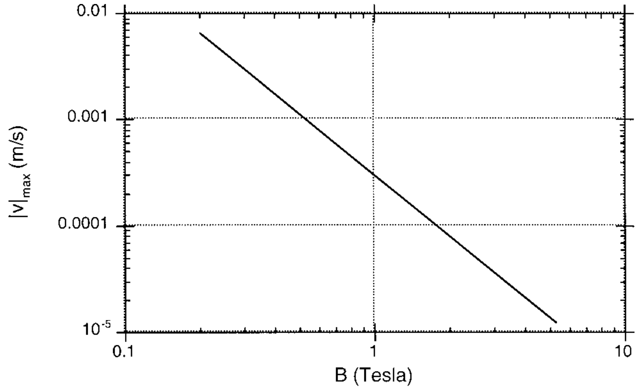

Fig. 3 Maximum magnitude of the velocity in the melt versus magnetic field strength for $0.2 \leq B \leq 5$ T

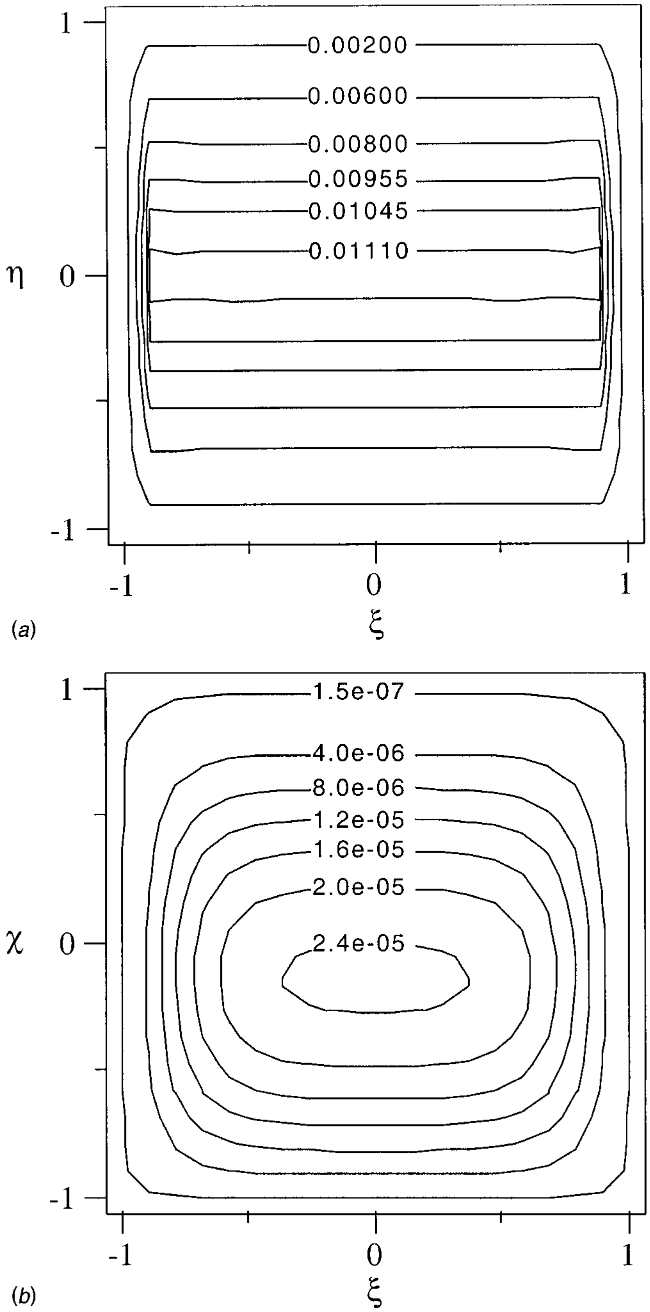

Fig. 4 Streamlines for $B=5$ T: (a) $\psi(\xi,\eta)$, and (b) $\psi_e(\xi,\chi)$

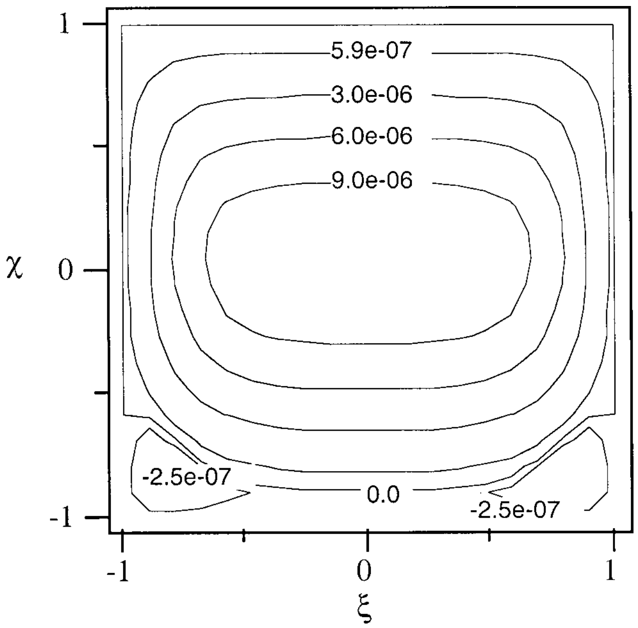

Fig. 5 Streamlines in the encapsulant $\psi_e(\xi,\chi)$ for $B=0.5$ T

melt, respectively, near the interface. Therefore the shear stress σ_{xy} at the interface is always positive, i.e., a force to the left on the bottom of the encapsulant and an equal force to the right on the top of the melt. The competition between the two buoyant convections, reflected by the continuity of u and of σ_{xy} at the interface, determines whether u at the interface is positive or negative. A positive value would reflect dominance by the encapsulant circulation, resulting in a clockwise circulation in the melt near the interface. A negative interfacial u would reflect dominance by the melt circulation, resulting in a clockwise circulation in the encapsulant near the interface. For all the cases considered here except for $B=5$ T, the interfacial u is negative, reflecting dominance by the buoyant convection in the melt, but this dominance decreases dramatically as the magnetic field strength is increased. For $B=5$ T, the encapsulant has a slight dominance which drives a positive interfacial u.

In Fig. 2, we present the dimensional interfacial shear stress for various magnetic field strengths. For $B=0.2$ T, the buoyant convection in the melt is relatively strong and produces a relatively large shear stress to the left on the bottom of the encapsulant. As the magnetic field strength is increased, the magnitude of the buoyant convection in the melt decreases roughly as B^{-2}, as reflected by our choice for the characteristic melt velocity in Eq. (1*a*). However, there is a jump in u across a Hartmann layer with an $O(\mathrm{Ha}^{-1})$ thickness adjacent to the encapsulant-melt interface, so that the interfacial shear stress decreases roughly as B^{-1} since the melt velocity varies as B^{-2} and the local y derivative varies as B. The effect of the EM damping is reflected in the dramatic decrease of the maximum magnitude of the melt velocity with increasing field strength which is presented in Fig. 3 for $0.2 \leq B \leq 5$ T. The maximum magnitude of the melt's velocity is 0.006593 m/s for $B=0.2$ T and is 0.00001156 m/s for $B=5$ T.

For $B=5$ T, the maximum and minimum dimensionless streamfunctions in the melt and in the encapsulant are 0.01133 and 2.53×10^{-5}, respectively, and the streamlines are plotted in Figs. 4(*a*) and 4(*b*). For this strong field, there is a significant electromagnetic (EM) damping of the flow, and the velocities in the two fluids are roughly the same order of magnitude where the maximum magnitude of the melt's velocity is 2.4 times larger than that of the encapsulant. The buoyant convection in the encapsulant drives a positive interfacial velocity in the melt and a clockwise circulation inside the Hartmann layer along $\eta=+1$. $u=0.146$

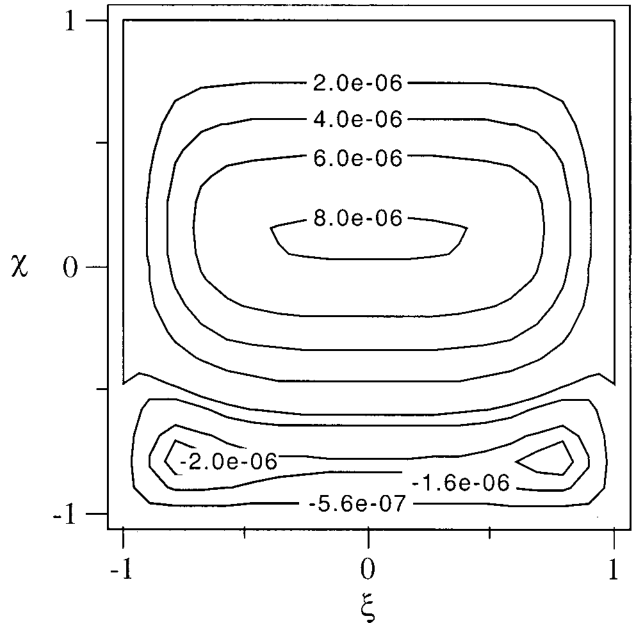

Fig. 6 Streamlines in the encapsulant $\psi_e(\xi,\chi)$ for $B=0.4$ T

along the interface at $\xi=0$. The interfacial shear stress of the slow-moving melt decreases the velocity of the encapsulant but does not drive flow in the opposite direction.

When the magnetic field strength is decreased to $B=0.5$ T, there is significantly less EM damping of the melt motion and the velocity of the melt is much larger. The circulation in the melt is entirely counterclockwise with $u<0$ along the interface. For $B=0.5$ T, the maximum magnitude of the melt's velocity is 0.001467 m/s and of the encapsulant's velocity is 0.000002319 m/s, as shown in Fig. 5. The melt drives two small clockwise cells in the encapsulant at $\xi=\pm1$ adjacent to the interface but the bulk of the encapsulant flows towards the hot wall at $\xi=+1$. The shear stress curve for $B=0.5$ T in Fig. 2 helps to explain this phenomena. The interfacial shear stress is equal to zero at $\xi=\pm1$, increases to a maximum as $|\xi|$ decreases, and then decreases to a value of about 0.0031 Pa in the middle. The two opposing cells are centered near the locations where the interfacial shear stress is maximum.

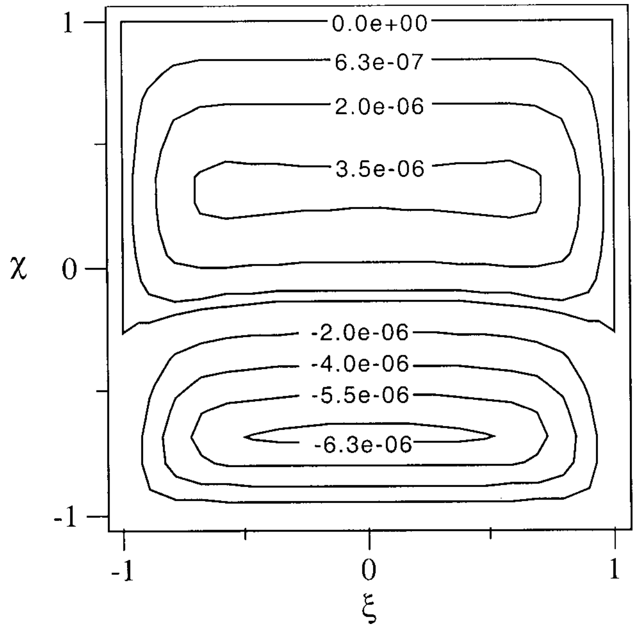

Fig. 7 Streamlines in the encapsulant $\psi_e(\xi,\chi)$ for $B=0.3$ T

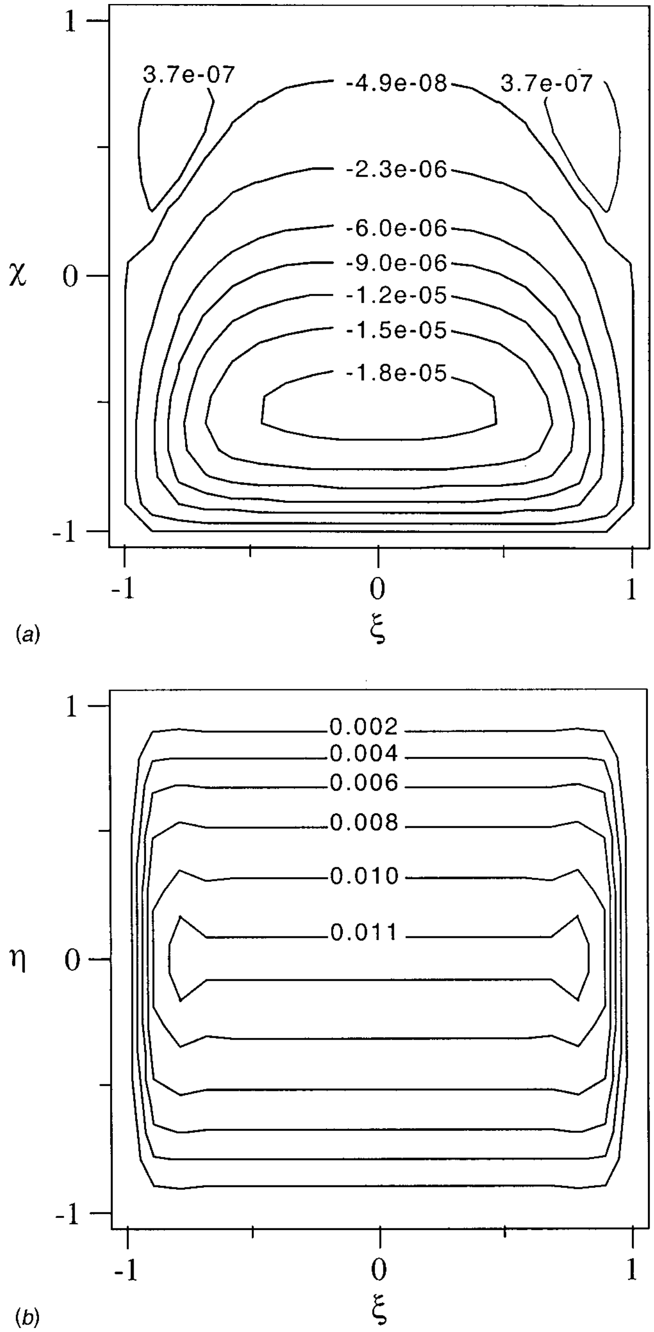

Fig. 8 Streamlines for $B=0.2$ T: (*a*) $\psi(\xi,\eta)$, and (*b*) $\psi_e(\xi,\chi)$

For $B=0.4$ T, we present the streamlines in the encapsulant in Fig. 6. The minimum and maximum streamfunctions in the encapsulant are -1.74×10^{-6} and 9.32×10^{-6}, respectively, while the maximum streamfunction in the melt is 0.01168. For $B=0.4$ T, the maximum magnitude of the melt's velocity is 0.002149 m/s which is 1014 times larger than that of the encapsulant. The interfacial shear stress is larger than that for $B=0.5$ T so that the two cells in the encapsulant at $\xi=\pm1$ have grown, as shown in Fig. 6. The larger interfacial shear stress provides a force which reverses the flow along the entire interface.

For $B=0.3$ T, the streamlines in the encapsulant are presented in Fig. 7. The maximum magnitude of the melt's velocity is

0.0033984 m/s which is 689 times larger than that of the encapsulant. The larger interfacial shear stress, as shown in Fig. 2 for $B=0.3\ T$, causes nearly half of the encapsulant's flow to reverse its direction. Here, the minimum and maximum streamfunctions in the encapsulant are -6.74×10^{-6} and 3.58×10^{-6}, respectively, while the maximum streamfunction in the melt is 0.01135.

When the field strength is decreased further to $B=0.2\ T$, the maximum streamfunction in the melt is 0.01134 and the minimum and maximum streamfunctions in the encapsulant are -2.1×10^{-5} and 6.37×10^{-7}, respectively, as shown in Figs. 8(*a*) and 8(*b*). The maximum magnitude of the velocity in the melt is 617 times that of the encapsulant and the interfacial shear stress shown in Fig. 2 has increased to 0.098 Pa in the middle of the fluids. This causes most of the encapsulant to circulate in the clockwise direction with two small counterclockwise circulations in the top of the encapsulant adjacent to the cold and hot walls.

The melt's flow clearly has a significant effect on the encapsulant's flow except for strong magnetic fields. However, the encapsulant has virtually no effect on the melt motion. To illustrate this point, we solved the equations governing the melt motion, i.e., Eqs. (3*a*) through (3*d*), with a rigid boundary at $\eta=+1$ so that we applied $u(\xi,+1)=0$ instead of boundary conditions (5*a*) and (6). In fact, when the maximum velocities with the encapsulant and with the rigid boundary are plotted together versus magnetic field strength in Fig. 3, the difference in the velocities are indistinguishable.

The key parameter is $(\lambda_\beta/\lambda_\mu)\mathrm{Ha}^2$ in Eq. (5*a*). As long as $(\lambda_\beta/\lambda_\mu)\mathrm{Ha}^2\ll1$, $u(\xi,+1)$ is roughly zero. $(\lambda_\beta/\lambda_\mu)\mathrm{Ha}^2$ only becomes $O(1)$ when Ha is very large. Then, as shown in Fig. 4(*a*) for $B=5\ T$, u of the interface and of the melt in part of the interface's Hartmann layer are positive. However, for $\mathrm{Ha}\gg1$, the Hartmann layer matches any jump in u with only an $O(\mathrm{Ha}^{-1})$ effect on the core flow through the Hartmann condition $v_c=\pm\mathrm{Ha}^{-1}\partial u_c/\partial x$, where c denotes an inviscid core region. Thus once B is large enough that the two convections are comparable, and the encapsulant's buoyant convection produces a positive interfacial u, the Hartmann layer is so thin that the effect of the positive interfacial u is negligible. For $B=5\ T$, the $u(\xi=0,\eta=+1)=+0.1457$ m/s.

Conclusions

The temperature gradient drives counter clockwise circulations in both the melt and encapsulant. These circulations alone would lead to positive and negative values of the horizontal velocity in the encapsulant and melt, respectively, near the interface. The competition between the two buoyant convections determines the direction of the horizontal velocity of the interface. For $B=5\ T$, there is significant EM damping of the melt motion and the encapsulant drives a positive interfacial velocity and a small clockwise circulation in the melt. For a much weaker field $B=0.1\ T$, the maximum velocity in the melt is hundreds of times larger than that of the encapsulant, thus causing nearly all the encapsulant to circulate in the clockwise direction.

In the present study, the encapsulant has virtually no effect on the melt motion except for very strong magnetic field strengths. Therefore, the implications for MLEC crystal growth are that the encapsulant-melt interface can be treated as a rigid boundary for crystal growth in a steady vertical magnetic field with a planar interface.

Acknowledgments

This research was supported by the National Aeronautics and Space Administration under grant NAG8-1817. The calculations were performed on the SGI Origin and IBM SP at the North Carolina Supercomputing Center in Research Triangle Park, NC.

Nomenclature

B = magnetic flux density
c_p = specific heat of the melt
c_{pe} = specific heat of the encapsulant
g = gravitational acceleration
Ha = Hartmann number
j_z = z component of the electric current density in the melt
$\mathrm{Pe}_{te,\mathrm{effective}}$ = effective thermal Péclet number for the encapsulant
Ψ = dimensionless streamfunction in the melt
Ψ_e = dimensionless streamfunction in the encapsulant
$\Psi_{e,\max}$ = dimensionless streamfunction in the encapsulant
k = thermal conductivity of the melt
k_e = thermal conductivity of the encapsulant
L = horizontal length of the melt or of the encapsulant
Ma_e = Marangoni number for the encapsulant
N = interaction parameter
p = deviation of the dimensional pressure in the melt from the hydrostatic pressure normalized by $\rho g\beta(\Delta T)L$
p_e = deviation of the dimensional pressure in the encapsulant from the hydrostatic pressure normalized by $\mu_e U_e/L$
Pe_t = thermal Péclet number for the melt
Pe_{te} = thermal Péclet number for the encapsulant
R_m = magnetic Reynolds number
T = deviation of the dimensional temperature in the melt from T_c normalized by (ΔT)
T_c = constant uniform temperature of the cold wall
T_e = deviation of the dimensional temperature in the encapsulant from T_c normalized by (ΔT)
T_h = constant uniform temperature of the hot wall
u = dimensionless horizontal velocity in the melt
u_e = dimensionless horizontal velocity in the encapsulant
U = characteristic velocity for the melt
U_e = characteristic velocity for the encapsulant
v = dimensionless vertical velocity in the melt
v_e = dimensionless vertical velocity in the encapsulant
x = dimensionless horizontal coordinate in the melt or in the encapsulant
$\hat{\mathbf{x}},\hat{\mathbf{y}},\hat{\mathbf{z}}$ = unit vectors in the Cartesian coordinate system
y = dimensionless vertical coordinate
z = dimensionless transverse coordinate

Greek Symbols

α = dimensionless depth of the melt
β = volumetric thermal expansion coefficient for the melt
β_e = volumetric thermal expansion coefficient for the encapsulant
χ = rescaled dimensionless vertical coordinate in the encapsulant
(ΔT) = characteristic temperature difference equal to (T_h-T_c)
η = rescaled dimensionless vertical coordinate in the melt
γ = dimensionless depth of the melt and encapsulant
Γ = interfacial surface tension
λ_β = ratio of $\rho_e\beta_e$ to $\rho\beta$
λ_μ = ratio of encapsulant's viscosity to the melt's viscosity
μ = dynamic viscosity of the melt
μ_e = dynamic viscosity of the encapsulant
ρ = density of the melt
ρ_e = density of the encapsulant
σ = electrical conductivity of the melt
ξ = rescaled dimensionless horizontal coordinate in the melt or in the encapsulant

References

[1] Hurle, D. T. J., and Series, R. W., 1994, ''Use of a Magnetic Field in Melt Growth,'' *Hanb Cryst Growth*, D. T. J. Hurle, ed., Elsevier Science Publishers, **2A**, pp. 261–285.

[2] Walker, J. S., 1999, ''Models of Melt Motion, Heat Transfer, and Mass Transport During Crystal Growth With Strong Magnetic Fields,'' *The Role of Magnetic Fields in Crystal Growth*, in *Prog Cryst Growth Charact Mater*, K. W. Benz, ed., Elsevier Science Publishers, **38**, pp. 195–213.

[3] Walker, J. S., and Ma, N., 2002, ''Convective Mass Transport During Bulk Growth of Semiconductor Crystals With Steady Magnetic Fields,'' *Annu Rev Heat Transfer*, Chang-Lin Tien, Vishwanath Prasad, and Frank Incropera, eds., Begell House, New York, **12**, pp. 223–263.

[4] Bliss, D. F., Hilton, R. M., and Adamski, J. A., 1993, ''MLEK Crystal Growth of Large Diameter (100) Indium Phosphide,'' J. Cryst. Growth, **128**, pp. 451–456.

[5] Bliss, D. F., Hilton, R. M., Bachowski, S., and Adamski, J. A., 1991, ''MLEK Crystal Growth of (100) Indium Phosphide,'' J. Electron. Mater., **20**, pp. 967–971.

[6] Morton, J. L., Ma, N., Bliss, D. F., and Bryant, G. G., 2001, ''Diffusion-Controlled Dopant Transport During Magnetically-Stabilized Liquid-Encapsulated Czochralski Growth of Compound Semiconductor Crystals,'' ASME J. Fluids Eng., **123**, pp. 893–898.

[7] Alchaar, S., Vasseur, P., and Bilgen, E., 1995, ''Natural Convection Heat Transfer in a Rectangular Enclosure With a Transverse Magnetic Field,'' J. Heat Transfer, **117**, pp. 668–673.

[8] Garandet, J. P., Alboussière, T., and Moreau, R., 1992, ''Buoyancy Driven Convection in a Rectangular Enclosure With a Transverse Magnetic Field,'' Int. J. Heat Mass Transf., **35**, pp. 741–748.

[9] Ozoe, H., and Okada, K., 1989, ''The Effect of the Direction of the External Magnetic Field on the Three-Dimensional Natural Convection in a Cubical Enclosure,'' Int. J. Heat Mass Transf., **32**, pp. 1939–1954.

[10] Ma, N., and Walker, J. S., 1996, ''Buoyant Convection During the Growth of Compound Semiconductors by the Liquid-Encapsulated Czochralski Process With an Axial Magnetic Field and With a Non-Axisymmetric Temperature,'' ASME J. Fluids Eng., **118**, pp. 155–159.

[11] Ma, N., Walker, J. S., Bliss, D. F., and Bryant, G. G., 1998, ''Forced Convection During Liquid Encapsulated Crystal Growth With an Axial Magnetic Field,'' ASME J. Fluids Eng., **120**, pp. 844–850.

[12] Hjellming, L. N., and Walker, J. S., 1987, ''Melt Motion in a Czochralski Crystal Puller With an Axial Magnetic Field: Motion Due to Buoyancy and Thermocapillarity,'' J. Fluid Mech., **182**, pp. 335–368.

[13] Bryant, G. G., Bliss, D. F., Leahy, D., Lancto, R., Ma, N., and Walker, J. S., 1997, ''Crystal Growth of Bulk InP From Magnetically Stabilized Melts With a Cusped Field,'' *IEEE Proceedings of the International Conference on Indium Phosphide and Related Materials*, pp. 416–419.

[14] Ma, N., and Walker, J. S., 2001, ''Inertia and Thermal Convection During Crystal Growth With a Steady Magnetic Field,'' J. Thermophys. Heat Transfer, **15**, pp. 50–54.

Buoyancy-Driven Flow Transitions in Deep Cavities Heated From Below

Chunmei Xia
e-mail: cxia@ecn.purdue.edu

Jayathi Y. Murthy
e-mail: jmurthy@ecn.purdue.edu

School of Mechanical Engineering,
Purdue University,
West Lafayette, IN 47907

A numerical investigation has been conducted of flow transitions in deep three-dimensional cavities heated from below. The first critical Rayleigh number, Ra_I, below which the flow is at rest, and the second critical Rayleigh number, Ra_{II}, for transition from steady state to oscillatory flow, have been found for cavities of aspect ratios Ar in the range 1–5. Transition to chaos has also been examined for these cases. The results show that $Ra_I=3583$, 2.545×10^4 and 5.5×10^5 and $Ra_{II}=4.07\times10^5$, 1.65×10^6 and 1.30×10^7 for aspect ratios of 1, 2, and 5 respectively. The route to chaos is P(Periodic) $\rightarrow QP_2$(Quasi-periodic with two incommensurate frequencies) $\rightarrow QP_3$(Quasi-periodic with three incommensurate frequencies) $\rightarrow N$(Chaotic) for $Ar=1$ with the Rayleigh number varying from 4.07×10^5 to 4.89×10^5. The route is P(Periodic) $\rightarrow P_2$(Periodic doubling) $\rightarrow I$(Intermittent) $\rightarrow P$(Periodic) $\rightarrow N$(Chaotic) for $Ar=2$ over a Ra range of 1.65×10^6 to 1.83×10^6. The interval between periodic and chaotic flow is very short for $Ar=5$. [DOI: 10.1115/1.1481356]

Keywords: Cavities, Enclosure Flows, Heat Transfer, Modeling, Natural Convection

Introduction

Rayleigh-Bénard convection in cavities is a classical problem and is important in a variety of engineering applications such as solar collector design, passive energy storage, crystal growth, and in emerging micro-manufacturing techniques such as LIGA [1]. In the past several decades, intensive theoretical, experimental, and numerical studies have been done, especially for infinite horizontal layers and relatively shallow cavities. The process of flow bifurcation and transition is governed by several critical Rayleigh numbers. Below the first critical Rayleigh number Ra_I, the fluid is at rest and heat transfer is only due to conduction. Steady state convective flows can be observed as Ra becomes larger than Ra_I. For Rayleigh numbers beyond the second critical value Ra_{II}, there is a transition from steady state to time-dependent flow. If the Rayleigh number is increased further, transition to chaos is observed.

The various flow patterns encountered during transition to chaos are most commonly characterized by their power spectrum. In addition, Lyapunov exponents [2] and the correlation dimension [3] have also been used to distinguish the various attractors quantitatively. Ra_I has been determined to be 1708 for an infinite layer [4,5], and is independent of the Prandtl number Pr. Davis [4] numerically calculated Ra_I for closed cavities with a linear temperature distribution on the lateral walls and with different aspect ratios. There are several steady flow patterns (denoted by S) past Ra_I. As mentioned in Ref. [6], these include zig-zag, cross-roll, Eckhaus, oscillatory, knot and skewed varicose instabilities, depending on the geometry of the enclosure and the Prandtl number. Gollub and Benson [7] found experimentally that the mean flow pattern in a box of $16.42\times27.72\times7.9$ mm is of the $2T$ type (2 parallel rolls whose axis are parallel to the short edge of the bottom) up to Ra_{II}. Stella and Bucchignani [8] found numerically the configuration to be $2T$ in a box of $3.5\times2.1\times1$ with $Pr=2.5$, and the soft-roll configuration in a box of $2.4\times1.2\times1$ with $Pr=5$. Mukutmoni and Yang [9] also found a $2T$ configuration numerically in a box of $3.5\times2.1\times1$. The flow may experience several temporal regimes after Ra_{II} before it becomes chaotic [6,10]. Typical regimes include: a periodic regime with one fundamental frequency (P); a subharmonic regime, also known as a period doubling regime (P_n), which contains frequencies which are one-half ($n=2$) or one-quarter ($n=4$) of the original frequency; a quasi-periodic regime (QP_n) with n incommensurate frequencies; phase locking (L) when the two frequencies in QP_2 lock into a constant rational ratio; intermittance (I) which results from the collision of a stable S and an unstable S; and finally, the nonperiodic or chaotic regime (N). Ra_{II} has been found to be around 30,000 to 37,960 for the $3.5\times2.1\times1$ box for $Pr=2.5$ [8,11].

There are many routes for the transition from steady state to chaos. Three main routes that lead to chaos have been classified and investigated. The Ruelle-Takens-Newhouse scenario [12], which may be represented by $S\rightarrow P\rightarrow QP_2\rightarrow N$, involves three Hopf bifurcations; the Feigenbaum sequence [13], a scenario in which an infinite cascade of period doublings (subharmonic bifurcations) leads to chaos, may be represented by $S\rightarrow P\rightarrow P_2\rightarrow P_4\ldots$; and the Pomeau-Manneville scenario [14], which involves flow intermittency (I), resulting from combinations of stable and unstable stationary attractors. Gollub and Benson [7] found four kinds of routes in their experiments: quasi-periodicity and phase locking for the box of $16.42\times27.72\times7.9$ mm and $Pr=5$, which can be symbolized as $S\rightarrow P\rightarrow QP_2\rightarrow L\rightarrow N$; subharmonic (period doubling) bifurcations for the same box and $Pr=2.5$, which can be expressed as $S\rightarrow P\rightarrow P_2\rightarrow P_4\rightarrow N$; three frequencies for $Pr=5$, which can be expressed as $S\rightarrow P(\rightarrow QP_2)\rightarrow QP_3\rightarrow N$; and intermittent noise which was observed for a box of $14.66\times28.85\times11.94$ mm and $Pr=5$. Bucchignani and Stella [10] numerically found the route as $S\rightarrow P\rightarrow P_2\rightarrow P_4\rightarrow N$ for a domain of $3.5\times2.1\times1$ and $Pr=2.5$, which agreed with experimental results [7] and the route as $S\rightarrow P\rightarrow QP_2\rightarrow L\rightarrow QP_2\times(\rightarrow QP_3)\rightarrow N$ for a domain of $2.4\times1.2\times1$ and $Pr=5$. Mukutmoni and Yang [11] numerically found the route to be $S\rightarrow P\rightarrow P_2\rightarrow QP\rightarrow N$ for the domain of $3.5\times2.1\times1$ and $Pr=2.5$. Leong et al. [15,16] experimentally and numerically investigated buoyant convection in a bottom-heated cubical cavity with a linear temperature profile on the sidewalls. Three different inclination angles were considered. Experimental results of the average Nusselt numbers on the hot and cold face were shown for Rayleigh numbers from 10^4 to 10^8.

In this paper we investigate numerically the flow behaviors and

---

Contributed by the Heat Transfer Division for publication in the JOURNAL OF HEAT TRANSFER. Manuscript received by the Heat Transfer Division May 18, 2001; revision received March 7, 2002. Associate Editor: M. Faghri.

transitions in deep closed cavities at Pr = 2.5. The published literature primarily addresses shallow cavities because viscous wall effects have widely been assumed to dominate in deep cavities, damping convection. The present work closes this gap in the existing literature. A second-order finite volume scheme is used to investigate the transition from quiescent flow to chaos, and critical Rayleigh numbers and the path of transition are identified.

Governing Equations

Three-dimensional incompressible flow of a Newtonian fluid is assumed for the purposes of this paper. The Boussinesq approximation is made to model buoyancy. The computational domain under consideration is shown in Fig. 1. The bottom wall is the hot wall and the top wall is the cold wall. All the side walls are adiabatic. Defining the following dimensionless quantities

$$X = x/h$$

$$Y = y/h$$

$$Z = z/h$$

$$t^* = t \cdot \alpha/h^2$$

$$U = uh/\alpha$$

$$V = vh/\alpha$$

$$W = wh/\alpha$$

$$P = ph^2/\rho\alpha^2$$

$$\theta = (T - T_c)/(T_h - T_c)$$

The corresponding dimensionless equations may be written as

$$\text{Continuity:}\quad \nabla \cdot \vec{V} = 0$$

$$\text{X-Momentum:}\quad \frac{\partial U}{\partial t^*} + \nabla \cdot (\vec{V}U) = -\frac{\partial P}{\partial X} + \text{Pr} \cdot \nabla^2 U$$

$$\text{Y-Momentum:}\quad \frac{\partial V}{\partial t^*} + \nabla \cdot (\vec{V}V) = -\frac{\partial P}{\partial Y} + \text{Pr} \cdot \nabla^2 V + \text{Ra}\ \text{Pr}\theta$$

$$\text{Z-Momentum:}\quad \frac{\partial W}{\partial t^*} + \nabla \cdot (\vec{V}W) = -\frac{\partial P}{\partial Z} + \text{Pr} \cdot \nabla^2 W$$

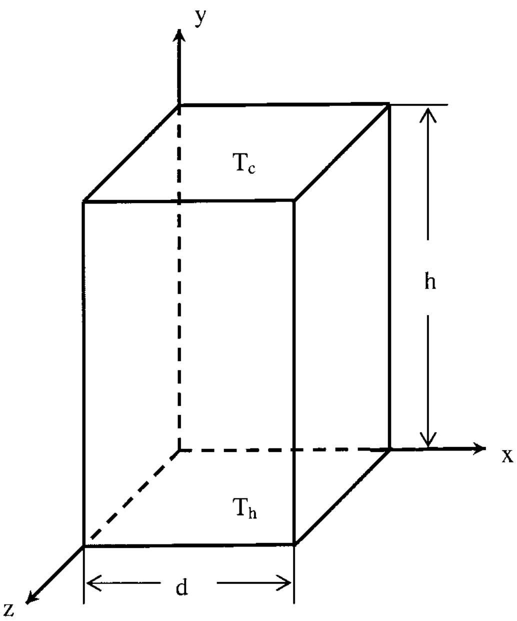

Fig. 1 Calculation domain

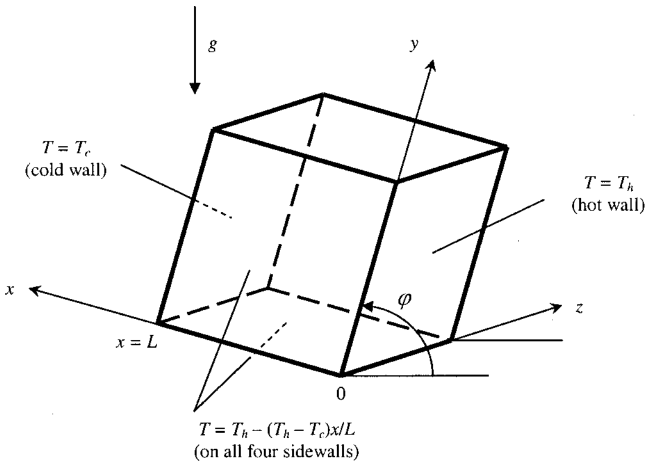

Fig. 2 Natural convection in cubical cavity

Table 1 Calculated average Nusselt number and relative error for steady flow

Ra		$\varphi = 0°$	Error	$\varphi = 45°$	Error	$\varphi = 90°$	Error
10^4	hot	1.209	2.97%	1.606	0.50%	1.518	0.13%
	cold	1.193	4.25%	1.588	1.61%	1.500	1.32%
4×10^4	hot	2.017	0.05%	2.589	1.13%	2.467	5.56%
	cold	1.996	1.10%	2.565	0.20%	2.443	4.54%
10^5	hot	3.640	3.73%	3.608	3.32%	3.207	3.55%
	cold	3.943	0.69%	3.577	2.43%	3.193	3.10%
10^6	hot					6.635	3.95%
	cold					6.616	3.65%

Table 2 Calculated average Nusselt number and relative error for unsteady flow

Ra		$\varphi = 0°$	Error	$\varphi = 45°$	Error	$\varphi = 90°$	Error
10^6	hot	8.300	5.29%	9.296	5.19%		
	cold	8.360	6.05%	9.280	5.01%		
10^7	hot			18.44	5.37%	13.88	6.93%
	cold			18.45	5.43%	13.80	6.32%
10^8	hot					28.31	5.67%
	cold					28.37	5.90%

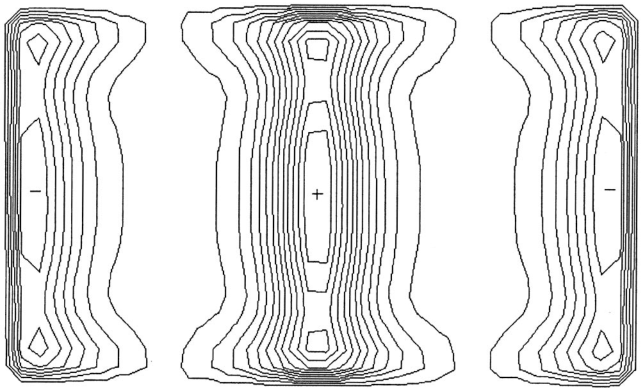

Fig. 3 2*T* configuration for a box of 16.42×27.72×7.9 mm (isolines of vertical velocity at horizontal middle plane for Ra = 3×10^4, Pr = 2.5)

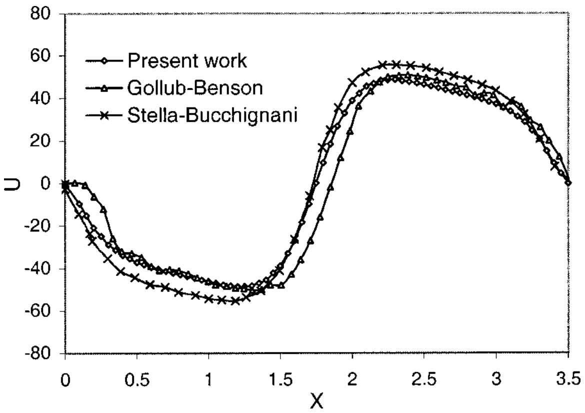

Fig. 4 Comparison with Gollub-Benson [7] and Stella-Bucchignani [8] (*V* velocity along *Y* at $X=1.651$ and $Z=0.875$ for $Ra=3\times10^4$, $Pr=2.5$)

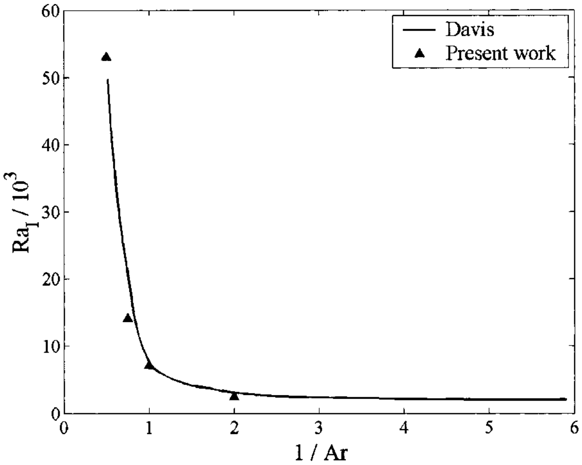

Fig. 5 Comparison of Ra_I with Davis [4]

Table 3 Maximum *U* velocity along the line at $Y=0.125$ and $Z=0.125$ for $Ar=2.0$, $Pr=2.5$, and $Ra=1.63\times10^5$ with different mesh densities

Mesh	m10	m15	m20	m25	m30	m40
uh/α	10.37	12.26	18.59	19.19	19.23	19.37

Table 4 Critical Rayleigh number for different aspect ratios

	Ar=1	Ar=2	Ar=5
Ra_I	3.583×10^3	2.543×10^4	5.5×10^5
Ra_{II}	4.07×10^5	1.65×10^6	1.30×10^7

$$\text{Energy:}\quad \frac{\partial\theta}{\partial t^*}+\nabla\cdot(\vec{V}\theta)=\nabla^2\theta$$

The nondimensional parameters governing the problem are the Rayleigh number Ra, the Prandtl number Pr and the aspect ratio Ar, which are defined as:

$$\mathrm{Ra}=\frac{g\beta(T_h-T_c)h^3}{\nu\alpha}$$

$$\mathrm{Pr}=\frac{\nu}{\alpha}$$

$$\mathrm{Ar}=h/d$$

Boundary Conditions. The boundary conditions for the problem are

$$\text{Bottom wall:}\quad \theta=1,\quad U=V=W=0$$

$$\text{Upper wall:}\quad \theta=0,\quad U=V=W=0$$

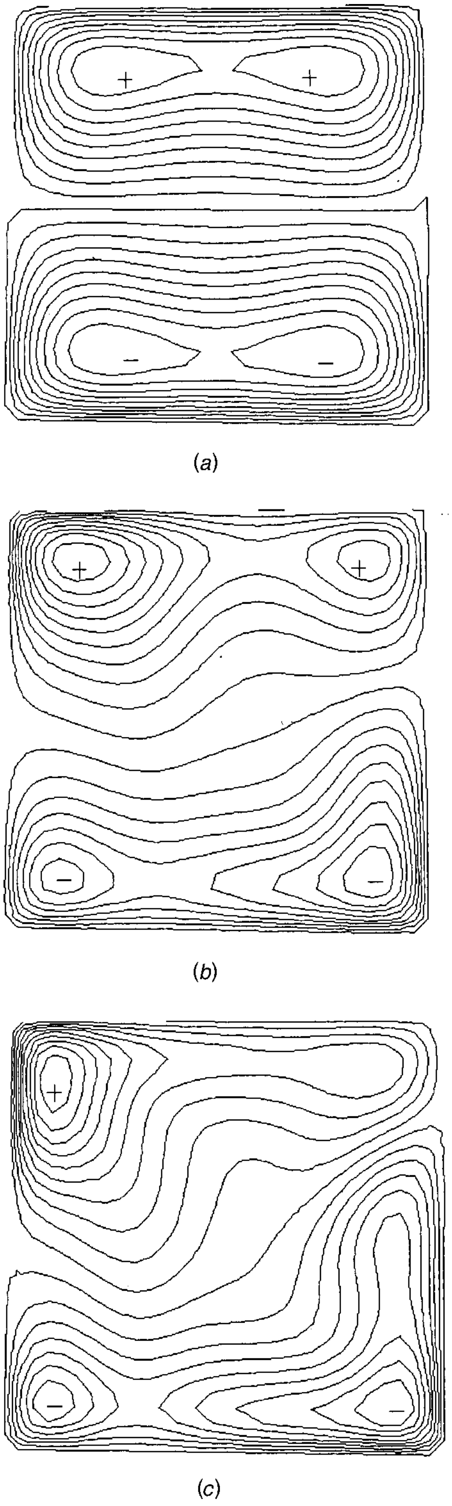

(*a*)

(*b*)

(*c*)

Fig. 6 Steady state flow pattern for Ar=1: (*a*) $Ra=2\times10^4$; (*b*) $Ra=10^5$; and (*c*) $Ra=2\times10^5$.

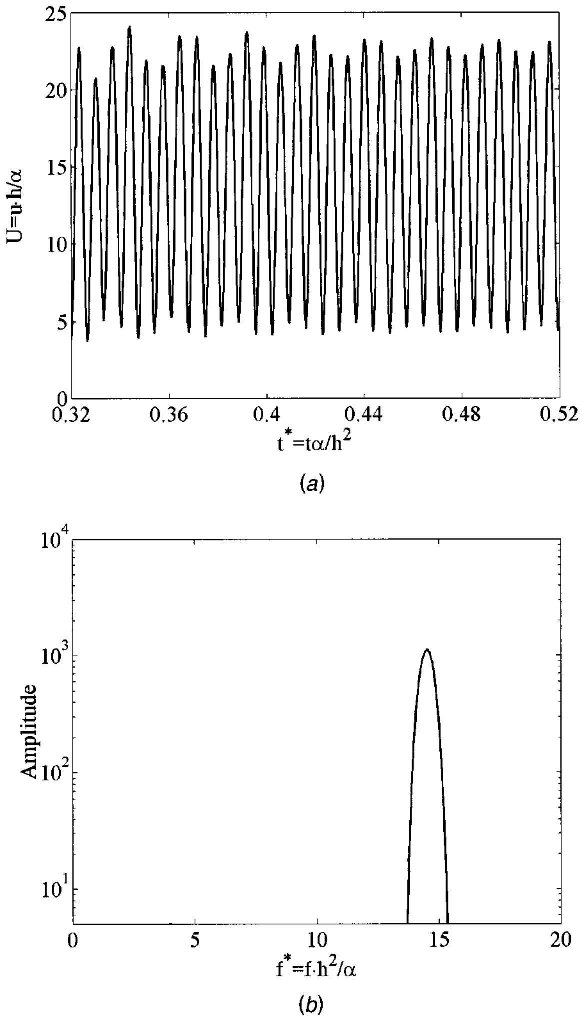

(*a*)

(*b*)

Fig. 7 Flow behavior at Ra=4.07×10^5 for Ar=1: (*a*) *U* velocity variation with time at point (*X*=0.7,*Y*=0.7,*Z*=0.7), Ar=1; and (*b*) Corresponding power spectrum.

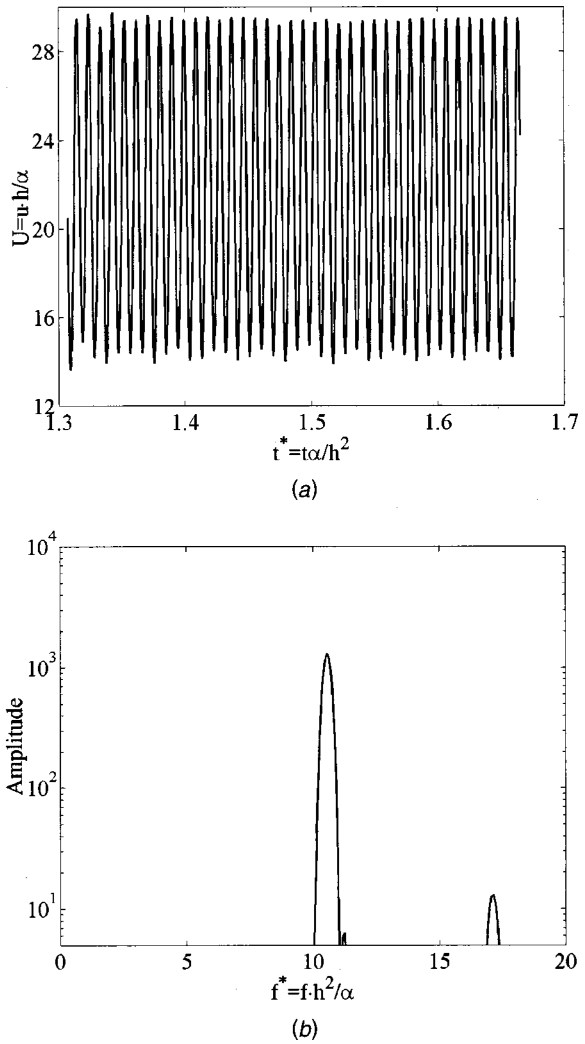

(*a*)

(*b*)

Fig. 8 Flow behavior at Ra=4.275×10^5 for Ar=1: (*a*) *U* velocity variation with time at point (*X*=0.7,*Y*=0.7,*Z*=0.7), Ar=1; and (*b*) corresponding power spectrum.

$$\text{Side walls: } \frac{\partial \theta}{\partial n}=0, \quad U=V=W=0$$

For the purposes of this study, the Prandtl number is fixed at 2.5. Three different aspect ratios, Ar=1, 2, and 5, are considered.

Numerical Method

A brief description of the numerical method is given here; details may be found in Mathur and Murthy [17]. An unstructured finite volume method is used. The calculation domain is divided to arbitrary unstructured polyhedral control volumes. A co-located formulation is used, with velocity, pressure and temperature being stored at cell centroids. The governing equations are integrated over the control volume to yield algebraic equations balancing incoming convective and diffusive fluxes with generation inside the control volume. A second-order upwind scheme is used for both the momentum and energy equations. For fluid flow, a sequential pressure-based algorithm, SIMPLE [18], is used. The unsteady formulation is also second-order accurate. The flow and energy equations are solved sequentially, using Picard iteration for non-linearity and coupling. At any time step, the solution is considered converged when normalized absolute residuals in the discrete equations summed over all cells are reduced by at least three orders of magnitude. In addition, the absolute normalized mass imbalance summed over all cells (see [18]) is decreased below 10^{-3}. The same criterion is used for steady-state computations.

Evaluation of Critical Rayleigh Numbers. To find the first critical Rayleigh number Ra_{I}, steady simulations were done starting with a Rayleigh number range across which the transition occurs, and using a bisection algorithm to detect the critical Rayleigh number. These computations were started from an initial guess of zero velocity and a uniform temperature field with $\theta=0$. To detect motion, three vertical lines in the domain were created at $(X=0.25/\mathrm{Ar}, Y=0.25/\mathrm{Ar})$, $(X=0.5/\mathrm{Ar}, Y=0.5/\mathrm{Ar})$ and $(X=0.75/\mathrm{Ar}, Y=0.75/\mathrm{Ar})$ and the steady temperature profiles on these lines were plotted. When Ra is lower than Ra_{I}, the temperature variation along these lines is strictly linear. For $\mathrm{Ra}>\mathrm{Ra}_{\mathrm{I}}$, the temperature along the three lines departs from linearity quite substantially. Using bisection, Ra_{I} was determined to an accuracy of better than 1 percent.

To find the second critical Rayleigh number $\mathrm{Ra}_{\mathrm{II}}$, unsteady flows were computed using the steady state results from Ra_{I} as the initial condition. The *U* velocity variation with time at point $(X=0.7/\mathrm{Ar}, Y=0.7/\mathrm{Ar}, Z=0.7)$ was recorded. The power spectrum of the frequencies contained in the signal was obtained to deter-

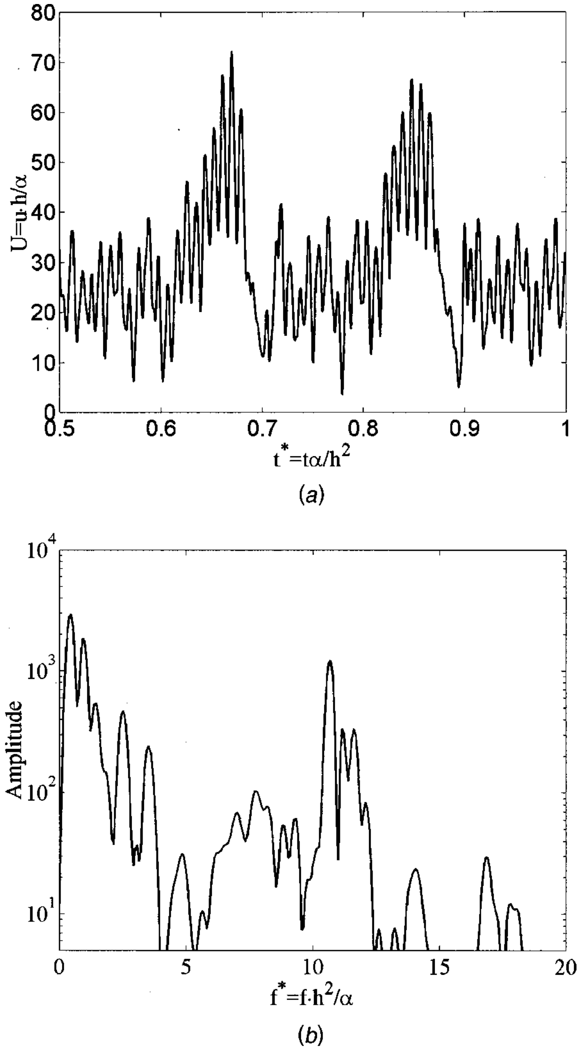

(a)

(b)

Fig. 9 Flow behavior at Ra=4.48×10^5 for Ar=1: (*a*) *U* velocity variation with time at point (*X*=0.7,*Y*=0.7,*Z*=0.7), Ar=1; and (*b*) corresponding power spectrum.

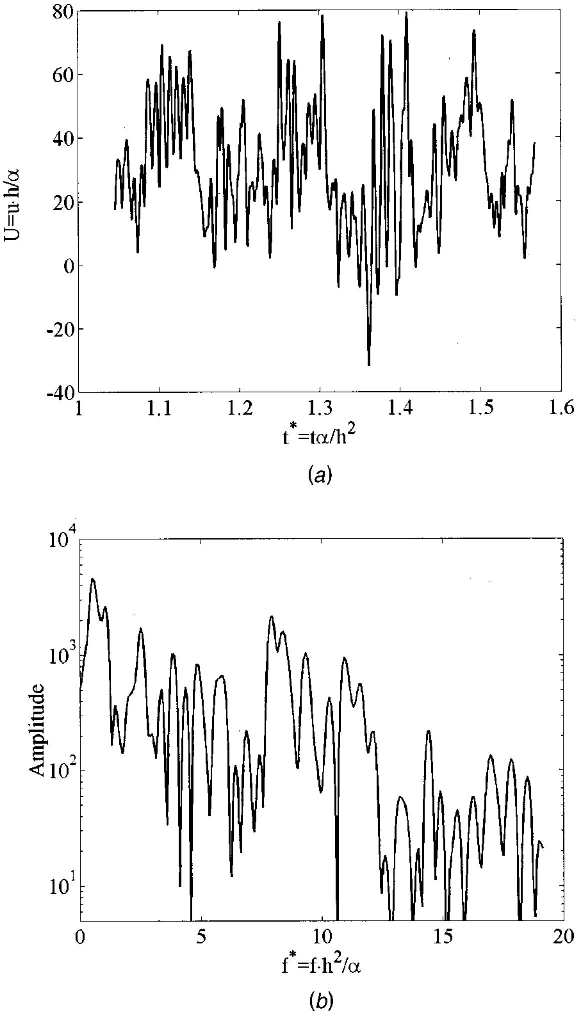

(a)

(b)

Fig. 10 Flow behavior at Ra=4.68×10^5 for Ar=1: (*a*) *U* velocity variation with time at point (*X*=0.7,*Y*=0.7,*Z*=0.7), Ar=1; and (*b*) corresponding power spectrum.

mine the nature of the transition. Again, the bisection method was used to determine Ra$_{\mathrm{II}}$ to an accuracy of better than 1 percent.

Comparison with Previous Work. To establish the validity of the numerical method, three different bottom-driven natural convection problems were computed, and results were compared to published numerical and experimental data.

Natural Convection in Inclined Cube. Leong et al. [15] studied natural convection in an air-filled cube with two opposing isothermal faces and the remaining four sides having a linear temperature variation from the cold face to the hot face, as shown in Fig. 2. They reported experimental values of the Nusselt number for three different inclinations: $\varphi=0$ deg (hot/cold face horizontal), $\varphi=90$ deg (hot/cold face vertical), and $\varphi=45$ deg (hot/cold face inclined at 45 deg), with 1 percent accuracy and 95 percent confidence.

We varied the mesh density to obtain an optimal mesh. A mesh of 30×30×30 gives an error in the average Nusselt number of 3.10 percent compared to the experimental results for $\varphi=90$ deg and Ra$=10^5$; and a mesh of 80×80×40 gives an error of 3.65 percent for $\varphi=90$ deg and Ra$=10^6$. As a compromise between accuracy and efficiency, we used a 30×30×30 mesh for the cases when Ra is equal or lower than 10^5, and an 80×80×40 mesh when Ra is equal or higher than 10^6. When unsteady calculations were necessary, we used a time step $\Delta t^*=3.17\times10^{-4}$ for Ra $=10^6$, $\Delta t^*=1\times10^{-4}$ for Ra$=10^7$ and $\Delta t^*=3.17\times10^{-5}$ for Ra$=10^8$. These values were arrived at by preliminary computations to ensure that the error is within 3–4 percent. It is possible that finer meshes would yield more accurate results, but time and computational resources do not allow further refinement, especially for unsteady flows.

The numerical results show that for $\varphi=0$ deg and $\varphi=45$ deg, the flow inside the cavity is steady when Ra is below 10^5 and that the flow becomes unsteady when Ra is above 10^6; for $\varphi=90$ deg, the flow is steady when Ra is below 10^6 and becomes unsteady when Ra is above 10^7. For steady flow, the calculated values of the average Nusselt number for the cold and hot faces and the error relative to the experimental results for the cold face are shown in Table 1. From Table 1, we can see that the average Nusselt number for the cold and hot faces are very close to each other, and the relative error is less than 5 percent for almost all the cases.

The unsteady flow we solved here includes: $\varphi=0$ deg (Ra $=10^6$), $\varphi=45$ deg (Ra$=10^6$ and Ra$=10^7$) and $\varphi=90$ deg (Ra $=10^7$ and Ra$=10^8$). We used the cold face temperature and zero velocity as the initial conditions for all the above cases. We recorded the variation of the average heat flux on the hot and cold

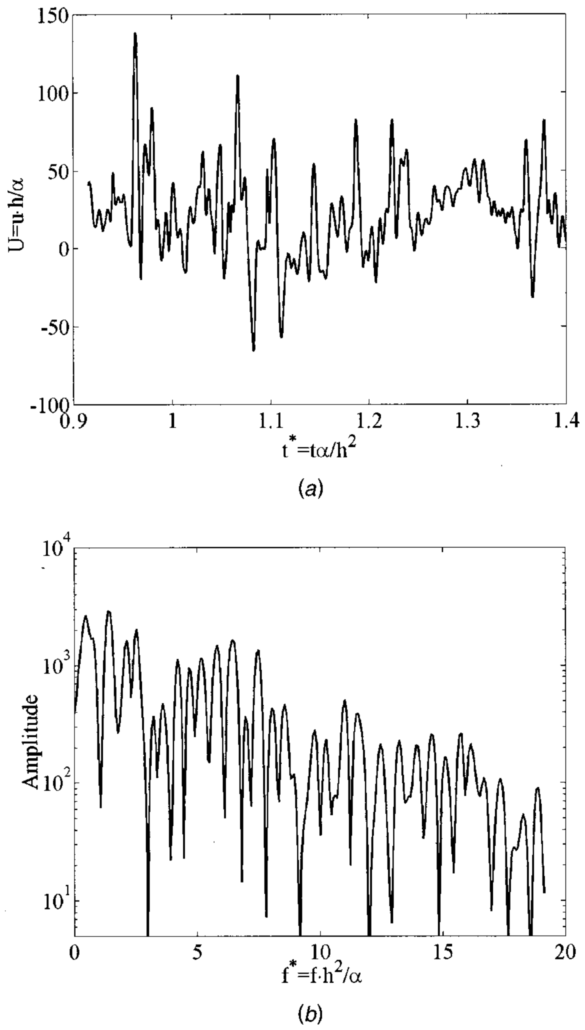

Fig. 11 Flow behavior at Ra=4.80×10^5 for Ar=1: (*a*) *U* velocity variation with time at point (*X*=0.7,*Y*=0.7,*Z*=0.7), Ar=1; and (*b*) corresponding power spectrum.

faces with time. The average Nusselt number reported is the average value of the spatially averaged Nu for the cold or the hot face at different time steps. The calculated values of the average Nusselt number for the cold and hot faces and the relative error with respect to the given experimental results for the cold face are shown in Table 2. The relative error is less than 7 percent for all the cases.

Bottom-Driven Natural Convection in Shallow Cavities. Calculations for a domain of 3.5×2.1×1 with Pr=2.5 and Ra=3 $\times 10^4$ were performed using the method described, and compared with the experimental data of Gollub and Benson [7] and with the numerical calculations of Stella and Bucchignani [8]. As in [7,8], a 2T configuration was found. This is shown in Fig. 3, which shows contours of the *U* velocity on the plane of $Z=0.5$. Quantitative comparison of the *U* velocity on the line $Y=1.651$, $Z=0.875$ with [7,8] are shown in Fig. 4. The velocity computed here falls between the Gollub and Benson [7] and the Stella and Bucchignani [8] results.

Computation of $\mathrm{Ra_I}$ *for Rectangular Cavities.* For cavities with square cross section and linear temperature distribution on the lateral side walls, we calculated $\mathrm{Ra_I}$ for different aspect ratios and compared them with the results of Davis [4], as shown in Fig. 5. The comparison with theory is quite good.

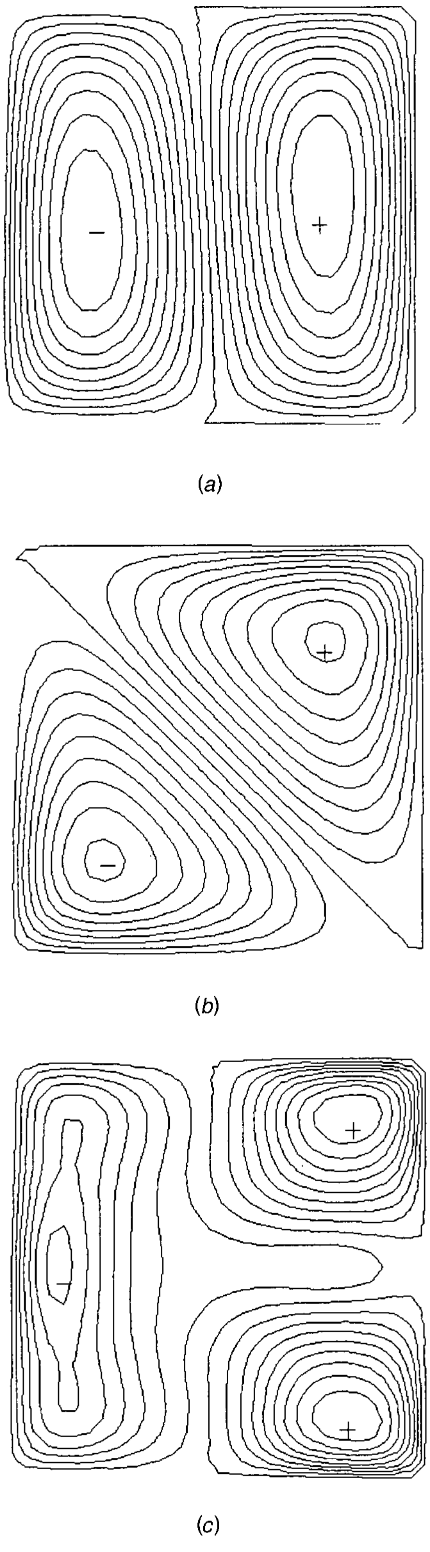

Fig. 12 Steady state flow pattern for Ar=2: (*a*) Ra=3×10^4; (*b*) Ra=1.22×10^5; and (*c*) Ra=1.62×10^6

Evaluation of Accuracy. A number of calculations were done with varying mesh densities to establish the numerical accuracy of the calculations done here. Computed values of the maximum *U* velocity along the line at $Y=0.125$ and $Z=0.125$ are shown in Table 3 for Ar=2.0, Pr=2.5, and Ra=1.63×10^5, where *m*10 means length *d* being divided into 10 cells and length h being

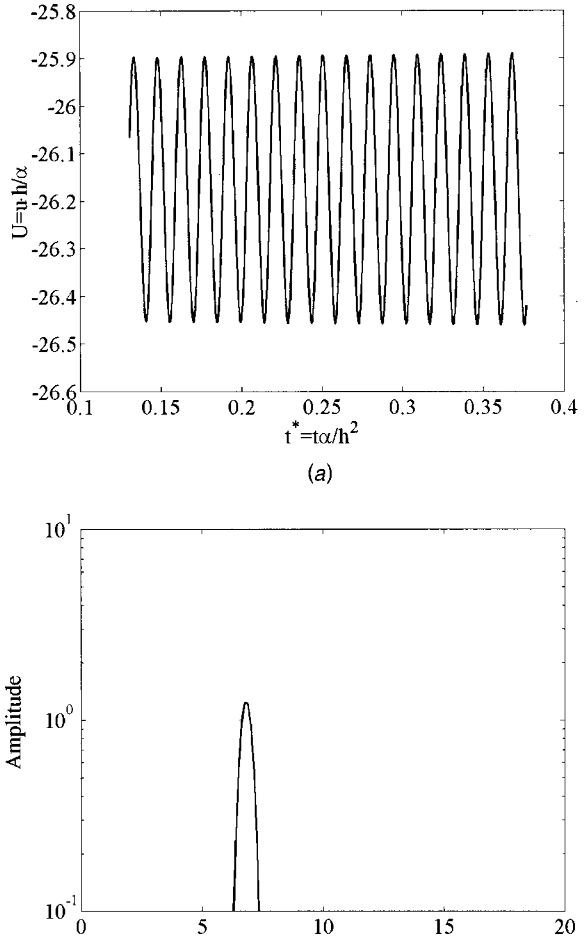

(*a*)

(*b*)

Fig. 13 Flow behavior at Ra=1.65×10⁶ for Ar=2: (*a*) *U* velocity variation with time at point (*X*=0.35,*Y*=0.35,*Z*=0.7), Ar =2; and (*b*) corresponding power spectrum.

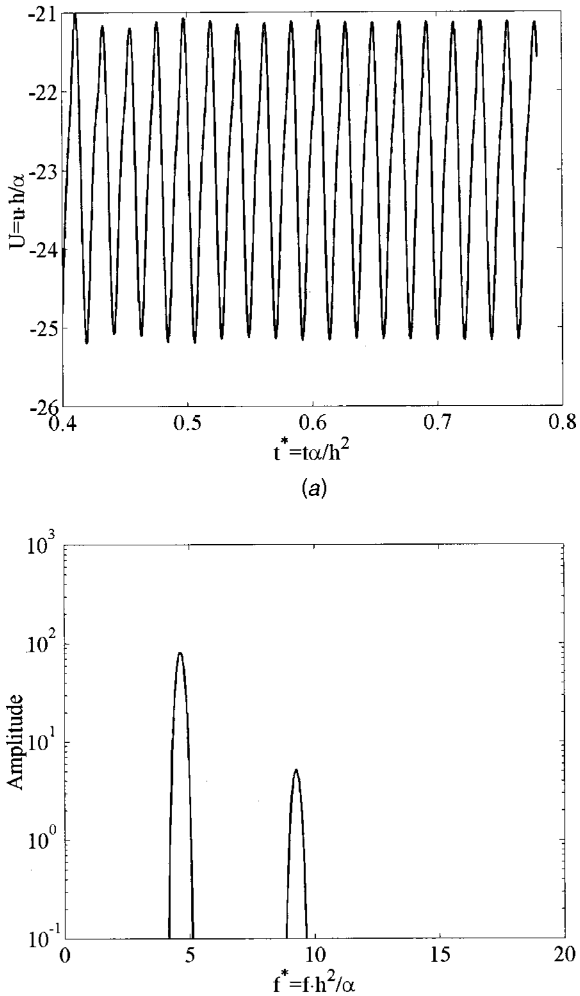

(*a*)

(*b*)

Fig. 14 Flow behavior at Ra=1.67×10⁶ for Ar=2: (*a*) *U* velocity variation with time at point (*X*=0.35,*Y*=0.35,*Z*=0.7), Ar =2; and (*b*) corresponding power spectrum.

divided into $10\cdot\mathrm{Ar}$ cells; meshes $m15$, $m20$, and so on are to be similarly interpreted. We see that a mesh of $30\times30\times60$ gives an error in the maximum velocity of 0.7 percent compared to a $40\times40\times80$ computation. Similar tests were done for other aspect ratios. Since our interest is in finding the critical Rayleigh numbers and the range of Ra for the transitions is of the same order as $\mathrm{Ra}_{\mathrm{II}}$, we use the same mesh size used in the steady state calculations. The final mesh size is $30\times30\times30$ for Ar=1, $30\times30\times60$ for Ar=2 and $25\times25\times125$ for Ar=5. When unsteady calculations are necessary, we use a time step $\Delta t^*=2.61\times10^{-4}$ for Ar =1 and Ar=2, and $\Delta t^*=5.23\times10^{-5}$ for Ar=5. These time-step values were chosen from the time-step independence studies and yield an error in the maximum velocity of under 1 percent.

Results

Critical Rayleigh numbers for the three aspect ratios investigated here are listed in Table 4. The behavior for each aspect ratio is described below.

Aspect Ratio Ar=1. For Ar=1, Ra_{I} has been found to be 3583 and $\mathrm{Ra}_{\mathrm{II}}$ is 4.07×10^5. The steady state flow pattern for $\mathrm{Ra}>\mathrm{Ra}_{\mathrm{I}}$ exhibits three distinct configurations before the flow becomes time-dependent. Fig. 6 shows contours of the V velocity on the plane $Z=0.5$ for three values of Ra between Ra_{I} and $\mathrm{Ra}_{\mathrm{II}}$. Fig. 6(*a*) is $1T$ configuration. There is only one roll in the cavity, with the fluid rising up along one vertical wall and flowing down the other. For higher Rayleigh numbers, a $2T$ configuration is encountered, as seen in Fig. 6(*b*). For yet higher Ra, a soft roll configuration, such as that shown in Fig. 6(*c*), is encountered. Here again, there are two rolls, but the axes of the two rolls are not parallel. The flow transitions to a periodic regime based on the third configuration.

Figures 7–11 illustrate the flow transitions from the periodic to the chaotic regime. Part (*a*) in these figures shows the U velocity variation with time at point $(X=0.7,Y=0.7,Z=0.7)$; part (*b*) presents the corresponding power spectrum. Figure 7 shows the behavior for $\mathrm{Ra}=4.07\times10^5$. A single fundamental nondimensional frequency, $f_1^*=14.5$, is found. The main frequency of the periodic flow increases as Ra increased. Figure 8 suggests a quasi-periodic regime as $\mathrm{Ra}=4.27\times10^5$ with two incommensurate frequencies: $f_1^*=10.6$, $f_2^*=17.1$ $(f_2^*/f_1^*=1.614)$. As Ra is increased further, other frequency components begin to appear. For $\mathrm{Ra}=4.48\times10^5$, as shown in Fig. 9(*b*), three peaks with significant amplitude are seen, at $f_1^*=0.14$, $f_2^*=0.92$, and $f_3^*=10.7$. Although there are other visible frequencies in the power spectrum, their amplitudes are one order smaller than the amplitude of the main frequencies. The regime may thus be classified as a QP_3 regime. Figure 10, corresponding to $\mathrm{Ra}=4.68\times10^5$, shows some of the

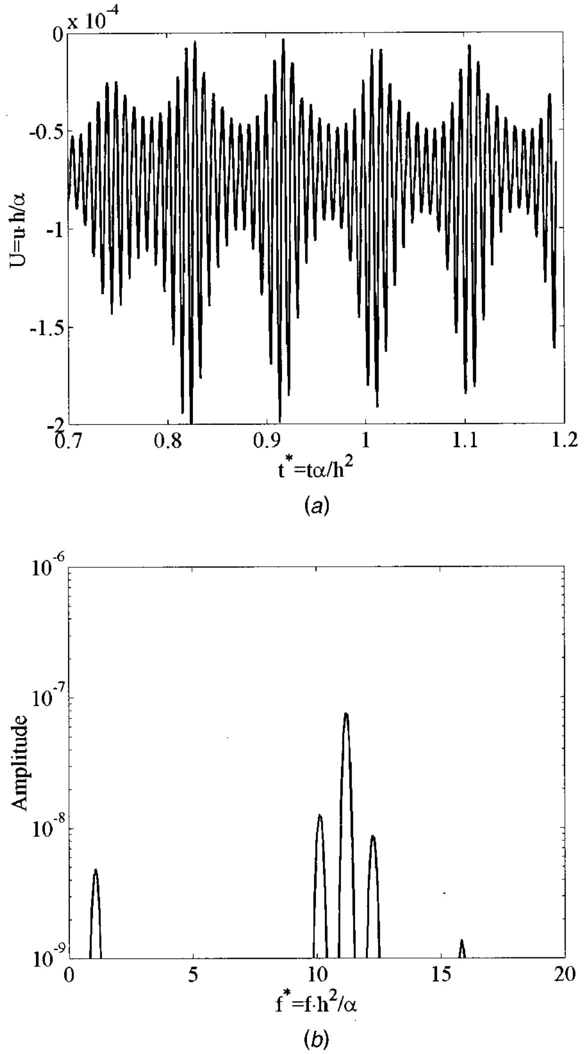

(a)

(b)

Fig. 15 Flow behavior at Ra=1.69×10⁶ for Ar=2: (*a*) *U* velocity variation with time at point (*X*=0.35,*Y*=0.35,*Z*=0.7), Ar =2; and (*b*) corresponding power spectrum.

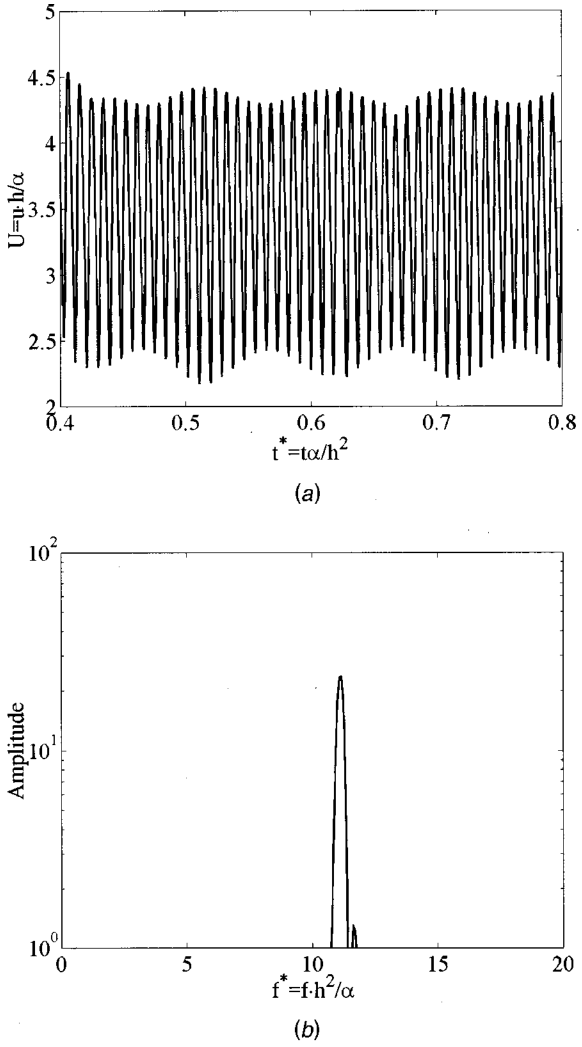

(a)

(b)

Fig. 16 Flow behavior at Ra=1.71×10⁶ for Ar=2: (*a*) *U* velocity variation with time at point (*X*=0.35,*Y*=0.35,*Z*=0.7), Ar =2; and (*b*) corresponding power spectrum.

characteristics of chaotic flow. Several peaks in the frequency spectrum may be identified; however, the difference in amplitude between the main frequencies and the other frequencies has decreased. The flow becomes chaotic by Ra$=4.89\times10^5$. The routes to chaos may be expressed as: $S\rightarrow P\rightarrow QP_2\rightarrow QP_3\rightarrow N$.

Aspect Ratio Ar=2. For Ar=2, the numerical results show that $\mathrm{Ra_I}=2.545\times10^4$ and $\mathrm{Ra_{II}}=1.65\times10^6$. As in the case of Ar =1, the steady state flow exhibits three main patterns before it becomes time-dependent. Contours of the V velocity on the middle plane $Z=0.5$ are shown in Fig. 12 for three Rayleigh numbers between $\mathrm{Ra_I}$ and $\mathrm{Ra_{II}}$. Figure 12(*a*) shows a 1T configuration at Ra$=3\times10^4$, with the flow rising up one vertical wall and falling along the opposite wall. As the Rayleigh number is increased to Ra$=1.22\times10^5$, the one-roll configuration persists, but the location of the roll has shifted so that the flow rises up along the corner and falls along the opposite corner. For yet higher Ra, a two-roll configuration is encountered. At Ra$=1.62\times10^6$, for example, the two-roll configuration consists of flow rising upwards along two adjacent corners and fall along the opposing face. The flow transitions to periodic flow based on this configuration.

Figure 13 shows the beginning of the periodic regime for Ar =2 as Ra$=1.65\times10^6$. The fundamental nondimensional frequency f_1^* is 6.8. A subharmonic cascade mechanism has been detected when Ra$=1.67\times10^6$. The fundamental frequency becomes 9.2 with a second frequency of 4.6, as shown in Fig. 14. Flow intermittency is detected by Ra$=1.69\times10^6$, where the flow becomes steady, as in Fig. 15. This is seen in the extremely low amplitude in Fig. 15(*b*). The flow becomes periodic again at Ra $=1.71\times10^6$ with one fundamental frequency f_1^* as 11.1, as in Fig. 16. When Ra$=1.83\times10^6$, the flow becomes chaotic, as shown in Fig. 17. The transition route is: $P\rightarrow P_2\rightarrow I\rightarrow P\rightarrow N$.

Aspect Ratio Ar=5. For Ar=5, $\mathrm{Ra_I}=5.5\times10^5$, and $\mathrm{Ra_{II}}=1.30\times10^7$. As in the case of Ar=1 and Ar=2, three main flow patterns have been found for steady state. At Ra$=5.6\times10^5$, a one-roll configuration similar to that in Fig. 12(*a*) has been found. The flow pattern for Ra$=2\times10^6$ is similar to that in Fig. 12(*b*). When Ra$=8\times10^6$, the one-roll pattern becomes twisted. The flow becomes time-dependent based on this configuration. The transition to chaos happens over an extremely short Ra range, making it difficult to reconstruct in detail. The flow becomes unsteady as Ra$=1.30\times10^7$ and becomes chaotic shortly thereafter.

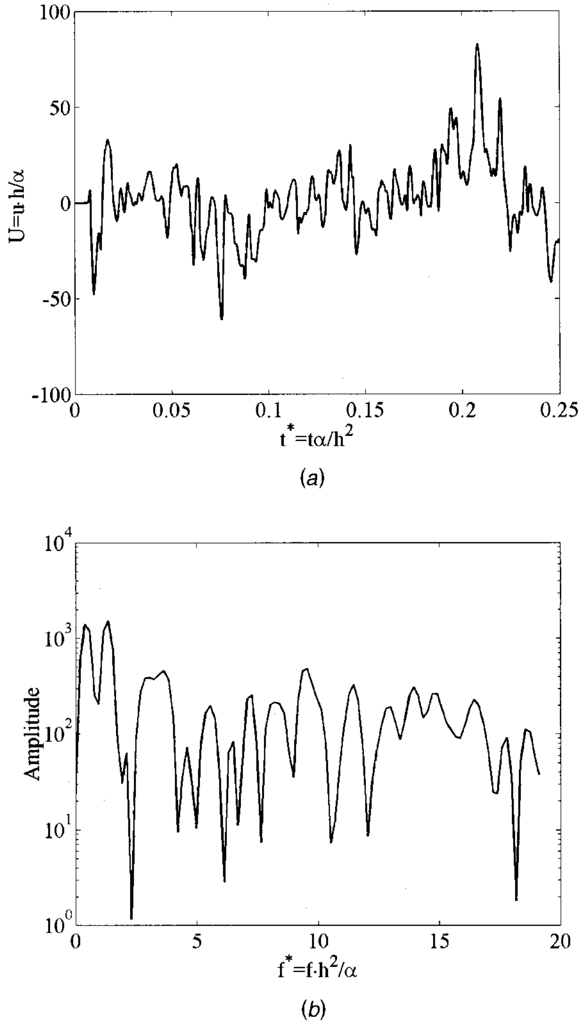

Fig. 17 Flow behavior at Ra=1.83×10^6 for Ar=2: (*a*) *U* velocity variation with time at point $(X=0.35, Y=0.35, Z=0.7)$, Ar =2; and (*b*) corresponding power spectrum.

Conclusions

Unsteady finite volume simulations of buoyancy-driven flows in deep cavities have been performed to determine flow transitions on the route to chaos. The first and second critical Rayleigh numbers have been determined. For aspect ratio Ar=1, a Ruelle-Takens-Newhouse based scenario, expressed as $S \rightarrow P \rightarrow QP_2 \rightarrow QP_3 \rightarrow N$, has been found. For aspect ratio Ar=2, a Feigenbaum sequence based scenario, expressed as $S \rightarrow P \rightarrow P_2 \rightarrow I \rightarrow P \rightarrow N$, has been found. For higher aspect ratios, the transition from the periodic to the chaotic regime happens vary rapidly with Rayleigh number, and precise transition mechanisms are difficult to identify.

The computations show that convection is restricted because of the presence of the sidewalls, especially for deeper cavities. Therefore, the critical Rayleigh numbers increase as the aspect ratio becomes higher and the Rayleigh number ranges for the different flow transitions also increase accordingly. Nevertheless, the computations demonstrate clearly that chaotic regimes with substantial mixing occur even in strongly constrained flows in deep cavities for Rayleigh numbers occurring in a variety of manufacturing processes. Further studies are underway to investigate open cavities of interest in micro-manufacturing processes such as LIGA for the high Prandtl numbers relevant to these processes.

Acknowledgments

The use of Fluent 5 from Fluent Inc. and support of J. Murthy and C. Xia by the Pennsylvania Infrastructural Technology Alliance (PITA) are gratefully acknowledged.

Nomenclature

Ar = Aspect ratio, $=h/d$
d = Width of cavity, m
f = Frequency, Hz
f^* = Nondimensional frequency
h = Depth of cavity, m
p = Pressure, Pa
P = Nondimensional pressure
Pr = Prandtl number
Ra = Rayleigh number
Ra_{I} = First critical Rayleigh number
$\mathrm{Ra}_{\mathrm{II}}$ = Second critical Rayleigh number
t = Time, s
t^* = Nondimensional time
T = Temperature, K
T_c = Cold wall temperature, K
T_h = Hot wall temperature, K
u = Velocity component in x-direction, m/s
U = Nondimensional velocity component in x-direction
v = Velocity component in y-direction, m/s
V = Nondimensional velocity component in y direction
$\overline{V}$ = Nondimensional velocity vector
w = Velocity component in z-direction, m/s
W = nondimensional velocity component in z direction
X = nondimensional length in x direction
Y = nondimensional length in y direction
Z = nondimensional length in z direction

Greek

α = thermal diffusivity, m^2/s
β = thermal expansion coefficient, 1/K
ν = kinematic viscosity, m^2/s
θ = nondimensional temperature
ρ = density, kg/m^3

References

[1] Griffiths, S. K., Nilson, R. H., et al., 1998, "Transport Limitations in Electrodeposition for LIGA Microdevice Fabrication," SPIE *Conference on Micromachining and Microfabrication Process Technology IV*, Santa Clara, California.
[2] Hakin, H., 1984, "*Instability Hierarchies of Self Organizing Systems and Devices*," in *Advanced Synergetics*, Springer-Verlag, Berlin.
[3] Grassberger, P., and Procaccia, I., 1983, "Characterization of Strange Attractors," Phys. Rev. Lett., **50**, pp. 346–349.
[4] Davis, S., 1967, "Convection in a Box: Linear Theory," J. Fluid Mech., **30**(3), pp. 465–478.
[5] Stork, K., and Muller, U., 1972, "Convection in a Box: Experiments," J. Fluid Mech., **54**(4), pp. 599–611.
[6] Yang, K. T., 1988, "Transitions and Bifurcations in Laminar Buoyant Flows in Confined Enclosures," ASME J. Heat Transfer, **110**, pp. 1191–1204.
[7] Gollub, J. P., and Benson, S. V., 1980, "Many Routes to Turbulent Convection," J. Fluid Mech., **100**, Part 3, pp. 449–470.
[8] Stella, F., and Bucchignani, E., 1999, "Rayleigh-Benard Convection in Limited Domains: Part 1—Oscillatory Flow," Numer. Heat Transfer, **36**, pp. 1–16.
[9] Mukutmoni, D., and Yang, K. T., 1993, "Rayleigh-Benard Convection in a Small Aspect Ratio Enclosure: Part 1—Bifurcation to Oscillatory Convection," ASME J. Heat Transfer, **115**, pp. 360–366.
[10] Stella, F., and Bucchignani, E., 1999, "Rayleigh-Benard Convection in Limited Domains: Part 2—Transition to Chaos," Numer. Heat Transfer, **36**, pp. 17–34.
[11] Mukutmoni, D., and Yang, K. T., 1993, "Rayleigh-Benard Convection in a Small Aspect Ratio Enclosure: Part 1—Bifurcation to Chaos," ASME J. Heat Transfer, **115**, pp. 367–376.

[12] Ruelle, D., Takens, F., and Newhouse, S. E., 1978, ‘‘Occurrence of Strange Axiom A Attractors Near Quasi Periodic Flows on T^m, $m \geqslant 3$,’’ Commun. Math. Phys., **64**, pp. 35–40.

[13] Feigenbaum, M. J., 1979, ‘‘The Onset Spectrum of Turbulence,’’ Phys. Lett., **A74**, pp. 375–378.

[14] Pomeau, Y., and Manneville, P., 1980, ‘‘Intermittent Transition to Turbulence in Dissipative Dynamic Systems,’’ Commun. Math. Phys., **74**, pp. 189–197.

[15] Leong, W. H., Hollands, K. G. T., and Brunger, A. P., 1998, ‘‘On a Physically Realizable Benchmark Problem in Internal Natural Convection,’’ Int. J. Heat Mass Transf., **41**(23), pp. 3817–3828.

[16] Leong, W. H., Hollands, K. G. T., and Brunger, A. P., 1999, ‘‘Experimental Nusselt Numbers for a Cubical-Cavity Benchmark Problem in Natural Convection,’’ Int. J. Heat Mass Transf., **42**, pp. 1979–1989.

[17] Mathur, S. R., and Murthy, J. Y., 1997, ‘‘A Pressure-Based Method for Unstructured Meshes,’’ Numer. Heat Transfer, **31**, pp. 195–216.

[18] Patankar, S. V., 1980, *Numerical Heat Transfer and Fluid Flow*, Hemisphere Publishing Corporation, New York.

Study of Mixing and Augmentation of Natural Convection Heat Transfer by a Forced Jet in a Large Enclosure

Shine-Zen (Joseph) Kuhn
University of California, Berkeley,
Department of Nuclear Eng.,
Berkeley, CA 94720-1730
e-mail: jkuhn1@txu.com

Hwan Kook Kang
Dae Hong Enterprise Co.,
30 Yangpyung-Dong-4ga,
Young Deung Po-Gu,
Seoul, Korea, 150-104

Per F. Peterson
University of California, Berkeley,
Department of Nuclear Eng.,
Berkeley, CA 94720-1730
e-mail: peterson@nuc.berkeley.edu

This paper presents an experimental study of gas mixing processes and heat transfer augmentation by a forced jet in a large cylindrical enclosure with an isothermal bottom heating/cooling surface. Cold/hot air was injected at several positions with varying pipe diameters and injection orientations, and was removed from the top of the enclosure. Under natural convection, the mean Nusselt number was correlated by the enclosure Rayleigh number $\mathrm{Ra}_D^{1/3}$*, and under strong forced convection, by the jet Reynolds number* $\mathrm{Re}_j^{2/3}$*. A combining rule for mixed convection was found for both the stabilizing (cooled surface) and destabilizing (heated surface) density gradients. Using the ratio of forced and free convection Nusselt numbers, this correlation could be further reduced to predict forced-jet augmentation as a function of the Archimedes number, with a correction factor to account for jet orientation and enclosure aspect ratio.* [DOI: 10.1115/1.1482081]

Keywords: Enclosure Flows, Fire, Heat Transfer, Impingement, Jets, Mass Transfer, Mixed Convection, Natural Convection

Introduction

Heat and mass transfer inside large enclosures is important in many applications, such as mixing process in the containment structures of passive light water reactors and other large stratified volumes, including high-level radioactive waste storage tanks, enclosure fires, chemical processing, and pollutant dispersal. For the AP-600 reactor containment design, the augmentation of condensation mass transfer caused by break-jet flows is of interest. The present study can be used to quantify the augmentation of heat removal rate under natural convection, generated by injection of a forced convection as during reactor blow down in a loss-of-coolant accident. For high-level liquid waste tanks, this work provides the basis for the evaluation of the performance of purge and ventilation systems to remove flammable gases generated from stored waste, and to maintain a well-mixed conditions in the gas space. In liquid high-level waste tanks, natural convection from the liquid surface to the gas space removes radiolysis-generated flammable gases. Injected gas jets, used to inert such tanks, can augment this mass transfer. When heavy gases such as benzene are generated and stable stratification can occur, the forced-convection augmentation can reduce the liquid temperature required to maintain adequate mixing and mass transfer.

For chemical processing, heat transfer in agitated vessels has been extensively studied with comprehensive coverage summarized by Sterbacek and Tausk [1], Uhl and Gray [2], and Penney [3]. Mechanical agitators are most often used to provide agitation. However, gas sparging and liquid jets injected into vessels are also used in some applications to provide mixing. To evaluate heat transfer in mechanically agitated and jet-agitated vessels, a general correlation form similar to the forced convection correlation is usually employed. In addition to the Reynolds, Prandtl, and viscosity ratio numbers, the general equation also contains several ratios of linear dimensions to describe the effect of the complex geometry on the fluid motion. The general equation is formulated as

$$\mathrm{Nu} = k\,\mathrm{Re}^a \mathrm{Pr}^b \left(\frac{\mu_b}{\mu_w}\right)^c \times f(\text{geometric factor}) \tag{1}$$

where Re is evaluated as the jet Reynolds number $\rho u d_j/\mu$ or impeller rotational Reynolds number $\rho N d_i^2/\mu$. Despite differences in mechanical impeller designs and tank geometry, the values of K typically fall within a relative narrow range from 0.33 to 0.74 for heat transfer to vessel walls, and from 0.02 to 0.08 for transfer to helical coils.

The geometric correlations can depend on several factors including the type of agitator (jet, propeller, and various turbines), heat transfer surfaces (vessel wall, helical coils and tube baffles), and geometric locations of agitator systems. As shown in Fig. 1 for a jet-agitated tank and a mechanically agitated tank, the geometric factor could include the following dimensionless length ratios,

$$f\left[\left(\frac{d_j}{D}\right)\left(\frac{d_i}{D}\right)\left(\frac{H}{D}\right)\left(\frac{Z}{D}\right)\left(\frac{w}{D}\right)\left(\frac{Z}{H}\right)\right] \tag{2}$$

The recirculation of fluid in a vessel to generate uniform mixing can be performed using a pump, which draws fluid from the vessel and returns the fluid to a nozzle. The fluid jet from the nozzle induces mixing and produces a large-scale circulating motion, which can reduce concentration, property, and temperature gradients. Some research, reported for the helical-coil heat transfer in a jet-agitated vessel, found that the ratio of nozzle diameter d_j to the tank diameter D has a weak effect on average heat transfer, where the geometric factor could be correlated with $(d_j/D)^{0.09}$. This work further suggested that jet orientation into the vessel did not play an important role. In present study for enclosures with a heated or cooled bottom surface, however, jet orientation is found to have a large effect on heat transfer.

Fossett and Prosser [4] studied the mixing of an aqueous Na_2CO_3 solution in tanks mixed by a jet. They carried out tests in a 1.50-m diameter, 0.92 m deep vessel in which a single jet was introduced to create large-scale recirculation flow patterns. The results of their jet mixing data suggested that the mixing time will be the same for jets nozzles of different diameters, if the effluent jet velocities are adjusted to provide the same momentum flux.

Contributed by the Heat Transfer Division for publication in the JOURNAL OF HEAT TRANSFER. Manuscript received by the Heat Transfer Division July 9, 2001; revision received March 14, 2002. Associate Editor: K. S. Ball.

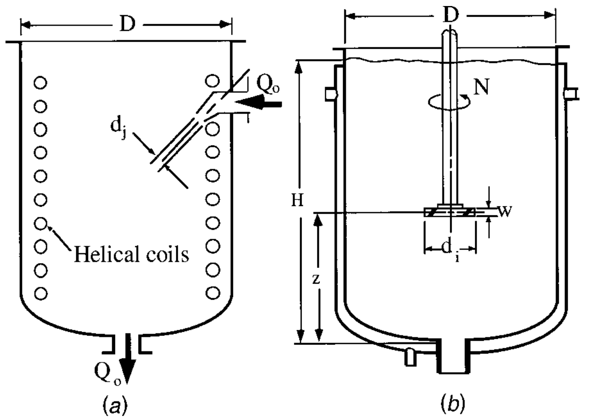

Fig. 1 Mixing processes for (*a*) jet-agitated, and (*b*) impeller-agitated vessels

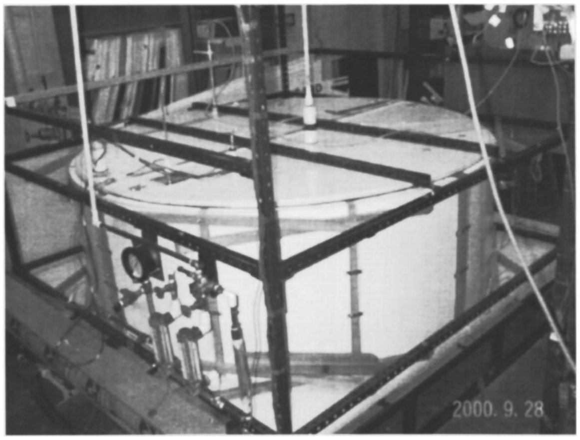

Fig. 2 Photo of the cylindrical enclosure experiment

Compared with limited information available for jet-agitated vessels, substantial research has been devoted to study the mechanically aided (impeller) heat transfer in agitated vessels. Investigation includes the geometric effects of impeller diameter ratio d_i/D, impeller height ratio Z/d_i and Z/H, thickness ratio w/D, and number of impeller blades (see Uhl and Gray [2], and Penney [3]). Others have studied the heat transfer phenomena in gas sparged vessels, such as Hart [5], and Nagata et al.[6], and a heat transfer correlation for gas-sparsed mixing of vessels was recommended by Hart [5] in the form:

$$\frac{h}{c_p \upsilon_s \rho} = 0.125\left(\frac{\upsilon_s \rho}{\mu g}\right)^{-0.25} \mathrm{Pr}^{-0.6} \tag{3}$$

where the heat transfer coefficient h is calculated by using the sparged-gas superficial velocity υ_s.

For natural convection inside enclosures with a horizontal heat transfer surface, some research work has been reported by Globe and Dropkin [7], and Catton and Edward [8]. Globe and Dropkin studied natural convection heat transfer in liquids confined by two horizontal plates and heated from below. Catton and Edward [8] further investigated effects of side walls on natural convection between horizontal plates, and found that, as the Rayleigh number was increased to 10^6 and above, the Nusselt numbers for various aspect ratios asymptotically reached the limit corresponding to the smallest aspect ratio used $(H/D=1)$. That implies that for large Rayleigh numbers extending into the turbulent regime, the size and thermal conductivity of the horizontally confining surfaces did not affect the mean heat transfer coefficient. The experiments performed by Globe and Droplin [7] also demonstrated that there has no significant effect of a lateral surface with low aspect ratio at high Rayleigh numbers. Experimental data reported by Catton and Edward [8] are limited to $\mathrm{Ra}<10^7$. Ulucakli [9] investigated the natural-convection heat transfer in a enclosure, heated partially from below by a disk-shaped surface and cooled from the top and the side, and the data were presented for $10^8<\mathrm{Ra}<10^{10}$. He found that, for large temperature differences between the heating surface and bulk, the mean heat transfer rates can be expressed in terms of conventional correlations, and the results were well correlated by the equation

$$\mathrm{Nu}_{dc} = 0.2\mathrm{Ra}_{dc}^{0.35} \tag{4}$$

where Nu_{dc} and Ra_{dc} are evaluated using the heating-disk diameter.

After reviewing of the previous work for mixing in agitated vessels and for natural convection inside enclosures, an experimental apparatus was constructed to measure the combined natural-and forced-convection heat transfer in a cylindrical enclosure mixed by an injected jet. The tests were designed to study the key parameters governing the heat transfer augmentation by a forced jet, and to investigate the effect of geometric factors, including jet diameter, jet injection orientation, enclosure geometry (aspect ratio), and the presence of flow obstructions. Flow velocity measurements were also performed to provide a better understanding of the flow patterns generated inside the enclosure, which have substantial effects on the effectiveness of enclosure mixing and heat transfer augmentation. Finally, a correlation is proposed using a weighted relation to balance the contributions of natural convection and forced convection to heat transfer.

Experimental Apparatus

In this experiment, a cylindrical enclosure was constructed with a diameter of 2.29 m and a maximum height of 0.8 m, with a vertically adjustable ceiling. The enclosure was designed as a 1/10-scale model of a Savannah River Plant high-level liquid waste tank. Figure 2 shows a picture of the experimental enclosure. At the bottom of the enclosure, a 3.18 mm thick copper plate (2.43 m long and 2.43 m wide) was installed. The copper plate could be heated or cooled by hot or cold water running through a total of 23 tubes soldered under the plate. This method provided a nearly isothermal heating/cooling surface for the experiment.

Nine sheathed J-type thermocouples with 0.508 mm diameter were embedded in the copper plate to measure the heating surface temperature. Due to the high thermal conductivity of copper and the arrangement of the heating tubes, the plate was shown to be nearly isothermal. Four T-type thermocouples were mounted in the inlet of heating water and another four in the outlet, creating a thermopile to measure the temperature difference for the calculation of total heat loss from the heating plate. Cold or hot air was injected into the enclosure with four different injection orientations using long tubes of 15 mm, 26 mm, and 53 mm I.D., and was removed at the top of the enclosure through two 53 mm diameter openings. The heat removal rate by the injected air was calculated from the temperature difference between the air inlet and outlet, and the air flow rate measured by a bank of parallel rotameters of different capacities. Temperatures inside the enclosure were measured with a vertical array of thermocouples designed to be traversed horizontally, measuring the vertical temperature distribution as well as the mean enclosure temperature.

A micromanometer device is applied to measure the flow velocity, using two gage liquids of small density difference. The gage liquids (water, and oil with a specific gravity of 0.9375) were immiscible. The heavier gage liquid filled the lower portion of the manometer U tube up to the 0-0 level (a half of the tube length), and lighter gage liquid was added to both sides, filling the upper U tube and two reservoirs placed on top of the U-tube. A large gage difference could be produced by a small pressure difference with this micromanometer device. A pitot tube was inserted into the tank with the opening directed upstream to the flow path and the other end connected to one of the micromanometer reservoir, which then measured the total pressure (static and dynamic). Another tube measuring static pressure is connected with the other reservoir. The flow velocity was then be determined by the gage difference in U tube, which represented the dynamic pressure head at the pitot-tube opening. Streeter and Wylie [10] discuss the use micromanometers.

Experimental Procedure

Experiments were first performed to investigate natural-convective heat transfer from the heated bottom surface. These results were used as the reference for subsequent evaluation of the heat transfer augmentation from combined natural and forced convection. The bottom surface was heated and maintained at constant temperatures ranging from 30° to 70°C, and heat was transferred by natural convection and removed from the enclosure top and sidewalls by conduction to the ambient. Tests were performed with enclosure heights of 42, 61, and 80 cm, giving enclosure aspect ratios H/D of 0.18, 0.27, and 0.35, respectively. An empirical heat transfer correlation for natural convection was obtained by correlating these experimental data.

With this correlation for natural-convection heat transfer inside the enclosure, combined natural- and forced-convection heat transfer was then studied. For a forced jet injected into the enclosure without internal obstructions, the geometric factors investigated included the use of three different enclosure aspect ratios, three different jet diameters and four different injection orientations. To study the effects of obstructions inside the enclosure, a total of 31 3.35 cm diameter (O.D.) tubes were inserted extending vertically from the ceiling to the bottom. Tests were performed to evaluate the effect of the tube structures on the mixing process. When the jet was directly obstructed by a tube located at various distances from the nozzle, momentum in the original flow direction was reduced due to a form drag.

The experiments investigated the effects of destabilizing density gradients by injecting cold air into the enclosure the bottom surface heated. The injected cold air temperature was approximately 21°C, and the mean temperature at the heating surface was controlled at around 60°C to minimize the effects of fluid property changes and to reduce the complexity for the comparison of geometric factors. Experiments were performed to investigate the effects of stabilizing density gradients, by injecting hot air into the enclosure with the bottom surface cooled. Under this condition, the buoyancy force stabilizes the flow close to the bottom surface and reduces heat transfer. The injected hot air temperature was approximately 52°C, and the mean temperature at the cooling surface was held around 12°C.

Temperature changes were carefully monitored inside the enclosure as well as on the heating surface. Data were collected only when the testing condition reached steady state. The reference temperature used to calculate the thermodynamic and transport properties of air was taken as the mean value measured by the vertical thermocouple array. Air was injected into the enclosure with Re_j (jet Reynolds numbers) from 3×10^3 to 3×10^6, and Ra_D (Rayleigh number scaled with enclosure diameter) inside the enclosure was in the order of $10^9\sim10^{10}$.

To investigate how different flow patterns can affect heat transfer augmentation, air was injected into the enclosure with four different injection orientations. Figure 3 illustrates the four orientations, and the five basic large-scale flow patterns that result. The orientations studied are:

A. Radial injection: injected horizontally across the enclosure center:

B. Azimuthal injection: injected horizontally at a 60 deg angle from radial injection.

C. Vertical/down injection near center: injected downward from the top at 23 cm from the enclosure center.

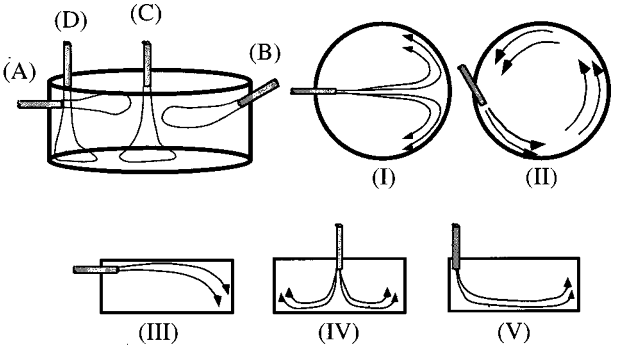

Fig. 3 Injection orientations and resulting large-scale recirculation patterns

D. Vertical/down injection near enclosure vertical wall: injected downward from the top at 10 cm from the enclosure vertical wall.

Error Analysis

The uncertainty of the temperature measurement, including errors from instrumentation and data acquisition system, was estimated to be ±0.1 °C. The uncertainty of the flow rate measurement for water was calibrated to be ±3 percent, and for air, depending on the range of flow measurement, was estimated between ±2 percent to ±5 percent. The corresponding maximum error was 18 percent for the calculated Nusselt number Nu_D, and 8 percent for the calculated Archimedes number Ar.

Experimental Results and Analysis

Part I Heat Transfer Augmentation with Destabilizing (Positive) Effect of Buoyancy Force.

Natural-Convection Heat Transfer in the Enclosure. Figure 4 shows the relationship between the Nusselt and Rayleigh numbers from the present data and the data of Uluckli [9]. These data can be well correlated by

$$\mathrm{Nu}_{nc}=0.15\mathrm{Ra}_D^{1/3} \tag{5}$$

where the 1/3 power and a constant value of 0.15 agrees with the natural-convection correlations for horizontal heating surface in open space. The results demonstrate that the lateral boundary and height-to-diameter ratio have a negligible effect on the turbulent natural-convection heat transfer at high Rayleigh numbers. Equation (5) is used as the reference to determine the heat transfer augmentation from combined natural and forced convection.

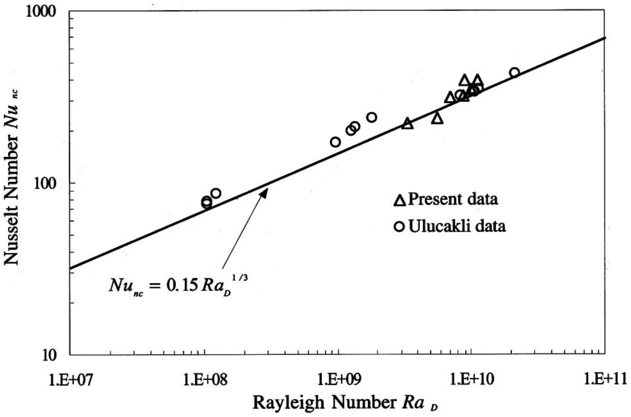

Fig. 4 Natural-convection heat transfer data

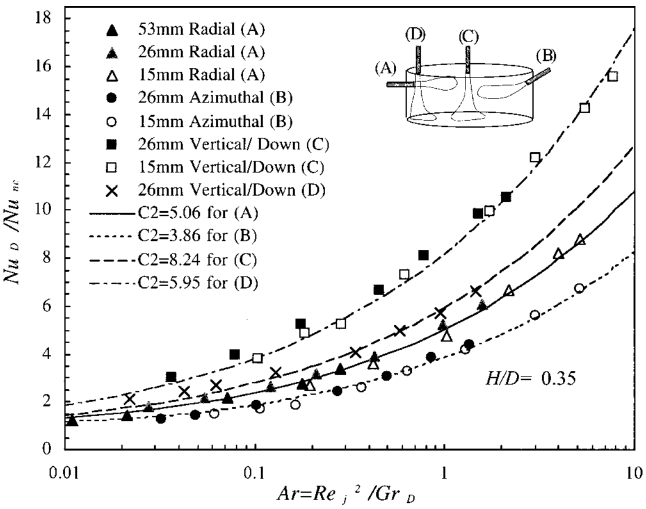

Fig. 5 Results for combined natural and forced-convection heat transfer

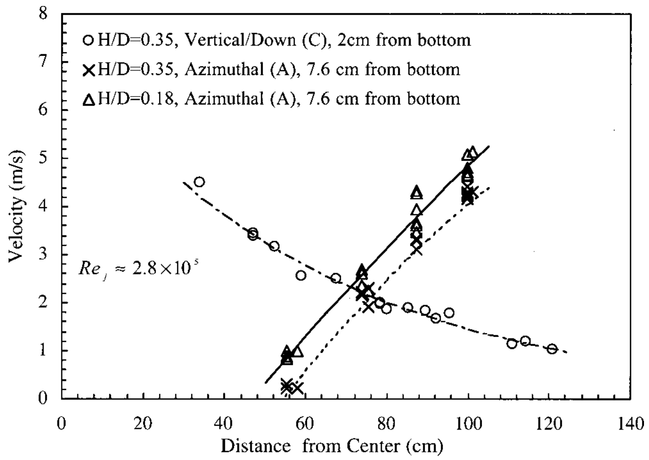

Fig. 6 Horizontal velocities at positions near the heated bottom surface

Combined Natural-and Forced-Convection Heat Transfer in the Enclosure. A general correlation form is employed to combine the natural- and forced-convection heat transfer in the enclosure, given by

$$\mathrm{Nu}_D^n=\mathrm{Nu}_{fc}^n\pm\mathrm{Nu}_{nc}^n \tag{6}$$

This combining rule was used by Churchill [11] to evaluate the mixed-convection heat transfer in external boundary layer flows as well as by Chen et al. [12] to evaluate transition heat transfer from laminar to turbulent film flows. This formulation uses a weighted relationship to balance the contributions from the separate correlations representing their extreme conditions. In the present study, a positive sign in Eq. (6) represents a destabilizing density gradient, and a negative sign a stabilizing gradient (with the minimum Nu value constrained to be zero). Following the common practice, an exponent of $n=3$ is adopted, and Eq. (5) is employed as the natural-convection part Nu_{nc}, and the correlation form of Eq. (1) as the forced-convection part Nu_{fc}.

It is found that the Nusselt numbers Nu_D, plotted against jet Reynolds number Re_j, are clustered into groups of trend lines in accordance with their injection orientations. At high Reynolds numbers the data are fitted best with Reynolds number to the 2/3 power ($\propto \mathrm{Re}_j^{2/3}$). The present data do not include a wide range of Pr, but from research summarized by Penney [3] for agitated vessels, a 1/3-power relation is used for the effect of Pr. Based on these arguments, Eq. (6) can be recast in the form

$$\frac{\mathrm{Nu}_D}{\mathrm{Nu}_{nc}}=\left\{\left[C_1\frac{\mathrm{Re}_j^{2/3}\mathrm{Pr}^{1/3}}{\mathrm{Ra}_D^{1/3}}\left(\frac{\mu_b}{\mu_w}\right)^{0.14}f(\text{geometric})\right]^3\pm1\right\}^{1/3} \tag{7}$$

where μ_b is the bulk air viscosity, and a 0.14 power for the viscosity property ratio is adopted. Equation (7) can then be further simplified using the Archimedes number $\mathrm{Ar}=\mathrm{Re}_j^2/\mathrm{Gr}_D$ and $\mathrm{Ra}_D=\mathrm{Gr}_D\mathrm{Pr}$, and by combining the constant C_1 and the geometric function,

$$\frac{\mathrm{Nu}_D}{\mathrm{Nu}_{nc}}=\left\{\left[C_2\mathrm{Ar}^{1/3}\left(\frac{\mu_b}{\mu_w}\right)^{0.14}\right]^3\pm1\right\}^{1/3} \tag{8}$$

As discussed previously, the constant k in Eq. (1) usually falls within the range of 0.35 to 0.74 for heat transfer to enclosure walls (not helical coil or tubes) in agitated tanks. Combining the constant in Eq. (5) for natural convection, C_2 is expected to fall in the range from 2.3 to 4.93. Figure 5 presents the heat transfer augmentation $\mathrm{Nu}_D/\mathrm{Nu}_{nc}$ versus Archimedes number under a destabilizing density gradient (with a heating surface at the bottom of the enclosure). The data, including four injection orientations and three jet diameters, are well correlated using Eq. (8) with a different constant C_2 for each injection orientation. It can be seen that changing the injection orientation changes the heat transfer augmentation significantly, while the geometric factor d_j/D has a very small effect. For the destabilizing density gradient the data for all injection orientations asymptotically approach 1 at low Archimedes number. This agrees with the prediction by Eq. (8) when heat transfer is dominated by natural convection.

The magnitude of augmentation is largest for vertical/down injection near the center (C), and followed by vertical/down injection near the wall (D), radial injection (A), and azimuthal injection (B). The constants C_2 correlated for radial (A) and azimuthal (B) injection, in general, fall within the expected range, while that for vertical/down injection (C) augmentation is clearly higher than expected.

To further understand the flow pattern, the air velocity was measured by the micromanometer device. Figure 6 presents the velocity in the horizontal direction measured near the bottom of the heating surface. For comparison, air was injected at $\mathrm{Re}_j\approx2.8\times10^5$ through a tube of 15 mm I.D. Three sets of data are included in this figure, including azimuthal injection with $H/D=0.35$, and 0.18, and vertical/down injection (C) with $H/D=0.35$. For azimuthal injection, the data is plotted at the positions measured from the vertical geometric center of the enclosure, and for vertical/down injection at the positions measured from the vertical jet center.

As illustrated in Fig. 3(II) air injection in the azimuthal direction induces circumferentially circulating motion. The flow velocity distribution in Fig. 6 shows approximately equal velocities for positions at the same radius from the enclosure center. It is also reveals that while there is strong horizontally circulating motion in the regions close to the wall, regions near the center experience little influence from forced flow motion, reaching an almost stagnant condition at the center. The delineation, separating the forced-convection dominated region near the wall and natural-convection dominated region near the center, makes the whole-volume mixing less effective, and thus reduces the average heat transfer augmentation. For $H/D=0.35$, approximately 25 percent of the bottom surface area was not subjected to the influence of forced convection under azimuthal injection, which explains the relatively low augmentation in this injection mode.

For radial injection, velocity measurement shows that after the expanded jet reaches the enclosure vertical wall, the jet undergoes a boundary layer transition and spreads as a wall jet both in horizontally circulating flow pattern (Fig. 3(I)) and also vertically downward pattern (Fig. 3(III)). The downward flow then turns and

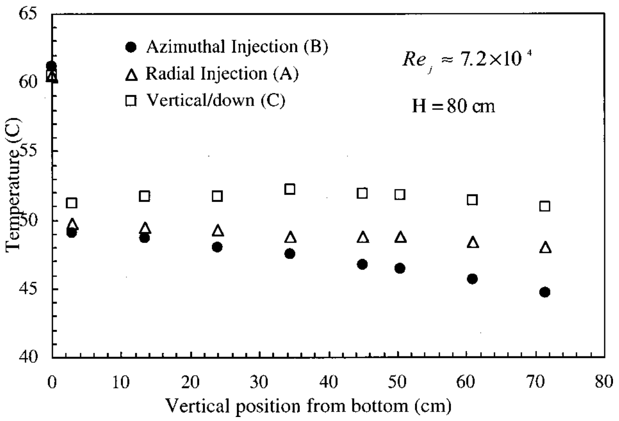

Fig. 7 Vertical temperature distributions in the enclosure

spreads across the bottom floor with decreasing velocity. The flow pattern generated by radial injection is found to be more productive in mixing the whole volume than is azimuthal injection, and gives a higher magnitude of heat transfer augmentation.

For vertical/down injection near enclosure vertical wall, Figure 3(V) shows the primary flow pattern. After the jet impinges on the floor, it transforms to a wall-jet flow spreading with decreasing velocity across the heating floor. This flow pattern mixes the cold injected air with hot air near bottom surface more effectively than in the cases discussed earlier. This explains why this orientation induces more effective augmentation than the radial and azimuthal injections.

The most effective injection orientation (Fig. 3(IV)) is vertical/down injection near the enclosure center. At high Re the augmentation is more than twice of that for azimuthal injection. After impinging on the floor surface, the vertical velocity component in jet core is decelerated and transformed into an accelerated horizontal flow. The horizontal wall jet spreads evenly outward with a velocity decreasing uniformly radially from the stagnant point, and then turns upward after reaching vertical walls. For this cylindrical enclosure this flow pattern proves to be most effective for uniform mixing. Figure 7 illustrates the vertical temperature distribution for three injection orientations, and shows that the enclosure volume is well mixed under vertical/down injection (C), and strongly stratified under azimuthal injection.

The heat transfer augmentation in vertical/down injection (C) occurs due both to the effective large-scale mixing flow pattern and the substantially augmented local heat transfer coefficient near jet impingement point. Jambunathan et al. [13] performed a detailed review of heat transfer data for single circular jet impingement. They concluded that the local heat transfer coefficient can be predicated as a function of jet Reynolds number, height to jet diameter ratio (L/d_j), and the ratio of radial distance from stagnation point to jet diameter (r/d_j). Following the results of Boguslawski and Popiel [14], the potential core radius affected by jet impingement is approximately four times the nozzle diameter. Several correlations are available for the prediction of local and average heat transfer coefficients in this region. The equation by Lee [15] can be used to estimate the average Nusselt number in this region,

$$\mathrm{Nu}_{r/d_j=4}=0.083\,\mathrm{Re}_j^{0.708}(L/d_j)^{0.144} \tag{9}$$

Based on the present experimental data, it is estimated that the average heat transfer coefficient inside the present enclosure will be increased by less than 13 percent due to the localized enhancement in the potential core region. Therefore, the majority of heat transfer augmentation by vertical/down impingement (C) is contributed by the effective large-scale mixing flow pattern.

The effect of jet orientation has not typically been included in agitated vessel correlations (e.g., Eq. (2)). The discrepancy is likely due to the different configurations of heat transfer surfaces in previous investigations. For an agitated vessel with the entire inner wall used as a heat transfer surface, the transport problem is different from a partially heated wall. The flow patterns of the wall jets generated by the injected fluid (or mechanical impeller) in different orientations does not significantly change the mean heat transfer rate if the entire inner tank wall is involved. However, if the wall is only partially heated or the heating source is localized in the enclosure, the effectiveness of heat transfer will be more strongly affected by the flow patterns, depending on which can mix better the cold injected fluid with localized hot fluid near the heat transfer surface. Therefore, injection orientation should not be neglected with localized heat transfer surfaces in enclosures.

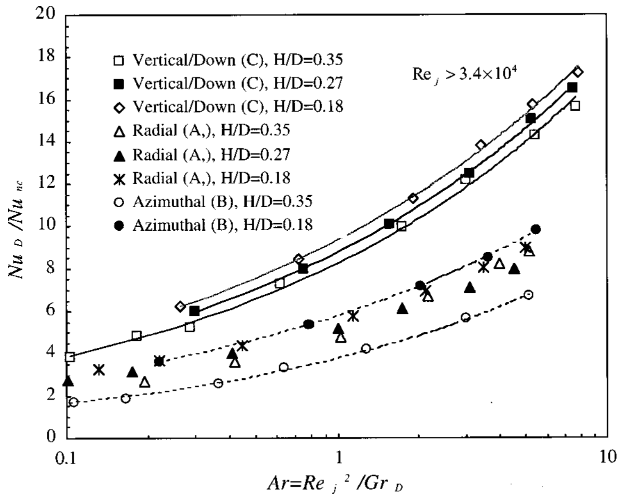

Fig. 8 Effect of aspect ratio on heat transfer augmentation

Effect of Enclosure Aspect Ratio. Figure 8 shows high-Re results for three different aspect ratios. In general, the heat transfer coefficient increases with decreasing aspect ratio for all three orientations presented. While the increase is small with decreasing aspect ratio for the radial (A) and vertical/down injections (C), the magnitude of the increase is relatively large for azimuthal injection (B). The solid trend lines in the upper part of the figure represent the increment due to the aspect ratio effect for vertical/down injection (C), and the dashed lines represent the large increment for azimuthal injection (B). From Figure 6 with enclosures of aspect ratios of 0.35 and 0.18, the circulating velocity induced by azimuthal injection increases with reducing aspect ratio, and the area affected by forced flow also extends further into the cylindrical center. This explains the larger increase of heat transfer augmentation for azimuthal injection with decreasing aspect ratio. Because the aspect ratio effect is not considered to be an important geometric factor, as shown in Eq. (2) for correlations for most of agitated vessels, here the same argument, as for jet orientation, applies regarding the greater importance of geometry localized heat transfer augmentation. Particularly for azimuthal injection a large increase of heat transfer is observed when the aspect ratio is reduced by half.

Table 1 summarizes the results for the correlated constants C_2 with positive buoyancy effect on the mixed convection inside the enclosure.

Effect of Obstructions Inside the Enclosure. To investigate the effect of flow obstructions, 31 tubes with 3.35 cm O.D. were inserted vertically from the top to the bottom of the enclosure. Experiments were performed to measure the variation of heat transfer under the conditions where the forced jet impinged directly on a tube at 10, 20, 38, and 63.5 cm from the injection nozzle. It is found that if the jet does not impinge on the tube

Table 1 C_2 values for injection orientation and aspect ratio

Injection Orientation	Aspect Ratio (H/D)		
	0.18	**0.27**	**0.35**
Radial (A)	5.43	5.29	5.06
Azimuthal (B)	5.72	4.76	3.86
Vertical/down (C)	9.08	8.69	8.24
Vertical/down (D)			5.95

before reaching the enclosure wall, the change of mean heat transfer coefficient can be small as long as the total cross-section area of tubes is much less than that of the flow area. If the jet hits a tube before reaching the enclosure wall, the loss of jet momentum in the flow direction can significantly affect the effectiveness of mixing the whole volume, and thus reduce the mean heat transfer coefficient. Figure 9 shows the results of jet impingement on tubes at certain distances from the injection nozzle.

The jet velocity profile downstream of the injection nozzle has been discussed by List [16], and is used here to estimate the momentum loss in the flow direction due to form drag with the impinged tube. Assuming that the tube diameter d_t is much smaller than expanded jet radius R, the fraction of momentum loss can be evaluated by

$$\frac{M_{\text{loss}}}{M}=\frac{\int_{-R}^{R} C_D \frac{\rho u(r)^2}{2} d_t dr}{\int_0^{R} \frac{\rho u(r)^2}{2} 2\pi r dr} \tag{9}$$

where C_D is the drag coefficient, and u the jet velocity. The distribution of velocity across a jet can be evaluated by (List [16])

$$u(r)=U_m e^{-(r/b)^2} \tag{10}$$

The evaluation of how the mean velocity U_m and width parameter b vary with the distance from the jet origin x, depends upon the evolution of the momentum flux, and can be determined from experimental measurements. For a given self-similar distribution of mean velocity and pressure, the width parameter is related to the jet radius by $b=R/\sqrt{2}$. Assuming $\rho \approx \rho_m$, Eq. (9) can be further simplified as

$$\frac{M_{\text{loss}}}{M}=\frac{\frac{C_D \rho_m U_m^2 d_t}{2}\int_{-\sqrt{2}b}^{\sqrt{2}b} e^{-(r/b)^4} dr}{2\pi \rho_m U_m^2 \int_0^{\sqrt{2}b} e^{-(r/b)^4} r dr}=0.327 C_D \frac{d_t}{b} \tag{11}$$

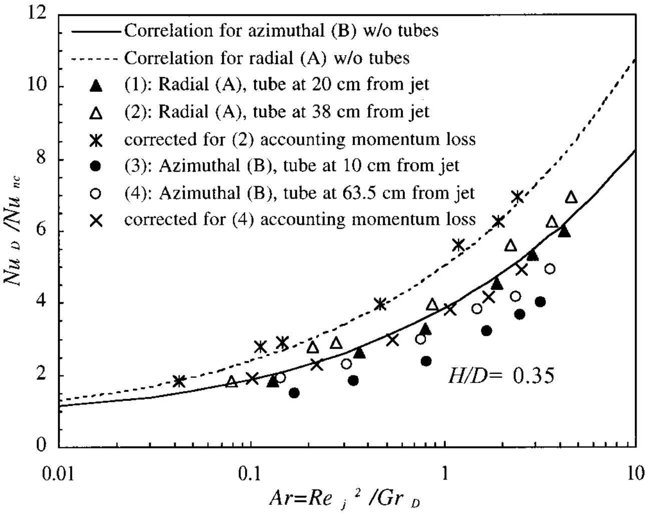

Fig. 9 Effect of tube obstructions inside the enclosure

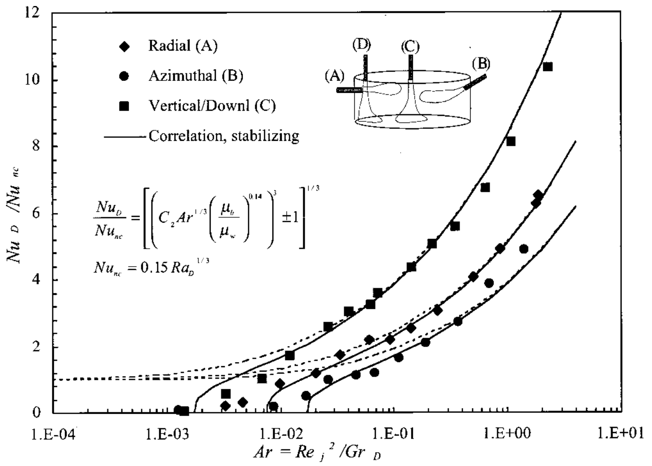

Fig. 10 Effect of stabilizing density gradient on mixed convection

The drag coefficient $C_D \approx 1.1$ and the experimental results from Fisher et al. [17] give $b/x=0.107$. Then the fraction of momentum loss can be estimated in terms of the distance from the jet origin and tube diameter by

$$\frac{M_{\text{loss}}}{M}=3.36\frac{d_t}{x} \tag{12}$$

By Eq. (12), 29.6 percent of momentum is lost in the flow direction after impingement on a 3.35 cm tube at 38 cm from the jet nozzle, and 17.7 percent of momentum is lost after impingement on a tube at 63.5 cm from the jet origin. By accounting for the momentum loss and the corresponding reduction of the jet Reynolds number, the resulting data shifts much closer to the correlations without tubes inside the enclosure. This information implies that the reduction of heat transfer augmentation by structures can be predicted by the loss of momentum in the jet. The large-scale motion induced by the jet dominates the large scale enclosure flow, and the augmentation of the heat transfer inside the enclosure.

Part II Heat Transfer Augmentation with Stabilizing (Negative) Effect of Buoyancy Force. For mixed convection with a stabilizing buoyancy force from a cooled bottom surface, a negative sign is used in Eqs. (6) and (8). Figure 10 shows the comparison with the experimental data. The dashed line represents the destabilizing (positive) effect of buoyancy force, and solid line represents the stabilizing (negative) buoyancy effect. As shown by the data, the augmentation ratio approaches close to 0 at low Archimedes numbers, with the weakening of forced convection and stabilizing effect of negative buoyancy force. Even though this combining rule to address stabilizing density gradients is rather crude, it generally fits the data well, and should be adequate for most engineering purposes.

Conclusions

The present experimental study has investigated heat transfer under combined natural convection and forced convection due to jet injection. Under natural convection, the average Nusselt number inside the large enclosure with heating surface at the bottom can be correlated by the Rayleigh number to the 1/3 power in the high-Rayleigh-number flow regime ($\mathrm{Ra}_D > 10^8$). Under forced convection with a strong jet, the data is well represented as a function of jet Reynolds number to the 2/3 power. The combining form of Eq. (6) is adequate to evaluate the mixed-convection heat transfer regime inside the enclosure. As shown by Eq. (8), the correlation can be formulated as a function of Archimedes number, fluid property factor, and geometric correlation, and correlates data well under both stabilizing and destabilizing buoyancy effects. The most important geometric factor is the jet injection orientation.

Augmentation is affected strongly by the flow patterns generated by different injection orientations, which, in turn, govern the effectiveness in large-scale mixing in the enclosure. As shown in Fig. 5, the heat transfer augmentation for vertical/down injection near the enclosure center can be two times the augmentation for azimuthal injection. The improved mixing is reflected in the vertical temperature distributions shown in Fig. 8. Depending on the injection orientation, the aspect ratio can also play an important role at low aspect ratios, particularly for azimuthal injection. In addition, the change of heat transfer augmentation, caused by obstructions inside enclosure, can also be important, and the reduction can be by considering the momentum loss from form drag.

Nomenclature

Ar = Archimedes number $(=\mathrm{Re}_j^2/\mathrm{Gr}_D)$
b = width parameter of velocity profile
β = coefficient of thermal expansion
c_p = specific heat at constant pressure
C_1 = constant
C_2 = constant
C_D = drag coefficient
d_i = impeller diameter
d_j = jet diameter
d_t = tube outer diameter (O.D.)
D = diameter of cylindrical enclosure
h = heat transfer coefficient
f = geometric factor
g = standard gravitational acceleration
Gr_D = enclosure Grashof number $(=g\beta(T_w-T_b)D^3/v^2)$
H = height of enclosure
I.D. = inner diameter
K = constant
k = thermal conductivity
L = distance between jet exit and impingement plate
n = constant
N = impeller rotational speed
Nu_D = Nusselt number inside the enclosure $(=hD/k)$
O.D. = outer diameter
Pr = Prandtl number
r = radial distance from stagnation point
ρ = density
R = radius of jet
Ra_D = enclosure Rayleigh number $(=\mathrm{Gr}_D\mathrm{Pr})$
Re_j = jet Reynolds number $(=\rho u d_j/\mu)$
T = temperature
μ = dynamic viscosity
v = kinematic viscosity
u = velocity
U_m = mean velocity
v_s = superficial velocity
w = width of impeller
x = distance from jet origin

Subscripts

b = bulk value
D = diameter of cylindrical enclosure
dc = disk
fc = forced convection
j = jet
m = mean value
nc = natural convection
w = wall

References

[1] Sterbacek, Z., and Tausk, P., 1965, *Mixing in the Chemical Industry*, Pergamon, London.
[2] Uhl, V. W., and Gary, J. B., 1966, *Mixing-Theory and Processing*, Vols. I and II, Academic, New York.
[3] Penney, W. R., 1983, *Agitated Vessels, Heat Exchanger Design Handbook*, E.U., Schlunder, ed., **2.2.6.2**, Hemisphere Publishing Corp., New York.
[4] Fossett, H., and Prosser, L. E., 1951, Trans. Inst. Chem. Engr. (London) **29**, pp. 322.
[5] Hart, W. F., 1976, ‘‘Heat Transfer in Bubble-Agitated Systems—A General Correlation,’’ Ind. Eng. Chem. Process Des. Dev., **15**(1), pp. 109–114.
[6] Nagata, S., et al., 1976, Study of Heat Transfer for Aerated Mixing Vessel and Aerated Tower, Heat Transfer Jpn. Res., **5**, No. 4, pp. 75–83.
[7] Globe, S., and Dropkin, D., 1959, ‘‘Natural Convection Heat Transfer in Liquids Confined by Two Horizontal Plates and Heated from Below,’’ J. Heat Transfer , **81**, pp. 24–27.
[8] Catton, I., and Edwards, D. K., 1967, ‘‘Effect of Side Walls on Natural Convection Between Horizontal Plates and Heated from Below,’’ J. Heat Transfer, **89**, pp. 295–299.
[9] Ulucakli, M. E., 1996, ‘‘Turbulent Natural Convection in an Enclosure with Localized Heating from Below,’’ Exp. Heat Transfer, **9**, pp. 305–321.
[10] Streeter, V. L., and Wylie, E. B., 1985, *Fluid Mechanics*, McGraw Hill, New York.
[11] Churchill, S. W., 1978, ‘‘A Comprehensive Correlating Equation for Laminar, Assisting, Forced and Free Convection,’’ AIChE J., **23**, pp. 10–16.
[12] Chen, S. L., Gerner, F. M., and Tien, C. L., 1987, ‘‘General Film Condensation Correlations,’’ Exp. Heat Transfer, **1**, pp. 93–107.
[13] Jambunathan, K., Kai, E., Moss, M. A., and Button, B. L., 1992, ‘‘A Review of Heat Transfer Data for Single Circular Jet Impingement,’’ Int. J. Heat Fluid Flow, **13**, pp. 106–115.
[14] Boguslawski, L., and Popiel, C. O., 1979, ‘‘Flow Structure of the Free Round Turbulent Jet in the Initial Region,’’ J. Fluid Mech., **90**, pp. 663–685.
[15] Lee, J., and Lee, S. J., 1999, ‘‘Stagnation Region Heat Transfer of Turbulent Axisymmetric Jet Impingement,’’ Exp. Heat Transfer, **12**, pp. 137–156.
[16] List, E. J., 1982, ‘‘Turbulent Jets and Plumes,’’ Annu. Rev. Fluid Mech., **14**, pp. 189–212.
[17] Fisher, H. B., List, E. J., Koh, R. C. Y., Imberger, J., and Brooks, N. H., 1979, *Mixing in Inland and Coastal Waters*, New York Academic.

Enhanced Convection or Quasi-Conduction States Measured in a Super-Conducting Magnet for Air in a Vertical Cylindrical Enclosure Heated From Below and Cooled From Above in a Gravity Field

Syou Maki
Graduate Student,
Interdisciplinary Graduate School of Engineering Sciences,
Kyushu University,
Kasuga Koen 6-1
Kasuga 816-8580, Fukuoka, Japan

Toshio Tagawa
Research Associate,

Hiroyuki Ozoe
Professor,
e-mail: ozoe@cm.kyushu-u.ac.jp

Institute of Advanced Material Study,
Kyushu University,
Kasuga Koen 6-1,
Kasuga 816-8580, Fukuoka, Japan

Magnetizing force was applied for natural convection of air in a shallow cylindrical enclosure heated from below and cooled from above. The cylinder measured 45 mm in diameter and 14.8 mm in height. The convection enclosure was located 66 mm above or below the coil center in the bore of a super-conducting magnet. The average Nusselt numbers were enhanced about twice at the location +66 mm above the coil center under 3.40 Tesla and decreased to $Nu = 1.12 \sim 1.28$ *at the location −66 mm below the coil center for the Rayleigh number from 3520 to 6980. These two locations were selected as the most effective positions for application of the magnetizing force in this super-conducting magnet. A model equation for magnetizing force was derived and numerically computed for* $Pr = 0.7$ *and* $Ra = 2100$ *and 7000. One turn coil was presumed as a model of thousand turns real superconductor. The magnetic strength is represented by a new parameter* γ *and varied from 2345 to 9124. By adjusting the location of the enclosure in the bore of the super-conducting magnet, the average Nusselt number of 1.14 at* $Ra = 2100$ *varied from 1.8 to 1.0001 depending on the magnetic strength, and that of 2.02 at* $Ra = 7000$ *varied from 2.6 to 1.0003. These data are plotted versus magnetic Rayleigh number* $Ra_m = Ra(\gamma \partial B_z^2 / \partial Z + 1)_{R=0, Z=0.5}$ *at the center of the enclosure and agreed well with Silveston's data for a classical nonmagnetic field.* [DOI: 10.1115/1.1482082]

Keywords: *Enhancement, Heat Transfer, Magnetic, Microgravity, Natural Convection*

1 Introduction

Through recent developments in super-conducting magnets strong magnetic-field gradients can be developed. These gradients can be used to produce large magnetizing forces in paramagnetic materials. The magnetizing force has been known for many years [1,2], but until recently it had been neglected almost completely. Braithwaite et al. [3] again highlighted this force for Benard convection of paramagnetic water solution to give larger or smaller heat transfer rates than the average heat transfer rate of a non-magnetic field, although they did not compare their findings with the data of Silveston [4]. Magnetizing force produces various interesting phenomena, and Wakayama and coworkers [5–9], and Kitazawa and coworkers [10–13] have reported many new findings and applications.

Air contains 21 percent of oxygen gas, which has exceptionally large positive value of magnetic susceptibility due to the parallel spin of electrons, and air also receives attractive force from a magnet. Depending on the location in the bore space of a super-conducting magnet, the geometrical gradient of magnetic induction differs. By choosing a suitable location, magnetizing force may be used to cancel or overcome gravitational force.

The present report examines experimentally and theoretically the effects of magnetizing force on the convection of air heated from below and cooled from above in a convection enclosure located in the bore space of a super-conducting magnet.

2 Experimental Setup

The experimental enclosure was a vertical cylinder of Plexiglas measuring 45 mm in diameter and 14.8 mm in height. This shallow enclosure was expected to provide similar heat transfer rates to those of Rayleigh-Benard convection in a very shallow layer. Air was selected as the experimental fluid. Air will also be used in the theoretical analysis to compare with experiments. The experimental enclosure was heated from below by a Nichrom wire, whose electric power was measured by both an ammeter (Digital multimeter 2000, Keithley) and a DC regulated voltmeter (Digital multimeter 7555, Yokogawa). The enclosure was cooled through a duct from a constant temperature bath (Lauda, RK20) regulated at 29.0°C The experimental fluid was heated and cooled through two copper plates of 3 mm in thickness. Two thermocouples of T type (accuracy 0.1 K) were inserted into two holes of 1 mm in diameter within the lower plate drilled up to 3 or 12 mm from the center of the enclosure. A hole of the same size was drilled in the upper plate for a thermocouple to measure the cooling plate temperature. An extra thermocouple was also placed outside the cylindrical enclosure. Thermocouple outputs were recorded every two minutes in a PC card data sampling system (NR-1000, KEYENCE). Sampled data were averaged for more than 80 data points. The experimental apparatus was placed in a Plexiglas cylinder of 72 mm in diameter which was surrounded by a bundle of tubes car-

---

Contributed by the Heat Transfer Division for publication in the JOURNAL OF HEAT TRANSFER. Manuscript received by the Heat Transfer Division September 24, 2001; revision received March 20, 2002. Associate Editor: F. B. Cheung.

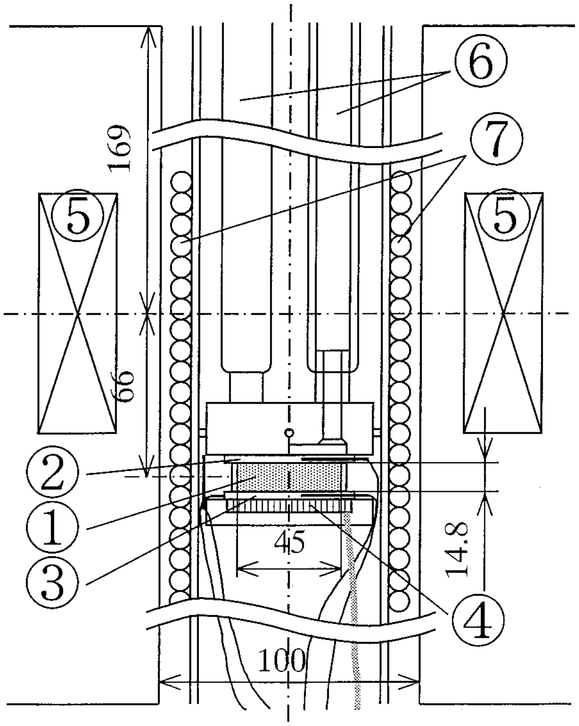

Fig. 1 Schematic view of the experimental apparatus located in the bore of a super-conducting magnet. ① Cylindrical enclosure; ② Cooled copper plate; ③ Heated copper plate; ④ Electric heater; ⑤ Magnetic coil; ⑥ Duct of running water; ⑦ Bundle of tubes.

rying water from another constant temperature bath kept at 29.0°C. This bundle of water tubes is to keep the whole experimental apparatus in a constant temperature environment. The whole apparatus was finally inserted into the bore space of a super-conducting magnet of 100 mm in diameter (5 T 100 ϕ, Helium-free super-conducting magnet, Sumitomo Heavy Industry, LTD., Japan). The setup is schematically shown in Fig. 1.

3 Experimental Results

3.1 Net Heat Flux. Natural convection in an enclosure occurs even with a heat flux as low as several watts. The difficulty in measuring natural convection experimentally lies in the evaluation of net heat flux through the fluid, especially for a low thermal conducting fluid like air. In the present experiment, a technique invented by Ozoe and Churchill [14] was again employed. The essence of this technique is that the experimental apparatus is turned upside-down, with the experimental fluid heated from above and cooled from below. Thermal conduction is induced by the temperature difference between the hot and cold plates, and the net conduction heat flux through the experimental fluid can be estimated by using the known thermal conductivity of air with Fourier's law. The difference between the total heat input through the electric heater and the theoretical conduction heat flux gives the heat loss from the electric heater to the environment. With several other heat inputs, we can obtain a linear relationship between the temperature difference $\Delta\theta$ and the electric heat supply Q. By subtracting conduction heat flux from each datum, we can obtain a linear relation for heat loss after least-square data reduction, as follows:

Conduction Curve

$$\Delta\theta = 13.12Q - 0.028 \tag{1}$$

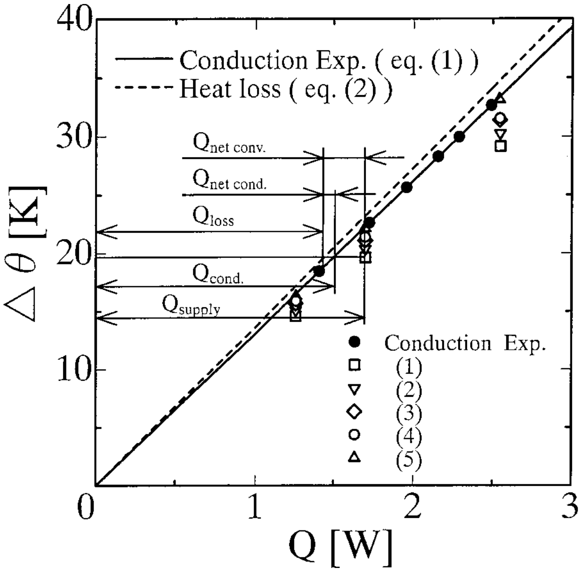

Fig. 2 Master plot for estimation of heat loss for the experiments in an enclosure heated from below and cooled from above. The solid line is obtained from conduction experiment with the enclosure placed upside-down. The dashed line is heat loss obtained from a conduction curve and will be employed for net heat flux in convection experiments.

	(1)	(2)	(3)	(4)	(5)
z_b [mm]	66	66	66	66	−66
$b_z(\partial b_z/\partial z)$ [T^2/m]	138	49.7	5.52	0	−138

Heat Loss Curve

$$\Delta\theta = 13.66Q - 0.029 \tag{2}$$

Figure 2 shows these curves. The solid (conduction) curve is Eq. (1) and the dashed (heat loss) curve is Eq. (2). The net heat conduction is the difference between curves (1) and (2). Then, convection experiments were carried out with the apparatus heated from below. For each total heat supply, the temperature difference between the hot and cold plates was measured. At each specific temperature difference $\Delta\theta$, the total heat supply minus heat loss calculated by Eq. (2) gives the net convection heat flux through the experimental fluid. These are indicated in Fig. 2 for one data point. The experimental average Nusselt number is given as follows.

$$\mathrm{Nu} = Q_{\mathrm{net\ conv}}/Q_{\mathrm{net\ cond}}, \tag{3}$$

The key idea of this technique is that the heat loss from the heater depends on the temperature of the heater itself without depending on the conduction or convection inside the enclosure. Error estimation in the average Nusselt number is mentioned briefly in the appendix.

3.2 Experimental Results With Magnetic Field. Measured data are plotted in Fig. 2 for various strengths of magnetic induction and locations of enclosure. Table 1 lists the experimental data. Experiments were carried out at two different locations, i.e., +66 mm above the coil center and −66 mm below the coil center. Magnetic induction has a geometrical distribution as shown later in the theoretical approach, and these two locations were selected to have the most axially aligned magnetizing force in the present super-conducting magnet.

Next, three different total heat inputs were tested. At each heat input, strengths of magnetic induction at the center of the enclosure were varied from 0 to 3.40 Tesla. Table 1 shows temperature difference $\Delta\theta = \theta_h - \theta_c$ and the Rayleigh number $\mathrm{Ra} = g\beta\Delta\theta h^3/(\alpha\nu)$, and the average Nusselt number calculated by Eq. (3). At the location of +66 mm, the average Nu number is

Table 1 Experimental results for air in a vertical cylindrical enclosure heated from below with an electric heater and cooled from above with isothermal coolant

Level of enclosure from coil center	Heater input Q [W]	b_z at r = 0 and mid height [Tesla]	$\Delta\theta$ [K]	Ra	Average Nu	$b_z(\partial b_z/\partial z)$ at r = 0 and mid height [T^2/m]	Ra_m
+66 mm	1.26	0	15.9	3800	1.97	0	3800
		0.680	15.7	3750	2.29	5.52	4910
		2.04	15.1	3620	3.38	49.7	13700
		3.40	14.6	3520	4.31	138	30600
	1.70	0	21.4	4910	2.03	0	4910
		0.680	21.1	4850	2.40	5.52	6360
		2.04	20.4	4710	3.36	49.7	17900
		3.40	19.6	4560	4.40	138	39900
	2.55	0	31.5	6720	2.47	0	6720
		0.680	31.4	6700	2.60	5.52	8820
		2.04	30.2	6510	3.63	49.7	25000
		3.40	29.1	6320	4.71	138	56100
−66 mm	1.26	3.40	16.3	3890	1.28	−138	−26100
	1.70	3.40	22.2	5060	1.12	−138	−34300
	2.55	3.40	33.2	6980	1.13	−138	−48300

enhanced with increasing strength of the magnetic field for all heat inputs. At 3.40 Tesla, the average Nu number is almost twice as large as that in the absence of a magnetic field. At the location of −66 mm, on the other hand, the average Nusselt numbers are 1.28 to 1.12, almost a conduction state. These are plotted in Fig. 3. The solid line is from Silveston's experimental data [4]. The data (4) represented by circles for absence of a magnetic field agree closely with Silveston's data. The data at $b_z(\partial b_z/\partial z)=5.52$, 49.7, and 138 T^2/m at +66 mm are larger than those at 0 T^2/m, showing enhancement by the magnetic fields, while the data for the enclosure located at −66 mm give Nusselt numbers as small as 1.12 to 1.28, i.e., almost a conduction state. These data suggest that magnetic field enhances or retards convection of air in an enclosure heated from below and cooled from above in the terrestrial state. This is because of the additional accelerating force produced by magnetizing force, as described hereafter.

4 Mathematical System Considered

In the numerical analyses, enclosures with an aspect ratio = diameter/height = 3 or 6 were considered.

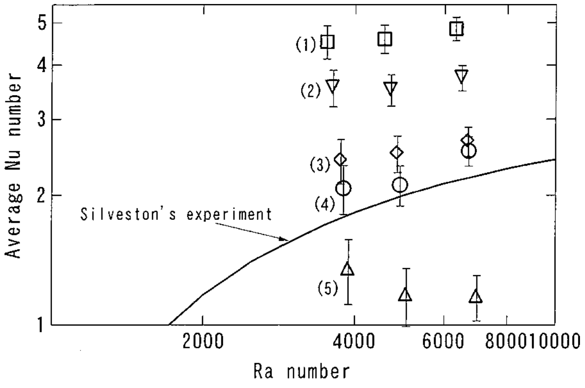

Fig. 3 Summary of experimental results. Solid line is from Silveston's experiment [4].

(1)	$z_b=+66$ mm and	$b_z(\partial b_z/\partial z)=138\ T^2/m$
(2)	$z_b=+66$ mm and	$b_z(\partial b_z/\partial z)=49.7\ T^2/m$
(3)	$z_b=+66$ mm and	$b_z(\partial b_z/\partial z)=5.52\ T^2/m$
(4)		$b_z(\partial b_z/\partial z)=0\ T^2/m$
(5)	$z_b=-66$ mm and	$b_z(\partial b_z/\partial z)=-138\ T^2/m$

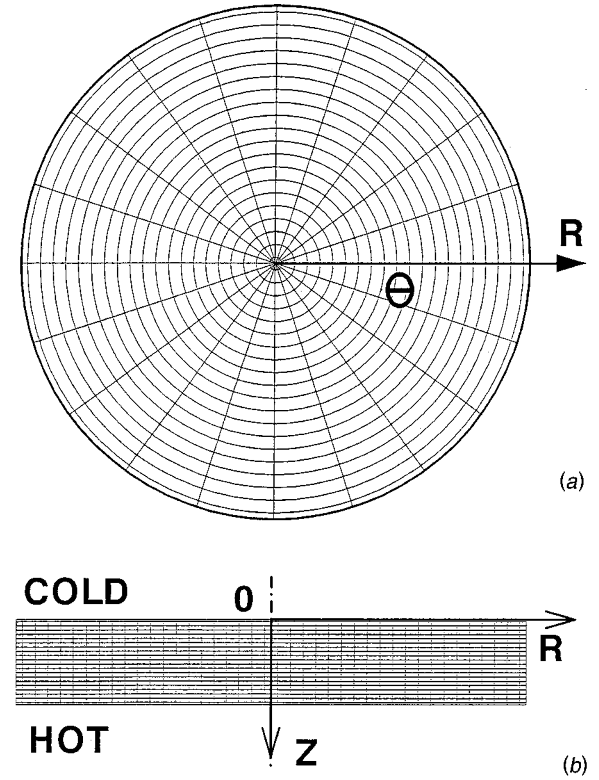

Fig. 4 Modeled vertical cylinder with computational grid lines for an enclosure with aspect ratio = 6: (*a*) top view, and (*b*) vertical side view.

Figure 4 shows the enclosure of aspect ratio = 6. A shallow vertical cylinder filled with air is heated from below and cooled from above. This system is expected to represent natural convection similar to Rayleigh-Benard convection in a regular gravity field. The cylinder was then located at various levels in the bore of a super-conducting magnet as shown in Fig. 5. The locations of the cylindrical enclosure correspond to 95, 55, 25, −25, −55, −95 mm in the bore of 100 mm in diameter. The magnetic coil diameter was presumed to be 180 mm. Figure 5(*a*) shows a vectorial representation of magnetic induction $\vec{B}$ due to the passage of electricity through the magnetic coil. Magnetic induction was computed by Biot-Savart's law below. A super-conducting magnet consists of a coil of several thousand turns but in the present

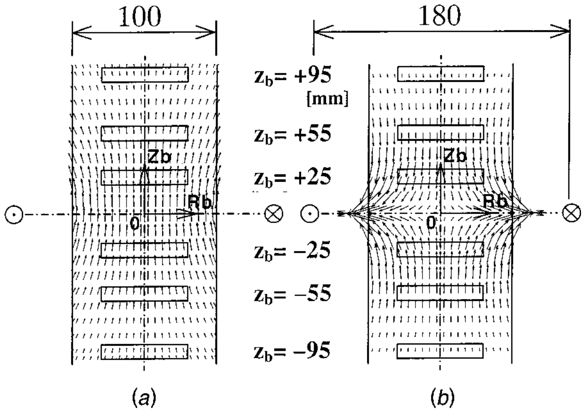

Fig. 5 Modeled location of enclosure at $z_b=95$, 55, 25, −25, −55, and −95 mm in the bore of 100 mm in diameter with a modeled magnetic coil: (*a*) magnetic induction vectors $\vec{B}$; and (*b*) magnetizing force vectors $\vec{\nabla}B^2$.

computations a coil of one turn was presumed for simplicity. Figure 5(*b*) shows a vectorial representation of magnetizing force $\vec{\nabla} B^2$ corresponding to Fig. 5(*a*), in a dimensionless scale of B. The magnetizing force is symmetrical in terms of the coil.

5 Mathematical Model Equations for Convection Due to Magnetizing and Gravitational Forces

Following our recent works [15,16], dimensionless model equations for the gravitational and magnetizing force fields are given as follows. They are an equation of continuity, an energy equation and momentum equations that include a magnetizing force term. Nondimensionalization followed Hellums and Churchill [17].

$$\vec{\nabla} \cdot \vec{U} = 0 \tag{4}$$

$$DT/D\tau = \nabla^2 T \tag{5}$$

$$\frac{D\vec{U}}{D\tau} = -\vec{\nabla} P + \mathrm{Pr}\nabla^2 \vec{U} - \mathrm{Ra}\cdot\mathrm{Pr}\cdot T\left[\gamma \vec{\nabla} B^2 + \begin{pmatrix} 0 \\ 0 \\ 1 \end{pmatrix}\right] \tag{6}$$

$$\vec{B} = -\frac{1}{4\pi} \oint \frac{\vec{R} \times d\vec{S}}{R^3}. \tag{7}$$

Equation (7) is Biot-Savart's law for the computation of magnetic induction. These sets of equations were approximated with finite difference equations and numerically solved with the initial and boundary conditions as follows.

$$\text{at } \tau = 0 \quad \vec{U} = T = 0$$

$$\text{at } Z = 0 \quad \vec{U} = 0, \quad T = -0.5$$

$$\text{at } Z = 1 \quad \vec{U} = 0, \quad T = +0.5$$

$$\text{at } R = 1.5 \text{ or } 3 \quad \vec{U} = 0, \quad \partial T/\partial R = 0$$

The above dimensionless equations were represented with fully three-dimensional cylindrical coordinate equations and solved numerically with the HSMAC (Highly Simplified Marker and Cell) [18] scheme for a staggered mesh system which is a finite difference computational scheme and widely employed. Characteristic dimensionless parameters are as follows:

$$\mathrm{Ra} = \frac{g\beta(\theta_h - \theta_c)h^3}{\alpha\nu}, \quad \mathrm{Pr} = \frac{\nu}{\alpha}, \quad \gamma = \frac{\chi_{m0} b_a^2}{\rho_0 \mu_m g h}$$

Variables are defined in the nomenclature. The parameter γ represents the strength of the magnetizing force versus the gravitational buoyant force. The reference magnetic induction b_a is proportional to the strength of electric current in a coil. This γ was derived by Tagawa et al. [15,16] in which its derivation is shown in detail. Tagawa et al. derived this following Bai et al. [9] in general.

6 Computed results

6.1 Effect of Computational Grid Size.

Numerical computations were first carried out without applying a magnetic field, to test the effect of grid size. Yamanaka et al. [19] and Hatanaka et al. [20] suggested the effect of axial grid size in studying the Rayleigh-Benard convection, and we compared axial grid numbers between 21×21×11 (radial×circumferential×axial) and 21^3. For an aspect ratio=6, at Ra=2100, Pr=0.7 and 21×21×11 grid numbers gave the average Nu=1.198, and 21^3 gave Nu=1.142. In comparison, Silveston's data give Nu=1.2 at Ra=2100. We decided to employ 21^3 grid size in the following analyses. The transient computation was carried out with dimensionless time increments of $\Delta\tau = 3\times10^{-7} - 10^{-5}$.

6.2 Computed Results.

The accelerating force acting on air in a cylinder consists of gravity force plus magnetizing force.

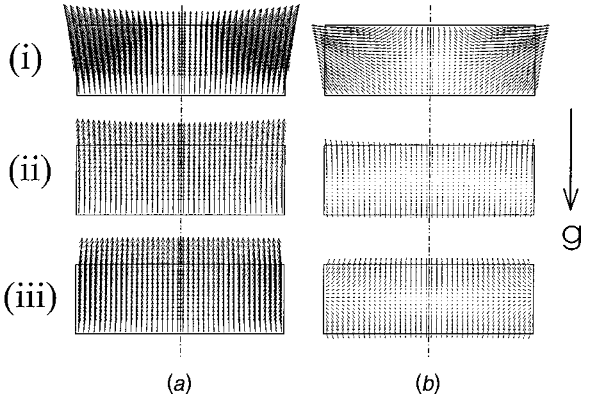

Fig. 6 Sample of the magnetizing force vectors for an enclosure 20 mm high and 60 mm in diameter in the bore of 100 mm in diameter with a coil 180 mm in diameter. (i) $z_b = -25$ mm, $\gamma = 292$ (ii) $z_b = -55$ mm, $\gamma = 350$ (iii) $z_b = -95$ mm, $\gamma = 1169$ (*a*) $\gamma\vec{\nabla} B^2$, (*b*) $\gamma\vec{\nabla} B^2 + (0,0,1)^T$

Depending on the location of the cylinder in the bore space, the net acceleration force for convection of air in the cylinder differs as shown in Fig. 6. Figure 6(*a*) shows a detailed vectorial representation of magnetizing force $\gamma\vec{\nabla} B^2$ in a cylinder at three locations below the coil. Figure 6(*b*) shows net accelerating force in addition to the gravity acceleration, $\gamma\vec{\nabla} B^2 + (0,0,1)^T$, in dimensionless representation.

Computed average Nusselt numbers for an enclosure with an aspect ratio=3 are listed in Table 2. This system corresponds to an enclosure of height $h = 20$ mm and 60 mm diameter in the bore of 100 mm in diameter with an electric wire of 180 mm in diameter. Three locations of the enclosure are −25, −55, and −95 mm from the coil center. Each value of γ was determined to cancel out the gravity force by the magnetizing force at the center of the enclosure. The average Nusselt number attains to 1.0002 at Ra=2100 and 1.001 at Ra=7000.

Figure 7 shows the computed isotherms and velocity vectors for the enclosure of aspect ratio=3, Pr=0.7, and Ra=7000. The top graph (1) shows the results without a magnetic field. Graphs (2) to (4) show the results at locations of −25, −55, and −95 mm in the bore as shown in Fig. 6. The side views in vertical cross-section are shown for (*b*) isotherms and (*c*) velocity vectors. When the enclosure is located at −55 mm as shown in (3), the net accelerating force disappears and a quasi-conduction state is attained. In (2) the convection is upward from a center due to the residual magnetizing force at the top corner, as shown for $z_b = -25$ mm in Fig. 6(*b*). On the other hand, the convection is downward from the top center due to the residual magnetizing force along the top plate, as shown in (iii) in Fig. 6(*b*).

Figure 8 shows transient responses of the average Nusselt number at Pr=0.7 and Ra=2100 for convection of air in a cylinder of aspect ratio=6 located at six different places from $z_b = 95$ to −95 mm in the bore of 100 mm in diameter as shown in Fig. 5. Mag-

Table 2 Computed average Nusselt number of natural convection at Pr=0.7 ($\gamma = 0$), and magnetizing force convection in the shallow cylinder of the aspect ratio=3. The enclosure height is 20 mm in the bore of 100 mm in diameter, with a coil 180 mm in diameter

z_b[mm]	γ	$b_z(\partial b_z/\partial z)\vert_{r=0,\,z=0.5}$ [T²/m]	Average Nusselt number	
			Ra = 2100	*Ra* = 7000
	0	0	1.069	2.074
(i) (−25)	292	−21.8	1.081	1.374
(ii) (−55)	350	−21.8	1.0002	1.001
(iii) (−95)	1169	−22.0	1.010	1.087

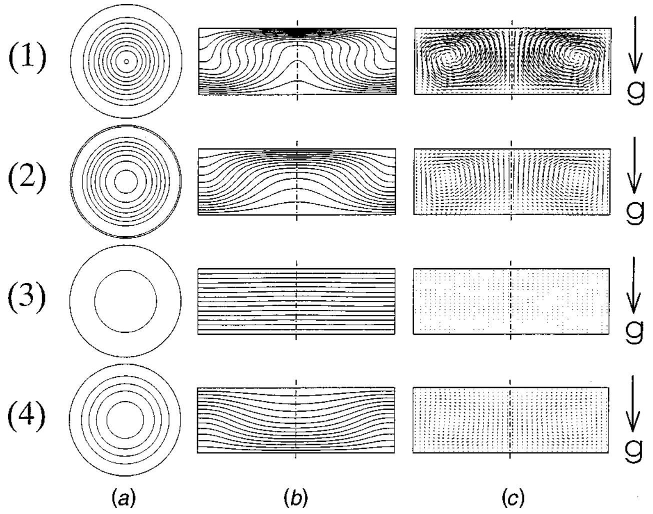

Fig. 7 Computed isotherms and velocity vectors for a cylinder of aspect ratio=3, Pr=0.7 and Ra=7000 with 21^3 grids. (1) $\gamma=0$, (2) $z_b=-25$ mm, $\gamma=292$, (3) $z_b=-55$ mm, $\gamma=350$, (4) $z_b=-95$ mm, $\gamma=1169$. (*a*) Top view of isotherms at $Z=0.5$. (*b*) Vertical side view of isotherm. (*c*) Vertical side view of velocity vectors.

nitudes of γ were chosen to give zero net acceleration at the center of the enclosure at locations $z_b=-25$, -55, and -95 mm, respectively. The same strengths were given for three upper symmetric locations. Curves (1) to (3) for $z_b=95$, 55, and 25 mm are oscillatory due to the enhanced acceleration, i.e., gravity force plus magnetizing force. Curves (4) to (6) show quick convergence almost to conduction in a cylinder located at lower levels than the magnetic coil, where net accelerating force is nearly zero. The magnitude of average Nusselt number decreased almost to unity, especially for curve (5) at $z_b=-55$ mm. The corresponding curves (not shown) at Pr=0.7 and Ra=7000 showed similar, but enhanced characteristics.

Table 3 Computed average Nusselt number in an enclosure of aspect ratio=6 at Pr=0.7 with 21^3 grids

Case no.	z_b[mm]	γ	$1+\gamma\partial B_z^2/\partial Z\,\|_{R=0,\,z=0.5}$	Nu at Ra = 2100	Nu at Ra = 7000
		0	1	1.142	2.017
(1)	95	9124	1.992	1.729	2.25
(2)	55	2815	1.995	1.825	2.56~2.64
(3)	25	2345	1.996	1.78~1.83	2.504
(4)	−25	2345	4.36×10^{-3}	1.091	1.406
(5)	−55	2815	5.22×10^{-3}	1.0001	1.0003
(6)	−95	9124	8.10×10^{-3}	1.011	1.105

Computed average Nusselt numbers for an enclosure of aspect ratio=6 are listed in Table 3. The top listed average Nusselt number at $\gamma=0$ is for natural convection only. The third column shows magnitude of dimensionless parameter γ, which represents the strength of magnetic reference value b_a, being proportional to the square of b_a. For cases no. (1) to (3), the enclosure is located in the upper part of the bore, and for (4) to (6) in the lower part. In (1) to (3), the average Nusselt number is increased, but in (4) to (6) it becomes almost unity, except in case (4) at Ra=7000. The combination of gravity force and magnetizing force can give various strengths of the net accelerating force, and thus various strengths of convection and heat transfer rate.

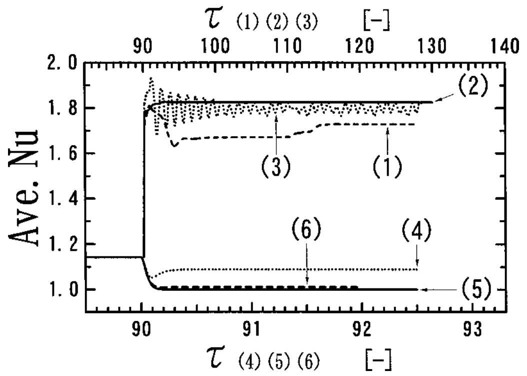

Fig. 8 Transient responses of the computed average Nusselt number for an enclosure of aspect ratio=6, Pr=0.7 and Ra=2100. Numbers (1) to (6) correspond to those in Tables 3, 4, and Fig. 9.

Figure 9 shows computed isotherms at Pr=0.7 and (*a*) Ra=2100, (*b*) Ra=7000 for the aspect ratio=6. Top view of the isotherms at $Z=0.5$ in the absence of a magnetic field is shown at the top. Convection is three-dimensional due to the shallow enclosure. Numbers (1) to (6) show side views of the isotherms located at six different levels in the bore of the super-conducting magnet as shown in Fig. 5. When the enclosure is located in the upper part of the coil, magnetizing force is added to the gravitational force to produce enhanced convection. Case no. (2) is most enhanced and not axisymmetric, but cases no. (4) to (6) are quite suppressed. These characteristics are enhanced further for Ra=7000. The result shown for case (5) indicates that an almost non-acceleration field will occur in the bore space of a superconducting magnet equivalent to non-gravity in a space.

7 Discussion

The experiments were carried out at ±66 mm from the coil center, where most of the radial component of acceleration becomes negligible. This is also the case for the computational model with a single coil, as shown in Fig. 6(ii)–(*b*) at ±55 mm.

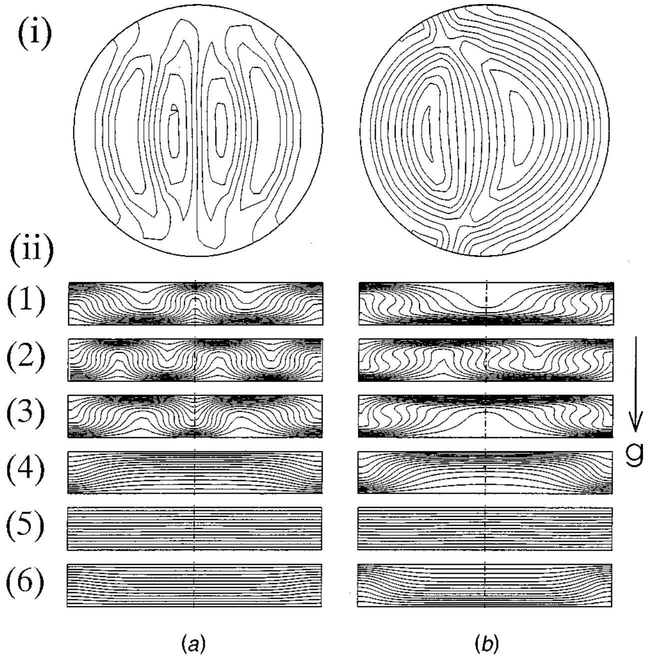

Fig. 9 Computed isotherms and velocity vectors for a cylinder of an aspect ratio=6, Pr=0.7 and (*a*) Ra=2100 and (*b*) Ra=7000. (i) Top view of isotherms at $\gamma=0$ and $Z=0.5$. (ii) Vertical side view of isotherms for cases (1) to (6). These cases correspond to those listed in Tables 3 and 4.

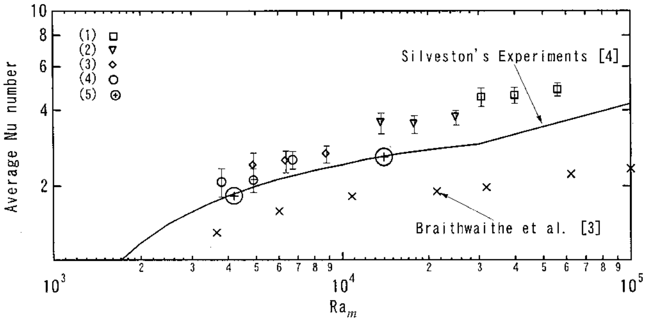

Fig. 10 Average Nusselt number plotted versus magnetic Rayleigh number Ra_m with the data by Silveston [4]. (1) Exp., $b_z(\partial b_z/\partial z)=138$ T^2/m. (2) Exp., $b_z(\partial b_z/\partial z)=49.7$ T^2/m. (3) Exp., $b_z(\partial b_z/\partial z)=5.5$ T^2/m. (4) Exp., $b_z(\partial b_z/\partial z)=0$ T^2/m. (5) Cal., Asp=6, $z_b=55$ mm, Ra=2100 and 7000, $Ra_m=4190$ and 13970.

As shown in Eq. (6), the acceleration force works by the last term of the right hand side of the equation. Thus total acceleration appears to be expressed by Ra $(\gamma\partial B_z^2/\partial Z|_{R=0,Z=0.5}+1)$ in the z-direction rather than Ra. We call this magnetic Rayleigh number, $Ra_m = Ra\,(\gamma\partial B_z^2/\partial Z|_{R=0,Z=0.5}+1)$ following Braithwaite et al.[3]. In Table 3, at $z_b=55$ mm, Nu=1.825 at $Ra_m=4190$ and 2.56–2.64 at $Ra_m=13965$. These Nu values are plotted with symbol of large cross-circles in Fig. 10 with the experimental data of Silveston and others. The agreement is almost perfect, even with the result for aspect ratio=6. Ra_m appears to give effective Rayleigh number almost exactly and should be suitable to represent the present system. This is also due to that the almost vertical vectors of magnetizing force cancel or overcome the gravity vectors as shown in Fig. 6(ii). Then, Ra_m was also computed for the experimental data in Table 1 and is shown in the last column. These data are also plotted in Fig. 10. Even with the difference in the magnetic strength, these data distribute along the data curve of Silveston for a non-magnetic field. The data by Braithwaite et al. [3] are also plotted. Their data for aqueous solution of gadolinium nitrate gave much smaller values than Silveston's. As seen in Fig. 10, both the theoretically computed Nusselt number and the experimental data for air show similar trends for the average Nusselt number versus the magnetic Rayleigh number, and we can conclude magnetic Rayleigh number closely represents the effective Rayleigh number with the magnetizing force in the present system.

Table 4 shows computed maximum velocity components and the dimensional equivalences for the enclosure of 10 mm in height and 60 mm in diameter. The dimensional magnitudes of $b_z(\partial b_z/\partial z)$ T^2/m are shown. The velocity of 1.29 cm/s without a magnetic field changes between 4.1 and 0.02 cm/s at Ra=2100, and that of 5.53 cm/s changes between 10 and 0.06 cm/s at Ra =7000. In this way, we can control the convection rate at will by changing the location and strength of magnetic induction, which is otherwise impossible under the terrestrial constant gravity field.

Table 4 Computed maximum velocity components and their dimensional equivalences for a cylinder of 10 mm in height and 60 mm in diameter. Pr=0.7, and 21^3 grids

Case no.	z_b [mm]	$b_z(\partial b_z/\partial z)\,\vert_{r=0,\,z=0.5}$ [T^2/m]	$U_{max}(u_{max}$[cm/s]) at Ra = 2100	$U_{max}(u_{max}$[cm/s]) at Ra = 7000
		0	5.88 (1.29 cm/s)	25.2 (5.53 cm/s)
(1)	95	21.8	15.65 (3.43 cm/s)	39.5 (8.66 cm/s)
(2)	55	21.9	15.75 (3.45 cm/s)	45.6~48.3 (9.99~10.6 cm/s)
(3)	25	21.9	18.3~18.8 (4.0~4.1 cm/s)	45.0 (9.85 cm/s)
(4)	−25	−21.9	4.90 (1.07 cm/s)	12.6 (2.77 cm/s)
(5)	−55	−21.9	0.08 (0.018 cm/s)	0.259 (0.057 cm/s)
(6)	−95	−21.8	1.56 (0.34 cm/s)	5.25 (1.15 cm/s)

8 Conclusion

Heat transfer rates were measured for convection of air in a vertical cylinder heated from below and cooled from above without and with an external magnetic field of a super-conducting magnet up to 3.40 Tesla. Depending on the location in the bore of a super-conducting magnet, the average Nusselt numbers were increased two fold or decreased to almost conduction state. These findings suggest that natural convection heat transfer rates can be freely controlled in the bore of a super-conducting magnet, which is otherwise difficult in a terrestrial laboratory.

Numerical computations were carried out for the natural convection of air in a shallow vertical cylindrical enclosure heated from below and cooled from above in a magnetic field. Depending on the location of the enclosure in the bore of a super-conducting magnet, the convection rate and the average heat transfer rate may be varied.

The theoretically computed average Nusselt numbers were plotted versus the magnetic Rayleigh number and found to agree with the experimental data by Silveston and others. The experimental data measured herein for air also distributed along the curve of Silveston's data versus the magnetic Rayleigh number, which appears to be an effective Rayleigh number for the magnetizing and gravity force field.

Appendix

Error Estimation in the Average Nusselt Number. The error bar in Figs. 3 and 10 were estimated as follows.
From Eq. (1),

$$Q_{\text{cond}}=\frac{\Delta\theta+0.028}{13.12}[W],\quad Q_{\text{net cond}}=\frac{\pi}{4}d^2k\,\frac{\Delta\theta}{h}$$

$$=\frac{\pi}{4}(0.045)^2(0.03)\,\frac{\Delta\theta}{0.0148}=0.00322\Delta\theta[W]$$

$$Q_{\text{loss}}=Q_{\text{cond}}-Q_{\text{net cond}}=\frac{\Delta\theta}{13.12}+\frac{0.028}{13.12}-0.00322\Delta\theta$$

$$=\frac{\Delta\theta+0.029}{13.66}=\frac{\Delta\theta+a}{b}[W]$$

$$\text{Nu}=\frac{Q_{\text{net conv}}}{Q_{\text{net cond}}}=\frac{Q_{\text{supply}}-Q_{\text{loss}}}{Q_{\text{net cond}}}=\frac{(IV)_\nu-\dfrac{\Delta\theta+a}{b}}{\dfrac{\pi}{4}d^2k\,\dfrac{\Delta\theta}{h}}$$

$$=\frac{4h}{\pi d^2k}\left\{\frac{1}{\Delta\theta}\left(IV-\frac{a}{b}\right)-\frac{1}{b}\right\}$$

The uncertainty in each variable is as follows:

- The height of the enclosure, $h+\delta h=(14.8\pm0.2)\times10^{-3}$ m
- The diameter of the enclosure, $d+\delta d=(45.0\pm0.5)\times10^{-3}$ m
- Temperature difference, $\delta\Delta\theta=\pm0.1$ K
- Temperature, $\delta\theta=\pm0.5$ K
- Thermal conductivity, $k=0.02614\times(340-\theta)/40.0+0.02900\times(\theta-300)/40.0$ W/(m·K)
- The coefficient of the Q_{loss} line, $a+\delta a=0.029\pm0.001$ K
- The coefficient of the Q_{loss} line, $b+\delta b=13.66\pm0.01$ K/W

For the data point of data (4) at Ra=3800 is given as follows:

$I_\nu=0.840434$ A, $V_\nu=1.50087$ V, $\theta_{\text{ave}}=38.81°$C, $\delta\theta=15.90$ K

$$\mathrm{Nu}_{\max}=\frac{4h_+}{\pi d_-^2 k_-}\left\{\left((IV)_\nu-\frac{a_-}{b_+}\right)\frac{1}{(\Delta\theta)_-}-\frac{1}{b_+}\right\}$$

$$=\frac{4((14.8+0.2)\times10^{-3})}{\pi((45.0-0.5)\times10^{-3})^2(0.02696)}\left\{\left(0.8404\times1.501-\frac{0.028}{13.67}\right)\frac{1}{15.8}-\frac{1}{13.67}\right\}=2.345$$

$$\mathrm{Nu}_{\min}=\frac{4h_-}{\pi d_+^2 k_+}\left\{\left((IV)_\nu-\frac{a_+}{b_-}\right)\frac{1}{(\Delta\theta)_+}-\frac{1}{b_-}\right\}$$

$$=\frac{4((14.8-0.2)\times10^{-3})}{\pi((45.0+0.5)\times10^{-3})^2(0.02703)}\left\{\left(0.8404\times1.501-\frac{0.030}{13.65}\right)\frac{1}{16.0}-\frac{1}{13.65}\right\}=1.808$$

Similar computations were carried out for other points and plotted in Figs. 3 and 10.

Nomenclature

$\vec{B}$ = $\vec{b}/b_a=(B_r,0,B_z)$, $[-]$
$\vec{b}$ = magnetic induction vector$=(b_r,0,b_z)$, $[T=\mathrm{Tesla}=\mathrm{Wb/m^2}=V\cdot\mathrm{s/m^2}]$
b_a = $\mu_m i/h$, [Tesla]
g = acceleration coefficient of gravity, [m/s^2]
Gr = $g\beta(\theta_h-\theta_c)h^3/\nu^2$, Grashof number
h = height of an enclosure, [m]
i = electric current in a coil, [A]
P = p'/p_a
p = pressure, [N/m^2]
p_0 = reference pressure without convection of gas, [N/m^2]
p' = perturbed pressure due to convection, [N/m^2]
p_a = $\rho_0(\alpha/h)^2$, [N/m^2]
Pr = ν/α, Prandtl number
Ra = Gr·Pr, Rayleigh number
Ra$_m$ = $\mathrm{Ra}(\gamma\partial B_z^2/\partial Z+1)_{R=0,Z=0.5}$, magnetic Rayleigh number at the center of an enclosure
r = radius, [m]
R = r/h
$d\vec{s}$ = coil element, [m]
$d\vec{S}$ = $d\vec{s}/h$
T = $(\theta-\theta_0)/(\theta_h-\theta_c)$
t = time, [s]
t_a = h^2/α, [s]
$\vec{U}$ = $\vec{u}/u_a$
$\vec{u}$ = velocity vector$=(u,v,w)$, [m/s]
u = radial velocity component of gas, [m/s]
u_a = α/h, [m/s]
v = circumferential velocity component of gas, [m/s]
w = z-directional velocity component of gas, [m/s]
Z = z/h
z = axial coordinate in a gravitational direction for convection in an enclosure (Fig. 4), [m]
z_b = location of an enclosure in the bore space (Fig. 5), [m]

Greek Letters

α = thermal diffusivity of gas, [m^2/s]
β = volumetric coefficient of expansion of gas due to temperature difference, [K^{-1}]
γ = $\chi_{m0}b_a^2/(g\mu_m h\rho_0)$
θ_h = hot wall temperature, [°C]
θ_c = cold wall temperature, [°C]
θ_0 = $(\theta_h+\theta_c)/2$, [°C]
μ = viscosity of gas, [Pa·s]
μ_m = magnetic permeability, [H/m]
ν = μ/ρ_0, [m^2/s]
ρ = density of gas, [kg/m^3]
ρ_0 = density of gas at θ_0, [kg/m^3]
τ = t/t_a
χ_{m0} = dimensionless magnetic susceptibility of gas

References

[1] Faraday, M., 1847, ''On the Diamagnetic Conditions of Flame and Gases,'' Philos. Mag., **31**(210), pp. 401–421.

[2] Pauling, L., Wood, R. E., and Sturdivant, J. H., 1946, ''An Instrument for Determining the Partial Pressure of Oxygen in a Gas,'' J. Am. Chem. Soc., **68**, pp. 795–798.

[3] Braithwaite, D., Beaugnon, E., and Tournier, R., 1991, ''Magnetically Controlled Convection in a Paramagnetic Fluid,'' Nature (London), **354**, pp. 134–136.

[4] Silveston, P. L., 1958, ''Wämedurchgang in waagerechten Flussigkeitsschichten,'' Part 1, Forsch, Ing. Wes., **24**, pp. 29–32 and pp. 59–69.

[5] Wakayama, N. I., 1991, ''Behavior of Flow Under Gradient Magnetic Fields,'' J. Appl. Phys., **69**(4), pp. 2734–2736.

[6] Wakayama, N. I., 1991, ''Effect of a Decreasing Magnetic Field on the Flow of Nitrogen Gas,'' Chem. Phys. Lett., **185**(5-6), pp. 449–451.

[7] Wakayama, N. I., 1993, ''Magnetic Promotion of Combustion in Diffusion Flames,'' Combust. Flame, **93**(3), pp. 207–214.

[8] Wakayama, N. I., Ito, H., Kuroda, Y., Fujita, O., and Ito, K., 1996, ''Magnetic Support of Combustion in Diffusion Flames Under Micro Gravity,'' Combust. Flame, **107**(1-2), pp. 187–192.

[9] Bai, B., Yabe, A., Qi, J., and Wakayama, N. I., 1999, ''Quantitative Analysis of Air Convection Caused by Magnetic-Fluid Coupling,'' AIAA J., **37**(12), pp. 1538–1543.

[10] Ikezoe, Y., Hirota, N., Nakagawa, J., and Kitazawa, K., 1998, ''Making Water Levitate,'' Nature (London), **393**, pp. 749–750.

[11] Ikezoe, Y., Hirota, N., Sakihama, T., Mogi, K., Uetake, H., Homma, T., Nakagawa, J., Sugawara, H., and Kitazawa, K., 1998, ''Acceleration Effect on the Rate of Dissolution of Oxygen in a Magnetic Field,'' (Japanese), Journal of Japan Institute of Applied Magnetics, **22**(4-2), pp. 821–824.

[12] Uetake, H., Nakagawa, J., Hirota, N., and Kitazawa, K., 1999, ''Nonmechanical Magnetothermal Wind Blower by a Superconducting Magnet,'' J. Appl. Phys., **85**(8), pp. 5735–5737.

[13] Nakagawa, J., Hirota, N., Kitazawa, K., and Shoda, M., 1999, ''Magnetic Field Enhancement of Water Vaporization,'' J. Appl. Phys., **86**(5), pp. 2923–2925.

[14] Ozoe, H., and Churchill, S. W., 1973, ''Hydrodynamic Stability and Natural Convection in Newtonian and Non-Newtonian Fluids Heated From Below,'' AIChE Symp. Ser., **69**(131), pp. 126–133.

[15] Tagawa, T., Shigemitsu, R., and Ozoe, H., 2002, ''Magnetizing Force Modeled and Numerically Solved for Natural Convection of Air in a Cubic Enclosure: Effect of the Direction of the Magnetic Field,'' Int. J. Heat Mass Transf., **45**, pp. 267–277.

[16] Kaneda, M., Tagawa, T., and Ozoe, H., 2002, ''Convection Induced by a Cusp-Shaped Magnetic Field for Air in a Cube Heated From Above and Cooled From Below,'' ASME J. Heat Transfer, **124**, pp. 17–25.

[17] Hellums, J. D., and Churchill, S. W., 1964, ''Simplification of the Mathematical Description of Boundary and Initial Value Problem,'' AIChE J., **10**, pp. 110–114.

[18] Hirt, C. W., Nichols, B. D., and Romero, N. C., 1975, ''A Numerical Solution Algorithm for Transient Fluid Flows,'' Los Alamos Scientific Laboratory, LA-5852.

[19] Yamanaka, Y., Kakimoto, K., Ozoe, H., and Churchill, S. W., 1998, ''Rayleigh-Benard Oscillatory Natural Convection of Liquid Gallium Heated From Below,'' Chem. Eng. J., **71**(3), pp. 201–206.

[20] Hatanaka, M., Tagawa, T., and Ozoe, H., 2000, ''Numerical Computation of Oscillatory Rayleigh-Benard Natural Convection of Gallium in a Rectangular Region With Aspect Ratios Equal to Five,'' *Proc. of Symposium on Energy Engineering in the 21st century (SEE 2000)*, Hong Kong, **1**, pp. 288–294.

The SK_N Approximation for Solving Radiative Transfer Problems in Absorbing, Emitting, and Isotropically Scattering Plane-Parallel Medium: Part 1

Zekeriya Altaç
e-mail: zaltac@ogu.edu.tr
Osmangazi University,
School of Engineering and Architecture,
Mechanical Engineering Department,
26480 Bati Meselik Eskisehir,
Turkey

A high order approximation, the SK_N method—a mnemonic for synthetic kernel—is proposed for solving radiative transfer problems in participating medium. The method relies on approximating the integral transfer kernel by a sum of exponential kernels. The radiative integral equation is then reducible to a set of coupled second-order differential equations. The method is tested for one-dimensional plane-parallel participating medium. Three quadrature sets are proposed for the method, and the convergence of the method with the proposed sets is explored. The SK_N solutions are compared with the exact, P_N, and S_N solutions. The SK_1 and SK_2 approximations using quadrature Set-2 possess the capability of solving radiative transfer problems in optically thin systems.

[DOI: 10.1115/1.1464130]

Keywords: *Emitting, Numerical Methods, Participating Media, Radiation, Scattering*

1 Introduction

Solving the radiative transfer problems in a participating medium requires the solution of either the radiative transfer equation (RTE) for intensity or the integral transfer equation for incident radiation and the heat fluxes. A number of numerical methods have been developed for solving either equation; however, each method has its own advantages and disadvantages.

The spherical harmonics, or P_N, approximation expands the angular dependence of the radiation intensity in terms of the spherical harmonics of the angular variables. A series of coupled differential equations that represent the space expansion coefficients must be solved. The drawback of this method is that low-order approximations are usually accurate in optically thick medium, for higher order approximations while mathematical complexity increase extremely rapidly, accuracy improves only slightly [1]. As a result of these complexities, very few multi-dimensional problems have been solved with the P_3 approximation, none with higher orders.

Increasingly, the discrete ordinates method (DOM) has become the dominant means for obtaining numerical solutions, especially in neutron transport, and, in the last decade, in radiative transfer. This method divides the global angular distribution of the radiation intensity into a specific number, *N*, of discrete directions. The transfer equation then becomes a system of *N* coupled linear equations with the angular intensity in these directions as variables. In the literature, high order DOM solutions in multi-dimensional geometries, are not encountered for thermal transfer analysis. Even in multi-dimensional neutron transport problems where high order discrete ordinates approaches are often used, the method exhibits so called the "ray effect," which is non-physical oscillations of intensity around the correct value [2]. In recent years, considerable effort has been expanded in deriving methods that eliminate or strongly mitigate the ray effect distortions that plague the discrete or discrete ordinates-like methods [2].

Radiative integral transfer equation (RITE) solutions completely eliminate the angular dependence of the incident radiation by integrating the radiative transfer equation over all solid angles. Because the angular variable is completely removed, the integral method is dimensionally simpler than the previously mentioned methods. On the other hand, the solution of this equation leads to dense matrices in multi-dimensional geometries which result in severe limitations on the number of grid points that can be treated without incurring prohibitive requirements for the computational memory and execution time.

The methods mentioned are being successfully used for solving complex engineering problems, including those involving convective heat transfer. However, there is still a need to solve the radiative transfer problems, especially in multi-dimensional geometries, in a much simpler fashion with reasonable accuracy at low cost. The Synthetic Kernel (SK_N) method deals with the integral equation and involves an exponential approximation to the transfer kernel. Then, the integral equation is reducible to a set of coupled second order differential equations for which proper boundary conditions can be derived. The method was proposed for solving integral neutron transport equation [3], and it was later successfully developed and applied to homogeneous, inhomogeneous, one- and multi-group constant source as well as eigenvalue problems in one- and two-dimensional optically thin systems [4–6]. The results agree well with the numerical solution of the integral equation. The method was also applied to an absorbing, emitting and isotropically scattering rectangular geometry, and the general SK_N equations for multi-dimensional complex geometries were given [7]. In the study, solutions with the SK_N method using Gauss quadrature set, along with, two types of boundary conditions that could be applied in rectangular geometries were discussed. The results for the radiative intensity and incident radia-

---

Contributed by the Heat Transfer Division for publication in the JOURNAL OF HEAT TRANSFER. Manuscript received by the Heat Transfer Division March 15, 2000; revision received October 9, 2001. Associate Editor: C. T. Avedisian.

tion were obtained with greater accuracy than the net radiative heat flux. In optically very thin systems, the reported relative errors for the intensity and incident energy solutions were on the order of 1–3 percent.

It should be noted that similar methods that rely on expanding real kernels into sums of exponential kernels have often been proposed and tried in the lowest orders. A method called exponential kernel approximation [1,8] was applied by Buckley [9] and Perlmutter and Siegel [10] to problems of radiative heat exchange inside cavity. Krook [11] describes a method which is the heart of the SK_N approximation. It was he who first proposed an approximation to exponential integral functions by finite sums of exponentials in plane parallel geometry. However, he did not extend his analysis to other geometries.

A method called the A_N approximation was developed by Coppa and Ravetto [12] and its theory was further investigated by Coppa et al. [13]. For systems of constant mean-free-path (mfp), the SK_N analysis is formally the same as theirs. They extended their analysis to one-dimensional cylinder and sphere and also investigated the Fourier transform of the Boltzmann equation for homogeneous systems leading to integro-differential equation in angle and transformed space. From this, they were able to show that many approximations are equivalent to the approximations of angular integrals by summation formulas, and that the choice of Gaussian summation parameters over the whole range of angles led to the P_N equations.

In this paper, the SK_N method has been not only applied to radiative transfer in plane parallel participating medium but also the additional two quadrature sets are developed and their convergence are compared with exact, and high order DOM and spherical harmonics solutions.

2 Analysis

A plane-parallel, absorbing, emitting, inhomogeneous, isotropically scattering medium at dimensionless temperature $\theta(\tau)$ with optical path τ_0 is considered. The walls are assumed to be opaque, diffusive reflectors and diffuse emitters and to have emissivities ε_1, ε_2 and reflectivities ρ_1, ρ_2. The emission of radiation from walls due to their temperatures are $\varepsilon_i \theta_i^4$, $(i=1 \text{ or } 2)$ where θ_i is the dimensionless temperature of wall i. The inhomogeneous property of the medium is due to assuming space dependent scattering albedo $\Omega_0(\tau)$.

The RTE for intensity is formally solved for outgoing and incoming intensities, $I^+(\tau,\mu)$ and $I^-(\tau,\mu)$, as described in Ref. [8]. The solution is straightforward, and therefore, the details of derivation of the integral equation are omitted. In the dimensionless radiative transfer equation, the dimensionless isotropic source term, $S(\tau)$, takes the form [8]

$$S(\tau)=[1-\Omega_0(\tau)]\theta^4(\tau)+\frac{1}{4\pi}\Omega_0(\tau)G(\tau) \tag{1}$$

where $G(\tau)$ is the dimensionless incident radiation obtained by integrating the monochromatic radiation intensity over the solid angle:

$$G(\tau)=2\pi\int_{-1}^{1} I(\tau,\mu')d\mu', \tag{2}$$

where $I(\tau,\mu)$ is the dimensionless radiation intensity, and μ is the angular cosine.

The dimensionless boundary conditions are written as

$$I^+(0)=\varepsilon_1\theta_1^4+2\rho_1\left\{I^-(\tau_0)E_3(\tau_0)+\int_0^{\tau_0} S(\tau')E_2(\tau')d\tau'\right\} \tag{3}$$

and

$$I^-(\tau_0)=\varepsilon_2\theta_2^4+2\rho_2\left\{I^+(0)E_3(\tau_0)+\int_0^{\tau_0} S(\tau')E_2(\tau_0-\tau')d\tau'\right\} \tag{4}$$

where $E_2(x)$ and $E_3(x)$ are the second and third order exponential integral functions [14].

Equations (3) and (4) pose two simultaneous equations and two unknowns to be solved for the wall intensities. Defining the following quantities

$$\alpha_1=\varepsilon_1\theta_1^4+2\rho_1\int_0^{\tau_0} S(\tau')E_2(\tau')d\tau' \tag{5}$$

and

$$\alpha_2=\varepsilon_2\theta_2^4+2\rho_2\int_0^{\tau_0} S(\tau')E_2(\tau_0-\tau')d\tau' \tag{6}$$

the dimensionless isotropic surface intensities are found to be

$$I^+(0)=\frac{\alpha_1+2\rho_1E_3(\tau_0)\alpha_2}{1-4\rho_1\rho_2E_3^2(\tau_0)} \tag{7}$$

and

$$I^-(\tau_0)=\frac{\alpha_2+2\rho_2E_3(\tau_0)\alpha_1}{1-4\rho_1\rho_2E_3^2(\tau_0)} \tag{8}$$

Then, the integral equation for the incident radiation is simply

$$G(\tau)=2\pi\left\{I^+(0)E_2(\tau)+I^-(\tau_0)E_2(\tau_0-\tau)\right.$$
$$\left.+\int_0^{\tau_0} S(\tau')E_1(|\tau-\tau'|)d\tau'\right\} \tag{9}$$

The net heat flux is defined as

$$q(\tau)=2\pi\int_{\mu=-1}^{1} \mu I(\tau,\mu)d\mu=q^+(\tau)-q^-(\tau) \tag{10}$$

where $q^+(\tau)$ and $q^-(\tau)$ are the incoming and outgoing radiative heat fluxes which can be written as

$$q^+(\tau)=2\pi\int_{\mu=0}^{1}\mu I(\tau,\mu)d\mu$$
$$=2\pi\left\{I^+(0)E_3(\tau)+\int_0^{\tau} S(\tau')E_2(\tau-\tau')d\tau'\right\} \tag{11}$$

and

$$q^-(\tau)=2\pi\int_{\mu=0}^{1}\mu I(\tau,-\mu)d\mu$$
$$=2\pi\left\{I^-(\tau_0)E_3(\tau_0-\tau)+\int_{\tau}^{\tau_0} S(\tau')E_2(\tau'-\tau)d\tau'\right\} \tag{12}$$

Equation (9) is a Fredholm integral equation of the second kind. Various techniques can be applied to solve Eq. (9) that gives the exact solution for the present problem. The heat fluxes can be calculated from Eqs. (10), (11), and (12).

3 The Derivation of the SK_N Equations

The first order exponential integral function $E_1(x)$ in Eq. (9) is replaced with the following approximation obtained by its Gauss quadrature integration:

$$E_1(x)=\int_0^1\frac{1}{\mu}e^{-x/\mu}d\mu \doteq \sum_{n=1}^{N}\frac{w_n}{\mu_n}e^{-x/\mu_n} \tag{13}$$

where w_n and μ_n's are quadrature weights and abscissas. These quadratures which are for various N values tabulated in Ref. [14] is referred to as Set-1 throughout this paper. The selection of the quadrature sets is discussed in section 4. Equation (9), then, takes the form

$$G(\tau)=f(\tau)+\int_0^{\tau_0}2\pi S(\tau')\sum_{n=1}^{N}\frac{w_n}{\mu_n}\exp\left(-\frac{|\tau-\tau'|}{\mu_n}\right)d\tau' \tag{14}$$

where

$$f(\tau)=2\pi\{I^+(0)E_2(\tau)+I^-(\tau_0)E_2(\tau_0-\tau)\} \tag{15}$$

Upon defining

$$G_n(\tau)=\frac{2\pi}{\mu_n}\int_0^{\tau_0}S(\tau')\exp\left(-\frac{|\tau-\tau'|}{\mu_n}\right)d\tau' \tag{16}$$

Eq. (14) can now be written as

$$G(\tau)=f(\tau)+\sum_{n=1}^{N}w_nG_n(\tau) \tag{17}$$

If we differentiate Eq. (16) twice with respect to τ, we get

$$-\mu_n^2\frac{d^2G_n(\tau)}{d\tau^2}+G_n(\tau)=4\pi S(\tau) \tag{18}$$

By making use of Eqs. (1) and Eq. (17) in Eq. (18), the following set of second order differential equations—the SK_N equations—are obtained

$$-\mu_n^2\frac{d^2G_n(\tau)}{d\tau^2}+[1-\Omega_0(\tau)w_n]G_n(\tau)=4\pi[1-\Omega_0(\tau)]\theta^4(\tau)+\Omega_0(\tau)\left\{f(\tau)+\sum_{\substack{m=1\\m\neq n}}^{N}w_mG_m(\tau)\right\}, \tag{19}$$

for $n=1,2,\ldots,N$.

The boundary conditions are given as

$$\frac{dG_n(0)}{d\tau}-\frac{G_n(0)}{\mu_n}=0 \tag{20}$$

and

$$\frac{dG_n(\tau_0)}{d\tau}+\frac{G_n(\tau_0)}{\mu_n}=0 \tag{21}$$

which are obtained by inspecting $G_n(\tau)$ and $dG_n(\tau)/d\tau$ at $\tau=0$ and $\tau=\tau_0$. These boundary conditions are mathematical boundary conditions in nature, and they are used regardless of the physical wall conditions. In the case of physical symmetry, $dG_n(\tau)/d\tau=0$ condition can be imposed.

The net heat flux can also be formulated by substituting an approximation for $E_2(x)$, which is obtained in a similar fashion as in Eq. (13).

$$E_2(x)\doteq\sum_{n=1}^{N}w_ne^{-x/\mu_n} \tag{22}$$

Substituting of Eqs. (11) and (12) into Eq. (10), applying the approximation from Eq. (22), and using $dG_n(\tau)/d\tau$ to simplify the integrals under the summation, the net radiative heat flux can be written as

$$q(\tau)=2\pi\{I^+(0)E_3(\tau)-I^-(\tau_0)E_3(\tau_0-\tau)\}-\sum_{n=1}^{N}w_n\mu_n^2\frac{dG_n(\tau)}{d\tau} \tag{23}$$

The outgoing and incoming radiation heat fluxes are computed from Eqs. (11) and (12) after the solution for the source term is obtained.

4 The Choice of Quadrature Sets

The choice of quadrature sets is open to debate since there are many ways to obtain such approximations. In this study, three quadrature sets are proposed, and their accuracy with respect to each other and the order of SK_N approximation is explored.

The first choice of the quadrature set, Set-1, is the N-point Gauss-Legendre quadratures in half interval [14]. Gauss-Legendre quadratures, which is applied for any arbitrary interval, yields the exact integral of any function which can be described by a polynomial of degree $(2N-1)$. Thus, using Set-1, as in Eq. (13), corresponds to the numerical integration $E_1(x)$; and in this study, it is used for any system regardless of its optical thickness.

To obtain Set-2, we start with the proposed exponential sum to $E_1(x)$. The moments of this approximation, $M_k(\tau_0)$, are evaluated for the real and the approximate exponential integral functions, and the first $2N$ moments are matched. This procedure leads to a nonlinear system of equations which is solved for the $2N$ unknowns. The moments are written as

$$M_k(\tau_0)=\int_0^{\tau_0}x^kE_1(x)dx=\sum_{n=1}^{N}\frac{w_n}{\mu_n}\int_0^{\tau_0}x^ke^{-x/\mu_n}dx,\quad \text{for } k=0,1,2,\ldots,(2N-1) \tag{24}$$

where τ_0 is the optical length in mfp. The solution of the nonlinear system of equations given with Eq. (24), in optically thick limit case $(\tau_0\to\infty)$ yields quadrature Set-1.

The sum of quadrature weights of Set-2 is less than unity for decreasing optical path. Another quadrature set, Set-3, was generated by imposing a condition that preserved the sum of the weights as unity. In the latter case, only the moments $k=0,1,2,\ldots,(2N-2)$ are considered, and the $2N$th condition is forced to be $\Sigma_nw_n=1$. The resulting set of nonlinear system of equations for both cases was solved to generate Set-2 and Set-3. A sample of quadrature sets for various optical thicknesses, used in this study, are provided in Table 1.

5 Results and Discussion

5.1 Benchmark Problems. Three benchmark problems have been set for testing of the SK_N method.

Benchmark Problem 1. The problem of radiative transfer in a plane-parallel slab with a constant scattering albedo and transparent boundaries, which has been solved by Çengel et al. [15], is considered. The only source in the medium is due to the externally isotropic unit incidence of radiation at the boundary $\tau=0$. In the present formulation, this boundary condition is achieved by setting $\varepsilon_1=\theta_1=1$, and $\varepsilon_2=\theta_2=\rho_1=\rho_2=0$ in Eqs. (3) and (4), yielding $I^+(0)=1$ and $I^-(\tau_0)=0$. The hemispherical reflectivity and transmissivity for slabs of various optical thicknesses ranging from $\tau_0=0.1$ to $\tau_0=10$ are determined for scattering albedos from $\Omega_0=0.2$ to $\Omega_0=0.995$.

The reflectivity and transmissivity are defined as

$$R=\frac{q^-(0)}{q^+(0)} \tag{25}$$

and

$$\Gamma=\frac{q^+(\tau_0)}{q^+(0)} \tag{26}$$

This benchmark problem was also solved with the P_N and the S_N approximations. The convergence of the results is compared with respect to the exact solutions.

Table 1 Quadrature Set-2 and 3 for various optical thicknesses

N	SET-2									
	$\tau_0=0.1$		$\tau_0=0.5$		$\tau_0=1$		$\tau_0=2$		$\tau_0=5$	
	μ_n	w_n	μ_n	w_n	μ_n	w_n	μ_n	w_n	μ_n	w_n
1	0.093831	0.423254	0.246967	0.775802	0.339450	0.898735	0.429341	0.971680	0.494833	0.999096
2	0.009727	0.028490	0.041573	0.115744	0.072553	0.194779	0.117233	0.300925	0.183475	0.444434
	0.162172	0.540949	0.388033	0.769834	0.511856	0.765194	0.631349	0.690612	0.750389	0.555279
3	0.003242	0.008585	0.013640	0.036015	0.025243	0.065974	0.044292	0.114084	0.080620	0.202675
	0.023066	0.041128	0.090479	0.144207	0.155567	0.224950	0.248212	0.314988	0.393525	0.407357
	0.217857	0.620171	0.468392	0.752458	0.596718	0.690097	0.713484	0.567920	0.828230	0.389904
	SET-3									
1	0.307715	1.000000	0.446874	1.000000	0.524329	1.000000	0.609291	1.000000	0.723454	1.000000
2	0.020747	0.065848	0.073617	0.203949	0.116247	0.300989	0.169657	0.412471	0.238769	0.548803
	0.388207	0.934152	0.560856	0.796051	0.645376	0.699011	0.727073	0.587529	0.817602	0.451197
3	0.004820	0.013139	0.020738	0.054922	0.036627	0.095156	0.060650	0.154060	0.101263	0.249966
	0.041770	0.088868	0.141826	0.230516	0.220205	0.306328	0.319112	0.372796	0.458308	0.427112
	0.437310	0.897994	0.622051	0.714562	0.706147	0.598516	0.783340	0.473145	0.863735	0.322922

Benchmark Problem 2. Four cases with various isotropically scattering, homogeneous participating medium at constant temperature and wall properties are considered:

Case 1, $\tau_0=1$, $\Omega_0=0.5$, $\theta=0$, $\theta_1=1$, $\varepsilon_1=0.5$, $\rho_1=0.5$, $\theta_2=0.5$, $\varepsilon_2=0.2$, $\rho_2=0.8$;
Case 2, $\tau_0=0.1$, $\Omega_0=0.9$, $\theta=0$, $\theta_1=1$, $\varepsilon_1=0.1$, $\rho_1=0.9$, $\theta_2=2$, $\varepsilon_2=0.9$, $\rho_2=0.1$;
Case 3, $\tau_0=0.5$, $\Omega_0=0.75$, $\theta=1$, $\theta_1=2$, $\varepsilon_1=1$, $\rho_1=0$, $\theta_2=1$, $\varepsilon_2=0$, $\rho_2=1$;
Case 4, $\tau_0=5$, $\Omega_0=0.95$, $\theta=0$, $\theta_1=1$, $\varepsilon_1=0.4$, $\rho_1=0.6$, $\theta_2=1$, $\varepsilon_2=0.6$, $\rho_2=0.4$.

Benchmark Problem 3. A plane-parallel slab geometry with space-dependent scattering albedo which was solved by Clements et al. [16], for linear and quadratic variations, is considered. Two additional albedo variations, exponential and cosine growing/damped oscillations, are introduced mainly to severely test the approximation and its effects with respect to spatially varying source term not only in the medium but also near the walls. To achieve this purpose, two alternatives for each albedo variations of linear, quadratic, exponential and cosine oscillations are considered featuring (1) albedo increasing from wall 1 to wall 2 and (2) albedo decreasing from wall 1 to wall 2. Boundary conditions are the same as those of presented in benchmark problem 1. The system has a constant optical path $\tau_0=1$, and the average value $\Omega_0(\tau)$ over the medium is equal to 0.5 in all cases.

5.2 Calculation of the Numerical Errors. There are mainly two reasons for selecting the computed the reflectivity and transmissivity for comparisons: (1) since they involve the incoming and outgoing heat fluxes of boundaries, they are a good indication of how well the boundary conditions are satisfied, (2) they are presented in terms of ratios, and any error in these parameters is strongly felt. To make the comparisons a severe one, relative per cent of a parameter p, denoting R or Γ, is computed as follows:

$$\text{Relative Error}=\left(\frac{p_{\text{exact}}-p_{\text{approx}}}{p_{\text{exact}}}\right)\times 100 \qquad (27)$$

This error representation results in a large value when the parameter p is very small, but accurate in 2–3 decimal places. The term "error" throughout this paper will be used to imply the relative per cent error computed by Eq. (27).

5.3 Numerical Solution Techniques. The optical distance is equally divided into 200 grid elements for all the methods in this study, allowing the same second order truncation errors in the finite difference representation of P_N, S_N, and SK_N equations. The integral equation, Eq. (9), is solved using "subtraction of singularity" technique [17]. In order to minimize the error in the numerical integration, Simpson's rule, which has a fourth order truncation error, is used for approximating the integrals. The resulting system of linear equations was solved using double precision LINPACK subroutines [18]. When the walls are black, the wall intensities are independent of the source term, the solution of Eq. (9) is obtained in a single step. However, when the walls are gray, the computation of the wall intensities requires the solution of incident energy which necessitates an iterative algorithm. In the algorithm used, first an initial estimate is made for the incident energy to compute the source term and intensities at the boundaries from Eqs. (1), (7), and (8). Then, using these wall intensities, Eq. (9) is solved. The source term is updated before computing the wall intensities to resolve Eq. (9). This procedure is repeated until the maximum relative error between two consecutive incident energy meets the convergence criterion $\xi<10^{-6}$. The procedure converges usually with less than 10 iterations for absorbing medium; however, in scattering medium convergence is rather slow—15 to 20 iterations.

The P_N equations were solved upon employing Marshak boundary condition [8]. When solving the P_N equations, the odd moments were eliminated, resulting in $(N+1)/2$ second order differential equations for the even moments. Then the finite difference equations, using second order discretization, were cast in block tridiagonal form, and direct solution of the difference equations using the Thomas algorithm [19] was applied.

In the S_N approximation, the numerical solution is achieved by using the standard diamond difference scheme with N-point Gauss quadratures in the whole range [2]. The resulting difference equations are iterated until the convergence criterion of $\xi<10^{-6}$ is met.

The SK_N equations were also solved using a second order finite-difference scheme. The numerical solution procedure is simple and straightforward, depending upon the nature of the problem, the solution algorithm is an iterative or a direct one that exploits block tridiagonal solution of the resulting system of linear equations. When the walls are black, finite-difference form of the

Table 2 Comparisons of grid sensitivity and computational time (CPU seconds) for Case 1

	Number of grids used									
	50		100		200		400		800	
Methods	Γ	CPU (sec)	Γ	CPU (sec)	Γ	CPU (sec)	Γ	CPU (sec)	Γ	CPU (sec)
Exact	0.346935	0.11	0.346923	0.37	0.346920	1.89	0.346920	17.26	0.346919	125.6
S_{128}	0.346869	0.42	0.346909	0.93	0.346913	2.24	0.346914	6.59	0.346914	13.98
P_{11}	0.347036	0.02	0.346965	0.03	0.346946	0.05	0.346942	0.11	0.346940	0.18
SK_1	0.346897	0.02	0.346874	0.03	0.346868	0.07	0.346866	0.11	0.346866	0.22
SK_2	0.346950	0.03	0.346927	0.06	0.346921	0.11	0.346919	0.22	0.346919	0.45
SK_3	0.346951	0.05	0.346928	0.09	0.346921	0.17	0.346919	0.35	0.346919	0.68
SK_4	0.346950	0.07	0.346927	0.12	0.346921	0.22	0.346919	0.46	0.346919	0.91
SK_5	0.346949	0.09	0.346927	0.15	0.346921	0.28	0.346919	0.58	0.346919	1.15

SK_N equations can be cast into block tridiagonal form just as in P_N method; otherwise, an iterative algorithm is applied. The algorithm used is basically the same as described for the RITE, but Eq. (19) is solved to obtain incident energy instead of Eq. (9).

5.4 Memory Requirement and Computational Time. If we let NG be the number of grids used and N be the order of an approximation, then the basic computational memory requirement for storage of the resulting system of algebraic equations are $NG\times(NG+1)$ for the RITE and $2\times N\times NG$ for S_N. If P_N equations are solved as a second order coupled differential equations, the memory requirement is $(N+1)\times(N+1)\times(2\times NG-1)/2$ for block tridiagonal system of equations or $(N+1)\times(2\times NG-1)$ for an iterative algorithm combined with the solution of tridiagonal system of equations for even moments. Basically the second order P_N equations for planar geometry and the SK_N equations have similar forms; thus the same memory requirements apply for both methods.

This study was carried out on a Pentium III 667 MHz processor with 128 Mb RAM. Several cases of grids ranging from 50 to 800 are considered to ensure grid independence of the presented solutions. In Table 2, a comparison of the computed transmissivity and computational times (cpu) obtained using the exact, P_{11}, S_{128} and SK_N (with Set-2) approximations up to the fifth order is given for Case 1 of benchmark problem 2. A comparison for the indicated grid configurations yields relative errors less than 0.002 percent with 200 grids for all approximations. The exact solution even for the smallest grid configuration, 50, is accurate at least in four decimal places as a result of the use of Simpson's integration rule.

For the number of grids of 100 to 800, cpu times of the exact solution are 0.37, 1.89, 17.26, and 125.6 seconds, respectively. Similarly, the cpu times for S_{128} are 0.93, 2.24, 6.59, and 13.98, while for the P_{11} these values result in 0.03, 0.05, 0.11, and 0.18 seconds, for 100 to 800 grids, respectively. These comparatively small cpu times of P_{11} are as a result of the direct solution of $6\times6\times NG$ block tridiagonal system of equations; however, this simplicity of the P_N equations and numerical treatment in planar geometry is difficult to extend to multi-dimensional geometries.

The cpu times of the SK_N approximation with other quadrature sets is the same since only the quadrature coefficients are replaced. The cpu times for 200 grids are 0.07, 0.11, 0.17, 0.22, and 0.28 sec while these figures for 800 grids are 0.22, 0.45, 0.68, 0.91, and 1.15 sec, for increasing orders of the SK_N approximation, respectively. A comparison of the cpu times with those of the other methods for 800 grids, which may be considered as a more realistic case in multi-dimensional problems, shows that the SK_2 and SK_3 approximations converge the exact solution in 0.22 and 0.45 sec. On the other hand, the cpu time with SK_5 approximation is 1.15 sec, making even higher order SK_N approximations cpu time-wise superior to S_{128} with 13.98 seconds and the exact method with 126.6 seconds.

5.5 The Spherical Harmonics and the Discrete Ordinates Solutions in Homogeneous Medium. Benchmark problem 1 was solved using RITE, and compared with the solutions of Ref. [15], the integral equation solutions were 5–6 decimal places in agreement with those reported. In addition to their solutions for albedos of 0.2, 0.8, and 0.995, exact solutions of $\Omega_0=0.5$ were added to the comparison set.

Benchmark problem 1 was also solved using the P_3, P_5, P_7, P_9, and P_{11} spherical harmonics, and the S_{12}, S_{24}, S_{64}, and S_{128} approximations. The results were truncated to five decimal places based on the error calculations. The relative errors for the transmissivity and reflectivity are tabulated in Table 3. As expected, both methods converge towards the exact solution as the order of approximations are increased, the largest errors being in absorbing medium ($\Omega_0<0.5$). As the medium becomes strongly scattering ($\Omega_0>0.5$), both approximations yield smaller errors. However, the convergence of optically very thin systems (0.1–0.5 mfp) is slower than moderately thin systems (1–2 mfps) with both methods. For optically thick systems, such as 10 mfp, convergence to the exact solutions in the order of 1 percent is reached at relatively low orders—S_{24} and P_9. The S_{64} and S_{128} solutions converge to the exact solutions for incident radiation and heat flux in 3–4 decimal places, and the errors are below 0.5 percent and 0.1 percent, respectively, with highest errors at $\tau_0=0.1$. On the other hand, convergence of the P_N approximation to the exact solution with increasing order is rather slow compared to that of the DOM. With P_3 approximation, errors of up to 60 percent for $\tau_0=0.1$ and absorbing medium are encountered; similarly for $\tau_0=10$ and absorbing medium, the errors of the reflectivities are in the range of 10–30 percent. These large errors are partly due to the exact values being very small combined with the definition of error by Eq. (27) yielding very high values. In these cases, where the errors were very large, the convergence was achieved in 2–3 decimal places. For P_{11} solutions, the errors are reduced to by at least 1/6th of those of P_3 for optically thin systems. When solutions for $\tau_0=0.1$ and absorbing medium are examined, the errors in the reflectivity are higher than those of transmissivity. To reach the accuracy levels of S_{128} for optically very thin systems, the P_N approximations of orders above 20 are needed.

5.6 The SK_N Approximation Solutions in Homogeneous Medium. The errors using the SK_N approximation of orders up

Table 3 Comparison of P_N and S_N with the exact solutions of the benchmark problem 1

Method	Ω_0	$\tau_0=0.1$		$\tau_0=0.5$		$\tau_0=1$		$\tau_0=2$		$\tau_0=5$		$\tau_0=10$	
		R	Γ	R	Γ	R	Γ	R	Γ	R	Γ	R	Γ
Exact	0.200	0.01460	0.84696	0.03715	0.47432	0.04394	0.24627	0.04608	0.07274	0.04628	0.00245	0.04635	0.00001
	0.500	0.03843	0.87044	0.10768	0.53499	0.13417	0.30671	0.14509	0.10706	0.14659	0.00529	0.14675	0.00004
	0.800	0.06493	0.89657	0.20562	0.62197	0.28015	0.41625	0.32796	0.19727	0.34176	0.02292	0.34218	0.00065
	0.995	0.08379	0.91521	0.29324	0.70178	0.44124	0.54884	0.59881	0.38155	0.76369	0.18923	0.82879	0.08667
S_{12}	0.200	-4.25[§]	0.34	-2.10	0.54	-1.62	0.42	-1.52	0.47	-1.51	0.41	-1.34	0
	0.500	-3.49	0.25	-1.72	0.43	-1.27	0.36	-1.17	0.39	-1.13	0.38	-1.02	-1.25
	0.800	-2.63	0.19	-1.27	0.36	-0.86	0.34	-0.71	0.35	-0.66	0.48	-0.58	-1.31
	0.995	-2.06	0.19	-0.90	0.37	-0.51	0.24	-0.29	-0.45	-0.11	-0.58	0.03	-1.23
S_{24}	0.200	-1.71	0.14	-0.57	0.11	-0.46	0.12	-0.41	0.12	-0.39	0.41	-0.24	0
	0.500	-1.43	0.11	-0.45	0.09	-0.35	0.10	-0.32	0.10	-0.29	0	-0.18	-0.05
	0.800	-1.11	0.08	-0.33	0.09	-0.23	0.09	-0.19	0.11	-0.17	-0.04	-0.10	-0.37
	0.995	-0.91	0.08	-0.24	0.10	-0.13	0.11	0.07	-1.19	0.02	-0.25	0.10	-0.87
S_{64}	0.200	-0.27	0.02	-0.08	0.02	-0.07	0.02	-0.04	0.01	-0.04	0	0.11	0
	0.500	-0.21	0.01	-0.07	0.01	-0.05	0.01	-0.05	0.02	-0.02	0	0.09	0
	0.800	-0.15	0.01	-0.05	0.01	-0.10	0.04	-0.02	0.02	0..01	0.13	0.08	0.05
	0.995	-0.14	0.01	-0.03	-0.01	-0.01	0	0.17	0.03	0.01	0.14	0.12	0.81
S_{128}	0.200	-0.07	0	-0.03	0	-0.01	0.01	0	0	-0.01	0	0.03	0
	0.500	-0.05	0	-0.01	0	-0.01	0	-0.01	0.01	-0.02	0	0.02	0
	0.800	-0.06	0	-0.01	0	-0.02	0.01	-0.01	0	0.01	0.02	0.06	0
	0.995	-0.04	0	-0.01	0	0	0	0.02	0.01	0.01	0.02	0.06	0.09
P_3	0.200	59.59	-0.32	40.92	1.56	35.48	2.18	34.29	-1.17	33.56	-4.90	31.26	0
	0.500	18.42	-0.53	9.31	0.37	7.54	0.98	7.25	-0.35	7.10	-3.02	6.70	0
	0.800	9.44	-0.63	2.79	-0.47	1.60	-0.13	1.37	-0.30	1.32	-1.00	1.29	-0.74
	0.995	7.11	-0.65	1.61	-0.67	0.53	-0.43	0.19	-0.29	0.06	-0.20	0.07	-0.14
P_5	0.200	34.45	-0.10	18.55	0.65	16.20	0.06	15.54	-0.82	14.67	0.82	12.08	0
	0.500	10.12	-0.24	3.99	0.20	3.41	-0.03	3.20	-0.53	3.04	0	2.62	0
	0.800	4.96	-0.32	1.02	-0.14	0.71	-0.16	0.61	-0.31	0.56	-0.26	0.55	-0.42
	0.995	3.70	-0.34	0.50	-0.21	0.19	-0.16	0.09	-0.14	0.03	-0.08	0.05	-0.06
P_7	0.200	22.26	-0.01	10.58	0.23	9.33	-0.21	8.79	-0.19	7.89	0	5.11	0
	0.500	6.25	-0.12	2.26	0.05	1.97	-0.17	1.79	-0.20	1.63	0	1.19	0
	0.800	2.93	-0.19	0.55	-0.08	0.43	-0.15	0.34	-0.17	0.30	-0.17	0.29	-0.14
	0.995	2.15	-0.20	0.24	-0.10	0.12	-0.10	0.05	-0.08	0.02	-0.05	0.05	-0.03
P_9	0.200	15.34	0.02	6.92	0.05	6.05	-0.16	5.62	-0.04	4.67	0	1.77	0
	0.500	4.14	-0.06	1.50	-0.02	1.28	-0.14	1.13	-0.08	0.98	0	0.51	0
	0.800	1.85	-0.11	0.38	-0.07	0.29	-0.11	0.21	-0.10	0.19	-0.09	0.18	-0.09
	0.995	1.35	-0.12	0.16	-0.07	0.09	-0.07	0.03	-0.05	0.02	-0.03	0.05	-0.02
P_{11}	0.200	11.2	0.03	4.90	-0.02	4.21	-0.09	3.86	-0.01	2.90	0	-0.09	0
	0.500	2.89	-0.03	1.09	-0.05	0.89	-0.09	0.78	-0.05	0.62	0	0.14	0
	0.800	1.23	-0.07	0.29	-0.06	0.20	-0.08	0.15	-0.07	0.13	-0.09	0.11	-0.02
	0.995	0.88	-0.08	0.13	-0.05	0.06	-0.05	0.02	-0.03	0.02	-0.02	0.05	-0.01

[§] Relative percent errors computed with Eq. (27) are truncated two decimal places.

to 3 with the three quadrature sets are tabulated in Table 4. The errors from SK_1 approximation for Set-1 and Set-3 increase with increasing scattering albedo. For Set-1, the errors are high for optically thin systems; for $\tau_0=0.1$ the errors change from 1.37 percent for $\Omega_0=0.2$ to 7.55 percent for $\Omega_0=0.995$. Similarly, for $\tau_0=0.5$ the errors range from 1.62 percent for $\Omega_0=0.2$ to 11.67 percent for $\Omega_0=0.995$ and for $\tau_0=1$ the errors range from 1.16 percent for $\Omega_0=0.2$ to 9.94 percent for $\Omega_0=0.995$. The best convergence for optically very thin systems is achieved with quadrature Set-2 in SK_1 approximation. However, errors still increase with increasing optical path. For optically thin systems, the solutions of 4–5 decimal places agreement was common. As the order of approximation is increased, the errors for optically thick systems is also reduced. For Set-3, the errors for optically thin systems are lower than Set-1 but worse than Set-2. However, for optically rather thick systems such as $\tau_0=5$ and $\tau_0=10$, the errors are as high as 30–40 percent. For example, the SK_1 approximation for $\Omega_0=0.5$ yields 25 percent errors in the transmissivity with all three sets. The exact value is 0.00004 while the computed values are 0.00003 with Set-1 and 2, and 0.00005 with Set-3. These values are in four decimal places in agreement with the exact value. On the other hand, the SK_1 approximation for $\Omega_0=0.8$ yields 46 percent error in the transmissivity with all sets. Again while the exact value is 0.00065, the computed values are 0.00035. The magnitude of these errors, here, can be partly attributed to truncation error.

The SK_2 approximation with Set-2 yielded solutions better than S_{128} and P_{11} approximations; in fact SK_1 approximation alone is

Table 4 Relative error for the solutions of the benchmark problem 1 with the SK_N approximation

Method	Ω_0	$\tau_0=0.1$		$\tau_0=0.5$		$\tau_0=1$		$\tau_0=2$		$\tau_0=5$		$\tau_0=10$	
		R	Γ	R	Γ	R	Γ	R	Γ	R	Γ	R	Γ
SK_1	0.200	1.37[*] 0[†] 0.34	0.02 0 0.01	1.62 0.03 1.00	0.10 0 0.06	1.16 0.18 1.43	0.06 0 0.10	0.93 0.50 2.00	-0.08 0.01 -0.01	0.91 0.86 2.79	1.22 1.22 -1.63	0.88 0.88 3.28	0 0 0
	0.500	3.62 0 0.88	0.16 0 0.04	4.56 0.10 2.87	0.77 -0.01 0.45	3.34 0.39 4.18	0.61 -0.04 0.89	2.43 1.14 5.71	-0.45 0.01 0.61	2.36 2.24 1.17	5.29 5.86 -11.53	2.31 2.31 9.40	25.0 25.0 -25.0
	0.800	5.96 0.02 1.52	0.43 0 0.11	8.42 0.12 5.34	2.43 -0.03 1.46	6.58 0.46 8.28	2.50 -0.16 3.47	4.15 1.46 11.59	-0.54 -0.51 5.39	3.63 3.39 15.77	6.54 7.55 -12.61	3.57 3.57 18.54	46.1 46.1 46.1
	0.995	7.55 0 1.93	0.69 0 0.17	11.67 0.10 7.48	4.37 -0.05 2.68	9.94 0.59 12.53	5.43 -0.36 7.28	5.66 0.79 19.45	0.96 -1.84 16.07	1.06 0.72 29.07	-6.35 -5.63 28.73	0.35 0.35 34.21	0.13 0.02 29.3
SK_2	0.200	0.62 0 0	0.01 0 0	0.16 0 0	0 0 0	0.07 0.02 0.02	0 0 0	0.09 0.02 0.07	0.03 0 0.01	0.06 0.04 0.11	0 0 0	0.06 0.04 0.17	0 0 0
	0.500	1.64 0 0	0.07 0 0	0.44 0 0.01	0.04 0 0	0.09 0.01 0.03	-0.06 0 0.01	0.15 0.01 0.09	0.17 0 0.07	0.15 0.08 0.27	-0.19 0 0	0.10 0.09 0.35	0 0 0
	0.800	2.76 0 0.03	0.20 0 0	0.77 0 0	0.13 0 0	-0.05 0 0.01	-0.24 0 0.03	0.08 0.01 0.07	0.25 -0.01 0.14	0.12 0.05 0.27	-0.09 -0.13 0.52	0.04 0.03 0.36	0 0 -0.31
	0.995	3.52 0 0.02	0.32 0 0	1.05 0 -0.01	0.25 0 0	-0.34 0 -0.02	-0.56 0 0.01	-0.29 -0.01 -0.05	-0.16 -0.01 0.06	-0.05 -0.04 -0.10	0.12 -0.07 0.21	-0.12 -0.12 -0.15	-0.14 -0.14 0.29
SK_3	0.200	0.25 -0.01 -0.01	0 0 0	-0.02 -0.01 -0.01	0 0 0	0.02 0.01 0.01	0 0 0	0.02 0.01 0.01	0 0 0	-0.01 -0.02 -0.01	0.16 0.16 0.16	-0.02 -0.02 -0.01	-10.0 -10.0 -10.0
	0.500	0.67 -0.01 -0.01	0.03 0 0	-0.05 0 0	-0.02 0 0	0.01 0 0	0.02 0 0	0.02 0 0	0.01 0 0	0 -0.02 -0.01	0.08 0.04 0.06	-0.05 -0.06 -0.04	0 0 0
	0.800	0.17 0.01 0.01	0.08 0 0	-0.14 0 0	-0.07 0 0	-0.02 0 0	0.02 0 0	0.02 -0.01 0	0.03 0 0	-0.01 -0.02 -0.02	0 -0.03 -0.01	-0.09 -0.10 -0.08	-0.07 -0.07 -0.07
	0.995	1.47 -0.01 -0.01	0.13 0 0	-0.25 0 0	-0.13 0 0	-0.09 0 0	-0.02 0 0	0.01 -0.01 -0.01	0.05 0 0	-0.03 -0.03 -0.03	-0.04 -0.02 -0.02	-0.10 -0.10 -0.10	-0.05 0 -0.06

[*] In each box, the values from top to bottom are the percent relative errors for Set-1, Set-2, and Set-3, respectively.

[†] The truncated error value in two decimal places is zero.

better than converged solutions of the P_{11} approximation for optically thin systems. The SK_2 and SK_3 approximations with quadrature sets 1 and 3 yielded errors of several percent for $\tau_0=0.1$ and $\tau_0=0.5$ while excellent agreement with exact solution is observed with Set-2 for all the cases. The magnitude of the errors in the computed transmissivity for $\tau_0=10$ are reduced.

In benchmark problem 2, four cases were considered. While S_{128} approximation yielded the maximum error of 0.002 percent (in Case 1), the P_{11} approximation yielded generally higher errors with the largest error being 0.47 percent in case 1. The results for the transmissivity and reflectivity in six decimal places for orders of SK_N approximation up to 4 are given in Table 5. The cases under consideration have been chosen from mostly scattering medium since the largest errors in low order SK_N approximations occurred in scattering medium. The results of the SK_1 approximation with Set-2 are in good agreement with the exact solutions. For optically thin systems 4–5 decimal places accuracy is normal, yielding errors of less than 0.25 percent with quadrature Set-2 while encountering several percent errors with other sets. The maximum errors, for sets 1 through 3, are 2.6 percent, 0.22 percent, 3.35 percent in Case 1, 1.01 percent, 0.0 percent, 3.98 percent in Case 2, 6.42 percent, 0.02 percent, 3.98 percent in Case 3, and 2.31 percent, 2.2 percent, 4.93 percent in Case 4. Using Set-2 yields substantial improvement in the results except in Case 4 which is not only optically thick but also purely scattering medium. It is noted that the order of the errors in this case are nearly identical with those of Set-1—2.3 percent and 1.96 percent. This is because, quadrature Set-2 is nearly identical to Gauss quadrature values of $\mu_1=0.5$ and $w_1=1$. Low order approximations for optically thick systems are not adequate.

The SK_2 approximation with Set-2 practically yields the exact results, the solutions with the other sets trailing behind but with substantial improvement. Using Set-1 resulted in the maximum error of 0.48 percent while this value in Set-3 is 0.15 percent. However, the SK_N approximation, with the exception of optically thick Case 4, yielded either the exact values or errors of less then 0.1 percent with sets 1 and 2 as the order was increased. The SK_N solutions with Set-2, for optically thin systems, are converging the exact solution much faster at low orders.

Changing the physical wall conditions has no adverse effect on the solution and convergence to the exact solutions as the order of the SK_N approximation is increased since the boundary terms that account for the emissions and reflections from the walls, Eqs. (17) and (23), are exactly preserved in the SK_N equations. However,

Table 5 Solutions of the benchmark problem 2

Method	Case 1		Case 2		Case 3		Case 4	
	R	Γ	R	Γ	R	Γ	R	Γ
Exact	0.226091	0.346920	1.103127	0.991760	0.659400	0.759848	0.701376	0.793224
S_{128}	0.226105	0.346913	1.103063	0.991764	0.659428	0.759848	0.701348	0.793188
P_{11}	0.225024	0.346946	1.103121	0.992834	0.659691	0.758842	0.701043	0.793020
SK_1	0.220205[‡] 0.225597 0.218508	0.343354 0.346868 0.342027	1.103028 1.103127 1.103102	0.981779 0.991760 0.989237	0.617055 0.659259 0.633124	0.730349 0.759807 0.741621	0.685152 0.685954 0.666815	0.777681 0.778898 0.760499
SK_2	0.226058 0.226087 0.226027	0.347069 0.346921 0.346860	1.103081 1.103127 1.103127	0.987153 0.991760 0.991728	0.656233 0.659401 0.659358	0.757730 0.759849 0.759816	0.701126 0.701510 0.700301	0.793063 0.793310 0.792501
SK_3	0.226047 0.226093 0.226092	0.346863 0.346921 0.346921	1.103108 1.103127 1.103127	0.989848 0.991760 0.991760	0.660313 0.659402 0.659402	0.760509 0.759849 0.759849	0.701555 0.701556 0.701547	0.793378 0.793384 0.793375
SK_4	0.226068 0.226092 0.226093	0.346898 0.346921 0.346922	1.103121 1.103127 1.103127	0.991118 0.991760 0.991760	0.659604 0.659402 0.659402	0.759989 0.759850 0.759850	0.701555 0.701553 0.701555	0.793384 0.793383 0.793385

[‡] The values from top to the bottom are solutions obtained using Set-1, Set-2, and Set-3, respectively.

the scattering albedo does have an effect on the solution and the convergence of the SK_N approximation, especially at low orders. This issue is discussed in detail in section 5.8.

5.7 The SK_N Approximation Solutions in Inhomogeneous Medium. The spatially varying scattering albedos cases described as benchmark problem 3 are solved with exact, S_{128}, and SK_N approximations. The reflectivity and transmissivity values are used in comparisons. The solution of the RITE for linearly and quadratically varying cases also reported in Ref. [16] were generated.

In Table 6, the reflectivity and transmissivity values, for linearly and quadratically varying albedo cases, are tabulated up to the fourth order SK_N approximations, using the three quadrature sets. In the $\Omega_0(\tau)=0.2+0.6\tau$ case, albedo increasing linearly from minimum value of 0.2 at wall 1 to maximum value of 0.8 at wall 2, the errors with SK_1, for reflectivity and transmissivity, are 2.47 percent, 0.99 percent; -0.07 percent, 0.04 percent and 3.27 percent, 1.31 percent, for Sets 1 through 3, respectively. The errors with SK_2 are dramatically reduced in magnitude yielding the exact solution with Set-2, while these errors are -0.19 percent and -0.03 percent using Set-1, and -0.02 percent and 0.01 percent using Set-3, respectively. As with the SK_3 approximation using Set-2 and 3 yields the exact solutions, using Set-1 results in -0.03 percent and 0.01 percent errors. In SK_4 approximation using Set-1, the errors are less than 0.01 percent, and with SK_3 and SK_4 using Set-2 and 3 are the converged exact solutions. In the

Table 6 Solutions for linearly and quadratically scattering albedo cases

Method	Scattering Albedo, $\Omega_0(\tau)$							
	$0.2+0.6\tau$		$0.8-0.6\tau$		$0.4-0.2\tau+0.6\tau^2$		$1-1.4\tau+0.6\tau^2$	
	R	Γ	R	Γ	R	Γ	R	Γ
Exact	0.089797	0.308978	0.188810	0.308978	0.108268	0.307972	0.216639	0.311079
S_{128}	0.089800	0.308959	0.188832	0.308964	0.108279	0.307956	0.216663	0.311064
SK_1	0.087580[§] 0.089863 0.086861	0.305916 0.308863 0.304931	0.178051 0.186555 0.176079	0.305917 0.308864 0.304932	0.105533 0.107989 0.104734	0.305617 0.307716 0.304742	0.201273 0.212532 0.198844	0.307061 0.310493 0.306015
SK_2	0.089964 0.089798 0.089811	0.309061 0.308978 0.308949	0.187832 0.188802 0.188703	0.309062 0.308979 0.308950	0.108212 0.108265 0.108221	0.307927 0.307977 0.307904	0.214606 0.216624 0.216374	0.310899 0.311084 0.311027
SK_3	0.089828 0.089797 0.089797	0.308960 0.308978 0.308978	0.188745 0.188813 0.188812	0.308961 0.308979 0.308979	0.108227 0.108269 0.108268	0.307891 0.307973 0.307972	0.216413 0.216645 0.216644	0.311033 0.311081 0.311081
SK_4	0.089792 0.089797 0.089797	0.308965 0.308978 0.308978	0.188801 0.188813 0.188813	0.308966 0.308979 0.308979	0.108254 0.108269 0.108269	0.307959 0.307972 0.307973	0.216621 0.216645 0.216645	0.311072 0.311080 0.311081

[§] The values from top to the bottom are solutions obtained using Set-1, Set-2, and Set-3, respectively.

Table 7 Solutions for exponential and cosine oscillating albedo cases

Method	Scattering Albedo, $\Omega_0(\tau)$							
	$0.790988\exp(-\tau)$		$0.790988\exp(-[1-\tau])$		$0.5+0.5\tau\cos 12\pi\tau$		$0.5+0.5(1-\tau)\cos 12\pi(1-\tau)$	
	R	Γ	R	Γ	R	Γ	R	Γ
Exact	0.180592	0.308307	0.098893	0.308307	0.133965	0.307242	0.137972	0.307242
S_{128}	0.180614	0.308294	0.098900	0.308290	0.133951	0.307180	0.137959	0.307180
SK_1	0.170986[§] 0.178490 0.169195	0.305675 0.308166 0.304749	0.096501 0.098844 0.095744	0.305674 0.308165 0.304748	0.129264 0.133224 0.128142	0.305006 0.306956 0.304150	0.132671 0.136631 0.131538	0.305007 0.306956 0.304150
SK_2	0.180579 0.179642 0.180454	0.308310 0.308350 0.308259	0.098892 0.098985 0.098883	0.308309 0.308349 0.308259	0.133632 0.133831 0.133753	0.307041 0.307012 0.306889	0.137050 0.137446 0.137236	0.307042 0.307013 0.306889
SK_3	0.180485 0.180595 0.180594	0.308260 0.308308 0.308308	0.098896 0.098893 0.098893	0.308256 0.308308 0.308307	0.133773 0.133944 0.133914	0.306885 0.307201 0.307147	0.137258 0.137924 0.137782	0.306886 0.307201 0.307148
SK_4	0.180574 0.180595 0.180596	0.308294 0.308308 0.308308	0.098884 0.098893 0.098893	0.308293 0.308307 0.308307	0.133824 0.133945 0.133950	0.306995 0.307207 0.307215	0.137439 0.137964 0.137976	0.306996 0.307208 0.307215

[§] The values from top to the bottom are solutions obtained using Set-1, Set-2, and Set-3, respectively.

$\Omega_0(\tau)=0.8-0.6\tau$ case, albedo decreases from maximum value of 0.8 at wall 1 to the minimum value of 0.2 at wall 2. The transmissivity values of five to six decimal places accuracy with the $\Omega_0(\tau)=0.2+0.6\tau$ case are observed yielding the same errors in transmissivity. The SK_1 errors for the reflectivities are 5.70 percent, 1.19 percent, and 6.74 percent for Set-1 through 3, respectively. The errors with SK_2 approximation are reduced to 0.52 percent, 0.004 percent, and 0.06 percent, for sets 1 through 3, respectively. In SK_3 approximation, using Set-2 and 3, converges to the exact solution on 5–6 decimal places while using Set-1 yields the error of 0.03 percent. On the other hand, the reflectivity error SK_4 approximation is 0.002 percent while the SK_3 and SK_4 approximation that uses Set-2 and 3 converges five decimal places of the exact solution. The errors in both reflectivity and transmissivity with S_{128} approximation yield errors of 0.01 percent or less for both cases.

In the $\Omega_0(\tau)=0.4-0.2\tau+0.6\tau^2$ case, albedo takes 0.4 and 0.8 values at wall 1 and at wall 2, respectively. The reflectivity and transmissivity errors with SK_1 approximation are 2.53 percent, 0.76 percent; 0.26 percent, 0.08 percent; and 3.26 percent, 1.05 percent, for sets 1 through 3, respectively. However, in SK_2 approximation, these errors are reduced below 0.05 percent for both the transmissivity and reflectivity. In SK_3 approximation using Set-1 yields 0.04 percent and 0.03 percent errors in reflectivity and transmissivity, respectively; these values in SK_4 approximation are reduced below 0.01 percent. The SK_2, SK_3, and SK_4 approximations using Set-2 and 3 yield 4–5 decimal places accurate solutions with increasing orders. In the $\Omega_0(\tau)=1-1.4\tau+0.6\tau^2$ case, albedo has the largest value of 1 at wall 1 decreasing towards to the value of 0.2 at wall 2. The reflectivity and transmissivity errors with SK_1 approximation are 7.09 percent, 1.29 percent; 1.90 percent, 0.19 percent; and 8.21 percent, 1.63 percent, for set 1 through 3, respectively. In SK_2 approximation, the maximum errors are observed in reflectivity with 0.94 percent, 0.01 percent, and 0.12 percent, for Set-1, Set-2, and Set-3 while the maximum error in the transmissivity is 0.06 percent in Set-1. The error in reflectivity using SK_3 approximation with Set-1 results in 0.1 percent while the errors with the other sets including those of the SK_4 is less than 0.01 percent yielding four decimal places accurate solutions.

In Table 7, the computed transmissivity and reflectivity values of benchmark problem 3 with the exact, S_{128} and the SK_N approximations are given for the exponential and cosine oscillating scattering albedos cases.

In the $\Omega_0(\tau)=0.790988\exp(-\tau)$ case, albedo decreasing from its maximum value of about 0.79 at wall 1 to its minimum value of about 0.29 at wall 2, the errors for the reflectivity and transmissivity for SK_1 are 5.32 percent, 0.85 percent; 1.16 percent, 0.05 percent; and 6.31 percent, 1.15 percent, for sets through 3, respectively. With SK_2 approximation, the reflectivity errors are reduced to 0.01 percent, 0.53 percent and 0.08 percent, in sets 1 through 3. Higher order SK_N approximations yield errors less than 0.06 percent with the errors being larger with Set-1 while Set-2 and Set-3 converge five decimal places accurate solutions with the exact solution. On the other hand, in the $\Omega_0(\tau)=0.790988\exp(-[1-\tau])$, albedo increases from about 0.29 value at wall 1 to about 0.79 value at wall 2. The errors for the reflectivity and transmissivity for SK_1 are 2.42 percent, 0.85 percent; 0.05 percent, 0.05 percent; and 3.18 percent, 1.15 percent, for Set-1, Set-2, and Set-3, respectively. The largest reflectivity error with -0.09 percent is in SK_2 approximation using Set-2 while the other sets produce errors less than 0.02 percent. While the SK_3 and SK_4 approximations using Set-1 converge the exact value in 5–6 decimal places, the maximum errors are 0.02 percent with SK_3 and 0.01 percent with SK_4 approximations.

In the $\Omega_0(\tau)=0.5+0.5\tau\cos 12\pi\tau$ case, scattering albedo oscillates around 0.5 while magnitude of the oscillations grow towards wall 2 where it takes the maximum value of 1.0. The errors for the reflectivity and transmissivity for SK_1 approximation are 3.51 percent, 0.73 percent; 0.55 percent, 0.09 percent; and 4.35 percent, 1.01 percent, for sets 1 through 3, respectively while, in SK_2 approximation, the errors in both reflectivity and transmissivity are reduced to 0.25 percent, 0.07 percent, 0.10 percent, 0.07 percent; and 0.16 percent, 0.11 percent. In SK_3 approximation, the errors using Set-1 yield 0.014 percent while the maximum errors using Set-2 and Set-3 are in reflectivity with 0.02 percent and 0.04 percent. The SK_4 approximation with Set-1 yield 0.11 percent error in reflectivity and 0.08 percent in transmissivity as the solutions with Set-2 and 3 yield four decimal places accurate solutions. On the other hand, in the $\Omega_0(\tau)=0.5+0.5(1-\tau)\cos 12\pi(1-\tau)$ case, starting from the value of 1.0 at wall 1 scattering albedo oscillations around 0.5 are damped towards wall

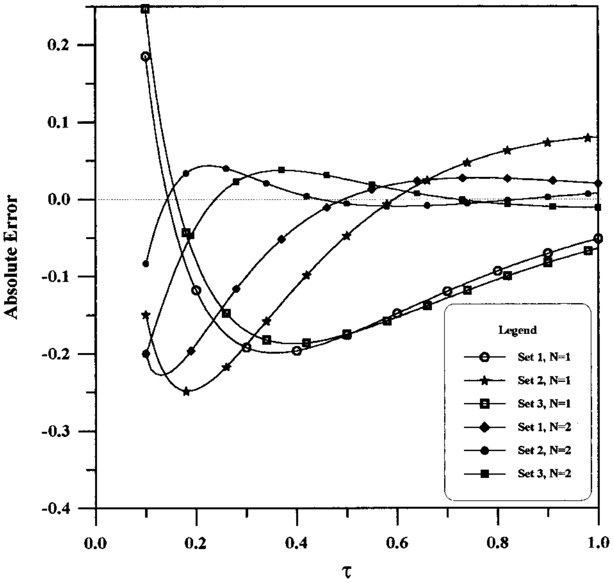

Fig. 1 The absolute errors of the first order exponential integral function using one- and two-term synthetic kernels with Set-1, 2, and 3

2. While the errors in transmissivity are about the same as in the case of $\Omega_0(\tau)=0.5+0.5\tau\cos 12\pi\tau$, the errors in reflectivities are generally higher and persistent in low order approximations. With SK_1 approximation, the reflectivity errors are, for SK_1 3.84 percent, 0.97 percent and 4.66 percent; for SK_2 0.67 percent, 0.38 percent and 0.53 percent; for SK_3 0.52 percent, 0.03 percent and 0.14 percent; for SK_4 0.39 percent, 0.01 percent, and -0.003 percent, for sets 1 through 3, respectively.

5.8 Accuracy of the Synthetic Kernels. To illustrate the behavior and the convergence of the SK_N approximation with increasing orders, we define the absolute error for the exact and the approximate first order exponential function as $E_1(\tau)-\Sigma_n w_n \exp(-\tau/\mu_n)/\mu_n$. The variation of absolute error, as a function of space, for $\tau_0=1$ and $N=1$ and 2 with three quadrature sets, is shown in Fig. 1. Here, the absolute error for the range $0.1\leqslant\tau\leqslant 1$ is depicted to allow an enlarged picture of the fit in the rest of the domain. In Fig. 1, the asymptotic behavior at $\tau=0$ is clearly visible for all sets. However, elsewhere in the interval, the absolute errors decrease in magnitude for increasing τ. For $N=2$, the magnitude of the errors are further decreased. Noting that the integrals of the exact and the approximate $E_1(\tau)$ over the optical domain are the first (zeroth) moment—$M_0(1)$—it is clear that the difference between the exact and the approximate moments will be zero for Set-2 and 3, while for Set-1 this difference yields -0.0132, -0.0034 and 0.0017, for $N=1$, 2 and 3, respectively. This implies that the integral of $S(\tau)E_1(\tau)$, in which the source term can be described by a polynomial of degree $(2N-1)$ or less in using Set-2 and a polynomial of degree $(2N-2)$ or less in using Set-3, will yield the exact value. This feature of Set-2 and 3 make them superior to Set-1 whereas Set-1 achieves this only when $N\rightarrow\infty$. However, the integrals involved, in Eqs. (9) and (16), do not exactly correspond the integrals over the optical domain since, for example the integral term in Eq. (9) can be, upon change of variables, written as

$$\int_{\tau'=0}^{\tau_0} S(\tau')E_1(|\tau-\tau'|)d\tau'=\int_{x=0}^{\tau} S(\tau-x)E_1(x)dx + \int_{x=0}^{\tau_0-\tau} S(\tau+x)E_1(x)dx \tag{28}$$

Thus, not only the zeroth but also the other spatial moments as applied to the RITE do not yield the exact integrals even for Set-2 and Set-3, except at $\tau=0$, though the magnitude of the errors made in Eq. (28) are much smaller with Set-2 and 3 than Set-1 in optically thin systems. Thus, the magnitude of source term and its profile near wall 1 where the errors of the approximate $E_1(\tau)$ are relatively greater will have greater impact onto the overall integration errors, especially SK_1 and SK_2 approximations.

In homogeneous absorbing medium ($\Omega_0\rightarrow 0$), the mentioned errors in low order approximations are further reduced since the magnitude of the source is reduced as well. On the other hand, for strongly scattering medium ($\Omega_0\rightarrow 1$) the source term will be greater than in the absorbing medium; thus both the synthetic kernel approximation and the integration errors combined have the full impact on the solution.

In inhomogeneous medium, the scattering albedo alternatives of $\Omega_0(\tau)=0.8-0.6\tau$, $\Omega_0(\tau)=1-1.4\tau+0.6\tau^2$, $\Omega_0(\tau)=0.790988\exp(-\tau)$ and $\Omega_0(\tau)=0.5+0.5(1-\tau)\cos 12\pi(1-\tau)$ turn out to be very good examples of displaying the importance of the source term behavior near wall 1. In comparison to the other scattering albedo alternatives where the source term is relatively small, the scattering albedos with larger values amplify the source near wall 1. The SK_N approximation performs remarkably well even under these circumstances, for example, in SK_1 approximation the maximum errors using Set-2 are 1.19 percent for linear, 1.9 percent for quadratic, 1.16 percent for exponential and 0.97 percent for cosine scattering albedos. With the SK_2 approximation the maximum errors using Set-2 are 0.01 percent for linear and quadratic, 0.53 percent for exponential and 0.38 percent for cosine scattering albedo cases. All of these maximum values are obtained in large albedo variations near wall 1. The accuracy is improved significantly with the SK_3 and SK_4 approximations yielding solutions, even in such worst cases, better than or equivalent to those of S_{128}.

Most of the errors encountered in the SK_N approximation were observed in the reflectivity rather than transmissivity. Foregoing error assessment could be extended to $E_2(x)$ and its synthetic approximation, Eq. (22). Here, the spatial moments of $E_2(x)$ also are not exactly preserved. In calculating the incoming heat flux, Eq. (12), at $\tau=0$, the integral of $S(x)E_2(x)$ is required over the optical domain which presents two kinds of error: (i) the source term near wall land (ii) low order of the synthetic kernel approximation. On the other hand, in the outgoing heat flux at $\tau=\tau_0$, Eq. (11), $S(x)E_2(\tau_0-x)$ term is integrated which reduces the source term magnitude with a weight function—namely, $E_2(\tau_0-x)$ which takes smaller values for $x=0$.

6 Conclusion

The SK_N approximation is applied to solve integral radiative transfer equations in plane parallel participating homogeneous and inhomogeneous medium. The solutions for the test cases are compared with the exact, S_N and P_N methods. In the SK_N approximation, one has to deal with a few second order coupled differential equations, and the angular dependence is completely eliminated from RTE. Based on the results presented, the following conclusions have been drawn:

1 The method is computationally very cheap and memory efficient. The cpu time with 800 grids for the exact, S_{128}, SK_2, and SK_5 are on the order of 100, 10, 0.4, and 1 seconds, respectively, which makes even higher approximations, such as SK_5, very attractive.

2 The significance of the accurate evaluation of spatial moments of $E_1(x)$ inherent in Eq. (24) is that, when the RTE equation is cast in its integral form, the integral is expressed accurately even though the approximation itself is grossly inaccurate near $x=0$. Thus an Nth order approximation yields the exact integral of $S(x)E_1(x)$ over the optical domain when $S(x)$ is described by a polynomial of degree $(2N-1)$ and $(2N-2)$ using Set-2 and 3,

respectively. This feature makes Set-2 inherently the best choice in low order approximations while the second best choice with exception of $N=1$ is Set-3.

3 The accuracy with the order of the SK_N approximation, with any quadrature set, also depends on the profile and the order of magnitude of the source term which is also influenced by scattering albedo. If the magnitude of the source term near the singular wall is small, the accuracy of the approximation for $N=1$ or 2 is improved drastically. The method performs remarkably well even in cases where a large or strong source term variations are encountered, as in exponential and cosine scattering albedo cases, yielding maximum errors up to 2 percent in SK_1 and 0.5 percent in SK_2.

4 It has been shown that the SK_3 and SK_4 approximations in most cases can be used to yield solutions comparable with S_{128} and P_{11}. Such high order approximations as SK_3 and SK_4 using Set-2 can be used to solve problems of various optical thicknesses and scattering albedo alternatives to yield errors of less than 0.1 percent if four or five decimal places accuracy in the solutions are desired. It is been also demonstrated that, the SK_1 approximation using Set-2 yields the exact solutions for optically very thin ($\tau_0 < 1$) medium, while solutions with errors of 1–2 percent in moderately thin (several mfps), and up to 5 percent in optically thick medium are observed. With SK_2 approximation the largest errors in optically thick medium are on the order of 0.5 percent. As the medium becomes absorbing ($\Omega_0 \rightarrow 0$), in optically thin cases, the exact solutions can be obtained with the SK_N approximation where low order DOM and P_N approximations present largest errors whereas in optically thick medium errors up to 1 percent are observed. On the other hand, for scattering medium ($\Omega_0 \rightarrow 1$), in low order approximations regardless for the optical thickness, the errors are higher than those of the absorbing medium yielding up to 8 percent in SK_1 and 0.15 percent in SK_2 using Set-2. But the accuracy in scattering medium is also improved with increasing order of SK_N approximation.

Acknowledgment

The author would like to thank the reviewers for their valuable comments and suggestion that have helped to improve the presented paper.

Nomenclature

$E_n(x)$ = nth order exponential integral function
G = dimensionless incident radiation $(=g/(n^2\sigma T_{\text{ref}}^4/\pi))$
$G_n(\tau)$ = functions defined by Eq. (16)
I = dimensionless radiative intensity $(=i/(n^2\sigma T_{\text{ref}}^4/\pi))$
Q = radiative heat flux
R = reflectivity
S = dimensionless isotropic source function $(=s/(n^2\sigma T_{\text{ref}}^4/\pi))$
T = temperature
$f(\tau)$ = boundary term defined by Eq. (15)
g = incident radiation function
i = radiative intensity
n = refractive index of the medium
s = source function
sgn = the sign function
q = dimensionless radiative heat flux $(=Q/(n^2\sigma T_{\text{ref}}^4/\pi))$
x = space variable
w_n = quadrature weights

Greek Symbols

Γ = transmissivity
Ω_0 = scattering albedo $(=\kappa/\beta)$
β = extinction coefficient
ε = wall emissivity
κ = absorption coefficient
μ = angular cosine
μ_n = quadrature abscissas
θ = dimensionless temperature $(=T/T_{\text{ref}})$
ρ = diffusive wall reflectivity
σ = Stefan-Boltzmann coefficient
τ = dimensionless optical variable $(=\beta x)$
τ_0 = optical path
ξ = convergence criterion

Subscripts

1 = boundary wall 1
2 = boundary wall 2
n = nth component of the SK_N equation
$-$ = outgoing heat flux or intensity
$+$ = incoming heat flux or intensity

Superscript

‘ = dummy integration variable

References

[1] Modest, M. F., 1993, *Radiative Heat Transfer*, McGraw Hill Inc.
[2] Lewis, E. E., and Miller, W. F., 1984, *Computational Methods of Neutron Transport*, John Wiley & Sons, Inc.
[3] Spinrad, B. I., and Sterbentz, J. S., 1985, ''Approximations to Neutron Transport Problems in Complex Geometries: I,'' Nucl. Sci. Eng., **90**, pp. 431–440.
[4] Altaç, Z., and Spinrad, B. I., 1990, ''The SK_N Method I: A High Order Transport Approximation to Neutron Transport Problems,'' Nucl. Sci. Eng., **106**, pp. 471–479.
[5] Spinrad, B. I., and Altaç, Z., 1990, ''The SK_N Method II: Heterogeneous Problems,'' Nucl. Sci. Eng., **106**, pp. 480–488.
[6] Altaç, Z., 1989, ''The SK_N approximation: A New Method for Solving the Integral Transport Equations,'' Ph.D. thesis, Iowa State University, Ames, IA.
[7] Altaç, Z., and Tekkalmaz, M., 2001, ''The SK_N approximation for Solving Radiation Transport Problems In Absorbing, Emitting, and Scattering Rectangular Geometries,'' *Proc. 3rd International Symposium on Radiation Transfer*, M. P. Mengüç and N. Selçuk, eds., Begell House Inc., New York, pp. 119–129.
[8] Özişik, M. N., 1973, *Radiative Transfer*, John Wiley & Sons, Inc.
[9] Buckley, H., 1928, ''On the Radiation from the Inside of a Circular Cylinder, Part I,'' Philos. Mag., **6**, pp. 447–457.
[10] Perlmutter, M., and Siegel, R., 1963, ''Effect of Specularly Reflecting Gray Surface on Thermal Radiation Through a Tube from its Heated Wall,'' ASME J. Heat Transfer, **85C**, pp. 55–62.
[11] Krook, M., 1955, ''On the Solution of Equation of Transfer I,'' Astrophys. J., **122**, pp. 488–497.
[12] Coppa, G., and Ravetto, P., 1982, ''An Approximate Method to Study the One-Velocity Neutron Integral Transport Equation,'' Ann. Nucl. Energy, **9**, pp. 169–174.
[13] Coppa, G., Ravetto, P., and Sumini, R., 1982, ''The A_N Method and the Spherical-Harmonics Approximation in Neutron Transport Theory,'' Ann. Nucl. Energy, **9**, pp. 435–437.
[14] Abramowitz, M., and Stegun, I. A., 1964, *Handbook of Mathematical Functions*, Dover Publications Inc.
[15] Çengel, Y., Özişik, M. N., and Yener, Y., 1984, ''Radiative Transfer in a Plane-parallel Medium with Space Dependent Albedo,'' Int. J. Heat Mass Transf., **27**, pp. 1919–1922.
[16] Clements, T. B., and Özişik, M. N., 1983, ''Effects of Stepwise Variation of Albedo on Reflectivity and Transmissivity of an Isotropically Scattering Slab,'' Int. J. Heat Mass Transf., **26**, pp. 1419–1426.
[17] Layolka, S. K., and Tsai, R. W., 1975, ''A Numerical Method for Solving Integral Equations of Neutron Transport-II,'' Nucl. Sci. Eng., **58**, pp. 317.
[18] Dongarra, J. J., Bunch, J. R., Moler, C. B., and Stewart, G. W., 1979, *LINPACK Users' Guide*, Society for Industrial and Applied Mathematics, Philadelphia, PA.
[19] Anderson, D. A., Tannehill, J. C., and Pletcher, R. H., 1984, *Computational Fluid Mechanics and Heat Transfer*, Hemisphere Publishing Corp.

Zekeriya Altaç
e-mail: zaltac@ogu.edu.tr
Osmangazi University,
School of Engineering and Architecture,
Mechanical Engineering Department,
26480 Bati Meselik-Eskisehir
Turkey

The SK_N Approximation for Solving Radiative Transfer Problems in Absorbing, Emitting, and Linearly Anisotropically Scattering Plane-Parallel Medium: Part 2

The SK_N (Synthetic Kernel) approximation is proposed for solving radiative transfer problems in linearly anisotropically scattering homogeneous and inhomogeneous participating plane-parallel medium. The radiative integral equations for the incident energy and the radiative heat flux using synthetic kernels are reduced to a set of coupled second-order differential equations for which proper boundary conditions are established. Performance of the three quadrature sets proposed for isotropic scattering medium are further tested for linearly anisotropically scattering medium. The method and its convergence with respect to the proposed quadrature sets are explored by comparing the results of benchmark problems using the exact, P_{11}, and S_{128} solutions. The SK_N method yields excellent results even for low orders using appropriate quadrature set. [DOI: 10.1115/1.1464131]

Keywords: *Emitting, Numerical Methods, Participating Media, Radiation, Scattering*

1 Introduction

Radiative integral transfer equation (RITE) is obtained by integrating radiative transfer equation (RTE) over the solid angle. In the RITE, physical wall boundary conditions appear as surface, while source terms containing absorption, scattering, and medium emission within the enclosure as volume integrals. Thus, the radiative integral equations do not require boundary conditions to be solved. The SK_N method, while preserving the surface integrals, or the physical boundary conditions, in their exact forms, approximates the RITE through a sum of exponentials—synthetic kernels—to its transfer kernels that are contained within the volume integrals. This feature of SK_N method allows a semi-analytic treatment of RTE. The approximate volume integrals are then reduced into a set of coupled differential equations; thus the solution of a system of linear equations of dense matrices is avoided. However, boundary conditions of mathematical in nature are needed to solve the SK_N equations for a given domain.

The SK_N approximation was applied by Altaç [1], and Altaç and Spinrad [2,3] to homogeneous and inhomogeneous neutron transport problems in one and two-dimensional geometries. One-dimensional slab, cylindrical and spherical absorbing, isotropically scattering homogeneous and stepwise inhomogeneous—typical of fuel cell neutronic calculations—problems were solved and compared with the solution of integral equation and discrete ordinates method (DOM) S_{32} [2,3]. The results of the SK_N approximation in homogeneous one-dimensional problems were three to four significant digit accurate with SK_3 and SK_4 solutions. The SK_N solutions for two-dimensional absorbing and isotropically scattering problems in rectangular medium, which were also typical of neutron transport calculations, were compared with those of integral transport equation, the nodal spherical harmonics P_5 and P_7, DOM D_{16} and Monte Carlo. The results were remarkably in good agreement with those of exact, DOM, P_7 and Monte Carlo in homogeneous and optically thin stepwise inhomogeneous medium. Furthermore, the solutions with the SK_N approximation did not exhibit so-called the ''ray effect'' [2,3]. The SK_N approximation was also applied to a radiative transfer problem of absorbing, emitting and isotropically scattering rectangular medium by Altaç and Tekkalmaz [4]. In the study, various optical configurations and scattering albedos were considered and incident energy; intensity and the net heat flux solutions were compared with those obtained by RITE. Also two types of boundary conditions that could be used in rectangular geometries were proposed. The results with SK_2 approximation for optically thin absorbing medium were in good agreement with the exact solutions yielding relative errors of 1–3 percent for the incident energy and the intensities. For optically thick and scattering medium, the relative errors of 10–20 percent in the net heat flux were encountered.

The foregoing studies used the Gauss quadratures in the half range to approximate the transfer kernels. However, various integration quadratures can be developed and used with the SK_N approximation that may potentially improve the accuracy of the approximation at low orders. A study that was carried out in plane-parallel isotropic scattering medium by Altaç [5] explored two additional quadrature sets: Set-2, Set-3, and Set-1 as being the Gauss quadratures in half range. In developing Set-2 and Set-3, respectively, $2N-1$ and $2N-2$ spatial moments of the first order exponential integral function of the real and the synthetic exponential integral functions were matched, and the resulting system of non-linear equations were solved [5]. The SK_1 approximation with Set-2 yields very accurate solutions for optically thin absorbing medium while highest percent errors are observed in strongly scattering or optically thick medium. The errors are dramatically reduced even with the SK_2 approximation using Set-2 and 3. The

---

Contributed by the Heat Transfer Division for publication in the JOURNAL OF HEAT TRANSFER. Manuscript received by the Heat Transfer Division March 15, 2000; revision received October 9, 2001. Associate Editor: C. T. Avedisian.

study also revealed that the magnitude the source term at $x=0$ strongly influences the accuracy of the solutions especially in low order approximations.

This study extends the SK_N approximation to linearly anisotropically scattering homogeneous and inhomogeneous medium, and the quadrature sets that were proposed in Ref. [5] were used to examine the convergence of the method to the exact solution with respect to quadrature sets used. It is also the intent of this study to analyze the sources of errors in the approximation that seem to be persistent in multi-dimensional geometries as well. In that respect, planar geometry is better suited to carry out and demonstrate this analysis since exact and high order approximation, such as S_{128} and P_{11}, solutions can be obtained rather easily, and it does not exhibit problems such as the "ray-effect."

2 Analysis

A plane-parallel, absorbing, emitting, inhomogeneous, linearly anisotropically scattering medium at dimensionless temperature $\theta(\tau)$ with optical path τ_0 is considered. The walls are assumed to be opaque, diffusive reflectors and diffuse emitters and to have emissivities $\varepsilon_1, \varepsilon_2$ and reflectivities ρ_1, ρ_2. The emission of radiation from walls due to their temperatures are $\varepsilon_i \theta_i^4$ ($i=1$ or 2) where θ_i is the dimensionless temperature of wall *i*. The medium is assumed to have a space-dependent scattering albedo $\Omega_0(\tau)$.

The dimensionless RTE for outgoing and incoming intensities, $I^+(\tau,\mu)$ and $I^-(\tau,\mu)$, in a plane-parallel geometry with linearly anisotropically scattering inhomogeneous medium can be written as [6]

$$\mu \frac{\partial I^{\pm}}{\partial \tau} + I^{\pm}(\tau,\mu) = S(\tau,\mu) \tag{1}$$

where μ is the angular cosine and τ the optical variable.

The dimensionless anisotropic source term takes the form [6]

$$S(\tau,\mu) = [1-\Omega_0(\tau)]\theta^4(\tau) + \frac{\Omega_0(\tau)}{4\pi}[G(\tau) + a_1 \mu q(\tau)] \tag{2}$$

where $G(\tau)$ is the incident radiation function, $q(\tau)$ is the net radiative heat flux, and a_1 is the coefficient of anisotropy.

Solving Eq. (1) for outgoing intensities and integrating it from $(0,\tau)$ gives

$$I^+(\tau,\mu) = I^+(0)e^{-\tau/\mu} + \int_0^{\tau} \frac{1}{\mu} S(\tau',\mu) e^{(\tau'-\tau)/\mu} d\tau', \quad \mu > 0 \tag{3}$$

Similarly, solving Eq. (1) for incoming intensities and integrating from (τ,τ_0) and rearranging for positive μ gives

$$\begin{aligned} I^-(\tau,-\mu) &= I^-(\tau_0)e^{-(\tau_0-\tau)/\mu} \\ &\quad + \int_{\tau}^{\tau_0} \frac{1}{\mu} S(\tau',-\mu) e^{-(\tau'-\tau)/\mu} d\tau', \quad \mu > 0 \end{aligned} \tag{4}$$

where $I^+(0)$ and $I^-(\tau_0)$ are the anisotropic wall intensities, and pertinent details are given in Appendix.

By definition, the dimensionless incident energy is

$$\begin{aligned} G(\tau) &= 2\pi \int_{-1}^{1} I(\tau,\mu) d\mu \\ &= 2\pi \int_0^1 I^+(\tau,\mu) d\mu + 2\pi \int_0^1 I^-(\tau,-\mu) d\mu \end{aligned} \tag{5}$$

Substitution of Eqs. (3) and (4) into Eq. (5) yields

$$\begin{aligned} G(\tau) &= f_1(\tau) + \int_0^{\tau_0} S_0(\tau') E_1(|\tau-\tau'|) d\tau' \\ &\quad + a_1 \int_0^{\tau_0} S_1(\tau') \operatorname{sgn}(\tau-\tau') E_2(|\tau-\tau'|) d\tau' \end{aligned} \tag{6}$$

where

$$f_1(\tau) = 2\pi[I^+(0)E_2(\tau) + I^-(\tau_0)E_2(\tau_0-\tau)] \tag{7}$$

$$S_0(\tau) = 2\pi[1-\Omega_0(\tau)]\theta^4(\tau) + \frac{1}{2}\Omega_0(\tau)G(\tau) \tag{8}$$

$$S_1(\tau) = \frac{1}{2}\Omega_0(\tau)q(\tau) \tag{9}$$

"sgn" is the sign function, and $E_1(x)$, $E_2(x)$, and $E_3(x)$ are the exponential integral functions of first, second and third order [7].

By definition of the net radiative heat flux, we write

$$q(\tau) = 2\pi \int_{-1}^{1} I(\tau,\mu)\mu d\mu = q^+(\tau) - q^-(\tau) \tag{10}$$

For incoming and outgoing components, after multiplying Eqs. (3) and (4) by $2\pi\mu$, we integrate over μ in the range (0,1) to get

$$\begin{aligned} q^+(\tau) &= 2\pi I^+(0)E_3(\tau) + \int_0^{\tau} S_0(\tau')E_2(\tau-\tau')d\tau' \\ &\quad + a_1 \int_0^{\tau} S_1(\tau')E_3(\tau-\tau')d\tau' \end{aligned} \tag{11}$$

and

$$\begin{aligned} q^-(\tau) &= 2\pi I^-(\tau_0)E_3(\tau_0-\tau) + \int_{\tau}^{\tau_0} S_0(\tau')E_2(\tau'-\tau)d\tau' \\ &\quad - a_1 \int_{\tau}^{\tau_0} S_1(\tau')E_3(\tau'-\tau)d\tau' \end{aligned} \tag{12}$$

Combining Eqs. (11) and (12) in Eq. (10) gives

$$\begin{aligned} q(\tau) &= f_2(\tau) + \int_0^{\tau_0} S_0(\tau') \operatorname{sgn}(\tau-\tau') E_2(|\tau-\tau'|) d\tau' \\ &\quad + a_1 \int_0^{\tau_0} S_1(\tau') E_3(|\tau-\tau'|) d\tau' \end{aligned} \tag{13}$$

where

$$f_2(\tau) = 2\pi[I^+(0)E_3(\tau) - I^-(\tau_0)E_3(\tau_0-\tau)] \tag{14}$$

Eqs. (6) and (13) constitute two coupled Fredholm integral equations of the second kind which need to be solved to obtain the exact solution. The anisotropic wall intensities are computed using Eq. (*A*4) and (A6) as described in the Appendix.

3 Derivation of the SK_N Approximation

We introduce the SK_N approximation by substituting the following approximations for the exponential integral functions into Eqs. (6) and (13)

$$E_m(x) = \int_{\mu=0}^{1} \mu^{m-2} e^{-x/\mu} dz \doteq \sum_{n=1}^{N} w_n \mu_n^{m-2} e^{-x/\mu_n}, \quad m=1,2,3 \tag{15}$$

where w_n and μ_n are the Gauss quadrature weights and abscissas [7].

Defining

$$G_n(\tau)=\frac{1}{\mu_n}\int_0^{\tau_0} S_0(\tau')\exp(-|\tau-\tau'|/\mu_n)d\tau' + a_1\int_0^{\tau_0} S_1(\tau')\text{sgn}(\tau-\tau')\exp(-|\tau-\tau'|/\mu_n)d\tau' \tag{16}$$

and

$$q_n(\tau)=\int_0^{\tau_0} S_0(\tau')\text{sgn}(\tau-\tau')\exp(-|\tau-\tau'|/\mu)d\tau' + a_1\mu_n\int_0^{\tau_0} S_1(\tau')\exp(-|\tau-\tau'|/\mu_n)d\tau' \tag{17}$$

Eqs. (6) and (13) can now be written as

$$G(\tau)=f_1(\tau)+\sum_{n=1}^{N} w_n G_n(\tau) \tag{18}$$

and

$$q(\tau)=f_2(\tau)+\sum_{n=1}^{N} w_n q_n(\tau) \tag{19}$$

Differentiating Eqs. (16) and (17) with respect to τ, we get

$$-\mu_n^2\frac{dG_n(\tau)}{d\tau}=q_n(\tau)-2a_1\mu_n^2 S_1(\tau) \tag{20}$$

and

$$\frac{dq_n(\tau)}{d\tau}=-G_n(\tau)+2S_0(\tau) \tag{21}$$

If we differentiate Eq. (20) with respect to τ to get,

$$-\mu_n^2\frac{d^2G_n(\tau)}{d\tau^2}=\frac{d}{d\tau}q_n(\tau)-2a_1\mu_n^2\frac{d}{d\tau}S_1(\tau) \tag{22}$$

and use the following relation along with Eqs. (9) and (21),

$$\frac{dq(\tau)}{d\tau}=[1-\Omega_0(\tau)][4\pi\theta^4(\tau)-G(\tau)] \tag{23}$$

we obtain the SK_N equations for inhomogeneous linearly anisotropically scattering plane-parallel medium as

$$-\mu_n^2\frac{d^2G_n(\tau)}{d\tau^2}+G_n(\tau)=4\pi[1-a_1\mu_n^2\Omega_0(\tau)][1-\Omega_0(\tau)]\theta^4(\tau) + \Omega_0(\tau)[1+a_1\mu_n^2[1-\Omega_0(\tau)]]G(\tau) - a_1\mu_n^2 q(\tau)\frac{d\Omega_0(\tau)}{d\tau} \tag{24}$$

Boundary conditions for the SK_N equations are derived by inspecting $G_n(\tau)$ and $dG_n(\tau)/d\tau$ at the walls, which turn out to be

$$\left[\frac{dG_n(\tau)}{d\tau}-\frac{1}{\mu_n}G_n(\tau)\right]_{\tau=0}=a_1\Omega_0(0)q(0) \tag{25}$$

and

$$\left[\frac{dG_n(\tau)}{d\tau}+\frac{1}{\mu_n}G_n(\tau)\right]_{\tau=\tau_0}=a_1\Omega_0(\tau_0)q(\tau_0) \tag{26}$$

Substituting q_n from Eq. (20) into Eq. (19) and using Eq. (9), the net heat flux is obtained.

$$q(\tau)=\frac{1}{1-a_1\Omega_0(\tau)\sum_{n=1}^{N} w_n\mu_n^2}\left\{f_2(\tau)-\sum_{n=1}^{N} w_n\mu_n^2\frac{dG_n(\tau)}{d\tau}\right\} \tag{27}$$

For $a_1=0$, integral equations, Eqs. (6) and (13), and the SK_N equations, Eqs. (24) and (27), are reduced to those for isotropic scattering [5].

4 Results and Discussion

4.1 Benchmark Problems. Three benchmark problems, labeled as 1, 2, and 3, which have been set for the testing of the SK_N method in isotropically scattering medium [5] were also used in this study for both forward $(a_1=1)$ and backward scattering $(a_1=-1)$ cases with the exception of benchmark problem 1. In benchmark problem 1, as the boundary conditions remain the same, only constant albedo cases of $\Omega_0=0.5$ and $\Omega_0=0.995$ for medium with optical thickness of $\tau_0=1$ are considered to test the method in scattering medium. Thus, most of the benchmark details are omitted here. The hemispherical reflectivity (R) and transmissivity (Γ) [5] are computed and compared with the results those of the exact, S_{128} and P_{11} solutions. The term error throughout this paper will be used to refer to the relative percent error of reflectivity or transmissivity with respect to their exact solutions.

4.2 Numerical Solution Techniques. The coupled integral equations, Eqs. (6) and (13), are solved using ‘‘subtraction of singularity’’ technique [8] on the first integral of Eq. (6) which has a singularity at $\tau=\tau'$. The numerical integration and solution scheme are basically the same as described in Ref. [5]. The system of linear equations is constructed to contain both integral equations leading to $2\times NG$ unknowns and a $(2\times NG)\times(2\times NG)$ square matrix, where NG is the number of grids used. If the walls are black, the integral equation solution is obtained with a single step. However, in the case of gray walls, the following iterative procedure is used: (i) an initial estimate is made for the incident energy and the net heat flux, (ii) intensities at the boundaries are computed from Eqs. (A4) and (A6), (iii) Eqs. (6) and (13) are solved for incident energy and net heat flux, (iv) the source terms, Eqs. (8) and (9), are updated before computing the wall intensities, and the procedure is repeated until the maximum relative error in the computed quantities meets the criterion $\xi<10^{-6}$.

The numerical solution of the SK_N equations, along with P_{11} and S_{128}, is given in Ref. [5]. The only difference between the linearly anisotropic and isotropic SK_N equations is limited with the right hand side of Eq. (24) and boundary conditions—Eqs. (25) and (26). Thus the same iterative algorithm also can be used.

4.3 Memory Requirements and Computation Time. The basic memory requirement to store resulting system of coupled integral equations becomes $4\times NG\times(NG+1)$; on the other hand, the memory requirements for the S_N, P_N, and SK_N equations remain the same as outlined for isotropic scattering treatments [5].

This study was carried out on a Pentium III 667 MHz processor with 128Mb RAM. The number of grids ranging from 50 to 800 are considered to ensure grid independence of the presented solutions. In Table 1, a comparison of the computed transmissivity and computational times (cpu seconds) obtained using the exact, P_{11}, S_{128}, and SK_N (with Set-1) approximations up to the fifth order are given for Case 1 of benchmark problem 2 with forward scattering. A comparison for the number of grids indicate that the exact and S_{128} solutions with 200 grids are the same with 800 grids, while relative errors of less than 0.002 percent with 200 grids is observed for other approximations. Therefore, the grid configuration of 200 was chosen to be the optimum for all the methods used.

For the number of grids of 100 to 800, computational times of the exact solution are 2.14, 19.72, 149.1, and 1129.3 sec, respec-

Table 1 Comparisons of grid sensitivity and computational time (CPU seconds) for Case 1

	Number of grids used									
	50		100		200		400		800	
Method	Γ	CPU (sec)	Γ	CPU (sec)	Γ	CPU (sec)	Γ	CPU (sec)	Γ	CPU (sec)
Exact	0.370286	0.33	0.370276	2.14	0.370273	19.72	0.370273	149.1	0.370273	1129.3
S_{128}	0.370251	0.44	0.370263	0.89	0.370266	2.34	0.370266	7.14	0.370266	14.35
P_{11}	0.370371	0.02	0.370298	0.03	0.370280	0.05	0.370279	0.11	0.370278	0.18
SK_1	0.366939	0.02	0.366924	0.04	0.366923	0.07	0.366924	0.11	0.366924	0.22
SK_2	0.370307	0.04	0.370295	0.07	0.370294	0.12	0.370295	0.23	0.370296	0.50
SK_3	0.370208	0.06	0.370196	0.10	0.370196	0.18	0.370197	0.35	0.370197	0.73
SK_4	0.370261	0.07	0.370249	0.12	0.370248	0.23	0.370249	0.48	0.370249	0.97
SK_5	0.370284	0.08	0.370272	0.14	0.370271	0.29	0.370272	0.59	0.370273	1.21

tively. Similarly, the cpu times for S_{128} are 0.89, 2.34, 7.14, and 14.35, while for the P_{11} the values result in 0.03, 0.05, 0.11 and 0.18 seconds, for 100 to 800 grids respectively. In the SK_N approximation, the cpu times for 200 grids are 0.07, 0.12, 0.18, 0.23, and 0.29 seconds while these figures for 800 grids are 0.22, 0.50, 0.73, 0.97, and 1.21 seconds, for $N=1$ through 5, respectively. A comparison of the cpu times with those of the other methods for 800 grids clearly indicate that the cpu time with SK_5 approximation yields 1.21 seconds, making even the SK_5 approximation cpu time-wise superior to S_{128} with 14.35 sec and the exact method with 1129.3 sec.

4.4 The SK_N Approximation in Homogeneous Medium. In Table 2, the reflectivity and transmissivity solutions of benchmark problem 1 with the exact integral equation, S_{128}, P_{11}, and the SK_N method up to the fourth order for $\Omega_0=0.5$ and $\Omega_0=0.995$ for backward and forward scattering cases are given. The errors with the S_{128} approximation is on the order of 0.02 percent or below resulting in 3–4 decimal places accurate solutions in both reflectivity and transmissivity. On the other hand, the maximum errors with the P_{11} solution, occurring in reflectivity, are on the order of 1 percent and 0.1 percent for $\Omega_0=0.5$ and $\Omega_0=0.995$, respectively.

The maximum errors with the SK_1 approximation turn out to be in the reflectivity as well, while the errors in the transmissivities are on the order of 1 percent. The maximum errors for $\Omega_0=0.5$ are 2.55 percent and 4.52 percent with Set-1, 0.44 percent and 1.04 percent with Set-2, and 3.28 percent and 5.92 percent with Set-3, each figure given for backward and forward scattering cases, respectively. The solutions with Set-2 are competing with the P_{11} solutions. Similarly, the maximum errors in the reflectivity for $\Omega_0=0.995$ are 8.53 percent and 11.94 percent, 1.85 percent and 2.98 percent, and 10.82 percent and 15.57 percent, for sets 1

Table 2 Comparison of the reflectivity and transmissivity solutions of benchmark problem 1

Method	$\Omega_0=0.5$				$\Omega_0=0.995$			
	$a_1=-1$		$a_1=1$		$a_1=-1$		$a_1=1$	
	R	Γ	R	Γ	R	Γ	R	Γ
Exact	0.168598	0.278195	0.094689	0.340098	0.508099	0.481988	0.353018	0.637061
S_{128}	0.168612	0.278181	0.094704	0.340082	0.508109	0.481957	0.353032	0.637029
P_{11}	0.167427	0.278463	0.093475	0.340402	0.507880	0.482203	0.352641	0.637434
SK_1	0.164295*	0.275805	0.090405	0.338338	0.464752	0.451708	0.310858	0.605501
	0.169337	0.278888	0.095672	0.336772	0.514166	0.490894	0.355123	0.618045
	0.163063	0.274932	0.089081	0.337842	0.453101	0.441801	0.298070	0.596725
SK_2	0.168451	0.278447	0.094643	0.340135	0.509229	0.485487	0.355145	0.639436
	0.169264	0.278318	0.095343	0.338542	0.512774	0.485020	0.352937	0.625841
	0.168661	0.278061	0.094793	0.339904	0.508594	0.481564	0.353797	0.636236
SK_3	0.168578	0.278166	0.094678	0.340033	0.508484	0.482156	0.353397	0.637108
	0.168976	0.278211	0.095056	0.339269	0.510696	0.483389	0.352787	0.630737
	0.168646	0.278149	0.094750	0.340035	0.508313	0.481829	0.353306	0.636706
SK_4	0.168587	0.278179	0.094674	0.340083	0.508046	0.481863	0.352876	0.636898
	0.168823	0.278183	0.094909	0.339623	0.509606	0.482679	0.352866	0.633346
	0.168624	0.278173	0.094721	0.340066	0.508221	0.481920	0.353146	0.636863

*All the SK_N solutions in each box from top to bottom are given for Set-1, 2, and 3, respectively.

Table 3 Transmissivity and reflectivity results for benchmark problem 2

Method	Case 1				Case 2			
	$a_1=-1$		$a_1=1$		$a_1=-1$		$a_1=1$	
	R	Γ	R	Γ	R	Γ	R	Γ
Exact	0.247211	0.325838	0.203071	0.370273	1.103106	0.994309	1.103144	0.988831
S_{128}	0.247224	0.325831	0.203087	0.370266	1.103054	0.994493	1.103095	0.989025
P_{11}	0.246159	0.325879	0.201988	0.370280	1.103089	0.994294	1.103128	0.988773
SK_1	0.241341[†] 0.248374 0.239564	0.321703 0.326879 0.320307	0.197385 0.202119 0.195597	0.366923 0.367011 0.365926	1.103007 1.103045 1.103001	0.984748 0.988533 0.984209	1.103048 1.103082 1.103043	0.978812 0.982406 0.978247
SK_2	0.247190 0.247989 0.247207	0.326084 0.326198 0.325707	0.203037 0.202832 0.203061	0.370294 0.368812 0.370097	1.103061 1.103103 1.103089	0.989998 0.994036 0.992670	1.103101 1.103139 1.103128	0.984309 0.988318 0.987106
SK_3	0.247175 0.247624 0.247239	0.325801 0.325981 0.325803	0.203013 0.202961 0.203094	0.370196 0.369500 0.370223	1.103088 1.103109 1.103108	0.992630 0.994617 0.994534	1.103128 1.103146 1.103146	0.987065 0.989027 0.989058
SK_4	0.247191 0.247445 0.247228	0.325818 0.325899 0.325823	0.203039 0.203016 0.203080	0.370248 0.369832 0.370246	1.103101 1.103108 1.103108	0.993871 0.994526 0.994517	1.103140 1.103146 1.103146	0.988364 0.988983 0.989040
	Case 3				Case 4			
Exact	0.663086	0.747328	0.655610	0.772745	0.712311	0.818042	0.691440	0.758653
S_{128}	0.663116	0.747331	0.655643	0.772746	0.712174	0.817941	0.691339	0.758558
P_{11}	0.663360	0.746305	0.655920	0.771672	0.711988	0.817864	0.691104	0.758423
SK_1	0.621276 0.667518 0.637162	0.716246 0.750412 0.728003	0.612713 0.650778 0.629035	0.744771 0.768484 0.755294	0.698197 0.700175 0.609920	0.804502 0.806442 0.726182	0.671864 0.670844 0.558039	0.742494 0.742529 0.604450
SK_2	0.659976 0.666400 0.663090	0.745144 0.749543 0.747226	0.652355 0.651830 0.655540	0.770682 0.769567 0.772590	0.712256 0.713025 0.711506	0.819325 0.819797 0.818788	0.690490 0.690176 0.689572	0.756439 0.756316 0.755895
SK_3	0.664017 0.665347 0.663124	0.748063 0.748814 0.747301	0.656471 0.652826 0.655572	0.773328 0.770450 0.772665	0.712711 0.712794 0.712702	0.819644 0.819701 0.819642	0.690882 0.690732 0.690876	0.756740 0.756663 0.756737
SK_4	0.663316 0.663594 0.663119	0.747506 0.747635 0.747330	0.655755 0.654883 0.655563	0.772847 0.772147 0.772693	0.712711 0.712726 0.712711	0.819650 0.819659 0.819650	0.690884 0.690851 0.690884	0.756746 0.756730 0.756748

[†] All the SK_N solutions in each box from top to bottom are given for Set-1, 2, and 3, respectively.

through 3, respectively. The errors, including the transmissivity data, always yield higher values in the forward scattering case in comparison to backward scattering cases. In SK_1 approximation, the results using Set-2 are superior to Set-1 and Set-3.

The maximum errors with the SK_2 approximation, for $\Omega_0=0.5$, using Set-1 and Set-3 are reduced drastically. The errors for both the reflectivity and the transmissivity are below 0.09 percent and 0.11 percent for Set-1 and Set-3, respectively. Similarly, the errors for $\Omega_0=0.995$ are reduced significantly with Set-1, Set-2, and Set-3 yielding the maximum errors 0.73 percent, 0.92 percent, and 0.22 percent, respectively. The convergence of the SK_2 approximation to the exact solutions with Set-1 and Set-3 are sharper than those obtained with Set-2. While the magnitude of the errors with Set-1 and Set-3 are almost identical for $\Omega_0=0.5$, for $\Omega_0=0.995$, in mostly scattering medium, Set-3 exhibits better performance.

The SK_3 solutions with Set-1 and Set-3 converge the exact solutions better than those with Set-2. The solutions with Set-1 and Set-3 are competing with each other yielding the maximum errors, for $\Omega_0=0.5$, 0.02 percent and 0.06 percent, and for $\Omega_0=0.995$, 0.11 percent and 0.08 percent, respectively. The maximum errors, on the other hand, with Set-2 are 0.39 percent and 0.99 percent, for $\Omega_0=0.5$ and $\Omega_0=0.995$, respectively. The magnitude of the errors with Set-1 and Set-3 are almost identical for $\Omega_0=0.995$ while for $\Omega_0=0.5$ using Set-1 is slightly better than using Set-3.

The maximum errors with the SK_4 approximation using Set-1 and Set-3 for both albedo solutions are below 0.04 percent while up to 0.58 percent errors are observed with Set-2. The magnitude of the maximum errors with Set-1 and Set-3 are almost identical.

In Table 3, the computed reflectivity and transmissivity solutions of benchmark problem 2 are tabulated. The reflectivity and transmissivity solutions obtained with the SK_N approximation are compared with the exact, S_{128} and P_{11} solutions. The solutions

Table 4 Transmissivity and reflectivity results for linearly varying albedo cases

Method	$\Omega_0(\tau)=0.2+0.6\tau$				$\Omega_0(\tau)=0.8-0.6\tau$			
	$a_1=-1$		$a_1=1$		$a_1=-1$		$a_1=1$	
	R	Γ	R	Γ	R	Γ	R	Γ
Exact	0.114744	0.280707	0.061266	0.342150	0.232790	0.280707	0.137797	0.342150
S_{128}	0.114748	0.280690	0.061272	0.342135	0.232812	0.280694	0.137821	0.342135
SK_1	0.112741‡	0.277181	0.059121	0.339154	0.222146	0.277175	0.127474	0.339159
	0.115812	0.281100	0.062286	0.338715	0.232207	0.281116	0.137595	0.338670
	0.111946	0.276202	0.058227	0.338509	0.220034	0.276195	0.125172	0.338514
SK_2	0.114928	0.280876	0.061445	0.342101	0.231704	0.280869	0.137008	0.342107
	0.115245	0.280814	0.061703	0.340629	0.233744	0.280820	0.138598	0.340583
	0.114836	0.280599	0.061373	0.341967	0.232796	0.280591	0.137901	0.341973
SK_3	0.114779	0.280715	0.061291	0.342107	0.232699	0.280707	0.137766	0.342112
	0.115023	0.280721	0.061509	0.341337	0.233334	0.280721	0.138243	0.341309
	0.114781	0.280669	0.061307	0.342084	0.232856	0.280662	0.137882	0.342089
SK_4	0.114742	0.280702	0.061257	0.342134	0.232780	0.280694	0.137790	0.342139
	0.114910	0.280698	0.061410	0.341682	0.233114	0.280694	0.138065	0.341667
	0.114764	0.280692	0.061285	0.342114	0.232827	0.280684	0.137842	0.342119

‡All the SK_N solution in each box from top to bottom are given for Set-1, 2, and 3, respectively.

with the S_{128} approximation yields in 3–4 decimal places accurate solutions with the maximum error of 0.02 percent in all the cases. On the other hand, in P_{11} approximation, the maximum errors are for Case 1, 0.43 percent and 0.53 percent, for Case 2, 0.01 percent, for Case 3, 0.14 percent, and for Case 4, 0.05 percent. This outcome is expected since the P_N approximations yielded good results in mostly scattering medium and/or optically thick systems.

In Case 1, the maximum errors, for Set-1 through 3, are 2.80 percent, 0.88 percent, 3.68 percent for SK_1, 0.08 percent, 0.39 percent, 0.05 percent for SK_2, 0.03 percent, 0.21 percent, 0.01 percent for SK_3 and 0.02 percent, 0.12 percent, 0.01 percent for SK_4. The results of SK_2 approximation using Set-1 and 3, are better than P_{11} and competing with those of S_{128}. The superiority of using Set-2 is limited to SK_1 approximation. On the other hand, the errors with Set-1 and 3 for $N \geqslant 2$ are equivalent to those obtained with S_{128}, and Set-3 solutions are slightly better than Set-1. The maximum errors in SK_1 and SK_2 approximations are in the reflectivity values of forward scattering case.

In Case 2, the maximum errors for Set-1 through 3 are 1.01 percent, 0.65 percent, 1.07 percent for SK_1, 0.46 percent, 0.05 percent, 0.17 percent for SK_2, 0.18 percent, −0.03 percent, 0.02 percent for SK_3 and 0.05 percent, 0.02 percent, 0.02 percent for SK_4. In SK_2 approximation using Set-2 yields solutions that compete with S_{128} approximation, and as the order of SK_N approximation is increased, the magnitude of the errors become identical to those of P_{11} solutions. The superiority of using Set-2 in SK_1 and SK_2 approximations is clear. However, as the order of approximation is increased Set-2 and Set-3 become competitive with Set-3 having a slight edge over the other sets. The maximum errors in SK_1 and SK_2 approximations are observed to be in the transmissivity values.

In Case 3, the maximum errors for Set-1 through 3 are 6.54 percent, 0.74 percent, 4.05 percent for SK_1, 0.50 percent, 0.58 percent, 0.02 percent for SK_2, −0.13 percent, 0.42 percent, 0.01 percent for SK_3 and 0.03 percent, 0.11 percent, 0.02 percent for SK_4. The SK_2 approximation using Set-3 produces results that are competing with those of S_{128} and P_{11}. Using Set-1 and 3 in the SK_N approximations of orders of $N \geqslant 2$ yields the exact solutions faster than Set-2, Set-3 being the best. On the other hand, Set-2 does well only in the SK_1 approximation. The large errors that are observed in SK_1 and SK_2 approximations are mostly in the reflectivity values, but the magnitude of the transmissivity errors are nearly those of reflectivities.

In Case 4, the maximum errors are observed in the reflectivity values of forward scattering case, and these errors for Set-1 through 3 are 2.83 percent, 2.98 percent, 20.33 percent for SK_1, 0.29 percent, 0.41 percent, 0.36 percent for SK_2, 0.25 percent, 0.30 percent, 0.25 percent for SK_3 and 0.25 percent for all sets for SK_4. The maximum errors with S_{128} and P_{11} approximations are 0.02 percent and 0.05 percent, respectively. Here, the SK_1 approximation with Set-1 yields slightly better results than with Set-2 and 3; however, as the order of the approximation is increased, the magnitude of the errors with all sets become identical. This is an expected trend since quadrature sets for optically thick limit case yield Set-1. The maximum errors of transmissivity and reflectivity are on the same order.

4.5 The SK_N Approximation in Inhomogeneous Medium. In Table 4, results for the reflectivity and transmissivity results using the SK_N approximation of up to the fourth order, along with S_{128}, for the cases of linearly varying scattering albedo are given. The discrete ordinates S_{128} solutions result in errors of less than 0.02 percent for all the cases considered. The maximum errors, in the approximations used, are observed in the computation of the reflectivity values, mostly in forward scattering cases. The maximum errors are registered in the $\Omega_0(\tau)=0.8-0.6\tau$ case which are for the SK_1 approximation are 7.49 percent, 1.66 percent, and 9.16 percent, using the Set-1, 2, and 3, respectively. The maximum errors are reduced to 0.57 percent, 0.71 percent, and 0.17 percent in SK_2; 0.04 percent, 0.40 percent, and 0.07 percent in SK_3; 0.01 percent, 0.24 percent, and 0.03 percent in SK_4, for sets 1, 2, and 3, respectively. The maximum errors in the $\Omega_0(\tau)=0.2+0.6\tau$ case are about half of those obtained from $\Omega_0(\tau)=0.8-0.6\tau$ case. The superiority of using Set-2 is again limited with the SK_1 approximation. As the order of the SK_N approximation is increased, the results of both albedo alternatives with Set-1 and Set-3 converge the exact solution faster than those with Set-2; and Set-1 and Set-3 yield identical error magnitudes with Set-1 being slightly better than Set-3.

In Table 5, a comparison of the results of the reflectivity and transmissivity for quadratically varying albedo cases is given. In

Table 5 Transmissivity and reflectivity results for quadratically varying albedo cases

Method	$\Omega_0(\tau)=0.4-0.2\tau+0.6\tau^2$				$\Omega_0(\tau)=1-1.4\tau+0.6\tau^2$			
	$a_1=-1$		$a_1=1$		$a_1=-1$		$a_1=1$	
	R	Γ	R	Γ	R	Γ	R	Γ
Exact	0.137407	0.279354	0.075084	0.341487	0.264968	0.282794	0.160394	0.344294
S_{128}	0.137418	0.279339	0.075095	0.341470	0.264991	0.282779	0.160421	0.344279
SK_1	0.134877[§]	0.27651	0.072488	0.339194	0.249634	0.278349	0.145612	0.340303
	0.138209	0.279748	0.075954	0.337723	0.262736	0.282780	0.158548	0.340264
	0.133989	0.275617	0.071491	0.338688	0.247046	0.277311	0.142819	0.339595
SK_2	0.137357	0.279413	0.075055	0.341294	0.262761	0.282702	0.158633	0.343974
	0.137957	0.279504	0.075605	0.339908	0.266076	0.282934	0.161197	0.342673
	0.137447	0.279203	0.075146	0.341263	0.264809	0.282657	0.160386	0.344091
SK_3	0.137369	0.279299	0.07504	0.341383	0.264694	0.282768	0.160229	0.344226
	0.137719	0.279384	0.075376	0.340645	0.265606	0.282819	0.160839	0.343418
	0.137449	0.279315	0.075132	0.341421	0.265045	0.282749	0.160490	0.344235
SK_4	0.137396	0.279349	0.075066	0.341472	0.264945	0.282787	0.160383	0.344288
	0.137593	0.279353	0.075258	0.341004	0.265348	0.282787	0.160663	0.343790
	0.137431	0.279339	0.075108	0.341452	0.265013	0.282771	0.160445	0.344265

[§] All the SK_N solutions in each box from top to bottom are given for Set-1, 2, and 3, respectively.

this case, too, the S_{128} solutions result in maximum errors of less than 0.02 percent. The maximum errors are recorded in reflectivity values of the $\Omega_0(\tau)=1-1.4\tau+0.6\tau^2$ case which in SK_1 approximation are 9.22 percent, 1.17 percent and 10.96 percent, for Set-1 through Set-3, respectively. The maximum errors are, respectively for sets 1, 2, and 3, reduced to 1.10 percent, 0.68 percent, 0.12 percent in SK_2; 0.10 percent, 0.28 percent, 0.06 percent in SK_3 and 0.02 percent, 0.17 percent, 0.03 percent in SK_4 approximations. The SK_1 and SK_2 approximations with Set-2 is superior in comparison to solutions with other sets. The maximum errors in $\Omega_0(\tau)=0.4-0.2\tau+0.6\tau^2$ case are about one-third or better of those obtained from $\Omega_0(\tau)=1-1.4\tau+0.6\tau^2$ case. The SK_4 solutions using Set-3 results in the same order of magnitude errors with those obtained with S_{128}. In SK_2 approximation while Set-1 yields slightly better results than Set-3, in the $\Omega_0(\tau)=0.4-0.2\tau+0.6\tau^2$ case, Set-3 shows better performance than Set-1 in the $\Omega_0(\tau)=1-1.4\tau+0.6\tau^2$ case. However, as order of the approximation is increased, both sets yield identical order of magnitude errors.

In Table 6, the reflectivity and transmissivity solutions for exponentially varying albedo cases are tabulated. Similarly, the S_{128} solutions yield the maximum errors of less than 0.02 percent. The maximum errors are recorded in reflectivity values of the $\Omega_0(\tau)=0.790988\exp(-\tau)$ case which in SK_1 approximation are 7.0 percent, 1.48 percent, and 8.6 percent, for Set-1 through Set-3, respectively. These errors are reduced to 0.71 percent, 0.59 per-

Table 6 Transmissivity and reflectivity results for exponentially varying albedo cases

Method	$\Omega_0(\tau)=0.790988\exp(-\tau)$				$\Omega_0(\tau)=0.790988\exp[-(1-\tau)]$			
	$a_1=-1$		$a_1=1$		$a_1=-1$		$a_1=1$	
	R	Γ	R	Γ	R	Γ	R	Γ
Exact	0.223302	0.279867	0.131211	0.341643	0.125954	0.279867	0.068013	0.341643
S_{128}	0.223324	0.279855	0.131236	0.341629	0.125961	0.279851	0.068020	0.341625
SK_1	0.213809[**]	0.276746	0.122028	0.339084	0.123773	0.276753	0.065726	0.339079
	0.222778	0.280312	0.131089	0.338056	0.126948	0.280297	0.069018	0.338096
	0.211883	0.275814	0.119924	0.338512	0.122934	0.275821	0.064782	0.338507
SK_2	0.224193	0.279997	0.131997	0.340056	0.126480	0.279992	0.068494	0.340097
	0.222255	0.279995	0.130432	0.341551	0.126058	0.280003	0.068124	0.341547
	0.223274	0.279730	0.131274	0.341445	0.126028	0.279737	0.068104	0.341441
SK_3	0.223173	0.279837	0.131134	0.341575	0.125961	0.279845	0.068011	0.341571
	0.223814	0.279887	0.131652	0.340793	0.126249	0.279888	0.068281	0.340818
	0.223365	0.279821	0.131292	0.341582	0.125993	0.279828	0.068058	0.341577
SK_4	0.223283	0.279853	0.131195	0.341631	0.125948	0.279861	0.068000	0.341627
	0.223607	0.279857	0.131477	0.341156	0.126130	0.279861	0.068173	0.341169
	0.223338	0.279844	0.131255	0.341612	0.125976	0.279851	0.068034	0.341608

[**] All the SK_N solutions in each box from top to bottom are given for Set-1, 2, and 3, respectively.

Table 7 Transmissivity and reflectivity results for cosine oscillation albedo cases

Method	$\Omega_0(\tau)=0.5+0.5\tau\cos 12\pi\tau$				$\Omega_0(\tau)=0.5+0.5(1-\tau)\cos 12\pi(1-\tau)$			
	$a_1=-1$		$a_1=1$		$a_1=-1$		$a_1=1$	
	R	Γ	R	Γ	R	Γ	R	Γ
Exact	0.168294	0.278679	0.094607	0.340686	0.172845	0.278679	0.098045	0.340686
S_{128}	0.168282	0.278620	0.094592	0.340620	0.172825	0.278620	0.098013	0.340622
SK_1	0.163785[††]	0.275927	0.090130	0.338531	0.167739	0.275943	0.092977	0.338524
	0.168840	0.279038	0.095308	0.336889	0.172825	0.279053	0.098127	0.336861
	0.162557	0.275053	0.088767	0.338040	0.166504	0.275071	0.091601	0.338033
SK_2	0.167948	0.278573	0.094331	0.340328	0.171918	0.278592	0.097199	0.340323
	0.168849	0.278599	0.095092	0.338846	0.173041	0.278618	0.098116	0.338813
	0.168192	0.278244	0.094523	0.340161	0.172228	0.278262	0.097449	0.340154
SK_3	0.168110	0.278348	0.094407	0.340288	0.172149	0.278366	0.097337	0.340283
	0.168655	0.278660	0.094932	0.339787	0.173223	0.278679	0.098311	0.339762
	0.168292	0.278536	0.094615	0.340518	0.172733	0.278554	0.097903	0.340512
SK_4	0.168161	0.278436	0.094454	0.340422	0.172338	0.278455	0.097507	0.340417
	0.168501	0.278633	0.094795	0.340157	0.173105	0.278651	0.098215	0.340140
	0.168304	0.278622	0.094623	0.340620	0.172911	0.278641	0.098059	0.340614

[††] All the SK_N solutions in each box from top to bottom are given for Set-1, 2, and 3, respectively.

cent, 0.13 percent in SK_2; 0.06 percent, 0.39 percent, 0.07 percent in SK_3 and 0.02 percent, 0.24 percent, 0.03 percent in SK_4, for sets 1 through 3, respectively. The maximum errors in the $\Omega_0(\tau)=0.790988\exp[-(1-\tau)]$ case are about half of those obtained from $\Omega_0(\tau)=0.790988\exp(-\tau)$ case. In both albedo cases, the superiority of Set-2 in SK_1 approximation remains unchallenged. However, in SK_2 approximation, Set-3 performs well in both exponential albedo cases, while higher order SK_N approximations indicate that the magnitude of the errors with Set-1 and Set-3 are identical.

In Table 7, the solutions and the errors for cosine oscillation albedo cases are tabulated. The S_{128} solutions yield the maximum errors less than 0.02 percent. The maximum errors are observed mostly in reflectivity values of the $\Omega_0(\tau)=0.5+0.5(1-\tau)\cos 12\pi(1-\tau)$ case with forward scattering which in SK_1 approximation yields errors of 5.17 percent, 1.12 percent, and 6.57 percent, for Set-1 through Set-3 respectively, making Set-2 superior to other sets. In SK_2 approximation, the maximum errors for Set-1, 2, and 3 are 0.86 percent, 0.61 percent, and 0.55 percent. These errors are further reduced to 0.72 percent, 0.34 percent, 0.14 percent in SK_3 and 0.39 percent, 0.20 percent, 0.04 percent in SK_4 approximations, for Set-1, 2, and 3, respectively. The SK_1 approximation for both albedo cases yield the same error of magnitude. However, for higher order approximations the maximum errors in the $\Omega_0(\tau)=0.5+0.5\tau\cos 12\pi\tau$ case are about one-third or better of those obtained from $\Omega_0(\tau)=0.5+0.5(1-\tau)\cos 12\pi(1-\tau)$ case. In the $\Omega_0(\tau)=0.5+0.5\tau\cos 12\pi\tau$ case, higher order SK_N approximations using Set-3 yields the exact solution faster; on the other hand, in the $\Omega_0(\tau)=0.5+0.5(1-\tau)\cos 12\pi(1-\tau)$ case Set-2 and Set-3 solutions compete with each other.

4.6 Error Assessment of the Synthetic Kernels. It was shown that the Synthetic Kernel for $E_1(x)$, though it fails at the singular point $x=0$ for all quadrature sets, oscillates around the correct value as it converges to $E_1(x)$ for increasing x. As the order of the approximation is increased the magnitude of the oscillations are reduced. While the integral of the approximation error for $E_1(x)$ over the optical domain is zero in Set-2 and 3, using Set-1, it approaches to zero with increasing N [5]. Since the derivation of SK_N equations for linearly anisotropically scattering case requires the use of three synthetic kernels for $E_1(x)$, $E_2(x)$, and $E_3(x)$, the error in the SK_N approximation consists of the errors made with all three synthetic kernels. Furthermore, as the exact spatial moments of $E_1(x)$ are preserved with Set-2 and 3, the exact spatial moments of $E_2(x)$ and $E_3(x)$ and their synthetic approximations are not necessarily preserved with either set.

To better understand the error sources in the SK_N approximation, it is appropriate and more meaningful to examine the first (zeroth) moments of the exponential integral functions involved over the optical domain. For that reason, we define the following error term—which gives the integrated errors within the computational domain:

$$e_m(\tau_0)=\int_0^{\tau_0}\left(E_m(x)-\sum_{n=1}^{N} w_n\mu_n^{m-2}e^{-x/\mu_n}\right)dx, \quad \text{for } m=1,2,3 \tag{28}$$

or, Eq. (28) after integration yields

$$e_m(\tau_0)=\frac{1}{m}-E_{m+1}(\tau_0)+\sum_{n=1}^{N} w_n\mu_n^{m-1}(e^{-\tau_0/\mu_n}-1) \tag{29}$$

Figure 1 depicts, as a function of optical thickness, the variation of $e_m(\tau_0)$, for $m=1$, 2, and 3, by one-term Synthetic Kernel approximations using Set-1, 2, and 3. In deriving Set-2 and 3, the first moment was, $e_1(\tau_0)$, zero [5]; thus, $e_1(\tau_0)$ for Set-2 and 3 is not shown in Fig. 1. It is seen that $e_1(\tau_0)$ for the approximation with Set-1 is predictably not zero, and it has the largest peak value of 0.1 at $\tau_0=0.15$. As it crosses zero ordinate at $\tau_0=0.82$, it reaches the minimum value of -0.023 at $\tau_0=1.5$. It then asymptotically approaches to zero. On the other hand, $e_2(\tau_0)$ decreases to the minimum value of -0.043 at $\tau_0=0.8$, then it converges to zero for increasing τ_0, while $e_3(\tau_0)$ steadily increases up to $\tau_0\approx 3$ where it converges to the value of 0.083. With Set-2 and Set-3, $e_2(\tau_0)$ reaches a maximum value of 0.11 at about $\tau_0=0.6$ then steadily declines and converges to zero at about $\tau_0\approx 6$. While $e_3(\tau_0)$ goes through the maximum value of 1.5 about $\tau_0=1$, and steadily converges to 0.083. However, $e_2(\tau_0)$ with Set-3, for increasing optical path diverges from zero instead converges to the value of -0.28 at $\tau_0=8$, while $e_3(\tau_0)$ reaches its maximum value of 0.034 at $\tau_0=0.4$ and then decreases steadily up to $\tau_0=8$.

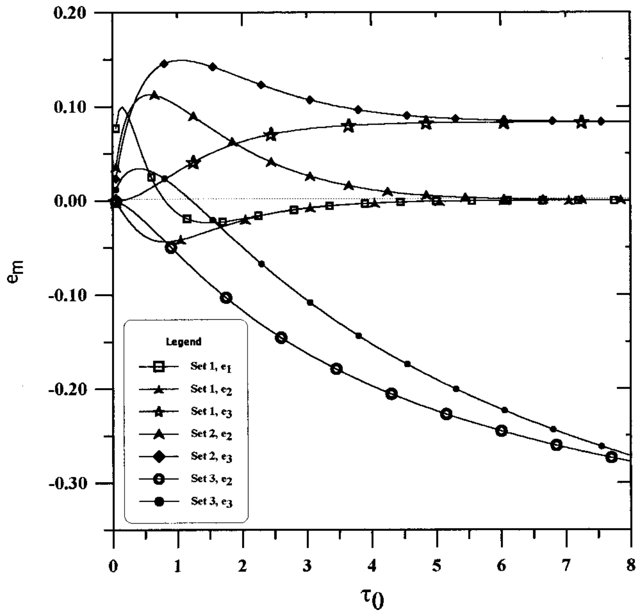

Fig. 1 Variation of e_m as a function optical thickness using one-term synthetic kernels with Set-1, 2, and 3 quadratures

Figure 2 depicts as a function of optical thickness the variation of $e_m(\tau_0)$, for $m=1$, 2 and 3, by two-term Synthetic Kernel approximations. In comparison to one-term approximations (Fig. 1), the magnitudes of $e_m(\tau_0)$ are reduced dramatically. For the same reason explained previously, $e_1(\tau_0)=0$ for Set-2 and 3. However, it turns out that for Set-3 $e_2(\tau_0)$ is also zero for $N\geqslant 2$. This outcome is not surprising; recalling $\Sigma_n w_n=1$ condition that was additionally imposed along with the $(2N-2)$ spatial moments, we set $m=1$ in Eq. (29) to obtain

$$e_1(\tau_0)=1-E_2(\tau_0)+\sum_{n=1}^{N} w_n e^{-\tau_0/\mu_n}-\sum_{n=1}^{N} w_n \tag{30}$$

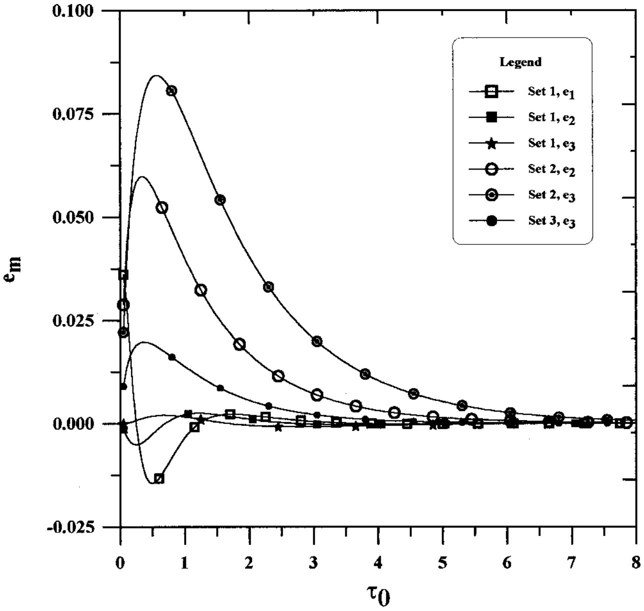

Fig. 2 Variation of e_m as a function optical thickness using two-term synthetic kernel with Set-1, 2, and 3 quadratures

When Eq. (30) is set to zero, Eq. (15) for $m=2$ is obtained. For Set-1, $e_1(\tau_0)$ declines sharply to a minimum value of -0.014 at $\tau_0=0.5$ where it proceeds to increase to the maximum value of 0.0023 at $\tau_0=1.75$ as it intersects zero ordinate at $\tau_0=1.23$. On the other hand, as $e_2(\tau_0)$ goes to the minimum value of -0.0051 at $\tau_0=0.25$ then it increases to its maximum value 0.0025 at $\tau_0=1.2$ followed by steady decline to $\tau_0=3.15$ where it is converges to zero. While $e_3(\tau_0)$ slightly increases to its maximum value of 0.0025 at $\tau_0=1.2$, then it steadily converges to zero for $\tau_0>3$. For Set-2, $e_2(\tau_0)$ has a large peak with the maximum value of 0.06 at $\tau_0=0.35$, then it declines to zero at $\tau_0=7.5$. And $e_3(\tau_0)$ exhibits similar shape as it reaches to its maximum value of 0.084 at $\tau_0=0.55$ followed a steady decline. For Set-3, $e_1(\tau_0)=e_2(\tau_0)=0$ while $e_3(\tau_0)$ has a maximum value of 0.02 at $\tau_0=0.35$ as it decreases steadily while converging to zero for $\tau_0>4$. Set-1 still has three major error components, as $e_1(\tau_0)$ exhibits sharp changes for $\tau_0<1.5$, $e_2(\tau_0)$ and $e_3(\tau_0)$ remain relatively stable in this interval, but for $\tau_0>4$ for $m=1$, 2 and 3, $e_m(\tau_0)\rightarrow 0$. Set-2, on the other hand, with two error components yields small errors in magnitude only for $\tau_0<0.25$ and in $0.25<\tau_0<4$ interval both components exhibit largest errors among the sets with two-point approximations as they approach zero for larger τ_0. Set-3, this time, has only $e_3(\tau_0)$ an error component which is relatively large for $\tau_0<1.5$; however, for $\tau_0>1.5$ its magnitude is reduced significantly.

As the order of SK_N approximation is increased, the order of magnitude of not only the integrals defined by Eq. (28) but also for the spatial moments of the exponential integral functions, which exhibit similar features, are reduced. But the SK_N approximation as it is applied to RITE does not ensure the exact integrals of the transfer kernels over the given domain; it yields two integrals over different intervals [5]. Since the radiative integral transfer equations are coupled integral equations, the nature of the error assessment also gets a bit complicated. Thus this part of the discussion especially for SK_1 approximation gives a relative idea about the magnitude of the errors that arise. If the source terms are nearly constant over the domain, we can relatively use Fig. 1 and 2 in determining the best quadrature set for a given optical thickness. Otherwise, especially in optically thin medium, where the errors are affected strongly by the magnitude and the behavior of the source terms near the singularity which requires higher order spatial moments to be satisfied, Fig. 1 and 2 should be accompanied by similar figures and analysis for the higher order moments. In view of the integrals and their magnitudes in Eqs. (6) and (13), we can state that three error components and those of the spatial moments have the following order of importance: $|e_1(\tau_0)|>|e_2(\tau_0)|>|e_3(\tau_0)|$ in the overall error assessment.

In Fig. 1, since $e_1(\tau_0)$ and $e_2(\tau_0)$ go to zero for $\tau_0>3$ and $e_3(\tau_0)$ converging the same value, Set-1 and Set-2 can be expected to give better solutions with one-term approximations. When we inspect the errors of benchmark problem 2, Case 4, we find that indeed Set-1 results are slightly better Set-2. For optically very thin medium, Case 2, the error components of Set-2 and 3 are very small, but the performance of Set-2 is better. Set-3, for various optical thicknesses, with large deviating $e_2(\tau_0)$ and $e_3(\tau_0)$ components does not seem to be appropriate in comparison to the other sets. Similarly, in Case 3, on the magnitude scale Set-2 and 3 seem to be equivalent, but the performance of Set-2 is better. For $\tau_0=1$, using one-term synthetic kernels, the integrated errors are $e_1(1)=-0.013$, $e_2(1)=-0.042$, and $e_3(1)=0.031$ for Set-1, $e_1(1)=0$, $e_2(1)=0.1012$, and $e_3(1)=0.15$ for Set-2 and $e_1(1)=0$, $e_2(1)=-0.056$, and $e_3(1)=0.013$ for Set-2 which these alone are not very conclusive. However, the inspection of the second spatial moments reveal that Set-2 should do better than the others since it satisfies two of the spatial moments. For that reason, it is believed that in almost all the cases, SK_1 approximation using Set-2 showed better performance.

As shown in Fig. 2, two-term synthetic kernels, for Set-1, though the magnitudes of $e_1(\tau_0)$ and $e_2(\tau_0)$ are fairly large compared to $e_3(\tau_0)$, all three of them converge zero for $\tau_0>4$ where it is expected to perform better. While $e_1(\tau_0)=0$ in Set-2, $e_2(\tau_0)$, and $e_3(\tau_0)$ are very large in the interval $0.2<\tau_0<6$, which indicate that only outside the interval reasonable solutions can be expected. Set-3, since $e_1(\tau_0)=e_2(\tau_0)=0$ is more likely to give the best performance in SK_2 approximation. The integrated errors for $\tau_0=1$ with two-term synthetic kernels, we have $e_1(1)=-0.0034$, $e_2(1)=0.0022$ and $e_3(1)=0.0016$ for Set-1, $e_1(1)=0$, $e_2(1)=0.04$ and $e_3(1)=0.074$ for Set-2 and $e_1(1)=e_2(1)=0$ and $e_3(1)=0.014$. These values indicate that the performance of Set-3 should be better than those of Set-1 and 2 with Set-1 being as the second best alternative. Furthermore, the same trend in the second moments are also observed, thus Set-3 in SK_2 approximation emerges as the best choice. In fact in most of the inhomogeneous scattering albedo cases Set-3 was the set that gave the best results in comparison to the others.

5 Conclusion

The SK_N equations for linearly anisotropically scattering inhomogeneous medium are derived and solved. The SK_N solutions are compared with those of exact, S_{128} and P_{11} approximations for homogeneous and inhomogeneous benchmark problems. Also an error assessment strategy is outlined for low order SK_N approximations. The study concludes the following:

1 The SK_N method is memory efficient and computationally very cheap. For the presented benchmark problem, while the cpu time for high order approximation such as SK_5 is 1.21 sec, it is 14.35 seconds for S_{128} and 1129.3 sec for the exact solutions. Additionally, this advantage of the SK_N approximation is maintained for various problems, yielding solutions in 1–2 sec with SK_5 approximation.

2 The accuracy of the SK_N method with any order of approximation basically depends on the requirement that the spatial moments of not only $E_1(x)$ but also $E_2(x)$ and $E_3(x)$ for the real and approximate kernels are satisfied. With strong scattering albedo or source term—$S_0(\tau)$ and $S_1(\tau)$—variations in the medium, low order approximations because of their inability to accurately represent the high order spatial moments will not yield as accurate solutions as higher order approximations. In the benchmark problems considered, the SK_1 approximation using Set-2 produces superior results in comparison to using Set-1 and 3; with errors 1 percent or less for optically thin systems and errors up to 3 percent for optically thick systems. In the SK_2 approximation while Set-1 and 3 yield better results in optically thin medium, Set-1 is slightly better in optically thick medium yielding errors less than 1 percent. For SK_3 approximations, in comparison to the exact solutions using Set-3 yields errors less than 0.6 percent, Set-1 on the order of 1 percent errors following it as the second best choice. With high order SK_N approximations—such as SK_4, solutions better than or comparable to S_{128} and P_{11} approximations are obtained.

3 Scattering albedo affects the accuracy of the approximation since it can amplify the magnitude of the source terms thereby amplifying the magnitude of the errors encountered in low order the SK_N approximations. Thus, the method yields higher errors in mostly scattering media. One way to overcome this problem is to increase the order of the approximation. In the pure absorber limit case, $\Omega_0\rightarrow 0$ and $N\rightarrow\infty$, the Synthetic Kernel formulations given with Eqs. (18) and (19), for any quadrature set, yield the exact integral equations; thus the SK_N approximation solutions become exact solutions.

4 Since three kernels are approximated, the choice of optimum quadrature set becomes an important factor in low order approximations. In this study, an optimum quadrature set selection strategy depending on the integrated errors of the exponential integral functions is outlined. This strategy, though it gives a relative idea, coupled with similar analysis for the spatial moments can be used as an aid in determining the optimum quadrature set for a given optical thickness.

5 The maximum errors in inhomogeneous problems are in the cases where scattering albedo is large near wall 1 where the approximate kernels are grossly inaccurate. These errors, generally showing up in the reflectivity values, are reduced with increasing order of the approximation.

Acknowledgment

The author would like to thank the reviewers for their valuable comments and suggestion that have helped to improve the presented paper.

Nomenclature

$E_n(x)$ = n^{th} order exponential integral function
G = dimensionless incident radiation $(=g/(n^2\sigma T_{\text{ref}}^4/\pi))$
$G_n(\tau)$ = functions defined by Eq. (16)
I = dimensionless radiative intensity $(=i/(n^2\sigma T_{\text{ref}}^4/\pi))$
Q = radiative heat flux
R = the reflectivity defined by Eq. (23)
S = dimensionless anisotropic source function $(=s/(n^2\sigma T_{\text{ref}}^4/\pi))$
$S_0(\tau)$ = source term defined by Eq. (8)
$S_1(\tau)$ = source term defined by Eq. (9)
T = temperature
a_1 = the coefficient of anisotropy
$e_m(x)$ = integrated error for m^{th} order exponential integral functions defined by Eq. (31)
$f_1(\tau)$ = boundary term defined by Eq. (7)
$f_2(\tau)$ = boundary term defined by Eq. (14)
g = incident radiation function
i = radiative intensity
n = refractive index of the medium
s = source function
sgn = the sign function
q = dimensionless radiative heat flux $(=Q/(n^2\sigma T_{\text{ref}}^4/\pi))$
$q_n(\tau)$ = functions defined by Eq. (17)
x = space variable
w_n = quadrature weights

Greek Symbols

Γ = transmissivity
Ω_0 = scattering albedo $(=\kappa/\beta)$
β = extinction coefficient
ε = wall emissivity
κ = absorption coefficient
μ = angular cosine
μ_n = quadrature abscissas
θ = dimensionless temperature $(=T/T_{\text{ref}})$
ρ = diffusive wall reflectivity
σ = Stefan-Boltzmann coefficient
τ = dimensionless optical variable $(=\beta x)$
τ_0 = optical path
ξ = convergence criterion

Subscripts

1 = boundary wall 1
2 = boundary wall 2
n = n^{th} component of the SK_N equation
$-$ = outgoing heat flux or intensity
$+$ = incoming heat flux or intensity

Superscript

$'$ = dummy integration variable

Appendix

The wall intensities can be determined from the formal solutions given by Eqs. (3) and (4) in the following manner. By setting $\tau=0$ in Eq. (4), we obtain

$$I^-(0,-\mu)=I^-(\tau_0)e^{-\tau_0/\mu}+\int_0^{\tau_0}\frac{1}{\mu}S(\tau',-\mu)e^{-\tau'/\mu}d\tau' \qquad \mu>0 \tag{A1}$$

by setting $\tau=\tau_0$ in Eq. (3), we obtain

$$I^+(\tau_0,\mu)=I^+(0)e^{-\tau_0/\mu}+\int_0^{\tau_0}\frac{1}{\mu}S(\tau',\mu)e^{(\tau'-\tau_0)/\mu}d\tau' \qquad \mu>0 \tag{A2}$$

The intensity of radiation, $I^+(0)$ for $0<\mu\leqslant 1$, leaving the wall at $\tau=0$ in the positive μ direction is

$$I^+(0)=\varepsilon_1\theta_1^4+2\rho_1\int_0^1 I^-(0,-\mu')\mu' d\mu' \tag{A3}$$

substitution of Eq. ($A1$) into Eq. ($A3$) and integration yields

$$I^+(0)=\varepsilon_1\theta_1^4+2\rho_1E_3(\tau_0)I^-(\tau_0)+2\rho_1\int_0^{\tau_0}[S_0(\tau')E_2(\tau') -a_1S_1(\tau')E_3(\tau')]d\tau' \tag{A4}$$

Similarly, the intensity of radiation, $I^-(\tau_0)$ for $-1\leqslant\mu<0$, leaving the wall at $\tau=\tau_0$ in the negative μ direction is

$$I^-(\tau_0)=\varepsilon_2\theta_2^4+2\rho_2\int_0^1 I^+(\tau_0,\mu')\mu' d\mu' \tag{A5}$$

Eq. ($A2$) is substituted in Eq. ($A5$) to give

$$I^-(\tau_0)=\varepsilon_2\theta_2^4+2\rho_2E_3(\tau_0)I^+(0)+2\rho_2\int_0^{\tau_0}[S_0(\tau')E_2(\tau_0-\tau') +a_1S_1(\tau')E_3(\tau_0-\tau')]d\tau' \tag{A6}$$

Eqs. ($A4$) and ($A6$) constitute two simultaneous equations and two unknowns—namely, $I^+(0)$ and $I^-(\tau_0)$ wall intensities. The solution of these equations are used.

References

[1] Altaç, Z., 1989, ''The SK_N approximation: A New Method for Solving the Integral Transport Equations,'' Ph.D. thesis, Iowa State University, Ames, IA.

[2] Altaç, Z., and Spinrad, B. I., 1990, ''The SK_N Method I: A High Order Transport Approximation to Neutron Transport Problems,'' Nucl. Sci. Eng., **106**, pp. 471–479.

[3] Spinrad, B. I., and Altaç, Z., 1990, ''The SK_N Method II: Heterogeneous Problems,'' Nucl. Sci. Eng., **106**, pp. 480–488.

[4] Altaç, Z., and Tekkalmaz, M., 2001, ''The SK_N approximation for Solving Radiation Transport Problems In Absorbing, Emitting, and Scattering Rectangular Geometries,'' *Proc. 3rd International Symposium on Radiation Transfer*, M. P. Mengüç and N. Selçuk, eds., Begell House Inc., New York, pp. 119–129.

[5] Altaç, Z., 2002, ''The SK_n Approximation for Solving Radiative Transfer Problems in Absorbing, Emitting, and Isotropically Scattering Plane-parallel Medium: Part I,'' ASME J. Heat Transfer, **124**(4), pp. 674–684.

[6] Özişik, M. N., 1973, *Radiative Transfer*, John Wiley & Sons, Inc.

[7] Abramowitz, M., and Stegun, I. A., 1964, *Handbook of Mathematical Functions*, Dover Publications Inc.

[8] Layolka, S. K., and Tsai, R. W., 1975, ''A Numerical Method for Solving Integral Equations of Neutron Transport-II,'' Nuclear Science & Engineering, **58**, pp. 317.

J. M. Goyhénèche[1]
e-mail: goyhenec@lcts.u-bordeaux.fr
Commissariat à l'Energie Atomique-Le Ripault,
BP 16, F 37260 Monts,
France

J. F. Sacadura
e-mail: cethil@insa-lyon.fr
Centre de Thermique de Lyon,
UMR CNRS 5008,
F 69621 Villeubrbanne Cedex,
France

The Zone Method: A New Explicit Matrix Relation to Calculate the Total Exchange Areas in Anisotropically Scattering Medium Bounded by Anisotropically Reflecting Walls

A new explicit matrix relation for the calculation of the total exchange areas (TEA) in emitting, absorbing and anisotropically scattering semi-transparent medium bounded by emitting, absorbing and anisotropically reflecting walls has been established. It has been used to directly determine the TEA as a function of radiative properties and geometry of the medium and its boundaries. Computation calls for direct exchange areas (DEA) and indirect exchange areas (IEA). A new definition of these exchange areas reduces their integration order and provides practical energy balance relations for their computation in the case of complex geometry elements. The new formulation is applied in the case of an emitting, absorbing and linearly anisotropic scattering semi-transparent slab bounded by black surfaces. This method is also applicable to nongray medium using the weighted sum of gray gases model. [DOI: 10.1115/1.1481359]

Keywords: *Heat Transfer, Participating Media, Radiation, Scattering, View Factors*

1 Introduction

The Zone Method, after Hottel and Sarofim [1], consists of decomposing a medium and its boundaries into N isothermal surface elements and M isothermal volume elements in order to compute the net radiative flux exchanged between all of these elements by

$$Q_{z_i z_j} = (Z_i Z_j) n^2 \sigma (T_i^4 - T_j^4) \tag{1}$$

where $(Z_i Z_j)$ (m^2) is called the *Total Exchange Area* (TEA) between the z_i and z_j elements. TEA represents the radiative power exchanged between the z_i and z_j elements after: (i) direct transfer, (ii) reflection onto surface elements, and (iii) scattering by volume elements. In case of a gray medium, the TEA does not depend on temperature. This particular case is the general field of application of the zone method. This method is however also applicable to a nongray medium using the weighted sum of gray gases model [2], but it is no more valid for semi-transparent media with temperature dependent radiative properties.

The aim of the zone method is to determine TEA as a function of the radiative properties and the geometry of the medium and its boundaries. J. J. Noble [3] proposed an explicit matrix relation for calculating TEA in an isotropic scattering medium bounded by opaque diffuse walls. In 1988, Tan and Lallemand [4] dealt with a non-scattering plane layer bounded by opaque or semi-transparent specular reflecting walls. Recently, Tan et al. [5] have extended the latter study to radiative transfer in a two-layer isotropic scattering semi-transparent composite bounded by specular reflecting walls, with spectrally dependent radiative properties. In 1988, Byun and Smith [6] developed the zone method for linearly anisotropic scattering medium. Their specific approach, however, cannot be extended to other anisotropic phase functions. In 1994, Yuen and Takara [7] formulated energy balances between surface and volume elements in anisotropically scattering semi-transparent medium bounded by opaque non-diffuse walls. In this very general study, new characteristic exchange areas for calculating exchanged radiative fluxes were proposed. Finally, Ma [8] validated the Yuen and Takara formulations to calculate the radiative transfer in a linear anisotropically scattering wall bounded by other black walls.

In studies dealing with anisotropically scattering media, TEA has never been expressed as an explicit function of radiative properties and geometry of the medium and its boundaries. Moreover, definition of characteristic exchange areas needs the numerical evaluation of high order integrals. In this work, a general matrix formulation of TEA is established from the global energy balance relations formulated by Yuen and Takara [7] and according to a similar approach to the one involved in the Noble analysis [3]. Besides, new definitions of characteristics exchange areas are proposed (detailed presentation in [9]). Finaly, interest of zone method is discussed.

In what follows, an absorbing, emitting and scattering gray medium bounded by absorbing, emitting and reflecting walls is considered. The medium is decomposed into M volume elements (of volume V_i) called g_i and its boundaries are discretized into N surface elements (of area A_i) called s_i.

2 The Zone Method in Emitting, Absorbing, and Isotropically Scattering Medium Bounded by Emitting, Absorbing, and Diffusely Reflecting Opaque Walls

2.1 Direct Exchange Areas. In isotropically scattering medium, the TEA will be expressed in terms of *Direct Exchange Area* (DEA). Hottel and Sarofim [1] defined DEA between two surface and/or volume elements

---

[1] Current address of the corresponding author: Laboratoire des Composites Thermostructuraux, UMR 5801, Domaine Universitaire, 3 allée de la Boétie, F 33600 Pessac, France.

Contributed by the Heat Transfer Division for publication in the JOURNAL OF HEAT TRANSFER. Manuscript received by the Heat Transfer Division March 30, 2001; revision received February 28, 2002. Associated Editor: J. P. Gore.

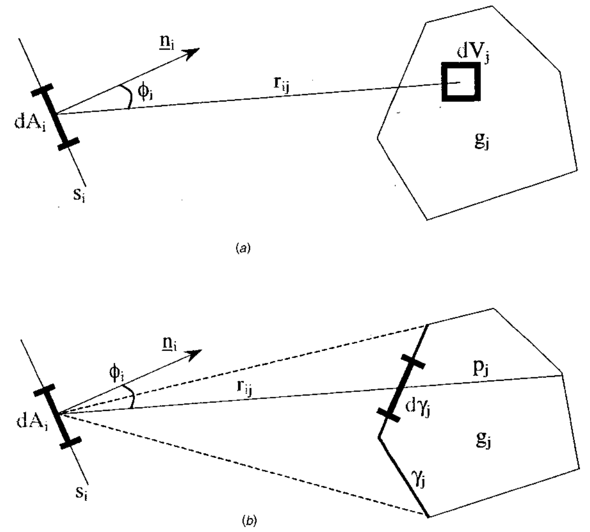

Fig. 1 Difference in surface-volume direct exchange area (DEA) definitions: (*a*) as defined by Hottel and Sarofin [1] Eq. (2) or by Yuen and Takara [7] Eq. (4); (*b*) as defined by Kheiri et al. [14] Eq. (3)

$$
\begin{aligned}
(s_is_j)&=\int_{A_i}\int_{A_j}e^{-\beta r_{ij}}\frac{\cos\phi_i\cos\phi_j}{\pi r_{ij}^2}dA_idA_j\\
(s_ig_j)&=\int_{A_i}\int_{V_j}\beta e^{-\beta r_{ij}}\frac{\cos\phi_i\cos\phi_j}{\pi r_{ij}^2}dA_idV_j\\
(g_ig_j)&=\int_{V_i}\int_{V_j}\beta^2 e^{-\beta r_{ij}}\frac{\cos\phi_i\cos\phi_j}{\pi r_{ij}^2}dV_idV_j
\end{aligned}
\tag{2}
$$

The DEA represents the part of energy emitted by a z_i (s_i or g_i) element and absorbed by a z_j element, after direct transmission between both elements. Many authors have used this formulation to compute DEA for various geometries using different methods. For example, Becker [10] gave analytic expressions in a parallelepipedic enclosure; Vercamen and Froment [11] proposed a numerical evaluation by a Monte-Carlo method for different geometries; Kim and Smith [12] dealt with cylindrical enclosure; and Tucker [13] established abacus to estimate DEA in a rectangular furnace.

Equations (2) call for 4th, 5th, and 6th order integrations (2nd order for surface integration and 3rd order for volume integration) to compute the surface-volume and volume-volume DEA. In 1990, Kheiri et al. [14] proposed a computation approach for surface-volume and volume-volume DEA with a reduced integration order, using an exponential formulation of the absorption and emission of radiative flux by volume elements (Fig. 1)

$$
\begin{aligned}
(s_ig_j)&=\int_{A_i}\int_{\gamma_j}e^{-\beta r_{ij}}(1-e^{-\beta p_j})\frac{\cos\phi_i\cos\phi_j}{\pi r_{ij}^2}dA_id\gamma_j\\
(g_ig_j)&=\int_{\gamma_i}\int_{\gamma_j}(1-e^{-\beta p_i})e^{-\beta r_{ij}}(1\\
&\quad -e^{-\beta p_j})\frac{\cos\phi_i\cos\phi_j}{\pi r_{ij}^2}d\gamma_id\gamma_j.
\end{aligned}
\tag{3}
$$

In these relations, γ_j represents the part of the g_j boundary directly seen from s_i. Finally, Yuen and Takara [7] proposed practical formulations of surface integration using scalar vector products

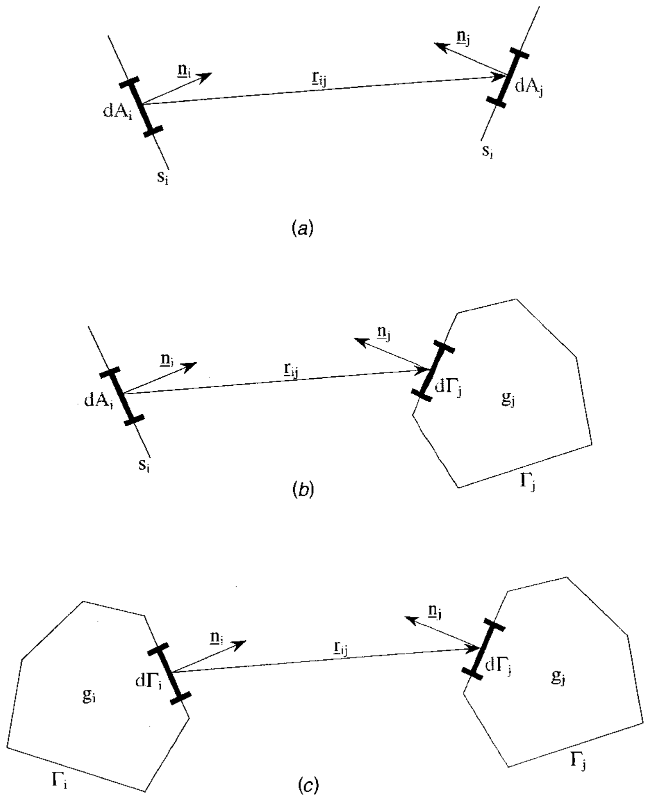

Fig. 2 Direct exchange area (DEA) as defined in this work Eq. (5): (*a*) surface-surface DEA; (*b*) surface-volume DEA; and (*c*) volume-volume DEA

$$
\begin{aligned}
(s_is_j)&=\int_{A_i}\int_{A_j}e^{-\beta r_{ij}}\frac{(\underline{n}_i\cdot\underline{r}_{ij})(\underline{r}_{ij}\cdot\underline{n}_j)}{\pi r_{ij}^4}dA_idA_j\\
(s_ig_j)&=\int_{A_i}\int_{V_j}\beta e^{-\beta r_{ij}}\frac{(\underline{n}_i\cdot\underline{r}_{ij})}{\pi r_{ij}^3}dA_idV_j
\end{aligned}
\tag{4}
$$

From these two improvements, a new expression of DEA can be proposed using scalar vector products and the integration of radiative flux over the boundaries Γ_i and Γ_j surrounding volume elements g_i and g_j (Fig. 2)

$$
\begin{aligned}
(s_is_j)&=\int_{A_i}\int_{A_j}e^{-\beta r_{ij}}\frac{(\underline{n}_i\cdot\underline{r}_{ij})(\underline{r}_{ij}\cdot\underline{n}_j)}{\pi r_{ij}^4}dA_idA_j\\
(s_ig_j)&=\int_{A_i}\int_{\Gamma_j}e^{-\beta r_{ij}}\frac{(\underline{n}_i\cdot\underline{r}_{ij})(\underline{r}_{ij}\cdot\underline{n}_j)}{\pi r_{ij}^4}dA_id\Gamma_j\\
(g_ig_j)&=\int_{\Gamma_i}\int_{\Gamma_j}e^{-\beta r_{ij}}\frac{(\underline{n}_i\cdot\underline{r}_{ij})(\underline{r}_{ij}\cdot\underline{n}_j)}{\pi r_{ij}^4}d\Gamma_id\Gamma_j
\end{aligned}
\tag{5}
$$

This definition of exchange areas reduces the order of integration to four and, as it will be seen latter, provides energy balance relations available in the case of complex geometry elements. A similar approach will be used to define other characteristic areas. In order to develop matrix formulations, all DEA are arranged in a unique $((N+M)\times(N+M))$ matrix $\underline{\underline{zz}}$

$$\underline{zz}=\begin{bmatrix}(s_1s_1) & \ldots & (s_1s_N) & (s_1g_1) & \ldots & (s_1g_M)\\ \ldots & \ldots & \ldots & \ldots & \ldots & \ldots\\ (s_Ns_1) & \ldots & (s_Ns_N) & (s_Ng_1) & \ldots & (s_Ng_M)\\ (g_1s_1) & \ldots & (g_1s_N) & (g_1g_1) & \ldots & (g_1g_M)\\ \ldots & \ldots & \ldots & \ldots & \ldots & \ldots\\ (g_Ms_1) & \ldots & (g_Ms_N) & (g_Mg_1) & \ldots & (g_Mg_M)\end{bmatrix} \tag{6}$$

2.2 Total Exchange Areas. The radiative flux arriving onto an element z_i (s_i or g_i) comes from all of surface and volume elements

$$\begin{gathered}A_iH_{s_i}=\sum_{p=1}^{N}(s_ps_i)W_{s_p}+\sum_{q=1}^{M}(g_qs_i)W_{g_q}\\ 4\beta V_iH_{g_i}=\sum_{p=1}^{N}(s_pg_i)W_{s_p}+\sum_{l=1}^{M}(g_qg_i)W_{g_q}\end{gathered} \tag{7a}$$

In these relations H_{z_i} represents the radiative flux arriving onto the z_i element, and W_{z_i} the radiative flux leaving the z_i element. The latter is composed of emission and reflection for the s_i surface element, or of emission and scattering for the g_i volume element

$$\begin{gathered}W_{s_i}=\varepsilon_iE_{s_i}+(1-\varepsilon_i)H_{s_i}\\ W_{g_i}=(1-\omega)E_{g_i}+\omega H_{g_i}\end{gathered} \tag{7b}$$

where E_{z_i} is the blackbody emissive power of the z_i element and ω is the scattering albedo. The net radiative flux Q_{z_i} lost by the z_i element is equal to the difference between the radiated flux leaving from z_i and arriving onto it

$$\begin{gathered}Q_{s_i}=A_i(W_{s_i}-H_{s_i})\\ Q_{g_i}=4\beta V_i(W_{g_i}-H_{g_i})\end{gathered} \tag{7c}$$

Moreover, the TEAs (ZZ) are defined by writing the net radiating flux Q_{z_i} lost by the z_i element in terms of blackbody emissive power

$$\begin{gathered}Q_{s_i}=\varepsilon_iA_iE_{s_i}-\sum_{p=1}^{N}(S_pS_i)E_{s_p}-\sum_{q=1}^{M}(G_qS_i)E_{g_q}\\ Q_{g_i}=4(1-\omega)\beta V_iE_{g_i}-\sum_{p=1}^{N}(S_pG_i)E_{s_p}-\sum_{q=1}^{M}(G_qG_i)E_{g_q}\end{gathered} \tag{7d}$$

In Eq. (7), the reflection and scattering phenomena are formulated by similar expressions [15]. Therefore, using z_i as a surface or a volume element, Eqs. (7(*a*)–7(*d*)) simply lead to

$$\hat{A}_iH_{z_i}=\sum_{k=1}^{N+M}(z_kz_i)W_{z_k} \tag{8a}$$

$$W_{z_i}=\hat{\varepsilon}_iE_{z_i}+(1-\hat{\varepsilon}_i)H_{z_i} \tag{8b}$$

$$Q_{z_i}=\hat{A}_i(W_{z_i}-H_{z_i}) \tag{8c}$$

$$Q_{z_i}=\hat{\varepsilon}_i\hat{A}_iE_{z_i}-\sum_{k=1}^{N+M}(Z_kZ_i)E_{z_k} \tag{8d}$$

In these relations, $\hat{A}_i$ and $\hat{\varepsilon}_i$ are the *Radiative Exchange Area* (REA) and the *Emissive Total Rate* (ETR) of the z_i element respectively. For the s_i surface elements: $\hat{A}_i=A_i$, $\hat{\varepsilon}_i=\varepsilon_i$; and for the g_i volume elements: $\hat{A}_i=4\beta V_i$, $\hat{\varepsilon}_i=1-\omega$. Then, it becomes easy to formulate Eq. (8) using the matrix expressions

$$\underline{\hat{A}}\cdot\underline{H}=\underline{zz}\cdot\underline{W}_z \tag{9a}$$

$$\underline{W}_z=\underline{\hat{\varepsilon}}\cdot\underline{E}+(\underline{I}-\underline{\hat{\varepsilon}})\cdot\underline{H} \tag{9b}$$

$$\underline{Q}=\underline{\hat{A}}\cdot(\underline{W}_z-\underline{H}) \tag{9c}$$

$$\underline{Q}=(\underline{\hat{\varepsilon}}\cdot\underline{\hat{A}}-\underline{ZZ})\cdot\underline{E} \tag{9d}$$

where $\underline{\hat{A}}$ represents the $((N+M)\times(N+M))$ diagonal matrix of REA, $\underline{\hat{\varepsilon}}$ the $((N+M)\times(N+M))$ diagonal matrix of ETR and $\underline{ZZ}$ the $((N+M)\times(N+M))$ matrix of TEA

$$\underline{ZZ}=\begin{bmatrix}(S_1S_1) & \cdots & (S_1S_N) & (S_1G_1) & \cdots & (S_1G_M)\\ \cdots & \cdots & \cdots & \cdots & \cdots & \cdots\\ (S_NS_1) & \cdots & (S_NS_N) & (S_NG_1) & \cdots & (S_NG_M)\\ (G_1S_1) & \cdots & (G_1S_N) & (G_1G_1) & \cdots & (G_1G_M)\\ \cdots & \cdots & \cdots & \cdots & \cdots & \cdots\\ (G_MS_1) & \cdots & (G_MS_N) & (G_MG_1) & \cdots & (G_MG_M)\end{bmatrix} \tag{10}$$

Finally, Eqs. (9(*a*)–9(*d*)) are combined to obtain the explicit matrix relation for the calculation of TEA

$$\underline{ZZ}=\underline{\hat{\varepsilon}}\cdot\underline{\hat{A}}\cdot[\underline{\hat{A}}-\underline{zz}\cdot(\underline{I}-\underline{\hat{\varepsilon}})]^{-1}\cdot\underline{zz}\cdot\hat{\varepsilon} \tag{11}$$

This relation is simpler than the Noble matrix expression [3], and is equivalent to the one proposed by Naraghi and Chung [15], obtained from a stochastic approach (multiple Markov chain theory). This result validates our approach in the particular case of an isotropically scattering medium.

2.3 Reciprocity and Energy Balance Relations. The definition of DEA and TEA allows the reciprocity relations

$$(z_iz_j)=(z_jz_i)\quad(Z_iZ_j)=(Z_jZ_i) \tag{12}$$

These relations imply symmetry for the DEA and TEA matrices. Otherwise, elementary energy balance relations are used to compute surface-volume and volume-volume DEA from surface-surface DEA calculated on a volume element boundary.

$$(s_ig_j)=\sum_{q=1}^{N_j}(s_i\Gamma_{jq}) \tag{13a}$$

$$(g_ig_j)=\sum_{p=1}^{N_i}\sum_{q=1}^{N_j}(\Gamma_{ip}\Gamma_{jq}) \tag{13b}$$

In these relations, Γ_{ij} represents the jth surface element of the ith volume element boundary. This kind of relation is very practical to compute DEA between complex geometry elements such as, for instance, those resulting from an unstructured mesh. Finally, the global energy balance relations are written in terms of DEA and TEA

$$\hat{A}_i=\sum_{k=1}^{N+M}(z_iz_k) \tag{14a}$$

$$\hat{\varepsilon}_i\hat{A}_i=\sum_{k=1}^{N+M}(Z_iZ_k) \tag{14b}$$

3 The Zone Method in Emitting, Absorbing, and Anisotropically Scattering Medium Bounded by Emitting, Absorbing, and Anisotropically Reflecting Opaque Walls

3.1 Indirect Exchange Areas. In an anisotropically scattering medium, the TEA will be expressed in terms of a *Direct Exchange Area* (DEA) and an *Indirect Exchange Area* (IEA). The IEA represents the part of power emitted by the z_i element and absorbed by the z_j element, after: (i) direct transfer between z_i and z_k, (ii) reflection by the s_k surface element *or* scattered by the g_k

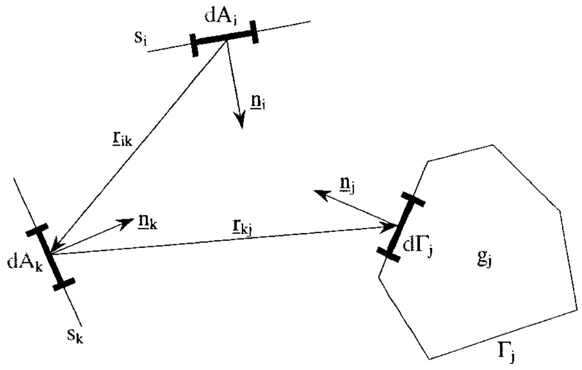

Fig. 3 $(s_i s_k g_j)$ **reflective indirect exchange area (IEA)**

volume element, and (iii) direct transfer between z_k and z_j (Fig. 3 and Fig. 4). For the reflection by the s_k surface element, IEAs are defined by

$$(s_i s_k s_j)=\int_{A_i}\int_{A_k}\int_{A_j} e^{-\beta r_{ik}}\rho_k''(\theta_{ikj}) \times e^{-\beta r_{kj}}\frac{(\underline{n}_i\cdot\underline{r}_{ik})(\underline{r}_{ik}\cdot\underline{n}_k)(\underline{n}_k\cdot\underline{r}_{kj})(\underline{r}_{kj}\cdot\underline{n}_j)}{\pi r_{ik}^4 r_{kj}^4}\,dA_i dA_k dA_j$$

$$(s_i s_k g_j)=\int_{A_i}\int_{A_k}\int_{\Gamma_j} e^{-\beta r_{ik}}\rho_k''(\theta_{ikj}) \times e^{-\beta r_{kj}}\frac{(\underline{n}_i\cdot\underline{r}_{ik})(\underline{r}_{ik}\cdot\underline{n}_k)(\underline{n}_k\cdot\underline{r}_{kj})(\underline{r}_{kj}\cdot\underline{n}_j)}{\pi r_{ik}^4 r_{kj}^4}\,dA_i dA_k d\Gamma_j \tag{15}$$

$$(g_i s_k g_j)=\int_{\Gamma_i}\int_{A_k}\int_{\Gamma_j} e^{-\beta r_{ik}}\rho_k''(\theta_{ikj}) \times e^{-\beta r_{kj}}\frac{(\underline{n}_i\cdot\underline{r}_{ik})(\underline{r}_{ik}\cdot\underline{n}_k)(\underline{n}_k\cdot\underline{r}_{kj})(\underline{r}_{kj}\cdot\underline{n}_j)}{\pi r_{ik}^4 r_{kj}^4}\,d\Gamma_i dA_k d\Gamma_j$$

In these relations, $\rho_k''(\theta_{ikj})$ denotes the bidirectional reflection coefficient of the s_k surface element. Equations (15) are equivalent to the expressions of Yuen and Takara [17] written in terms of volume integration for $(s_i s_k g_j)$ and $(g_i s_k g_j)$. In the case of isotropic reflecting boundaries, $\rho_k''(\theta_{ikj})=\rho_k/\pi$, where ρ_k represents the bihemispherical reflection coefficient of s_k surface element and Eq. (15) leads to

$$(z_i s_k z_j)=\frac{(z_i s_k)\rho_k(s_k z_j)}{A_k} \tag{16}$$

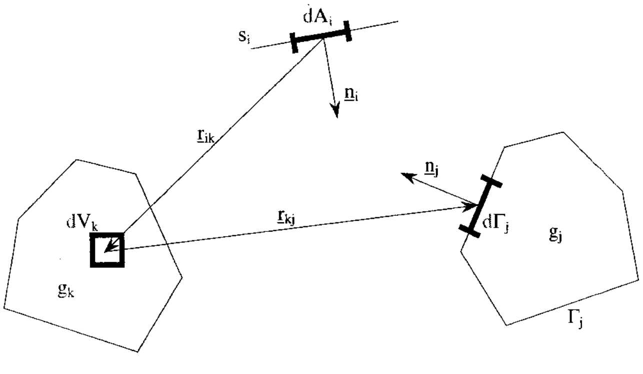

Fig. 4 $(s_i g_k g_j)$ **scattering indirect exchange area (IEA)**

For the scattering by a g_k volume element, IEA are defined by

$$(s_i g_k s_j)=\int_{A_i}\int_{V_k}\int_{A_j} e^{-\beta r_{ik}}\omega\beta\Phi(\theta_{ikj}) \times e^{-\beta r_{kj}}\frac{(\underline{n}_i\cdot\underline{r}_{ik})(\underline{r}_{kj}\cdot\underline{n}_j)}{\pi r_{ik}^3 r_{kj}^3}\,dA_i dV_k dA_j$$

$$(s_i g_k g_j)=\int_{A_i}\int_{V_k}\int_{\Gamma_j} e^{-\beta r_{ik}}\omega\beta\Phi(\theta_{ikj}) \times e^{-\beta r_{kj}}\frac{(\underline{n}_i\cdot\underline{r}_{ik})(\underline{r}_{kj}\cdot\underline{n}_j)}{\pi r_{ik}^3 r_{kj}^3}\,dA_i dV_k d\Gamma_j \tag{17}$$

$$(g_i g_k g_j)=\int_{\Gamma_i}\int_{V_k}\int_{\Gamma_j} e^{-\beta r_{ik}}\omega\beta\Phi(\theta_{ikj}) \times e^{-\beta r_{kj}}\frac{(\underline{n}_i\cdot\underline{r}_{ik})(\underline{r}_{kj}\cdot\underline{n}_j)}{\pi r_{ik}^3 r_{kj}^3}\,d\Gamma_i dV_k d\Gamma_j$$

In these relations, $\Phi(\theta_{ikj})$ denotes the phase function of the medium. Equations (17) are equivalent to expressions from Yuen and Takara [7] written in terms of volume integration for $(s_i g_k g_j)$ and $(g_i g_k g_j)$. In the case of an isotropically scattering medium, $\Phi(\theta_{ikj})=1$ and the Eq. (17) leads to

$$(z_i g_k z_j)=\frac{(z_i g_k)(1-\omega)(g_k z_j)}{4\beta V_k} \tag{18}$$

3.3 Total Exchange Areas. For convenience, the *Indirect Exchange Rates* (IER) must be defined

$$(z_i s_k z_j^0)=\frac{(z_i s_k z_j)}{(s_k z_j)} \quad (z_i g_k z_j^0)=\frac{(z_i g_k z_j)}{(g_k z_j)} \tag{19}$$

The radiative flux leaving the z_i element in the direction of the z_j element is denoted by $W_{z_i z_j}$. This flux is composed of emission and reflection for the s_i surface element, or by emission and scattering for the g_i volume element

$$W_{s_i s_j}=\varepsilon_i E_{s_i}+\sum_{p=1}^{N}(s_p s_i s_j^0)W_{s_p s_i}+\sum_{q=1}^{M}(g_q s_i s_j^0)W_{g_q s_i}$$

$$W_{s_i g_j}=\varepsilon_i E_{s_i}+\sum_{p=1}^{N}(s_p s_i g_j^0)W_{s_p s_i}+\sum_{q=1}^{M}(g_q s_i g_j^0)W_{g_q s_i} \tag{20a}$$

$$W_{g_i s_j}=(1-\omega)E_{g_i}+\sum_{p=1}^{N}(s_p g_i s_j^0)W_{s_p g_i}+\sum_{q=1}^{M}(g_q g_i s_j^0)W_{g_q g_i}$$

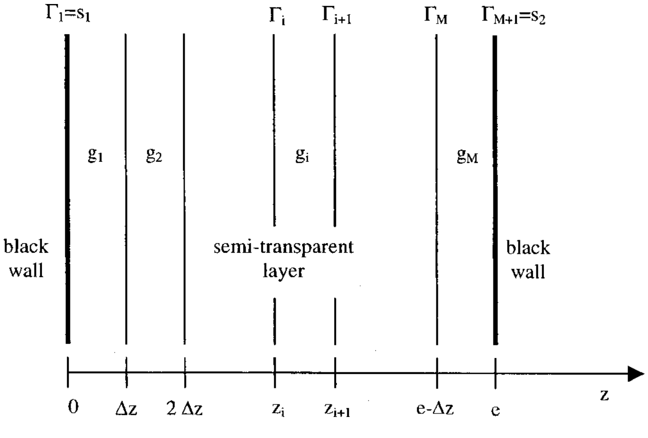

Fig. 5 Application: purely anisotropic scattering layer bounded by black walls

$$W_{g_ig_j}=(1-\omega)E_{g_i}+\sum_{p=1}^{N}(s_pg_ig_j^0)W_{s_pg_i}+\sum_{q=1}^{M}(g_qg_ig_j^0)W_{g_qg_i}$$

The net radiative flux lost by the z_i element is equal to the difference between the radiative flux leaving z_i and arriving onto it

$$Q_{s_i}=\sum_{p=1}^{N}(s_is_p)[W_{s_is_p}-W_{s_ps_i}]+\sum_{q=1}^{M}(s_ig_q)[W_{s_ig_q}-W_{g_qs_i}] \tag{20b}$$

$$Q_{g_i}=\sum_{p=1}^{N}(g_is_p)[W_{gs_is_p}-W_{s_pg_i}]+\sum_{q=1}^{M}(g_ig_q)[W_{g_ig_q}-W_{g_qg_i}]$$

Moreover, TEAs are always defined by writing the net radiated flux lost by the z_i element in terms of blackbody emissive power

$$Q_{s_i}=\varepsilon_iA_iE_{s_i}-\sum_{p=1}^{N}(S_pS_i)E_{s_p}-\sum_{q=1}^{M}(G_qS_i)E_{g_q} \tag{20c}$$

$$Q_{g_i}=4(1-\omega)\beta V_iE_{g_i}-\sum_{p=1}^{N}(S_pG_i)E_{s_p}-\sum_{q=1}^{M}(G_qG_i)E_{g_q}$$

In Eq. (20), the reflection and scattering phenomena are formulated by similar expressions. Consequently, using z_i as a surface or volume element, Eqs. (20) simply lead to

$$W_{z_iz_j}=\hat{\varepsilon}_iE_{z_i}+\sum_{k=1}^{N+M}(z_kz_iz_j^0)W_{z_kz_i} \tag{21a}$$

$$Q_{z_i}=\sum_{k=1}^{N+M}(z_iz_k)[W_{z_iz_k}-W_{z_kz_i}] \tag{21b}$$

$$Q_{z_i}=\hat{\varepsilon}_i\hat{A}_iE_{z_i}-\sum_{k=1}^{N+M}(Z_kZ_i)E_{z_k} \tag{21c}$$

Then, it becomes easy to formulate Eq. (21) under the matrix expressions

$$\underline{W}_{zz}=\underline{P}\cdot\underline{\hat{\varepsilon}}\cdot\underline{E}+\underline{zzz}^0\cdot\underline{L}\cdot\underline{W}_{zz} \tag{22a}$$

$$\underline{Q}=\underline{zz}^0\cdot(\underline{I}-\underline{L})\cdot\underline{W}_{zz} \tag{22b}$$

$$\underline{Q}=(\underline{\hat{\varepsilon}}\cdot\underline{\hat{A}}-\underline{ZZ})\cdot\underline{E} \tag{22c}$$

where $\underline{zzz}^0$ represents $((N+M)^2\times(N+M)^2)$ matrix of IER:

$$\underline{zzz}^0=\begin{bmatrix}\cdots & \cdots & & & & & \\ \cdots & \cdots & & & & & \\ & & (z_1z_kz_1^0) & \cdots & (z_1z_kz_{N+M}^0) & & \\ & & \cdots & \cdots & \cdots & & \\ & & (z_1z_kz_{N+M}^0) & \cdots & (z_{N+M}z_kz_{N+M}^0) & & \\ & & & & & \cdots & \cdots \\ & & & & & \cdots & \cdots\end{bmatrix} \tag{23}$$

In these relations, $\underline{zz}^0$ denotes a new matrix arrangement of DEA, I represents the identity matrix, and $\underline{L}$ and $\underline{P}$ the transformation matrices (Appendix 1). Finally Eqs. (22(a)–22(c)) are combined to obtain an explicit matrix relation to calculate TEA

$$\underline{ZZ}=\underline{\hat{\varepsilon}}\cdot\underline{\hat{A}}-\underline{zz}^0\cdot(\underline{I}-\underline{L})\cdot(\underline{I}-\underline{zzz}^0\cdot\underline{L})^{-1}\cdot\underline{P}\cdot\underline{\hat{\varepsilon}} \tag{24}$$

In the case of an isotropic scattering medium bounded by isotropic reflecting walls, IER are computed by Eqs. (16,18,19)

$$(z_iz_kz_j^0)=\frac{(z_iz_k)(1-\hat{\varepsilon}_k)}{\hat{A}_k} \tag{25}$$

and Eq. (24) leads to Eq. (11).

3.4 Reciprocity and Energy Balance Relations. The reciprocity relations of TEA and DEA (Eq. (12)) are obviously still valid. Besides, if $\rho''(\theta_{ikj})=\rho''(\theta_{jki})$ and $\Phi(\theta_{ikj})=\Phi(\theta_{jki})$, then the IEA satisfy reciprocity relations

$$(s_iz_ks_j)=(s_jz_ks_i) \tag{26}$$

These relations imply symmetry for the IEA matrix but not for the IER matrix. Elementary energy balance relations are used to compute surface-volume and volume-volume IEA from surface-surface IEA calculated on a volume element boundary

$$(s_iz_kg_j)=\sum_{q=1}^{N_j}(s_iz_k\Gamma_{jq})\qquad(g_iz_kg_j)=\sum_{p=1}^{N_i}\sum_{q=1}^{N_j}(\Gamma_{ip}z_k\Gamma_{jq}) \tag{27}$$

Finally, global energy balances are written in terms of IEA

$$(z_iz_k)(1-\hat{\varepsilon}_k)=\sum_{j=1}^{N+M}(z_iz_kz_j) \tag{28}$$

4 Application

A purely anisotropic scattering layer $(\omega=1)$ bounded by black walls is considered (Fig. 5). The medium is decomposed into M volume elements numbered from 1 to M and its boundaries are decomposed into $N=2$ surface elements s_1 and s_2. Layer thickness is denoted by e and the volume element thickness by $\Delta z=e/M$. Each volume element g_i is confined by $N_i=2$ virtual surface elements Γ_i and Γ_{i+1} located at coordinates z_i and z_{i+1}. Consequently: $s_1=\Gamma_1$ and $s_2=\Gamma_{M+1}$. An anisotropic linear phase function is set to the medium: $\Phi=1+x\cos\theta_{ikj}$. The aim of this application is to compute the total exchange area S_1S_1 in order to compare results to reference ones.

The DEA between any Γ_i and Γ_j surface elements ($\underline{n}_i$ and $\underline{n}_j$ in opposite directions) of the wall is calculated by the classical relation [1]

$$(\Gamma_i\Gamma_j)=2E_3(\beta\Delta z_{ij}) \tag{29}$$

where $E_3(t)=\int_0^1\mu e^{-t/\mu}d\mu$ is the 3rd order integro-exponential function, and $\Delta z_{ij}=|z_j-z_i|$ the distance between both surface elements. Direct application of this relation between s_1 and s_2 yields

$$(s_1s_2)=(\Gamma_1\Gamma_{M+1}) \tag{30}$$

The elementary energy balance relations (Eq. (13)) are then used to compute surface-volume and volume-surface DEA

Table 1 Total exchange area S_1S_1 in purely anisotropic scattering slab, computed with:$^{\rm i}$ $M=20$,$^{\rm ii}$: $M=30$,$^{\rm iii}$: $M=100$ volume elements. Three significant digits for the results of [16], [17], and [8]; four significant digits for the others.

x	Reference	τ=0.1	τ=0.5	τ=1	τ=2	τ=3	τ=10
-1	**this work Eq. (24)**	**0.1050**$^{\rm i}$	**0.3545**$^{\rm i}$	**0.5164**$^{\rm ii}$	**0.6764**$^{\rm ii}$	**0.7564**$^{\rm ii}$	**0.9089**$^{\rm ii}$
-0.7	[16]	0.099	0.337	0.495		0.740	
	[17]	0.099	0.339	0.495			
	[6]	0.0987	0.3367	0.4954	0.6567		0.9026
	[8]	0.099	0.338	0.497		0.741	
	this work Eq. (24)	**0.0988**$^{\rm i}$	**0.3375**$^{\rm i}$	**0.4967**$^{\rm ii}$	**0.6581**$^{\rm ii}$	**0.7406**$^{\rm ii}$	**0.9014**$^{\rm ii}$
0.0	[18]	0.0843		0.4466			0.8833
	[19]			0.4466	0.6099		0.8833
	[16,17]	0.084	0.296	0.447			0.891
	[20]				0.6099		
	[6]	0.0843	0.2958	0.4465	0.6099		0.8828
	this work Eq. (11)	**0.0843**$^{\rm iii}$	**0.2958**$^{\rm iii}$	**0.4466**$^{\rm iii}$	**0.6099**$^{\rm iii}$	**0.6978**$^{\rm iii}$	**0.8832**$^{\rm iii}$
	this work Eq. (24,25)	**0.0843**$^{\rm i}$	**0.2958**$^{\rm i}$	**0.4465**$^{\rm ii}$	**0.6096**$^{\rm ii}$	**0.6978**$^{\rm ii}$	**0.8804**$^{\rm ii}$
	this work Eq. (24,17)	**0.0843**$^{\rm i}$	**0.2958**$^{\rm i}$	**0.4465**$^{\rm ii}$	**0.6096**$^{\rm ii}$	**0.6978**$^{\rm ii}$	**0.8804**$^{\rm ii}$
0.7	[16,17]	0.069	0.250	0.389		0.642	
	[6]	0.0694	0.2496	0.3872	0.5482		0.8529
	[8]	0.070	0.251	0.390		0.645	
	this work Eq. (24)	**0.0695**$^{\rm i}$	**0.2506**$^{\rm i}$	**0.3891**$^{\rm ii}$	**0.5507**$^{\rm ii}$	**0.6440**$^{\rm ii}$	**0.8531**$^{\rm ii}$
1	[19]			0.3577	0.5154		0.8351
	[6]	0.0628	0.2279	0.3577	0.5154		0.8348
	this work Eq. (24)	**0.0631**$^{\rm i}$	**0.2302**$^{\rm i}$	**0.3619**$^{\rm ii}$	**0.5214**$^{\rm ii}$	**0.6164**$^{\rm ii}$	**0.8386**$^{\rm ii}$

$$
\begin{aligned}
(s_1g_j) &= (\Gamma_1\Gamma_j) - (\Gamma_1\Gamma_{j+1}) \\
(s_2g_j) &= (\Gamma_{M+1}\Gamma_j) - (\Gamma_{M+1}\Gamma_{j+1}) \qquad (31) \\
(g_ig_j) &= (\Gamma_{i+1}\Gamma_j) - (\Gamma_{i+1}\Gamma_{j+1}) - (\Gamma_i\Gamma_j) + (\Gamma_i\Gamma_{j+1})
\end{aligned}
$$

Reciprocity relations (Eq. (12)) allow to complete extra-diagonal terms of DEA matrix. Finally, the DEA global energy balance relations (Eq. (14)) are used to compute (s_is_i) and (g_ig_i)

$$
(s_is_i) = 1 - \sum_{\substack{k=1 \\ k\neq i}}^{N+M} (s_iz_k) \quad (g_ig_i) = 4\beta\Delta z - \sum_{\substack{k=1 \\ k\neq i}}^{N+M} (g_iz_k) \qquad (32)
$$

In the case of black boundaries, reflective IEA are equal to zero: $(z_is_kz_j)=0$. Moreover, scattering IEA between any surface elements Γ_i, and Γ_j of the wall is calculated by the relation

$$
(\Gamma_i g_k \Gamma_j) = \frac{\omega}{4\beta\Delta z} 4 I_{\Gamma_i \cdot g_k \cdot \Gamma_j} \qquad (33)
$$

where geometric integral $I_{\Gamma_i, g_k, \Gamma_j}$ is given by

$$
\begin{aligned}
I_{\Gamma_i, g_k, \Gamma_i} = \int_0^1 \int_0^1 & e^{-\beta[\Delta z_{ki}/\mu_i + \Delta z_{kj}/\mu_j]} [1 - e^{-\beta\Delta z/\mu_i}] \varphi(\mu_i, \mu_j) \\
& \times [1 - e^{-\beta\Delta z/\mu_j}] \mu_i \mu_j d\mu_i d\mu_j \qquad (34)
\end{aligned}
$$

and linear anisotropic phase function integrated over azimuth variable yields

$$
\varphi(\mu_i, \mu_j) = \begin{cases} z_i < z_k < z_j & : \ 1 + x\mu_i\mu_j \\ z_i, z_j < z_k \ \text{ or } \ z_k < z_i, z_j & : \ 1 - x\mu_i\mu_j \end{cases} \qquad (35)
$$

Direct application of Eq. (33) between s_1 and s_2 yields

$$
(s_1 g_k s_2) = (\Gamma_1 g_k \Gamma_{M+1}) \qquad (36)
$$

Then, elementary energy balance relations (Eq. (27)) are used to compute surface-volume and volume-surface IEA

$$
\begin{aligned}
(s_1 g_k g_j) &= (\Gamma_1 \Gamma_j) - (\Gamma_1 \Gamma_{j+1}) \\
(s_2 g_k g_j) &= (\Gamma_{M+1} \Gamma_j) - (\Gamma_{M+1} \Gamma_{j+1}) \\
(g_i g_k g_j) &= (\Gamma_{i+1} \Gamma_j) - (\Gamma_{i+1} \Gamma_{j+1}) - (\Gamma_i \Gamma_j) - (\Gamma_i \Gamma_{j+1})
\end{aligned}
\tag{37}
$$

Reciprocity relations (Eq. (26)) allow to complete extra-diagonal terms of IEA matrix. Finally, global energy balance relations (Eq. (28)) are used to compute $(z_i g_j g_j)$ and $(g_i g_i g_i)$ DEA

$$
\begin{aligned}
(z_i g_j g_j) &= (z_i g_j)\omega - \sum_{\substack{k=1 \\ k \neq j}}^{N+M} (z_i g_j z_k) \quad (i \neq j) \\
(g_i g_i g_i) &= (g_i g_i)\omega - \sum_{\substack{k=1 \\ k \neq i}}^{N+M} (g_j g_i z_k)
\end{aligned}
\tag{38}
$$

The symmetry of the wall provides relations between exchange areas. Using this relations reduces the number of DEA and IEA calculations. TEA are computed using the explicit matrix relation (Eq. (24)). The global energy balance (Eq. (14)) provides a validation of the results. Numerical values are compared to reference data in Table I, for different wall optical thickness $\tau = \beta e$ and different anisotropic factor x values.

The calculated value of $S_1 S_1$ compares very well with those obtained by various methods such as: previous versions of zone method [6,8], analytical solution [16,19], successive approximations [17], the normal mode expansion technique [18] and an iterative approach with spherical harmonics method used for the initial guess [20]. A large number of elements is chosen to provide a reference solution with Eq. (11) in the case of an isotropic scattering wall. For $x=0$, $S_1 S_1$ calculated with the isotropic simplification (Eq. (25)) is close to $S_1 S_1$ calculated with the complete formulation of scattering IEA (Eq. (17)), both being in good agreement with results obtained by Eq. (11). In the other cases, Eq. (24) provides good results with a moderate number of elements, which has to be increased, of course, when the optical thickness increases.

5 Advantages of the Zone Method

The advantage of the zone method appears clearly when solving a nonstationary (either coupled or not) heat transfer problem. In this case, the temperature field is the solution of both coupled partial derivative equations, energy equation and radiative transfer equation:

$$
\nabla q_R = \rho C \frac{\partial T}{\partial t} \tag{39}
$$

$$
\nabla i(M,\vec{\Delta}) = (1-\omega)\beta i_b(M,\vec{\Delta}) + \frac{\omega\beta}{4\pi}\int_{4\pi} \Phi(\vec{\Delta},\vec{\Delta}')\, i(M,\vec{\Delta}')\, d\Omega' \tag{40}
$$

where q_R represents the radiative flux

$$
q_R = \int_{4\pi} i(M,\vec{\Delta})\vec{\Delta}\, d\Omega \tag{41}
$$

The numerical solution of this problem is generally obtained using a spatial mesh of the domain and a directional discretisation of the radiant intensity. Both partial derivative equations are formulated in terms of discrete algebrical equations for each element and each direction. Then, a numerical procedure leads to the radiant intensity $i_{ij} = i(M_i, \vec{\Delta}_j)$ and the temperature $T_i = T(M_i)$, for each node M_i and each direction $\vec{\Delta}_j$. This computation has to be done for each time step.

Using the zone method, the radiative source on each isothermal element at the temperature T_i is directly expressed in terms of TEAs

$$
\nabla q_R = \frac{1}{V_i} \sum_{k=1}^{N+M} (Z_k Z_i) n^2 \sigma (T_k^4 - T_i^4) \tag{42}
$$

The numerical solution is then obtain by: (i) computing the complete total exchange area matrix; and (ii) solving the energy equation for each time step.

The zone method only requires the spatial decomposition of the domain (the directional behavior of the radiant intensity is integrated in the TEAs computation), whereas others methods additionally require the directional discretisation of the radiant intensity. It is the reason why the zone method leads to accurate results. Moreover, the relations developped in this work allow an explicit determination of the TEAs as a function of the radiative properties and the geometry of the medium and its boundaries. These TEAs can be directly used to compute the radiative source. It is the advantage of these explicit relations. Finally, to solve the nonstationary problem, TEAs are computed before the time iterations, as an initialising procedure, and then used at each time step. It is the reason why the zone method allows a quick numerical determination of the temperature in the case of nonstationary heat transfer. This advantage is much more important for solving coupled heat transfer problems [2,4,5,9].

6 Conclusion

A new explicit matrix relation for the calculation of TEA in emitting, absorbing and anisotropic scattering semi-transparent medium bounded by emitting, absorbing and anisotropically reflecting walls has been established. It allows the computation of TEA as a function of the radiative properties and the geometry of the medium and its boundaries. This method is applicable to nongray medium, using the weighted sum of gray gases model. Moreover, new formulations of DEA and IEA have been proposed. They enable the computation of the characteristic exchange areas in the case of complex elements like unstructured meshes. At our knowledge, such an application of the zone method has never been dealt with so far. It provides a large range of investigation for a method which has always been considered as a reference one in terms of accuracy.

Appendix 1

Definition of Matrixes $\underline{zz}^0$, $\underline{L}$, and $\underline{P}$. Transformed DEA matrix $\underline{zz}^o((N+M)\times(N+M)^2)$ is defined by

$$
\underline{zz}^0 = \begin{bmatrix}
\underline{s_1 z_j} & & 0 & & & \\
 & \cdots & & & 0 & \\
0 & & \underline{s_N z_j} & & & \\
 & & & \underline{g_1 z_j} & & 0 \\
 & 0 & & & \cdots & \\
 & & & 0 & & \underline{g_M z_j}
\end{bmatrix}
$$

$$
\text{with}\quad
\begin{aligned}
\underline{s_i z_j} &= [(s_i s_1) \ \cdots \ (s_i s_N) | (s_i g_1) \ \cdots \ (s_i g_M)] \\
\underline{g_i z_j} &= [(g_i s_1) \ \cdots \ (g_i s_N) | (g_i g_1) \ \cdots \ (g_i g_M)]
\end{aligned}
$$

The vector of radiative outgoing flux $\underline{W}_{zz}((N+M)^2\times 1)$ and the transformed vector of radiative outgoing flux $\underline{W}^f_{zz}((N+M)^2\times 1)$ are defined by

$$
\underline{W}_{zz} = \begin{bmatrix}
\underline{W}_{s_1 z_j} \\ \cdots \\ \underline{W}_{s_N z_j} \\ \underline{W}_{g_1 z_j} \\ \cdots \\ \underline{W}_{g_M z_j}
\end{bmatrix}
\qquad
\underline{W}^f_{zz} = \begin{bmatrix}
\underline{W}^f_{z_i s_1} \\ \cdots \\ \underline{W}^f_{z_i s_N} \\ \underline{W}^f_{z_i g_1} \\ \cdots \\ \underline{W}^f_{z_i g_M}
\end{bmatrix}
$$

with $\underline{W}_{z_iz_j}=\begin{bmatrix} W_{z_iz_1} \\ \cdots \\ W_{z_iz_{N+M}} \end{bmatrix}$ and $\underline{W}^f_{z_iz_j}=\begin{bmatrix} W_{z_1z_j} \\ \cdots \\ W_{z_{N+M}z_j} \end{bmatrix}$

Then matrix $\underline{L}((N+M)^2\times(N+M)^2)$ transforms $\underline{W}_{zz}$ to $\underline{W}^f_{zz}$ by

$$\underline{W}^f_{zz}=\underline{L}\cdot\underline{W}_{zz}$$

Moreover, the vector of blackbody emissive power $\underline{E}((N+M)\times 1)$ and the transformed vector of blackbody emissive power $\underline{E}^f((N+M)^2\times 1)$ are defined by

$$\underline{E}=\begin{bmatrix} E_{s_1} \\ \cdots \\ E_{s_N} \\ E_{g_1} \\ \cdots \\ E_{g_M} \end{bmatrix} \qquad \underline{E}^f=\begin{bmatrix} E_{s_1}\underline{I}_{N+M} \\ \cdots \\ E_{s_N}\underline{I}_{N+M} \\ E_{g_1}\underline{I}_{N+M} \\ \cdots \\ E_{g_M}\underline{I}_{N+M} \end{bmatrix}$$

where $\underline{I}_{N+M}$ represents the $((N+M)\times 1)$ identity vector. Then, matrix $\underline{P}((N+M)^2\times(N+M))$ transforms $\underline{E}$ into $\underline{E}^f$ by

$$\underline{E}^f=\underline{P}\cdot\underline{E}$$

In practice, it is not necessary to store $\underline{L}$ and $\underline{P}$ matrixes but simply to program the transformations they do.

Nomenclature[2]

Quantities

$\hat{A}$ = Radiative Exchange Area (REA), m^2
$\hat{\varepsilon}$ = Emissive Total Rate (ETR)
C = specific heat, J/kg K
Δz = volume elements thickness, m
c = wall thickness, m
E_{z_i} = blackbody emissive power of z_i element, W/m^2
H_{z_i} = radiative flux arriving onto z_i element, W/m^2
i = radiant intensity, W/m^2 sr
i_b = blackbody radiant intensity, W/m^2 sr
$\underline{I}$ = identity matrix
n = refractive index
$\underline{n}_i$ = normal vector of ith differential surface element,
N, M = number of surface and volume elements respectively
$\underline{N}_i$ = surface elements number of Γ_i
Ω = solid angle, sr
p_j = distance across g_j volume element in the direction defined by r_{ij}, m
q_R = radiative flux, W/m^2
Q_{z_i} = net radiative flux lost by z_i element, W
$Q_{z_iz_j}$ = net radiative flux exchanged between z_i and z_j elements, W
ρ = density, kg/m^3
ρ'' = bidirectional reflection coefficient
r_{ij} = distance between two differential elements, m
θ_{ikj} = angle between incident and reflected (or scattered) ray, rad
W_{z_i} = radiative flux leaving z_i element, W/m^2
$W_{z_iz_j}$ = radiative flux leaving z_i element in direction of z_j element, W/m^2
zz = Direct Exchange Area (DEA), m^2
$\underline{zz}^0$ = DEA matrix with peculiar arrangement, m^2
ZZ = Total Exchange Area (TEA), m^2
zzz = Indirect Exchange Area (IEA), m^2
zzz^0 = Indirect Exchange Rate (IER)

Elements

γ_j = part of Γ_j boundary surface element directly seen from z_i element
Γ_i = boundary surface of g_i volume element
Γ_{ij} = jth part of Γ_i boundary surface element
s, S = surface element
g, G = volume element
z, Z = generalized notation for elements

General features

(quantity into brackets) = scalar value of exchange area
underline type quantity = vector or matrix

References

[1] Hottel, H. C., and Sarofim, A. F., 1967, *Radiative Transfer*, McGraw-Hill, New York.
[2] Olsommer, B., von Spakovsky, M., and Favrat, D., 1997, "*Transfert de chaleur par rayonnement dans un four d'incinération industriel: application de la méthode des zones*," Revue Générale de Thermique, **36**, pp. 125–134.
[3] Noble, J. J., 1975, "*The Zone Method: Explicit Matrix Relations for Total Exchange Areas*," Int. J. Heat Mass Transf., **18**, pp. 261–269.
[4] Tan, H. P., and Lallemand, M., 1989, "*Transcient Radiative-Conductive Heat Transfer in Flat Glasses Submitted to Temperature, Flux and Mixed Boundary Conditions*," Int. J. Heat Mass Transf., **32**, pp. 795–810.
[5] Tan, H. P., Wang, P. Y., and Xia, X. L., 2000, "*Transcient Coupled Radiation and Conduction in an Absorbing and Scattering Composite Layer*," J. Thermophys. Heat Transfer, **14**, pp. 77–87.
[6] Byun, K. H., and Smith, T. F., 1988, "*Development of the Zone Method for Linearly Anisotropic Scattering Media*," Journal of Quantitative Spectroscopy and Radiative Transfer, **34**, pp. 591–604.
[7] Yuen, W. W., and Takara, E. E., 1994, "*Development of a Generalized Zonal Method for the Analysis of Radiative Transfer in Absorbing and Anisotropically Scattering Media*," Numer. Heat Transfer, Part B, **25**, pp. 75–96.
[8] Ma, A. K., 1995, "*Generalized Zoning Method in One-Dimensional Participating Media*," ASME J. Heat Transfer, **117**, pp. 520–523.
[9] Goyhénèche, J. M., 1997, "*Modélisation et caractérisation thermique à très haute température de matériaux poreux en carbone destinés à l'isolation thermique des corps de rentrée dans l'atmosphère*," Ph.D. thesis, Institut National des Sciences Appliquées, order No 97ISAL0043, Lyon.
[10] Becker, H. B., 1977, "*A Mathematical Solution for Gas-to-Surface Radiative Exchange Area for a Rectangular Parallelepiped Enclosure Containing a Gray Medium*," ASME J. Heat Transfer, **99**, pp. 203–207.
[11] Vercamen, H. A. J., and Froment, G. F., 1980, "*An Improved Zone Method Using Monte-Carlo Techniques for the Simulation of Radiation in Industrial Furnaces*," Int. J. Heat Mass Transf., **23**, pp. 329–337.
[12] Kim, T. K., and Smith, T. F., 1985, "*Radiative and Conductive Transfer for a Real Gas in a Cylindrical Enclosure With Gray Walls*," Int. J. Heat Mass Transf., **28**, pp. 2268–2277.
[13] Tucker, R. J., 1986, "*Direct Exchange Areas for Calculating Radiation Transfer in Rectangular Furnaces*," ASME J. Heat Transfer, **108**, pp. 707–710.
[14] Kheiri, A., Tanguier, J. L., Bour, D., Mainard, R., and Kleinclauss, J., 1990, "*Transfert de chaleur dans les milieux semi-transparents: adaptation de la méthode des zones de Hottel aux milieux optiquement épais*," *Proceedings SFT-90 Conference*, Nantes, pp. 37–40.
[15] Naraghi, M. H. N., and Chung, B. T. F., 1985, "*A Unified Matrix Formulation for the Zone Method: A Stochastic Approach*," Int. J. Heat Mass Transf., **28**, pp. 245–251.
[16] Dayan, A., and Tien, C. L., 1975, "*Heat Transfer in a Gray Planar Medium With Linear Anisotropic Scattering*," ASME J. Heat Transfer, **97**, pp. 391–397.
[17] Yuen, W. W., and Tien, C. L., 1980, "*A Successive Approximation Approach to Problems in Radiative Transfer With Differential Formulation*," ASME J. Heat Transfer, **102**, pp. 86–91.
[18] Bleach, H. L., Ozisik, M. N., and Siewert, C. E., 1971, "*Radiative Transfer in Linearly-Anisotropic-Scattering, Conservative and Non-Conservative Slabs With Reflective Boundaries*," Int. J. Heat Mass Transf., **14**, pp. 1551–1565.
[19] Busbridge, I. W., and Orchard, S. E., 1967, Astrophys. J., **149**, p. 655.
[20] Sutton, W. H., and Ozisik, M. N., 1979, "*An Iterative Solution for Anisotropic Radiative Transfer in a Slab*," ASME J. Heat Transfer, **101**, pp. 695–698.

---

[2] Symbols not appearing in the nomenclature comply with the JHT Common Symbol List.

Shou-Shing Hsieh
Sun Yat-Sen Professor of Mechanical and
Electro-Mechanical Engineering,
Dean of Engineering,
Fellow ASME

Chung-Guang Ke
Graduate Student

Department of Mechanical and Electro-
Mechanical Engineering,
National Sun Yat-Sen University,
Kaohsiung, Taiwan 80424

Bubble Dynamic Parameters and Pool Boiling Heat Transfer on Plasma Coated Tubes in Saturated R-134a and R-600a

An optical method for measuring the bubble dynamic data subject to an isolated bubble model is presented at low heat flux ($q \leqslant 1\ kW/m^2$); while the operating heat fluxes are up to 30 kW/m^2. By simultaneous measurements of departure diameters, velocities, frequencies and nucleation site densities, the heat transfer contribution of an individual active site is evaluated. A single phase heat transfer correlation was used to model the present heat transfer data. The test specimens consisted of tubes with porous copper (Cu) and molybdenum (Mo) plasma coated surfaces. The porosity (ε), the thickness of the porous layer (δ), and the mean pore diameter (η) of the tested tubes are the following: $0.055 \leqslant \varepsilon \leqslant 0.057$, $100 \leqslant \delta \leqslant 300\ \mu m$, and $3 \leqslant \eta \leqslant 4\ \mu m$. The tests were carried out using R-134a and R-600a as working fluid at a saturation temperature of 18°C and with low and moderate heat fluxes ($\leqslant$1 kW/m^2) for boiling visualization and related measurements ($\leqslant$30 kW/m^2). [DOI: 10.1115/1.1481360]

Keywords: *Boiling, Bubble Growth, Enhancement, Heat Transfer, Refrigeration*

1 Introduction

It is known that nucleate boiling is characterized by the formation of vapor bubbles from fixed sites randomly distributed on a heating surface. Moreover, enhanced boiling surfaces would generally create more bubbles and, consequently, result in a higher heat transfer performance. Although plenty of studies of boiling heat transfer have been devoted to enhanced surfaces [1–6], due to the highly complex nature of boiling and difficulty in measurements such as the determination of key boiling parameters such as bubble departure diameter, velocity, frequency, and active nucleation site density, aspects of the boiling heat transfer mechanisms on enhanced surfaces remain unclear.

Previous studies have employed several photographic techniques to determine the above-stated bubble dynamic data. Few of them have applied the data to predict each component of the total heat flux (latent heat, natural convection, and micro convection) as well as to validate their boiling models.

Barthau [7] proposed an optical method for measuring the active nucleation size density on a tube immersed in R-114 at various pressures. The heat transfer contribution of an individual active site is found to decrease with increasing pressure and to decrease strongly with increasing heat flux. Small increases of the bubble departure diameter and of the bubble frequency have been observed with increasing heat flux.

Ammerman et al. [8] developed a unique method to determine the vapor volumetric flow rate as well as boiling dynamic data above a heated wire within a saturated liquid FC-72 utilizing a single photograph and Laser-Doppler anemometry. Overall contributions to the total heat flux from four nucleate boiling heat transfer mechanisms were determined.

In recent years, environmental concerns over the use of CFCs as working fluids in refrigeration and air-conditioning plants have led to the development of alternative fluids. Among these alternatives, R-134a and R-600a are used as substitutes for the commonly used CFC-12. Moreover, considerable effort has recently been made to find ways to design more compact and efficient evaporators for the process and refrigeration industries based on CFCs/non-CFCs. Industries are currently undergoing a massive conversion process from CFC to HFC (like R-134a) or HC (like R-600a). The conversion establishes a need for refrigerant data on the substitute refrigerants such as R-134a and R-600a used in this study.

In spite of foregoing merits, these methods (e.g., Barthau [7] and Ammerman et al. [8]) have the disadvantage of being limited to either special types of fluids or to special types of heating surfaces. Therefore, more accurate and detailed study of the bubble dynamic data especially for bubble departure velocity from coated enhanced surfaces in R-134a and R-600a are needed. Mertz et al. [9] reported an experimental study for tubes with wires in compact two phase heat exchangers. Very recently, Hsieh and Yang [10] performed a series of pool nucleate boiling heat transfer experiments from coated surfaces with porous copper (Cu) and molybdenum (Mo) and helically wrapped with wire on copper surfaces immersed in saturated R-134a and R-600a.

This paper is a continuation of the work of Hsieh and Yang [10] to broaden our fundamental understanding of the mechanisms of pool boiling heat transfer on plasma coated tubes in saturated R-134a and R-600a.

2 LDV Measurements and Videography

2.1 LDV Measurements for Bubble Velocity and Bubble Departure Frequency. The present system is a commercial two color, four beam DANTEC fringe-type LDV system, operated in the backward scatter mode, with the general layout shown in Fig. 1 which is similar to that of Hsieh et al. [11]. Standard DANTEC 55× modular optics and a model Stabilite 2016 4W Special Physics Ar^+ laser are mounted on a two-dimensional, traversing system. Two separate LDV channels are formed by use of color separation of beams with wavelengths 514.5 nm (green light) and 488.0 nm (blue light). These two beams form orthogonal fringes by means of a standard DANTEC two channel optical train. These two sets of fringes allow the simultaneous measurement of two

---

Contributed by the Heat Transfer Division for publication in the JOURNAL OF HEAT TRANSFER. Manuscript received by the Heat Transfer Division July 27, 2001; revision received March 12, 2002. Associate Editor: D. B. R. Kenning.

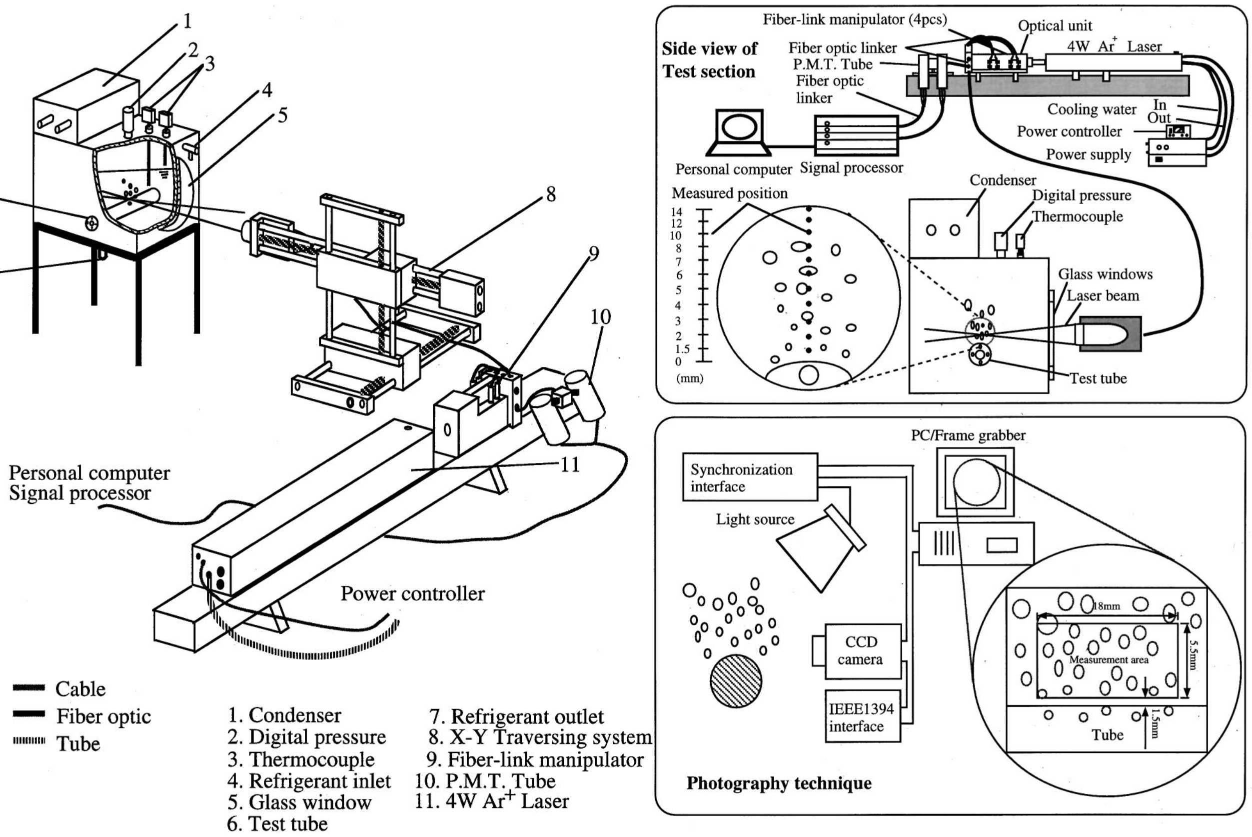

Fig. 1 Photography technique and LDV facility schematic for recording bubble dynamic data

orthogonal velocity components. The transverse velocity component is measured using the 488.0 nm beam, while the 514.5 nm beam measures a streamwise velocity component. A combined counter-type signal processor (Dantec model 57H00) with functions of counter, buffer interface and coincidence filter, which is interfaced with a LEO (Intel-486) PC in the direct access mode, was employed for data processing. Statistical data were based on a sample size of 320,000 measurements with a sampling frequency of approximately 400 samples/s, from which the time-averaged values were determined.

The laser-Doppler signal from the photomultiplier was fed to a signal processor and then measured with a frequency counter. The digital value of the Doppler frequency shift f_D, the characteristic wavelength of the laser λ, and the half-angle between the beams $\theta/2$ are translated to streamwise u and transverse v velocity components, respectively, by the equation:

$$u/or\ \ v=\frac{\lambda_{u/or\ \ v}f_D}{2\sin(\theta/2)} \tag{1}$$

Data were taken whenever a signal was validated. Moreover, the departure frequency of the bubble can be simultaneously measured.

In addition, various sources of uncertainty contribute to the random and system errors in the mean velocity measurements. These include index of refraction effects that alter the half-angle between the beams and the optical probe volume location; velocity bias, filter bias, and velocity gradient broadening; and finite size of the data samples. The visual optical probe volume positioning uncertainty was kept less than ±0.01 mm by the careful determination of an initial reference location and using stepping motors with incremental steps equal to 50 μm.

2.2 Videography for Bubble Dynamic Parameters (d_b and n). A JVC Model Gr-DVM 70 gated, intensified, high resolution CCD video camera with a motion analyzing system was used to visualize the boiling phenomena in the test sections as also shown in Fig. 1. This system was used to capture single-frame images of vapor bubbles above the heated surface, and it can provide images at a speed of 30 frames per second. Such a technique is the same as the work reported by Ammerman et al. [8]. The illumination provided by one LPL-BROM CINE 500 W floodlight was filtered through a diffuser for the videography. The field of view is 18 $\times$5.5 mm in the horizontal and vertical directions, respectively. Video images were synchronized and transferred to an IBM 586 PC, where they were digitized by a 640$\times$480 frame grabber board and analyzed by image processing software. There are eleven positions (points) to be measured (one value/measured point) as indicated in Fig. 1. Unlike Hsieh and Yang [10], a single photo method following Ammerman et al. [8] was applied to analyze the present measuring data to obtain the bubble departure diameter. The nucleation site density was measured for different heat fluxes by photographing the test tubes with a high speed camera at 30 frames/s. The flash duration used was less than 50 nanoseconds and the camera is capable of shutter speeds up to 1/500th of a second. The photograph was projected on a screen to obtain sufficient magnification, and the bubbles corresponding to nucleation sites on the surface were thus counted.

3. Experimental Setup and Procedure

3.1 Test Facility and Test Section. The experimental apparatus, including the measurement positions, is similar to that of Hsieh and Yang [10]. It consists of a rectangular container with the dimensions of 300$\times$370$\times$300 mm made of stainless steel (see

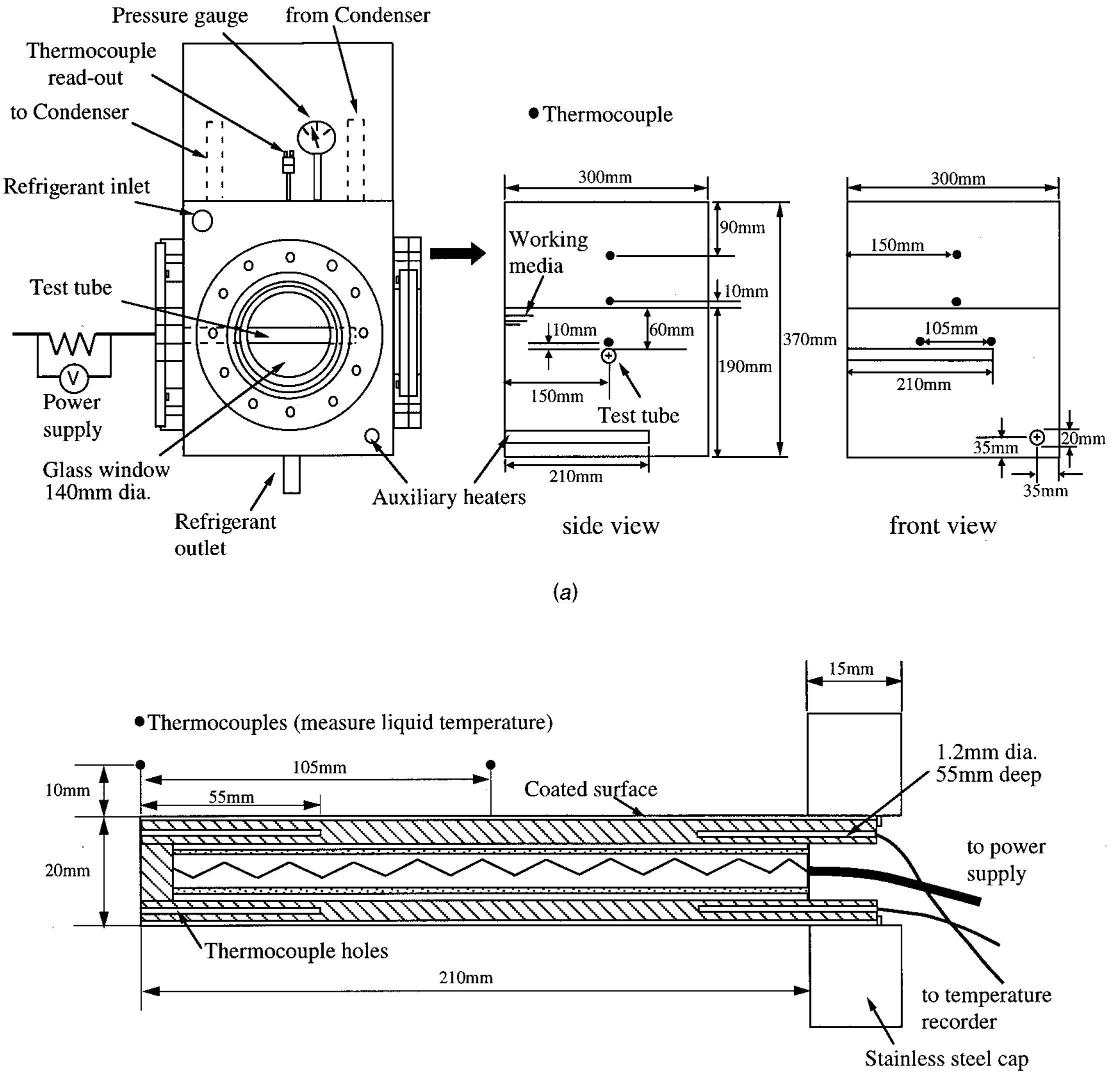

(*a*)

(*b*)

Fig. 2 (*a*) Test section; (*b*) Thermocouple positions and test specimen

Fig. 2 for details). Saturated nucleate pool boiling data were taken on a smooth tube and two plasma coated tubes with R-134a and R-600a as working fluids. More than six runs for each tube were conducted. Some of these tests were repeated after several months to verify the reproducibility. The tested tube was designed to simulate a portion of a typical rod in a refrigerant-flooded evaporator. It was fabricated from a copper tube. The test specimen is soldered to a flange at one end of the tank. The copper tubes were 20 mm in outer diameter, with an inner diameter of 12 mm. Each cartridge heater was 220 mm long with an actual heated length of

Table 1 The specification and dimensions of the present coated tubes studied

Tube No. (designated symbol)	surface(coating material)	thickness of porous layer $\delta(\mu m)$	surface roughness $Ra(\mu m)$	porosity ε	mean pore diameter $\eta(\mu m)$
Tube1 (S)	Smooth	—	0.07	—	—
Tube2 (CM)	Mo	300	7.24	0.055	3
Tube3 (Cu)	Cu	100	7.84	0.057	4
Note：All tubes considered have OD 20mm and ID 10mm with a length 210mm					

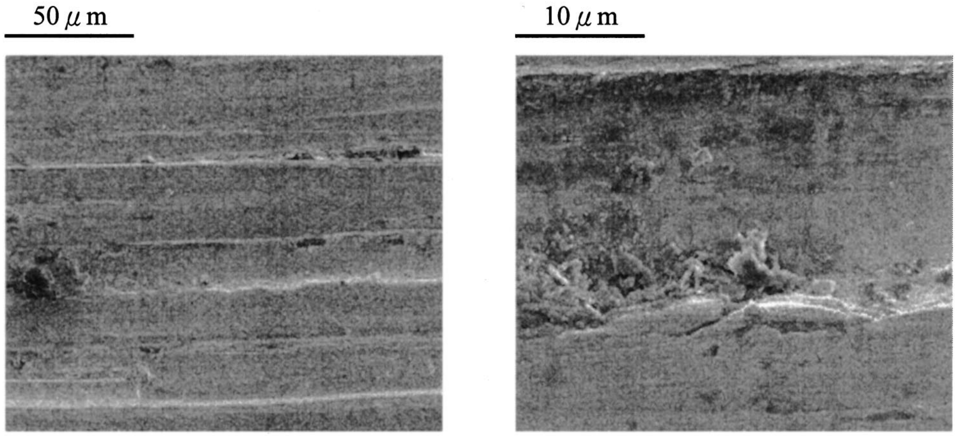

Smooth(×1000)-top Smooth(×5000)-top

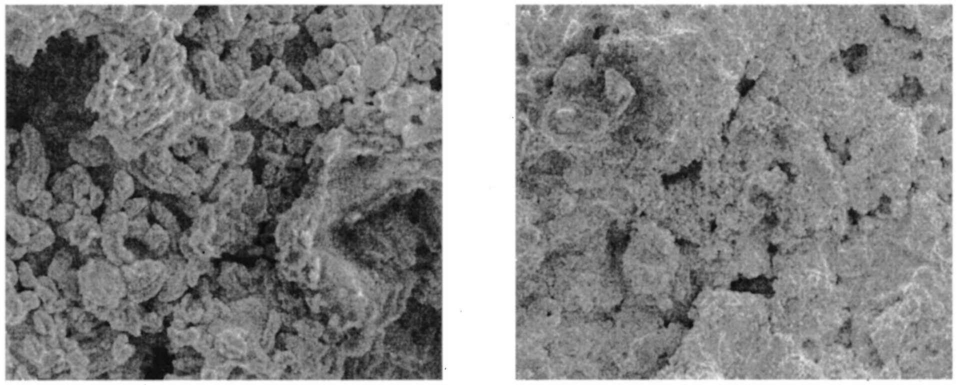

Mo(×1000)-side Mo(×5000)-side

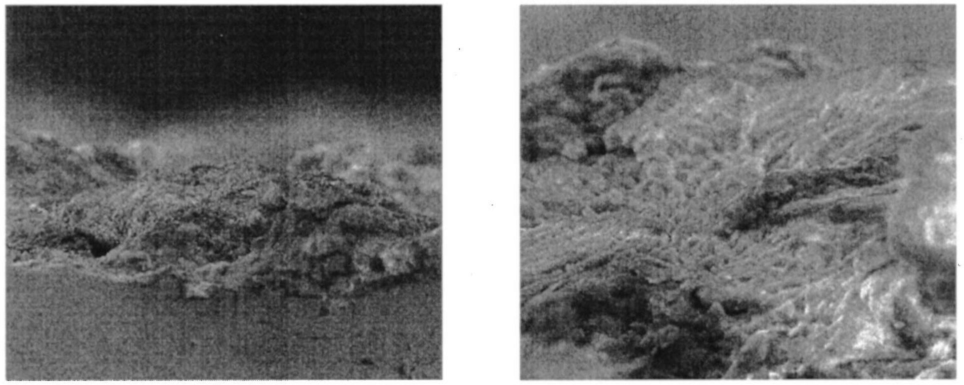

Mo(×1000)-top (*a*) Mo(×5000)-top

Fig. 3 SEM observations for test tubes

210 mm and 11.95 mm in diameter with a maximum power output 378 W and was inserted into the copper tube. The test section included both smooth and treated surfaces.

Both increasing and decreasing heat flux of boiling data were obtained but only the data for decreasing heat flux are shown. Table 1 depicts the dimensions of the test tubes. The tubes with coated surfaces were provided by Metal Industrial Research and Development Center (MIRDC) of Taiwan. Because one of the objectives is to investigate the surface roughness effect on boiling behavior, the tested surfaces including smooth surfaces were examined by an SEM. Figure 3 shows these results. The characteristics of the coated surfaces (e.g., the porosity (ε), thickness of layer (δ), and the surface roughness (Ra)) were calculated following the same procedure as indicated by Hsieh and Yang [10]. The r.m.s. roughness values (Ra) in the circumferential direction ranged from 0.07 μm for the smooth tubes (S) to 7.84 μm for the tubes coated with copper (Cu), the corresponding porosity (ε) from 0 to 0.057 and mean pore diameter (δ) 0 to 4 μm, Table 1. Boiling on the heated surfaces was illuminated, photographed and measured through windows at the sides of the apparatus. Tube wall and pool bulk temperatures were also measured.

3.2 Experimental Procedure. The primary measurements consist of tube wall and pool bulk temperatures, and the power to

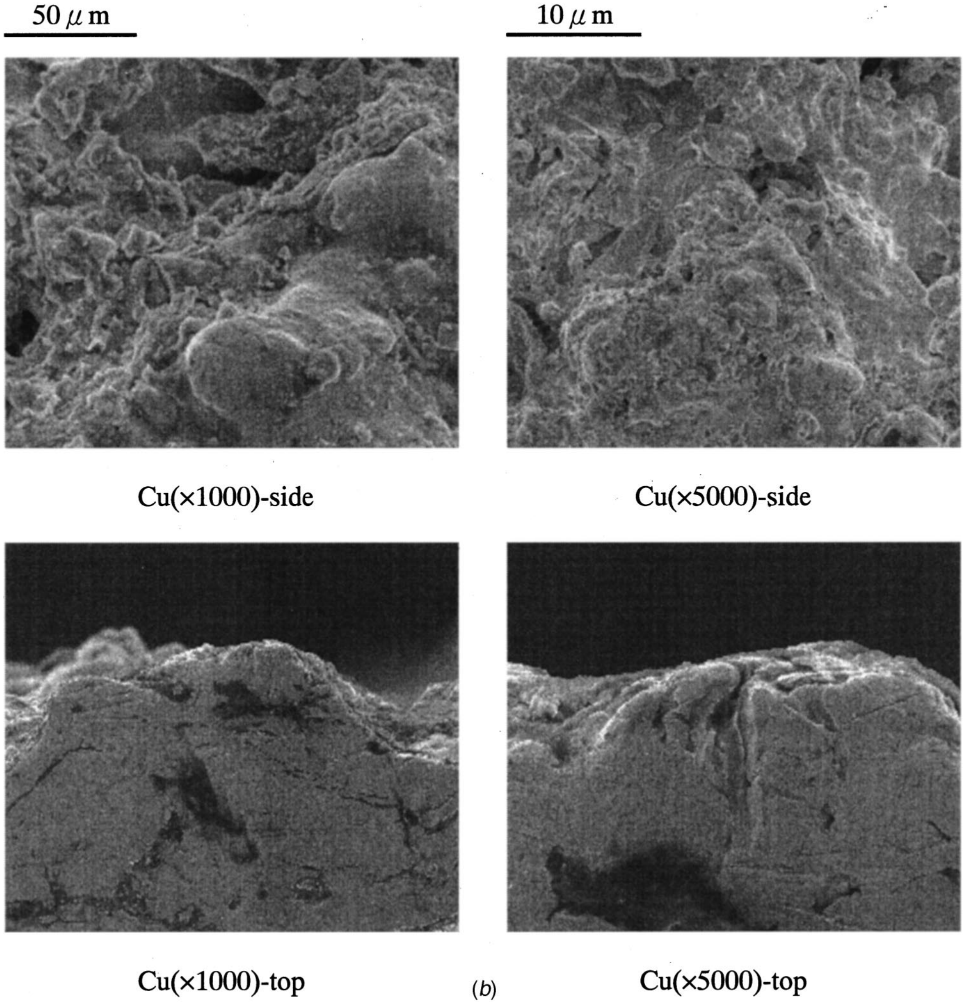

Cu(×1000)-side Cu(×5000)-side

Cu(×1000)-top (b) Cu(×5000)-top

Fig. 3 (***continued***)

the heater. Four *T* type sheath thermocouples with diameters of 1.1 mm as shown by Hsieh and Yang [10] located at the middle of the tube are used to measure the tube wall temperature. Four *T* type thermocouples, two just right above the tube surface, one positioned at the center and one at the end of the tube length, respectively, are used to measure the pool temperature, and the liquid was maintained at its saturation temperature at the corresponding operating pressures. The temperature difference between these two points was within ±0.1°C at the maximum power input. A variac-controlled AC power supply, a current shunt (15 Ω with 1 percent accuracy), and two precision multimeters, one for current and one for voltage measurement, provided the measurement and control of the input of electric power with an accuracy of ±1 percent. The other two thermocouples were used to measure the vapor temperature and were positioned along the tube about 10 and 105 mm respectively above the liquid free surface (see Hsieh and Yang [10] for details).

Prepared test sections were cleaned with chlorinol and water and finally with acetone. The tank was cleaned with acetone before each run. Once the evaporator tube was installed, the system was evacuated to a pressure of about 30 Pa. If no leaks were detected over a 24 h interval, the evaporator was charged with the working fluid from a reservoir to a level of 60 mm above the top of the tube. This resulted in a vapor pressure of about 537 kPa (R-134a) and 284 kPa (R-600a), respectively.

The power was applied to the pool to degas the test fluids at a heat flux of 30 kW/m^2 for 1.5 h and 1 h, respectively. The saturation temperature at the measured pressure was compared to the pool temperature measured by the thermocouples (within ±0.1°C). The power supplied to the test section was gradually, and slowly, reduced to zero. The test pool was maintained close to the saturation temperature with an auxiliary heater for about 40 min; then the heater was switched off to minimize convective effects. The heating power supplied to the test section was slowly and gradually increased to almost 30 kW/m^2 for heat transfer measurements. Due to the bubble coalescence at high heat fluxes, boiling visualization tests were employed for only heat fluxes up to 1 kW/m^2. Both increasing and decreasing heat flux data were taken in order to obtain more accurate data and to observe boiling hysteresis (not shown). For the decreasing data, the heat flux was reduced from 30 kW/m^2 in pre-determined steps by means of a variac. It generally took about 30 min to achieve steady-state conditions after the power level was changed. A steady-state condition was assumed when the temperatures in the center of the test tube did not vary by more than 0.1°C over 2 min.

During all the tests, the saturation temperature was kept near 18°C for both R-134a and R-600a, respectively. Test liquids were carefully prepared and kept clean to avoid the contamination; however, uncontrolled contamination may still occur. More detailed relevant properties of the refrigerants in this study can be found in Hsieh and Yang [10]. All the data were obtained and reduced with a computer-controlled data acquisition system. Room temperature was maintained at 25°C, so that heat losses from the test section were almost constant during all experiments.

Table 2 Maximum possible measurement errors

Quantity	Systematic error	Random error
ΔT	○ ±2.06% ◎ ±1.58%	○ ±2.49% ◎ ±2.32%
d	○ ±1.40% ⊙ ±0.44%	○ ±1.28% ⊙ ±0.40%
q	○ ±10.6% ◎ ±3.10%	○ ±10.2% ◎ ±2.34%
h	○ ±10.8% ◎ ±3.48%	○ ±10.5% ◎ ±3.30%
n	○ ±5.16% ⊙ ±3.67%	○ ±4.87% ⊙ ±3.24%
f	±6.24%	±5%
T	±1.3%	±1.1%
x	±0.05mm	±0.01mm
y	±0.05mm	±0.01mm
z	±0.05mm	±0.01mm
U_T	±7.5%	±6.6%
U/U_T	±8.7%	±8.26%

Note: ○ denotes 0.6kW/m^2 ⊙ denotes 1kW/m^2 ◎ denotes 30kW/m^2

4 Data Reduction and Uncertainty Analysis

For each power input, the heat transfer coefficient was calculated on the basis of bulk fluid saturation temperature (T_{sat}), tube heat flux (q), and the average value (T_{avg}) of the four tube wall temperatures. The heat transfer coefficient at each power input was then calculated, following $h = Q/[A(T_{\text{avg}} - T_{\text{sat}})]$.

Using the method of Kline and McClintock [12], uncertainty estimates were made considering the errors of the instruments, the measurement variance, geometry uncertainty and calibration errors for the heat flux, temperature, and bubble dynamic parameter measurements. The uncertainty in the wall superheat was dominated by the uncertainty in the wall temperature measurements. The values of the four wall temperatures were recorded and compared to examine variation caused either by nonuniformities in the cartridge heater or by the test tube soldering and assembly procedure. Wall superheat uncertainty can be attributed primarily to thermocouple calibration (±0.1°C) and temperature correction from the thermocouple reading to the reference surface. The maximum variation of the four measured wall temperatures was ±0.3°C at the maximum heat flux (≅30 kW/m^2). The uncertainty in the saturation temperature was estimated to be less than ±0.1°C.

Substrate conduction heat losses were quantified at different heat flux conditions by solving three-dimensional conduction problems with a finite-difference solver. This loss varied between 10.2 % and 0.2 % for heat flux conditions between 0.8 kW/m^2 to 30 kW/m^2, respectively. The other primary contributor to heat flux uncertainty was heated surface area. For instance, it is about ±4 % for Tube 3 (Cu) coated surface at $q = 0.8$ kW/m^2. Combining these effects lead to overall uncertainty estimates in heat flux of 11.2 % at the lowest heat input. Based on these uncertainties, it indicates the uncertainty of the wall heat transfer coefficient to be about ±15 % at $q = 0.8$ kW/m^2.

Accuracy of the bubble diameter measurements is estimated to be within ±1.9 %/ or ±0.6 % at the minimum/or maximum heat flux with an extreme high space resolution (~9.5 nm) of CCD camera. The uncertainty in the number of bubbles was found within ±7.1 % for the minimum and ±4.9 % for the maximum heat flux. Uncertainty estimates for time is ±1.7 %. The frequencies reported are average values and the observed fluctuations in frequency are less than ±8 %. The data presented refer to individual and isolated bubbles. Of the uncertainties specifically attributable to the LDA technique, filter bias, velocity bias, and gradient broadening were carefully examined. Filter bias was avoided. The maximum velocity bias was estimated to be less than 10 % but typically, it was about 10 %. The effect of gradient broadening seems negligible. Calculation of the mean results in statistical uncertainties of ±12 % for mean velocity at the largest heat flux level. Table 2 summarizes the estimates of maximum inaccuracy (systematic error) and imprecision (random error) associated with each measurements.

5 Results and Discussion

5.1 General Observations. Due to the random microstructure of the present enhanced tubes, bubble departure diameters are generally very random, which fitted over the range of 50–500 μm at the same heat flux. Smaller bubble diameters were found for enhanced surfaces than for the smooth tube. However, bigger bubbles were found for R-600a test refrigerant. Bubble agglomeration was found at $q > 1$ kW/m^2. These features could be seen from a set of typical photographs shown in Fig. 4. In fact, as heat flux increases, bubble coalescence takes place especially for plasma coated surfaces (Figs. 4(*c*) and 4(*e*)).

Like Hsieh and Yang [10], the mechanism which described the boiling process from porous structures of the present plasma coating surfaces can be explained as follows; it appears that the heat is conducted to a liquid layer at the upper surface of the porous structure. This conduction supposedly occurs through the matrix formed by the solid portion of these wick and liquid in the porous spaces. It is recognized that the vapor bubbles exist within the pores formed by the void space between two solid portions. Heat is transferred by conduction through the solid matrix and then by conduction across the liquid portion. The pores within the matrix are interconnected so that liquid can be supplied to the pores and vapor can pass through the matrix to the tube surface. As vapor is generated within a pore, the pressure in the vapor increases [1]. When the pressure is sufficiently high, it overcomes the surface tension retention force and the vapor is forced through the interconnected channels (pores) to the liquid.

5.2 Local Bubble Velocity and Final Velocity. The LDV system was used to determine an average of measured instantaneous bubble velocities at each height following Ammerman et al. (1996). Figure 5 indicates that the local bubble departure velocity along the bubble rising path above the smooth test tube for R-134a at different heat flux levels. Also included in Fig. 5 are the results from Ammerman et al. [8] for comparison. Local averaged bubble velocity increases along the rising path until a critical velocity (final velocity) is approached at a height of 8 mm above the tube for all studied cases. This behavior is in excellent agreement with the results of Ammerman et al. [8].

However, the magnitude of the present study is consistently lower (25~30 percent) than that of Ammerman et al. at the corresponding height due to different working medium used. The reason for this behavior is that, initially, the buoyancy force caused the bubble to accelerate when departing from the tube. Eventually, however, the drag force on the bubble balances the buoyancy force which results in a constant velocity thereafter. Since the present bubbles generated from the surfaces are very small (~0.1 mm), surface tension forces are often strong enough

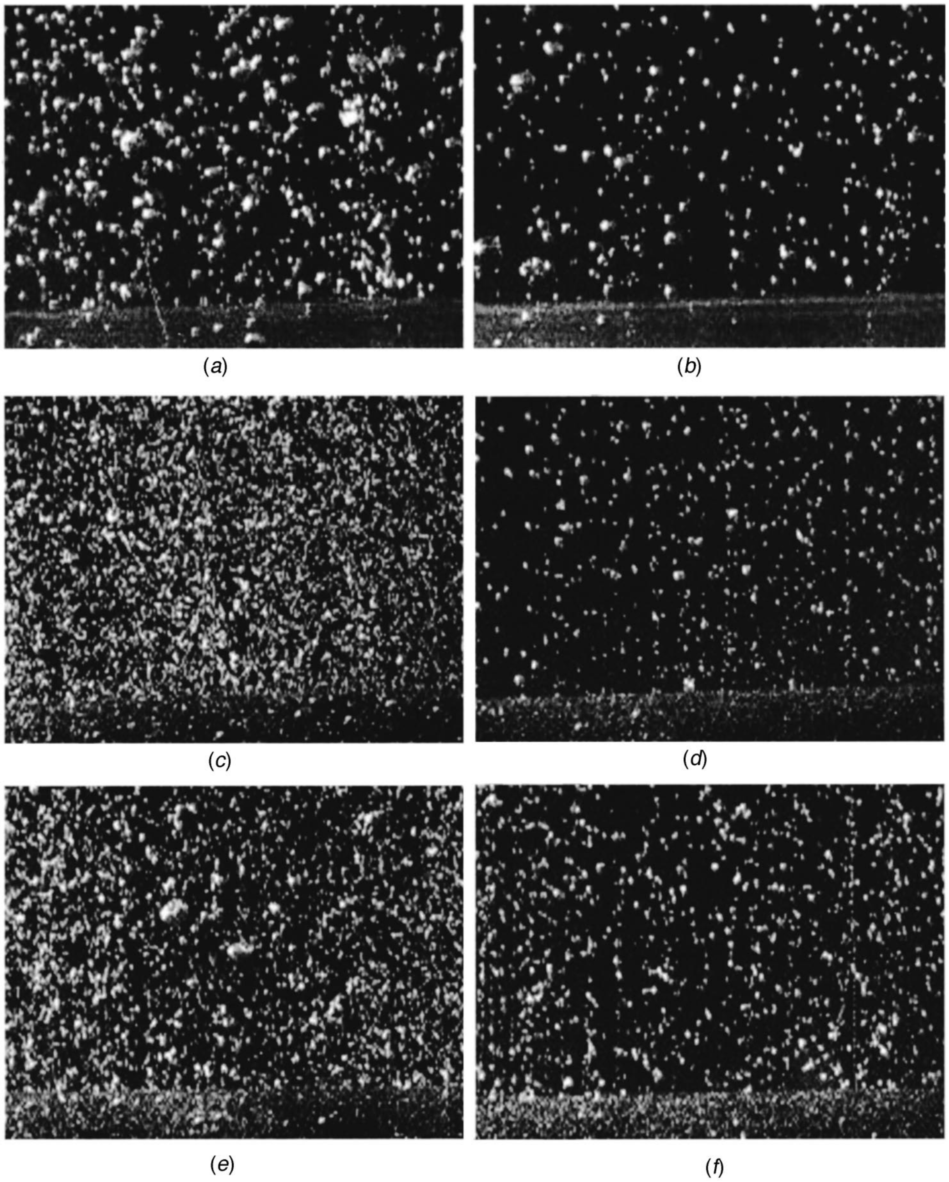

Fig. 4 Illustration of boiling visualizations: (*a*) smooth tube 1 kW/m^2, R-134a; (*b*) smooth tube 0.6 kW/m^2, R-134a; (*c*) coated tube (Mo) 1 kW/m^2, R-134a; (*d*) coated tube (Mo) 0.6 kW/m^2, R-134a; (*e*) coated tube (Cu) 1 kW/m^2, R-134a; (*f*) coated tube (Cu) 0.6 kW/m^2, R-134a; (*g*) smooth tube 1 kW/m^2, R-600a; (*h*) smooth tube 0.6 kW/m^2, R-600a; (*i*) coated tube (Mo) 1 kW/m^2, R-600a; (*j*) coated tube (Mo) 0.6 kW/m^2, R-600a; (*k*) coated tube (Cu) 1 kW/m^2, R-600a; and (*l*) coated tube (Cu) 0.6 kW/m^2, R-600a.

to maintain the spherical shape. The traditional Stokes' law may not apply due to the failure of the no-slip condition to hold at a mobile interface.

Further observations of the local average bubble velocity for different test tubes are presented in Fig. 6, and it indicates that with a higher heat flux, a higher local velocity was reached due to a higher driving force applied. The velocity in Fig. 6 also strongly suggests that such a value seems independent of the surface condition of test tubes.

Local bubble velocity distribution versus bubble diameter can be found in Figs. 7(*a*)–(*c*) for smooth and plasma coated surfaces for different heat fluxes. Figure 7(*a*) indicates a nearly linear velocity increases with bubble diameter for R-600a with about ±10 percent scatter in the range of $0.47 < d < 0.55$ mm. As heat flux increases, bubble departure velocity increases. For instance, at $q = 1$ kW/m^2 final velocity can be reached to 0.19 m/s with a corresponding bubble diameter of 0.57 mm for R-600a. The same finding can be seen in Fig. 7(*b*) for R-134a with smaller values of both velocity and diameter. With plasma coated surfaces, the bubble diameter becomes even smaller (about 1/3) and, in turn, this also results in a smaller final velocity (1/2) due to a resultant smaller buoyancy. Table 3 lists results from Fig. 7 with comparisons from the calculated values based on Stokes' Theorem [14] and previous investigation, Rohsenow [15]. Naturally, the differences can be seen due to a quite simple model for each.

In summary, experimental final velocities for vapor bubbles rising in R-134a and R-600a are presented in Fig. 8(*a*). As one may note, due to the present very small bubbles ($d \leq 0.35$ mm), surface tension forces are often strong enough to maintain the spherical shape. As a result, most of the present bubbles are within the spherical bubble regime especially for R-134a test fluid. However, for R-600a, the bubble size seems bigger ($d > 0.35$ mm), they belong to the ellipsoidal regime. Some of the spread in the data may be partly due to the experimental scatter and partly due to the surface contamination. The wide variance in the data perhaps reflects uncontrolled contamination of the R-600a. It is recognized

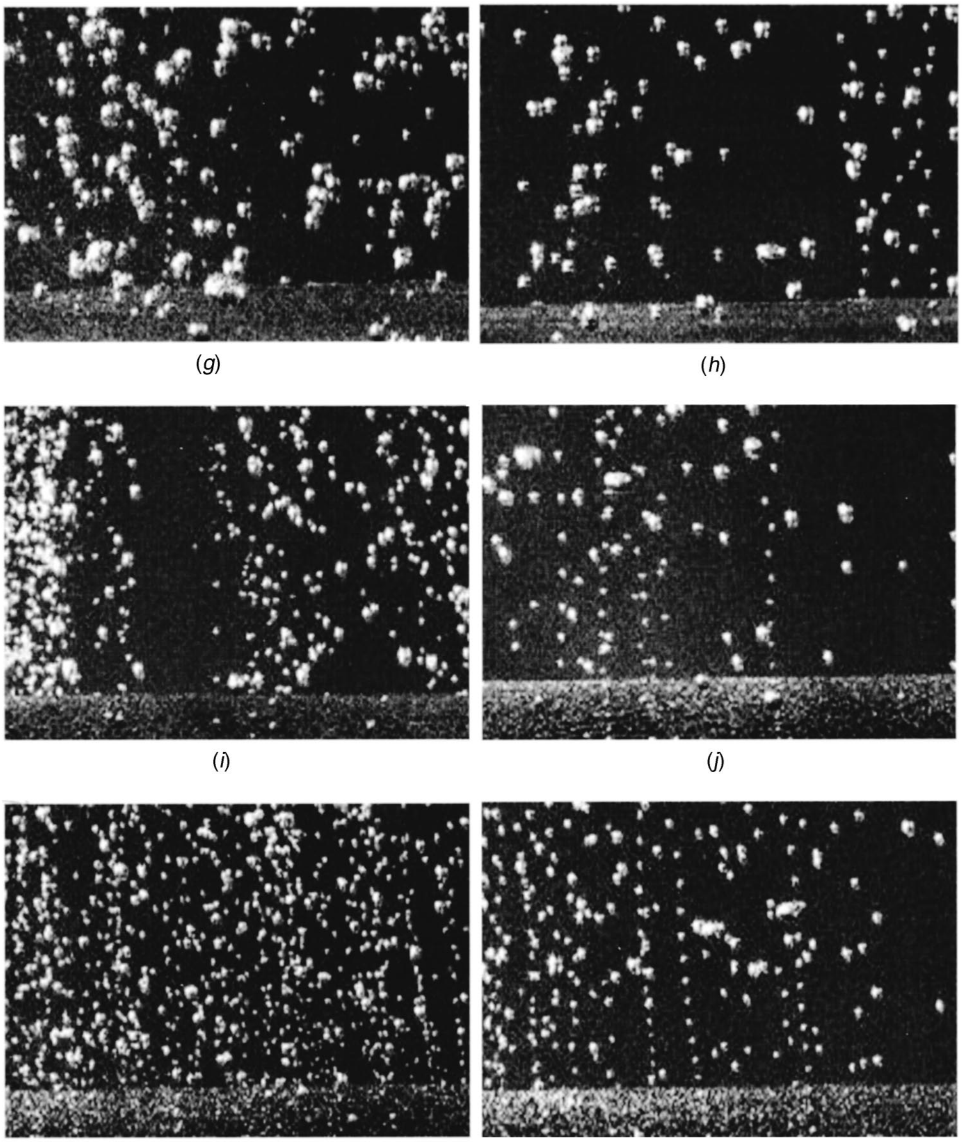
(*g*) (*h*)

(*i*) (*j*)

(*k*) (*l*)

Fig. 4 (***continued***)

that the final velocity is a complex function of the bubble diameter, also evidenced by Figs. 7(*a*)–(*c*), because of the distortion of the bubble shape, and ultimately because of the oscillation of large bubbles as they rise through the test refrigerants. The present data for spherical regime were also correlated followed the correlation described by Clift et al. [13] and results were also shown in Fig. 8(*a*) and it is found that all the experimental data fall within ±20 percent band as shown in Fig. 8(*b*). The curves converge for small spherical bubbles and for large bubbles where surface tension forces is not important any more.

5.3 Bubble Departure Frequency. The bubble dynamics for R-134a and R-600a are seen to depend on heat flux. After the onset of nucleate boiling, single bubbles occur close to the heated wall. As the heat flux increases, bubble coalescence takes place as stated before. Then, bubble growth after departure, and bubble agglomeration may occur ($q > 1\ \mathrm{kW/m^2}$). This behavior is more pronounced as the heat flux increases. For visualization tests ($q \leqslant 1\ \mathrm{kW/m^2}$), the bubble diameter increase after departure is mainly due to the liquid (outside the bubble) pressure becoming smaller as the bubble rises along its path. For both R-134a and

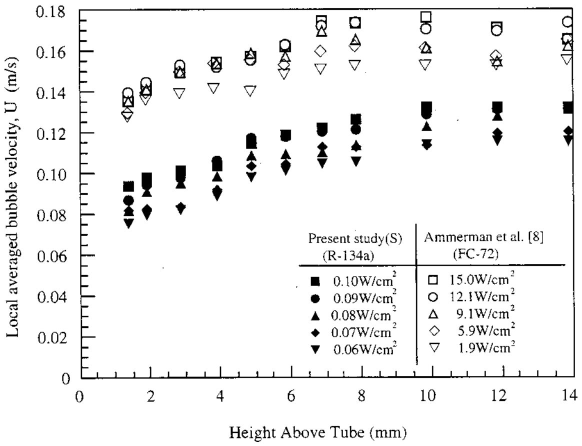

Fig. 5 Local averaged bubble velocity distribution versus vertical position

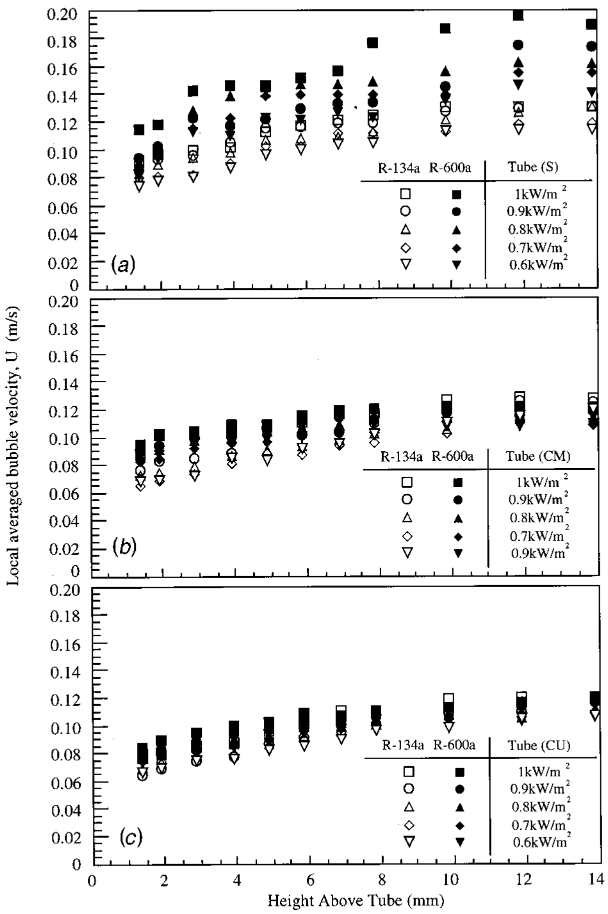

Fig. 6 Local averaged bubble velocity versus vertical position

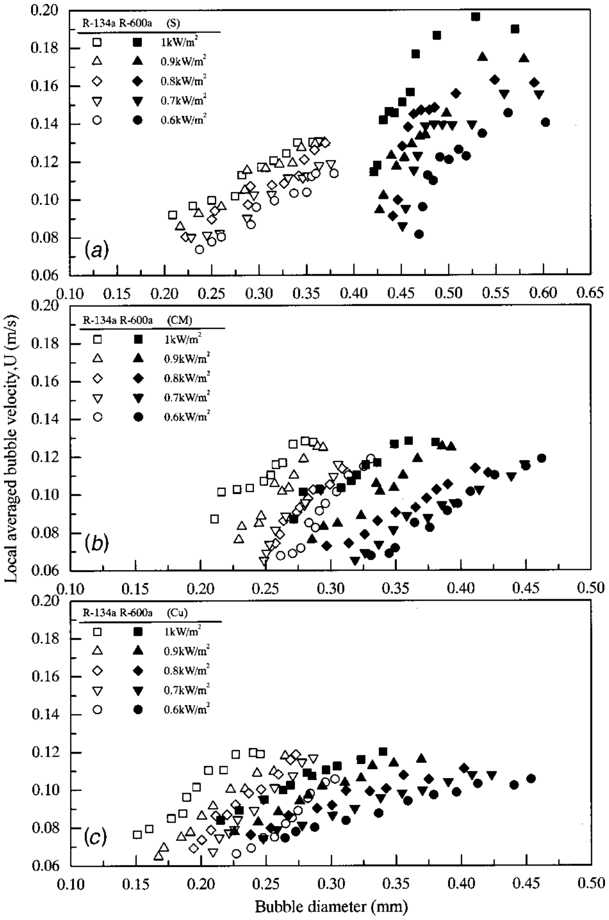

Fig. 7 Bubble diameter versus bubble velocity

R-600a, the departure diameter was observed to slightly decrease with increasing heat flux (not shown) which is in agreement with Hsieh and Yang [10]. The bubbles tend to have a spherical shape small diameters ($\leqslant 0.35$ mm) to an elliptic shape for large diameters (> 0.35 mm).

With bubble velocities known, individual bubble frequencies can be directly counted from LDV signal process. Frequency is shown versus heat flux in Figs. 9(*a*) and (*b*), respectively, for R-134a and R-600a. Again, the frequency increases rapidly versus heat flux in the partially developed boiling regime. A corresponding increase in active nucleation sites was also found, which is similar to the results reported by Ammerman et al. [8] and Hsieh and Yang [10]. However, the present results seem consistently lower for both R-134a and R-600a than those of Hsieh and Yang [10], also shown in Fig. 9 for comparison, due to different measuring technique used.

5.4 Nucleation Site Density (*n*). The nucleation site densities (n) were estimated (counted) from the photographs. The nucleation size densities as a linear function of the heat flux for smooth and plasma coated tubes for both test refrigerants are shown in Fig. 10. The nearly linear increase of n with q of the present data is different from the data obtained in Barthau's work [5] where a nearly quadratic increase was found for a horizontal tube in R-114. It can also be seen from Fig. 10 that, for coated tubes, the nucleation site density obviously increases for a given heat flux for each test fluid. This kind of increasing behavior of the nucleation site density has also been found previously [16]. Also, the heat flux is known as a function of the degree of wall superheat ΔT, namely $q \sim (\Delta T)^m$, where m is about 3. In addition, the present nucleation site density has also something to do with the geometry as well as nucleate boiling bubble dynamic results. In order to correlate the increasing nucleation site density, the parameters of the plasma coated surfaces N_{cf} and λ were developed. N_{cf} represents the competing forces of viscosity of liquid phase and capillarity [17], $N_{cf} = \mu_l^2/\eta\rho_l\sigma$, η is the average pore diameter and $\lambda = \eta/\delta$ is the geometric scale factor. The correlation has the following form (Fig. 11):

$$n = c\ \mathrm{Pr}^{1.63}\lambda^{-0.12}N_{cf}^{0.051}(\Delta T)^{3.12}, \tag{2}$$

where $c = 150/\mathrm{m}^2\ \mathrm{K}^{3.12}$

$$3.793 \leqslant \mathrm{Pr} \leqslant 3.982$$

$$1\times10^{-2} \leqslant \lambda \leqslant 4\times10^{-2}$$

$$1.089\times10^{-3} \leqslant N_{\mathrm{cf}} \leqslant 1.574\times10^{-3}$$

The present exponent of (ΔT) was found to be 3.12 and the effect due to surface condition is significant in spite of two coated surfaces considered herein.

5.5 Heat Transfer and Correlations for Nucleate Boiling. Heat transfer results can be found from the boiling curves for smooth and two coated surfaces in both R-134a and R-600a. Heat transfer coefficient h versus heat flux q was plotted in Fig. 12(*a*). Generally speaking, the best heat transfer performance was found for Tube 3 (Cu) followed by Tube 2 (CM) and Tube 1 (S) and is found to be insensitive to bubble local velocity. However, it is directly proportional to departure frequency and active nucleation site density.

Following Nakayama and co-workers, the latent heat flux from the present surfaces can be found by using

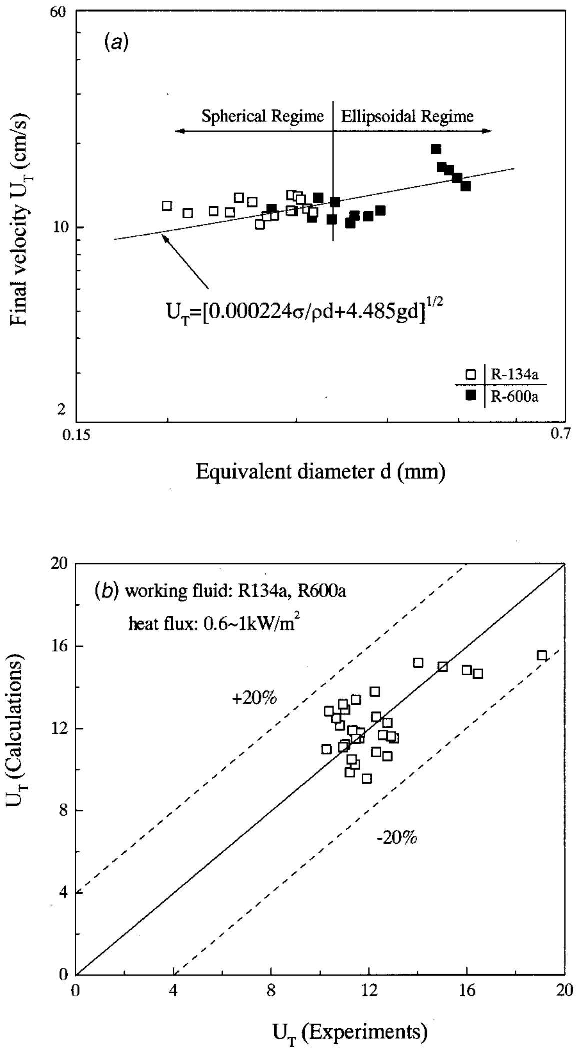

Fig. 8 ***U_T* versus *d* and the deviation of *U_T* correlation with experimental results**

$$q_f=(n)(\pi\overline{d_b^3}/6)\overline{f}h_{fg}\rho_v \tag{3}$$

where $\overline{d_b}$ is the average bubble departure diameter and f is the average departure frequency. The upper part of Fig. 12(*b*) illustrates the ratios of the latent heat flux to the total heat flux for the present coated surfaces, while the lower part of this figure indicates the sensible heat flux ratio which was obtained by subtracting the latent flux ratio from 1.0. Like previous studies [7,18], as the total heat flux increases, the value of the latent heat flux ratio decreases for coated surfaces (e.g., from 0.85 at 0.6 kW/m^2 down to 0.45 at 1 kW/m^2 for Tube 3 (Cu) in R-600a) as compared to that of smooth tube for coated surfaces, the latent heat takes most part of heat transfer contribution at low heat flux (e.g., up to 0.8 at 0.6 kW/m^2 for Tube 2 (CM) in R-600a). On the other hand, for smooth surfaces, the sensible heat accounts for most of the heat transfer contribution.

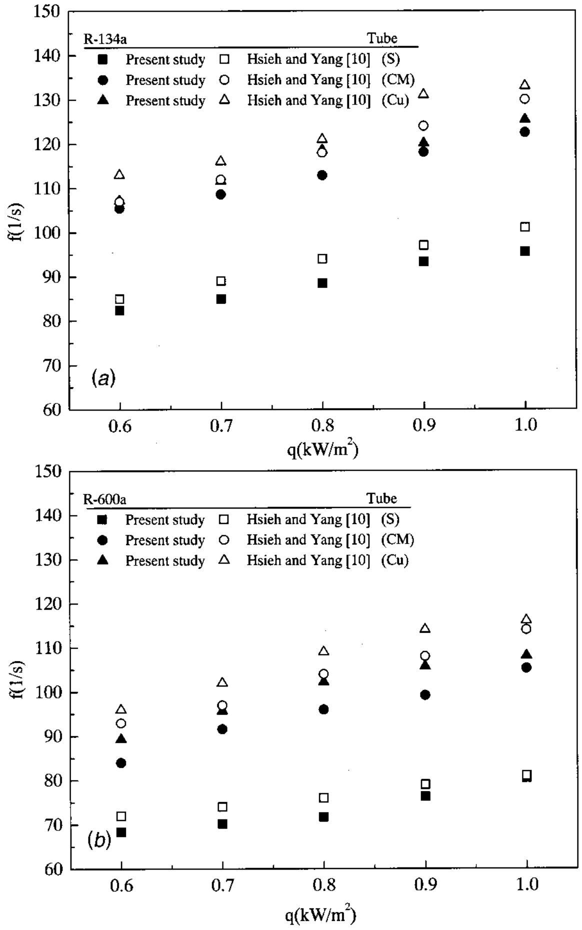

Fig. 9 Bubble departure frequency as function of heat flux

Table 3 Final velocity for the smooth tube and comparison with theoretical results

Heat flux	Present study U_T (m/s)		Rohsenow (average vapor velocity $U_{avg}=\frac{q}{\rho_v h_{fg}}$) U_{avg} (m/s)		Stokes' law ($U_T=\frac{\left(\frac{d}{4}\right)^2}{3\mu_v}(\rho_l-\rho_v)g$) U_T (m/s)	
	R-134a (S)	R-600a (S)	R-134a (S)	R-600a (S)	R-134a (S)	R-600a (S)
1k W/m^2	0.13	0.19	0.000208	0.000397	0.133	0.193
0.9k W/m^2	0.128	0.164	0.000187	0.000358	0.136	0.2
0.8k W/m^2	0.125	0.16	0.000166	0.000318	0.137	0.208
0.7k W/m^2	0.116	0.15	0.000146	0.000278	0.14	0.216
0.6k W/m^2	0.113	0.14	0.000125	0.000238	0.140	0.222

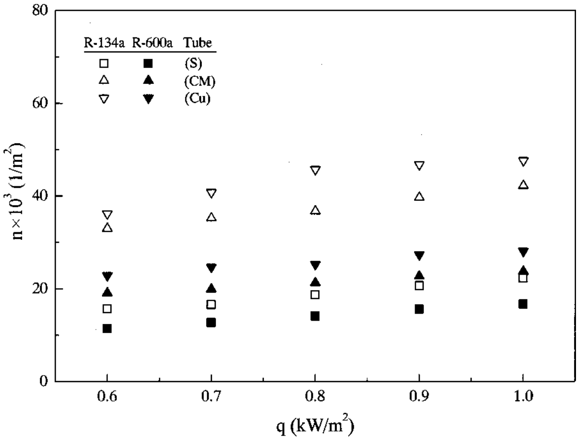

Fig. 10 Nucleation site density with heat flux

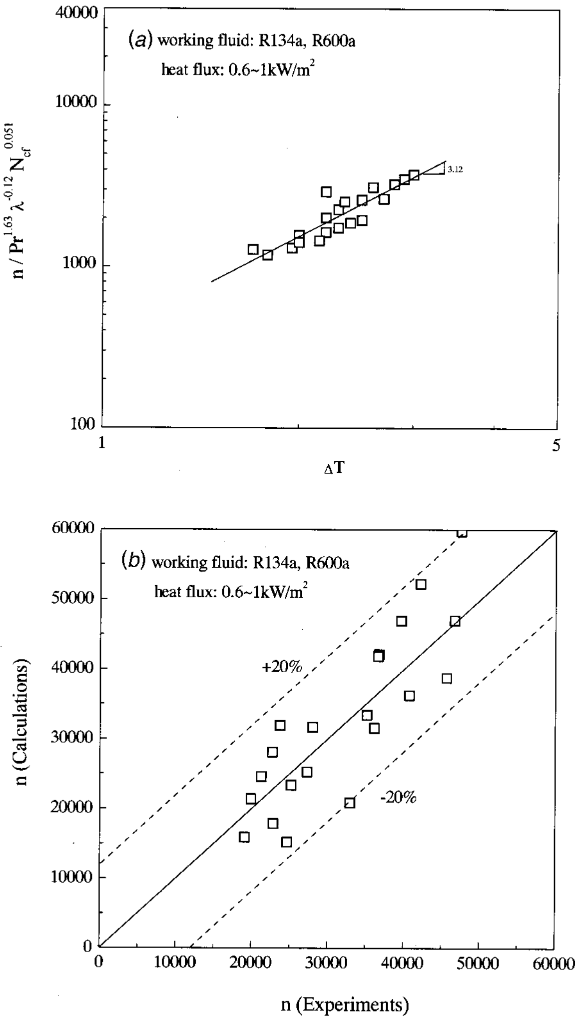

Fig. 11 *n* as a function of the relevant parameters

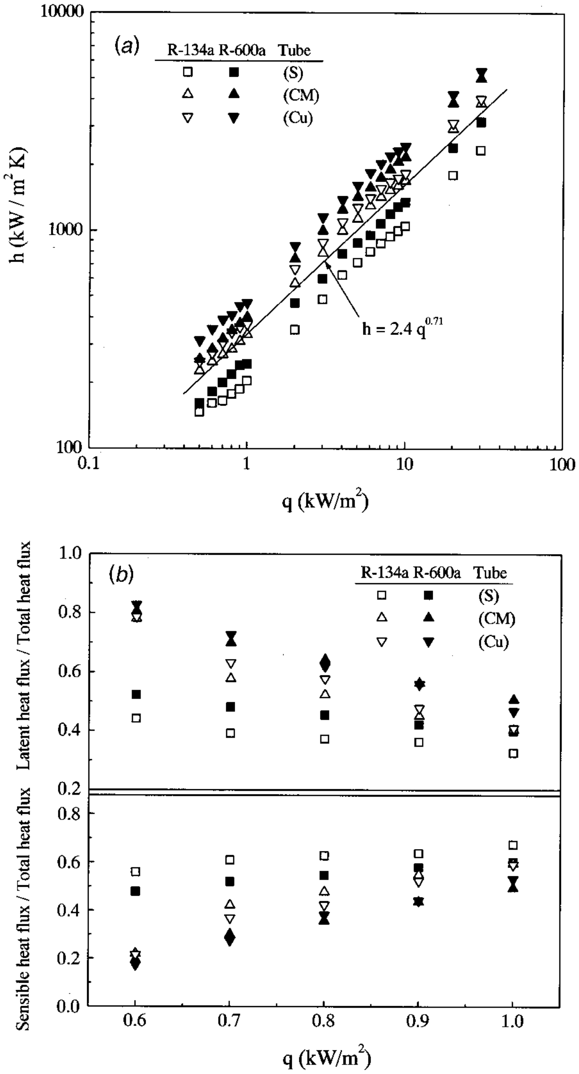

Fig. 12 (*a*) Heat transfer coefficient versus heat flux and (*b*) latent/sensible heat flux ratios for enhanced surfaces

The present results can provide some details to model nucleate boiling heat transfer and fluid motion. The following modeling effort was made based on Rohsenow's model described in [15] with Re_b redefined using the measured bubble departure diameter as a characteristic length. Figure 13(*a*) depicts such a correlation. This again proves that it is possible to adapt a single-phase forced-convection heat transfer correlation to nucleate pool boiling for phasma coated surfaces at very low heat fluxes. The enhancement effect can be clearly noted when comparing the coefficient (=0.29) of the present correlation to that of the Dittus-Boelter correlation (=0.023). Figure 13(*b*) shows the plot of the correlation. The correlation predicts 99 percent of the data within ±20 percent.

Conclusions

Bubble dynamic parameters and pool boiling heat transfer on two plasma coated tubes in saturated R-134a and R-600a at low and moderate heat flux were studied. Since the present visualization is subject to an isolated bubble model, the observations are therefore irrelevant to practical conditions. Nevertheless, the present results may still provide some information at low heat fluxes for bubble dynamics study. The results lead to the following conclusions:

1 Local bubble velocity distribution along its rising path as well as a final velocity was found. A linear increase in local bubble velocity was also noted for both R-134a and R-600a. However, the local velocity and bubble diameters for R-600a are consistently higher than those of R-134a. As a result, the final velocity in R-134a is almost half the value in R-600a. A final velocity correlation was obtained, based on Clift et al. [13].

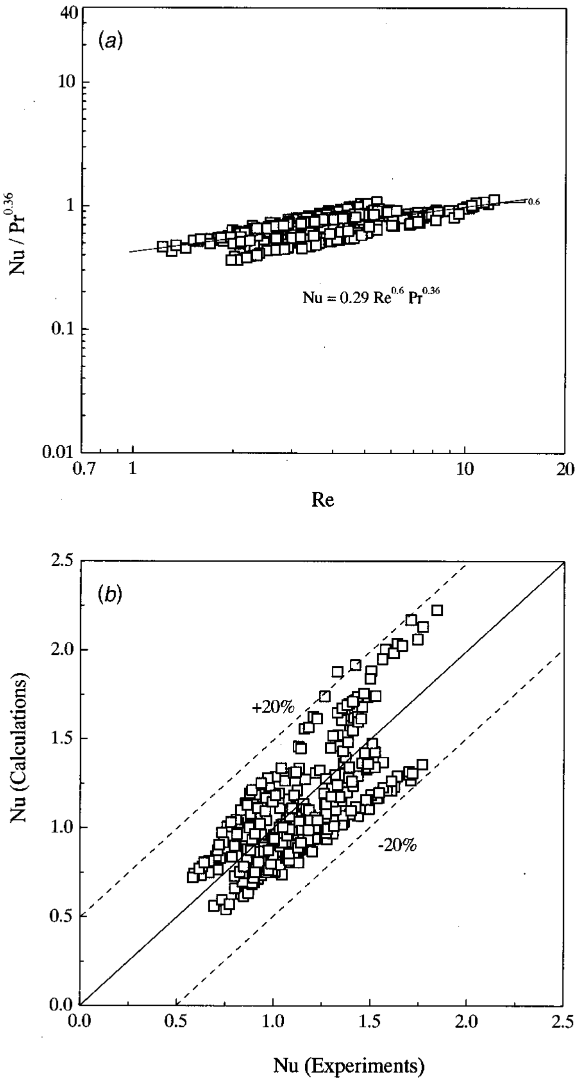

Fig. 13 Heat transfer with experimental data

2 Bubble dynamics were found to be dependent on the heat flux for both R-134a and R-600a. The departure diameter was also observed to decrease slightly with increasing heat flux, while the bubble frequency increases.

3 Nucleation site density is markedly increased for the present coated surfaces as compared to that of the smooth surface and it is a linear function of the heat flux. A relevant functional relationship with the geometric factors and some related parameters (e.g., λ, N_{cf} . . . etc.) for present coated surfaces and the heat flux (in terms of the degree of wall superheat ΔT) was found.

4 Again, in agreement with previous studies [5,18], the latent heat transfer is found to be significant at $q \leqslant 0.8\ \mathrm{kW/m^2}$ for plasma coated surfaces. Following Rohsenow's model [15], a modified Nu correlation with a new defined Re_b in terms of the present measured bubble departure diameter was developed.

Acknowledgment

This work was supported by a research grant (NSC 89-2212-E110-026) from National Science Council, Taiwan, R.O.C.

Nomenclature

A = heated tube area, $\pi d_o L$
C_p = specific heat at constant pressure, kJ/kgK
d = local bubble diameter, mm
d_b = bubble departure diameter measured at an elevation of 1.5 mm from the heating surface, mm
d_o = outside diameter of test tube, mm
f = bubble departure frequency, s^{-1}
f_D = Doppler frequency used in Eq. (1)
h = boiling heat transfer coefficient, W/mK
h_{fg} = latent heat, kJ/kg
k = thermal conductivity, W/mK
L = length of test tube, mm
N = number of bubble generated
N_{cf} = a dimensionless group, $\mu_l^2/\eta\rho_1\sigma$
n = active nucleation site density, sites/m^2
Nu = Nusselt number, hd_b/k
P = pressure, kPa
Q = heat transfer rate, W
q = heat flux (Q/A), W/m^2
Ra = roughness, μm
Re_b = Reynolds number based on bubble departure diameter, $qd_b/\mu_1 h_{fg}$
ΔT = temperature difference, K
ΔT_{sat} = degree of wall superheat, K
U = local bubble velocity, m/s
U_{avg} = average vapor velocity, m/s
U_T = bubble final velocity, m/s
u, v = velocity component used in Eq. (1), m/s

Greek Symbols

δ = porous layer thickness, μm
ϵ = porosity, (%)
η = average pore diameter, μm
θ = helical angle, degree or radian
λ = geometric scale factor, η/δ
μ = dynamic viscosity, Ns/m
ρ = density, kg/m^3
σ = surface tension, N/m

subscripts

avg = average
b = bubble
l = liquid
s = smooth tube
sat = saturation
v = vapor
- = average

References

[1] Thome, J. R., 1990, *Enhanced Boiling Heat Transfer*, Hemisphere Publishing Corporation, New York, pp. 28–63.
[2] Hsieh, S.-S., and Hsu, P.-T., 1994, "Nucleate Boiling Characteristics of R-114, Distilled Water (H_2O) and R-134a on Plain and Rib Roughened Tube Geometries," Int. J. Heat Mass Transf., **37**, pp. 1423–1432.
[3] Hsieh, S.-S., and Weng, C. J., 1997, "Nucleate Pool Boiling from Coated Surfaces in Saturated R-134a and R-407c," Int. J. Heat Mass Transf., **40**, pp. 519–532.
[4] Hsieh, S.-S., and Weng, C. J., 1997, "Nucleate Pool Boiling Heat Transfer Coefficients of Distilled Water (H_2O) and R-134a/Oil Mixtures from Rib-Roughened Surfaces," ASME J. Heat Transfer, **119**, pp. 142–151.
[5] Gorenflo, D., 1966, "Zum Warmeubergang bei der Blasen verdampfung on Rippenrohren," Ph.D. dissertation. TH Karlsruhe, Germany.
[6] Webb, R. L., and Pais, C., 1992, "Nucleate Pool Boiling Data for Five Refrigerants on Plain, Integral-Fin and Enhanced Tube Geometries," Int. J. Heat Mass Transf., **35**, pp. 1893–1904.
[7] Barthau, G., 1992, "Active Nucleate Site Density and Pool Boiling Heat Transfer-An Experimental Study," Int. J. Heat Mass Transf., **35**, pp. 271–278.
[8] Ammerman, C.-N., You, S.-M., and Hong, Y.-S., 1996, "Identification of Pool Boiling Heat Transfer Mechanisms from a Wire Immersed in Saturated FC-72 Using a Single-Photo/LDA Method," ASME J. Heat Transfer, **118**, pp. 117–123.
[9] Mertz, R., Groll, M., Marvillet, Ch., and Hesselgreaves, J. E., 1994, "Enhanced Static Heat Transfer Surfaces for Compact Two-Phase Heat Exchangers," Heat Recovery Syst. CHP, **14**, pp. 493–506.
[10] Hsieh, S.-S., and Yang, T.-Y., 2001, "Nucleate Pool Boiling from Coated and Spirally Wrapped Tubes in Saturated R-134a and R-600a at Low and Moderate Heat Flux," ASME J. Heat Transfer, **123**, pp. 257–270.

[11] Hsieh, S.-S., Chen, P.-J., and Chin, H.-J., 1999, ''Turbulent Flow in a Rotating Two Pass Smooth Channel,'' ASME J. Fluids Eng., **121**, pp. 725–734.

[12] Kline, S. J., and McClintock, F. A., 1953, ''Describing Uncertainties in Single Sample Experiments,'' Mech. Eng. (Am. Soc. Mech. Eng.), **75**, pp. 3–8.

[13] Clift, R., Grace, J. R., and Weber, M. E., 1978, *Bubbles, Drops, and Particles*, Academic Press, Inc., New York. pp. 171.

[14] Middleman, S., 1998, *An Introduction to Fluid Dynamics*, John Wiley and Sons, Inc., New York, pp. 199.

[15] Carey, V. P., 1992, *Liquid-Vapor Phase Change Phenomena*, Hemisphere Publishing Corp., Washington, pp. 223.

[16] Benjamin, R. H., and Balakrishnan, A. R., 1997, ''Nucleate Site Density in Pool Boiling of Saturated Pure Liquids: Effect of Surface Microroughness and Surface and Liquid Physical Properties,'' Exp. Therm. Fluid Sci., **15**, pp. 32–42.

[17] Rudemiller, G. R., and Lindsay, J. D., 1990, ''An Investigation of Boiling Heat Transfer in Fibrous Porous Media,'' *Heat Transfer 1990, Proceedings of the Ninth International Heat Transfer Conference*, **5**, pp. 159–164.

[18] Nakayama, W., Daikoku, T., Kuwahara, H., and Nakajima, T., 1980, ''Dynamic Model of Enhanced Boiling Heat Transfer on Porous Surfaces-Part I: Experimental Investigation,'' ASME J. Heat Transfer, **102**, pp. 445–450.

Onset of Nucleate Boiling and Active Nucleation Site Density During Subcooled Flow Boiling

Nilanjana Basu

Gopinath R. Warrier

Vijay K. Dhir
e-mail: vdhir@seas.ucla.edu

Mechanical and Aerospace Engineering
Department,
University of California, Los Angeles,
Los Angeles, CA 90095-1597

The partitioning of the heat flux supplied at the wall is one of the key issues that needs to be resolved if one is to model subcooled flow boiling accurately. The first step in studying wall heat flux partitioning is to account for the various heat transfer mechanisms involved and to know the location at which the onset of nucleate boiling (ONB) occurs. Active nucleation site density data is required to account for the energy carried away by the bubbles departing from the wall. Subcooled flow boiling experiments were conducted using a flat plate copper surface and a nine-rod (zircalloy-4) bundle. The location of ONB during the experiments was determined from visual observations as well as from the thermocouple output. From the data obtained it is found that the heat flux and wall superheat required for inception are dependent on flow rate, liquid subcooling, and contact angle. The existing correlations for ONB underpredict the wall superheat at ONB in most cases. A correlation for predicting the wall superheat and wall heat flux at ONB has been developed from the data obtained in this study and that reported in the literature. Experimental data are within ±30 percent of that predicted from the correlation. Active nucleation site density was determined by manually counting the individual sites in pictures obtained using a CCD camera. Correlations for nucleation site density, which are independent of flow rate and liquid subcooling, but dependent on contact angle have been developed for two ranges of wall superheat—one below 15°C and another above 15°C. [DOI: 10.1115/1.1471522]

Keywords: *Boiling, Heat Transfer, Nucleonics, Phase Change, Two-Phase*

Introduction

To develop a mechanistic model for subcooled flow boiling one needs to understand the partitioning of the wall heat flux. The first step in partitioning of wall heat flux is to identify the different heat transfer mechanisms involved. Upstream of the location of Onset of Nucleate Boiling (ONB), single phase heat transfer prevails. With the presence of bubbles different heat transfer mechanisms come into play. As such, location of ONB marks the boundary between single and two phase heat transfer. Nucleation site density (N_a) information is necessary to determine the amount of evaporative energy carried away by bubbles lifting off from the wall.

A detailed literature review of parameters involved in subcooled flow boiling has been performed by Warrier and Dhir [1]. Several studies have been performed in the past for ONB of which the notable ones are discussed here. Hsu [2] was the first to postulate the criteria for the boiling inception. According to his criteria, for an embryo to evolve into a bubble, the minimum temperature surrounding the bubble (the temperature at the tip of the bubble) should be at least equal to the saturation temperature corresponding to the pressure inside the bubble. The pressure inside the bubble is higher than the surrounding liquid, and the pressure difference can be expressed in terms of the Young-Laplace equation ($\Delta P = 2\sigma/r_b$) for a spherical bubble. The corresponding saturation temperature inside the bubble can be approximately found from the Clausius-Clapeyron equation as,

$$T - T_{\mathrm{sat}} = \frac{2\sigma T_{\mathrm{sat}}}{r_b \rho_v h_{fg}}. \tag{1}$$

Assuming a linear temperature drop in the thermal boundary layer, one can express the temperature profile in the boundary layer as,

$$T - T_l = (T_w - T_l)\left(1 - \frac{y}{\delta_t}\right). \tag{2}$$

For a particular wall superheat, applying Hsu's criteria while geometrically relating bubble radius, r_b, and cavity radius, r_c, to the distance of the bubble tip from the wall, a quadratic equation is obtained which gives the range of nucleating cavities for a given wall superheat as,

$$\{r_{c,\min}, r_{c,\max}\} = \frac{\delta_t C_2}{2C_1} \frac{\Delta T_w}{\Delta T_w + \Delta T_{\mathrm{sub}}} \times \left[1 \mp \sqrt{1 - \frac{8 C_1 \sigma T_{\mathrm{sat}}(p_l)(\Delta T_w + \Delta T_{\mathrm{sub}})}{\rho_v h_{fg} \delta_t (\Delta T_w)^2}}\right], \tag{3}$$

where $C_1 = 1 + \cos\phi$ and $C_2 = \sin\phi$. Equation (3) is shown graphically in Fig. 1. Hsu considered a truncated bubble sitting on a cavity mouth and assumed the bubble to be part of a sphere. Bergles and Rohsenow [3] stated that on commercial surfaces there will be a wide range of cavity sizes present and as such incipience will be independent of surface conditions. While accounting for variation of physical properties with pressure, Bergles and Rohsenow obtained an empirical expression for the heat flux at ONB in terms of system pressure as,

$$q_{w,\mathrm{ONB}} = 15.6 P^{1.156} (\Delta T_w)^{P^{2.3/0.0234}}, \tag{4}$$

where P is in psia, $q_{w,\mathrm{ONB}}$ is in BTU/ft^{2}hr, and T in °F. Their experiments were conducted with water on stainless steel (SS) and nickel surfaces and covered a range of pressures from 15 to 2000 psia. Sato and Matsumara [4] analytically developed an equation for expressing the wall heat flux at ONB condition in terms of the wall superheat. Their analysis was based on application of Hsu's criteria and tangency condition of Eq. (1) and Eq. (2). The super-

---

Contributed by the Heat Transfer Division for publication in the JOURNAL OF HEAT TRANSFER. Manuscript received by the Heat Transfer Division October 9, 2001; revision received February 1, 2002. Associate Editor: F. B. Cheung.

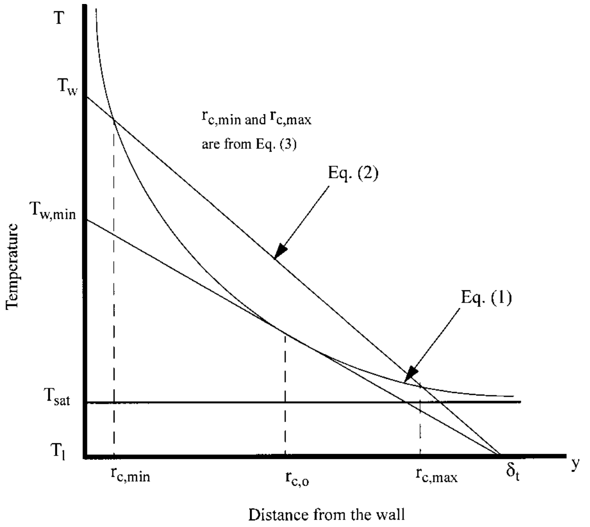

Fig. 1 Inception criteria

heat corresponds to the minimum superheat required for inception and the wall heat flux can be related to the wall superheat as,

$$q_{w,\mathrm{ONB}} = \frac{k_l h_{fg} \rho_v (\Delta T_w)^2}{8\sigma T_{\mathrm{sat}}}. \tag{5}$$

Davis and Anderson [5] extended this analysis and introduced the contact angle as a variable for the ONB condition. Their analysis gave the heat flux condition at ONB as,

$$q_{w,\mathrm{ONB}} = \frac{k_l h_{fg} \rho_v (\Delta T_w)^2}{8C_1\sigma T_{\mathrm{sat}}}, \tag{6}$$

where C_1 is same as in Eq. (3). They also showed that Bergles and Rohsenow's graphical solution closely represents the analytical expressions for hemispherical bubbles (Eq. (5)) and takes care of the property variation in terms of the pressure term. All of these expressions mostly tend to underpredict the incipience wall superheat.

Kandlikar et al. [6] numerically solved the flow field to obtain the stagnation point on the bubble. Their numerical results show that the stagnation distance from the wall is at $1.1r_b$. Using the liquid temperature in the boundary layer at this distance as the temperature for the tip of the bubble, they derived from the inception criteria the range of nucleating cavities as,

$$\{r_{c,\mathrm{min}} r_{c,\mathrm{max}}\} = \frac{\delta_t \sin\phi}{2.2} \frac{\Delta T_w}{\Delta T_w + \Delta T_{\mathrm{sub}}} \times \left(1 \mp \sqrt{1 - \frac{9.2\sigma T_{\mathrm{sat}}(\Delta T_w + \Delta T_{\mathrm{sub}})}{\rho_v h_{fg} \delta_t (\Delta T_w)^2}}\right). \tag{7}$$

They also noted from flow boiling experiments of subcooled water on a polished aluminum surface that keeping the flow rate and wall temperature constant, as the subcooling is reduced, the minimum cavity radius decreases slightly but the maximum cavity radius and range of nucleating cavity sizes increases considerably. Increasing the flow rate reduced the thermal boundary layer thickness and in turn reduced the range of nucleating cavity sizes.

Several studies have been conducted on boiling inception using refrigerants. Yin and Abdelmessiah [7] studied incipience of R11 on a vertical SS tube of 11.81 mm ID. Hino and Ueda [8] studied boiling incipience using R113 on SS surfaces and postulated that the incipience occurs when the liquid temperature equals the superheat corresponding to the maximum cavity radius available on the surface. From their R113 data they concluded that the cavity size ranged from 0.22 to 0.34 μm. Bar-Cohen and Simon [9] gave a summary of superheat excursions at inception for various refrigerants available in the literature and a brief review of the mechanisms that may be responsible for the delayed nucleation for refrigerants. You et al. [10] studied saturated pool boiling of R113 on chromel and platinum surfaces at atmospheric pressure. Chin [11] studied flow boiling of R11 in a vertical channel at a pressure of 1.4 bar. The heater material was Haynes 230. Incipience data was correlated using the minimum wall superheat given by the tangency condition and then multiplying that value by introducing an empirically found correction factor for wall superheat. However, this factor, as mentioned in the work is only applicable to those set of data only.

Hahne et al. [12] studied incipience in subcooled flow boiling for a well wetting liquid (R12) and came up with a model applicable for other refrigerants also. For well wetting liquids, they stated that vapor nuclei in cavities even in the size corresponding to minimum wall superheat for inception (tangency condition) may be displaced or diminished. As such, Eq. (5) may not be applicable to well wetting liquids. They assumed that for such liquids, a nucleus is necessary for incipience and that is given by the largest of the remaining nuclei on the surface. They developed a correlation for the prediction of the heat flux and wall superheat required for incipience based on this radius r^*, which is the largest of all the nuclei present on the surface, and calculated r^* from their data for R12 as,

$$\frac{2\sigma}{r^*} = 1.54 \text{ bar}. \tag{8}$$

Assuming negligible temperature drop in the thin liquid layer of thickness r^* adjacent to the wall, they predicted the wall superheat and wall heat flux at incipience as,

$$\Delta T_{w,\mathrm{ONB}} = \frac{2\sigma T_{\mathrm{sat}}}{r^* \rho_v h_{fg}}, \tag{9}$$

and

$$q_{w,\mathrm{ONB}} = h_{\mathrm{sp}} \left[\frac{2\sigma T_{\mathrm{sat}}}{r^* \rho_v h_{fg}} + (T_{\mathrm{sat}} - T_l) \right]. \tag{10}$$

Hahne et al. applied their correlation successfully to data available in the literature for different refrigerants like R113, R11, and R12, covering a wide range of velocities, subcooling, and pressures. However, for each refrigerant they utilized a different constant for $2\sigma/r^*$.

Tong et al. [13] studied boiling incipience of highly wetting liquids. For highly wetting liquids which have very small static contact angles, ϕ_s, the advancing dynamic contact angles, ϕ_d, (which may vary with velocity of the interface) can be large enough to trap gas and vapor in the cavities and initiate nucleation. Consequently the incipience superheat may lie below the value required for quiescent pool boiling. Based on their analysis and application of the model to existing data, they found that the embryo radius has to be corrected by a factor $f(=r/r_c)$ from that of the cavity size available on the surface. The factor was found to be a function of ϕ_d, ϕ_s, and β. The factor, for small ϕ_d and ϕ_s is expressed as,

$$f=\left\{\frac{\dfrac{\sin(\phi_d-2\beta)}{\sin(\phi_d-\beta)\sin\beta}}{\dfrac{\cos(\phi_s-\beta)}{\tan\beta}+[2-3\sin(\phi_s-\beta)+\sin(\phi_s-\beta)]\dfrac{\left[\dfrac{\tan\beta}{\tan(\phi_d-\beta)}-1\right]^2}{\left[1-\dfrac{\tan\beta}{\tan(\phi_d-\beta)}\right]^{3/2}}}\right\}^{1/3}. \tag{11}$$

However, in developing the function f, no experimental corroboration of the fact that indeed conical cavities do exist on a surface was provided. Wang and Dhir [14] found that at least on Copper surfaces most of the nucleating cavities were of reservoir type. The inception wall superheat was expressed as,

$$\Delta T_{w,\mathrm{ONB}}=\frac{2\sigma T_{\mathrm{sat}}}{f r_c \rho_v h_{fg}}. \tag{12}$$

Celata et al. [15] studied ONB in a horizontal uniformly heated steel channel of diameter 8 mm and length 100 mm. Water was the test fluid. They used pressure drop measurements to determine the location of ONB. Their definition of the ONB location is the point where the pressure drop from experimental data deviates from the single phase values. Based on their results, they concluded that ONB location is dependent on velocity and liquid subcooling while system pressure has negligible effect.

Literature review on ONB shows that most of the correlations are based on minimum superheat criteria (tangency condition as shown in Fig. 1) from Hsu's postulation. These correlations generally underpredict the actual superheat required for inception. Inception will occur at this superheat only when the corresponding cavity size is available on the surface. For well wetting liquids, the available cavity size is reduced as shown by Hahne et al. None of the past studies have experimentally investigated the explicit influence of contact angle on inception.

Several studies have been performed on N_a which give the functional dependence of N_a on q_w, ΔT_w, or available r_c. Some notable studies in this field are discussed here. Jakob [16] first reported the relationship between N_a and q_w. His observations were, however, limited to low heat flux cases, as at higher heat fluxes, bubbles at neighboring sites begin to merge. Gaertner and Westwater [17] found the functional dependency of active nucleation site density with wall heat flux to be,

$$N_a \sim q_w^{2.1}. \tag{13}$$

They used a technique in which nickel salts dissolved in water were deposited on the copper-heater surface when boiling occurred. By counting the number of holes in the deposited nickel layer an estimate of the active nucleation site density was obtained. Hsu and Graham [18] summarized earlier works of several investigators regarding the relationship between active nucleation site density and heat flux. Their work showed that in general the exponent of the heat flux varies between 1 and 2.1.

Sultan and Judd [19] reported nucleation site density data for water boiling at 1.013 bar on a copper surface. Their observed number densities were several times higher than those reported by Gaertner and Westwater. This difference could be attributed to the increased surface wettability due to nickel deposit in Gaertner and Westwater's experiment.

Mikic and Rohsenow [20] were the first to relate active site density to the sizes of the cavities present on the surface and expressed the functional dependence of active nucleation site density on cavity size for commercial surfaces as,

$$N_a \sim \left[\frac{D_s}{D_c}\right]^m, \tag{14}$$

where m is an empirical constant (= 6.5) and D_c is given by,

$$D_c=\frac{4\sigma T_{\mathrm{sat}}}{\rho_v h_{fg}\Delta T_w}. \tag{15}$$

Bier et al. [21] expressed N_a as a function of cavity size. Their expression is given as,

$$\ln N_a=\ln(N_{\max})\left[1-\left[\frac{D_c}{D_s}\right]^m\right], \tag{16}$$

where $N_{\max}$ is the value corresponding to $D_c=0$. The value of the exponent m was found to depend on the surface preparation procedure. For Freon-115 and Freon-11, boiling on copper surfaces the values of exponent m is 0.42 and 0.26. Cornwell and Brown [22] studied active nucleation site density of water boiling at 1.013 bar on a copper surface, with surface condition varying from smooth to rough, and related the dependence of active site density on wall superheat from their study as,

$$N_a \sim \Delta T_w^{4.5}. \tag{17}$$

From the cavity size data obtained using an electron microscope, they also related cavity size to total number of cavities present on the surface, N_s, as,

$$N_s \sim \frac{1}{D_c^2}. \tag{18}$$

They justified their observed functional dependence on wall superheat by assuming only conical cavities existed on the surface and that gas/vapor needed to be trapped in the cavities before any nucleation could occur.

Yang and Kim [23] first attempted to predict quantitatively the active nucleation sites from knowing the size and cone angle of the cavities actually present on the surface. Using an electron microscope and a differential interference contrast microscope, they obtained the cavity probability density function involving cavity size (ranging from 0.65 to 6.2 μm) and β. The size distribution was found to fit a Poisson distribution while a normal distribution was used for β. They used Bankoff's [24] criteria to determine which cavities will trap gas. This condition is given as $\phi>2\beta$. By combining the probability distribution functions and this criteria, they related N_a to the average of $\overline{N}_s$ on the surface as,

$$\begin{aligned}N_a=\overline{N}_s\int_0^{\phi_s/2}[(2\pi)^{1/2}]^{-1}\exp[-(\beta-\overline{\beta})^2/(2s^2)]d\beta\\ \times\left(\int_{D_c}^{D_s}\lambda e^{-(\lambda D_c)/2}dD_c\right),\end{aligned} \tag{19}$$

where $\overline{\beta}$ is the mean value of cone half angle, and λ and s are statistical parameters. These parameters are dependent on surface preparation procedure and the material of the surface. Gaertner [25] first observed that active nucleation sites were randomly located and could be expressed in terms of Poisson's distribution function. Sultan and Judd [19] concluded the same from their observations.

Kocamustafaogullari and Ishii [26] developed a relation for active nucleation site density in pool boiling from the data available in the literature. They also applied the correlation to the few forced convection nucleate boiling data available. Their correlation expressed active nucleation site density in dimensionless form as a function of dimensionless minimum cavity size and density ratio. The correlation was valid for system pressures ranging from 1.0 to 198.0 bar. Their correlation is given as,

$$N_a^* = f(\rho^*) r_c^{*-4.4}, \tag{20}$$

where $N_a^* = N_a D_d^2$, $r_c^* = r_c/(D_d/2)$, $r_c = 2\sigma T_{\mathrm{sat}}/\rho_v h_{fg}\Delta T_w$, $D_d = 0.0012(\Delta\rho/\rho_g)^{0.9} D_{dF}$, $\rho^* = (\rho_v - \rho_g)/\rho_g$, the density function $f(\rho) = 2.157\times 10^{-7}\rho^{*-3.2}(1+0.0049\rho^*)^{4.13}$, and D_{dF} is the Fritz diameter given by,

$$D_{dF} = 0.0208\phi_s\sqrt{\frac{\sigma}{g(\rho_l - \rho_v)}}. \tag{21}$$

Wang and Dhir [14] were the first to perform a systematic study of the effect of contact angle on the density of active nucleation sites. In the experiments, pool boiling of water at 1.013 bar was studied on vertical copper surfaces for contact angles ranging from 18 deg to 90 deg. Copper surfaces were prepared by a well defined procedure and the contact angle was varied by controlling the degree of oxidation of the surface. The cumulative number density of cavities and their shapes were obtained with an electron microscope, while the number of active sites were counted from the still pictures. It was found that the cavities that nucleate are mostly the reservoir type rather than the conical type (were shallow cavities), which was the usual assumption in most studies that has been done in the past. The actual cavity size was corrected by multiplying it with a shape factor $f_d(=0.89)$ to account for the irregular shape of the cavities. The corrected size was related to the wall superheat for nucleation as given in Eq. (15). It was found that the there was a strong influence of wettability on active nucleation site density. For surfaces with $18\ \mathrm{deg} \leqslant \phi_s \leqslant 90$ deg, they correlated N_a with corrected D_c as,

$$N_a = 5.0\times 10^5 (1-\cos\phi_s) D_c^{-6.0}. \tag{22}$$

In Eq. (22), N_a is in sites/cm^2 and D_c is in μm. Equation (22) is valid for values of D_c smaller than 5.8 μm.

Zeng and Klausner [27] obtained experimental data for N_a during flow boiling of R113 on a horizontal $25\ \mathrm{mm}\times 25\ \mathrm{mm}$ test section with a nichrome heating strip. Their experiments were performed for varying vapor quality at inlet, system pressure and wall heat flux. They studied the effect of vapor velocity, liquid velocity, liquid film thickness, system pressure, and wall heat flux on N_a. Although no correlation was developed, they concluded that even if N_a is dependent on r_c, it is not sufficient for correlating N_a. From their data, they concluded that velocity, heat flux, and system pressure have a strong effect on N_a.

Literature review on N_a shows very limited experimental studies have been conducted in subcooled flow boiling. The effect of subcooling and velocity have not been quantified and as such no correlation is available for N_a in subcooled flow boiling.

The objective of the present study is to identify the parameters affecting ONB and N_a in subcooled flow boiling, compare the experimental data with existing correlations, and develop new correlations as necessary. Several experiments were conducted covering a wide range of flow rates, liquid subcooling, and heat fluxes on a copper flat plate test surface and a nine-rod bundle with zircalloy-4 cladding.

Experimental Apparatus

The schematic of the flow loop is shown in Fig. 2. The flow loop consists of two tanks, each with a volume of 1.25 m^3, a centrifugal pump, turbine flow meter, bypass line, preheater and test section. Tank #1, which was used as the supply tank, is also fitted with immersion heaters (13.5 kW total power) to degas and preheat the distilled water used in the experiments. The preheater consisted of a 210 kW (480 V, 3 phase) flanged immersion heater fitted vertically onto a stainless steel container. The power to the immersion heater is controlled using a 480 V, 350 A silicon controlled rectifier (SCR) power controller (Phasetronics). Using the power controller and thermocouple outputs, it is possible to control the liquid subcooling accurately. Thermocouples and pressure transducers are installed at the inlet and exit of the heating section. Two types of test surfaces were used in this study: (1) flat plate and (2) nine-rod bundle.

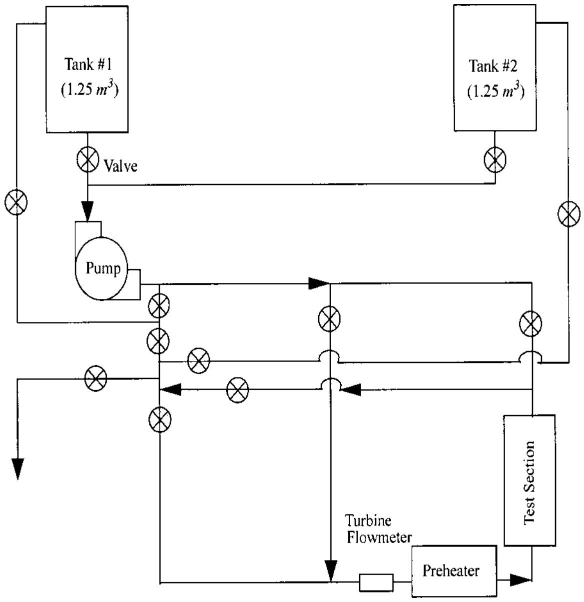

Fig. 2 Schematic of test loop

Test Surface 1—Flat Plate. For this test surface, the flow channel is 1.83 m long, of which the heated section is 0.30 m. A 0.61 m long flow development section is provided upstream of the heated section, while a 0.30 m long section is provided downstream of the heated section. In addition, transition sections, each 0.30 m long, are provided upstream and downstream of the test section. A flow straightener is also placed at the inlet of the flow developing section. The cross section of the flow channel is shown in Fig. 3. The flow channel is almost square in cross section with a flow area of 16.33 cm^2. The copper block, which is heated, is mounted flush with one of the inside walls of the flow channel, while pyrex glass windows are provided on the other three sides of the channel. The glass windows help in visual observation of the flow. Figure 4 shows the dimensions of the copper block and the placement of the thermocouples at each axial location. The temperatures measured by these embedded thermocouples are

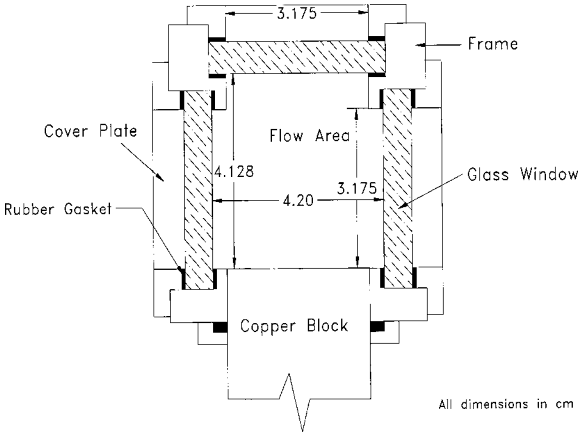

Fig. 3 Cross section of the test chamber for flat plate

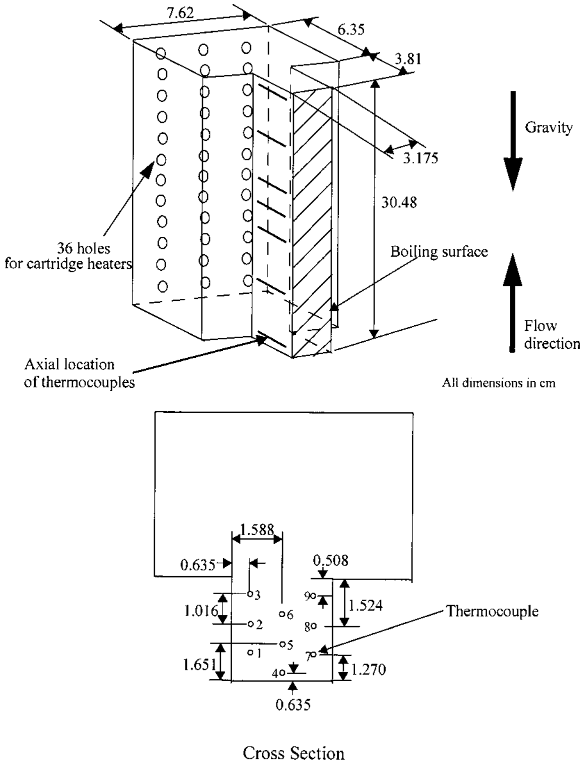

Fig. 4 Copper heating block and thermocouple placement

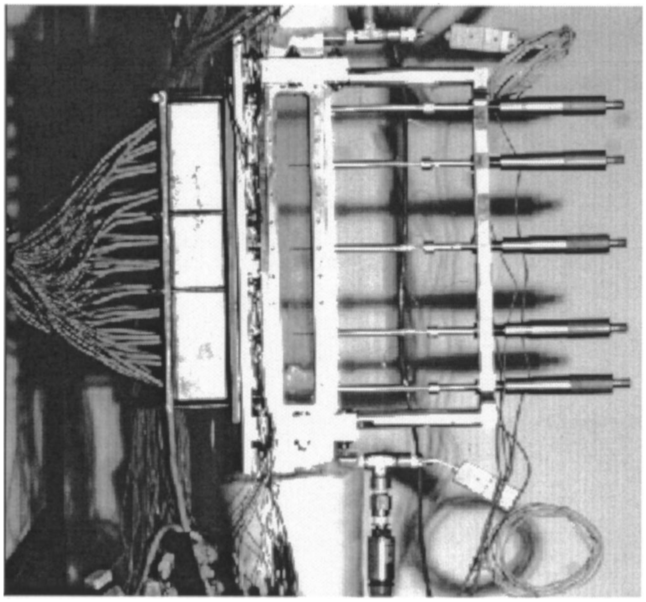

Fig. 5 Photograph of the test chamber for flat plate test surface

used to determine the temperature and heat flux at the surface (boiling surface). The thermocouples (K-type, 0.81 mm diameter) are located at seven different axial locations along the length of the copper block. At each axial location, there are nine thermocouples (labeled 1 through 9) embedded in the block at discrete locations normal to the heating surface, as can be seen from the cross section of the copper block shown in Fig. 4. Thus, a total of 63 thermocouples are placed in the copper block. The heating of the copper block is achieved using 36 cartridge heaters embedded in the back of the copper block. These cartridge heaters were arranged such that the heat flux at the boiling surface is uniform. Since each cartridge heater has a maximum power rating of 750 W, the total installed power in the test section is 27 kW. The power supplied to the cartridge heaters, and hence to the copper block, is controlled with a 240 V, 50 A, SCR power controller (Phasetronics).

Figure 5 shows a photograph of the assembled test section with the various pressure and temperature sensors mounted on it. Five microthermocouples (K-type, 0.25 mm diameter) are mounted in the test chamber to measure the liquid temperature profile adjacent to the test surface. These microthermocouples are connected to micrometers making it possible to traverse the width of the channel. They are used to measure liquid temperatures at axial distances of 0.64 cm, 6.48 cm, 15.25 cm, 24.00 cm and 29.86 cm, respectively from the leading edge of the copper block.

Test Surface 2—Nine-Rod Bundle. In this case we have a heated length of 0.91 m with a 0.36 m long flow development section in the upstream side and 0.15 m section in the downstream side. Transition sections of length 0.20 m are provided at both the upstream and the downstream side. Figure 6 shows the cross-section of the nine-rod bundle heating section. Glass windows are provided on all sides so as to aid visual observations. The diameter of the rods (1.11 cm OD) and the pitch (1.429 cm) of the 3 ×3 square arrangement are typical of those found in a pressurized water reactor. Zircalloy-4 has been chosen as the cladding material and the cladding is Joule heated using a 100 kW DC power supply. The wall thickness of the cladding is 0.015 cm. This value was chosen so that the maximum power could be generated for the current rating of the power supply. Power to the cladding is provided using copper bus bars mounted at the ends of the test section (at the inlet and exit of the heated section). Though this configuration disturbs the flow it was found to provide a better alternative for supplying power to the cladding. The wall temperatures of the rods are measured at various axial and radial locations using miniature thermocouples mounted inside the thin-walled tubes as shown in Fig. 7. These thermocouples are mounted in slots machined in solid lava rods which are placed inside the zircalloy-4 tubes.

The thermocouples are attached and covered with a nonconducting cement all throughout except at the tips where they are covered with electrically insulated but thermally conducting cement. Moveable microthermocouples are mounted at various axial location along the flow channel to measure the liquid temperature profile. The arrangement of the microthermocouples and the ther-

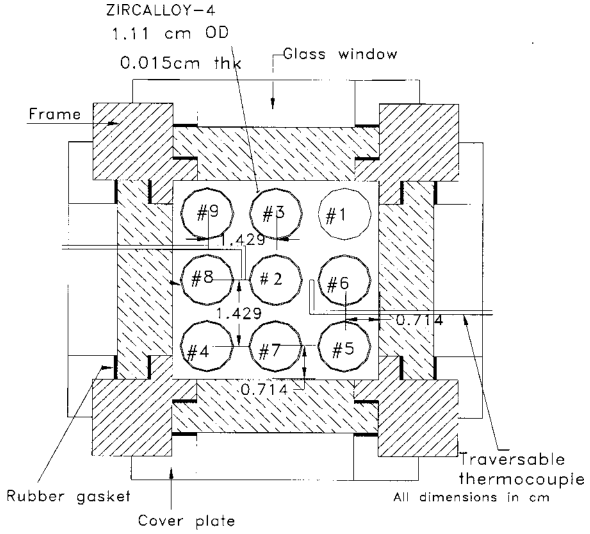

Fig. 6 Cross section of the test surface for nine-rod bundle

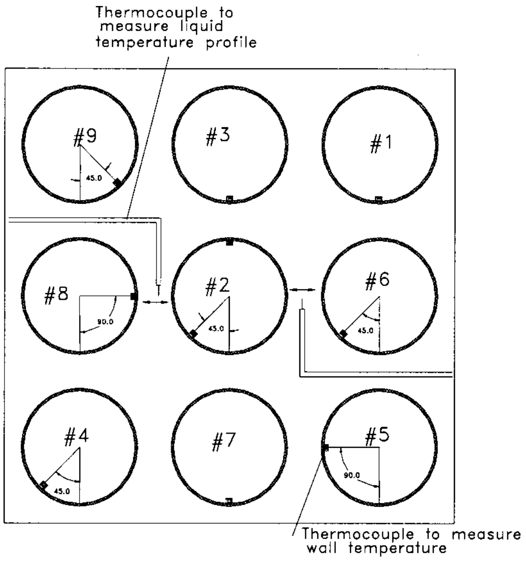

Fig. 7 Arrangement of thermocouples at a given axial plane

mocouples within the rod at a given axial plane are shown in Fig. 7. Thermocouples are placed at six axial locations starting at 1.27 cm from the leading edge of the rod-bundle and thereafter at regular intervals of 17.78 cm. The average heat generation rate (and hence the heat flux) was calculated using the voltage and current supplied ($\text{power}=IV$, $I=\text{current}$, $V=\text{voltage}$).

Experimental Procedure. Several subcooled flow boiling experiments were performed while varying the flow rate and inlet subcooling with water at one atmosphere pressure. Prior to each experiment, tank #1 was filled with distilled water and was heated. The water was degassed by boiling it for approximately three hours and thereafter it was cooled to the required temperature. During an experiment, water was pumped from tank #1 through the flowmeter, inline preheater, and the test section before being discharged into tank #2. The liquid flow rate was controlled using the valves placed at the preheater inlet and the bypass line. The power to the boiling surface was turned on once the required flow rate and liquid subcooling levels at inlet were achieved. After the test heater reached steady state, all the required temperature measurements were taken. A 16-bit data acquisition system (Strawberry Tree, Model DS-16-8-TC) was used to record the temperatures. The boiling phenomena occurring at the heater surface was recorded using a high-speed CCD camera (HSIS 2000 from KSV Instruments Ltd.). The wall heat flux was computed from the temperature gradients measured in the copper heating block. The uncertainty in q_w is due to the uncertainty in temperature difference, thermocouple placement and thermal conductivity. The percentage uncertainty decreased with increase in heat flux. The computed uncertainty for 20 W/cm^2 is ±9.4 percent, while that for 96 W/cm^2 is ±8.5 percent. The heater surface temperature was obtained by extrapolating the measured interior temperatures to the surface and its uncertainty is in the range of ±0.4°C to ±0.8°C.

For the rod bundle, the heat flux was obtained from the measured input power and rod surface area. The uncertainty mainly arises due to the difference in cladding thickness which gives rise to variation in resistance of the rods. The uncertainty is estimated to be about 8 percent. The surface temperature for the rod bundles was obtained from the readings of the miniature thermocouples placed inside the thin walled tubes. The uncertainty, after correction for temperature drop across the tube wall was made, is about ±0.2°C to ±0.4°C. The uncertainty in the measured liquid temperature is ±0.2°C.

Before each test case, the surface was prepared and ϕ_s was measured. The following procedure was adopted while oxidizing the copper boiling surface. The surface was first polished using 600 grit sand paper for about one minute (approximately 200 strokes). This was then followed by polishing using 1200 grit crocus cloth for about five minutes (approximately 1000 strokes). The final polishing of the surface was done using a hand held buffing machine (for about five minutes). The surface was then cleaned using isopropyl alcohol and acetone. The oxidation of the surface was achieved by heating the copper surface in air (copper block was horizontal with boiling surface facing upwards). While heating the block, the power supplied to the copper block was fixed at 325 W ($\text{current}=4\,A$, $\text{voltage}=27\,V$). With this power, it took approximately four hours for the block to reach steady state (the steady state temperature was about 217°C). After steady state was reached, the heating was continued for another 45 minutes. The power was then turned off and the block was allowed to cool. Once the block had cooled to room temperature (in about five hours), the contact angle was measured. The static contact angle was measured by placing small droplets of water at various locations (about 10 to 15) on the copper surface and taking photographs of these droplets. The photographs were taken using a CCD camera. From these photographs the contact angles were measured. Thereafter the copper block was installed in the test section. The unoxidized surface was prepared in a very similar manner, except that the surface was not heated. The measured ϕ_s for the oxidized surface was $30\ \text{deg} \pm 3\ \text{deg}$, whereas that for the unoxidized surface was about 90 deg.

Most of the 30 deg and some of the 90 deg test cases for which N_a was obtained, were single heat flux experiments for which ϕ_s after the experiment did not change much (only about 2 deg) from that prior to the experiment. Some of the experiments with an initially unoxidized surface ($\phi_s=90\ \text{deg}$) were performed for multiple heat fluxes keeping the flow rate and liquid subcooling constant. For these test cases, ϕ_s decreased by about 10 deg to 15 deg by the end of the experiment (duration of the experiment was about two hours). This change in ϕ_s was due to the oxidation of the copper test surface during the experiments at higher heat fluxes. In order to quantify ϕ_s during these experiments, the duration of the experiments and the change in color of the test surface were recorded, from which ϕ_s were approximately identified. For the rod bundle case, the ϕ_s was found to be 57 deg before the rod bundle was assembled into the test section. The uncertainty in the measured ϕ_s is about ±3 deg.

Results and Discussion

The experiments covered a range of mass fluxes, G, varying from 124 to 886 $\text{kg/m}^2\,\text{s}$, $\Delta T_{\text{sub,in}}$ varying from 6.6 to 52.5°C, q_w from 2.5 to 96.3 W/cm^2 and ϕ_s varying from 30 deg to 90 deg for the flat plate test surface. For the rod bundle ($\phi_s=57\ \text{deg}$), experiments for ONB were performed for G varying from 186 to 631 $\text{kg/m}^2\,\text{s}$, $\Delta T_{\text{sub,in}}$ varying from 1.7 to 46.0°C and q_w varying from 1.6 to 14.3 W/cm^2.

Onset of Nucleate Boiling. The onset of nucleate boiling is the location where the first vapor bubbles appear on the heater surface. In the experiments, the ONB location was identified by visual observations as well as temperature and heat flux data. Though in all test cases, a few bubbles were observed at the edges of the heater surface, the ONB location was identified as the point where bubbles were first observed in the middle (away from the edges) of the heater surface in the transverse direction. Visual observation of ONB location was validated with that determined from heat transfer coefficients versus axial location (h-z) plots. With inception of boiling, for the same flow rate and liquid subcooling, the heat transfer coefficient will deviate from the corresponding single phase value. Figure 8 shows the h-z plots for $G=346\ \text{kg/m}^2\,\text{s}$ and $\Delta T_{\text{sub,in}}=26.5°\text{C}$ for different q_w on the flat plate test surface. The lowest heat flux case of 6 W/cm^2 is a single-phase case whereas those for higher heat fluxes are two-phase cases. Comparing the h-z plot for the single-phase case of

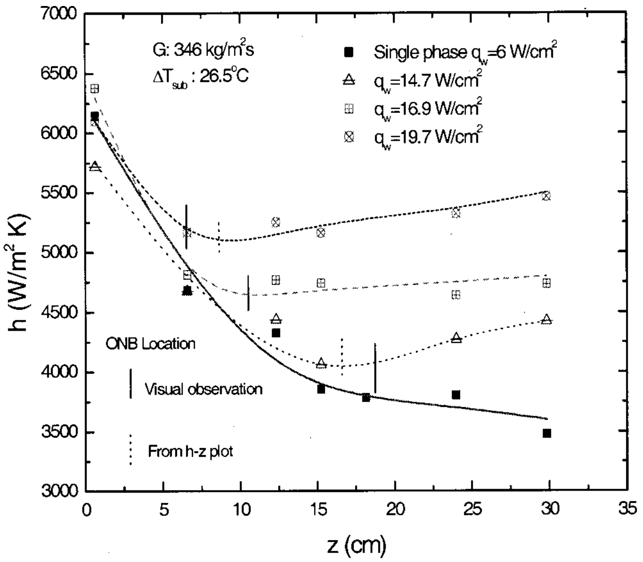

Fig. 8 Heat transfer coefficient as a function of axial distance for different heat fluxes for mass flux=346 kg/m^2 s and inlet liquid subcooling=26.5°C

$q_w = 6$ W/cm^2 and that of the two-phase case ($q_w = 14.7$ W/cm^2), we can identify the location of ONB as the point where the heat transfer coefficient deviates from the corresponding single phase value at a particular location. The location of ONB from heat transfer data is found to be 16.5 cm from the leading edge, whereas from visual observation the ONB is found to occur at 18.0 cm from the leading edge. The ONB location obtained from visual observation as well as that from *h-z* plot for different heat fluxes are marked in the plot as vertical bars. The ONB location obtained from visual observations appear to agree with that discerned from the heat flux data (on an average within ±8 percent for all cases). Also, from these plots it is evident that the ONB location moves down towards the inlet as the q_w increases. Keeping all other parameters constant, the *h-z* plots upstream of ONB for all q_w values match well with the single-phase case. The small variations as seen in the plot are within the uncertainty of the evaluation of the heat transfer coefficient (for this case about ±15 percent). The variation in the axial location at which ONB occurs is plotted in Fig. 9 as a function of $\Delta T_{w,\mathrm{ONB}}$. From Fig. 9, it can be seen that keeping all the parameters the same, as G increases from 346 kg/m^{2}s to 886 kg/m^{2}s, the ONB at the same z location occurs at higher ΔT_w. A similar effect is seen when ΔT_{sub} increases. Also, inception occurs at a lower ΔT_w for larger values of ϕ_s.

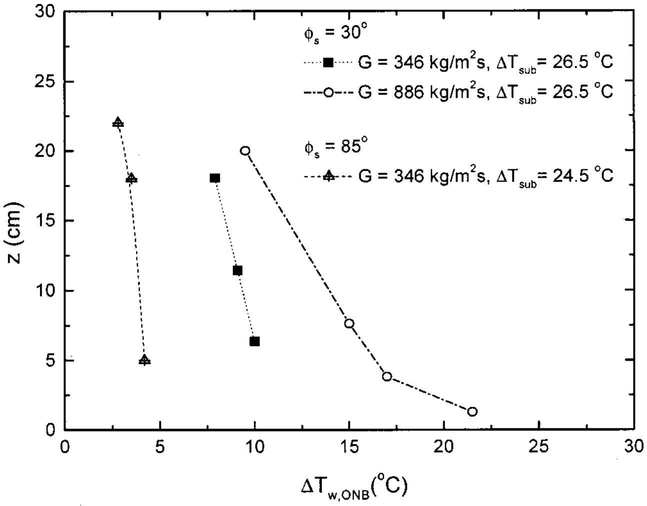

Fig. 9 Variation of ONB location with $\Delta T_{w,\mathrm{ONB}}$ for various flow rates and contact angles

A comparison of $\Delta T_{w,\mathrm{ONB}}$ data obtained in this study with the predictions from past studies is shown in Table 1. It is found that for flat plate ($\phi_s = 30$ deg), the $\Delta T_{w,\mathrm{ONB}}$ correlations of Bergles and Rohsenow (Eq. (4)), Sato and Matsumara (Eq. (5)), and Davis and Anderson (Eq. (6)), underpredict $\Delta T_{w,\mathrm{ONB}}$ in most cases. For the rod bundle, ($\phi_s = 57$ deg) all the predictions match quite well with the experimental data. In general, the previous correlations tend to underpredict $\Delta T_{w,\mathrm{ONB}}$ as wettability of the surface increases.

New Proposal. The tangency condition in the implementation of Hsu's criterion yields the minimum wall superheat at nucleation. However, the onset of nucleate boiling at the predicted minimum wall superheat is contingent upon the following two conditions:

1. the corresponding cavity is available on the surface
2. the cavity is not flooded (i.e., it contains gas or vapor)

The distribution of cavities of different sizes and shapes strongly depends on the manufacturing conditions and the procedure that is used to polish the surface. How many of these cavities are flooded depends on the shape of the cavities and the wettability of the surface. According to Wang and Dhir [14], for a cavity to trap gas or vapor the contact angle should be greater than the cavity mouth angle. It can be an arduous task to determine the size and shape of cavities that are present on a commercial surface. It should be further noted that even with this information it would be very difficult to identify specific cavities that nucleate at a given wall superheat. In this study cavity size distribution and shapes of cavities present on the heater surfaces were not determined. A detailed study of cavity size distribution and active sites identification has been previously performed by Wang and Dhir [14]. In the absence of such knowledge, in this work it is proposed that the probability of finding an unflooded cavity of the size corresponding to the minimum wall superheat calculated from Hsu's criterion diminishes as the wettability of the surface increases. However, the size of the available cavity is proportional to that obtained from the minimum superheat criterion. As such, the available cavity size can be expressed as,

$$D_c = D_c^0 F, \tag{23}$$

where the correction factor F (which depends on ϕ_s) is obtained empirically and D_c^0 is obtained by invoking the minimum superheat criterion as,

$$D_c^0 = \left[\frac{8\sigma T_{\mathrm{sat}} k_l}{\rho_v h_{fg} q_w}\right]^{1/2}. \tag{24}$$

Under the assumption that the nucleating cavity is much smaller than δ_t, the wall temperature for inception corresponding to D_c is obtained from the following equations:

$$P_v - P_l = \frac{4\sigma}{D_c}, \tag{25}$$

$$\Delta T_{w,\mathrm{ONB}} = T_{\mathrm{sat}}(P_v) - T_{\mathrm{sat}}(P_l). \tag{26}$$

When the calculated wall superheat is not too high, $\Delta T_{w,\mathrm{ONB}}$ in terms of D_c can be approximated as,

$$\Delta T_{w,\mathrm{ONB}} \equiv T_{w,\mathrm{ONB}} - T_{\mathrm{sat}} = \frac{4\sigma T_{\mathrm{sat}}}{D_c \rho_v h_{fg}}. \tag{27}$$

Prior to ONB, single-phase flow prevails on the heater surface, an expression for wall heat flux in terms of the single-phase heat transfer coefficient (which may or may not depend on the axial location) can be written as,

Table 1 Comparison of experimental $\Delta T_{w,\mathrm{ONB}}$ with predictions from past studies

	G (kg/m²s)	ϕ_s (deg)	ΔT_{sub} (°C)	$q_{w,\mathrm{ONB}}$ (W/cm²)	$\Delta T_{w,\mathrm{ONB}}$ (°C)	Bergles and Rohsenow Eq. (4) $\Delta T_{w,\mathrm{ONB}}$ (°C)	Sato and Matsumara Eq. (5) $\Delta T_{w,\mathrm{ONB}}$ (°C)	Davis and Anderson Eq. (6) $\Delta T_{w,\mathrm{ONB}}$ (°C)
Flat Plate	124	30	50.3	21.3	10	6.5	6.3	8.7
	346	30	26.5	17.4	9.1	5.9	5.8	7.9
	346	30	50.3	26.0	10.0	7.1	7.1	9.6
	868	30	26.5	57	17	10.4	10.6	14.5
	886	30	52.5	70	16	11.3	11.6	15.8
Rod Bundle	186	57	2.2	3.2	2.7	2.7	2.5	3.1
	336	57	9.6	8.0	4.0	4.1	3.9	4.9
	336	57	38.6	13.3	4	5.2	5.0	6.3
	596	57	1.7	5.4	3.3	3.4	3.2	4.0

* Water is the test liquid.

$$q_{w,\mathrm{ONB}} = h_{\mathrm{sp}}(z)\Delta T_{w,\mathrm{ONB}} + h_{\mathrm{sp}}(z)(T_{\mathrm{sat}} - T_l(z)). \tag{28}$$

From the available data, it is found that the function F can be expressed as

$$F = 1 - \exp\left[-\left(\frac{\pi\phi_s}{180}\right)^3 - 0.5\left(\frac{\pi\phi_s}{180}\right)\right], \tag{29}$$

where ϕ_s is expressed in degrees. For determining the form of Eq. (29), it must be kept in mind that as $\phi_s \rightarrow 0$, all the cavities will be flooded and hence $F \rightarrow 0$. Also as $\phi_s \rightarrow 90$ deg, $F \rightarrow 1$. The final form of the equation was chosen based on the experimental data (from present and past studies) with ϕ_s ranging from 1 deg to 85 deg, and taking into considerations the above mentioned extreme limits. Most of the predicted wall superheats and wall heat fluxes match the experimental data to within ±30 percent as shown in Figs. 10 and 11. In calculating the predicted values, the h_{sp} values used were the experimental values obtained at lower heat fluxes for the same flow rate.

Included in Figs. 10 and 11 are also the other experimental data available in the literature. The static contact angle for the data of Bergles and Rohsenow [3] is taken to be 38 deg (water on stainless steel, water on nickel). For Hahne et al.'s [12] data for R-12 and copper surface, ϕ_s is assumed to be 6 deg. Contact angles information available in the literature for different refrigerant and surfaces are listed in Tong et al.'s [13] paper. Their work reports ϕ_s values ranging from 2 deg to 5 deg for R113 on stainless steel, less than 5 deg for R11 on copper, and between 0 deg to 1 deg for FC-72 on stainless steel. For the predicted values plotted in Fig. 10, for R113, R11, and FC-72, the ϕ_s values are chosen appropriately. For example, $\phi_s = 5$ deg for R113 on stainless steel, chromel, and platinum, $\phi_s = 4$ deg for R11 on stainless steel and Haynes metal, and $\phi_s = 1$ deg for FC-72 on nichrome. It should be noted that pool boiling data for R113 [10] are also included in Fig. 10. Most of the plotted data were obtained at atmospheric pressure or close to it, except for Bergles and Rohsenow's data for water in nickel tube for which the pressure was 137 bar and Hahne et al.'s data for which the pressure was 7.5 bar. Figures 10 and 11 show that the present model predicts $\Delta T_{w,\mathrm{ONB}}$ and $q_{w,\mathrm{ONB}}$ within ±30 percent for a wide range of system pressures, static contact angles, flow rates, and liquid subcoolings. All of the data plotted in Fig.

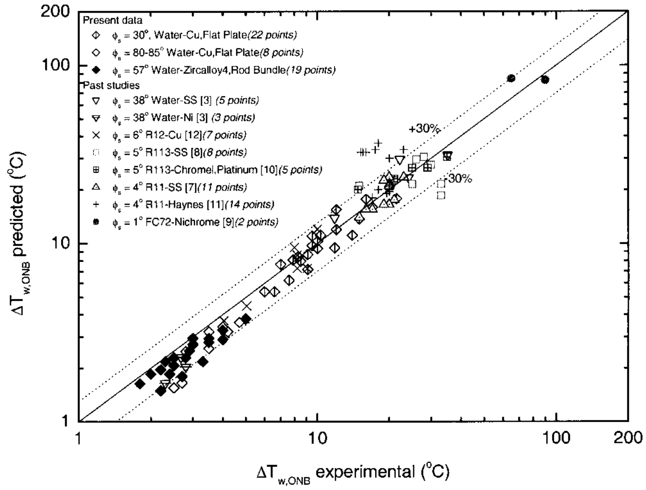

Fig. 10 Comparison of predicted and experimental $T_{w,\mathrm{ONB}}$ values

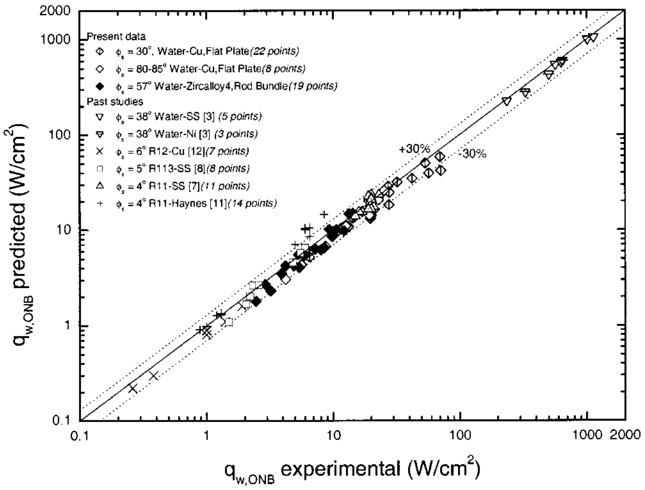

Fig. 11 Comparison of predicted and experimental $q_{w,\mathrm{ONB}}$ values

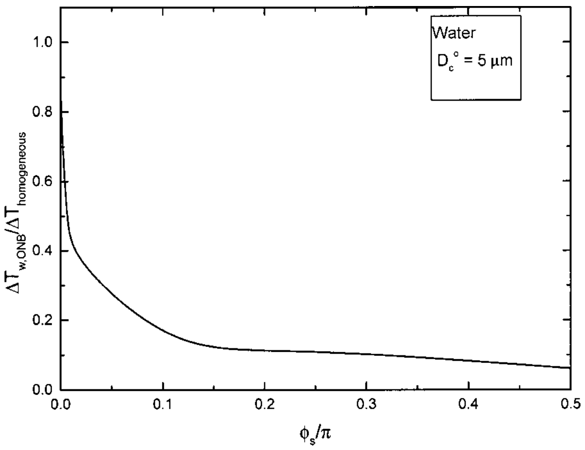

Fig. 12 Inception superheat variation with contact angle for water

10 and obtained from literature could not be shown in Fig. 11 because of lack of information regarding the exact local subcooling and/or the heat transfer coefficient. From the above model, for given values of G, $\Delta T_{\rm sub}$, and ϕ_s, it is possible to predict the axial location at which inception would occur, when a given q_w is imposed on the surface. Equation (28) is valid for all liquids and for both laminar and turbulent flow regimes as long as position dependent value of $h_{\rm sp}$ is used.

It should be noted that as ϕ_s decreases, $\Delta T_{w,\rm ONB}$ approaches the superheat required for homogeneous nucleation. This is shown in Fig. 12, which is a plot of the normalized heterogeneous inception temperature as a function of ϕ_s, for $D_c^o = 5$ μm. The inception superheat is normalized with the homogeneous nucleation superheat (213 °C for water). The plot shows that the inception temperature increases with decreasing contact angle, and approaches the homogeneous nucleation temperature for very low contact angles.

For highly wetting liquids, Tong et al. [13] found a correction factor for the size of nucleating cavities, given by Eq. (11). A quantitative comparison of the $\Delta T_{w,\rm ONB}$ values predicted using the present correlation with that predicted from Eqs. (11) and (12), could not be made because evaluation of superheat from Eq. (12) requires an a priori knowledge of β and ϕ_d. As stated earlier, in the absence of detailed information regarding the size and shape distribution of cavities present on the heater surface, any model relying on such information cannot be used to predict $\Delta T_{w,\rm ONB}$. In the present work an approach is taken where the available data are used to empirically correlate the function F. The deviation in the predicted $\Delta T_{w,\rm ONB}$ values using function F can occur if the experimental conditions (such as dissolved gas content of the liquid) are substantially altered from those that existed in the experiments representing the database. Ranges of all the data shown in Figs. 10 and 11 are listed in Table 2. Complete details of all the experimental data obtained in present work can be found in the report by Warrier et al. [28].

Active Nucleation Site Density. The active nucleation site density was measured from the high-speed motion pictures taken of the heater surface during boiling. These pictures were taken from the front of the heater surface using a CCD camera. The CCD camera (HSIS 2002) has a resolution of 256×256 pixels over viewing area and a maximum frame rate of 1220 frames/second. Pictures were taken at various axial locations along the heater surface. The recorded movies were then played back and the number of active nucleation sites counted manually. The ac-

Table 2 Experimental conditions for ONB data

Investigators	Working fluid and Surface	P (bar)	ϕ_s (deg)	G (kg/m^{2}s)	$\Delta T_{\rm sub}$ (°C)	$\Delta T_{\rm w,ONB}$ (°C)	$q_{\rm w,\,ONB}$ (W/cm^2)
Present work	Water on Cu	1.03	30	124 - 868	7.8 - 52.5	6 - 21.5	6.5 -71
		1.03	80 - 85	256 - 886	6.6 - 25.6	2.5 - 4.7	6.6 - 25.6
	Water on Zr-4	1.03	57	186 - 631	1.7 - 38.6	1.8 - 5.0	1.6 - 14.3
Bergles and Rohsenow [3]	Water on SS	2.62	38	3130 - 16200	74.8 - 80	11.8 - 35.2	336 - 1130
	Water on Ni	137.5	38	1890 - 5672		2.6 - 2.67	331 - 646
Hahne *et al.* [12]	R12 on Cu	7 - 8.1	6	200 - 2250	2.2 - 10.8	4.0 - 9.16	0.26 - 4.5
Hino and Ueda [8]	R113 on SS	1.47	5	514 - 1240	20 - 30.6	10 - 33	1.5 - 5.5
You *et al.* [10]	R113 on Cr, Pt	1	5	pool	saturated	14.8 - 35	1.6 - 4.6
Yin and Abdelmessiah [7]	R11 on SS	1.6	4	126 - 611	6 - 20	15 - 23	0.5 - 2.0
Chin [11]	R11 on Haynes-230	1.41-1.81	4	292.5 - 5257	4.74 - 11.57	11 - 20	0.88 - 8.5
Bar-Cohen and Simon [8]	FC-72 on Ni	1	1	3260 - 6535	12.6 -13.4	63, 90	87

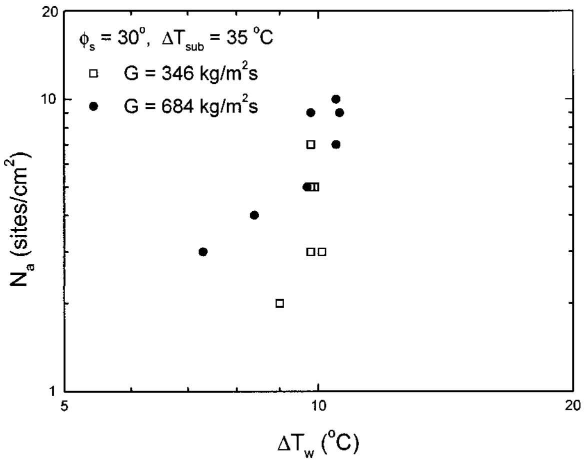

Fig. 13 Comparison of N_a for two different mass fluxes

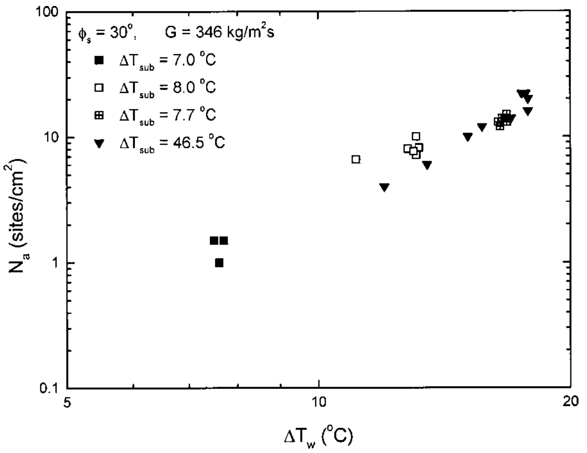

Fig. 14 Comparison of N_a for different liquid subcooling

tive nucleation site density was calculated by dividing the total number of active nucleation sites by the area over which the camera was focused. In partial nucleate boiling, where discrete bubbles are present on the surface, the active sites could be easily discerned from the pictures. However, at higher wall superheats, adjacent bubbles begin to merge making it difficult to accurately count the number of individual active sites.

To overcome this problem, a technique similar to the that used by Wang and Dhir [9] was employed. In this technique, once the required wall superheat was reached, colder water (at about 60 °C) stored in tank #2 was pumped through the test chamber for about two or three minutes. The increased subcooling caused the bubbles to decrease in size and eliminate merger, thereby facilitating the observation of individual sites. As pointed out by Wang and Dhir, this raises the possibility that if the subcooling is high, the liquid-vapor interface may be pushed back into the cavity, thereby giving the appearance that the site has been deactivated. Pictures taken before and after the cold water was introduced, showed that though the bubbles decreased in size, they did not completely disappear. The error due to deactivation is expected to be small, since the wall superheat and heat flux changed insignificantly after the cold water was introduced.

Figure 13 shows a comparison of the N_a values measured for two different values of G. Figure 14 shows the N_a values measured for different values of ΔT_{sub}. The data shown in Figs. 13 and 14 were obtained using the flat plate surface for $\phi_s = 30$ deg. No systematic effect of G and ΔT_{sub} on N_a are observed in Figs. 13 and 14. From these figures it appears that for a given ϕ_s, the dependence of N_a on ΔT_w is independent of both G and ΔT_{sub}. The active nucleation site density as a function of ΔT_w for different contact angles, for both the flat plate and rod bundle, is shown in Fig. 15. An increase in either ΔT_w or ϕ_s (i.e., decrease in surface wettability) results in an increase in N_a. The increase in N_a with increase in ϕ_s can also be clearly seen in the photographs shown in Fig. 16 for the same wall superheat of 12 °C Correlations of Kocamustafaogullari and Ishii [26] and Wang and Dhir [14] are also plotted in Fig. 15. Also included are the experimental data of Zeng and Klausner [27]. The data plotted in Fig. 15 shows significant scatter. However, this is not unexpected, since at very low number densities, ($N_a \sim 1$ site/cm^2), and with the focussing area being in the range of 1.4 cm^2 to 1.6 cm^2 for flat plate test surface, missing just one nucleation site can cause a large error. At higher wall superheats, with increase in N_a, it becomes difficult to measure the exact number of nucleation sites due to merger of bubbles from neighboring sites. Only one experiment for $\phi_s = 30$ deg, $G = 346$ kg/m^{2}s, and ΔT_w greater than 20 °C was performed with the cold water technique mentioned earlier. Figure 15 shows that at higher ΔT_w values (i.e., lower D_c values), N_a increases more rapidly with ΔT_w. From the data it appears that this transitional dependency of N_a on ΔT_w occurs at about 15 °C wall superheat.

Wang and Dhir [14] also observed this transition, but at a wall superheat of 12°C. Kocamustafaogullari and Ishii's [26] correlation underpredicts the nucleation site density obtained in the current experiment as shown in Fig. 15. Wang and Dhir's correlation matches well with the experimental data for wall superheats higher than 15°C. As mentioned earlier, it should be noted that this correlation was developed for $D_c < 5.8\ \mu$m which corresponds to a $\Delta T_w > 12$°C for water. For lower wall superheats, Wang and Dhir did not propose any correlation for N_a. However, in their work they empirically found, N_s (in sites/cm^2), the number density of all cavities present on the surface, as a function of D_c,

$$N_s = 9\times 10^3 D_c^{-2.0} \quad (D_c^* \geq 5.8\mu\text{m}). \tag{30}$$

In Eq. (30), D_c is in μm and $D_c = f_d D_c^*$, where the shape factor f_d is 0.89 and D_c^* is the measured cavity size. The number of nucleating cavities is less than the total number of available cavities as only a fraction of these cavities trap gas or vapor. The dependence of N_s on D_c (and hence ΔT_w) given by Eq. (30) is the same as what has been measured in the present work, for $\Delta T_w < 15$°C.

Based on the present data, two correlations have been developed for N_a as a function of both wall superheat (ΔT_w) and contact angle (ϕ_s). These correlations are given as:

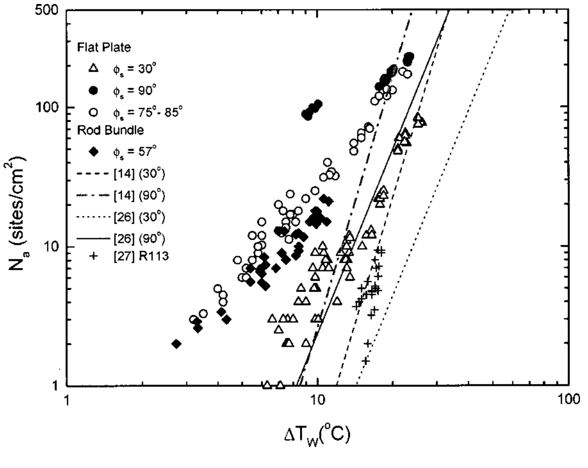

Fig. 15 Active nucleation site density data

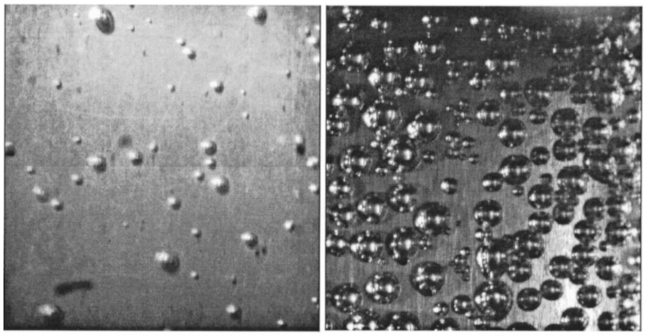

(*a*) (*b*)

Fig. 16 Comparison of heater surface during nucleate boiling, (*a*) $\phi_s=30$ deg and (*b*) $\phi_s=90$ deg

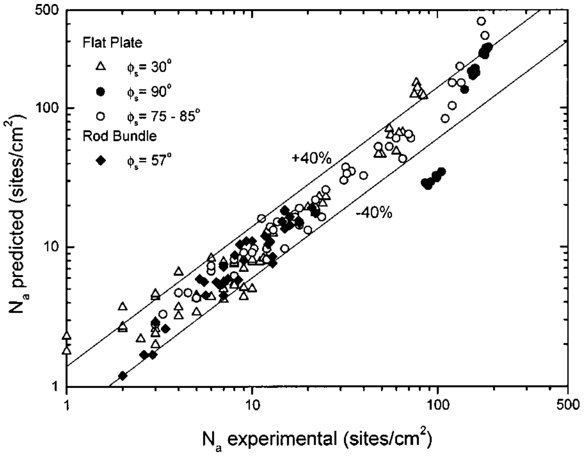

Fig. 17 Comparison of predicted and experimental N_a values

$$N_a=0.34[1-\cos(\phi_s)]\Delta T_w^{2.0} \quad \Delta T_{w,\mathrm{ONB}}<\Delta T_w<15°, \quad (31)$$

$$N_a=3.4\times10^{-5}[1-\cos(\phi_s)]\Delta T_w^{5.3} \quad \Delta T_w\geqslant 15°. \quad (32)$$

These correlations should be valid for other liquids and pressures and are applicable for $\Delta T_w>\Delta T_{w,\mathrm{ONB}}$. The power of ΔT_w in Eq. (32) is 5.3 whereas Wang and Dhir's correlation had $\Delta T_w^{6.0}$. The contact angle dependency is the same as that proposed by Wang and Dhir. Also, for lower superheats, $N_a\sim\Delta T_w^{2.0}$ which is the same dependence given by Eq. (30) (i.e., $N_s\sim D_c^{-2.0}$ which is equivalent to $N_s\sim\Delta T_w^{2.0}$). Figure 17 shows a comparison of the N_a values obtained experimentally with those predicted from Eqs. (31) and (32). It is seen that most of the data are correlated within ±40 percent.

Zeng and Klausner [27] obtained N_a data during flow boiling in a horizontal channel. In their experiments the heat flux was kept constant while the liquid velocity, liquid layer thickness, and the vapor quality at inlet were varied. Their results showed that for a constant heat flux, changing the liquid or vapor velocity had a significant effect on N_a. Another way of interpreting these results is as follows: since the heat flux was always kept constant, changing the liquid or vapor velocity will result in changing the heat transfer coefficient and in turn the wall superheat. This change in the wall superheat will in turn change the measured N_a values. The plot of their N_a data with ΔT_w for various mass fluxes, liquid film thickness, vapor and liquid velocities, shows that $N_a\sim\Delta T_w^{5.6}$ (as shown in Fig. 15) which is close to the dependence obtained in the present work, for higher range of wall superheats. However, converting the N_a dependence on velocity (from the data reported in the paper) to that on wall superheat gives $N_a\sim\Delta T_w^{3.75}$. This was obtained by assuming that for turbulent flows, $Nu\sim u^{0.8}$ and given that $N_a\sim u^{-3.0}$ (as reported in their paper). However, their data show considerable scatter. The scatter in the data at low wall superheats can be due to the uncertainty that is inherent in determining N_a when only a few sites are present in the area of interest. Table 3 lists the ranges of N_a data shown in the plots. Details of all the N_a data obtained in the present study can be found in Warrier et al. [28].

Summary

The dependence of the onset of nucleate boiling and active nucleation site density on different subcooled flow boiling parameters have been quantified. Unlike most of the previous studies the functional dependence of inception superheat or heat flux on flow rate, local liquid subcooling, static contact angle, and axial location has been accounted for. The present model explicitly takes into account the influence of static contact angle as it has been successfully applied to various liquids-surface pairs, including refrigerants. The correlation can be used to determine the location of ONB given the various system and flow parameters. The validity of the ONB correlation has been shown for the following range of parameters: (i) ϕ_s: 1 deg to 85 deg, (ii) system pressure: 1.0 bar to 137.5 bar, (iii) local liquid subcooling: 1.7°C to 80.0°C, and (iv) velocity: pool to 17 m/s.

It is found that the nucleation site density depends only on static contact angle and wall superheat. The effect of velocity and local liquid subcooling is implicit in the relation between local heat flux and wall superheat and they do not affect the nucleation site density independently. Nucleation site density data for water

Table 3 Test conditions for N_a data

Investigators	Working fluid and Surface	P (bar)	ϕ_s (deg)	G (kg/m^{2}s)	ΔT_{sub} (°C)	ΔT_w (°C)	q_w (W/cm^2)	N_a (sites/cm^2)
Present work	Water on Cu	1.03	30	235 - 684	7.0 - 46.5	6.3 - 26.5	6.5 - 96.3	1 - 84
		1.03	75 - 85	256 - 886	6.6 - 25.6	3.2 - 23.1	12.6 - 70.0	3 -180
		1.03	90	346	10.2 -12.9	9.2 - 23.5	16.0 - 94.4	86 - 230
	Water on Zr-4	1.03	57	186 - 631	1.7 - 38.6	2.8 - 11.1	3.0 - 14.3	2 -22
Zeng and Klausner [27]	R113 on nichrome	1.3	-	214	-	14 -18	1.9	1 - 9.5

is correlated as a function of static contact angle and wall superheat. The correlations developed for N_a covered a range of static contact angles varying from 30 deg to 90 deg and superheats ranging from 3°C to 26.5°C.

Acknowledgment

This work received support from the U.S. Nuclear Regulatory Commission.

Nomenclature

D = diameter
D_c^o = cavity diameter corresponding to the tangency condition
D_s = maximum cavity diameter present on the surface
G = mass flux
h = heat transfer coefficient
h_{fg} = latent heat
k = thermal conductivity
N_a = active nucleation site density
N_s = cumulative site density
P = pressure
q = wall heat flux
r = radius
T = temperature
ΔT_w = wall superheat ($T_w - T_{\text{sat}}$)
ΔT_{sub} = liquid subcooling ($T_{\text{sat}} - T_l$)
u = velocity
y = normal distance from the wall
z = axial direction (along flow)

Greek

β = cone half angle
δ = boundary layer thickness
ϕ = contact angle
ρ = density
σ = surface tension

Subscripts

b = bubble
c = cavity
d = dynamic
g = gas
in = inlet
l = liquid
ONB = onset of nucleate boiling
s = static
sat = saturation
sp = single-phase
sub = subcooling
t = thermal
v = vapor
w = wall

References

[1] Warrier, G. R., and Dhir, V. K., 1999, ‘‘Review of Experimental and Analytical Studies on Low Pressure Subcooled Flow Boiling,’’ *Proceedings of the 5th ASME/JSME Joint Thermal Engineering Conference*, Paper AJTE99-6233, CD-ROM Edition.

[2] Hsu, Y. Y., 1962, ‘‘On the Size Range of Active Nucleation Cavities on a Heating Surface,’’ ASME J. Heat Transfer, **84**, pp. 207–216.

[3] Bergles, A. E., and Rohsenow, W. M., 1964, ‘‘The Determination of Forced-Convection Surface-Boiling Heat Transfer,’’ ASME J. Heat Transfer, **1**, pp. 365–372.

[4] Sato, T., and Matsumara, H., 1964, ‘‘On the Conditions of Incipient Subcooled Boiling With Forced Convection,’’ Bull. JSME, **7**(26), pp. 392–398.

[5] Davis, E. J., and Anderson, G. H., 1966, ‘‘The Incipience of Nucleate Boiling in Forced Convection Flow,’’ AIChE J., **12**(4), pp. 774–780.

[6] Kandlikar, S. G., Mizo, V., Cartwright, M., and Ikenze, E., 1997, ‘‘Bubble Nucleation and Growth Characteristics in Subcooled Flow Boiling of Water,’’ *National Heat Transfer Conference*, ASME, HTD-342, pp. 11–18.

[7] Yin, S. T., and Abdelmessih, A. H., 1977, ‘‘Prediction of Incipient Flow Boiling From Uniformly Heated Surface,’’ AIChE Symp. Ser., **73**(164), pp. 236–243.

[8] Hino, R., and Ueda, T., 1985, ‘‘Studies on Heat Transfer and Flow Characteristics in Subcooled Flow Boiling-Part I. Boiling Characteristics,’’ Int. J. Multiphase Flow, **11**(3), pp. 269–281.

[9] Bar-Cohen, A., and Simon, T. W., 1988, ‘‘Wall Superheat Excursions in the Boiling Incipience of Dielectric Fluids,’’ Heat Transfer Eng., **9**, pp. 19–31.

[10] You, S. M., Simon, T. W., Bar-Cohen, A., and Tong, W., 1990, ‘‘Experimental Investigation of Nucleate Boiling Incipience with a Highly-Wetting Dielectric Fluid (R113),’’ Int. J. Heat Mass Transf., **33**(1), pp. 105–117.

[11] Chin, Y., 1997, ‘‘An Experimental Study of Flow Boiling in a Narrow Channel: From Convection to Nucleate Boiling,’’ Ph.D. thesis, University of Houston, Houston, TX.

[12] Hahne, E., Spindle, K., and Shen., N., 1990, ‘‘Incipience of Flow Boiling in Subcooled Well Wetting Fluids,’’ *Proceedings 9th International Heat Transfer Conference*, Israel, **2**, pp. 69–74.

[13] Tong, W., Bar-Cohen, A., Simon, T. W., and You, S. M., 1990, ‘‘Contact Angle Effects on Boiling Incipience of Highly Wetting Liquids,’’ Int. J. Heat Mass Transf., **33**(1), pp. 91–103.

[14] Wang, C. H., and Dhir, V. K., 1993, ‘‘Effect of Surface Wettability on Active Nucleation Site Density During Pool Boiling of Water on a Vertical Surface,’’ ASME J. Heat Transfer, **115**, pp. 659–669.

[15] Celata, G. P., Cumo, M., and Mariani, A., 1997, ‘‘Experimental Evaluation of the Onset of Subcooled Flow Boiling at High Liquid Velocity and Subcooling,’’ Int. J. Heat Mass Transf., **40**(12), pp. 2879–2885.

[16] Jakob, M., 1949, *Heat Transfer*, Wiley, New York.

[17] Gaertner, R. F., and Westwater, J. W., 1960, ‘‘Population of Active Sites in Nucleate Boiling Heat Transfer,’’ Chem. Eng. Prog., Symp. Ser., **56**, pp. 39–48.

[18] Hsu, Y. Y., and Graham, R. W., 1976, *Transport Processes in Boiling and Two-Phase Systems*, Hemisphere Publishing Corporation, Washington DC.

[19] Sultan, M., and Judd, R. L., 1978, ‘‘Spatial Distribution of Active Sites and Bubble Flux Density,’’ ASME J. Heat Transfer, **100**, pp. 56–62.

[20] Mikic, B., and Rohsenow, W. M., 1969, ‘‘A New Correlation of Pool Boiling Data Including the Effect of Heating Surface Characteristics,’’ ASME J. Heat Transfer, **91**, pp. 245–250.

[21] Bier, K., Gorenflo, D., Salem, M., and Tanes, Y., 1978, ‘‘Pool Boiling Heat Transfer and Size of Active Nucleation Centers for Horizontal Plates With Different Surface Roughness,’’ *Proceedings of 6th International Heat Transfer Conference*, Toronto, **1**, pp. 151–156.

[22] Cornwell, K., and Brown, R. D., 1978, ‘‘Boiling Surface Topography,’’ *Proceedings of 6th International Heat Transfer Conference*, Toronto, **1**, pp. 157–161.

[23] Yang, S. R., and Kim, R. H., 1988, ‘‘A Mathematical Model of Pool Boiling Nucleation Site Density in Terms of Surface Characteristics,’’ Int. J. Heat Mass Transf., **31**, pp. 1127–1135.

[24] Bankoff’s, S. G., 1958, ‘‘Entrapment of Gas in Spreading of Liquid Over a Rough Surface,’’ AIChE J., **4**, pp. 24–26.

[25] Gaertner, R. F., 1963, ‘‘Distribution of Active Sites in the Nucleate Boiling of Liquids,’’ Chem. Eng. Prog., Symp. Ser., **59**, pp. 52–61.

[26] Kocamustafaogullari, G., and Ishii, M., 1983, ‘‘Interfacial Area and Nucleation Site Density in Boiling Systems,’’ Int. J. Heat Mass Transf., **26**(9), pp. 1377–1387.

[27] Zeng, L. Z., and Klausner, J. F., 1993, ‘‘Nucleation Site Density in Forced Convection Boiling,’’ ASME J. Heat Transfer, **115**, pp. 215–221.

[28] Warrier, G. R., Basu, N., and Dhir, V. K., 2001, ‘‘Subcooled Boiling for Low Pressures,’’ Progress Report for USNRC Task Order No. 5., UCLA ENG-01-224.

Ying-Xin Wang

Ling Zheng

Joel L. Plawsky

Peter C. Wayner, Jr.
e-mail: wayner@rpi.edu

The Isermann Department of Chemical
Engineering, Rensselaer Polytechnic Institute,
Troy, NY 12180-3590

Optical Evaluation of the Effect of Curvature and Apparent Contact Angle in Droplet Condensate Removal

The microscale transport processes in droplet condensation and removal due to interfacial phenomena were studied. In particular, this paper concerns the movement of a condensed ethanol sessile drop into a concave liquid film in the corner. An improved image analyzing procedure was used to evaluate the curvatures and contact angles for both the drop and the concave corner meniscus at different condensation rates. The experimental results demonstrated that the condensate removal rate was a function of the curvature and contact angle, which self-adjust to give the necessary force field. The use of a dimensionless, shape dependent, force balance was demonstrated. For small drops, the intermolecular force was found to be much larger than the gravitational force and dominated droplet removal. Microscale pressure fields can be experimentally measured whereas interfacial temperature differences cannot. [DOI: 10.1115/1.1466460]

Keywords: *Condensation, Image Processing, Interferometry, Microscale, Visualization*

Introduction

The pressure gradient due to changes in the intermolecular force field, which is a function of the shape, temperature, and composition, controls the fluid flow and heat transfer processes in thin microscale liquid-vapor systems [e.g., [1–8]]. For example, thin film evaporation in the grooves of heat transfer devices has been extensively studied [e.g., [9–20]]. Herein, the use of a Constrained Vapor Bubble (CVB) heat exchanger to study the microscale transport processes due to interfacial phenomena in dropwise condensation is described. A schematic of the CVB is presented in Fig. 1. It consists mainly of a quartz cell (square cross section; inside dimensions, 3 mm×3 mm; outside dimensions, 5.5 mm ×5.5 mm; length, 40 mm), a heater on the top, and coolers on each side of the cell located at 20mm from the top. The axial temperature profile on the flat surface was measured using thermocouples (which are not shown) placed at 2 mm intervals. Since temperature $T_1 > T_2$, energy flows from End (1) to End (2) by conduction in the walls and by an evaporation, vapor flow and condensation mechanism. Some heat is lost to the surroundings from the entire length. Details regarding the experimental setup can be found in Wang et al. [21]. As shown in Fig. 1, the vertical CVB in the earth's gravitational field is divided into three different regions, which includes Region I (the dry region), Region II (the evaporator region), and Region III (the condenser region). There is a ''pressure jump'' at the liquid-vapor interface, $P_l - P_v$, due to the anisotropic stress tensor near interfaces. The condensate flows from End (2) to End (1) against gravity and frictional force because of the intermolecular force field which is a function of the film profile. The details of the film profile and therefore, the pressure field, are measured optically. Below, the description and use of an improved image analyzing procedure to determine the characteristics of the droplet removal portion of this process is emphasized.

To obtain a partially wetting ethanol/quartz system, the quartz cell is heated to a high temperature during fabrication. Figures 2 and 3 show a comparison of the isothermal ethanol film at 24°C in the initial cell and a cell ''modified'' by heating above 1000°C during fabrication. The ethanol film in Fig. 3 becomes partially wetting on the surface of the modified quartz cell because heating to a high temperature makes the surface more hydrophobic by removing surface hydroxyl groups [22]. In the initial cell, there is a relatively thick film of adsorbed ethanol ($\delta \approx 50$ nm based on relative reflectivity) above the contact angle of $\theta = 0$. The apparent contact angle in the modified cell is $\theta = 4.9$ deg. The procedure to obtain these angles is discussed below. Herein, we discuss the optically observed details of the droplet condensation process occurring in Region III with partially wetting ethanol on the modified surface. A schematic of a cross-section of the cell in Region III is given in Fig. 4 where ethanol forms both a drop on the quartz surface and a concave film in the corner. Before pure ethanol was introduced into the evacuated CVB heat exchanger, it was distilled to remove the non-condensable gases.

The interfacial characteristics of both equilibrium and dynamic sessile drops have been extensively studied. For example, the details of the equilibrium shape of the fluid interface in the microscopic contact line region have been described using the augmented Young-Laplace equation [23–34]. Although all these details are important for the complete understanding of the processes addressed, a macroscopic force balance based on only the curvature and apparent contact angle is used herein to obtain significant new insights concerning droplet removal. Although the use of a macroscopic force balance obviates the current need to address more of the microscopic details below a film thickness of $\delta = 0.1$ μm, it is anticipated that this work will be subsequently extended to study these details.

The effect of changes in the apparent contact angle on contact line motion has also been extensively studied. Essentially, using the assumption of a low vapor pressure liquid without phase change, hydrodynamic and surface diffusion models were developed for forced spreading [35–43]. An example of its importance to stability was given by Sharma and Jameel [44]. To reconcile these models, accurate measurement of the contact angle is needed [35]. Herein, using a unique experimental design, the measured shape change due to condensation gives the driving force for flow.

As shown in Fig. 2, the region of dropwise condensation was viewed through an ordinary light microscope with illumination

---

Contributed by the Heat Transfer Division for publication in the JOURNAL OF HEAT TRANSFER. Manuscript received by the Heat Transfer Division December 4, 2000; revision received October 22, 2001. Associate Editor: A. Majumdar.

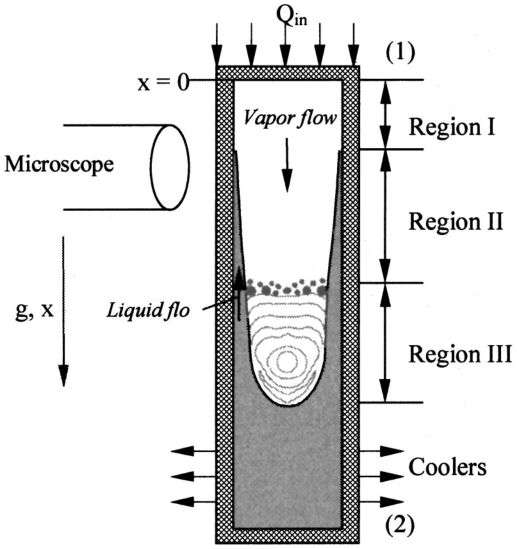

Fig. 1 A schematic drawing of three different regions of the vertical CVB

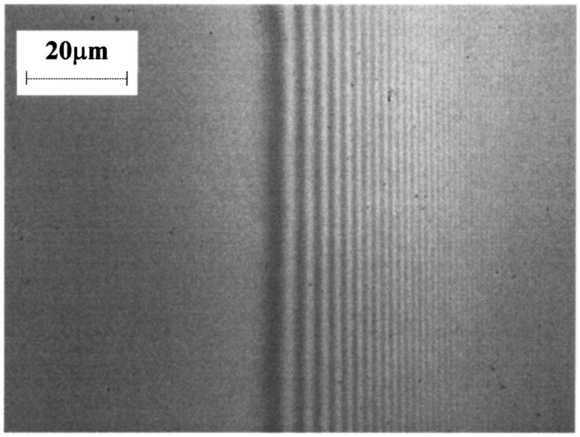

Fig. 2 The completely wetting ethanol film in the initial cell with a contact angle $\theta=0$

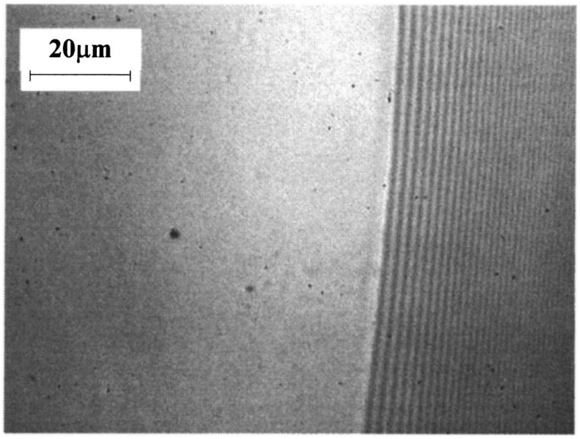

Fig. 3 The partially wetting ethanol film in the modified cell with a contact angle $\theta=4.9$ deg ($x=3$ mm)

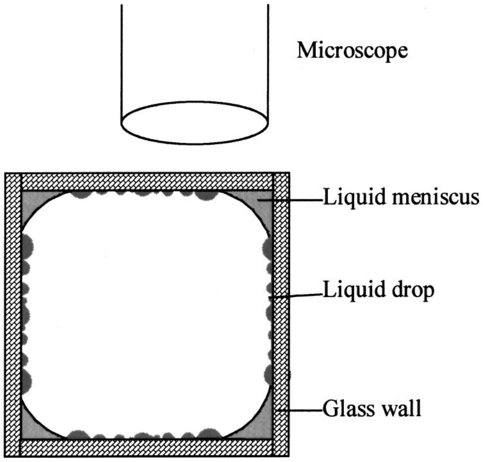

Fig. 4 Dropwise condensation in Region III

through a 50× objective and captured using a video camera. Near the corner, where the convex condensed drop coexists with the concave thin liquid film, the liquid flow occurs from the drop to the concave liquid film because of the differences in the curvatures and the apparent contact angles. The main purpose of this paper is to propose an improved image analyzing procedure to measure the curvatures and contact angles for both the drop and the meniscus in the corner. A force balance is then used to evaluate the movement of the drop to the meniscus due to intermolecular forces.

Since Schmidt et al. [45] reported that the heat transfer coefficient of dropwise condensation is much higher than that of film condensation, dropwise condensation has been extensively studied [e.g., [46–50]]. The dropwise condensation process includes initial droplet formation, growth, removal, and re-nucleation on re-exposed sites. When a droplet grows to a size that can not be sustained by surface tension forces, it is removed from the surface by gravity, external forces or drag forces resulting from the surrounding surface conditions [51]. Tanasawa et al. [52] measured the dependence of the heat transfer coefficient on the departing drop diameter, using the gravitational, centrifugal, and steam shear forces to change the departing drop diameter. Yamali and Merte [53] designed a centrifuge to study the effect of body forces on dropwise condensation heat flux under controlled subcooling. Wang et al. [54] gave an initial report on the departure of a single condensed drop into a concave liquid film due to the intermolecular force gradient. This paper extends the description of these studies by first detailing the image analyzing technique developed and then using it to compare the removal of drops at different condensation rates. An enhanced understanding of the effect of interfacial phenomena is thereby obtained.

Force Balance

A brief description of the force balance used in Ref. [54] is given next. Consider a drop close to the liquid meniscus in the corner shown in Fig. 5: the condensed drop is assumed to be a spherical cap, whereas the meniscus in the corner is a portion of a cylindrical surface. Changes in the intermolecular force field cause the pressure difference between liquid drop and liquid in the corner. Using the following augmented Young-Laplace equation, the shape of the interface gives the pressure field for microscale liquid flow in the liquid:

$$P_v - P_l = \sigma_l K + \Pi \tag{1}$$

where K is the curvature ($K<0$ for convex and $K>0$ for concave). A force balance that relates viscous losses to interfacial forces due to curvatures and apparent contact angles gives-

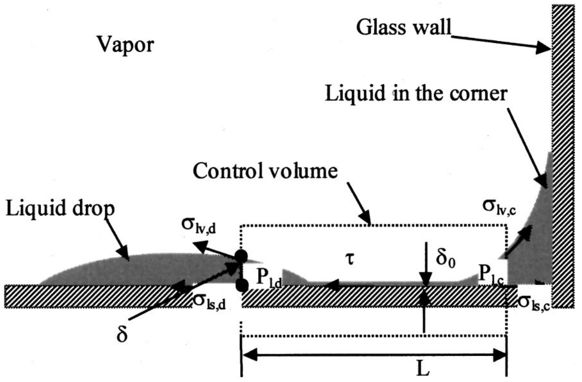

Fig. 5 Macroscopic force balance

$$\tau L=\sigma_l(-\cos\theta_d+\cos\theta_c)+\delta(-\sigma_l K_d+\sigma_l K_c) \tag{2}$$

where τ is the average shear stress over the length L, L is the distance between the thickness δ in the drop and the corner meniscus, and $\theta<90$ deg is the apparent contact angle. The subscripts d and c denote the drop and corner meniscus. The right hand side of Eq. (2) is the driving force for liquid flow per unit width (F/d_s) between the drop and the meniscus. It is the decrease in chemical potential that causes the spontaneous flow. For the purpose of discussion, we assume that d_s is the width of the liquid drop. The selection of this characteristic width does not affect the value of the dimensionless experimental data given on the rhs of Eq. (3). In both the liquid drop and corner meniscus, δ is taken to be the film thickness of the 0th order of destructive fringes, 0.1 μm, where the apparent contact angles were measured. Using a large value of the film thickness at the ends of the control volume obviates the need to discuss the disjoining pressure, which is important at thickness $\delta<0.1$ μm.

Equation (2) can be rewritten in dimensionless form by dividing by σ_l to give the dimensionless difference in free energy for spontaneous condensate removal,

$$\frac{F}{d_s\sigma_l}=\frac{\tau L}{\sigma_l}=(-\cos\theta_d+\cos\theta_c)+\delta(-K_d+K_c) \tag{3}$$

The left hand side of Eq. (3) represents the ratio of the resistance force due to shear to the surface free energy of a flat bulk liquid. It is equal to the sum of two terms due to the contact angle difference and the capillary pressure difference. Using the improved image analyzing technique proposed next, the apparent contact angles and curvatures can be obtained accurately from the film thickness profiles of the drop and the meniscus.

Image Analyzing Technique

A high power microscope was rotated and situated on an adjustable stage, so that the naturally occurring interference fringes of the drop and liquid film in the corner of the vertical CVB could be viewed and evaluated using image analyzing interferometry. Of particular relevance to our experimental technique is the pioneering work by Sharp [55], who used the interference of monochromatic light reflected at the liquid-vapor and liquid-solid interfaces in a thin liquid film to visualize an evaporation liquid film at the base of bubbles on glass during nucleate boiling. Jawurek [56] employed high-speed interference photography to simultaneously determine the detailed shape and thickness of the microlayer. Voutsinos and Judd [57] investigated the growth and evaporation of the microlayer underlying a bubble forming on a glass heater surface using laser interferometry and high speed photography. Using Interferometry, Renk and Wayner [58,59] measured the shape of a stationary ethanol meniscus formed on a horizontal glass substrate as a function of the evaporative heat flux. To evaluate the effect of concentration gradients, Wayner et al. [8] studied evaporation in the contact line region of a mixture on a silicon wafer using Interferometry and Huang et al. [60] used the CVB. Chen and Wada [61] studied the isothermal spreading dynamics of a drop edge using a laser light interference microscopy method. Kihm and Pratt [62] presented a Fizeau interferometry technique to determine the complete contours of thin film thickness variations of evaporating pentane menisci. Microscale patterning of contact line instabilities have also been studied using Interferometry [63–67].

Film Profile. The interference fringes resulting from the reflection of monochromatic light at both the liquid-vapor and liquid-solid interfaces in the CVB were used to determine the thickness profile of the meniscus. Destructive interference occurs when the optical paths of the two reflected beams is such that they are out of phase by π. In our case, $n_v<n_l<n_s$. Therefore, there is a phase shift equal to π at each interface. The constructive interference occurs when the two reflected beams are in phase. Herein, monochromatic light ($\lambda=543.5$ nm) from a Hg-arc with a narrow band filter is used to illuminate the cell. Ethanol ($n_l=1.359$, $\sigma_l=0.0225$ Nm) is used as working fluid. With a 50× objective, each of the 640×480 pixels measures the average reflectivity (thickness) of a region with a diameter of 0.1777 μm. The recorded images were analyzed using image processing. Using the proposed new analytical technique, the measured liquid thickness profile gives both the curvature and apparent contact angle.

Curvature. For example, DasGupta et al. [68] and Karthikeyan et al. [69] used image analyzing interferometry to measure curvatures for a completely wetting fluid. The curvature (K) is defined as

$$K=\frac{\dfrac{d^2\delta}{dy^2}}{\left[1+\left(\dfrac{d\delta}{dy}\right)^2\right]^{3/2}} \tag{4}$$

A simplified expression was obtained by assuming that the square of the slope, $(d\delta/dy)^2$, was very small compared to one. The film profile was assumed to be a parabola whose curvature was a constant in this approximation. The square root of film thickness, $\delta^{1/2}$, was then plotted against the distance, y, and the profile appeared to be a straight line in the thicker portion of the meniscus. The curvature was then obtained from the slope of the profile, which is a constant,

$$K=\frac{1}{r}=2\left(\frac{d\delta^{1/2}}{dy}\right)^2 \tag{5}$$

This treatment is applicable only in the completely wetting system for the isothermal case [52] and the adiabatic region of the non-isothermal case [53]. In the cases of high rates of phase change and/or partially wetting systems, a steep film profile is obtained. The plot, $\delta^{1/2}$ versus y, bends instead of being a straight line. Thus, the slope, $d\delta^{1/2}/dy$, is not a constant. The second derivative of the parabola can no longer account for these variations. In addition, we found that this technique could not be used to obtain the apparent contact angle. Herein, an improved analytical technique is proposed to overcome these difficulties and evaluate both the curvature and the apparent contact angle for both the partially wetting fluid and the completely wetting fluid. Instead of using the definition of the curvature, we considered the film profile in the corner to be a part of a circle, the curvature can then be obtained from the radius of the circle. In addition, an extension of this method discussed later gives the correct spherical shape of the drop in the equilibrium limit.

Theoretical Formulation for the Concave Liquid Film in the Corner. Figure 6 represents one of the corners of a container with a general vertex angle of α. The corner is partially filled with the liquid, and the liquid forms an apparent finite contact angle of

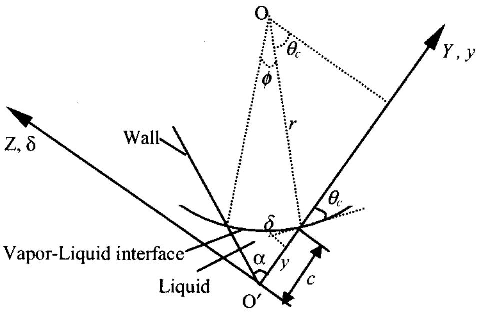

Fig. 6 One of the corners of a container with a vertex angle, α

θ_c on the interior wall of the container. The coordinate axes are labeled on the figure. The *Z*-axis represents the thickness of the liquid film (δ). The *Y*-axis, which corresponds to one side of the container wall, represents the location of the film thickness profile. The vapor-liquid interface is assumed to be a part of a circle, the center of the circle is located at point *O*. The local validity of this assumption is demonstrated by the final fit of the model to the experimental data. The coordinate of point *O* $(r \cos \theta_c, c + r \sin \theta_c)$ is easily derived from geometric relations, where $c = r \sin \phi/2/\sin \alpha/2$, $\phi = \pi - (2\theta_c + \alpha)$. The shape of the vapor-liquid interface at the corner of a container can thus be expressed as,

$$(\delta - r \cos \theta_c)^2 + (y - c - r \sin \theta_c)^2 = r^2 \tag{6}$$

Rearranging Eq. (6) while using the negative square root,

$$y = c + r \sin \theta_c - \sqrt{r^2 - (\delta - r \cos \theta_c)^2} \tag{7}$$

The two unknowns, r and θ_c, can be obtained simultaneously by best fitting the experimental film thickness profile, $\min(\Sigma_{i=1}^{N}(y_{\mathrm{exp},i} - y_{\mathrm{theo},i})^2)$, where N is the total number of dark and bright fringes. The subscripts exp and theo denote the experimental data and theoretical values using Eq. (7), respectively. The curvature (K) is obtained from the reciprocal of the radius of curvature. In our particular case of square cross section, $\alpha = \pi/2$.

Verification of the Technique. To verify this technique, isothermal experimental data obtained with apolar pentane was used to evaluate a theoretical model. Use of the completely wetting apolar pentane/quartz system to evaluate the measurement error minimizes the influence of uncertain factors such as local variations in the contact angles.

For an isothermal vertical CVB illustrated in Figure 1 ($Q_{\mathrm{in}} = Q_{\mathrm{out}} = 0$), the sum of the disjoining and the capillary pressures equals the hydrostatic pressure,

$$\Delta(\Pi + \sigma_l K) = (\rho_l - \rho_v) g \Delta x \tag{8}$$

where ρ_l and ρ_v represent the densities of the liquid and vapor, respectively. x is the axial distance in the vertical cell. As marked in Fig. 1, zero represents the top of the vapor bubble in the cell. Figure 7 gives an example of typical interference fringes which represent the film thickness profile of pentane in the corner of the cell. The uniformly bright part represents the thin film on the flat surface of the cell. Using Eq. (7) to best fit the experimental film thickness profile presented in Fig. 8, an apparent contact angle of 0 deg and a curvature of the meniscus in the corner of the cell of 5190 m^{-1} were obtained. Neglecting the disjoining pressure Π in the thicker portion of the film, $\delta > 0.1$ μm, gives,

$$\Delta K = \frac{(\rho_l - \rho_v) g \Delta x}{\sigma_l} \tag{9}$$

The curvatures obtained experimentally along the axial direction were compared with the theoretical results from Eq. (9). Figure 9 shows the comparison of the experimental and theoretical pentane

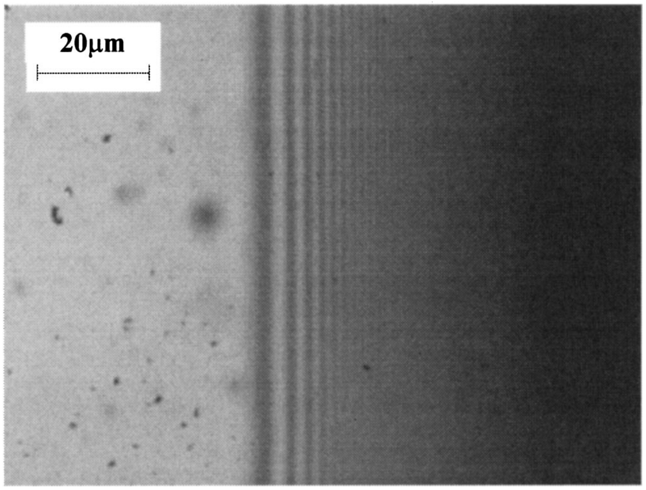

Fig. 7 Typical interference fringes for a curved thin film of pentane in the corner of the cell

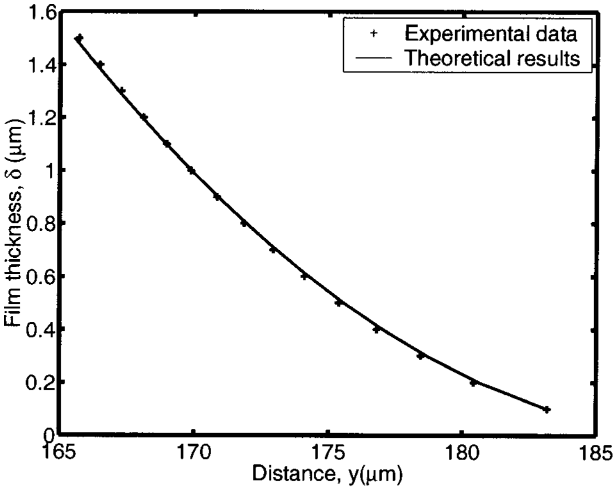

Fig. 8 Film thickness profiles of pentane in the corner of the cell

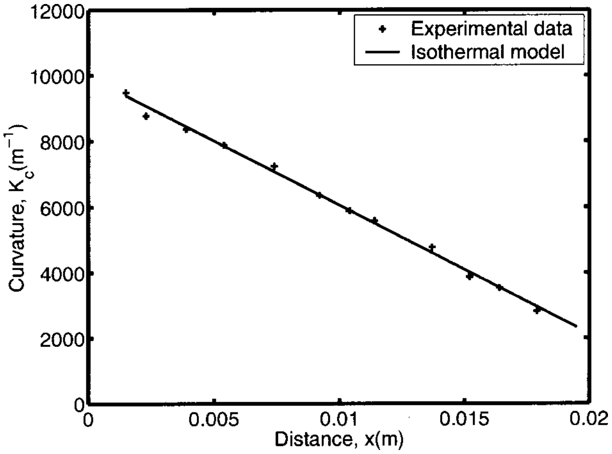

Fig. 9 Comparison of analyzed experimental curvature profiles with modeling results based on Eq. (9)

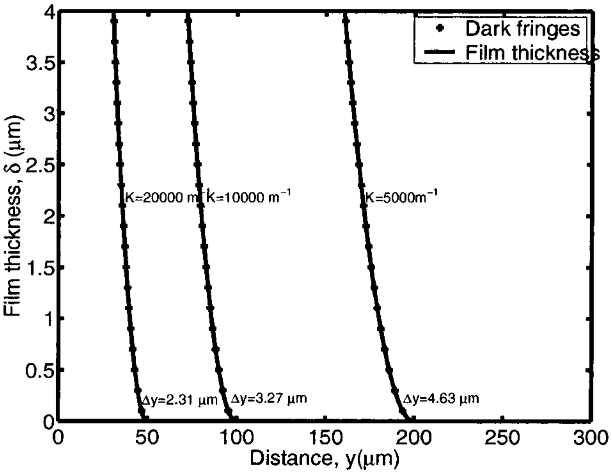

Fig. 10 Theoretical film thickness profiles showing theoretical locations of dark fringes for different curvatures with $\theta_c = 0$ deg obtained using Eq. (7)

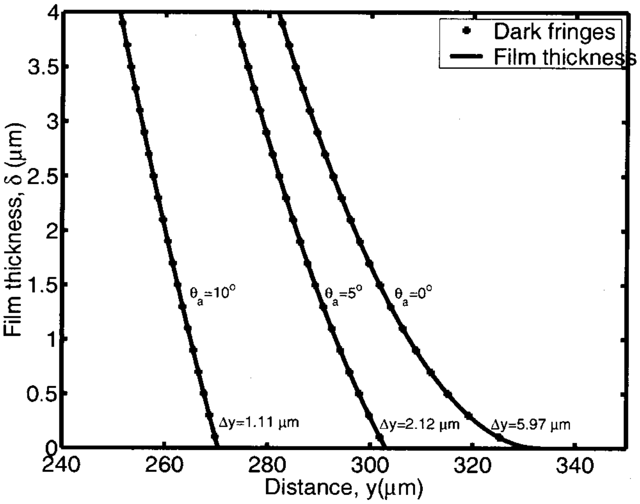

Fig. 11 Theoretical film thickness profiles showing theoretical locations of dark fringes for different apparent contact angles for $K = 3000\ \mathrm{m}^{-1}$ obtained using Eq. (7)

curvatures along the axial distance in the vertical isothermal CVB with a bubble length of 22 mm. The experimental curvatures were in good agreement with the theoretical results. The average deviation of experimental results from the modeling results is 1.8 percent.

Effect of Curvature on Film Thickness Profile. The following theoretical results are presented to enhance the understanding of the pictures. Using Eq. (7), a series of theoretical film thickness profiles with different curvatures with the contact angle of zero for the pentane/quartz system is presented in Fig. 10. The circles in the plot represent the destructive fringes obtained from Eq. (7). For example, the circle sign at 0.101 μm denotes the 0th order destructive fringe, at 0.302 μm it denotes the 1st order destructive fringe. As can be seen, the spacing between two consecutive destructive fringes becomes smaller as the film thickness increases, which can be observed in Fig. 7. The spacing between the two consecutive destructive fringes also decreases as the curvature increases. For the film thickness profile with $K = 5000\ \mathrm{m}^{-1}$, the spacing between the 0th and 1st orders of destructive fringes is 4.63 μm; For $K = 10000\ \mathrm{m}^{-1}$ and $K = 20000\ \mathrm{m}^{-1}$, the spacings are 3.27 μm and 2.31 μm, respectively. Each pixel in our experimental system measured the reflectivity of an area with a diameter of 0.1777 μm.

Effect of Apparent Contact Angle on Film Thickness Profile. For a partially wetting system, liquid forms a finite contact angle on the wall of the container. Taking the ethanol/quartz system with a curvature of 3000 m^{-1} as an example, the film thickness profiles with assumed different contact angles obtained using Eq. (7), are shown in Fig. 11. As the contact angle increases, the spacing between two consecutive dark fringes decreases. At $\theta_c = 0$ deg, the spacing between the 0th and 1st orders of the dark fringes is 5.97 μm; At $\theta_c = 5$ deg and 10 deg, the spacings reduce to 2.12 μm and 1.11 μm, respectively. It is interesting to note that the film thickness profile at $\theta_c = 10$ deg is very steep and appears to be a straight line without curvature, however, it is actually a part of a circle with the curvature of 3000 m^{-1}.

Theoretical Formulation for the Convex Liquid Drop on the Surface. Equation (6) describes the shape of a concave liquid film in the corner of a container using a YZ-coordinate system. Since a liquid drop forms a convex vapor-liquid interface on the flat surface, the curvature of the liquid drop on the flat surface can not be obtained by directly applying the above equations. Experimentally, we can obtain the film thickness profile (δ'_{exp}) of the mid-plane of the drop. Therefore, for a mid-plane through the drop, we introduce a $Y'Z'$-coordinate system for a single radius of curvature shown in Fig. 12 with the origin at point O'' and with the Y'-axis directed along the flat surface line $O''B$. The $Y'Z'$-system is devised so that theoretical film thickness profiles can be compared with experimental data. The Z'-axis represents the film thickness (δ') of the drop, and Y'-axis represents the location (y') of the film thickness. In order to obtain the curvature of the drop by applying Eq. (6), we need to determine the transformation between the YZ-system and $Y'Z'$-system. In our case, $\alpha = \pi/2$. By geometrical derivations, the points in the YZ-system can be expressed in the $Y'Z'$-system by the following coordinate transformation

$$y = c - \frac{y' + \delta'}{\sqrt{2}} \tag{10a}$$

$$\delta = \frac{y' - \delta'}{\sqrt{2}} \tag{10b}$$

where δ and y denote the film thickness and the location of the film thickness in the YZ-system, respectively. δ' and y' denote the film thickness and the location in the $Y'Z'$-system. Substituting Eqs. (10a) and (10b) into Eq. (6) and rearranging gives

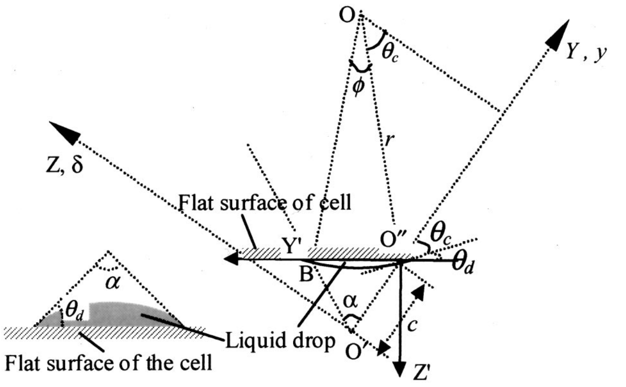

Fig. 12 Coordinate transformation for the drop on the flat surface

$$y' = -\frac{1}{2}\{\sqrt{2}r(-\cos\theta_c + \sin\theta_c) + \sqrt{2r^2(-\cos\theta_c + \sin\theta_c)^2 - 4[(\delta')^2 + \sqrt{2}r\delta'(\cos\theta_c + \sin\theta_c)]}\} \quad (11)$$

The two unknowns, r and θ_c, can be obtained simultaneously by best fitting the experimental film thickness profile of the drop. The contact angle of the drop is then given by $\theta_d = \pi/4 - \theta_c$, and the curvature is $K_d = 2/r$ since the drop is assumed to be a spherical cap.

Experimental Results and Discussions

The thickness profiles of ethanol in Figs. 2 and 3 are given in Fig. 13. As can be seen, the thickness profile of ethanol on the modified surface cell is much steeper than that on the initial surface cell. The ethanol/quartz system changes from completely wetting in the initial cell to partially wetting in the modified cell. The equilibrium apparent contact angle of the ethanol-modified quartz system is 4.9 deg.

In the region of dropwise condensation, the vapor first condensed into small discrete liquid drops on the flat surface of the vertical quartz cell. These small drops then grew and coalesced into larger drops, which were then absorbed into the meniscus in the corner. This sequence then repeated. For example, three pictures of the same location recorded over a period of 0.33 seconds are presented in Fig. 14. Time $t = 0$ is a relative time as close to the start of a cycle as we can measure with a standard video camera. Near the corner of the quartz cell, instead of falling under the gravitational force, the condensed drops are driven into the concave liquid film by the natural pressure gradient due to interfacial phenomena, which can be accurately analyzed using the image analyzing technique described above. Two local cases with different condensation rates shown in Figs. 15 and 16(*a*) are now discussed using the sessile drops indicated by the arrows. Figures 15 and 16 were recorded at different locations and absolute times.

Since the coolers are located 20 mm from the top, the base of the longer vapor bubble (Case II) is closer to the cooler, therefore, the condensation rate in the longer bubble is larger. For Case I in Fig. 15, the length of the vapor bubble is 7 mm. For Case II in Figure 16(*a*), the length of the vapor bubble is 10 mm. It is clearly seen that the liquid film in the corner in Fig. 16(*a*) is more spread out due to the larger condensation rate. Figure 16(*b*) gives a clearer view of the spreading liquid film portion in the corner adjacent to that in Fig. 16(*a*). For each bubble length, the condensation rate is also a function of axial position.

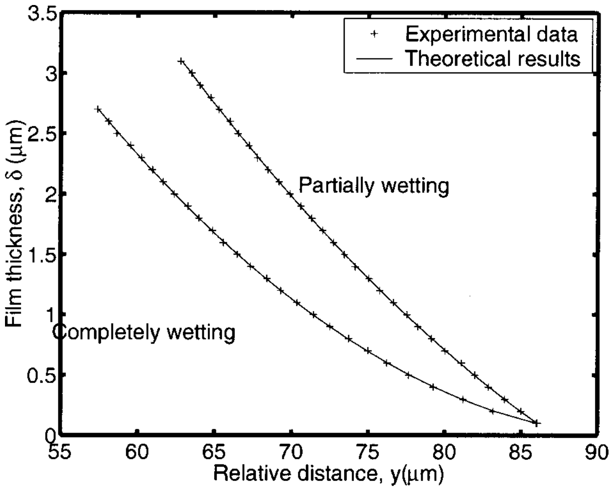

Fig. 13 Comparison of thickness profiles of ethanol film on the initial and modified surfaces ($x = 3$ mm)

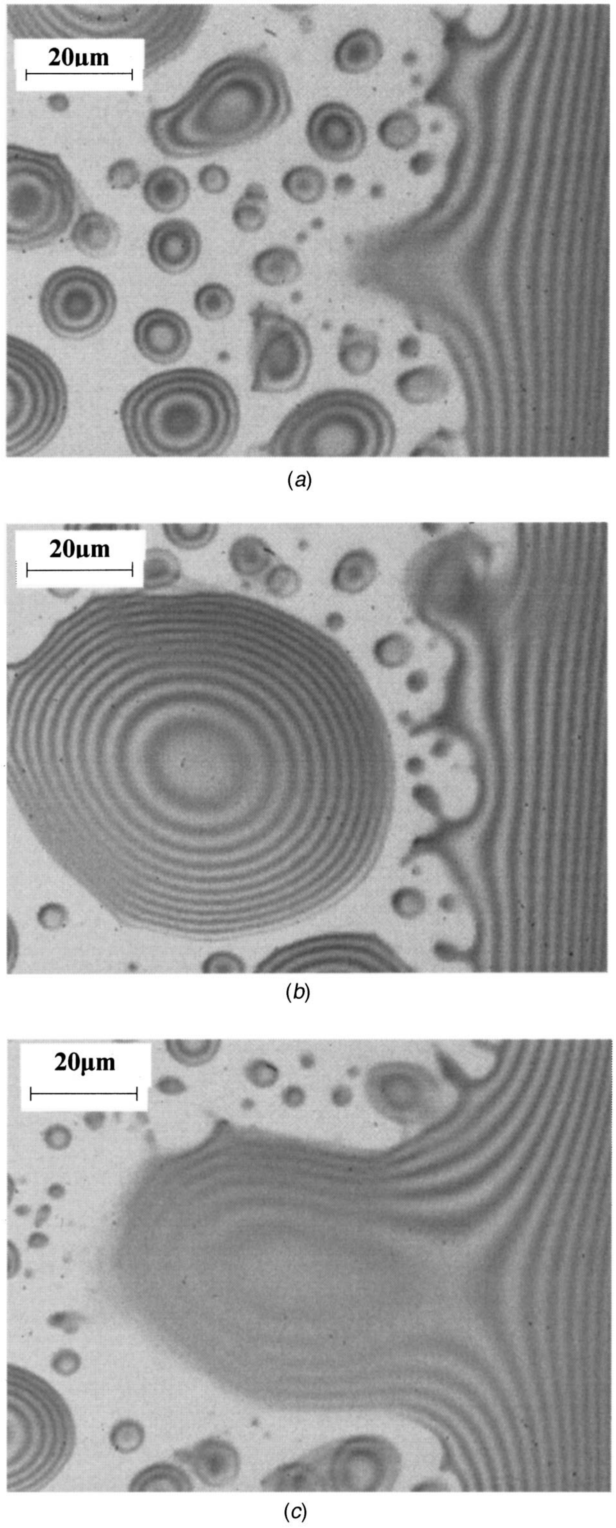

(*a*)

(*b*)

(*c*)

Fig. 14 (*a*) Dropwise condensation of ethanol at $x = 3$ mm ($t = 0$ sec); (*b*) Dropwise condensation of ethanol at $x = 3$ mm ($t = 0.27$ sec); and (*c*) Dropwise condensation of ethanol at $x = 3$ mm ($t = 0.33$ sec).

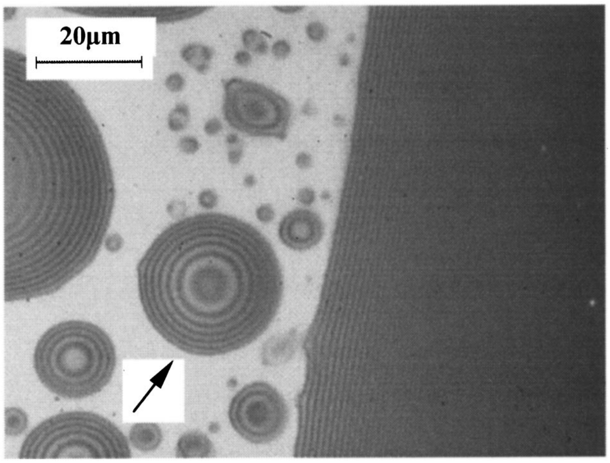

Fig. 15 Case I: Dropwise condensation at lower condensation rate ($x=3$ mm)

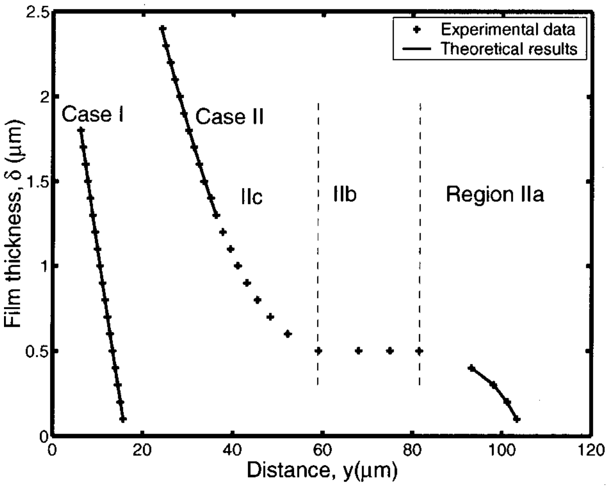

Fig. 17 Film thickness profiles in the corner

A comparison of the film thickness profiles in the corner is given in Fig. 17. The film thickness profile in the corner in Case I, which has an apparent contact angle of 9.6 deg (at 0.1 μm) and a curvature of $2.38\times10^{3}\ \mathrm{m}^{-1}$, is much steeper than the profile in Case II. For Case II, the meniscus bulges at the beginning, then flattens out, and then the film thickness increases gradually. We find that this change in sign in the curvature at the contact line is important to obtain the necessary additional driving force for the increased flow in Case II. At the convex front marked as Region IIa in Fig. 17, the curvature is $-3.68\times10^{3}\ \mathrm{m}^{-1}$. In Region IIb, the curvature is near zero. In Region IIc, the curvature of the thick film in the corner is $2.22\times10^{3}\ \mathrm{m}^{-1}$. As demonstrated by Zheng et al. [70], the evaluation of the uncertainties associated with the presented image processing procedure is a complex function of the pixel resolution of the optical system, the number of dark fringes which can be recorded to obtain the curvature (which is a function of the value of the curvature and optical magnification), the apparent contact angle, the wavelength of the light, and the refractive index of the liquid. In our optical system, the resolution was 0.1777 um/pixel. We calculated the uncertainties presented in Table 1 using the procedures presented in [70]. Note that the sign convention for the curvature is negative for the convex meniscus, positive for the concave meniscus. According to the simplified Young-Laplace equation for the thick film where the disjoining pressure can be neglected, the horizontal pressure difference in the meniscus can be obtained from the sum of the absolute values of curvatures of the convex front (Region IIa) and the thick film (Region IIc). Hence, the value of the horizontal pressure difference between the bulging film (Region IIa) and the meniscus (Region IIc) is 133 N/m^2, which is 2.7 times larger than that (50 N/m^2) between the spreading flat film (Region IIb) and the meniscus (Region IIc). The shape of the meniscus in Case II provides much more driving force for condensate removal than that in Case I. The meniscus absorbs the drop into the corner by this intermo

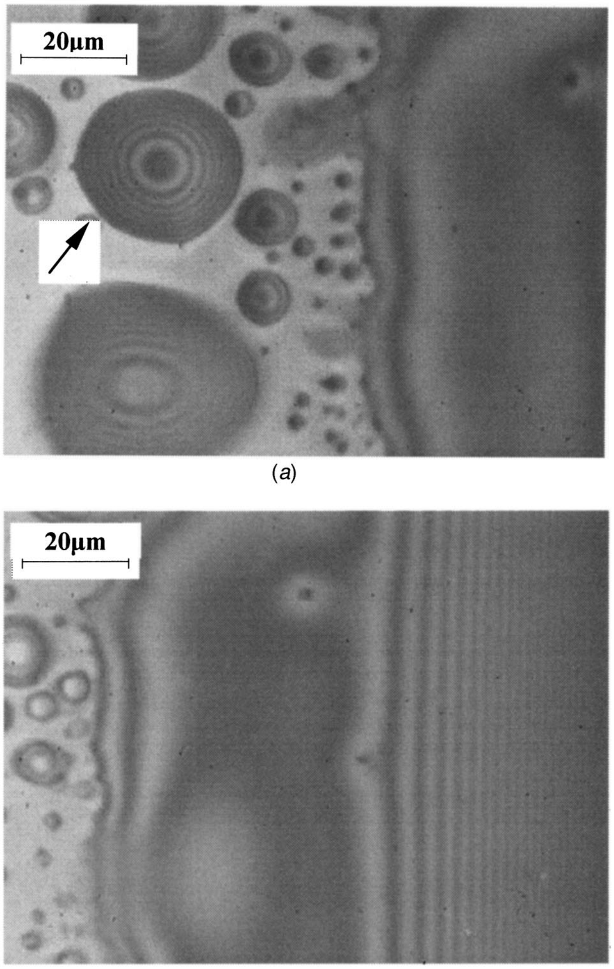

(*a*)

(*b*)

Fig. 16 (*a*) Case II: Dropwise condensation at higher condensation rate: an extension of the picture is given in Fig. 16(*b*) ($x=6$ mm); (*b*) Case II: Spreading liquid film in the corner which shows the extension of Fig. 16(*a*) ($x=6$ mm).

Table 1 Values of the different terms in the force balance (Eq. 3) evaluated at $\delta=0.1\ \mu$m

Case	I	II
d_s [m]	$2.83\text{x}10^{-5}$	$2.93\text{x}10^{-5}$
θ_d	9.6°	9.9°
θ_c	9.5°	2.5°
K_d [m^{-1}]	$-2.65\text{x}10^{4}\pm6.29\%$	$-2.41\text{x}10^{4}\pm5.60\%$
K_c [m^{-1}]	$2.38\text{x}10^{3}\pm8.59\%$	$3.68\text{x}10^{3}\pm2.18\%$
$(-\cos\theta_d+\cos\theta_c)$	$2.90\text{x}10^{-4}$	$1.39\text{x}10^{-2}$
$\delta(-K_d+K_c)$ [N/m]	$2.92\text{x}10^{-3}$	$2.04\text{x}10^{-3}$
$\dfrac{F}{d_s\sigma_l}$	$3.21\text{x}10^{-3}$	$1.59\text{x}10^{-2}$
$\dfrac{F}{\rho_l g V_d}$	$8.88\text{x}10^{2}$	$3.09\text{x}10^{3}$

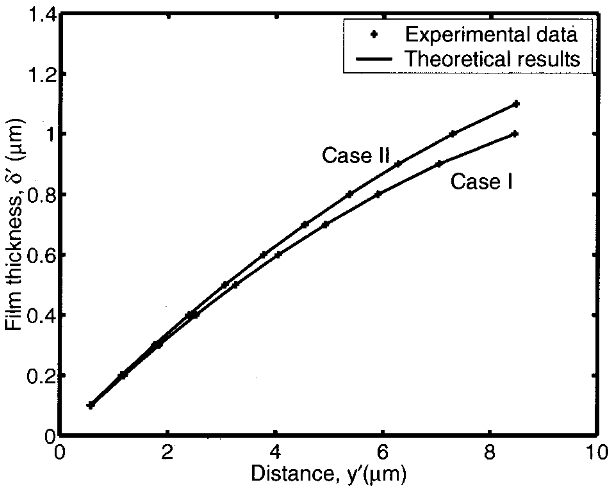

Fig. 18 Film thickness profiles at the mid-plane of the drops

lecular force gradient, then the condensate flows up to the region of evaporation by the vertical axial curvature gradient. The film profile is self-adjusting to obtain the necessary force. These initial discussions demonstrate that the details of the two-dimension pressure field can be obtained for future analyses.

For now, Eq. (3) is used to analyze the macroscopic removal force between the drop and the meniscus. Table 1 summarizes the values of the terms at $\delta=0.1$ μm and the driving force for these two cases. Although the curvature difference term between the drop and liquid meniscus in Case II becomes a little smaller compared to that in Case I due to the convex front of the meniscus in Region IIa, the contact angle difference term plays a dominant role in the change in the driving force. The dimensionless difference in free energy for the drop removal in Case II, $F/d_s\sigma_l$, is 1.59×10^{-2}, which is 5 times larger than that for Case I. A comparison of drop profiles is presented in Fig. 18, where we find that the contact angles and curvatures of the drops are slightly different. However, as discussed above, the contact angles of the meniscus in the corner are quite different. Consequently, the drop removal force in Case II is much larger than that in Case I because of the change in the corner profile.

For the drop close to the corner, we find that the effect of gravity on droplet movement towards the corner becomes insignificant. The ratio of the horizontal driving force between the drop and the meniscus to the vertical gravitational force on the drop ($F/\rho_l g V_d$) is 8.88×10^2 for Case I, and 3.09×10^3 for Case II. However, gravity does have a large effect on axial flow in the corner of the vertical system. The removal rate is obtained by dividing the mass of the drop by the time period for removal. The removal rate for Case II is 5.26×10^{-12} kg/s, which is 2.3 times larger than that (2.34×10^{-12} kg/s) for Case I. These results demonstrate that the evaluation of both the body and the interfacial pressure forces enhance the understanding of the mechanism for efficient removal of drops from a condenser surface. When the system is used in microgravity, the gravitational force becomes insignificant for all orientations. A physical understanding of the effects of the liquid-vapor interfacial pressure and temperature jumps on the local evaporation/condensation heat flux, q''_{lv}, can be obtained using the following equation which includes both the Kelvin and Clapeyron effects on the vapor pressure [3]:

$$q''_{lv}=m''h_{fg}=h^{id}_{lv}(T_{lv}-T_v)+h^{kl}_{lv}(P_l-P_v) \tag{12}$$

where

$$h^{id}_{lv}=\left(\frac{C^2M}{2\pi RT_{lv}}\right)^{0.5}\frac{MP_vh^2_{fg}}{RT_vT_{lv}},\quad h^{kl}_{lv}=\left(\frac{C^2M}{2\pi RT_{lv}}\right)^{0.5}\frac{V_{lM}P_vh_{fg}}{RT_{lv}}$$

According to Eq. (12) condensation is promoted by subcooling and hindered by high liquid film pressure.

The interfacial pressure difference is obtained using Eq. (1) with the thickness profile. The pressure level in the vapor, which is uniform because of minimum resistance to vapor flow, is measured using a pressure transducer. For our isothermal system at 24°C, the vapor pressure measurement was 60 mmHg which is the thermodynamic value of 56 mmHg plus an apparent error of 4 mmHg. The difference is believed due to non-condensibles which did not change. During heat transfer studies, the vapor pressure correlated with the temperature in the region of condensation. However, the interfacial temperature difference is too small to measure and must be obtained from modeling thermal conduction. This can be evaluated using two overall heat balances: (1) a mass balance based on the measured volume of the drops which gives the average heat flux ($q''_{lv}=-1.86\times10^3$ W/m^2 for Case I, $q''_{lv}=-3.28\times10^3$ W/m^2 for Case II); and (2) a numerical calculation of conduction in the glass which is to be done. Finally, a numerical example of the sensitivity of the magnitude of the interfacial temperature difference can be obtained using Eq. (12) with the measured pressure jump and heat flux: $(T_{lv}-T_v)=-1.09\times10^{-4}$ K for the drop in Figure 15, and -1.51×10^{-4} K for the drop in Fig. 16(*a*). Obviously, these temperature differences are too small to measure. However, they indicate that Marangoni flows were probably insignificant in the region analyzed. This conclusion was supported by the interference profiles in the region analyzed. We note that future studies under different conditions may alter this conclusion. Although they are both important, we find that the pressure field is much easier to measure than the temperature field in these heat transfer studies.

Conclusions

1 An improved image analyzing procedure, which can be used to obtain simultaneously the curvature and apparent contact angle of the meniscus in the corner of the cell, was proposed and verified. Using a coordinate transformation, it can also be applied to the convex liquid drop.

2 The apparent contact angles and curvatures of the meniscus in the corner and the sessile drop were a function of the heat flux.

3 The condensate removal rate was a function of changes in the contact angle and curvature which self-adjust to give the necessary force field.

4 The use of a dimensionless, shape dependent, macroscopic force balance to analyze condensate removal was demonstrated.

5 Near the corner, the intermolecular force was up to 3000 times larger than the gravitational force and dominated droplet removal.

6 Microscale pressure fields can be experimentally measured, whereas interfacial temperature differences cannot.

Acknowledgments

This material is based on work supported by the National Aeronautics and Space Administration under grants # NAG3-1834 and NAG3-2351. Any opinions, findings, and conclusions or recommendations expressed in this publication are those of the authors and do not necessarily reflect the view of NASA.

Nomenclature

C = accommodation constant
C_l = geometric coefficient
c = liquid-wall contact line length
d_s = width of the liquid drop
h_{fg} = latent heat of vaporization
K = curvature
L = length in Figure 5
M = molecular weight
m'' = interfacial mass flux

n = refractive index
P = pressure
R = gas constant
r = interfacial radius of curvature
V_{lM} = molar volume of the liquid
x = axial distance along the CVB axis
y = distance in the direction normal to CVB axis

Greek Characters

α = vertex angle of the quartz cell
δ = film thickness
θ = apparent contact angle
Π = disjoining pressure
σ = surface tension
τ = shear stress
ϕ = defined in Fig. 6

Subscripts

1,2 = arbitrary number of location index
c = liquid film in the corner
d = liquid drop on the flat surface
exp = experimental data
l = liquid
lv = liquid-vapor interface
s = solid
theo = theoretical results
v = vapor

Superscripts

$'$ = coordinate system for the liquid drop on the flat surface

References

[1] Derjaguin, B. V., Nerpin, S. V., and Churaev, N. V., 1965, ''Effect of Film Transfer upon Evaporation of Liquids from Capillaries,'' Bulletin Rilem, **29**, pp. 93–98.
[2] Potash, M., Jr., and Wayner, P. C., Jr., 1972, ''Evaporation From a Two-Dimensional Extended Meniscus,'' Int. J. Heat Mass Transf., **15**, pp. 1851–1863.
[3] Wayner, P. C., Jr., 1991, ''The Effect of Interfacial Mass Transport on Flow in Thin Liquid Films,'' Colloids Surf., A, **52**, pp. 71–84.
[4] Swanson, L. W., and Herdt, G. C., 1992, ''Model of the Evaporating Meniscus in a Capillary Tube,'' ASME J. Heat Transfer, **114**, pp. 434–441.
[5] Stephan, P., and Busse, C. A., 1992, ''Analysis of the Heat Transfer Coefficient of Grooved Heat Pipe Evaporator Walls,'' Int. J. Heat Mass Transf., **35**, pp. 383–391.
[6] Sharma, A., 1998, ''Equilibrium and Dynamics of Evaporating or Condensing Thin Fluid Domains: Thin Film Stability and Heterogeneous Nucleation,'' Langmuir, **14**, pp. 4915–4928.
[7] Wilson, S. K., Davis, S. H., and Bankoff, S. G., 1999, ''The Unsteady Expansion and Contraction of a Long Two-Dimensional Vapor Bubble Between Superheated or Subcooled Parallel Plates,'' J. Fluid Mech., **391**, pp. 1–27.
[8] Wayner, P. C., Jr., Tung, C. Y., Tirumala, M., and Yang, J. H., 1985, ''Experimental Study of Evaporation in the Contact Line Region of a Thin Film of Hexane,'' ASME J. Heat Transfer, **107**, pp. 182–189.
[9] Kamotani, Y., 1978, ''Evaporator Film Coefficients of Grooved Heat Pipes,'' *Proceedings of 3rd International Heat Pipe Conference*, American Institute of Aeronautics and Astronautics, pp. 128–130.
[10] Holm, F. W., and Goplen, S. P., 1979, ''Heat Transfer in the Meniscus Thin Film Region,'' ASME J. Heat Transfer, **101**, pp. 543–547.
[11] Moosman, S., and Homsy, S. M., 1980, ''Evaporating Menisci of Wetting Fluids,'' J. Colloid Interface Sci., **73**, pp. 212–223.
[12] Mirzamoghadam, A. V., and Catton, I., 1988, ''A Physical Model of the Evaporating Meniscus,'' ASME J. Heat Transfer, **110**, pp. 201–207.
[13] Xu, X., and Carey, V. P., 1990, ''Film Evaporation From a Micro-Grooved Surface-An Approximate Heat Transfer Model and Its Comparison with Experimental Data,'' Journal of Thermophysics and Heat Trans., **4**, pp. 512–520.
[14] Stephan, P., and Busse, C. A., 1992, ''Analysis of the Heat Transfer Coefficient of Grooved Heat Pipe Evaporator Walls,'' Int. J. Heat Mass Transf., **35**, pp. 383–391.
[15] Swanson, L. W., and Herdt, G. C., 1992, ''Model of the Evaporating Meniscus in a Capillary Tube,'' ASME J. Heat Transfer, **114**, pp. 434–441.
[16] Hallinan, K. P., Chebaro, H. C., Kim, S. J., and Chang, W. S., 1994, ''Evaporation from an Extended Meniscus for Nonisothermal Interfacial Conditions,'' J. Thermophys. Heat Transfer, **8**, pp. 709–716.
[17] Swanson, L. W., and Peterson, G. P., 1994, ''Evaporating Extended Meniscus in a V-Shaped Channel,'' J. Thermophys. Heat Transfer, **8**, pp. 172–180.
[18] Swanson, L. W., and Peterson, G. P., 1995, ''The Interfacial Thermodynamics of Micro Heat Pipes,'' ASME J. Heat Transfer, **115**, pp. 195–201.
[19] Khrustalev, D., and Faghri, A., 1995, ''Thermal Characteristics of Conventional and Flat Miniature Axially-Grooved Heat Pipes,'' ASME J. Heat Transfer, **117**, pp. 1048–1054.
[20] Peterson, G. P., and Ha, J. M., 1998, ''Capillary Performance of Evaporating Flow in Micro Grooves: An Approximate Analytical Approach and Experimental Investigation,'' ASME J. Heat Transfer, **120**, pp. 743–751.
[21] Wang, Y-X., Plawsky, J., and Wayner, P. C., Jr., 2000, ''Heat and Mass Transfer in a Vertical Constrained Vapor Bubble Heat Exchanger using Ethanol,'' *34th National Heat Transfer Conference*, Pittsburgh, PA, Paper NHTC2000-12201.
[22] Hautman, J., and Klein, M. L., 1991, ''Microscopic Wetting Phenomena,'' Phys. Rev. Lett., **67**, pp. 1763–1766.
[23] Sharma, A., 1993, ''Equilibrium Contact Angles and Film Thicknesses in the Apolar and Polar Systems: Role of Intermolecular Interactions in Coexistence of Drops with Thin Films,'' Langmuir, **9**, pp. 3580–3586.
[24] Derjaguin, B. V., 1955, ''Definition of the Concept and Determination of the Disjoining Pressure,'' Colloid J. USSR, **17**, pp. 191–197.
[25] Renk, F., Wayner, P. C., Jr., and Homsy, G. M., 1978, ''On the Transition Between a Wetting Film and a Capillary Meniscus,'' J. Colloid Interface Sci., **67**, pp. 408–414.
[26] Wayner, P. C., Jr., 1980, ''Interfacial Profile in the Contact Line Region of a Finite Contact Angle System,'' J. Colloid Interface Sci., **77**, pp. 495–500.
[27] White, L. R., 1977, ''On Deviation from Young's Equation,'' J. Chem. Soc., Faraday Trans. 1, **73**, pp. 390–398.
[28] Zasadzinski, J. A. N., Sweeney, J. B., Davis, H. T., and Scriven, L. E., 1987, ''Finite Element Calculations of Fluid Menisci and Thin-Films in a Model Poroud Media,'' J. Colloid Interface Sci., **119**, pp. 108–116.
[29] Philip, J. R., 1977, ''Unitary Approach to Capillary Condensation and Adsorption,'' J. Chem. Phys., **66**, pp. 5069–5075.
[30] de Gennes, P. G., 1985, ''Wetting: Statics and Dynamics,'' Rev. Mod. Phys., **57**, pp. 827–863.
[31] Wong, H., Morris, S., and Radke, C. J., 1992, ''Three-Dimensional Menisci in Polygonal Capillaries,'' J. Colloid Interface Sci., **148**, pp. 317–336.
[32] Wayner, P. C., Jr., 1993, ''Spreading of a Liquid Film with a Finite Contact Angle by the Evaporation/Condensation Process,'' Langmuir, **9**, pp. 294–299.
[33] Martynov, G. A., Starov, V. M., and Churaev, N. V., 1977, ''Hysteresis of the Contact Angle at Homogeneous Surfaces,'' Colloid J. USSR, **39**, pp. 406–417.
[34] Brochard, F., 1989, ''Motions of Droplets on Solid Surfaces Induced by Chemical or Thermal Gradients,'' Langmuir, **5**, pp. 432–438.
[35] Schneemilch, M., Hayes, R. A., Petrov, J. G., and Ralston, J., 1998, ''Dynamic Wetting and Dewetting of a Low-Energy Surface by Pure Liquids,'' Langmuir, **14**, pp. 7047–7051.
[36] Petrov, P. G., and Petrov, J. G., 1992, ''Combined Molecular-Hydrodynamic Approach to Wetting Kinetics,'' Langmuir, **8**, pp. 1762–1767.
[37] Cherry, B. W., and Holmes, C. M., 1969, ''Kinetics of Wetting of Surfaces by Polymers,'' J. Colloid Interface Sci., **29**, pp. 174–176.
[38] Miller, C. A., and Ruckenstein, E., 1974, ''The Origin of Flow During Wetting of solids,'' J. Colloid Interface Sci., **48**, pp. 368–373.
[39] Lopez, J., Miller, C. A., and Ruckenstein, E., 1976, ''Spreading Kinetics of Liquid Drops on Solids,'' J. Colloid Interface Sci., **56**, pp. 460–468.
[40] Ruckenstein, E., and Dunn, C. S., 1977, ''Slip Velocity during Wetting of Solids,'' J. Colloid Interface Sci., **59**, pp. 135–138.
[41] Huh, C., and Scriven, L. E., 1969, ''Shapes of Axisymmetric Fluid Interfaces of Unbounded Extent,'' J. Colloid Interface Sci., **30**, pp. 323–337.
[42] Petrov, P. G., and Petrov, J. G., 1995, ''Extrapolated Dynamic Contact Angle and Viscous Deformation of a Steady Moving Meniscus at a Vertical Flat Wall,'' Langmuir, **11**, pp. 3261–3268.
[43] Dussan, E. B., Rame, E., and Garoff, S., 1991, ''On Identifying the Appropriate Boundary Conditions at a Moving Contact Line. An Experimental Investigation,'' J. Fluid Mech., **230**, pp. 97–116.
[44] Sharma, A., and Jameel, A. T., 1993, ''Nonlinear Stability, Rupture, and Morphological Phase Separation of Thin Fluid Films on Apolar and Polar Substrates,'' J. Colloid Interface Sci., **161**, pp. 190–208.
[45] Schmidt, E., Schurig, W., and Sellschop, W., 1930, ''Versuche uber die Kondensation von Wasserdampf in Film- und Tropfenform,'' Tech. Mech. Thermodyn., **1**, pp. 53–63.
[46] Jakob, M., 1936, ''Heat Transfer in Evaporation and Condensation—II,'' Mech. Eng. (Am. Soc. Mech. Eng.), **58**, pp. 729–739.
[47] Welch, J. F., and Westwater, J. W., 1961, ''Microscopic Study of Dropwise Condensation,'' *Proceedings of International Heat Transfer Conference*, ASME, Part II, pp. 302–309.
[48] McCormick, J. L., and Baer, E., 1963, ''On the Mechanism of Heat Transfer in Dropwise Condensation,'' J. Colloid Sci., **18**, pp. 208–216.
[49] Umur, A., and Griffith, P., 1965, ''Mechanism of Dropwise Condensation,'' ASME J. Heat Transfer, **87**, pp. 275–282.
[50] Haraguchi, T., Shimada, R., and Takeyama, T., 1990, ''Observation of the Initial Drop Formation Mechanism in Dropwise Condensation Using a Microscope (Film Growth Hypothesis as Suggested by Three Experiments),'' Trans. JSME, **56**, pp. 2697–2703.
[51] Merte, H., Jr., and Yamali, C., 1983, ''Profile and Departure size of Condensation Drops on Vertical Surfaces,'' Waerme- Stoffuebertrag., **17**, pp. 171–180.
[52] Tanasawa, I., Ochiai, J., Utaka, Y., and Enya, S., 1976, ''Experimental Study on Dropwise Condensation (Effect of Departing Drop Size on Heat-transfer Coefficients),'' Trans. JSME, **42**, pp. 2846–2852.
[53] Yamali, C., and Merte, H., Jr., 1999, ''Influence of Sweeping on Dropwise Condensation with Varying Body Force and Surface Subcooling,'' Int. J. Heat Mass Transf., **42**, pp. 2943–2953.

[54] Wang, Y-X., Plawsky, J., and Wayner, P. C., Jr., 2000, ''Optical Measurement of Microscale Transport Processes in Dropwise Condensation,'' Microscale Thermophys. Eng., **5**, pp. 55–69.

[55] Sharp, R. R., 1964, ''The Nature of Liquid Film Evaporation During Nucleate Boiling,'' *NASA-TND1997*.

[56] Jawurek, H. H., 1969, ''Simultaneous Determination of Microlayer Geometry and Bubble Growth in Nucleate Boiling,'' Int. J. Heat Mass Transf., **12**, pp. 843–848.

[57] Voutsinos, C. M., and Judd, R. L., 1975, ''Laser Interferometric Investigation of the Microlayer Evaporation Phenomena,'' ASME J. Heat Transfer, **97**, pp. 88–93.

[58] Renk, F. J., and Wayner, P. C., Jr., 1979, ''An Evaporating Ethanol Meniscus, Part I: Experimental Studies,'' ASME J. Heat Transfer, **101**, pp. 55–58.

[59] Renk, F. J., and Wayner, P. C., Jr., 1979, ''An Evaporating Ethanol Meniscus, Part II: Analytical Studies,'' ASME J. Heat Transfer, **101**, pp. 59–62.

[60] Huang, J., Karthikeyan, M., Plawsky, J., and Wayner, P. C., Jr., 1998, ''Experimental Study and Modeling of the Effect of Low-Level Impurities on the Operation of the Constrained Vapor Bubble,'' *Space Technology and Applications International Forum (2nd Conference on Applications of Thermophysics in Microgravity) Part I, American Institute of Physics Conference Proceedings 420*, Woodbury, NY, pp. 446–451.

[61] Chen, J. D., and Wada, N., 1992, ''Edge Profiles and Dynamic Contact Angles of a Spreading Drop,'' J. Colloid Interface Sci., **148**, pp. 207–222.

[62] Kihm, K. D., and Pratt, D. M., 1999, ''Contour Mapping of Thin Liquid Film Thickness Using Fizeau Interferometer,'' *Proceedings of the 33rd National Heat Transfer Conference*, Albuquerque, NM, Paper NHTC99-224.

[63] Kataoka, D. E., and Troian, S. M., 1999, ''Patterning Liquid Flow on the Microscopic Scale,'' Nature (London), **402**, pp. 794–797.

[64] Cazabat, A. M., Heslot, F., Troian, S. M., and Charles, P., 1990, ''Fingering Instability of Thin Spreading Films Driven by Temperature Gradients,'' Nature (London), **346**, pp. 824–826.

[65] Silvi, N., and Dussan, E. B., 1985, ''On the Rewetting of an Inclined Solid Surface by a Liquid,'' Phys. Fluids, **28**, pp. 5–7.

[66] Jerrett, J. M., and deBruyn, J. R., 1992, ''Fingering Instability of a Gravitationally Driven Contact Line,'' Phys. Fluids A, **4**, pp. 234–242.

[67] Williams, R., 1977, ''The Advancing Front of a Spreading Liquid,'' Nature (London), **266**, pp. 153–154.

[68] DasGupta, S., Plawsky, J. L., and Wayner, P. C., Jr., 1995, ''Interfacial Force Field Characterization in a Constrained Vapor Bubble Thermosyphon,'' AIChE J., **41**, pp. 2140–2149.

[69] Karthikeyan, M., Huang, J., Plawsky, J. L., and Wayner, P. C., Jr., 1998, ''Experimental Study and Modeling of the Intermediate Section of the Nonisothermal Constrained Vapor Bubble,'' ASME J. Heat Transfer, **120**, pp. 166–173.

[70] Zheng, L., Wang, Y.-X., Plawsky, J. L., and Wayner, P. C., Jr., 2002, ''Accuracy of Measurements of Curvature and Apparent Contact Angle in a Constrained Vapor Bubble Heat Exchanger,'' Int. J. Heat Mass Transf., **45**, pp. 2021–2030.

Forced Convective Heat Transfer in Metallic Fibrous Materials

Devarakonda Angirasa
Member ASME
Thermacore International Inc.,
780 Eden Road,
Lancaster, PA 17601, U.S.A.

A numerical study is reported for high Reynolds number forced convection in a channel filled with rigid metallic fibrous materials of high porosity. The effects of convective and form inertia, viscous shear, and thermal dispersion are all considered together. Inertia and thermal dispersion are modeled. The numerical results suggest that heat transfer rate increases with increasing Reynolds number within a range, but not significantly beyond that range. The heat transfer rate also increases with stagnant thermal conductivity, and decreases with Darcy number. The fiber thickness was found to have significant influence on thermal dispersion. The range of applicability of the local volume averaging in terms of the significant parameters is discussed. [DOI: 10.1115/1.1470491]

Keywords: Channel Flow, Dispersion, Forced Convection, Modeling, Porous Media

Introduction

Forced convection through rigid metallic fibrous materials can be used for substantial enhancement of heat transfer rates while still maintaining surface temperatures at a reasonably low value. Given these characteristics, fibrous metallic blocks are well suited for use as high-performance heat spreaders or dissipaters in industrial applications. Various metallic fibrous blocks are commercially available, which are inexpensive and can be manufactured to the desired porosity and permeability. In the current investigation, a numerical model is developed to predict the forced convection heat transfer rates using such a porous medium. The resulting model can be used to aid in the design and optimization of the metallic fibrous heat dissipaters.

Convective heat transfer in a fibrous medium involves the formation of complex flow and temperature fields around individual fibers. As pointed out by Beavers and Sparrow [1], flow separation may occur around the fibers at higher velocities. While this leads to a larger pressure-drop, the associated mixing substantially enhances the heat transfer rate. In addition, when the fluid-saturated fibrous material has a larger effective thermal conductivity than the fluid alone, the heat dissipation from the bounding surface is enhanced, helping to keep the surface temperature within acceptable limits.

Nield and Bejan [2] and Kaviany [3] presented a modern account of convective heat transfer in porous media. A majority of the previous investigations of convection in porous media have been based on the Darcy flow model, which does not consider convective inertia, form drag and viscous shearing effects. These factors are important, particularly in high Reynolds number flows. Since the fluid flows through a complex tortuous path through the fibrous medium, it is not possible to model the flow in full detail. However, the effects of the fibrous matrix, the local recirculation around the individual fibers, and the thermal dispersion can be incorporated into the conservation equations through a volume-averaging process. While this averaging procedure provides a mechanism by which the desired conservation equations can be made applicable to the bulk flow and heat transfer in fibrous media, it clouds the local effects of recirculation and dispersion, leaving two quantities to be determined empirically: the form coefficient, C_F, and the dispersion conductivity, k_d. As a result, these two parameters must be obtained either through experimentation or additional modeling. For a history of the theoretical developments of flow through porous media, see Lage [4].

Following the earlier work of Whitaker [5] and Slattery [6], Vafai and Tien [7,8] investigated the effects of the quadratic form drag term and the solid boundary on flow, heat and mass transfer in a porous medium. They utilized the local volume averaging technique to develop the conservation equations. Vafai [9] and Vafai et al. [10] theoretically and experimentally studied the influence of variable porosity on the transport phenomena. Kaviany [11] studied heat transfer in a channel for fully-developed flow situation by neglecting the quadratic drag term and axial conduction. A boundary layer type of flow and heat transfer along a flat plate embedded in a porous medium was studied by Beckermann and Viskanta [12] by neglecting the form drag. Vafai and Kim [13] obtained an exact solution for forced convection in a channel by considering fully-developed flow. Nield et al. [14] studied forced convection in a fluid-saturated porous medium channel with isothermal and isoflux boundaries, while Nield et al. [15] considered the effect of the temperature-dependent viscosity.

Beavers and Sparrow [1] conducted a series of experiments to determine the friction coefficients for a family of metallic fibrous materials saturated with water. The form coefficient, C_F, and the permeability, K, were obtained in terms of the flow rates and the pressure-drop. Koch and Brady [16] obtained expressions for the effective diffusivity of fibrous media in terms of the permeability and velocity, using an ensemble averaging technique.

In the current investigation, two-dimensional forced flow through a channel filled with metallic fibrous media, as shown in Fig. 1, is considered. The rigid fibrous medium has high uniform porosity and isotropic properties. One of the channel walls is heated, while the other is assumed to be adiabatic. Detailed flow and thermal fields are numerically modeled with the consideration of convective and form drag, viscous shearing effects, and thermal dispersion. The form drag and dispersion effects are modeled from the experimental data of Beavers and Sparrow [1] and the theory of Koch and Brady [16], respectively. Heat transfer coefficients are presented in terms of Reynolds number, Re, and Darcy number, Da.

Analysis

For low porosity and steady flow rates of incompressible fluids, the empirical Darcy formula is expressed as [17]

$$\frac{\Delta p}{\Delta x} = \frac{\mu}{K} u \tag{1}$$

where u is the average velocity in the flow direction, x. This equation is valid strictly for very low velocity flows. Reynolds [18] first suggested the quadratic drag form

---

Contributed by the Heat Transfer Division for publication in the JOURNAL OF HEAT TRANSFER. Manuscript received by the Heat Transfer Division February 23, 2001: revision received January 25, 2002. Associated Editor: J. G. Georgiadis.

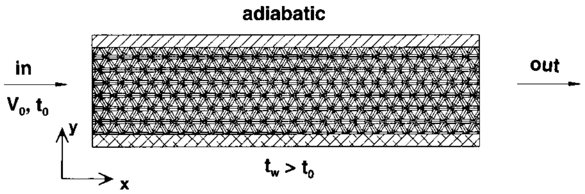

Fig. 1 Physical configuration

$$\frac{\Delta p}{\Delta x} = Au + Bu^2 \tag{2}$$

where A and B are dimensional constants. This came to be known as the Forchheimer law [17].

Equation (2) was used by Green and Duwez [19] to correlate experimental data for friction factor in terms of Reynolds number. Ward [20] obtained the following expression

$$\frac{dp}{dx} = \frac{\mu u}{K} + \frac{c\rho u^2}{\sqrt{K}} \tag{3}$$

in which c is a dimensionless constant. Ward [20] mistakenly thought that the value of c was a universal constant. However, the experimental data of Brownell et al. [21], Green and Duwez [19], and Beavers and Sparrow [1] do not support this.

To account for the viscous shearing effect, Brinkman [22] proposed a modified Darcy law of the form

$$\nabla p = -\frac{\mu}{K}\mathbf{v} + \mu'\nabla^2\mathbf{v} \tag{4}$$

where μ' is the effective viscosity of the medium. It is common practice to assume it to be the fluid viscosity, μ. This model is expected to be valid at very high values of porosity.

The volume averaged conservation equations which resemble the Navier-Stokes and energy equations have been derived by Slattery [23] and Vafai and Tien [7]. This formulation is employed in the present analysis. Consider a two-dimensional channel of length L and height H, filled with fibrous material and fully saturated with a fluid (Fig. 1). The temperature of one of the walls is assumed to be t_w and the other wall is adiabatic. The fluid flows through the inlet of the channel with a constant and uniform velocity, V_0 and temperature, t_0. The flow in the channel can be described using the following volume-averaged conservation equations of mass and momentum

$$\nabla\cdot\langle\mathbf{v}\rangle = 0 \tag{5}$$

$$\frac{\rho_f}{\varphi^2}\left(\varphi\frac{\partial\langle\mathbf{v}\rangle}{\partial\tau} + (\langle\mathbf{v}\rangle\cdot\nabla)\langle\mathbf{v}\rangle\right) = -\nabla\langle p\rangle - \frac{\mu_f}{K}\langle\mathbf{v}\rangle - \rho_f\frac{C_F}{\sqrt{K}}|\langle\mathbf{v}\rangle|\langle\mathbf{v}\rangle + \mu_f\nabla^2\langle\mathbf{v}\rangle \tag{6}$$

respectively. In the above formulation, $\langle\,\rangle$ represents the aforementioned volume-averaged quantities. The momentum equation, Eq. 6, can be split into the three component equations for the coordinate system of choice. For the current investigation, a Cartesian coordinate system will be utilized.

The convective inertia term on the left-hand side of Eq. 6 is important when the flow is developing, i.e., at the entrance of the channel and for flow through a high porosity medium such as the one considered here. The first two terms on the right-hand side, when isolated, form the well-known Darcy formula for fluid flow in porous media. The third term accounts for the local acceleration and separation around individual fibers, which occurs in high Reynold number flows [1]. The quantity $|\langle\mathbf{v}\rangle|$, for a two-dimensional flow, is given by

$$|\langle\mathbf{v}\rangle| = \sqrt{\langle u\rangle^2 + \langle v\rangle^2} \tag{7}$$

The last term in Eq. 6 accounts for the viscous shear, and it provides means to improve the no-slip wall condition.

For an isotropic fibrous medium, φ, C_F, and K are independent of direction and are constants for a given medium and fluid. For this case, assuming thermal equilibrium between the two phases, the volume-averaged homogeneous energy equation can be expressed as

$$(\rho C_P)_f\left(\sigma\frac{\partial\langle t\rangle}{\partial\tau} + \langle\mathbf{v}\rangle\cdot\nabla\langle t\rangle\right) = \nabla\cdot(k_o\nabla\langle t\rangle + k_d\nabla\langle t\rangle) \tag{8}$$

where, σ is the ratio of heat capacities of the stagnant medium and the fluid and k_o is the stagnant thermal conductivity of the saturated fibrous medium. The stagnant conductivity can be either measured experimentally or estimated from the porosity and the thermal conductivities of the solid and the fluid.

Nondimensional Parameters and Equations. The nondimensional variables are defined in nomenclature. The space coordinates are scaled with the length of the channel, L, and the velocities with the uniform inlet velocity, V_0. For convenience, the brackets, $\langle\,\rangle$ are dropped in the subsequent formulation as it is understood here that these are volume-averaged quantities.

The length of the channel, L, rather than its height, H, is chosen as the length scale, since the height of the heat dissipater may be determined. Hence, the nondimensional channel height, H/L, is left as a parameter in the analysis. This aspect ratio determines the height of the domain of computation in the Y-direction, and can be independently prescribed in the calculations. With the use of these nondimensional variables, the continuity and momentum equations for a two-dimensional flow can be transformed to

$$\frac{\partial U}{\partial X} + \frac{\partial V}{\partial Y} = 0 \tag{9}$$

$$\varphi\frac{\partial U}{\partial\tau^*} + U\frac{\partial U}{\partial X} + V\frac{\partial U}{\partial Y} = -\varphi\frac{\partial P}{\partial X} - \frac{\varphi^2}{\mathrm{Re\,Da}}U - \frac{C_F\varphi^2}{\sqrt{\mathrm{Da}}}U_M U + \frac{\varphi}{\mathrm{Re}}\left(\frac{\partial^2 U}{\partial X^2} + \frac{\partial^2 U}{\partial Y^2}\right) \tag{10}$$

$$\varphi\frac{\partial V}{\partial\tau^*} + U\frac{\partial V}{\partial X} + V\frac{\partial V}{\partial Y} = -\varphi\frac{\partial P}{\partial Y} - \frac{\varphi^2}{\mathrm{Re\,Da}}V - \frac{C_F\varphi^2}{\sqrt{\mathrm{Da}}}U_M V + \frac{\varphi}{\mathrm{Re}}\left(\frac{\partial^2 V}{\partial X^2} + \frac{\partial^2 V}{\partial Y^2}\right) \tag{11}$$

The nondimensional parameters appearing in the momentum equations are the Reynolds number, Re, and the Darcy number, Da, which are defined in the nomenclature.

The magnitude of the volume-averaged dimensionless velocity, U_M, is given by

$$U_M = \sqrt{\frac{u^2 + v^2}{V_0^2}} \tag{12}$$

The two momentum equations, Eqs. (10) and (11) may be combined into one vorticity-transport equation as [24]

$$\varphi\frac{\partial\omega}{\partial\tau^*} + U\frac{\partial\omega}{\partial X} + V\frac{\partial\omega}{\partial Y} = -\frac{\varphi^2}{\mathrm{Re\,Da}}\omega - \frac{C_F\varphi^2 U_M}{\sqrt{\mathrm{Da}}}\omega - \frac{C_F\varphi^2}{\sqrt{\mathrm{Da}}}\left(U\frac{\partial U_M}{\partial Y} - V\frac{\partial U_M}{\partial X}\right) + \frac{\varphi}{\mathrm{Re}}\left(\frac{\partial^2\omega}{\partial X^2} + \frac{\partial^2\omega}{\partial Y^2}\right) \tag{13}$$

where the vorticity, ω, is given by

$$\omega=\frac{\partial U}{\partial Y}-\frac{\partial V}{\partial X} \tag{14}$$

Here, a nondimensional stream function, ψ, can be defined, such that

$$U=\frac{\partial \psi}{\partial Y} \quad \text{and} \quad V=-\frac{\partial \psi}{\partial X} \tag{15}$$

From Eqs. (14) and (15), it follows that

$$\omega=\frac{\partial^2 \psi}{\partial X^2}+\frac{\partial^2 \psi}{\partial Y^2} \tag{16}$$

The vorticity-transport equation, Eq. (13), implicitly satisfies the mass conservation equation, Eq. (9). Equations (13) and (16) can be solved for the two variables, ω and ψ, with φ, Re and Da as parameters, provided C_F is known.

The energy equation, Eq. (8), is converted to nondimensional form with a dimensionless temperature as defined in nomenclature. The dispersion conductivity, k_d, requires empirical determination. Using the ensemble averaging analysis of Koch and Brady [16], k_d may be expressed as

$$(k_d)_x=\frac{\rho C_p \lambda_x \sqrt{K}|\mathbf{v}|}{\ln\left(\dfrac{1}{1-\varphi}\right)} \quad \text{and} \quad (k_d)_y=\frac{\rho C_p \lambda_y \sqrt{K}|\mathbf{v}|}{\ln\left(\dfrac{1}{1-\varphi}\right)} \tag{17}$$

where λ_x and λ_y are constants. With these transformations the nondimensional energy equation in two-dimensional form can be written as

$$\sigma\frac{\partial T}{\partial \tau^*}+U\frac{\partial T}{\partial X}+V\frac{\partial T}{\partial Y}=\left(\frac{k_o}{k_f}\frac{1}{\text{Re Pr}}\right)\left(\frac{\partial^2 T}{\partial X^2}+\frac{\partial^2 T}{\partial Y^2}\right)+\frac{\lambda_x\sqrt{\text{Da}}}{\ln\left(\dfrac{1}{1-\varphi}\right)}\frac{\partial}{\partial X}\left(U_M\frac{\partial T}{\partial X}\right)+\frac{\lambda_y\sqrt{\text{Da}}}{\ln\left(\dfrac{1}{1-\varphi}\right)}\frac{\partial}{\partial Y}\left(U_M\frac{\partial T}{\partial Y}\right) \tag{18}$$

where σ is the ratio of heat capacities of the stagnant medium and the fluid, k_o/k_f is the ratio of thermal conductivities of the stagnant medium and the fluid, and Pr is the Prandtl number of the fluid. For the main flow aligned with the x-direction, the values of λ have been obtained by Koch and Brady [16] as

$$\lambda_x=\frac{57\pi^3}{160}, \quad \text{and} \quad \lambda_y=\frac{3\pi^3}{320} \tag{19}$$

The implication of Eqs. (17–19) is that even when the temperature gradients in the flow direction are small, the diffusion terms in the streamwise direction still must be retained in the energy equation to account for dispersion, since λ_x has a value substantially larger than λ_y.

The dispersion conductivity given by Eq. (17) was derived for bulk flow in the x-direction with an average velocity of $|\mathbf{v}|$. In the near wall region, dispersion is expected to be insignificant and the molecular diffusion comparatively larger. Since the dispersion conductivity directly depends on the magnitude of the local velocity, and is brought to zero adjacent to the wall, when the Laplacian term in the momentum equation is retained, with the no-slip boundary condition, Eq. (17) is then physically meaningful.

Two additional constraints for the validity of Eq. (17) for dispersion conductivity are given as follows

$$1\ll|\text{Pe}_l| \quad \text{and} \quad \sqrt{\frac{\ln(\varepsilon^{-1})}{\varepsilon}}\ll|\text{Pe}_a| \tag{20}$$

where

$$\text{Pe}_l=\text{Re Pr}\sqrt{\text{Da}} \quad \text{and} \quad \text{Pe}_a=\text{Re Pr}\sqrt{\text{Da}}\left(\frac{a}{\sqrt{K}}\right) \tag{21}$$

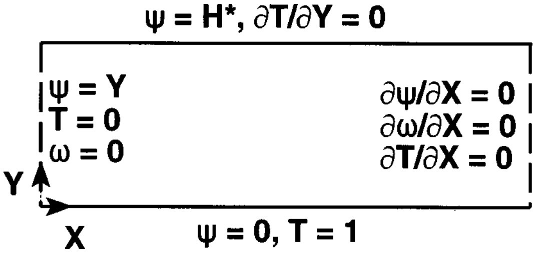

Fig. 2 Numerical boundary conditions

The fiber radius, a, may be estimated from the following expression [16,25]

$$K^{-1}\approx\frac{20}{3a^2}\frac{\varepsilon}{\ln\varepsilon^{-1}} \tag{22}$$

The average Nusselt number is defined as

$$\text{Nu}=\frac{\bar{h}L}{k_o}=\int(-\partial T/\partial Y)|_{Y=0}dX \tag{23}$$

Since the nondimensional parameters, Re, Da, and Nu, are dependent on channel length by definition, they can easily be converted to other definitions. For instance, a Nusselt number based on channel height, H, may be obtained by multiplying Nu in Eq. (23) with H/L.

The stagnant thermal conductivity of the saturated fibrous medium, k_0, is higher than the thermal conductivity of the fluid. Hence, care must be exercised in the interpretation of the Nusselt number defined by Eq. (23) when compared to the Nusselt number with the viscous flow of the fluid alone (i.e., without the fibrous medium in place). For such a comparison, the Nusselt number in Eq. 23 may be multiplied by the conductivity ratio, k_0/k_f.

Numerical Procedure

The convective terms in Eqs. (13) and (18) were discretized with upwind differencing due to stability considerations [24]. The diffusion terms were discretized with a central difference formulation. The vorticity transport equation, Eq. (13), was solved by the alternating direction implicit (ADI) scheme as described by Roache [24]. Solution for the stream function equation, Eq. (16), was obtained by the successive over relaxation (SOR) method. The stream function equation was iterated at each time-step of the solution of the vorticity transport equation. Both absolute and relative error criteria were used to check for the steady-state solution. The same type of criteria were used for the convergence test of the stream function equation. Uniform grid spacings were employed. The energy equation utilized the flow field solution. The ADI method mentioned above was used again for the numerical solution of the energy equation, Eq. (18).

The numerical boundary conditions are shown in Fig. 2. At the inlet of the channel, a constant velocity was prescribed. At the outlet of the channel the flow was assumed to be fully developed, and the convective heat transfer term was dominant. Wall vorticities were evaluated using a first order formula [26]. The initial conditions were

$$\tau^*=0, \quad \omega=0, \quad T=0, \quad U=0, \quad \text{and}$$
$$V=0 \text{ for all } X \text{ and } Y \tag{24}$$

The numerical solutions were tested for grid-dependence. In the results to follow 61×151 grid points were utilized for the numerical computations. This gave an error estimate of less than one percent for the field variables when compared to those obtained on

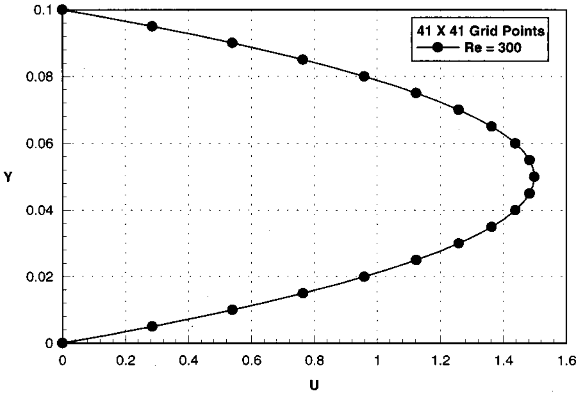

Fig. 3 Velocity profile for fully-developed viscous flow in a channel: $X=1$, $H^*=0.1$, $\varphi=1$, and $C_F=0$

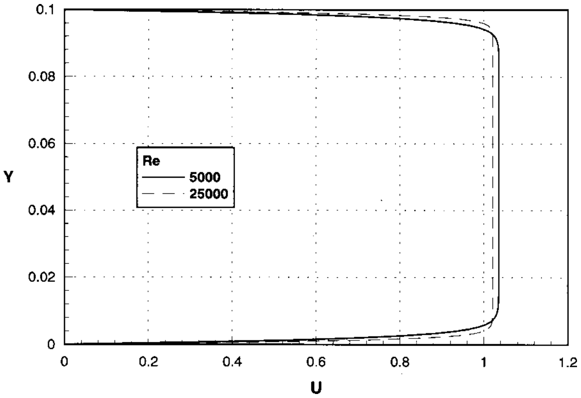

Fig. 4 Velocity profiles in the fully-developed flow region: Da $=5\times10^{-6}$, $\varphi=0.95$

41×121 grid points. The average Nusselt number was obtained by numerically integrating Eq. (23) with Simpson's open ended formula [27]. The numerical code was validated for the classical case of viscous fluid flow in a channel, and the numerical results compared very well with the analytical solution [28] as shown in Fig. 3. This was achieved by setting $\varphi=1$, Da=1, and $C_F=0$ in Eq. (13). A moderate value of 300 was chosen for Reynolds number so for the outflow boundary conditions in Fig. 2 to be valid. Then Eqs. (13) and (16) were solved by setting zero the first term on the right hand side of Eq. (13).

Results and Discussion

A series of numerical calculations was performed for different parametric values. The effect of the Reynolds number on flow field and heat transfer will be discussed first. This is followed by the variation of the Darcy number, and the thermal conductivity ratio. The Prandtl number was assumed to be 7.0 for all calculations. Thermal dispersion depends on fluid velocities and the mixing of the fluid as it flows through the complex tortuous paths around the fibers. For dispersion to be an effective transport mechanism, the permeability and the porosity need to be large to felicitate this mechanism. A high value for φ of 0.95 was assumed. The value of the form coefficient, C_F, was taken to be 0.075 as recommended by the experimental work of Beavers and Sparrow [1]. The nondimensional height of the channel was held at 0.1.

The stagnant conductivity of the fibrous medium, k_0, depends on the thermal conductivities of the solid and the fluid, the porosity of the medium, and the relative orientation of the fibers, which, while important, is difficult to quantify. The stagnant conductivity can be bounded using the arithmetic average of the two conductivities, which yields too high a value of k_o, and the harmonic mean, which is too low. It is, therefore, desirable to measure the stagnant conductivity experimentally. For the numerical calculations presented here the ratio of thermal conductivities, k_o/k_f, was assumed to be 2.0, except for the last set where the effects of variation in this term will be considered.

The ratio of heat capacities, σ, is significant when transient solutions for the energy equation, Eq. (18) are desired. In the present work, the focus is on steady-state solutions, hence, the unsteady term is utilized merely to march the equation in time to its steady-state solution. Three different values of σ, 0.8, 1.0, and 1.1 resulted in identical steady-state solutions. For the results that follow, the value of σ was prescribed to be 1.0.

Figure 4 illustrates the velocity profiles for two values of Reynolds number. For both cases, the velocity varies linearly near the wall and there is a large core of constant velocity. A smooth transition exists between these two different regimes and it is clear from the velocity profiles that the numerical solutions satisfy mass conservation with the core accelerating to compensate for the deceleration near the solid boundary. At the higher Reynolds number, the velocity gradient near the wall is expectedly steeper. Fully developed flow conditions prevailed at a short distance (<0.2) from the entrance of the channel for the entire range of Re considered here. The "boundary layer" thickness remained constant thereafter.

The corresponding temperature profiles are shown in Fig. 5. For higher Reynolds number, the temperature profile is steeper resulting in a larger temperature gradient at the wall (Fig. 7). Figure 6 presents a plot of isotherms. From Figs. 5 and 6, it is apparent that the unheated adiabatic bounding surface of the channel is at the inlet temperature. This suggests that the thermal layer remained close to the heated wall and did not penetrate very far towards the other wall. The fundamental assumption of the volume average analysis is that there are significant number of pores and fibers present in a representative volume of the medium over which the averaging is performed. However, very small channel heights may impose restrictions on the validity of the volume averaging process as discussed. The isotherms expectedly are closely packed near the entrance of the channel yielding larger local Nusselt number (Fig. 7).

The local wall temperature gradients are presented in Fig. 7. As shown, the local heat transfer rate decreases with increasing distance from the channel inlet as the transfer medium absorbs more energy along the direction of flow. The average Nusselt number data appear in Fig. 8 for Reynolds number ranging from 5000 to 25,000. Although the heat transfer rate is substantially higher in this Reynolds number range when compared to that of viscous flow through a channel, it is interesting to note that there is only a marginal increase in Nu with a much larger increase in Re. This

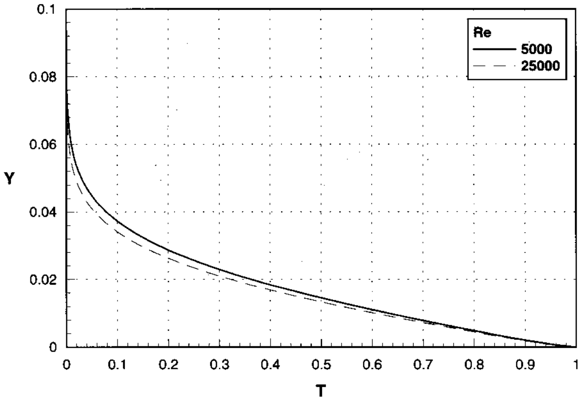

Fig. 5 Temperature profiles at $X=1$: Da$=5\times10^{-6}$, $k_0/k_f=2$, $\varphi=0.95$, and Pr$=7$

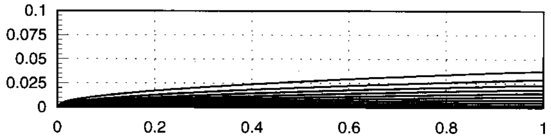

Fig. 6 Isotherms for Re=5000, Da=5×10^{-6}, φ=0.95, and k_0/k_f=2

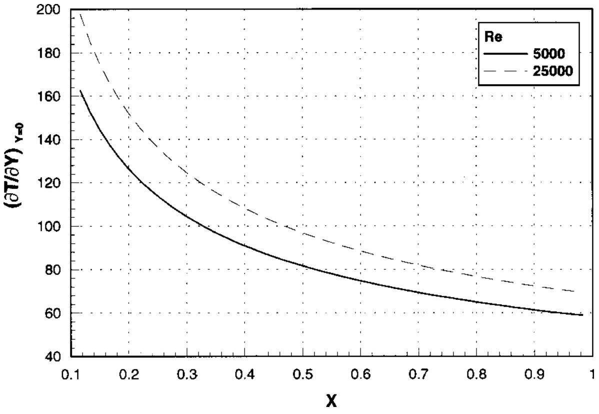

Fig. 7 Local wall-temperature gradients: Da=5×10^{-6}, φ =0.95

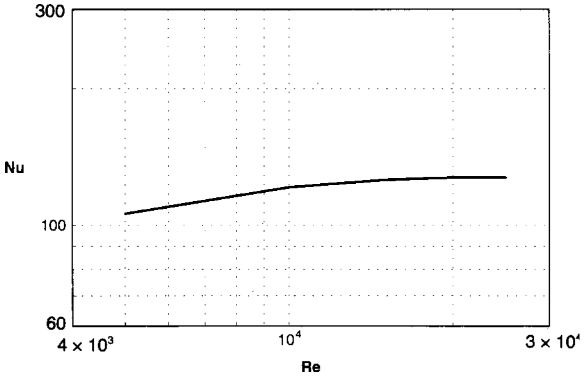

Fig. 8 Average Nusselt number: Da=5×10^{-6}, k_0/k_f=2, φ =0.95, and Pr=7

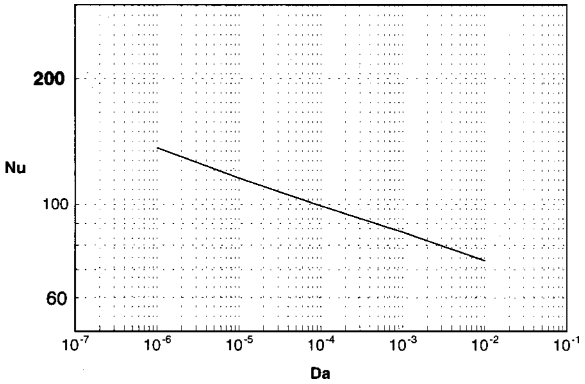

Fig. 9 Average Nusselt number: Re=10^4, k_0/k_f=2.0, and φ =0.95

Table 1 C_F=0.075, φ=0.95, Re=10^4, and Da=10^{-6}

k_0/k_f	Nu	(k_0/k_f) Nu
1.0	153.3	153.3
1.25	148.5	185.6
1.5	144.2	216.3
1.75	140.2	245.4
2.0	136.5	273.0

suggests that while the use of the fibrous medium enhances heat transfer, fluid inlet velocity beyond some relatively high value will not further enhance the heat transfer. It appears that the limit of thermal dispersion is reached here. The experimental work of Beavers and Sparrow [1] clearly demonstrated that the quadratic inertial term containing C_F is important even for moderate velocities. The current numerical study appears to suggest that the effective use of fluid flow around thin fibers for better mixing is a preferable method of enhancing the heat transfer, rather than just continuing to increase the flow velocity.

To understand the most significant mechanisms that contribute to enhanced heat transfer in fibrous media, the Darcy number was varied while holding all other parameters constant. The average Nusselt number is illustrated in Fig. 9 as a function of the Darcy number. Comparing Figs. 8 and 9, it is clear that a lower Darcy number rather than a higher Reynolds number produces significant increases in heat transfer. When porosity does not change, a lower Darcy number can be achieved through thinner fibers. This can be explained with the relation for permeability in terms of porosity and fiber thickness, Eq. (22). For constant porosity, thin fibers lead to lower permeability and hence, smaller Darcy numbers. Thinner fibers spread the flow more evenly and promote better mixing of the fluid, which results in larger heat transfer rates. It should be noted, however, that there may be manufacturing limitations for thinner fibers.

Although the thermal conductivity ratio, k_o/k_f, may depend on either the porosity or permeability or both, the variation of the ratio helps understand the effect of the type of solid material utilized for the fibrous medium. Table 1 lists the values of the average Nusselt number obtained for different k_o/k_f. While the change in the Nusselt number appears to be insignificant, the heat transfer coefficient increases substantially with an increase in k_o/k_f. A better way to characterize this effect is to examine the product (k_o/k_f) Nu, which accounts for the combined effect.

Conclusions

A comprehensive numerical model was developed to study the forced convection heat transfer in rigid metallic fibrous materials. Numerical results were presented for liquid cooling using water and metallic fibrous heat dissipaters. Empirical models were used to include the effects of inertia and thermal dispersion associated with high Reynolds number flows.

The current numerical model allows the variation of one significant parameter while keeping all the others constant, which typically is not possible in experiments. Hence the numerical model can assist in the design and choice of fibrous heat sinks. While high Reynolds number flow is desirable for effective heat dissipation, distinction here is made between the two different flow velocity regimes. At very low velocities, the Darcy model is valid, and the thermal dispersion is insignificant. Hence, it is not the preferred range of Reynolds number. In the higher range of Re, i.e., >5000, further increases in Re do not bring about substantial enhancement in heat transfer. This can be accomplished by thinner fibers reducing the Darcy number.

Here again, two ranges of Darcy number need to be demarcated. At the lower end, $K<10^{-6}$, the porosity and the flow rates will be rather low for thermal dispersion to be present. For the higher range of Darcy number comprised of higher porosities and permeability, dispersion increases with decreasing permeability. For the randomly oriented fibrous media, lowering the permeability in the high porosity range corresponds to thinner fibers. As a result, in the manufacturing of the fibrous material, the best heat transfer performance can be obtained by maximizing the porosity and making the fibers as thin as possible. By so doing, the fluid velocities will be lower, with the corresponding savings of pressure drop and the associated pumping capacity.

For $\mathrm{Re}\lesssim 5\times 10^3$, and $\mathrm{Da}\lesssim 10^{-6}$, the numerical calculations were unstable and no meaningful solutions could be obtained. In these lower ranges of Re and Da, the simple Darcy law is perhaps more appropriate. Numerical solutions were not possible for $\mathrm{Re}=1000$ even with $\mathrm{Da}=10^{-2}$. From the experience gained through the numerical calculations, the realistic values of Reynolds number and Darcy number for dispersion to be significant are $5000\lesssim \mathrm{Re}\lesssim 25000$ and $10^{-6}\lesssim \mathrm{Da}\lesssim 10^{-5}$. Outside these ranges, the physical assumptions made in arriving at the volume-averaged conservation equations, Eqs. (6) and (8), break down. The main assumption is that in a representative volume of the medium over which the averaging process is performed, there are large number of pores and fibers. A very large Darcy number indicates a large value of fiber thickness (fiber thickness is proportional to the square root of permeability) relative to the channel length which is invalid for the volume average analysis. A very low value of Darcy number indicates low permeability and hence much smaller void relative to solid phase. As the Darcy number increases the limit of viscous fluid flow is approached. Much lower values of Darcy number lead to low velocity and low porosity Darcy flow where dispersion is absent.

Materials of large thermal conductivity are desirable for the fibrous heat dissipaters because they produce higher stagnant conductivities. The numerical results suggest that even a marginal increase in the stagnant conductivity can significantly enhance heat transfer coefficients. The thermal performance of the fibrous heat dissipaters thus depends on the choice of the material, and the manufacturing of the fibrous materials with high porosity and thin fibers.

Nomenclature

a = fiber radius
A,B = dimensional constants
c = dimensionless constant
c_p = specific heat at constant pressure
Da = Darcy number $=K/L^2$
C_F = form coefficient
h = average convective heat transfer coefficient
H = channel height
H^* = nondimensional channel height $=H/L$
k = thermal conductivity
K = permeability of the fibrous medium
l = Brinkman's screening length $=\sqrt{K}$
L = channel length
Nu = average Nusselt number $=hL/k_0$
p_f = volume averaged pressure of the fluid
P = nondimensional pressure $=\phi p_f/\rho V_0^2$
Pe_a = Péclet number based on fiber radius $=\mathrm{Re}\,Pr\sqrt{\mathrm{Da}}(a/\sqrt{K})$
Pe_l = Péclet number based on Brinkman's screening length $=\mathrm{Re}\,Pr\sqrt{\mathrm{Da}}$
Pr = fluid Prandtl number $=v/\alpha$
Re = Reynolds number $=V_0L/v$
t = temperature
T = nondimensional temperature $=t-t_0/t_w-t_0$
u,v = volume averaged velocity components in x, and y directions, respectively
U,V = volume averaged nondimensional velocity components $(u/V_0,\ v/V_0)$
$\mathbf{v}$ = volume averaged velocity vector
V_0 = inlet velocity
x,y = Cartesian coordinates
X,Y = nondimensional cartesian coordinates $(x/L,\ y/L)$

Greek

α = thermal diffusivity of the fluid $=(k/\rho c_p)_f$
ε = volume fraction of the fibers $=(1-\varphi)$
φ = porosity
λ = constant parameter
ψ = stream function
μ = dynamic viscosity of the fluid
μ' = effective dynamic viscosity of the medium
ν = kinematic viscosity
ρ = density
σ = ratio of heat capacities of the stagnant medium, and the fluid $=(\rho c_p)_0/(\rho c_p)_f$
τ = time
τ^* = nondimensional time $=\tau V_0/L$
ω = vorticity

Subscripts

f = fluid
0 = stagnant medium
d = thermal dispersion

References

[1] Beavers, G. S., and Sparrow, E. M., 1969, "Non-Darcy Flow Through Fibrous Porous Media," ASME J. Appl. Mech., **36**, pp. 711–714.
[2] Nield, D. N., and Bejan, A., 1999, *Convection in Porous Media*, 2nd ed., Springer-Verlag, New York.
[3] Kaviany, M., 1995, *Principles of Heat Transfer in Porous Media*, 2nd ed., Springer-Verlag, New York.
[4] Lage, J. L., 1998, "The Fundamental Theory of Flow Through Permeable Media From Darcy to Turbulence," in *Transport in Porous Media*, D. B. Ingham and I. Pop, eds., Pergamon, Oxford, pp. 1–30.
[5] Whitaker, S., 1969, "Advances in Theory of Fluid Motion in Porous Media," Ind. Engrg. Chem., **61**, pp. 14–28.
[6] Stattery, J. C., 1969, "Single-Phase Flow Through Porous Media," AIChE J., **15**, pp. 866–872.
[7] Vafai, K., and Tien, C. L., 1981, "Boundary and Inertia Effects on Flow and Heat Transfer in Porous Media," Int. J. Heat Mass Transf., **24**, pp. 195–203.
[8] Vafai, K., and Tien, C. L., 1982, "Boundary and Inertia Effects on Convective Mass Transfer in Porous Media," Int. J. Heat Mass Transf., **25**, pp. 1183–1190.
[9] Vafai, K., 1984, "Convective Flow and Heat Transfer in Variable-Porosity Media," J. Fluid Mech., **147**, pp. 233–259.
[10] Vafai, K., Alkire, R. L., and Tien, C. L., 1985, "An Experimental Investigation of Heat Transfer in Variable Porosity Media," ASME J. Heat Transfer **107**, pp. 642–647.
[11] Kaviany, M., 1985, "Laminar Flow Through a Porous Channel Bounded by Isothermal Parallel Plates," Int. J. Heat Mass Transf., **28**, pp. 851–858.
[12] Beckermann, C., and Viskanta, R., 1987, "Forced Convection Boundary Layer Flow and Heat Transfer Along a Flat Plate Embedded in a Porous Medium," Int. J. Heat Mass Transf., **30**, pp. 1547–1551.
[13] Vafai, K., and Kim, S. J., 1989, "Forced Convection in a Channel Filled With a Porous Medium: An Exact Solution," ASME J. Heat Transfer, **111**, pp. 1103–1106.
[14] Nield, D. A., Junqueira, S. L. M., and Lage, J. L., 1996, "Forced Convection in a Fluid-Saturated Porous-Medium Channel With Isothermal or Isoflux Boundaries," J. Fluid Mech., **322**, pp. 201–214.
[15] Nield, D. A., Porneala, D. C., and Lage, J. L., 1999, "A Theoretical Study, With Experimental Verification, of the Temperature-Dependent Viscosity Effect on the Forced Convection Through a Porous Medium Channel," ASME J. Heat Transfer, **121**, pp. 500–503.
[16] Koch, D. L., and Brady, J. L., 1986, "The Effective Diffusivity of Fibrous Media," AIChE J., **32**, pp. 575–591.
[17] Muskat, M., 1937, *The Flow of Homogeneous Fluids Through Porous Media*, McGraw-Hill, New York.
[18] Reynolds, O., 1901, *Papers on Mechanical and Physical Subjects*, 2(44), Cambridge University Press, pp. 51–105.
[19] Green, L., and Duwez, P., 1951, "Fluid Flow Through Porous Metals," ASME J. Appl. Mech., **18**, pp. 39–45.
[20] Ward, J. C., 1964, "Turbulent Flow in Porous Media," ASCE J. Hydraulics Div., **90**, pp. 1–12.
[21] Brownell, L. E., Dombrowski, H. S., and Dickey, C. A., 1950, "Pressure Drop Through Porous Media," Chem. Eng. Prog., **46**, pp. 415–422.
[22] Brinkman, H. C., 1947, "A Calculation of the Viscous Force Exerted by a

Flowing Fluid on a Dense Swarm of Particles,'' Appl. Sci. Res., **A1**, pp. 27–34.

[23] Slattery, J. C., 1972, *Momentum, Energy and Mass Transfer in Continua*, McGraw-Hill, New York.

[24] Roache, P. J., 1998, *Fundamentals of Computational Fluid Dynamics*, Hermosa, Albuquerque, NM.

[25] Spielman, L., and Goren, S. L., 1968, ''Model for Predicting Pressure Drop and Filtration Efficiency in Fibrous Media,'' Envi. Sci. Tech., **2**, pp. 279–287.

[26] Anderson, D. A., Tannehill, J. C., and Pletcher, R. H., 1984, *Computational Fluid Mechanics and Heat Transfer*, Taylor & Francis; Chap. 9.

[27] Press, W. H., Teukolsky, S. A., Vetterling, W. T., and Flannery, B. P., 1992, *Numerical Recipes: The Art of Scientific Computing*, 2nd ed., Cambridge University Press, New York; Chap. 4.

[28] Shames, I. H., 1992, *Mechanics of Fluids*, 3rd ed., McGraw-Hill, New York; Chap. 7.

Heat and Fluid Flow Within an Anisotropic Porous Medium

A. Nakayama
Professor

F. Kuwahara
Associate Professor

T. Umemoto
Graduate Student

T. Hayashi
Graduate Student

Department of Mechanical Engineering,
Shizuoka University,
3-5-1 Johoku, Hamamatsu, 432 Japan

A numerical experiment at a pore scale using a full set of Navier-Stokes and energy equations has been conducted to simulate laminar fluid flow and heat transfer through an anisotropic porous medium. A collection of square rods placed in an infinite two-dimensional space has been proposed as a numerical model of microscopic porous structure. The degree of anisotropy was varied by changing the transverse center-to-center distance with the longitudinal center-to-center distance being fixed. Extensive calculations were carried out for various sets of the macroscopic flow angle, Reynolds number and degree of anisotropy. The numerical results thus obtained were integrated over a space to determine the permeability tensor, Forchheimer tensor and directional interfacial heat transfer coefficient. It has been found that the principal axes of the permeability tensor (which controls the viscous drag in the low Reynolds number range) differ significantly from those of the Forchheimer tensor (which controls the form drag in the high Reynolds number range), The study also reveals that the variation of the directional interfacial heat transfer coefficient with respect to the macroscopic flow angle is analogous to that of the directional permeability. Simple subscale model equations for the permeability tensor, Forchheimer tensor and directional Nusselt number have been proposed for possible applications of VAT to investigate flow and heat transfer within complex heat and fluid flow equipment consisting of small scale elements.
[DOI: 10.1115/1.1481355]

Keywords: *Convection, Heat Transfer, Laminar, Modeling, Porous Media*

Introduction

The concept of local volume-averaging theory, namely, VAT (Cheng [1], Quintard and Whitaker [2]), widely used in the study of porous media (Kaviany [3], Nield and Bejan [4], Vafai [5]), may be exploited to investigate the flow and heat transfer within complex heat and fluid flow equipment consisting of small scale elements which one does not want to grid (Nakayama et al. [6]). For example, the hot and cold fluid passages in a compact heat exchanger can be treated as two distinct porous media with highly anisotropic permeabilities. It is quite likely that one has to appeal to the volume-averaged set of equations with some subscale model, when he performs CFD calculations of engine nacelles to account for bundles of hydraulic tubes, ribs and some other obstructions (DesJardin [7]). There are a number of other situations in which one needs to introduce macroscopic and subscale models to describe complex equipment. However, in order to apply these macroscopic governing equations based on VAT such as introduced by Nakayama et al. [6] for analyzing the complex heat and fluid flow equipment, one must model the flow resistance associated with subscale solid elements (modeled as an anisotropic porous medium) and also the heat transfer between the flowing fluid and the subscale elements, beforehand.

The microscopic numerical results obtained at a pore scale can be processed to extract the macroscopic hydrodynamic and thermal characteristics in terms of the volume-averaged quantities. A great deal of effort has been directed towards this endeavor (Kuwahara et al. [8], Nakayama and Kuwahara [9]). In the fundamental study of turbulent flow through an isotropic porous medium, Nakayama and Kuwahara [10] pointed out that the smaller eddies (i.e., turbulent mixing rather than mechanical dispersion) must be modeled first, as in the case of LES, and started with the Reynolds averaged set of the governing equations and integrated them over a representative control volume to obtain the set of macroscopic equations, namely, the equations of continuity, momentum, energy, turbulence kinetic energy and its rate of dissipation. The unknown model parameters including the interfacial heat transfer coefficient, permeability and Forchheimer constants were determined by carrying out exhaustive numerical experiments using a periodic array of square rods and then integrating these microscopic results over a unit porous structure (Nakayama and Kuwahara [10] and Kuwahara et al. [11]), Their study can be generalized to treat anisotropic porous media, which may represent complex heat and fluid flow equipment consisting of synthetic structural elements.

In this study, we shall essentially follow their procedure to investigate laminar flow and thermal non-equilibrium heat transfer through a collection of square rods placed anisotropically, so as to make a first step towards establishing a general numerical procedure based on VAT for analyzing complex heat and fluid flow equipment in reality. A series of direct numerical experiments using a structural model are conducted for various sets of the macroscopic flow angle, Reynolds number and degree of anisotropy, to determine the permeability tensor, Forchheimer tensor and directional interfacial heat transfer coefficient, purely from the first principles without any empricizm.

Numerical Model and Periodic Boundary Conditions

Let us consider a macroscopically uniform flow with an angle α through an infinite number of square rods placed in an anisotropic fashion, as shown in Fig. 1. All square rods, which may be regarded as heat sinks (or sources), are maintained at a constant temperature T_w, which is lower (or higher) than the temperature of the flowing fluid. The macroscopic velocity field follows

$$\langle \vec{u} \rangle = |\langle \vec{u} \rangle| (\cos \alpha \vec{l} + \sin \alpha \vec{m}) \tag{1}$$

where $\langle a \rangle$ denotes the volume average, namely,

$$\langle a \rangle = \frac{1}{V} \int_V a\,dV \tag{2}$$

Contributed by the Heat Transfer Division for publication in the JOURNAL OF HEAT TRANSFER. Manuscript received by the Heat Transfer Division October 4, 2001; revision received March 1, 2002. Associate Editor: M. Faghri.

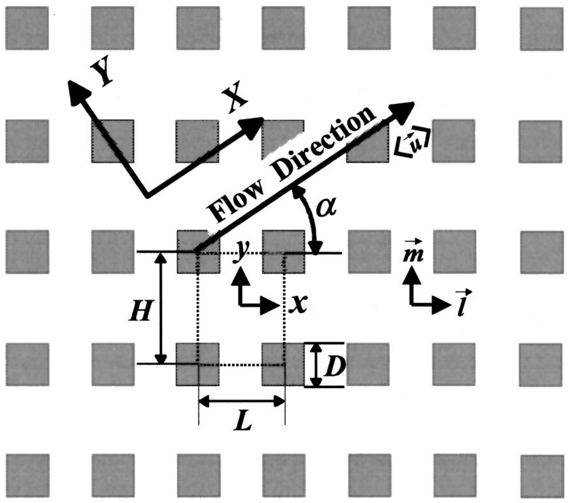

Fig. 1 Physical model and its coordinate system

The representative elementary volume V, which should be smaller than a macroscopic characteristic length, can be taken as $L\times H$ for this periodic structure. Due to the periodicity of the model, only one structural unit as indicated by dashed lines in the figure may be taken as a calculation domain. The governing equations for the fluid phase are given as follows

$$\nabla\cdot\vec{u}=0 \tag{3}$$

$$\rho_f(\nabla\cdot\vec{u})\vec{u}=-\nabla p+\mu_f\nabla^2\vec{u} \tag{4}$$

$$\rho_f c_{p_f}\nabla\cdot(\vec{u}T)=k_f\nabla^2 T \tag{5}$$

where the subscripts *f* stand for the fluid phase. At the periodically fully developed stage, the velocity distribution at the exit of the structural unit must be *identical* to that at the inlet, whereas the temperature profile at the exit must be *similar* to that at the inlet. (Note that the situation is analogous to the case of forced convection in a channel with isothermal walls.) Thus, the boundary, compatibility and periodic constraints are given according to Nakayama et al. [12] and Kuwahara et al. [11] as follows

On the solid walls:

$$\vec{u}=\vec{0} \tag{6}$$

and

$$T=T_w \tag{7}$$

On the periodic boundaries:

$$\vec{u}|_{x=-L/2}=\vec{u}|_{x=L/2} \tag{8a}$$

$$\vec{u}|_{y=-H/2}=\vec{u}|_{y=H/2} \tag{8b}$$

$$\int_{-H/2}^{H/2}u\,dy\bigg|_{x=-L/2}=\int_{-H/2}^{H/2}u\,dy\bigg|_{x=L/2}=H\cos\alpha\langle|\vec{u}|\rangle \tag{9a}$$

$$\int_{-L/2}^{L/2}v\,dx\bigg|_{y=-H/2}=\int_{-L/2}^{L/2}v\,dx\bigg|_{y=H/2}=L\sin\alpha\langle|\vec{u}|\rangle \tag{9b}$$

$$(T-T_w)|_{x=L/2}=\tau^{L\cos\alpha/(L\cos\alpha+H\sin\alpha)}(T-T_w)|_{x=-L/2} \tag{10a}$$

$$(T-T_w)|_{y=H/2}=\tau^{H\sin\alpha/(L\cos\alpha+H\sin\alpha)}(T-T_w)|_{y=-H/2} \tag{10b}$$

where

$$\tau=\frac{(T-T_w)|_{x=L/2,\,y=H/2}}{(T-T_w)|_{x=-L/2,\,y=-H/2}} \tag{10c}$$

Table 1 Effect of grid number on $-(\partial\langle p\rangle^f/\partial s)/(\rho|\langle\vec{u}\rangle|^2/L)$ at $\alpha=0$ deg

Re_L	Grid system 91x91	Grid system 181x181
10	7.80	7.82
100	0.836	0.835
600	0.154	0.154

Note that the thermal periodicity as given by Eqs. (10*a*) and (10*b*) must be satisfied, since the microscopic temperature field, when averaged spatially within a local control volume, should lead to the macroscopic temperature field whose gradient aligns with the macroscopic velocity vector in s direction, such that the macroscopic energy equation reduces to

$$\rho_f c_{pf}|\langle\vec{u}\rangle|\frac{d\langle T\rangle^f}{ds}=-h_f\alpha_f(\langle T\rangle^f-\langle T\rangle^s) \tag{11a}$$

where the net heat transfer from the fluid phase to the solid phase through a specific interfacial area a_f (i.e., interfacial area per unit volume) is given by $h_f a_f(\langle T\rangle^f-\langle T\rangle^s)$ where $\langle T\rangle^f$ and $\langle T\rangle^s$ denote the intrinsically averaged temperature of fluid phase and that of solid phase, respectively. This equation naturally yields

$$\langle T\rangle^f-(T)^s=(\langle T\rangle^f-(T)^s)_{\mathrm{ref}}\exp\left(-\frac{a_f h_f}{\rho_f c_{p_f}|\langle\vec{u}\rangle|}(s-s_{\mathrm{ref}})\right) \tag{11b}$$

since the interfacial heat transfer coefficient h_f is expected to be constant for the periodically fully developed heat and fluid flow (Kuwahara et al. [11]). It can easily be confirmed that the foregoing macroscopic equation is possible only when the microscopic temperature field satisfies Eqs. (10*a*) and (10*b*).

Computations may be made using the dimensionless equations based on the absolute value of the Darcian (apparent) velocity vector $|\langle\vec{u}\rangle|$, and the longitudinal center-to-center distance L as reference scales. For carrying out a series of numerical calculations, it may be convenient to use the Reynolds number based on L as $\mathrm{Re}_L=|\langle\vec{u}\rangle|L/\nu_f$, which can readily be translated into the Reynolds number based on the size of square rod D as follows

$$\mathrm{Re}_D=|\langle\vec{u}\rangle|D/\nu_f=\left((1-\phi)\frac{H}{L}\right)^{1/2}\mathrm{Re}_L \tag{12}$$

where the porosity is given by $\phi=1-(D^2/HL)$. In this study, the ratio H/L is set to 1, 3/2, and 2 to investigate the effects of the degree of the anisotropy, whereas the ratio D/L is fixed to 1/2 for all calculations.

The governing equations (3) to (5) subject to the foregoing boundary and compatibility conditions were numerically solved using SIMPLE algorithm proposed by Patankar and Spalding [13]. Convergence was measured in terms of the maximum change in each variable during an iteration. The maximum change allowed for the convergence check was set to 10^{-5}, as the variables are normalized by appropriate references. The hybrid scheme is adopted for the advection terms. Further details on this numerical procedure can be found in Patankar [14] and Nakayama [15]. All computations have been carried out for a one structural unit $L\times H$ using non-uniform grid arrangements with 91×91, to ensure that the results are independent of the grid system. In Table 1, the results of the macroscopic pressure gradient obtained using the 91×91 grid system and 181×181 grid system are compared to confirm mesh invariance. All computations were performed using the computer system at Shizuoka University Computer Center.

Microscopic Velocity Field and Macroscopic Pressure Gradient

Two distinct sets of velocity vector plots obtained for two different arrays $H/L=1$ and 3/2, with $\alpha=0$ deg and 45 deg are

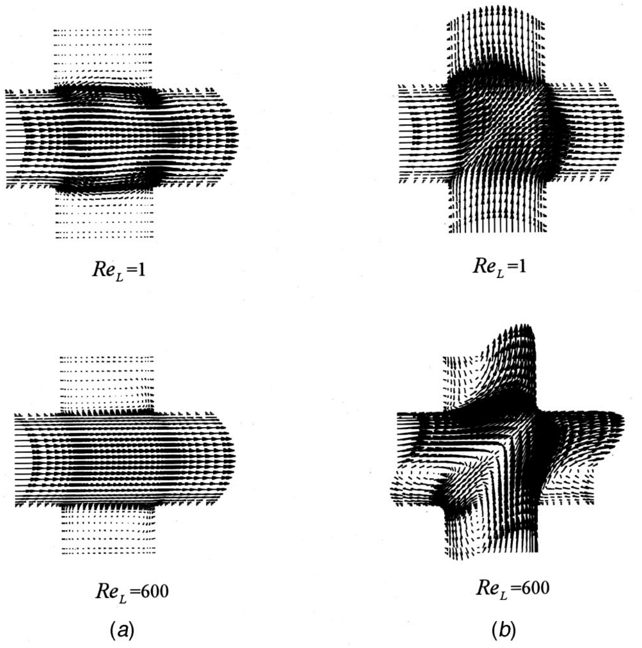

Fig. 2 Velocity vector plots ($H/L=1$) (*a*) $\alpha=0$ deg (*b*) $\alpha=45$ deg

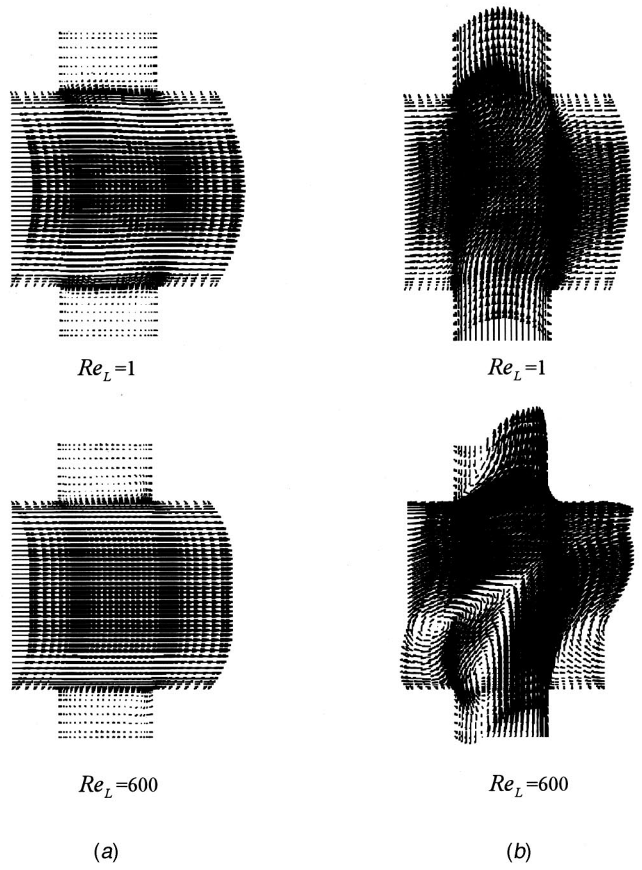

Fig. 3 Velocity vector plots ($H/L=3/2$) (*a*) $\alpha=0$ deg (*b*) $\alpha=45$ deg

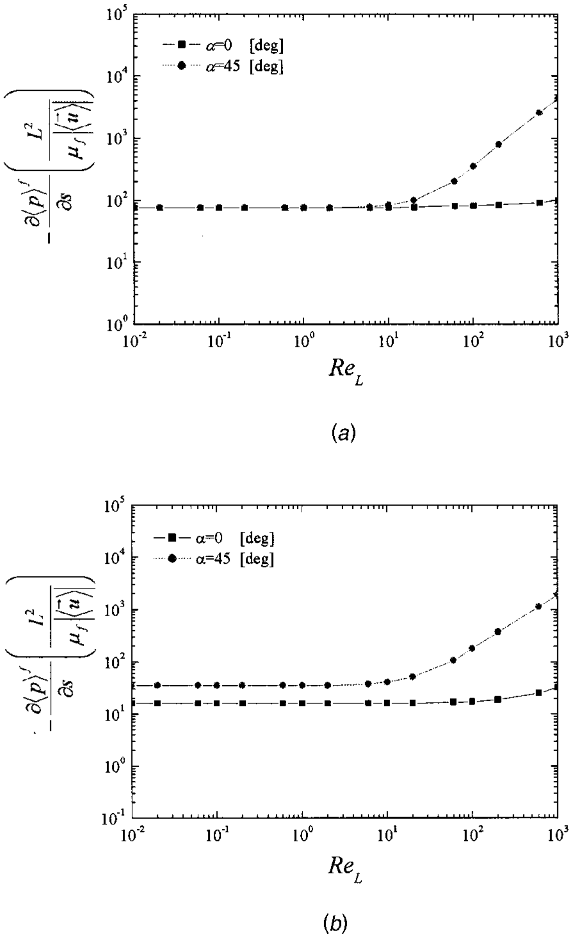

Fig. 4 Dimensionless plot of pressure gradient for a low Reynolds number range: (*a*) $H/L=1$ and (*b*) $H/L=3/2$

presented in Figs. 2 and 3 for two different Reynolds numbers, namely, $\mathrm{Re}_L=1$ and 600. When the Reynolds number is comparatively small, the viscous force contribution to the pressure drop predominates over the inertial contribution. As the Reynolds number increases, flow separation takes place for $\alpha=45$ deg, such that the inertial contribution to the pressure drop becomes significant, whereas the flow field for $\alpha=0$ deg remains to be of the channel flow type such that the inertial contribution is negligibly small. From these velocity vector plots, we may expect that the resulting macroscopic pressure drop for a fixed mass flow rate is rather insensitive to the macroscopic flow direction for low Reynolds number flows (especially for $H/L=1$), while it becomes sensitive to the flow direction as either the Reynolds number or the degree of anisotropy (H/L) increases.

The macroscopic pressure gradient (i.e., the gradient of the intrinsic average pressure $\langle p\rangle^f$ measured along the macroscopic flow direction s) may readily be evaluated using the microscopic numerical results as

$$-\frac{\partial\langle p\rangle^f}{\partial s}=\frac{\cos\theta}{L(H-D)}\int_{-(H-D)/2}^{(H-D)/2}(p|_{x=-L/2}-p|_{x=L/2})dy+\frac{\sin\theta}{H(L-D)}\int_{-(L-D)/2}^{(L-D)/2}(p|_{y=-H/2}-p|_{y=H/2})dx \tag{13}$$

The pressure gradient results are assembled in Figs. 4, in terms of the dimensionless pressure gradient against the Reynolds number. All data show that the dimensionless pressure gradient stays constant for $\mathrm{Re}_L\leqslant 10$, as we expected from the velocity vector plots in Figs. 2 and 3. For the case of nonzero macroscopic flow angle, the pressure gradient increases drastically as Re_L goes beyond 10 in which the porous inertial contribution becomes appreciable as compared with the viscous (Darcian) contribution.

Determination of Permeability Tensor

As in the study of Nakayama et al. [6], Forchheimer extended Darcy's law (Forchheimer [16]) may be extended for the case of anisotropic porous medium as follows:

$$-\frac{\partial\langle p\rangle^f}{\partial x_i}=(\mu_f K_{f_{ij}}^{-1}+\rho_f b_{f_{ij}}|\langle\vec{u}\rangle|)\langle u_j\rangle \tag{14}$$

where $\langle u_k\rangle\langle u_k\rangle=|\langle\vec{u}\rangle|^2$. When the velocity (Reynolds number) is low, the equation reduces to Darcy's law as

$$-\frac{\partial\langle p\rangle^f}{\partial x_i}=(\mu_f K_{f_{ij}}^{-1}+\rho_f b_{f_{ij}}|\langle\vec{u}\rangle|)\langle u_j\rangle\cong\mu_f K_{f_{ij}}^{-1}\langle u_j\rangle \tag{15}$$

For the orthotropic media (having three mutually orthogonal principal axes) such as shown in Fig. 1, the permeability tensor may be modeled following Dullien [17] as

$$K_{f_{ij}}^{-1}=(l_i l_j)/K_{f_1}+(m_i m_j)/K_{f_2}+(n_i n_j)/K_{f_3} \tag{16}$$

such that

$$-\frac{\partial\langle p\rangle^f}{\partial x_i}\cong\mu_f K_{f_{ij}}^{-1}\langle u_j\rangle=\left(\frac{\cos\alpha}{K_{f_1}}l_i+\frac{\cos\beta}{K_{f_2}}m_i+\frac{\cos\gamma}{K_{f_3}}n_i\right)|\langle\vec{u}\rangle| \tag{17}$$

where

$$\cos\alpha=\frac{l_j\langle u_j\rangle}{|\langle\vec{u}\rangle|},\ \cos\beta=\frac{m_j\langle u_j\rangle}{|\langle\vec{u}\rangle|},\ \cos\gamma=\frac{n_j\langle u_j\rangle}{|\langle\vec{u}\rangle|} \tag{18}$$

are the directional cosines of the macroscopic velocity vector, such that

$$\cos^2\alpha+\cos^2\beta+\cos^2\gamma=1$$

Thus, the directional permeability measured along the macroscopic flow direction s is given by

$$\frac{1}{K_{f_n}}=\frac{\cos^2\alpha}{K_{f_1}}+\frac{\cos^2\beta}{K_{f_2}}+\frac{\cos^2\gamma}{K_{f_3}} \tag{19}$$

such that

$$-\frac{\partial\langle p\rangle^f}{\partial s}=\frac{\mu_f}{K_{f_n}}|\langle\vec{u}\rangle| \tag{20}$$

or, in dimensionless form, as

$$-\frac{\partial\langle p\rangle^f}{\partial s}\frac{L^2}{\mu_f|\langle\vec{u}\rangle|}=\frac{L^2}{K_{f_n}} \tag{21}$$

Thus, the directional permeability K_{f_n} may readily be determined by reading the intercept of the ordinate variable in Fig. 4, where $-(\partial\langle p\rangle^f/\partial s)(L^2/\mu_f|\langle\vec{u}\rangle|)$ is plotted against Re_L.

The numerical results of the directional permeability, thus obtained for two sets of rod arrangements, are presented in Fig. 5 as a function of the macroscopic flow angle α. These numerical data follow closely along the solid curves based on the model Eq. (19), which, for the two-dimensional case, reduces to

$$\frac{1}{K_{f_n}}=\frac{\cos^2\alpha}{K_{f_1}}+\frac{\sin^2\alpha}{K_{f_2}} \tag{22}$$

since $\cos\beta=\sin\alpha$. It is interesting to note that the effect of the macroscopic flow angle α on the permeability is totally absent for the case of the arrangement $H/L=1$. This is due to the fact that the flow field at low Reynolds number is very much like that of fully-developed channel flow. Naturally, for the case of $H/L=1$, the flow resistances for both x and y directions stay the same so that the permeability loses its directional variation. The coefficients determined by fitting the numerical data against Eq. (22) are listed in Table 2. The result $L^2/K_{f_n}=76$ (or $D^2/K_{f_n}=76/4=19$ irrespective of α) obtained for $H/L=1$ ($\phi=0.750$) agrees well with the correlation for isotropic media, proposed by Kuwahara et al. [8] on the basis of numerical experiments, namely,

$$D^2/K_f=120(1-\phi)^2/\phi^3 \tag{23}$$

On the other hand, the comparison between the values based on the foregoing correlation and those obtained by averaging the directional permeability over the macroscopic flow angle as

$$\frac{1}{K_f}\equiv\frac{2}{\pi}\int_0^{\pi/2}\frac{1}{K_{f_n}}d\alpha\cong\frac{1}{2}\left(\frac{1}{K_{f_1}}+\frac{1}{K_{f_2}}\right) \tag{24}$$

reveals that the presence of the anisotropy in the structure nearly doubles Darcian flow resistance (i.e., halves the permeability) for the fixed porosity and rod size.

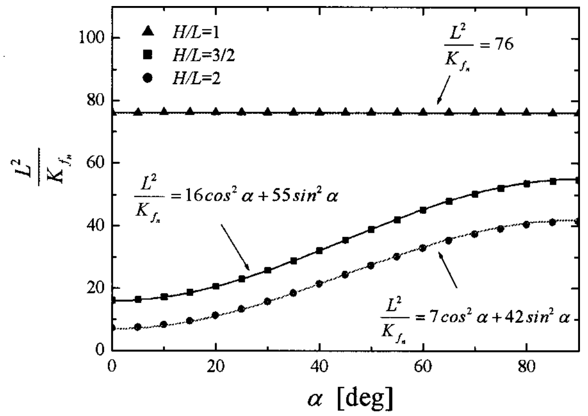

Fig. 5 Directional permeability

Table 2 Coefficients for macroscopic pressure gradient

H/L (ϕ)	L^2/K_{f_1}	L^2/K_{f_2}	$b_{f_1}L$	$b_{f_2}L$	$bb_{f_1}L$
1 (0.750)	76	76	0.2	0.2	8.5
3/2 (0.833)	16	55	0.1	0.6	3.5
2 (0.875)	7	42	0.05	0.8	1.6

Determination of Forchheimer Tensor

When the velocity (Reynolds number) is sufficiently high, the Forchheimer term describing the form drag predominates over the Darcy term such that

$$-\frac{\partial\langle p\rangle^f}{\partial x_i}=(\mu_f K_{f_{ij}}^{-1}+\rho_f b_{f_{ij}}|\langle\vec{u}\rangle|)\langle u_j\rangle\cong\rho_f b_{f_{ij}}|\langle\vec{u}\rangle|\langle u_j\rangle \tag{25}$$

Usually, the principal axes of the permeability tensor $K_{f_{ij}}^{-1}$ do not coincide with those of the Forchheimer tensor $b_{f_{ij}}$. For the orthotropic media in consideration, however, the tensors $b_{f_{ij}}$ should be symmetric and they must also satisfy the following symmetric conditions:

$$\left.\frac{\partial b_{f_n}}{\partial\alpha}\right|_{\alpha=0,\pi/2}=\left.\frac{\partial b_{f_n}}{\partial\beta}\right|_{\beta=0,\pi/2}=\left.\frac{\partial b_{f_n}}{\partial\gamma}\right|_{\gamma=0,\pi/2}=0 \tag{26}$$

where

$$b_{f_n}\equiv b_{f_{ij}}\frac{\langle u_i\rangle\langle u_f\rangle}{|\langle\vec{u}\rangle|^2} \tag{27}$$

is the directional Forchheimer coefficient measured along the macroscopic flow direction s. One of the simplest functions that satisfy these conditions may be:

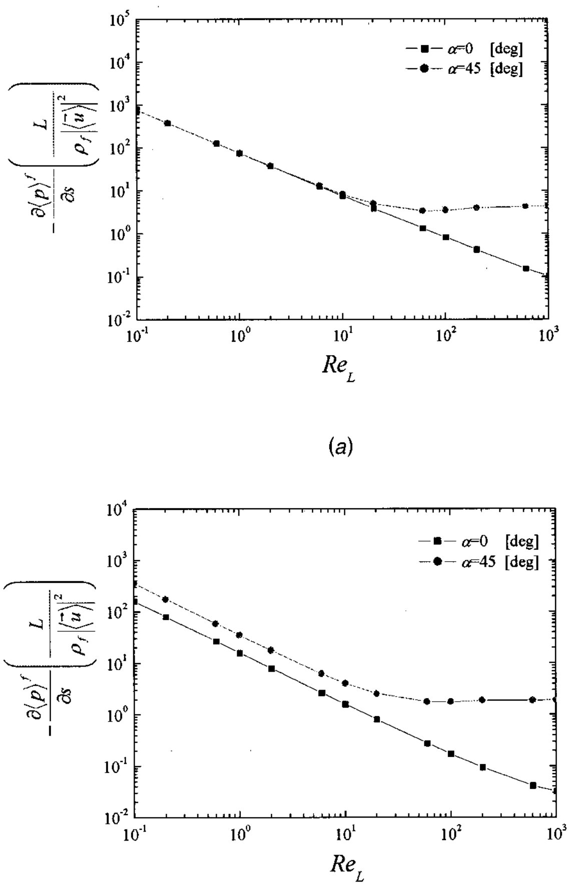

(a)

(b)

Fig. 6 Dimensionless plot of pressure gradient for a high Reynolds number range: (a) $H/L=1$ and (b) $H/L=3/2$

$$b_{f_{ij}}=b_{f_1}(l_il_j)+b_{f_2}(m_im_j)+b_{f_3}(n_in_j)+bb_{f_1}\cos\alpha\cos\beta((l_im_j)+(l_jm_i))+bb_{f_2}\cos\beta\cos\gamma((m_in_j)+(m_jn_i))+bb_{f_3}\cos\gamma\cos\alpha((n_il_j)+(n_jl_i)) \quad (28)$$

which results in

$$b_{f_n}=b_{f_1}\cos^2\alpha+b_{f_2}\cos^2\beta+b_{f_3}\cos^2\gamma+2bb_{f_1}\cos^2\alpha\cos^2\beta+2bb_{f_2}\cos^2\beta\cos^2\gamma+2bb_{f_3}\cos^2\gamma\cos^2\alpha \quad (29)$$

such that

$$-\frac{\partial\langle p\rangle^f}{\partial s}=\frac{\mu_f}{K_{f_n}}|\langle\vec{u}\rangle|+\rho_f b_{f_n}|\langle\vec{u}\rangle|^2 \quad (30)$$

or, in dimensionless form, as

$$-\frac{\partial\langle p\rangle^f}{\partial s}\frac{L}{\rho_f|\langle\vec{u}\rangle|^2}=\frac{L^2}{K_{f_n}\mathrm{Re}_L}+b_{f_n}L \quad (31)$$

Re-plotting the results of macroscopic pressure gradient in terms of $-(\partial\langle p\rangle^f/\partial s)(L/\rho_f|\langle\vec{u}\rangle|^2)$ as shown in Fig. 6 and reading the horizontal asymptotes, we can readily determine the directional Forchheimer constant b_{f_n}. Figure 7 shows the numerical results of the directional Forchheimer coefficient obtained for three sets of rod arrangement as a function of the macroscopic flow angle α. In the same figure, the solid curves generated from the model Eq. (29) are also presented. For this two-dimensional case, the model equation reduces to

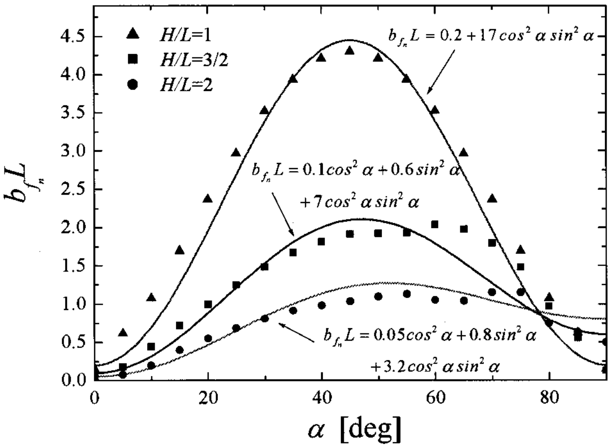

Fig. 7 Directional Forchheimer coefficient

$$b_{f_n}=b_{f_1}\cos^2\alpha+b_{f_2}\sin^2\alpha+2bb_{f_1}\cos^2\alpha\sin^2\alpha \quad (32)$$

where the constants in the model equation must be determined according to the particular subscale array in consideration. It is interesting to note that the numerical results for the cases $H/L=3/2$ and 2 show two consecutive peaks, while the model Eq. (32) yields only one peak (the first peak). The second peak appears when the macroscopic flow angle reaches roughly $\tan^{-1}(H/L)$. Note that, for the case of $H/L=1$, this second peak coincides with the first one. Unfortunately, the model equation is incapable of describing the second peak. Thus, we determine the coefficients b_{f_1}, b_{f_2}, and bb_{f_1} by fitting the numerical results against the curves based on the model Eq. (32), such that the total error diminishes over the entire range $0\leqslant\alpha\leqslant\pi/2$. The resulting values for the coefficients are listed in Table 2.

The mean value of Forchheimer coefficient may be obtained by averaging the directional Forchheimer coefficient over the macroscopic flow angle as

$$b_f\equiv\frac{2}{\pi}\int_0^{\pi/2}b_{f_n}d\alpha\cong\frac{1}{2}(b_{f_1}+b_{f_2})+\frac{1}{4}bb_{f_1} \quad (33)$$

which yields $b_fL=2.33$, 1.23, and 0.83 for $\phi=0.750$, 0.833, and 0.875 (i.e., $H/L=1$, 3/2, and 2), respectively. These values are quite close to those ($b_fL=2.51$, 1.29, and 0.89) obtained numerically by Nakayama and Kuwahara [9] for isotropic media (See Fig. 7 in Nakayama and Kuwahara [9]). Thus, unlike the permeability, the mean Forchheimer coefficient for the fixed porosity and rod size is fairly insensitive to the degree of the anisotropy in the structure.

Microscopic Temperature Field and Determination of Interfacial Heat Transfer Coefficient

Typical temperature fields obtained for the fluid with $\mathrm{Pr}_f=1$ passing through different arrays $H/L=1$ and 3/2, with $\alpha=0$ deg and 45 deg are presented in Figs. 8 and 9 for two different Reynolds numbers, namely, $\mathrm{Re}_L=1$ and 600. (Note that the corresponding velocity fields are shown in Figs. 2 and 3.) The isotherms obtained at low Reynolds numbers exhibit similar patterns, which are typical for the case of pure thermal conduction. For the case of high Reynolds number flow at $\alpha=45$ deg, the temperature

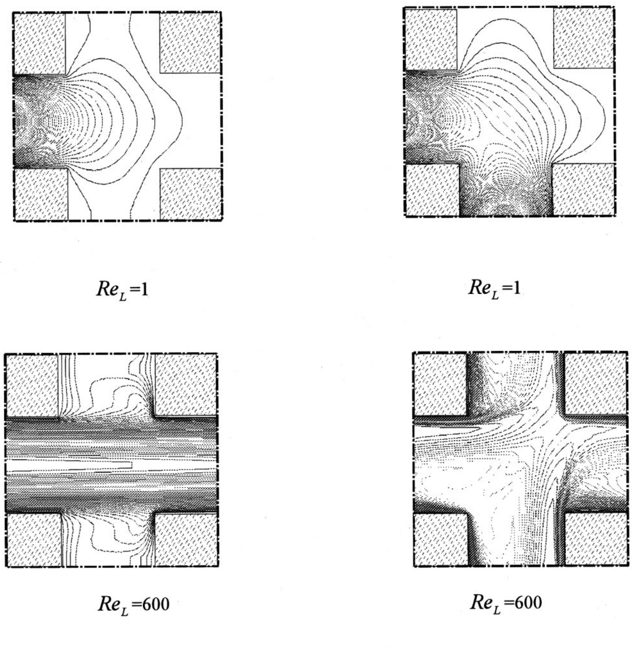

(*a*) (*b*)

Fig. 8 Isotherms ($H/L=1, \mathrm{Pr}_f=1$): (*a*) $\alpha=0$ deg and (*b*) $\alpha=45$ deg

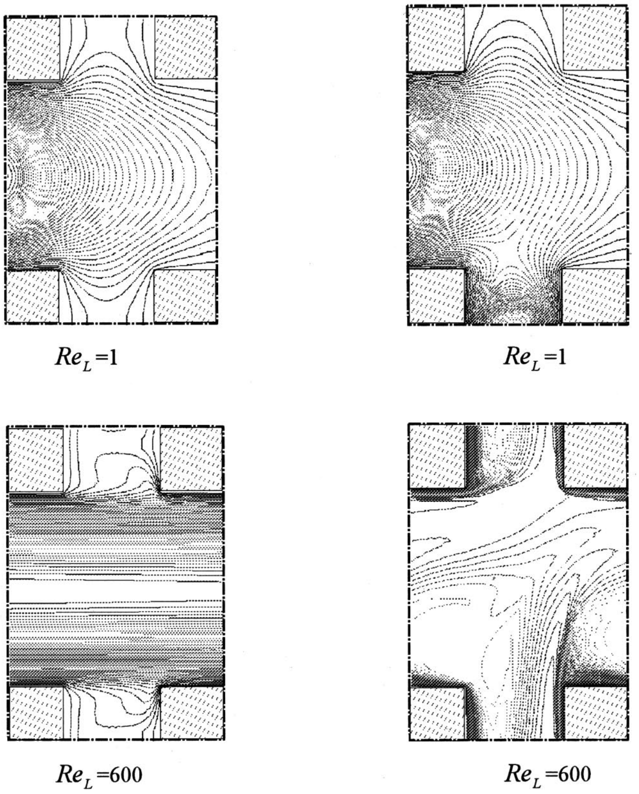

(*a*) (*b*)

Fig. 9 Isotherms ($H/L=3/2, \mathrm{Pr}_f=1$): (*a*) $\alpha=0$ deg and (*b*) $\alpha=45$ deg

pattern becomes very much complex. A thin thermal boundary layer covers over the windward surface of the rod, and it gets thicker over the leeward surface, as can be seen from Figs. 8 and 9, where comparatively uniform temperature fields prevail within recirculation regions.

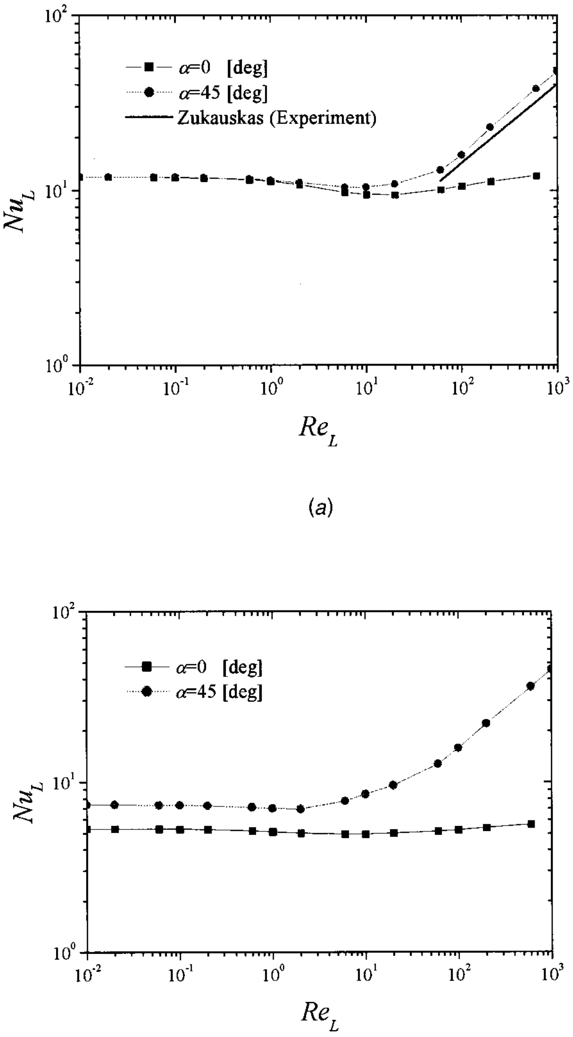

(*a*)

(*b*)

Fig. 10 Effect of Reynolds number on Nusselt number: (*a*) $H/L=1$ and (*b*) $H/L=3/2$

As demonstrated by Kuwahara et al. [11], the interfacial heat transfer coefficient may be obtained by substituting the microscopic temperature results into the following equation:

$$h_f \equiv \frac{\frac{1}{V}\int_{A_{\mathrm{int}}} k_f \nabla T \cdot d\vec{A}}{(\langle T\rangle^s - \langle T\rangle^f)} \tag{34}$$

A_{int} is the total interface between the fluid and solid, while $d\vec{A}$ is its vector element pointing outward from the fluid side to solid side.

The resulting values of the interfacial convective heat transfer coefficient h_f are presented in terms of the Nusselt number $\mathrm{Nu}_L = h_f L/k_f$ against Re_L in Fig. 10. The figure suggests that the lower and higher Reynolds number data follow two distinct limiting lines for the case of non-zero α. The lower Reynolds number data stay constant for the given array and flow angle, whereas the high Reynolds number data vary in proportion to $\mathrm{Re}_L^{0.6}$.

Another series of computations changing the Prandtl number, conducted following Kuwahara et al. [11], revealed that the exponents associated with the Reynolds and Prandtl numbers are the same as those Wakao and Kaguei [18] observed as collecting and

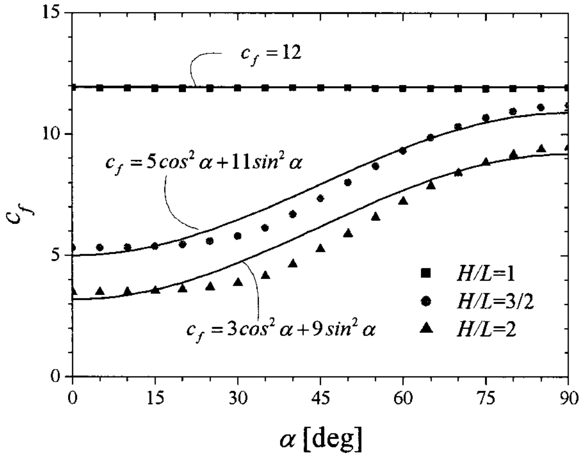

Fig. 11 Effect of α on the coefficient c_f

scrutinizing reliable experimental data on interfacial convective heat transfer coefficients in packed beds. The similarity, albeit the difference in the Reynolds number dependence, between the Nusselt number Nu_L (in Fig. 10) and the macroscopic pressure gradient (in Fig. 4) is noteworthy, which prompts us to model the directional Nusselt number as follows

$$\mathrm{Nu}_L \equiv \frac{h_f L}{k} = c_f + d_f \mathrm{Re}_L^{0.6} \mathrm{Pr}_f^{1/3} \tag{35}$$

As shown in Fig. 10(*a*), the results obtained for $\alpha = 45$ deg and $H/L = 1$ closely follow the experimental correlation obtained by Zukauskas [19] for the heat transfer from the circular tubes in staggered banks (i.e., Eq. (39) in Zukauskas [19] where $\mathrm{Nu}_f \cong \mathrm{Nu}_L/2$ and $\mathrm{Re}_f \cong \mathrm{Re}_L$ since $D/L = 1/2$).

Following the procedure similar to the one adopted for determining the directional permeability, the coefficient $c_f \equiv \mathrm{Nu}_L|_{\mathrm{Re}_L \to 0}$ for each macroscopic flow angle is evaluated and plotted in Fig. 11, using the low Reynolds number data. The similarity between c_f (Fig. 11) and L^2/K_{f_n} (Fig. 5) is obvious, which leads us to introduce a functional form as follow:

$$c_f = c_{f_1} \cos^2 \alpha + c_{f_2} \cos^2 \beta + c_{f_3} \cos^2 \gamma \tag{36}$$

Thus, for the two-dimensional case in consideration, it reduces to

$$c_f = c_{f_1} \cos^2 \alpha + c_{f_2} \sin^2 \alpha \tag{37}$$

The coefficient d_f, on the other hand, may be modeled as

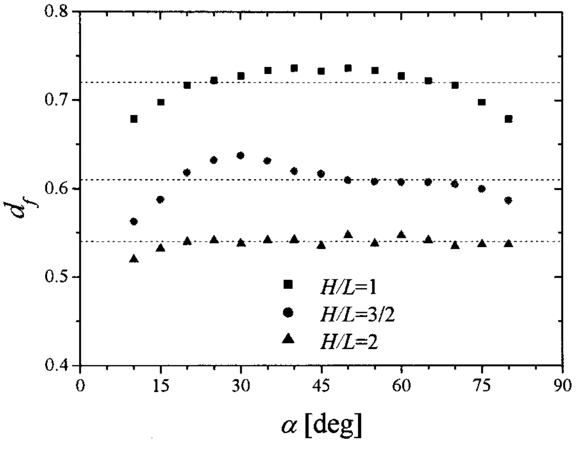

Fig. 12 Effect of α on the coefficient d_f

Table 3 Coefficients for directional Nusselt number

H/L (ϕ)	c_{f_1}	c_{f_2}	$d_f = d_{f_1}^{0.3}$
1 (0.750)	12	12	0.72
3/2(0.833)	5	11	0.61
2 (0.875)	3.2	9.2	0.54

$$d_f = (d_{f_1} \cos^2 \alpha + d_{f_2} \cos^2 \beta + d_{f_3} \cos^2 \gamma)^{0.3} \tag{38}$$

such that the effective velocity which takes account of the three-dimensional yaw effect conforms with the empirical expression used in the hot-wire anemometry

$$u_{\mathrm{eff}} \propto |\langle \vec{u} \rangle| (d_{f_1} \cos^2 \alpha + d_{f_2} \cos^2 \beta + d_{f_3} \cos^2 \gamma)^{1/2}$$

The coefficient d_f may be determined using the data $\mathrm{Nu}_L/\mathrm{Re}_L^{0.6}\mathrm{Pr}_f^{1/3}$ in the high Reynolds number range. The resulting values of d_f are presented in Fig. 12. Unlike the Forchheimer coefficient b_{f_n}, the coefficient d_f stays roughly constant for almost all the macroscopic flow angles, indicating $d_{f_1} \cong d_{f_2}$ for this collection of square rods. However, for the cases of $\alpha = 0$ and $\pi/2$ (in which the fluid flows along the principal axis of the structure), the coefficient d_f drops abruptly to zero. It can be confirmed from Fig. 10 that the Nusselt number for the case of $\alpha = 0$ remains at the same level as c_f even for the high Reynolds number range such that $d_f \cong 0$. (Note that this is analogous to the case of fully-developed channel flow. However, in reality, the macroscopic flow direction rarely coincides with the principal axes, since even small disturbances at a sufficiently high Reynolds number make the flow deviate from the axis.) This insensitivity of Nu_L to α in the high Reynolds number range may be attributed to the thermal dispersion, namely, the enhanced mechanical dispersion due to the presence of obstacles, which makes the temperature field fairly insensitive to the macroscopic flow angle α. Thus, for the two-dimensional case in consideration, the directional Nusselt number may be given by

$$\mathrm{Nu}_L = c_{f_1} \cos^2 \alpha + c_{f_2} \sin^2 \alpha + d_{f_1}^{0.3} \mathrm{Re}_L^{0.6} \mathrm{Pr}_f^{1/3} \tag{39a}$$

or

$$\mathrm{Nu}_D = \frac{1}{2}(c_{f_1} \cos^2 \alpha + c_{f_2} \sin^2 \alpha) + \frac{d_{f_1}^{0.3}}{2^{0.4}} \mathrm{Re}_D^{0.6} \mathrm{Pr}_f^{1/3} \tag{39b}$$

Naturally, the coefficients in the foregoing model equation depend on that particular geometrical configuration of the subscale structure. The values obtained using the present model for $H/L = 1$, 3/2, and 2 are listed in Table 3.

Concluding Remarks

In this study, we have established a systematic modeling procedure to describe the macroscopic pressure gradient and interfacial heat transfer coefficient needed in the macroscopic transport equations for analyzing fluid flow and local thermal non-equilibrium heat transfer within an anisotropic porous medium. We may utilize the resulting expressions for the macroscopic hydrodynamic and thermal tensors to conduct macroscopic calculations for fluid flow and non-local thermal equilibrium heat transfer through complex manmade structures, using the macroscopic equations based on VAT. Nakayama et al. [20] have recently proposed such macroscopic energy equations based on Hsu's closure model [21]. In order to apply these macroscopic equations to practical problems, both mechanical dispersion tensor and tortuosity tensor must be modeled accordingly. Such investigations for anisotropic porous media are underway.

Nomenclature

$\vec{A}$ = surface area vector
A_{int} = total interface between the fluid and solid
$b_{f_{ij}}, b_{f_n}$ = Forchheimer tensor, directional Forchheimer coefficient
c_{p_f} = specific heat at constant pressure
c_f, d_f = coefficients associated with Nusselt number
D = size of square rod
H, L = size of structural unit
h_f = interfacial convective heat transfer coefficient
$K_{f_{ij}}, K_{f_n}$ = permeability tensor, directional permeability
u, v = microscopic velocity components in the x and y directions
T = microscopic temperature
p = microscopic pressure
k = thermal conductivity
Re_L = Reynolds number based on L and the macroscopically uniform velocity
Re_D = Reynolds number based on D and the macroscopically uniform velocity
V = elementary representative volume
x, y = Cartesian coordinates
α, β, γ = angles between the macroscopic velocity vector and principal axes
ν = kinematic viscosity
ρ = density
μ = viscosity
ϕ = porosity

Subscripts and superscripts

f = fluid
s = solid

Special symbols

$\langle\ \rangle$ = volume-average
$\langle\ \rangle^{f,s}$ = intrinsic average

References

[1] Cheng, P., 1978, ‘‘Heat Transfer in Geothermal Systems,’’ Adv. Heat Transfer, **14**, pp. 1–105.
[2] Quintard, M., and Whitaker, S., 1993, ‘‘One and Two Equation Models for Transient Diffusion in Two-Phase Systems,’’ Adv. Heat Transfer, **23**, pp. 269–464.
[3] Kaviany, M., 1995, *Principles of Heat Transfer in Porous Media*, 2nd ed., Springer Verlag, New York.
[4] Nield, D. A., and Bejan, A., 1998, *Convection in Porous Media*, Springer-Verlag, New York.
[5] Vafai, K., 2000, *Handbook of Porous Media*, Marcel Dekker, Inc., New York.
[6] Nakayama, A., Kuwahara, F., Naoki, A., and Xu, G., 2001, ‘‘A Three-Energy Equation Model Based on a Volume Averaging Theory for Analyzing Complex Heat and Fluid Flow in Heat Exchangers,’’ *Proc. Int. Conf. Energy Conversion and Application*, Wuhan, China, (ICECA'2001), pp. 506–512.
[7] DesJardin, P. E., 2001, private communication.
[8] Kuwahara, F., Nakayama, A., and Koyama, H., 1994, ‘‘Numerical Modeling of Heat and Fluid Flow in a Porous Medium,’’ *Proc. 10th Int. Heat Transfer Conf.*, **5**, pp. 309–314.
[9] Nakayama, A., and Kuwahara, F., 2000, ‘‘Numerical Modeling of Convective Heat Transfer in Porous Media Using Microscopic Structures,’’ *Handbook of Porous Media*, Vafai, K. ed., Marcel Dekker, Inc., New York, pp. 441–488.
[10] Nakayama, A., and Kuwahara, F., 1999, ‘‘A Macroscopic Turbulence Model for Flow in a Porous Medium,’’ ASME J. Energy Resour. Technol., **121**, pp. 427–433.
[11] Kuwahara, F., Shirota, M., and Nakayama, A., 2001, ‘‘A Numerical Study of Interfacial Convective Heat Transfer Coefficient in Two-Energy Equation Model for Convection in Porous Media,’’ Int. J. Heat Mass Transf., **44**, pp. 1153–1159.
[12] Nakayama, A., Kuwahara, F., Kawamura, Y., and Koyama, H., 1995, ‘‘Three-Dimensional Numerical Simulation of Flow Through a Microscopic Porous Structure,’’ *Proc. ASME/JSME Thermal Engineering Conf.*, **3**, pp. 313–318.
[13] Patankar, S. V., and Spalding, D. B., 1972, ‘‘A Calculation Procedure for Heat, Mass and Momentum Transfer in Three-Dimensional Parabolic Flows,’’ Int. J. Heat Mass Transf., **15**, pp. 1787–1806.
[14] Patankar, S. V., 1980, *Numerical Heat Transfer and Fluid Flow*, Hemisphere, Washington, DC.
[15] Nakayama, A., 1995, *PC-Aided Numerical Heat Transfer and Convective Flow*, CRC Press, pp. 177–250.
[16] Forchheimer, P. H., 1901, ‘‘Wasserbewegung durch Boden,’’ Z. Ver. Dtsch. Ing., **45**, pp. 1782–1788.
[17] Dullien, F. A. L., 1979, *Porous Media: Fluid Transport and Pore Structure*, Academic Press, pp. 215–219.
[18] Wakao, N., and Kaguei, S., 1982, *Heat and Mass Transfer in Packed Beds*, Gorden and Breach Sci. Publishers, New York, pp. 243–295.
[19] Zukauskas, A., 1987, ‘‘Heat Transfer from Tubes in Crossflow,’’ Adv. Heat Transfer, **18**, pp. 87–159.
[20] Nakayama, A., Nakayama, A., and Xu, G., 2001, ‘‘A Two-Energy Equation Model in Porous Media,’’ Int. J. Heat Mass Transf., **44**, pp. 4375–4379.
[21] Hsu, C. T., 1999, ‘‘A Closure Model for Transient Heat Conduction in Porous Media,’’ ASME J. Heat Transfer, **121**, pp. 733–739.

M. Belghazi
Research Student,
Groupement pour la Recherche sur les
Echangeurs Thermiques (GRETh),
CEA Grenoble,
17, avenue des martyrs,
38054 Grenoble cedex 9, France

A. Bontemps
Professor,
Laboratoire des Ecoulements Géophysiques et
Industriels (LEGI/GRETh),
Université Joseph Fourier,
Grenoble, France,
CEA Grenoble, 17, avenue des martyrs,
38054 Grenoble cedex 9, France
e-mail: andre.bontemps@cea.fr

C. Marvillet
Research Engineer,
Groupement pour la Recherche sur les
Echangeurs Thermiques (GRETh),
CEA Grenoble,
17, avenue des martyrs,
38054 Grenoble cedex 9, France

Condensation Heat Transfer on Enhanced Surface Tubes: Experimental Results and Predictive Theory

Condensation heat transfer in a bundle of horizontal enhanced surface copper tubes (Gewa C+ tubes) has been experimentally investigated, and a comparison with trapezoidal shaped fin tubes with several fin spacing has been made. These tubes have a specific surface three-dimensional geometry (notched fins) and the fluids used are either pure refrigerant (HFC134a) or binary mixtures of refrigerants (HFC23/HFC134a). For the pure fluid and a Gewa C+ single tube, the results were analyzed with a specifically developed model, taking into account both gravity and surface tension effects. For the bundle and for a pure fluid, the inundation of the lowest tubes has a strong effect on the Gewa C+ tube performances contrary to the finned tubes. For the mixture, the heat transfer coefficient decreases dramatically for the Gewa C+ tube.

[DOI: 10.1115/1.1459728]

Keywords: Bundles, Condensation, Finned Surfaces, Zeotropic Mixture, Horizontal Tubes

Introduction

A large number of specifically designed enhanced surface tubes have been tested to find the best surface geometry for condensing either pure fluids or vapor mixtures. These surfaces can be classified according to three types: one-dimensional surfaces (smooth tubes), two-dimensional surfaces (with transverse plain fins) and three-dimensional surfaces (with interrupted fins, spines, etc . . .). Theoretical models to predict the heat transfer coefficient for single low-finned tubes with trapezoidal (or rectangular) fins have been well developed since the 1940s, in particular by the pioneering work of Beatty and Katz [1]. Their model assumed that condensate is drained via gravity only. They neglected surface tension forces, which generally have an important role at the fin tip, since they are responsible for the draining of condensate from the tip to the fin flanks, and because the major part of heat transfer occurs at the fin tip. The surface tension forces also have a non-beneficial effect due to condensate retention along the underside of the tube. Theoretical models combining both gravity and surface tension forces, are used to predict the Heat Transfer Coefficient (HTC) of a single horizontal tube with sufficient accuracy (Karkhu and Borovkov [2], Webb et al. [3], Honda and Nozu [4], Adamek and Webb [5], Rose [6], Sreepathi et al. [7]). The most simple proposed by Rose [6], is a semi-empirical model for a horizontal tube having trapezoidal fins. An enhancement ratio $\varepsilon_{\Delta T}$ is defined as the ratio of the heat transfer coefficient for a finned tube to that for a plain tube, based on plain tube area at the fin root diameter for the same ΔT ($\Delta T = T_{\text{sat}} - T_w$). To compare his model to experimental results, Rose used various finned tubes with different pitches, heights and diameters as well as various fluids (water, ethylene glycol, methanol, R113, R11, R12 . . .).

Since the work of Gregorig, [8], many theoretical studies to optimize the fin profiles of two-dimensional circumferential fins have been carried out. Adamek [9] in his theoretical approach assumed the condensate to be drained by surface tension forces only and showed that around the fin crest the best heat transfer is given by a profile curvature depending on the path length at a power of -0.5 instead of 2.0 as proposed by Gregorig. More recently, Zhu and Honda [10] and Honda and Kim [11] have performed numerical calculations to optimize the fin profiles of two-dimensional circumferential fins.

There are other numerical approaches to optimize enhanced surfaces. Honda and Makishi [12] in a two dimensional adaptation showed that by creating a circumferential rib on a fin, the values of the HTC can be 27 to 58 percent higher than the best performing fin profile proposed in the previous studies. Further three-dimensional adaptations to extended surfaces have been carried out. The first systematic investigation was by Webb et al. [13] but does not allow a conclusive opinion to be drawn. Honda et al. [14,15] compared the heat transfer performance of several two-dimensional and three-dimensional fin geometries. Their results showed that the heat transfer performance of the best two-dimensional and those of the tested three-dimensional tubes are comparable. A specific type of three-dimensional fin was realized by Wang et al. [16] by creating radial ridges on the fin flanks. They found that the heat transfer performance was 30 to 40 percent higher than commercially available three-dimensional fin tubes.

The results obtained for a single tube cannot be extended to a tube bundle and a fin profile optimized for a single tube can be non-optimized for a tube bundle making, these models for a single tube inapplicable to tube banks, since the heat transfer in the lower rows is affected by condensate inundation and the HTC is lower for these tubes. It has been shown that, in this case, three-dimensional geometries are not favorable (Webb and Murawski [17], Honda et al. [14,15]). In the literature there are several approaches to this problem. The simplest consists of multiplication of the heat transfer for a single tube by a factor less than unity, taking into account the row position in the bundle.

In this paper, experiments were carried out to determine the HTC during condensation of R134a and a zeotropic mixture of R23 and R134a, on horizontal tubes with three-dimensional enhanced surfaces. A new type of notched fin tube (called Gewa C+ tube) has been studied and the results have been compared to those obtained for smooth tubes or integral-fin tubes with trapezoidal fins. This notched tube can be considered as a combination

---

Contributed by the Heat Transfer Division for publication in the JOURNAL OF HEAT TRANSFER. Manuscript received by the Heat Transfer Division January 25, 2001; revision received October 30, 2001. Associate Editor: M. K. Jensen.

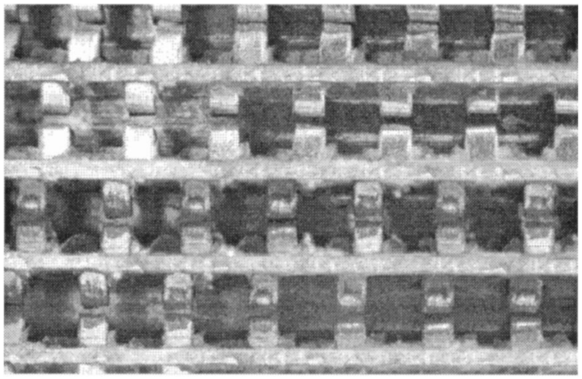

Fig. 1 Optical microscope view of a notched fin tube (Gewa C+)

of the enhanced tube with a circumferential rib (Honda and Kim [11]) with the tube having radial ridges on the fin flank (Wang et al. [16]). The notches seen in Fig. 1 can be considered as part of a rib and the space between notches as radial ridges. One can expect that such a fin geometry will be efficient in condensation heat transfer.

There are few experiments on condensation of HFC134a on low finned tubes. In the work of Blanc et al. [18] the HTC on trapezoidal fin tubes (K26) is compared with another type of finned tube as well as with current theories. Honda et al. [19] measured the row-by-row heat transfer coefficients of HFC134a condensing on a bundle of tubes having 26 fins/inch and a diameter at the fin root of 15.8 mm. Their results are slightly lower than those of Blanc et al., Cheng and Wang [20], and Agrawal et al. [21] conducted experiments on condensation of HFC134a using several types of low finned tubes. For a vertical column of three tubes with trapezoidal fins no significant inundation effect is observed [20]. The variation of the HTC in function of ΔT for a single tube was carried out by Agrawal et al. [21].

Studies covering the condensation of zeotropic mixtures are essentially confined to flat plates and smooth tubes. Hijikata and Himeno [22] conducted experiments using horizontal finned tubes during condensation of the binary mixture (90 percent R113+ 10 percent R114), and they found that the tube with high fins (3 mm) is better than the one with small fins (0.8 mm). Honda et al. [23] conducted experiments during condensation of a downward-flowing zeotropic mixture HFC123/HFC134a (about 9 percent HFC134a at the test section inlet), on a 13×15 (columns ×rows) staggered bundle of horizontal low finned tubes. Their experimental data show that both the heat and the mass transfer coefficients increased with the row number up to the third (or the second) row, then decreased monotonically with increasing row number, finally to increase at the last row.

Experimental Apparatus and Reduction of Data

The experimental apparatus consists of a thermosyphon refrigerant loop and a forced circulation coolant (water) loop (Fig. 2). The test rig used in this investigation is basically the same as that used in the previous study by Belghazi et al. [24].

In the refrigerant loop the vapor is generated in a boiler heated with hot water which is itself heated electrically. The vapor flows towards the test section, passes vertically downwards and condenses outside the water cooled tubes. The test section (Fig. 3) is a stainless steel duct and contains a staggered copper tube bank consisting of 13 rows, each of 2 (even rows) or 3 tubes (odd rows). The cross-hatched tubes are dummies (no heat exchange), while the others are active. Half tubes are attached to the vertical walls of the test section in order to eliminate vapor by-pass. A metallic rod with a diameter of 11 mm was inserted in each active tube in order to increase the water velocity. In this way the heat transfer is enhanced on the coolant side. The horizontal tube pitch is 24 mm, whereas the vertical pitch is 20 mm. The length of the tubes is 300 mm. The characteristics of the tested tubes are given in Table 1. Since the water flow rate is equally distributed in all active tubes (it is controlled by means of 13 rotameters, one on each row), it is deduced from the water flow rate in the coolant loop, measured by an electromagnetic flow meter, with an accuracy of ±0.5 percent. The vapor velocity is less than 2 m/s and the vapor temperature inlet was maintained at 40°C. Temperatures were measured by type E thermocouples (Chromel-Constantan) with a precision of ± 0.05°C. The vapor temperature is measured by five thermocouples (T06, T07, T08, T09, and T10) in the test section. These thermocouples indicate the same temperatures (T_{sat}) during the condensation of HFC134a, in contrast to the condensation of HFC23/HFC134a, where the vapor temperature decreases from the inlet to the outlet of the test section. The temperatures indicated by the five thermocouples are interpolated in order to obtain the vapor temperature in the neighborhood of each row.

In this study, commercial tubes (Wieland-Werke AG) are used, having a wall thickness of about 1 mm. An indirect Wilson plot method which measures the vapor-side heat transfer coefficient without measuring the wall temperature is employed.

From the measured water temperatures in the mixing chambers at the inlet and the outlet of each tube and from the measured vapor temperature in the neighborhood of each row, the overall HTC is calculated as follows:

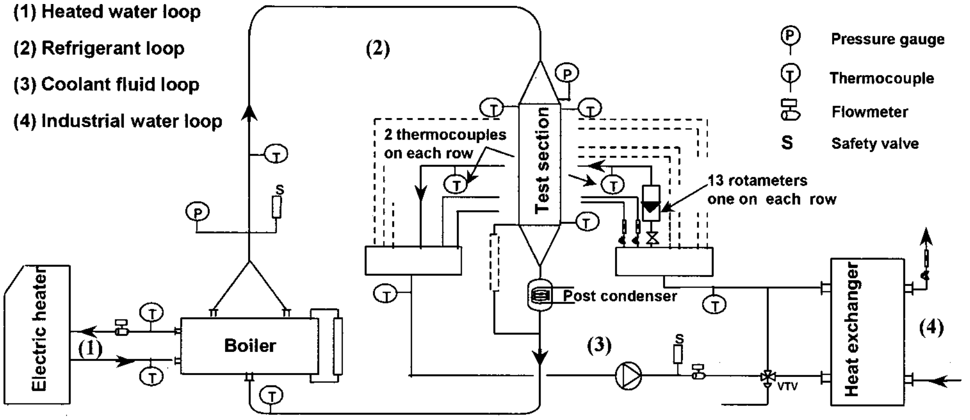

Fig. 2 Test rig

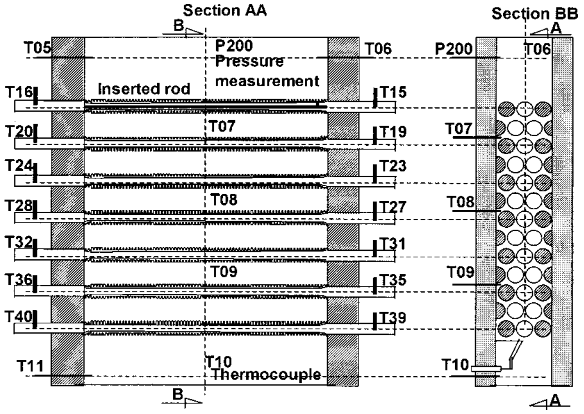

Fig. 3 Test section

Table 1 Tube dimensions (mm). See nomenclature for definitions. (The uncited dimensions are proprietary.)

Tube	*Dr*	*De*	*Di*	*p*	*h*	*t*
smooth	16.8	16.8	14.2	---	---	---
K11	16	18.9	14	2.31	1.45	0.38
K19	16	18.9	14	1.34	1.45	0.33
K26	15.8	18.8	14	0.97	1.5	0.25
K32	16.2	18.8	14	0.82	1.3	0.2
K40	16.3	18.9	14.4	0.635	1.3	0.16
Gewa C+	17	---	14	---	---	---

$$U=\frac{\dot{m}_c C_{p,c}}{\pi D_r L_{\text{tube}}}\mathrm{Ln}\left(\frac{T_{v,j}-T_{c,j,\text{in}}}{T_{v,j}-T_{c,j,\text{out}}}\right) \tag{1}$$

where j refers to the row number, c to the cooling water, v to the vapor, *in* and *out* to the cooling water input and output respectively. The reference area is that outside a bare tube, D_r being either the external diameter of a smooth tube or the diameter at the fin root for enhanced tubes.

The vapor-side HTC, α_e, is calculated via the following relation:

$$\frac{1}{\alpha_e}=\frac{1}{U}-\frac{1}{\alpha_i}\frac{D_r}{D_i}-\frac{D_r}{2\lambda_w}\ln\left(\frac{D_r}{D_i}\right) \tag{2}$$

α_i is the inner heat transfer coefficient determined with the Gnielinski correlation (Gnielinski [25]):

$$\mathrm{Nu}_G=\frac{(f/2)(\mathrm{Re}_c-1000)\mathrm{Pr}_c}{1+12.7(f/2)^{1/2}(\mathrm{Pr}_c^{2/3}-1)} \tag{3}$$

where f is the friction factor determined from the following expression:

$$f=(1.58\ \mathrm{Ln}(\mathrm{Re}_c)-3.28)^{-2} \tag{4}$$

Re_c is the hydraulic Reynolds given by:

$$\mathrm{Re}_c=\frac{\rho_c\dot{V}_c D_h}{\mu_c} \tag{4-bis}$$

The Gnielinski correlation has been chosen because it has a wide range of applicability, $2300<\mathrm{Re}_c<5\ 10^6$ and $0.5<\mathrm{Pr}_c<2000$. Thus, it covers both the transition and the turbulent flow regimes. In our case, the Reynolds number was varied between 2,400 and 12,000.

The inner HTC α_i is expressed as:

Table 2 *B* values

Tube	Gewa C+	K40	K32	K26	K19	K11
B	1.07	1.19	0.99	0.98	1.08	0.92

$$\alpha_i=B\cdot\mathrm{Nu}_G\cdot\frac{\lambda_C}{D_h} \tag{5}$$

where the coefficient B is determined by the Wilson plot procedure (Wilson [26]). To determine the B coefficient a specific loop was built with a water/water countercurrent double pipe heat exchanger. The inner tube is the same as used in the condensation experiments. To enhance the accuracy on the α_i value, the outer HTC in this specific loop was maintained to a high value. The uncertainty δB was determined using Moffat's method [27]. Table 2 gives the B values for all tubes tested.

The relative uncertainty of the vapor-side HTC is strongly depending on the experimental conditions. For example, for condensation on the first row the uncertainties are less than 20 percent, 17 percent, 21 percent, 17 percent, 14 percent, and 15 percent for the K11, K19, K26, K32, K40, and Gewa C+, respectively. For the whole bundle, the uncertainties are reported on the figures. Details of the uncertainty calculations are given in the appendix.

Experimental Results

Pure Fluid (HFC 134a)

Single Tube. Figure 4 shows the evolution of the HTC of the first row with temperature difference ΔT, during condensation of pure HFC134a on all tubes tested and on a smooth tube (Belghazi et al. [24]). It can be seen that K32 has the best performance compared to the other trapezoidal fin tubes. A fin spacing of about 0.6 mm is then an optimum in order to have the best heat transfer coefficient during condensation of HFC134a. The notched fin tube presents a better HTC than the K32 tube, because notches located at the middle of the fin height enhance surface tension effects at the fin tip. The film condensate is thinner and heat transfer performances are better.

To predict the Gewa C+ HTC a theoretical model based on the Nusselt approach but taking the surface tension into account, has been developed.

Tube Bundle. Figure 5 shows the evolution of the heat transfer coefficient along the bundle. It can be seen that the inundation effect (impinging of deep rows by condensate flowing from upper rows) is important for Gewa C+ tubes in contrast to trapezoidal fin tubes (Signe, [28]) where the deterioration of the HTC is not important. It is also noticed that the higher the vapor mass velocity G, the greater the Gewa C+ HTC deterioration in the tube

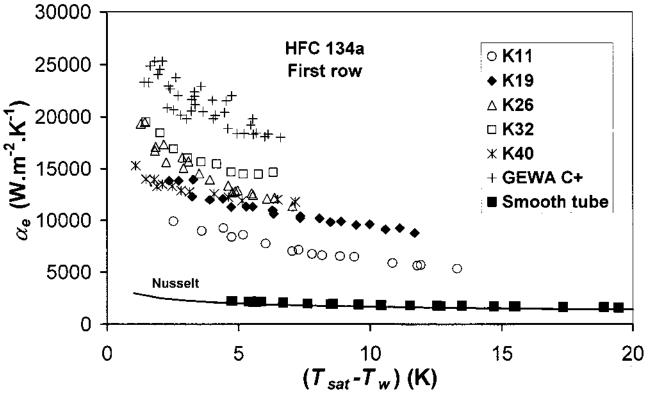

Fig. 4 Heat transfer coefficient of the first row during condensation of HFC134a

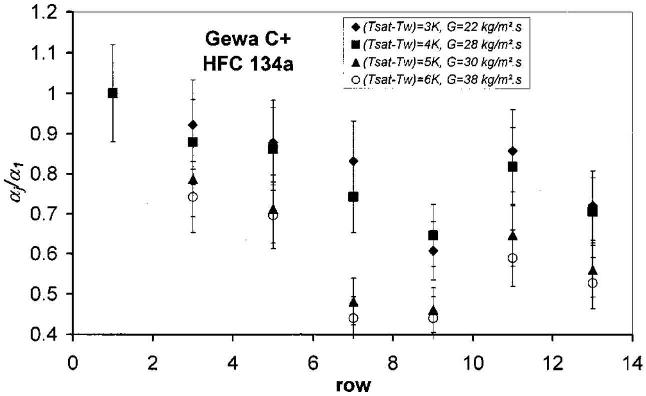

Fig. 5 Evolution of the Gewa C+ HTC along the bundle during condensation of HFC 134a

bundle, in contrast to the integral fin tubes where the deterioration of the HTC is more important when G decreases (Belghazi, [29]). Indeed, the Gewa C+ has low notched fins and retains condensate formed on the upper rows. Then, even if the vapor mass velocity increases, the inundation effect controls the heat transfer because the condensate flow increases also.

Mixtures

Single Tube. Figure 6 shows the evolution of the HTC during condensation of two mixtures (3 percent and 6 percent HFC23) of HFC23/HFC134a on K19 and Gewa C+ tubes. A deterioration of the mixture HTC is noted due to the mass transfer induced by the more volatile component (HFC23) which accumulates in the liquid-vapor interface and constitutes a diffusion layer which acts as a thermal resistance. Such deterioration has been also observed by Hijikata and Hemino [22], who measured the vapor-side HTC during condensation of R113 and several compositions of the mixture R113/R114.

Contrary to the case of the pure fluid it can be seen from Fig. 6 that the Gewa C+ has a HTC comparable to that of the K19 tube. Indeed, as the Gewa C+ tube has low fins compared to the other fin tubes, its fins are flooded by the diffusion layer (Fig. 7), and performance is poorer. For 6 percent HFC 23 and for low ΔT's, where the diffusion layer controls the heat transfer, the K19 and Gewa C+ HTC values tend to the smooth tube HTC values, since the diffusion layer is very thick and screens the fins. The finned tube is seen as a smooth tube.

Tube Bundle. During condensation of mixture outside the Gewa C+ bundle the HTC may increase or decrease from the top to the bottom of the tube bank, depending on the heat flux (Fig. 8). Such effects have already been observed by Signe [28] who noted that the HTC on a bundle of smooth tubes increases throughout the bundle. This effect was explained by the fact that the condensate formed on upper rows disturbs the diffusion layer, which gives an amelioration of the heat transfer.

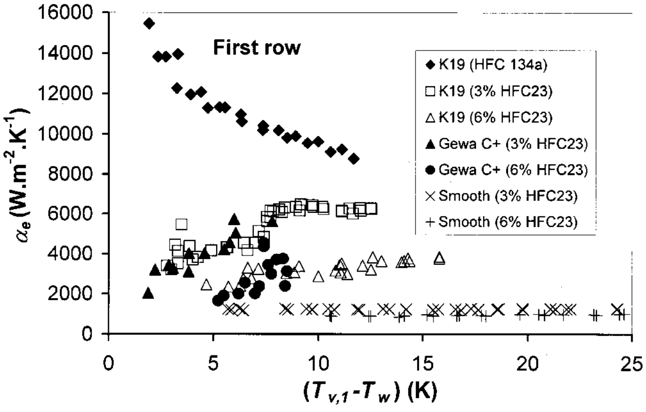

Fig. 6 Evolution of mixture HTC on Gewa C+ and K19 tubes

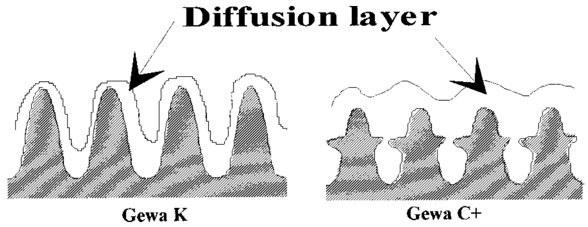

Fig. 7 Flooding of fins by the gaseous diffusion layer

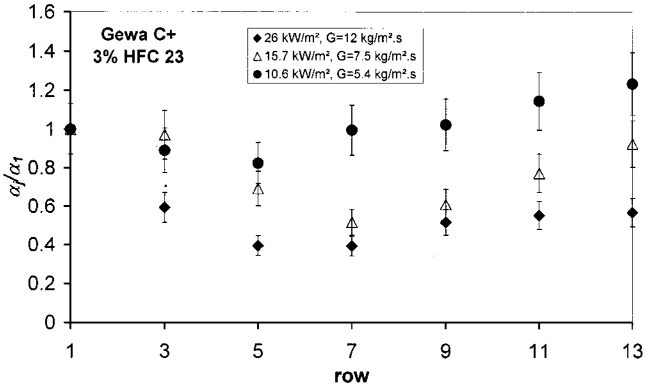

Fig. 8 Evolution of the ratio α_j/α_l as a function of the row number

Theoretical Model

As shown in Fig. 9, the Beatty and Katz model [1] underestimates the HTC of the Gewa C+ tube, because it neglects the surface tension effects which are enhanced by notches located at the fin flanks (Fig. 11). To develop a model predicting the HTC on the Gewa C+ tube, the tube circumference is divided into a flooded and an unflooded part.

The flooded part located at the bottom of the tube is referred to as an area submerged completely by the condensate because of capillary retention. It is assumed that there is no heat transfer in this part of the tube. The retention angle Φ (Fig. 10) is calculated by the Rudy and Webb equation [30]:

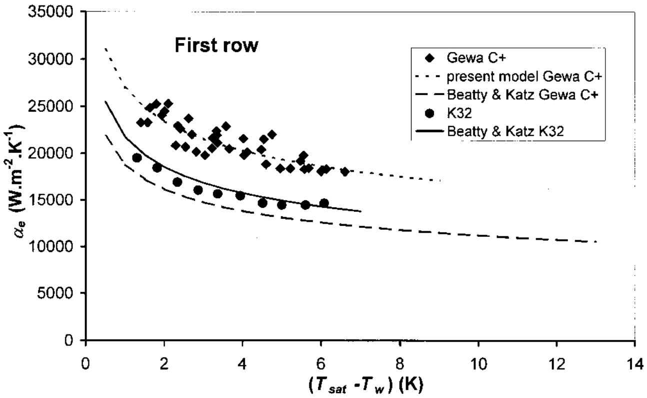

Fig. 9 Experimental and predicted HTC during condensation of HFC 134a on Gewa C+ and K32 tubes

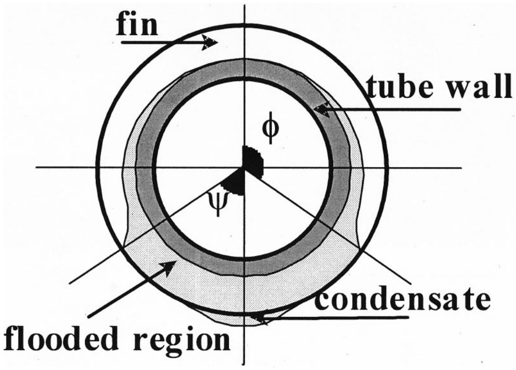

Fig. 10 Retention angle

$$\Phi = \cos^{-1}\left(\frac{4\sigma}{\rho_l g b D_e} - 1\right) \tag{6}$$

The unflooded region is divided into four regions:

- region I: referred as the upper part of the fin, located above the notches
- region II: fin area beneath notches
- region III: fin area located between notches
- region IV: the interfin channel

It is assumed that the condensate is drained by surface tension in regions I and III, and by gravity in regions II and IV.

The model is based on the Nusselt expressions for condensation on a vertical plate (Eq. (7)), and on horizontal smooth tubes (Eq. (8))

$$\alpha_{\text{plate}} = 0.943\left(\frac{\lambda_l^3 \rho_l(\rho_l - \rho_v) g \Delta h_v}{\mu_l (T_{\text{sat}} - T_w) L}\right)^{1/4} \tag{7}$$

$$\alpha_{\text{tube}} = 0.728\left(\frac{\lambda_l^3 \rho_l(\rho_l - \rho_v) g \Delta h_v}{\mu_l (T_{\text{sat}} - T_w) D}\right)^{1/4}. \tag{8}$$

where L and D are plate length and tube diameter, respectively.

For regions I and III where only surface tension forces drain condensate, Nusselt's expression (Eq. (7)) is modified by replacing $\rho_l g$, which is a gravity volume force, by an equivalent in terms of surface tension.

Generally the condensation of a fluid having a liquid-vapor interface radius (see Fig. 12) which varies along the wall, induces a pressure variation along that interface. An expression for this was given by (Gregorig, [7]):

$$\frac{dP_l}{ds} = \frac{d(\sigma/r)}{ds} \tag{9}$$

In term of a volume force Eq. (9) can be written:

$$dF_\sigma = \sigma \frac{d(1/r)}{ds} dV \tag{10}$$

where dV is a condensate volume control.

For a condensate film surface having two different radii r_t and r_b as shown in Fig. 12, the curvature derivative can be written as:

$$\frac{d(1/r)}{ds} \approx \frac{1}{h}\left(\frac{1}{r_b} - \frac{1}{r_t}\right) \tag{11}$$

where h is the fin height.

This nevertheless represents a strong assumption, which will be justified a posteriori.

Combining Eq. (10) and (11) gives:

$$\frac{dF_\sigma}{dV} \approx \frac{\sigma}{h}\left(\frac{1}{r_b} - \frac{1}{r_t}\right) \tag{12}$$

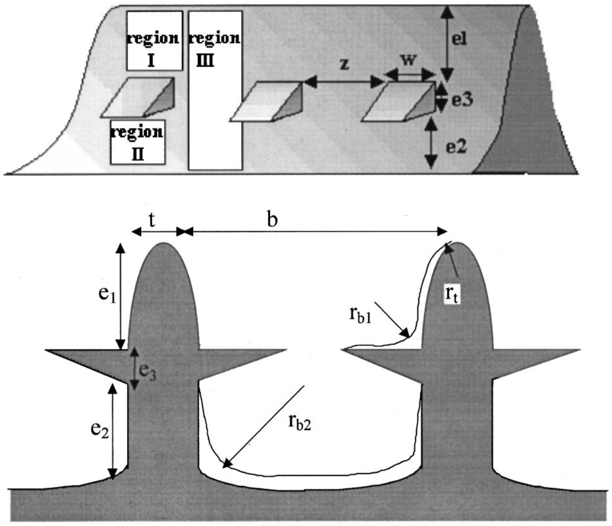

Fig. 11 The shape of the Gewa C+ tube. Definitions of parameters used

The Gewa C+ HTC, calculated with reference to the surface of tube having D_r as a diameter, is a function of the HTCs of regions I, II, III, and IV and is given by:

$$\alpha_p A_r = \eta(\alpha_{\text{I}} A_{\text{I}} + \alpha_{\text{II}} A_{\text{II}} + \alpha_{\text{III}} A_{\text{III}}) + \alpha_{\text{IV}} A_{\text{IV}} \tag{13}$$

where η is the fin efficiency, given by:

$$\eta = \frac{\tanh(mh)}{mh} \tag{14}$$

with

$$m = \left(\frac{2\alpha_p}{\lambda_w t}\right)^{1/2} \tag{15}$$

α_p being determined by an iterative procedure.

Parameters given in Eq. (13) are defined as follows:

$$A_{\text{I}} = 2\frac{\Phi}{\pi} K w e_1 / p \tag{16}$$

$$A_{\text{II}} = 2\frac{\Phi}{\pi} K w e_2 / p \tag{17}$$

$$A_{\text{III}} = 2\frac{\Phi}{\pi} K z h / p = 2\frac{\Phi}{\pi} K z (e_1 + e_2 + e_3)/p \tag{18}$$

$$A_{\text{IV}} = 2\frac{\Phi}{\pi} K \pi D_r b / p \tag{19}$$

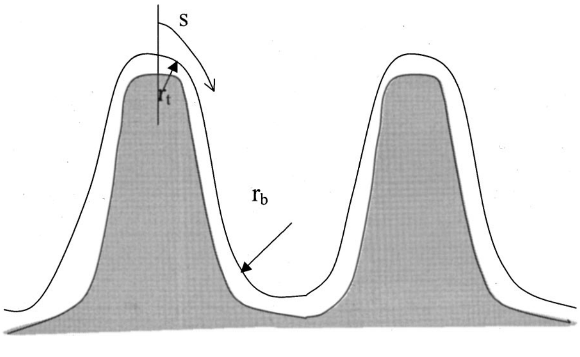

Fig. 12 Variation of the vapor interface radius

$$A_r = \pi D_r \, ,$$

where K is the number of elemental parts of the fin (region I, II, III plus notches. Fig. 11) on one side of a fin flank and p is the fin pitch.

Assuming that (Fig. 11):

$$r_t = t/2; \quad r_{b1} = -b/4; \quad r_{b2} = -b/2$$

the acting force in the region I is given by:

$$\left.\frac{dF_\sigma}{dV}\right|_{\text{Region I}} = \frac{\sigma}{e_1}\left(\frac{1}{r_t} + \frac{1}{r_{b1}}\right) = \frac{\sigma}{e_1}\left(\frac{2}{t} + \frac{4}{b}\right) \tag{20}$$

Substituting $\rho_l g$ in Eq. (7) by Eq. (20) leads to:

$$\alpha_{\text{I}} = 0.943\left(\frac{\lambda_l^3(\rho_l - \rho_\nu)\Delta h_\nu}{\mu_l(T_{\text{sat}} - T_w)e_1}\right)^{1/4}\left(\frac{\sigma}{e_1}\left(\frac{2}{t} + \frac{4}{b}\right)\right)^{1/4} \tag{21}$$

In the same manner in region III:

$$\left.\frac{dF_\sigma}{dV}\right|_{\text{Region III}} = \frac{\sigma}{h}\left(\frac{1}{r_t} + \frac{1}{r_{b2}}\right) = \frac{2\sigma}{h}\left(\frac{1}{t} + \frac{1}{b}\right) \tag{22}$$

$$\alpha_{\text{III}} = 0.943\left(\frac{\lambda_l^3(\rho_l - \rho_\nu)\Delta h_\nu}{\mu_l(T_{\text{sat}} - T_w)h}\right)^{1/4}\left(\frac{2\sigma}{h}\left(\frac{1}{t} + \frac{1}{b}\right)\right)^{1/4}. \tag{23}$$

In region II, the condensate is drained by gravity and the HTC is given by:

$$\alpha_{\text{II}} = 0.943\left(\frac{\lambda_l^3\rho_l(\rho_l - \rho_\nu)g\Delta h_\nu}{\mu_l(T_{\text{sat}} - T_w)e_2}\right)^{1/4} \tag{24}$$

The HTC in the interfin channel is given using Eq. (8) by:

$$\alpha_{\text{channel}} = 0.728\left(\frac{\lambda_l^3\rho_l(\rho_l - \rho_\nu)g\Delta h_\nu}{\mu_l(T_{\text{sat}} - T_w)D_r}\right)^{1/4} \tag{25}$$

The condensate formed on fins is collected within the interfin channel, so that the actual HTC corresponding to the region IV is smaller than the one calculated by Eq. (25) since film condensate is thicker. To take this phenomenon into account another version of the Nusselt formula is used (Eq. (26)):

$$\alpha_{\text{IV}} = 1.51\,\text{Re}_f^{-1/3}\left(\frac{\nu_l^2}{\lambda_l^3 g}\right)^{-1/3} \tag{26}$$

where

$$\text{Re}_f = 4\,\frac{\Gamma}{\mu_l} \quad \text{and} \quad \Gamma = \Gamma_{\text{channel}} + \Gamma_{\text{fin}}$$

$$\Gamma_{\text{channel}} = \frac{\alpha_{\text{channel}}(T_{\text{sat}} - T_w)A_{\text{IV}}}{\Delta h_\nu} \tag{27}$$

$$\Gamma_{\text{fin}} = \eta\,\frac{(\alpha_{\text{I}}A_{\text{I}} + \alpha_{\text{II}}A_{\text{II}} + \alpha_{\text{III}}A_{\text{III}})(T_{\text{sat}} - T_w)}{\Delta h_\nu} \tag{28}$$

Figure 9 shows that the present model predicts very accurately the Gewa C+ HTC, without adjusting any parameter. The deviation from experimental results is less than 10 percent.

Conclusion

The present investigation allows the following concluding remarks to be drawn:

- Experimental data for condensation of HFC134a on five commercially available copper integral fin tubes show an optimum fin spacing of about 0.6 mm.
- The Gewa C+ tube (notched tube) has been tested and gives an enhancement of about 30 percent compared to the best integral fin tubes (K32). Notches drawn on fin flanks enhance the surface tension effect. During condensation of HFC134a, the higher the vapor mass velocity, the greater the Gewa C+ HTC deterioration in the tube bundle. However, from an industrial point of view, the usual ΔT is about 3K, and in this case the inundation effect is not significant.
- For the mixtures, experimental results show that, due to the zeotropic character of the mixture tested (HFC23/HFC134a), the HTC deteriorates dramatically. Contrary to the pure fluid case, the Gewa C+ tube gives no enhancement compared to the K19 tube.
- The model developed for a single Gewa C+ tube, takes into account surface tension effects, and predicts accurately the present experimental data.
- Work is currently in progress to develop a model, based on the condensation curve method, predicting heat transfer during condensation of binary mixtures outside a bundle of Gewa C+.

Acknowledgment

The authors acknowledge with thanks Wieland-Werk AG for their contribution to this work.

Nomenclature

A = heat exchange surface area, m^2
A_r = surface of a plain tube, m^2
b = fin spacing, m
C_p = heat capacity, J kg^{-1} K^{-1}
D_0 = diameter of the metallic rod, m
D_e = diameter at the fin tip, m
D_h = hydraulic diameter, m
D_i = inner diameter, m
D_r = tube diameter at the fin root, m
e_1 = distance from fin tip to notch, m
e_2 = distance from notch to fin root, m
e_3 = thickness of a notch, m
f = friction factor
F = force, N
g = gravity, m s^{-2}
G = vapor mass velocity, kg m^{-2} s^{-1}
h = fin height, m
K = number of elemental parts on fin's flank
L = plate length, m
L_{tube} = tube length, m
$\dot{m}$ = mass flow rate, kg s^{-1}
p = fin pitch, m
P = pressure, Pa
$\dot{Q}$ = heat flow rate, W
r = curvature radius, m
r_{b1}, r_{b2}, r_t = curvature radii, m
s = curvilinear coordinate, m
t = fin thickness, m
T = temperature, K
U = overall heat transfer coefficient, W m^{-2} K^{-1}
$\dot{V}$ = volumetric flow rate, m^3 s^{-1}
w = notch width, m
z = space between notches, m

Greek

α_e = vapor side HTC, W m^{-2} K^{-1}
α_i = inner HTC, W m^{-2} K^{-1}
α_p = predicted HTC, W m^{-2} K^{-1}
ΔT = $(T_{\text{sat}} - T_w)$ or $(T_{\text{v,j}} - T_{\text{w}})$, K
Δh_ν = latent heat, J kg^{-1}
Γ = condensate lineic mass flow rate, kg s^{-1} m^{-1}
Φ = flooding angle, rad
λ = thermal conductivity, W m^{-1} K^{-1}
μ = dynamic viscosity, Pa s
ν = kinematic viscosity, m^2 s^{-1}
ρ = density, kg m^{-3}
σ = surface tension, N m^{-1}
η = fin efficiency

Indices

I, II, III, IV = region's index
c = coolant
e = external
f = film condensate
G = refers to Gnielinski
i = internal
in = water inlet
j = row index
l = liquid
out = water outlet
r = at fin root
t = fin tip
v = vapor
w = wall
σ = refers to surface tension

Dimensionless Numbers

Nu = Nusselt number
Pr = Prandtl number
Re = Reynolds number

Appendix

The single sample uncertainty of external heat transfer coefficient, $\delta\alpha_e$, is written as:

$$\bullet \quad \delta\alpha_e = \sqrt{\left(\frac{\partial\alpha_e}{\partial U}\,\delta U\right)^2 + \left(\frac{\partial\alpha_e}{\partial\alpha_i}\,\delta\alpha_i\right)^2} \tag{A-1}$$

where

$$\frac{\partial\alpha_e}{\partial U} = \frac{1}{U^2\left\{\frac{1}{U} - \frac{1}{\alpha_i}\frac{D_r}{D_i} - \frac{D_r}{2\lambda_w}Ln\left(\frac{D_r}{D_i}\right)\right\}^2} \tag{A-2}$$

and

$$\frac{\partial\alpha_e}{\partial\alpha_i} = -\frac{1}{\alpha_i^2\left\{\frac{1}{U} - \frac{1}{\alpha_i}\frac{D_r}{D_i} - \frac{D_r}{2\lambda_w}Ln\left(\frac{D_r}{D_i}\right)\right\}^2} \tag{A-3}$$

In the same way:

$$\bullet \quad U = \frac{\dot m_c C_p}{\pi D_r} Ln\left(\frac{T_\nu - T_{c,\mathrm{in}}}{T_\nu - T_{c,\mathrm{out}}}\right) \tag{A-4}$$

$$\delta U = \sqrt{\left(\frac{\partial U}{\partial \dot m_c}\,\delta\dot m_c\right)^2 + \left(\frac{\partial U}{\partial T_\nu}\,\delta T_\nu\right)^2 + \left(\frac{\partial U}{\partial T_{c,\mathrm{out}}}\,\delta T_{c,\mathrm{out}}\right)^2 + \left(\frac{\partial U}{\partial T_{c,\mathrm{in}}}\,\delta T_{c,\mathrm{in}}\right)^2} \tag{A-5}$$

The flowmeter used has a precision of 0.5 percent, and the thermocouples have an uncertainty of 0.05 K.

$$\bullet \quad \alpha_i = B\cdot \mathrm{Nu}_G\frac{\lambda_c}{D_h} \tag{A-6}$$

$$\delta\alpha_i = \sqrt{\left(\frac{\partial\alpha_i}{\partial B}\,\delta B\right)^2 + \left(\frac{\partial\alpha_i}{\partial \mathrm{Nu}_G}\,\delta\mathrm{Nu}_G\right)^2} \tag{A-7}$$

Using Moffat's method [27] it was found that δB is equal to 0.1, 0.09, 0.04, 0.12, 0.03 and 0.05 for K11, K19, K26, K32, K40 and Gewa C+ respectively.

For each point $\delta\mathrm{Nu}_G$ is calculated as follows:

$$\delta\mathrm{Nu}_G = \frac{\partial\mathrm{Nu}_G}{\partial\,\mathrm{Re}}\,\delta\,\mathrm{Re} \tag{A-8}$$

where Nu_G is given by equations (3) and (4).

$$\delta\,\mathrm{Re} = \frac{4\rho_c}{\pi\mu_c(D_i + D_0)}\,\delta\dot V_c \tag{A-9}$$

Finally the maximum relative uncertainty of the external HTC $\delta\alpha_e/\alpha_e$ for the first row of the bundle is equal to 20 percent, 17 percent, 21 percent, 17 percent, 14 percent and 15 percent for the K11, K19, K26, K32, K40 and Gewa C+ respectively. For the bundle the uncertainties are reported on the figures 5 and 8.

References

[1] Beatty, K. O., and Katz, D. L., 1948, "Condensation of Vapors on Outside of Finned Tubes," Chem. Eng. Prog., **44**, pp. 55–77.

[2] Karkhu, V. A., and Borovkov, V. P., 1971, "Film Condensation of Vapor at Finely Finned Horizontal Tubes," Heat Transfer-Sov. Res., **3**(2), pp. 183–191.

[3] Webb, R. L., Rudy, T. M., and Kedzierski, M. A., 1985, "Prediction of Condensation Coefficient on Horizontal Integral-Fin Tubes," ASME J. Heat Transfer, **107**, pp. 369–376.

[4] Honda, H., and Nozu, S., 1987, "A Prediction Method for Heat Transfer During Film Condensation on Horizontal Low Integral-Fin Tubes," ASME J. Heat Transfer, **109**, pp. 218–225.

[5] Adamek, T., and Webb, R. L., 1990, "Prediction of Film Condensation on Horizontal Integral-Fin Tubes," Int. J. Heat Mass Transf., **33**(8), pp. 1721–1735.

[6] Rose, J. W., 1994, "An Approximation Equation for the Vapor-Side Heat-Transfer Coefficient for Condensation on Low-Finned Tubes," Int. J. Heat Mass Transf., **37**, pp. 865–875.

[7] Sreepathi, L. K., Bapat, S. L., and Sukhatme, S. P., 1996, "Heat Transfer During Film Condensation of R-123 Vapor on Horizontal Integral-Fin Tubes," Journal of Enhanced Heat Transfer, **3**(2), pp. 147–164.

[8] Gregorig, R., 1954, "Film Condensation on Finely Rippled Surfaces with Consideration of Surface Tension," Z. Angew. Math. Phys., **5**, pp. 36–49.

[9] Adamek, T., 1981, "Bestimmung der Kondensation-grossen auf Feingewellten Oberflachenzur Auslegun Optimaler Wandprofile," Waerme- Stoffuebertrag., **15**, pp. 255–270.

[10] Zhu, H.-R., and Honda, H., 1993, "Optimization of Fin Geometry of a Horizontal Low-Finned Condenser Tube," Heat Transfer-Jpn. Res., **22**(4), pp. 372–386.

[11] Honda, H., and Kim, K., 1995, "Effect of Fin Geometry on the Condensation Heat Transfer Performance of a Bundle of Horizontal Low-Finned Tubes," J. Enhanced Heat Transfer, **2**(1–2), pp. 139–147.

[12] Honda, H., and Makishi, O., 1995, "Effect of Circumferential Rib on Film Condensation on a Horizontal Two-Dimensional Fin Tube," J. Enhanced Heat Transfer, **2**(4), pp. 307–315.

[13] Webb, R. L. Keswani, S. T., and Rudy, T. M., 1982, "Investigation of Surface Tension and Gravity Effects in Film Condensation," *Proc. Int. Heat Transfer Conf.*, Washington, **5**, pp. 175–180.

[14] Honda, H., Uchima, B., Nozu, S., Nakada, H., and Torigoe, E., 1991, "Film Condensation of R-113 on In-Line Bundles of Horizontal Finned Tubes," ASME J. Heat Transfer, **133**(2), pp. 479–486.

[15] Honda, H., Uchima, B., Nozu, S., Torigoe, E., and Imai, S., 1992, "Film Condensation of R-113 on Staggered Bundles of Horizontal Finned Tubes," ASME J. Heat Transfer, **114**(2), pp. 442–449.

[16] Wang, S. P., Hijikata, K., and Deng, S. J., 1990, "Experimental Study on Condensation Heat Transfer Enhancement by Various Kinds of Integral Finned Tubes," *Condensers and Condensation*, Proc. 2nd Int. Symp., pp. xv–xxiii.

[17] Webb, R. L., and Murawski, C. G., 1990, "Row Effect for R-11 Condensation on Enhanced Tubes," ASME J. Heat Trasfer, **112**, pp. 768–775.

[18] Blanc, P., Bontemps, A., and Marvillet, C., 1994, "Condensation Heat Transfer of HCFC22 and HFC134a Outside a Bundle of Horizontal low Finned Tubes," *Proc. Symp. CFC's, The Day After*, Padova, Italy, pp. 635–642.

[19] Honda, H., Takamatsu, H., Takada, N., and Yamasaki, T., 1995, "Condensation of HFC 134a and HFC 123 in a Staggered Bundle of Horizontal Finned Tubes," *Proc. Eurotherm No. 47*, Heat Transfer in Condensation, pp. 110–115, Paris.

[20] Cheng, W. Y., and Wang, C., 1994, "Condensation of R-134a on Enhanced Tubes," ASHRAE Trans., **10**(1), pp. 809–817.

[21] Agrawal, K. N., Moharty, P., Kumar, R., and Varma, H. K., 1999, "Enhancement of Heat Transfer Rates During Condensation of Refrigerants Over Horizontal Finned Tubes," *Proc. Symp. Two Phase Flow Modelling and Experimentation*, **1**, pp. 505–510.

[22] Hijikata, K., and Himeno, N., 1990, "Condensation of Azeotropic and Nonazeotropic Binary Vapor Mixtures," Annu. Rev. Heat Transfer, **3**, Chap. 2, pp. 39–83.

[23] Honda, H., Takuma, M., and Takada, N., 1999, ''Condensation of Downward-Flowing Zeotropic Mixture HFC-123/HFC-134a on a Staggered Bundle of Horizontal Low-Finned Tubes,'' ASME J. Heat Transfer, **121**, pp. 405–412.

[24] Belghazi, M., Bontemps, A., Signe, J. C., and Marvillet, C., 2001, ''Condensation Heat Transfer of a Pure Fluid and Binary Mixture outside a Bundle of Smooth Horizontal Tubes. Comparison of Experimental Results and a Classical Model,'' Int. J. Refrig., **24**(8), pp. 841–855.

[25] Gnielinski, V., 1976, ''New Equation for Heat and Mass Transfer in Turbulent Pipe and Channel Flow,'' Int. Chem. Eng., **16**(2), pp. 359–368.

[26] Wilson, E. E., 1915, ''A Basis for Rational Design of Heat Transfer Apparatus,'' Trans. ASME, **37**, pp. 47–70.

[27] Moffat, R. J., 1988, ''Describing the Uncertainties in Experimental Results,'' Exp. Therm. Fluid Sci., **1**, pp. 3–17.

[28] Signe, J. C., 1999, ''Condensation de Mélanges Non Azéotropes de Fluides Frigorigènes *à* l'Extérieur d'un Faisceau de Tubes Horizontaux,'' Ph.D. thesis, Université Joseph Fourier, Grenoble, France.

[29] Belghazi, M., 2001, ''Condensation d'un fluide pur et de mélanges zéotropes à l'extérieur d'un faisceau de tubes à surface améliorée,'' Ph.D. thesis, Université Joseph Fourier, Grenoble, France.

[30] Rudy, T. M., and Webb, R. L., 1985, ''An Analytical Model to Predict Condensate Retention on Horizontal Integral-Fin Tubes,'' ASME J. Heat Transfer, **107**, pp. 361–368.

Experimental Study of Surface-Mounted Obstacle Effects on Heat Transfer Enhancement by Using Transient Liquid Crystal Thermograph

W. M. Yan
Professor
Mem. ASME
e-mail: wmyan@hfu.edu.tw

R. C. Hsieh
Graduate Student

Department of Mechanical Engineering,
Huafan University,
Shih-Ting, Taipei, Taiwan 22305,
Republic of China

C. Y. Soong
Professor
Mem. ASME
Department of Aeronautical Engineering,
Feng Chia University,
Seatwen, Taichung, Taiwan 40745,
Republic of China
e-mail: cysoong@fcu.edu.tw

Effects of surface-mounted obstacles on the local heat transfer enhancement of a base plate are investigated by using transient liquid crystal thermograph technique. To explore the geometry effects of short obstacles, the height less than one hydraulic diameter (d), three cross-sectional shapes of obstacles, i.e., circular, square and diamond, with variations in number of obstacles, obstacle spacing, and free-stream Reynolds number are considered. The maximum number of the obstacles in tandem array is 3 and the spacing between obstacles is 1d, 2d, or 4d. The free-stream Reynolds number ranges from 2100 to 4200. The experimental results reveal that the local heat transfer enhancement in front of leading circular and square obstacles are better than the diamond one, while the influenced area by the obstacle of the diamond shape is most remarkable. The present results disclose that an intermediate height (0.5d) of the protruding elements is more beneficial to the heat transfer enhancement in wake of the obstacle. With the sweepback leading edge of the top surface, the diamond and circular obstacles produce vortical flow across the obstacles and thus enhance heat transfer downstream in wake. Increasing Reynolds number leads to an enhancement in heat transfer performance. The number of and the spacing between the obstacles in tandem array are also influential factors to the flow structure and heat transfer enhancement on the basic plate. [DOI: 10.1115/1.1459729]

Keywords: *Heat Transfer Enhancement, Transient Liquid Crystal Technique, Surface-Mounted Obstacles, Horse-Shoe Vortex, Vortex Wake*

1 Introduction

Enhancement of heat transfer performance can be achieved by mounting turbulence promoters or roughness elements on the walls of flow passages. Various obstacles are employed to alter the flow patterns, enhance mixing, and/or strengthen the vortical flow and, in turn, increase heat exchange between the wall and the fluids. For example, turbulence promoter of pin-fin type is a typical application of mounting protrusion elements on a surface or in a flow passage to improve heat transfer performance. This class of heat transfer enhancement techniques has been employed in a variety of practical applications, e.g., compact heat exchangers and internal cooling of gas turbine blades, just to name only a few. On the other hand, in electronic equipment cooling applications, circuit board with a number of chips mounted on is a most common configuration. It is therefore important to understand the mechanism of the surface-mounted obstacles influencing the flow structure and its effects on heat transfer performance. Tremendous amount of the related investigations has appeared in literature. There is no attempt to make an exhaustive review, but only some typical ones will be mentioned.

As to the flow over a surface with obstacles mounted, a number of experimental studies have dealt with the associated flow structure, e.g., Sparrow et al. [1], Goldstein et al. [2], Chyu and Natarajan [3,4], Yoo et al. [5], Natarajan and Chyu [6], Meinders et al. [7,8], etc. The previous results indicated the complex structure of the three-dimensional flow field around a cubic obstacle, in which the horse-shoe vortex, corner vortex and the wake of counter-rotating vortices appear. The fluid over the top of the obstacle may generate separation bubble and migrates downstream over the re-circulation zone behind the obstacle. Finally, the flow reattaches the base plate in the wake region. As to the case of two cubic obstacles in tandem, the flow structure becomes more complicated and the geometric arrangement must be one of the significantly influential factors. Ishii and Honami [9], Pierce and Tree [10], Eckerle and Awad [11], and Baker [12] studied the formation of horse-shoe vortex and its oscillatory nature. Schofield and Logan [13] explored the effects of obstacle geometry and shear flow on the perturbation and recovery regions behind the obstacle. Martinuzzi and Tropea [14] investigated the effect of the cross-stream width-to-height aspect ratio on the flow structure around the junction of the base plate and the obstacle. For the case of multi-obstacle, Igarashi and Takasaki [15] studied three obstacles in tandem. It was disclosed that the incident boundary layer thickness is closely related to the laminar-to-turbulent transition. Recently, Morris and Garimella [16] measured the temperature distributions downstream the obstacle, they found the differences in thermal characteristics of the laminar and turbulent wake flows.

As to the transport characteristics on the surfaces with obstacles mounted on, Sparrow et al. [1], Goldstein and Karni [17], and Goldstein et al. [18] disclosed that main stream boundary layer characteristics influences the vortex formation and the local mass/heat transfer rates around the obstacle. Igarashi [19–21] studied local and average heat transfer rates over the rectangular cylinder of various aspect ratios at angles of attack, and he also proposed Nusselt number correlations. Later on, Yoo et al. [5] and Natarajan and Chyu [6] studied the effects of angle of attack on the mass transfer performance of cubic obstacle. The influences of horse-shoe and corner vortices on the local surface mass transport rates

---

Contributed by the Heat Transfer Division for publication in the JOURNAL OF HEAT TRANSFER. Manuscript received by the Heat Transfer Division March 19, 2001; revision received July 26, 2001. Associate Editor: C. Amon.

around the cubic obstacle was investigated by Chyu and Natarajan [3]. They disclosed that the maximum average transport rate on the two sidewalls of the cube is attributed to the contribution of the horse-shoe vortex.

Geometric configuration is another one of the influential factors to the development of the flow pattern and the heat/mass transfer rates. Fisher and Eibeck [22] compared the influences of a circular and tapered circular (teardrop-shaped) cylinders on the heat transfer rate of the base plate. They found the tapered one provides a higher local heat transfer enhancement along the centerline downstream of the obstacle; while the circular cylinder enhances heat transfer over a larger region than a streamlined obstacle. Based on their experimental results, Chyu and Natarajan [4] claimed that the horse-shoe vortex formed upstream and the arch-shaped vortex behind the obstacle are generated due to the configuration of the base plate and the obstacle. They also compared the reattachment lengths downstream the obstacles and listed them in an order of long to short as: diamond (square prism with 45 deg rotation around its own axis), cube, circular cylinder, triangular cone, and semi-sphere. Recently, by using infrared thermograph, liquid crystal, and the surface oil flow visualization techniques, Meinders et al. [7,8] investigated the vortical flow structure and the local heat transfer from an array of wall-mounted cubes.

Since the flow around surface-mounted obstacles is a pure three-dimensional one involving complicated flow physics in the presence of vortex-wall and vortex-vortex interactions. For this class of heat transfer experiments, whole field measurement is more appropriate than the conventional thermocouple measurements of local heat transfer rates. The whole field techniques include Naphthalene sublimation, infrared thermograph, liquid crystal thermograph, etc. Among these, due to its merits in measuring local thermal characteristics, the transient liquid crystal thermograph becomes increasingly important in a variety of heat transfer experiments, e.g., Martinez-Botas et al. [23], Ekkad and Han [24], Han and Ekkad [25], Chyu et al. [26], Critoph et al. [27], Hwang and Cheng [28], etc. The present work employs this relatively new technique of surface temperature measurement to investigate the effects of protruding obstacles on heat transfer enhancement over the base plate. In reviewing the previous literature, it is found that the most of the previous studies either focus on the obstacle surfaces or on the base plate heat and mass transfer with effects of the long protrusions, e.g., $H/d=1$ to 12 in the work of Goldstein et al. [18]. The present study emphasizes effects of the short obstacles of the height less than one hydraulic diameter (d). Three cross-sectional shapes of obstacles, i.e., circular, square and diamond, with variations in number of obstacles, obstacle spacing, and free-stream Reynolds number are considered.

2 Experimental Facility and Model

The present test facility consists of (1) small wind tunnel, (2) hot stream generator, (3) data acquisition system, (4) image acquisition and processing system, (5) liquid crystal, and (6) test models. The schematic diagram of the arrangement is shown in Fig. 1. The wind tunnel is of 100 mm×100 mm test section. The hot stream coming from a generator with an outlet of 65 mm diameter flows through a 200 mm long expansion section, 150 mm long settling chamber, honeycomb, 50 mm long buffer zone, five layers of screens and, finally, enters the test section. The hot stream generator has both flowrate and temperature modulations. In the present work, the exit fluid temperature of the generator was set to be 70°C, while the fluid temperature at the inlet of the test section is about 63°C.

The test model assembly as shown in Fig. 2 consists of a base plate and obstacles all made of acrylic material. The base plate is of 250 mm×100 mm×8 mm (length×width×thickness) with leading edge sharpened. The obstacles are of circular, square, and diamond cross-sections and all have hydraulic diameter $d=20$ mm. Three heights of the obstacles, $H/d=1$, 0.5, and 0.25, are adopted. The origin of the Cartesian coordinates (x = streamwise, y = transverse, z = normal) is located on the base plate and under the center of the bottom surface of the leading

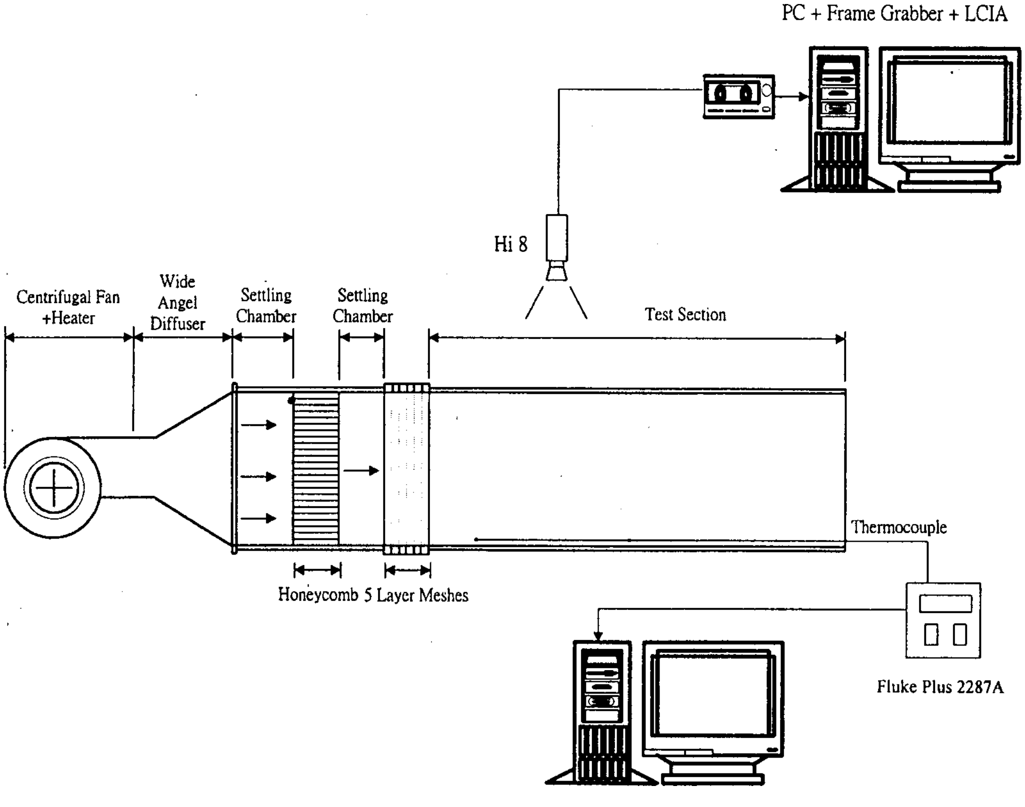

Fig. 1 Experimental apparatus

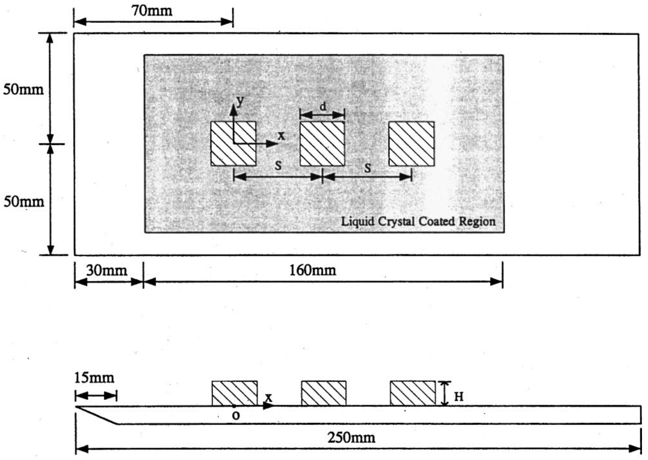

Fig. 2 Obstacle-plate model assembly

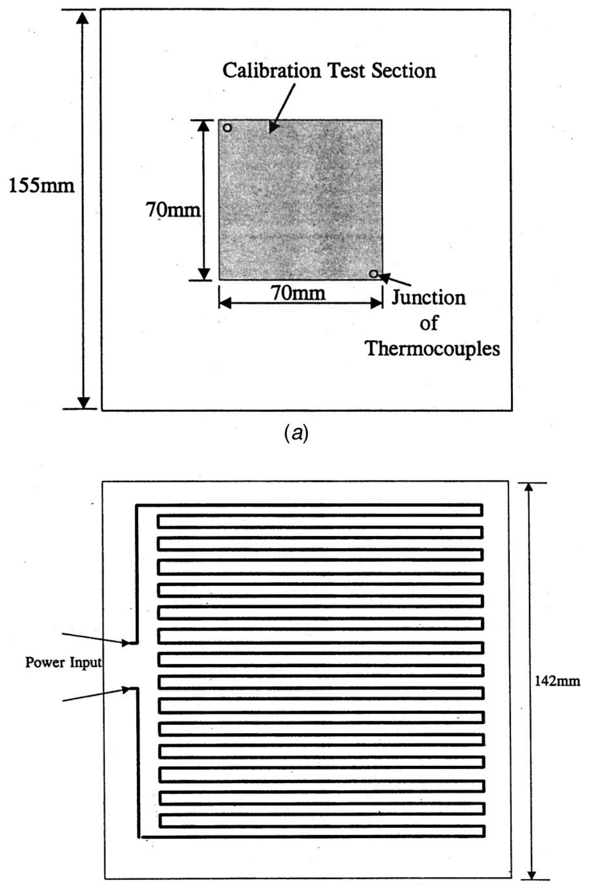

(*a*)

(*b*)

Fig. 3 Calibration test model: (*a*) calibration test model plate; and (*b*) heating element.

obstacle. Three conditions of free stream velocity, $u_\infty = 4.0$, 3.3, and 2.0 m/s corresponding to the Reynolds numbers Re=4200, 3500, and 2100, respectively, are considered. To examine the effects of the obstacle spacing, cases of two and three obstacles placed in tandem are studied. The liquid crystal (Type BM/R38C5W/C17-10, Hallcrest Co.) was sprayed over the heat transfer surface to form a thin-film of thickness of the order 10^{-3} cm. For this thin layer of liquid crystal, Ireland and Jones [29] has demonstrated that the time scale for color change is of the order 10^{-3} s, which is far shorter than the time scale of the measuring process. This liquid crystal has a color-changing range of 5°C in which its color changes in the order of clear, red, green, blue, and then back to clear. To provide a better contrast for color intensity, a layer of black paint is used as background on backside of the acrylic plate.

The theoretical background of the data reduction and the experimental procedure of the transient liquid crystal technique are omitted here for saving the space. The interested readers may find the related information elsewhere, e.g., Ekkad and Han [24].

3 Calibration and Verification

The light condition of the environment is very influential to recording and identification of the liquid crystal color information. In the present work, the whole test section is covered in a dark room with the specified light source at the specified location. Before the experiment, an initial calibration with a test plate made of copper, as shown in Fig. 3(*a*), was performed. The upper surface is coated by the thermochromic liquid crystal; while on the lower surface a film heater, Fig. 3(*b*), and two thermocouples for monitoring the temperature variation were installed. Under the well-controlled illumination condition, the color intensity corresponding to various temperatures were recorded and used as the reference for the data analysis in the subsequent experiments.

In an unsteady experiment like the present one, the thermal boundary condition of the plate is neither uniform wall temperature nor uniform heat flux. Butler and Baughn [30] investigated the problem theoretically and, for a flat plate, they proposed an appropriate local Nusselt number correlation based on the uniform wall temperature results and a transient modification of the wall temperature. By using their result, therefore, the local heat transfer coefficient on base plate in the present transient liquid crystal measurement, h_{xc}, is evaluated by the correction formula,

$$h_{xc}=h_x/(T^*)^{4.9/\mathrm{Re}^{0.2}} \tag{1}$$

where h_x and T^*, respectively, denote the local heat transfer coefficient over a flat plate of uniform wall temperature and modified wall temperature function, viz.

$$h_x=0.332k\mathrm{Pr}^{1/3}(u_\infty/\nu x)^{1/2} \tag{2}$$

and

$$T^*=(T_\infty-T_{LC})/(T_\infty-T_o) \tag{3}$$

where T_o, T_∞, and T_{LC} denote initial, free-stream, and liquid crystal sensed temperatures, respectively. Figure 4 shows a comparison of the present measurements and the laminar flow theory by Butler and Baughn [30]. It is observed that the noticeable deviation appears in the leading edge region. Flow turbulence in experiment and the approximations invoked in the pure laminar flow theory are the possible reasons for the discrepancy. However,

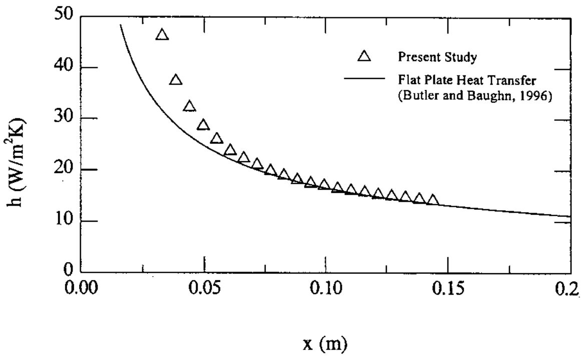

Fig. 4 Comparison of the present measurements on a flat plate with the previous theory

the theoretical predictions and measurements become very close in the region sufficiently downstream, say $x > 0.06$ m from the leading edge. This verifies the appropriateness of the present measurements and provides a guideline in installation of the obstacles.

4 Results and Discussion

In the following, the heat transfer enhancement results are displayed in the form of ratio of h/h_o, where h_o denotes heat transfer coefficient of flat plate without obstacle effects. In all of the contours, the heat transfer remarkably enhanced regions with $h/h_o > 1.3$ are denoted by various colors as indicated in the figures. The data reduction for the region near the root of the protruding elements is rather troublesome, noise to optical signal may emerge especially for low values of h/h_o. To retain the quality of the data presentation, the regions of relatively weaker heat transfer enhancement with $h/h_o < 1.3$ are displayed in white.

4.1 Single Obstacle. In Fig. 5, (*a*) circular, (*b*) square, and (*c*) diamond obstacles of height $H/d = 1$, 0.5 and 0.25 in a flow at $\mathrm{Re} = 3500$ are employed to examine the influences of obstacle height on the heat transfer enhancement over the base plate. In Fig. 5(*a-a*) (Here first letter "*a*" denotes circular shape, and the second letter "*a*" stands for height $H/d = 1$), with an obstacle of $H/d = 1$ protruding the main stream, the horse-shoe (HS) vortex formed in front of the obstacle-plate junction strongly enhances the local heat transfer. The HS vortex sweeps downstream along the two sides of the obstacle. In these regions, vortical flow motion enhances the heat exchange between the fluids and the base plate. Therefore, the HS vortex strength can be characterized by the local heat transfer enhancement. Besides the base region of low heat transfer rate immediately behind the obstacle, considerable heat transfer enhancement appears downstream due to the action of the HS vortex. The shear flow roll up over the circular edge of the obstacle top surface, similar to that from leading edge of the swept wings, may generate a pair of vortices, which is relatively weaker and is pushed toward centerline by the HS vortex downstream in the near wake region. Along the centerline of the wake, there is a region of relatively high transport rate, which is a consequence under the effects of combined HS vortex and the above-mentioned vortical flow from the top of the obstacle. The maximum enhancement ($h/h_o \approx 3$) falls into the region around the reattachment point. It is also observed that, due to low pressure of the near wake, a neck of the HS vortex trail appears a little upstream the attachment point. As the obstacle height reduced to $0.5d$, the h/h_o contours in Fig. 5(*a-b*) show a reduction in the enhancement ratio and also a shrink in the influenced area. With this shorter obstacle, higher reattachment heat transfer rate due to a stronger impact appears in the wake region. While a too short obstacle, $H/d = 0.25$ in Fig. 5(*a-c*), only very slightly distorts the main flow. It results in a weaker vortex system and smaller reattachment impact and, in turn, lower heat transfer enhancement. The two spots of slightly enhanced heat transfer are due to reattachment of flow with the pair of swept vortices coming from the top surface. For higher obstacles, say $H/d = 0.5$ and 1, the two counter-rotating vortices approach towards each other before reattachment and the two spots merge into one.

Figure 5(*b*) shows the results of flow over a base plate with the presence of a cubic (square) obstacle. The situation of $H/d = 1$ is somewhat similar to that in Fig. 5(*a*). The differences from the circular obstacle are the relatively strong HS vortex effect and the small enhancement effects in the wake region. As the obstacle height reduces, it is observed that the horse shoe vortex effect becomes weak in the head-on stagnation region but concentrates at the corners. Since there is no swept leading edge of the top surface, therefore, no clue of swept vortices and vortical flow

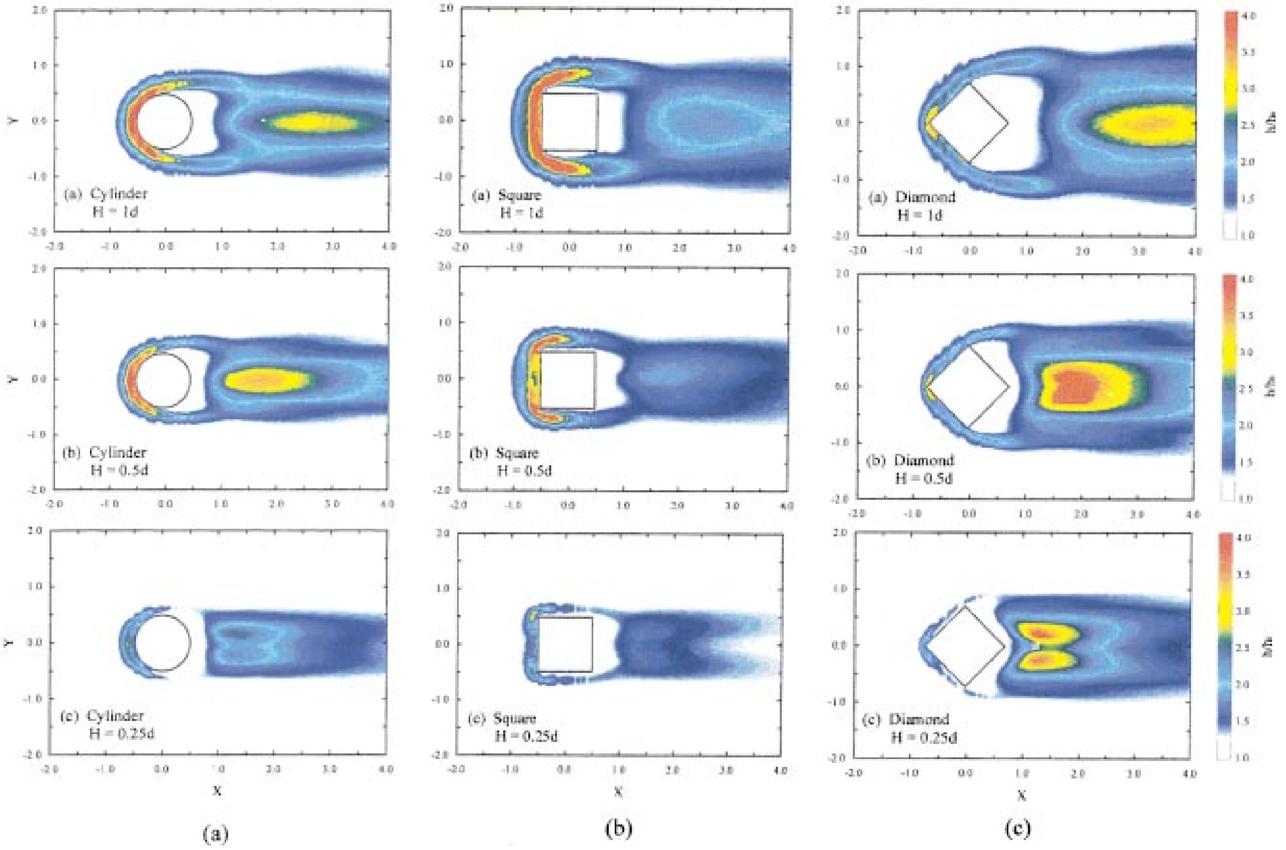

Fig. 5 Effects of obstacle height and cross-section geometry on base plate heat transfer enhancement at Re=3500: (*a*) circular; (*b*) square; and (*c*) diamond obstacles.

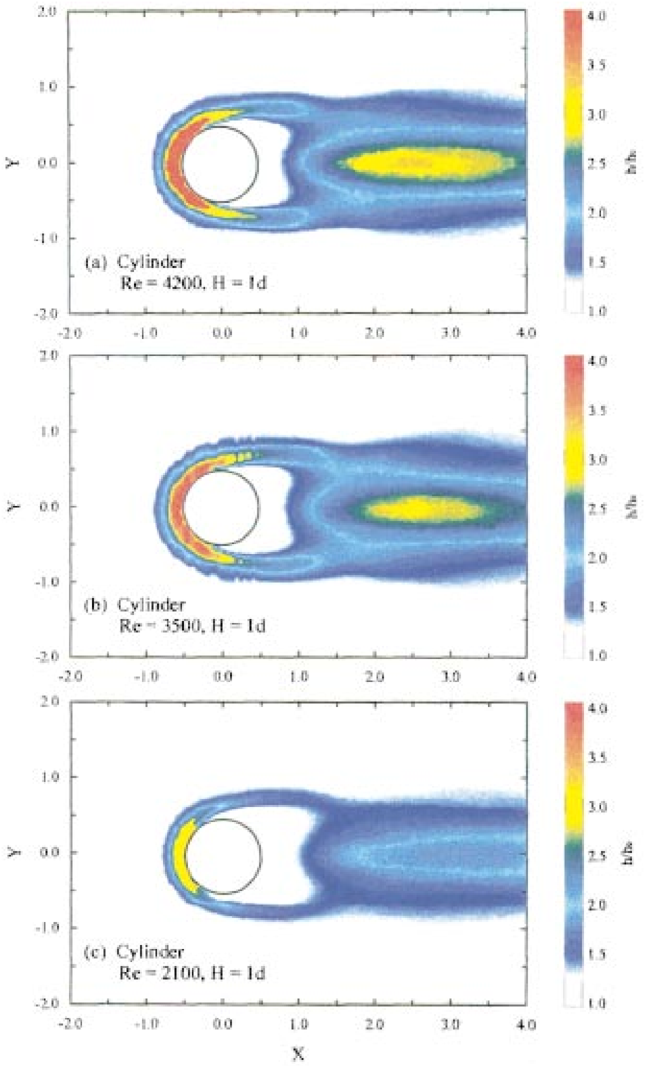

Fig. 6 Reynolds number effects on heat transfer enhancement of base plate with a circular obstacle of $H=d$: (*a*) Re=4200; (*b*) Re=3500; and (*c*) Re=2100.

attachment displayed. For the case of diamond obstacle in Fig. 5(*c*), without presence of a stagnation region of head-on impingement, the HS vortex and its enhancement effect are weak. However, the influenced area is relatively larger due to larger blockage or frontal area. The higher the obstacle is, the larger the wake region of low heat transfer is. Also due to the sweep of the windward edge of the top surface, the pair of wing-tip-like vortices from the top surface accompanies the reattachment process downstream the obstacle. In a previous paper, Natarajan and Chyu [6] mentioned the wing-tip-like vortices over a diamond obstacle, but they only concentrated their attentions on the effects of the heat transfer on the obstacle surfaces not that on the base plate. For the case of higher obstacle, $H/d=1$, the vortices from the top surface are relatively weaker and are squeezed into one by the HS vortex, see Fig. 5(*c-a*). As the height is reduced as that in Figs. 5(*c-b*) and 5(*c-c*), the HS vortex becomes weaker. However, due to small size in obstacle height, the pair of wing-tip-like vortices (i.e., vortices like that originated from the leading edge of a sweepback/delta wing) from the two swept leading edges of top surface have no chance to merge into one before they reattach the base plate. Therefore, two noticeably enhanced regions appear in the reattachment region. This sweptback vortex effect can be also observed in Fig. 5(*a-c*) of short circular obstacles, but it is not the case for a square obstacle in which the leading-edge of the upper surface is flat and normal to the on-coming flow.

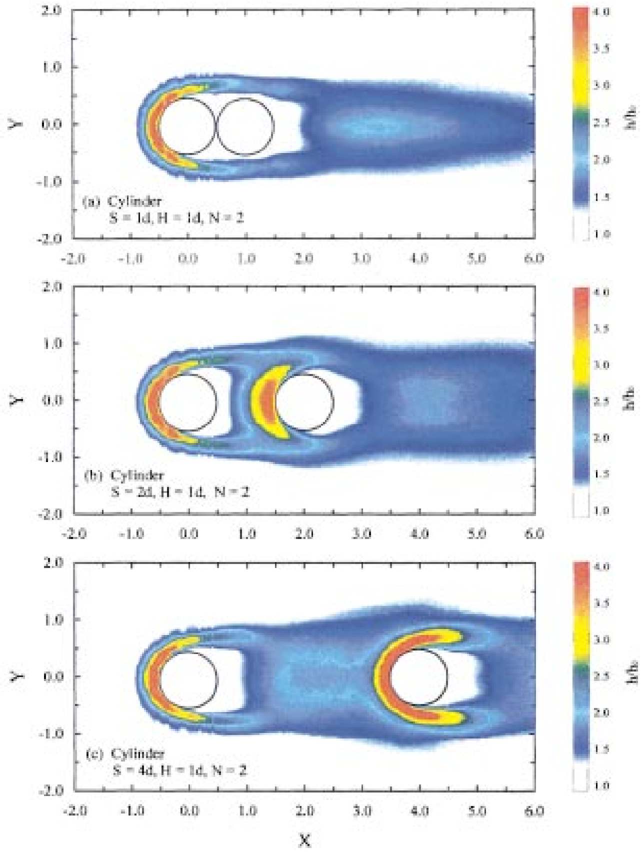

Fig. 7 Effects of obstacle spacing on the heat transfer enhancement of base plane with circular obstacles

The Reynolds number effects are shown in Fig. 6, in which it is observed that more pronounced heat transfer enhancement can be obtained at a higher Reynolds number. Since in flows at higher Re, larger velocity gradient in boundary layer and streamwise pressure gradient of on-coming flow result in a stronger HS vortex in front of the obstacle. The high Reynolds number also leads to a strong forced convection effect on reattachment process. Therefore, heat transfer enhancement increases with the increasing Reynolds number.

4.2 Obstacles in Tandem. As the obstacles are arranged in tandem, the spacing becomes one of the very important parameters in dealing with flow structure and the associated heat transfer performance. Figure 7 displays the heat transfer enhancement contours for two circular obstacle of height d with spacing $S/d=1$, 2, and 4. The two close obstacles in Fig. 7(*a*) perform as an equivalent streamlined body and elongate the axial flow path over the top surface. Comparing with the case of single obstacle, the reattachment process and the heat transfer enhancement become moderate. Increasing the spacing to $2d$, see Fig. 7(*b*), the flow over the leading obstacle impinges on the root region of the second one and enhances heat transfer there. Further increase in spacing, i.e., $S/d=4$ in Fig. 7(*c*), the flow between the obstacles has the chance to redevelop after attachment and forms a new HS vortex around the second obstacle. Due to the superimposed effects from the trail of the first HS vortex, it is noted that the enhancement in the region of the second HS vortex is larger than that of the first one. Although there is no significant effect on the upstream HS by the changes in spacing, the heat transfer enhancement region in Fig. 7(*c*) is obviously the largest one in the three arrangements of different spacing. Effects of the obstacle height

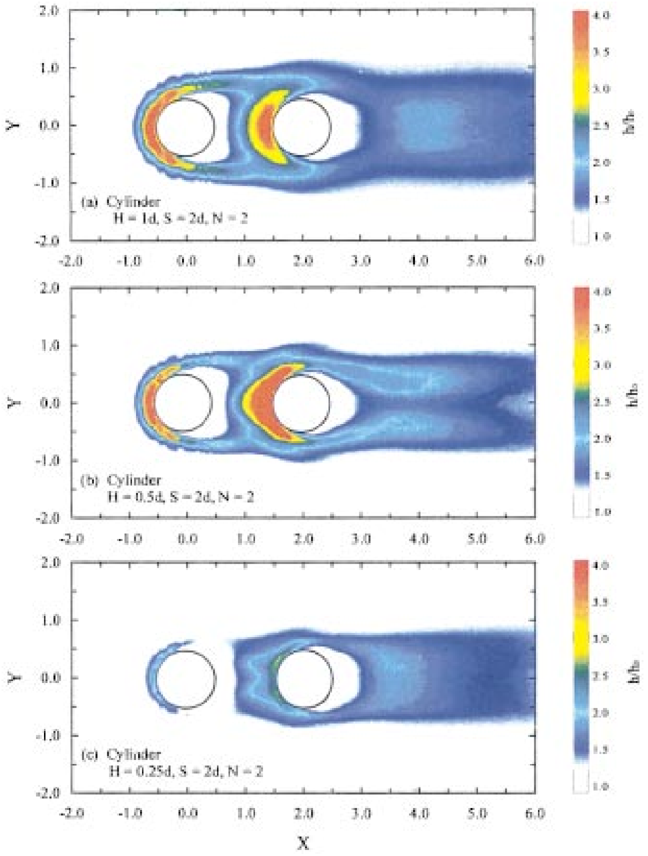

Fig. 8 Effects of Obstacle height on the heat transfer enhancement of base plate with circular obstacles

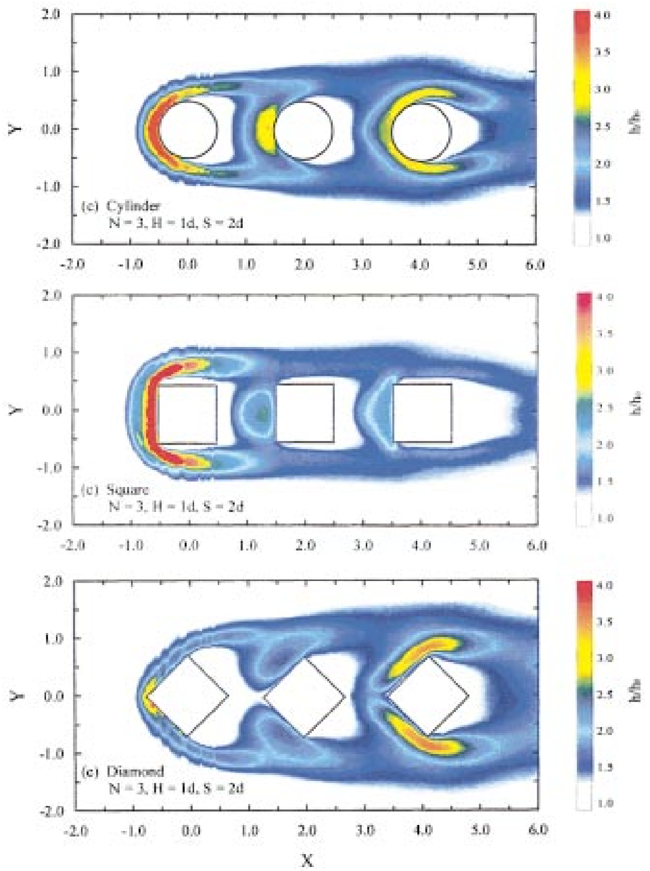

Fig. 9 Base plate heat transfer enhancement with tandem array of three obstacles of $H/d=1$ and $S/d=2$ at Re=3500

are shown in Fig. 8. Comparing 8(*a*) and 8(*b*), it can be inferred that the reattachment point behind the leading obstacle moves forward as the obstacle is shortened. The vortex trails in 8(*b*) show that the attached flow redevelops in front of the second obstacle and forms a new HS vortex. The combining effects of the reattachment and the HS vortex between the two obstacles generate a relatively better heat transfer enhancement in the root region of the second obstacle. While, as mentioned in the discussion of single obstacle, the effects reduce dramatically as the obstacles shortened to $H/d=0.25$, see Fig. 8(*c*). In the sense of overall performance, the case of $H/d=1$ in Fig. 8(*a*) shows the largest area of heat transfer enhancement.

Heat transfer characteristics associated with tandem array of three obstacles are shown in Fig. 9. By using the circular obstacles as a typical example, it is revealed that the heat transfer in front of the second obstacle in Fig. 9(*a*) is lower than that of the corresponding case of two-obstacle array shown in Fig. 7(*b*). The presence of the third obstacle has a blockage effect on the flow coming from the upstream region between the leading and the second obstacles and thus reduces the heat convection in the region. As to the flow around the third obstacle, the relatively high heat transfer rate is a consequence of the newly developed HS vortex and the complex interaction of the on-coming vortices upstream. For the corresponding cases of square and diamond obstacles in Figs. 9(*b*) and 9(*c*), both have some similar qualitative nature in these aspects. In Fig. 9(*b*), however, the heat transfer enhancement in the downstream part of the leading obstacle is different from the other two cases and it is the lowest one among the three obstacle shapes. The circular and diamond shapes both have a sweepback windward surface, which is different from the flat one of the square obstacle. As to the influenced region of diamond-shaped obstacles is the largest one.

5 Concluding Remarks

By employing the transient liquid crystal thermography technique, enhancement of surface heat transfer by short obstacles ($H/d\leqslant 1$) has been studied. Besides the measurements of the heat transfer over the base plate surface, it is demonstrated that the near-surface flow structure can be reasonably inferred from the contours of the local heat transfer coefficients. More physical insights into the mechanisms of heat transfer enhancement can be provided by the present investigation. Based on the present measurements and the analysis for the range of parameters: $2100\leqslant \mathrm{Re}\leqslant 4200$, $0.25\leqslant H/d\leqslant 1$, and $1\leqslant S/d\leqslant 4$, the following conclusions can be drawn.

1 In general, an obstacle protruding flow over a surface may generate a horse-shoe vortex structure in front of the windward side of the obstacle. For a single obstacle of a fixed height, the strength of the horse-shoe vortex in order is square>circular>diamond. As to the reattachment region behind the obstacles, however, the heat transfer enhancement ratios have the order of diamond>circular>square. By inspecting the surface heat transfer contours, it is inferred that the wing-tip-like vortices generated by the flow over top surface of the diamond obstacle have major contribution on the heat transfer enhancement in reattachment region. The circular obstacles also have this kind of sweepback vortex effect due to its circular (windward) edge of the top surface.

2 The obstacle height is a very influential factor to the horse-shoe vortex as well as to the vortical wake behind the obstacle. The strength of the horse-shoe vortex and the area of the heat transfer enhancement both increase with obstacle height. While for the heat transfer performance in the wake region of the single obstacle, the height $H/d=0.5$ is the most efficient among the

present three heights considered. Both too high and too short obstacles weaken the impact of reattachment and the local heat transfer enhancement in the wake region behind the obstacle.

3 For tandem arrays of the two-obstacle and three-obstacle, the horse-shoe vortex around the leading obstacle is not altered noticeably. The heat transfer in the region between two obstacles is noticeably changed with the shape of the obstacles. The better heat transfer performance can be obtained by appropriate combination of height of and spacing between the obstacles. The former controls the vortex flow strength and the latter influences the reattachment process and the redevelopment of the downstream wake flow. As an example in the present work, the tandem array of two circular obstacles at a fixed Reynolds number Re=3500, favorable heat transfer performance can be obtained with $(H/d, S/d)=(1,4)$, (1, 2), and (0.5, 2).

4 Comparing with a two-obstacle tandem array at corresponding conditions, the heat transfer in the region between the leading and the second obstacles in a three-obstacle array is relatively lower. However, the presence of the third protrusion element may further enhance the local heat transfer. As to the effect of obstacle geometry on the heat transfer performance associated to the three-obstacle array, circular and diamond shapes both are better than the square one. Although the array of the diamond obstacles influences larger area of the base plate, its near wake immediately behind the obstacles shows relatively worse heat transfer performance, which also implies a larger wake and larger pressure loss. Considering all the information provided by the present measurements, it is reasonable to infer that the tandem array of the circular obstacles with proper height and spacing of obstacles might be more attractive in a design of surface heat transfer enhancement.

5 The vortex motion in this flow configuration dominates the heat transfer enhancement on the base plate. Therefore, to understand the vortical flow structure and vortex interactions under the conditions of various obstacle heights, a well-designed flow visualization experiment is most worthwhile. The present liquid crystal thermograph results are very useful to the interpretation of flow structure especially the surface flow pattern.

Acknowledgment

This work is sponsored by the National Science Council of Taiwan, R.O.C., through the grant number NSC 89-2212-E211-005.

Nomenclature

d = hydraulic diameter of obstacle (0.02 m)
H = height of the obstacles (m)
h = heat transfer coefficient of base plate with obstacles (W/m^2K)
h_o = heat transfer coefficient of base plate without obstacles (W/m^2K)
h_x = heat transfer coefficient of base plate at uniform wall temperature (W/m^2K)
h_{xc} = modified heat transfer coefficient of base plate (W/m^2K)
N = number of obstacles
Re = Reynolds number, $u_\infty d/v$
S = spacing between obstacles (m)
T = temperature (°C or K)
T_o = initial temperature (°C or K)
T_∞ = free-stream temperature (°C or K)
T^* = dimensionless temperature of liquid crystal, $(T_\infty - T_{LC})/(T_\infty - T_o)$
T_{LC} = liquid crystal temperature for green (°C or K)
u_∞ = free-stream velocity (m/s)
x, y, z = Cartesian coordinates (m)

Greek symbols

ν = kinematic viscosity (m^2/s)

References

[1] Sparrow, E. M., Stahl, T. J., and Traub, P., 1984, ''Heat Transfer Adjacent to the Attached End of a Cylinder in Crossflow,'' Int. J. Heat Mass Transf., **27**(2), pp. 233–242.
[2] Goldstein, R. J., Yoo, S. Y., and Chung, M. K., 1990, ''Convective Mass Transfer From a Square Cylinder and Its Base Plate,'' Int. J. Heat Mass Transf., **33**(1), pp. 9–18.
[3] Chyu, M. K., and Natarajan, V., 1991, ''Local Heat/Mass Transfer Distributions on the Surface of a Wall-Mounted Cube,'' ASME J. Heat Transfer, **113**, pp. 851–857.
[4] Chyu, M. K., and Natarajan, V., 1996, ''Heat Transfer on the Base Surface of Three-Dimensional Protruding Elements,'' Int. J. Heat Mass Transf., **39**(14), pp. 2925–2935.
[5] Yoo, S. Y., Goldstein, R. J., and Chung, M. K., 1993, ''Effects of Angle of Attack on Mass Transfer from a Square Cylinder and Its Base Plate,'' Int. J. Heat Mass Transf., **36**(2), pp. 371–381.
[6] Natarajan, V., and Chyu, M. K., 1994, ''Effect of Flow Angle-of-Attack on the Local Heat/Mass Transfer from a Wall-Mounted Cube,'' ASME J. Heat Transfer, **116**, pp. 552–560.
[7] Meinders, E. R., Hanjalic, K. and Van Der Meer, T. H., 1998, ''Similarity and Dissimilarity Between the Surface Heat Transfer and the Flow Structure in Turbulent Flows Over Surface-Mounted Cubes,'' *Proc., 11th Int. Heat Transfer Conference*, **3**, pp. 51–56.
[8] Meinders, E. R., Van Der Meer, T. H., and Hanjalic, K., 1998, ''Local Convective Heat Transfer from an Array of Wall-Mounted Cubes,'' Int. J. Heat Mass Transf., **41**(2), pp. 335–346.
[9] Ishii, J., and Honami, S., 1986, ''A Three-Dimensional Turbulent Detached Flow With a Horseshoe Vortex,'' ASME J. Eng. Gas Turbines Power, **108**, pp. 125–130.
[10] Pierce, F. J., and Tree, I. K., 1990, ''The Mean Flow Structure on the Symmetry Plane of a Turbulent Junction Vortex,'' ASME J. Fluids Eng., **112**, pp. 16–22.
[11] Eckerle, W. A., and Awad, J. K., 1991, ''Effect of Freestream Velocity on the Three-Dimensional Separated Flow Region in Front of a Cylinder,'' ASME J. Fluids Eng., **113**, pp. 37–44.
[12] Baker, C. J., 1991, ''The Oscillation of Horseshoe Vortex System,'' ASME J. Fluids Eng., **113**, pp. 489–495.
[13] Schofield, W. H., and Logan, E., 1990, ''Turbulent Shear Flow over Surface Mounted Obstacle,'' ASME J. Fluids Eng., **112**, pp. 376–385.
[14] Martinuzzi, R., and Tropea, C., 1993, ''The Flow Around Surface-Mounted, Prismatic Obstacles Placed in a Fully Developed Channel Flow,'' ASME J. Fluids Eng., **115**, pp. 85–92.
[15] Igarashi, I., and Takasaki, H., 1992, ''Fluid Flow Around Three Rectangular Blocks in a Flat-Plate Laminar Boundary Layer,'' Exp. Heat Transfer, **5**, pp. 17–31.
[16] Morris, G. K., and Garimella, S. V., 1996, ''Thermal Wake Downstream of a Three-Dimensional Obstacle,'' Exp. Therm. Fluid Sci., **12**, pp. 65–74.
[17] Goldstein, R. J., and Karni, J., 1984, ''The Effect of a Wall Boundary-Layer on Local Mass Transfer from a Cylinder in Crossflow,'' ASME J. Heat Transfer, **106**, pp. 260–267.
[18] Goldstein, R. J., Chyu, M. K., and Hain, R. C., 1985, ''Measurement of Local Mass Transfer on a Surface in the Region of the Base of a Protruding Cylinder with a Computer-Controlled Data Acquisition System,'' Int. J. Heat Mass Transf., **28**(5), pp. 977–985.
[19] Igarashi, T., 1985, ''Heat Transfer From a Square Prism to an Air Stream,'' Int. J. Heat Mass Transf., **28**(1), pp. 175–181.
[20] Igarashi, T., 1986, ''Local Heat Transfer from a Square Prism to an Air Stream,'' Int. J. Heat Mass Transf., **29**(5), pp. 777–784.
[21] Igarashi, T., 1987, ''Fluid Flow and Heat Transfer Around Rectangular Cylinders (The Case of a Width/Height Ratio of a Section of 0.33∼1.5),'' Int. J. Heat Mass Transf., **30**(5), pp. 893–901.
[22] Fisher, E. M., and Eibeck, P. A., 1990, ''The Influence of a Horseshoe Vortex on Local Convective Heat Transfer,'' ASME J. Heat Transfer, **112**, pp. 329–335.
[23] Martinez-Botas, R. F., Lock, G. D., and Jones, T. V., 1995, ''Heat Transfer Measurements in an Annular Cascade of Transonic Gas Turbine Blades Using the Transient Liquid Crystal Technique,'' ASME J. Turbomach., **117**, pp. 425–431.
[24] Ekkad, S. V., and Han, J. C., 1996, ''Heat Transfer Inside and Downstream of Cavities Using Transient Liquid Crystal Method,'' AIAA J. Thermophysics and Heat Transfer, **10**(3), pp. 511–516.
[25] Han, J. C., and Ekkad, S. V., 1996, ''Turbine Blade Cooling and Heat Transfer Measurement Using a Transient Liquid Crystal Image Method,'' Invited Paper for the 5th Colloquium on Turbomachinery Seoul National University Seoul, Korea, pp. 263–302.
[26] Chyu, M. K., Ding, H., Downs, J. P., and Soechting, F. O., 1998, ''Determination of Local Heat Transfer Coefficient Base on Bulk Mean Temperature Using a Transient Liquid Crystal Technique,'' Exp. Therm. Fluid Sci., **18**, pp. 142–149.
[27] Critoph, R. E., Holland, M. K., and Fisher, M., 1998, ''Comparisons of Steady

State and Transient Methods for Measurement of Local Heat Transfer in Plate Fin-Tube Heat Exchangers Using Liquid Crystal Thermography with Radiant Heating,'' Int. J. Heat Mass Transf., **42**, pp. 1–12.

[28] Hwang, J. J., and Cheng, C. S., 1999, ''Augmented Heat Transfer in a Triangular Duct by Using Multiple Swirling Jets,'' ASME J. Heat Transfer, **121**, pp. 683–690.

[29] Ireland, P. T., and Jones, T. V., 1987, ''The Response Time of a Surface Thermometer Employing Encapsulated Thermochromic Liquid Crystals,'' J. Phys. E, **20**, pp. 1195–1199.

[30] Butler, R. J., and Baughn, J. W., 1996, ''The Effect of the Thermal Boundary Condition on Transient Method Heat Transfer Measurements on a Flat Plate With a Laminar Boundary Layer,'' ASME J. Heat Transfer, **118**, pp. 831–837.

Forced Convection Heat Transfer Enhancement Using a Self-Oscillating Impinging Planar Jet

Cengiz Camci
Mem. ASME
e-mail: c-camci@psu.edu

Frank Herr[1]

Turbomachinery Heat Transfer Laboratory,
The Pennsylvania State University,
Department of Aerospace Engineering,
223 Hammond Building,
University Park, PA 16802

Impinging jets are widely used in the local enhancement of heat removed from internal passages of gas turbine blades. Arrays of stationary jets are usually impinged on surfaces of internal cooling passages. The current practice is to benefit from the high heat transfer coefficients existing in the vicinity of the jet impingement region on a target wall. The present study shows that a self-oscillating impinging-jet configuration is extremely beneficial in enhancing the heat removal performance of a conventional (stationary) impinging jet. In addition to a highly elevated stagnation line Nusselt number, the area coverage of the impingement zone is significantly enhanced because of the inherent sweeping motion of the oscillating coolant jet. When an oscillating jet ($Re=14{,}000$) is impinged on a plate normal to the jet axis ($x/d=24$ hole to plate distance), a typical enhancement of Nu number on the stagnation line is about 70 percent. The present paper explains detailed fluid dynamics structure of the self-oscillating jet by using a triple decomposition technique on a crossed hot wire signal. The current heat transfer enhancement levels achieved suggest that it may be possible to implement the present self-oscillating-impinging-jet concept in future gas turbine cooling systems, on rotating disks, glass tempering/quenching, electronic equipment cooling, aircraft de-icing, combustors and heat exchangers. [DOI: 10.1115/1.1471521]

Keywords: *Convection, Enhancement, Heat Transfer, Jets, Turbulence*

Introduction

The advancement of high performance thermal systems has stimulated interest in methods to improve heat transfer rates, especially on the coolant side of hot surfaces. Considerable efforts have been made to increase heat transfer rates by implementing passive enhancement methods that require no direct consumption of external power. The present study deals with a heat transfer enhancement method using planar cooling jets in a self-sustained oscillatory flow mode. Utilizing an impinging jet in oscillatory mode has great cooling potential for hot section components. This method is based on the enhancement of turbulent mixing processes on the coolant side of hot surfaces by generating additional turbulent mixing via periodic oscillations in the impingement region. The term ''oscillation'' is used for the periodic flapping motion of the jet in a direction normal to orifice/nozzle axis. An obvious advantage of using self-sustained oscillations is that the power for oscillation is drawn from the existing flow field. The oscillations can easily be generated by a simple orifice/nozzle configuration that has no moving components even in relatively small coolant passages. The flapping motion of the turbulent planar jet spreads the effective thermal transport features over a relatively large impingement area on the target plate. A typical enhancement of Nu number near the stagnation line can be as high as 70 percent over stationary jet values.

Stationary impinging jets are widely used to provide high local mass/momentum/heat transfer in a variety of applications including gas turbine cooling, paper drying, helicopter rotor blade deicing system, glass manufacturing, food processing etc. Impingement jet systems are popular because of the relative ease of controlling the specific area needed to be cooled/heated/dried and high local heat transfer rates on the target surface. Reviews of earlier heat transfer studies on stationary impinging jets are given in Martin [1] and Goldstein et al. [2]. Gardon and Cobonpue [3] described the rate of heat transfer to an impinging jet as proportional to the difference between the target plate temperature and the adiabatic wall temperature, which varied from point to point on the impingement surface. Gardon and Akfirat [4] noted that the level of turbulence in the jet had a significant effect on the rate of heat transfer between the target plate and the stationary jet. Heat transfer from a flat surface to an oblique impinging jet was studied by Goldstein and Franchett [5] and Foss [6]. Most studies have involved jets of the same temperature as the ambient fluid. However, when the temperature of the jet is different from that of the ambient air, entrainment of ambient air into the jet complicates the heat transfer problem, Goldstein et al. [7] and Goldstein and Seol [8]. Stationary impinging jet based cooling arrangements are currently extremely popular in gas turbine cooling engineering and process engineering.

Fluidic oscillatory nozzles as simple and effective mixing devices have been used by Viets [9]. An extension of the fluidic nozzle concept to supersonic flow conditions is described by Raman et al. [10]. These are detailed fluid mechanics studies geared towards using the unsteady motion to actively control viscous flow near surfaces. The current study uses the fluidic oscillating nozzle as a heat transfer augmentation method for general heat transfer applications. The self-oscillating impinging jet improves thermal transport via periodic flapping motion of the jet. The area coverage of the impingement zone is also greatly enlarged by the flapping motion. Details of the analytical flow model for the self-oscillating-impinging jet used in this study is given by Herr and Camci [11]. The analytical model based on a corrected similarity technique is validated via hot wire measurements using a crossed wire. A decomposition approach wa used to identify the contribution due to the deterministic jet oscillations and

---

[1] Present address: Tenneco Corp., Walker Eng. Center, 3901 Willis Road, Grass Lake, Michigan, 49240

Contributed by the Heat Transfer Division for publication in the JOURNAL OF HEAT TRANSFER. Manuscript received by the Heat Transfer Division June 30, 2000; revision received February 15, 2002. Associate Editor: J. G. Georgiadis.

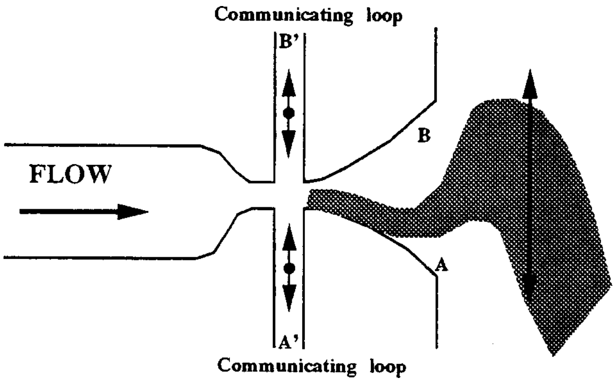

Fig. 1 A planar jet with self-sustained oscillations

stochastic turbulent fluctuations. The governing equations are derived for oscillating flows with fixed flapping frequency. At a given time, the oscillatory flow field can be approximately described by the solution of a stationary jet flow obtained from a nozzle/orifice attached to a relative reference frame that is oscillating at a prescribed frequency. The corrected similarity solution predicts the axial/lateral mean velocity measurements and oscillation kinetic energy data well, Herr [12].

Oscillation of the planar jet flow enhances transport process near the target plate because of the existence of additional inertia forces (oscillation stress) and additional thermal fluxes (oscillation heat flux). Experiments show that most of the kinetic energy in the oscillatory jet is contained in the deterministic unsteady part. The magnitude of the unsteady kinetic energy convection due to the flapping motion of the jet is about three times of that due to turbulence. The individual terms of the kinetic energy conservation equation sampled/evaluated from the measured crossed hot wire data show that the convection of kinetic energy in oscillatory flows is stronger than the convection due to turbulent fluctuations.

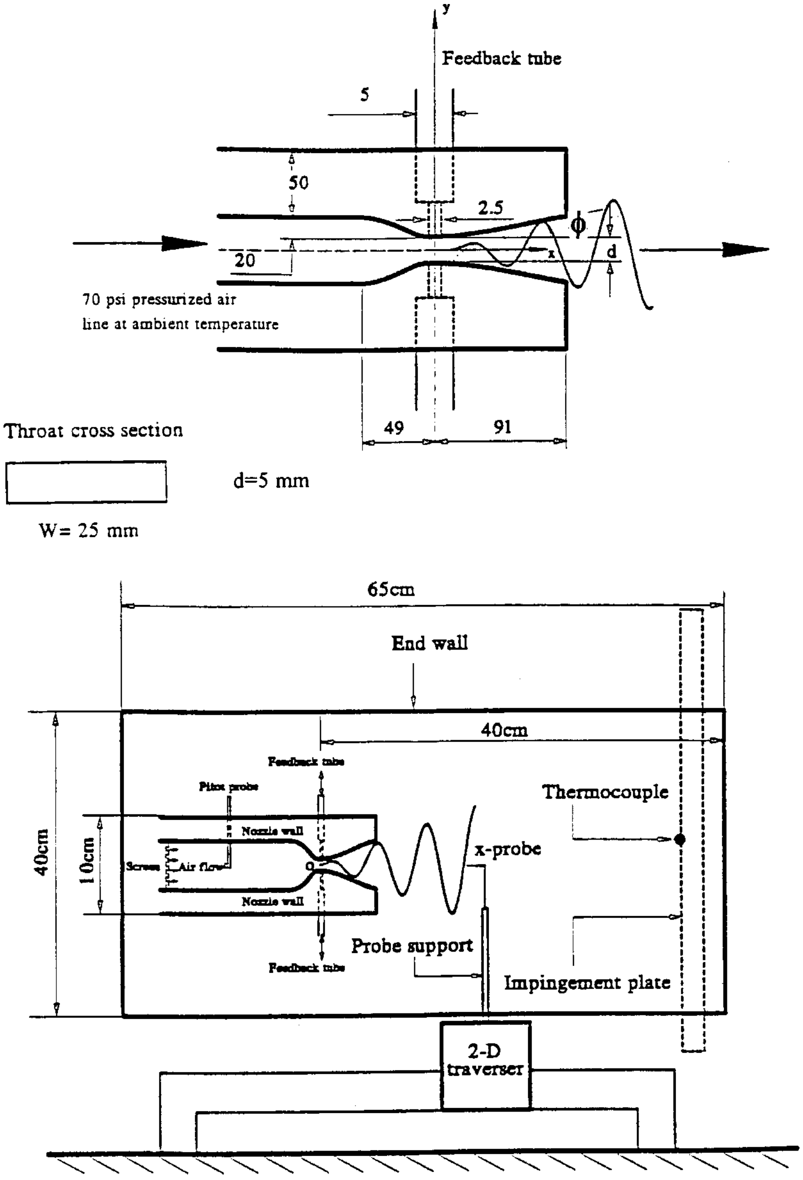

Fig. 2 Geometrical details of the nozzle and the experimental setup for the self-oscillating impinging jet experiments

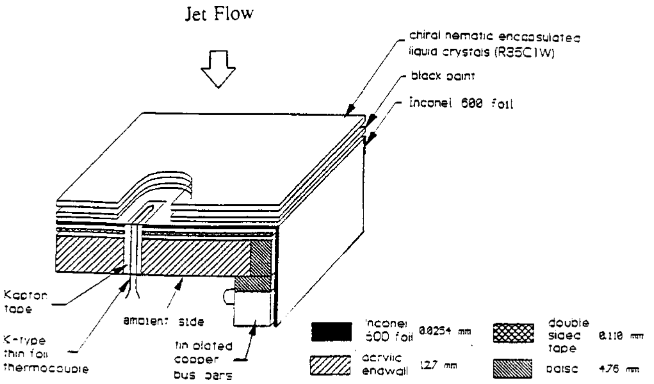

Fig. 3 Heat transfer surface construction

It is concluded that deterministic unsteadiness enhances transport process significantly, Herr and Camci [13]. Oscillation increases convection and diffusion significantly.

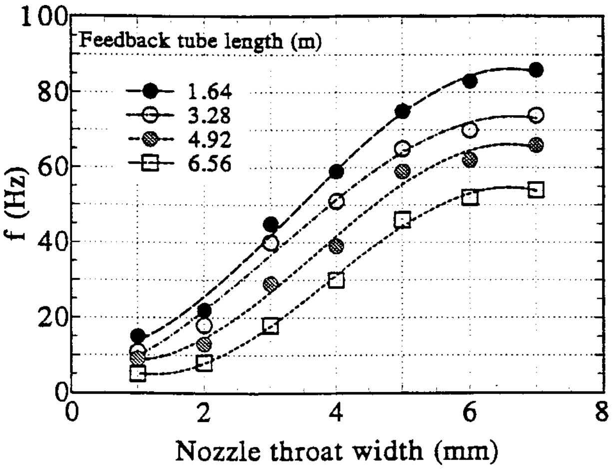

Fig. 4 Effect of nozzle throat width and communicating tube length on oscillation frequency of the jet, (ϕ=20 deg)

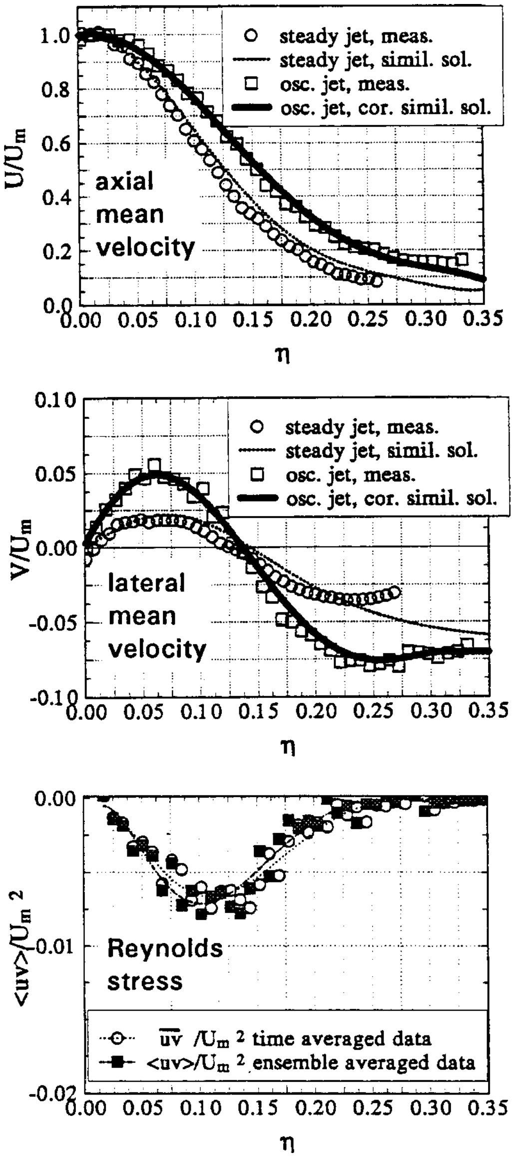

Fig. 5 Axial, lateral mean velocity profiles and Reynolds stresses in oscillating jet

Enhancement of impingement heat transfer using a self-oscillating circular nozzle is described in Page et al. [14]. This acoustic excitation technique is based on the matching of the shear tone and organ pipe frequency of the pipe's finite length. The flow visualization studies revealed free transverse wave oscillations and enhanced vortex shedding. A collar extension approach results in enhancements in surface transport phenomena. An oscillation frequency of 5000 Hz from a self-oscillating nozzle resulted in measurable heat transfer coefficient enhancement. The nozzle-to-plate distance varied between diameters. Azevedo et al. [15] used a mechanical rotating ball valve to generate pulsations in axial velocity of a circular jet. The axial velocity in time varies between a peak and a minimum in each period created by valve rotations. This approach results in degradation in heat transfer coefficients on the impingement plate. The nozzle to plate distance varies between 2 to 10 diameters. The authors claim that the type of pulsations generated in this study adds energy primarily on the large scale, with little superimposed small scale turbulence. Liu and Sullivan [16] studied heat transfer from an acoustically excited circular impinging jet. The investigation is performed with a nozzle having an exit diameter of 12.7 mm and a nozzle to plate spacing less than two diameters. A loudspeaker attached to one side of a rectangular plenum chamber induces organ pipe resonance in the chamber producing pane-wave excitation at the jet exit. The perturbation velocity can be adjusted between 0.05 percent and 0.18 percent in a frequency range from 600 to 2500 Hz. A small nozzle-to-plate spacing (less than two diameters), the local heat transfer in the wall jet region can be significantly affected by exciting the impinging jet. The heat transfer near the stagnation point remains unchanged. The random vortical structures enhance the local heat transfer. The strong large-scale well-organized vortices formed after the stable pairing induce the unsteady separation of the wall boundary layer and hence, lead to the local heat transfer reduction. Mladin and Zumbrunnen [17] use a rotating ball mechanism to generate a planar air jet with pulsations. The nozzle-to-plate separation distance varies between 0 to 10 nozzle widths with a pulse amplitude ranging from 0 to 50 percent of the mean flow velocity. Pulsation frequencies range from 0 to 80 Hz corresponding to Strouhal numbers below 0.106 based on nozzle width and jet discharge velocity. Heat transfer enhancements up to 12 percent near the nozzle mid-plane due to surface renewal effects and up to 80 percent at distances downstream due to increased turbulence levels are measured where both the pulse amplitude and Strouhal number are the highest. Pulses of small amplitude and low frequency induces a quasi-steady behavior at small separation distances, with no significant effect on the time averaged heat transfer near the nozzle mid plane. However, at

Table 1 Estimates of the precision index and bias error values used for the uncertainty analysis

	Precision index	Bias Error	Uncertainty
q_{gen}	1.0 %	0.3 %	1.0 %
q_{cond}	5.5 %	5.9 %	8.1 %
q_{rad}	1.6 %	1.9 %	2.5 %
$(T_w\text{-}T_{char})$	2.7 %	2.6 %	3.4 %

larger separation distances, increased turbulence associated with the decay of the flow pulse enhanced the time averaged heat transfer away from the nozzle mid plane by up to 20 percent.

All of the studies reviewed in the previous paragraph focus on the nozzle to plate distances less than 10 jet diameters (or widths). Although Page et al.'s [14] study uses a self-sustained oscillation mode that does not require external power to maintain pulsations, Liu and Sullivan [16], Mladin and Zumbrunnen [17] and Azevedo et al. [15] use loudspeaker and rotating ball valve arrangements that are powered externally. The current study is different from the studies summarized in this paragraph for two main reasons. First, the nozzle-to-impingement plate distance of the current study $(24<x/d<60)$ is geared towards engineering applications that can be found in food processing, drying, gas turbine cooling, glass tempering and aeronautical de-icing systems. The second main difference is in the character of unsteady jet motion imposed. The current study benefits from a self-oscillating impinging jet configuration that improves thermal transport via periodic flapping motion of the jet. The area coverage of the flapping fluid motion that is influencing the impingement plate zone is much greater than the coverage of all other studies reviewed in this section. Although the jets acoustically excited (or mechanically oscillated by a rotating ball valve) usually develop strong longitudinal oscillations they influence a limited impingement area on the target plate. The current self-oscillating planar jet in flapping mode has relatively larger area coverage on the target plate.

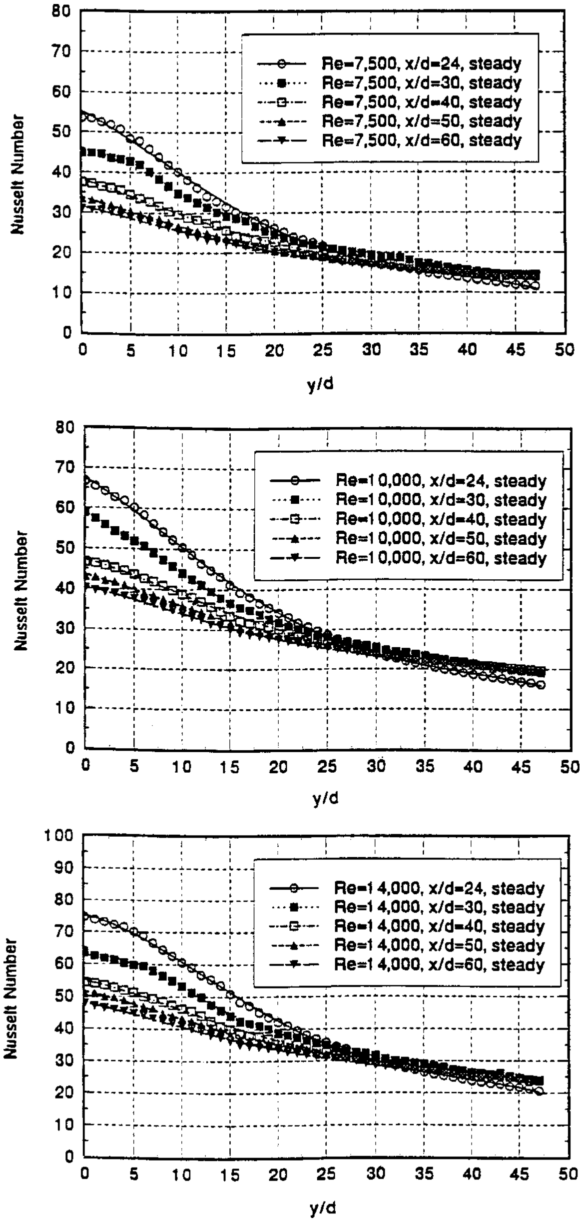

Fig. 6 Stationary jet Nusselt number distributions on impingement plate, influence of Reynolds number and impingement plate location *x*/*d*, baseline data set

The present study focuses on the heat transfer aspects of self-oscillating impinging jets used in thermal system engineering. High-resolution heat transfer measurements are presented in a Re number range between 7500 and 14,000 $(24<x/d<60)$. This range is sufficiently wide for many current thermal engineering applications. It is possible to implement the present self-oscillating-impinging-jet concept in future gas turbine cooling systems, on rotating disks, in electronic equipment cooling, aircraft de-icing systems and heat exchanger systems.

Experimental Setup and Procedures

Oscillating Jet Assembly. The operation principle of an oscillatory jet is based on the fact that a jet exiting into space between two sufficiently near walls is bi-stable, i.e., may attach to either wall. In addition, a small pressure gradient across the jet at the throat may cause the jet to detach one wall and attach to the opposite one. A simple fluidic nozzle representation of the oscillatory jet used in this study is shown in Fig. 1. The air flows through a nozzle shaped contraction, past two communication ports, into an expansion section. The output ports are attached to each other via a communication loop. Due to the proximity of the wall at the nozzle throat, the jet is bi-stable and must attach to one of the walls. Consider the jet to be attached to wall *A*. Due to large amount of entrainment into the jet, the pressure at the control port A' is relatively low while the pressure at the port B' is relatively high. Since the ports are attached to each other by a feedback loop, a compression wave travels from port B' to port A' tending to raise the pressure there and push the jet off the wall. Simultaneously, an expansion wave originates at port A' and travels to port B', tending to lower the pressure there and pull the jet onto the wall *B*. Thus, in a well designed nozzle, the jet will oscillate between walls *A* and *B* at a frequency determined by the length of the line connecting ports A' and B' and the line diameter. The frequency is also a weak function of the stagnation pressure entering the nozzle. The improved mixing characteristics of the oscillatory jet are seen in the increased spread angle and in the voids of stagnant gas that are entrained between the waves of the oscillation, Herr and Camci [11,13]

The flow and heat transfer tests for the current oscillating jet concept have been performed using precision Aluminum nozzles. The planar nozzle sections are precision-machined using fine, spline fitted coordinate points. The nozzle pieces are enclosed in 1.25 cm thick plexiglass sidewalls as shown in Fig. 2. A regulated laboratory compressed air supply is fed into the nozzle. The jet emerges from the nozzle having $d=5$ mm throat width (nozzle height is $W=25$ mm) at a typical mean velocity of 25 m/s $(\mathrm{Re}=10^4)$. To study the oscillation caused by the mechanism described above, the unsteadiness of other means must be minimum. With two communicating ports closed, the velocity at the throat

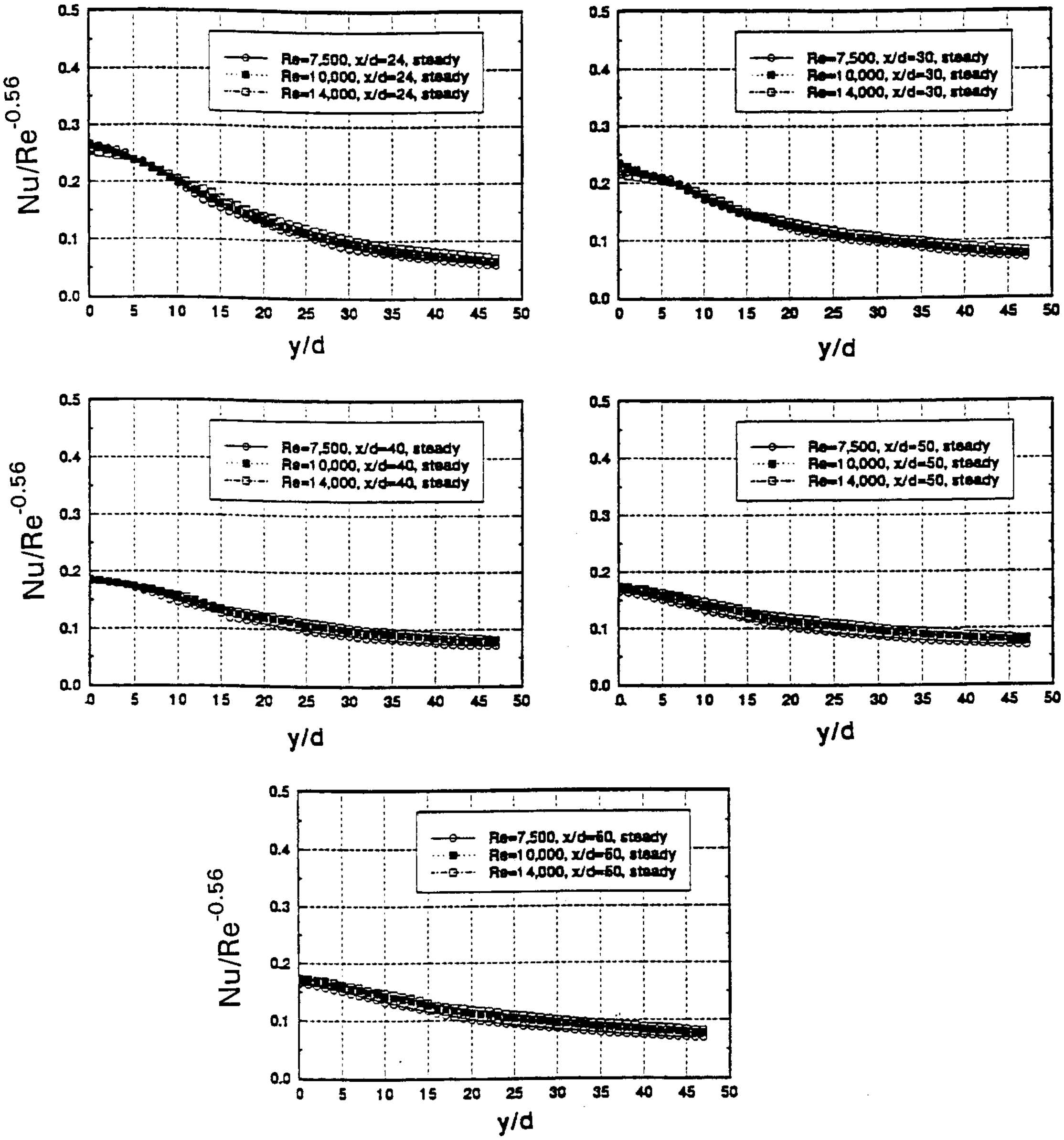

Fig. 7 Impingement plate heat transfer distribution from stationary jet, Nu/Re$^{-0.56}$ distribution for all Reynolds numbers in function of *y/d*

has been kept constant within 1 percent. For steady-flow situation, the jet is laminar, having a turbulence intensity of approximately 0.1 percent at the exit plane. The oscillation frequency of the jet is in the range of 10–100 Hz. This frequency is controlled by the stagnation pressure, nozzle throat width, and the length/diameter of the communicating loop. Other details of the experimental set-up can be found in Herr [12].

Steady/Unsteady Flow Field Measurements. Instantaneous velocity measurements have been taken with a TSI 1249A-T1.5 miniature 90 deg crossed hot wire probe and a TSI 1210-T1.5 general purpose single sensor probe using TSI series 1050 constant temperature anemometer. The single sensor probe has been used to measure the jet exit flow at the nozzle throat plane. The crossed wire probe has been calibrated in a velocity range from 0.5 to 40 m/s using a full velocity-yaw angle calibration scheme (±45 deg). The specific calibration scheme is the one defined by Lueptow et al. [18] and modified by Panchepakesan and Lumley [22]. This stretching coordinate transformation approach improves the measurement resolution at low velocities. Unsteady flow data are sampled at a rate of 10 KHz for 5 seconds. A local averaging technique is used to detect the fronts of the periodical signals and 100 periods are ensemble averaged. Details of the current crossed hot-wire measurement method are presented in Herr [12].

Heat Transfer Measurements on the Target Plate. The target heat transfer surface, located downstream of the nozzle is shown in Fig. 2. The target plate to nozzle distance has been varied from 24 to 60 nozzle throat width "*d*" during the experiments. The impingement plate is made up of 1.25 cm thick clear acrylic. The heat transfer surface is a composite system that includes a double-sided tape layer, Inconel heater foil, black backing paint, a liquid crystal thermo-indicator layer and flush mounted surface thermocouples. Details of the composite heat transfer surface are shown in Fig. 3. A low resistivity rectangular steel foil (Inconel-600) has been used as a constant heat flux surface on the target plate. The resistance of the steel foil has been accurately determined using a Keithley 580 micro-ohmmeter to an uncertainty of ±0.001 Ω. A DC current reversal method removing unwanted offset voltages has been used. This technique lowers

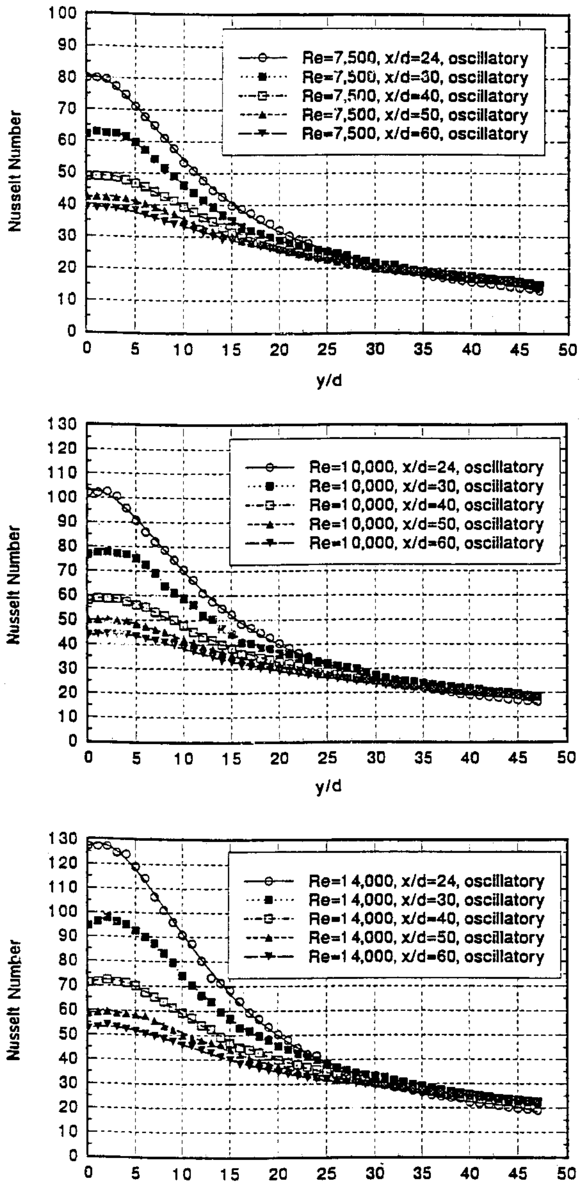

Fig. 8 Self-oscillating-jet Nusselt number distributions on impingement plate, influence of Reynolds number and impingement plate location *x/d*

random noise in resistance measurements. Wall temperature measurement on the heat transfer has been made by using several flush-mounted thin-foil thermocouples of K type. Details of the heat transfer surface construction area given in Wiedner and Camci [19] and Herr [12]. Flush mounted thermocouples have been inlaid in several spanwise locations along the impingement plate and the junctions have been located at mid-point, Fig. 3, Herr [12]. The impingement plate shown in Fig. 2 has been traversed in the *y*-direction. The ambient side temperature of the heat transfer surface has also been monitored continuously for conduction heat loss calculations. The losses from the impingement side to the ambient side have been considered in the calculation of the convective heat transfer coefficient. A variable current DC power supply has been used to heat the constant heat flux surface. The jet and the ambient air in the laboratory are at the same temperature. The convective heat transfer coefficient is defined as,

$$h = q_{\mathrm{conv}}/(T_w - T_{\mathrm{char}}) \tag{1}$$

where q_{conv} is convective heat flux rate, T_w the wall temperature and T_{char} the characteristic temperature. The Nusselt number for this problem is based on the nozzle throat width d,

$$\mathrm{Nu} = hd/k. \tag{2}$$

In the present study, the reference temperature T_{char} is taken as the total temperature of the jet, T_o. The uniform wall heat flux value over the rectangular surface was fixed at a constant level for all tests. The heat flux generated by Joule heating of the steel foil is balanced by convective, conductive and radiative heat flux,

$$q_{\mathrm{gen}} = q_{\mathrm{conv}} + q_{\mathrm{cond}} + q_{\mathrm{rad}}. \tag{3}$$

The conduction heat loss from the impingement side to the back side of the plate is assumed to be one-dimensional,

$$q_{\mathrm{cond}} = k_{\mathrm{plate}} \partial T/\partial y = k_{\mathrm{plate}}(T_w - T_{w,\mathrm{back}})/H \tag{4}$$

where T_w is the wall temperature on the heat flux surrace, $T_{w,\mathrm{back}}$ is the temperature of the back side of the target plate, and H is the thickness of the target plate. During a typical run, conduction losses account for approximately 6–12 percent of the generated heat flux. Radiation heat transfer was estimated using the assumptions of black body emissivity and thermal equilibrium between the jet and sidewalls. The shape factors were approximated using an enclosure model and considering each surface as black. The radiation heat flux is approximately 3–9 percent of the local generated heat flux.

Experimental Uncertainties. The final experiment uncertainty estimates of the current study are described using the method given by Kline and McClintock [20]. The uncertainty levels presented are analogous to 95 percent coverage or 20:1 odds. A crossed hot wire sensor has been used to measure *x* and *y*-components of the instantaneous velocity field in which temperature variation in the flow field is not significant. The Inconel strip heater used in constant heat flux measurements on the target plate has been disconnected from the DC power supply during hot wire measurements. This approach assures an isothermal flow field that is essential for high quality hot-wire measurements. The instantaneous field has then been de-composed into mean, deterministic and random parts for further analysis. The sources of error in hot wire measurement include flow field temperature variations, thermal inertia of the sensors, probe misalignment, sampling time errors, constant temperature anemometer noise. The cut-off frequency used has been selected as 4 kHz with an overheat ratio of 1.6. It has been noted from a power spectral density calculation that, energy content of the flow is extremely small for the frequencies higher than 600 Hz. A 0.5 deg alignment error is assumed in the uncertainty analysis. This error contributes 0.1 percent to the total error. The predicted error in instantaneous velocity measurements is about 1 percent. A detailed account of the error analysis on hot wire measurements is presented in Herr [12].

The heat transfer measurements on the constant heat flux surface are influenced from the errors made in the determination of wall temperature T_w, total temperature T_o of the jet (ambient), heat flux measurement, throat width measurement and absolute error in thermal conductivity *k* of air. Our experiments by varying the black paint and liquid crystal layer thickness showed that the wall temperature error $\delta(T_w - T_{\mathrm{char}})/(T_w - T_{\mathrm{char}})$ is less than 3.4 percent. This error is already included in the final uncertainty value of Nusselt number 6.3 percent approximately. Estimates of the precision index and bias error values for the main measured quantities in the uncertainty analysis are given in Table 1. Further details of the uncertainty analysis are presented in Herr [12].

Experimental Results and Discussion

Jet Half Width and Effective Mixing. A useful indication of effective mixing in a jet is the variation of the jet half width in axial direction. The definition of the half width at any streamwise

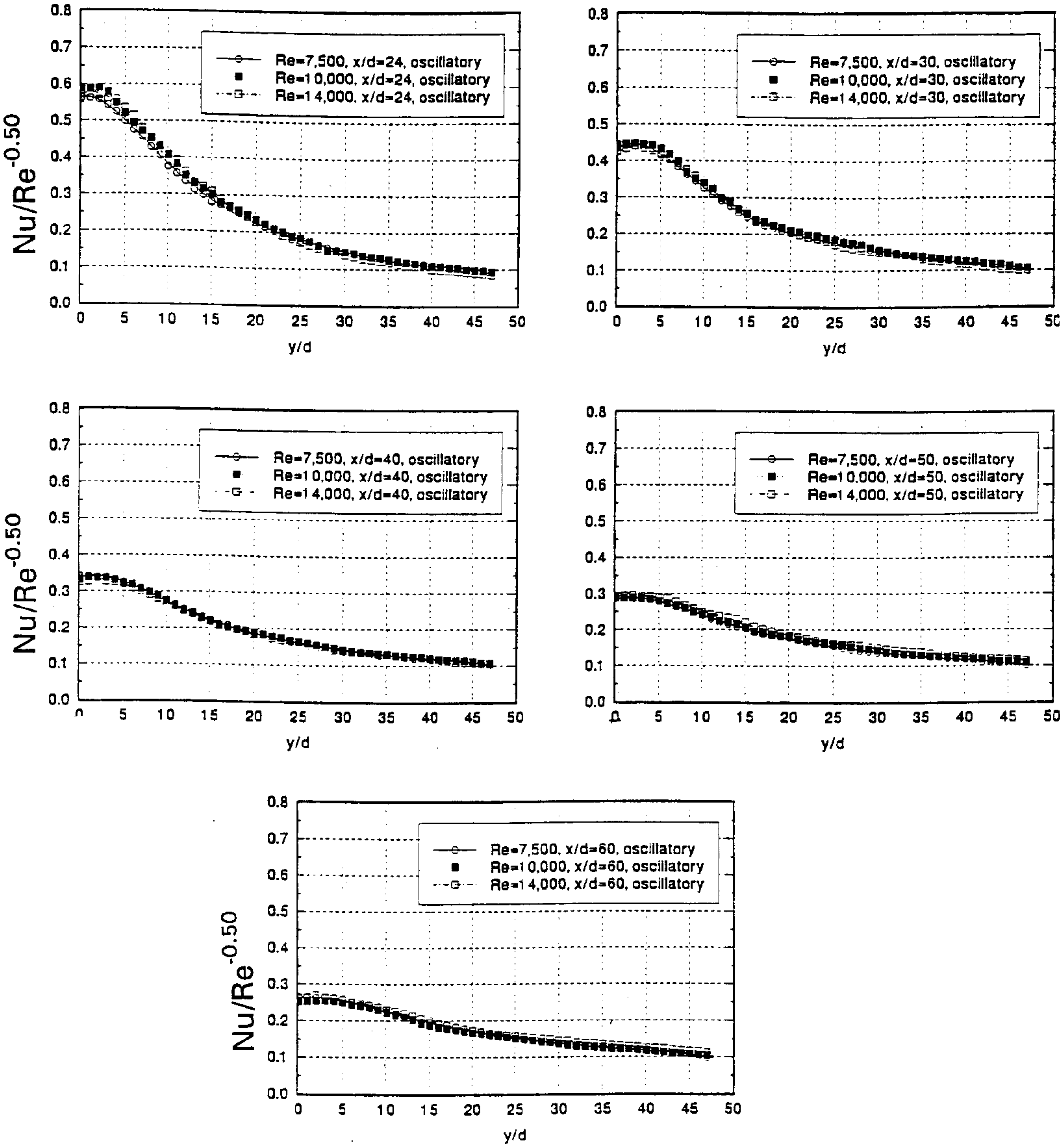

Fig. 9 Impingement plate heat transfer distribution from oscillating jet, Nu/Re$^{-0.50}$ distribution for all Reynolds numbers in function of *y/d*

position is the distance between the jet centerline and the point where the local velocity is equal to half of the centerline velocity. Current experiments clearly show that the introduction of the oscillatory motion dramatically increases the jet half width. At $x/d = 60$, (Re=10,000), the half width from a stationary jet is about 8 times the nozzle throat width *d*. However, when the same jet is put into a self-oscillatory motion, the half width increases to 13 times the throat width, Herr [12]. This observation is closely related to the fact that a cooling jet in a flapping motion covers a much wider impingement area when compared to a stationary jet. Enhanced turbulent transport with effective mixing is spread over a much larger impingement zone on the target surface via the use of an oscillating jet.

Frequency of Self-Sustained Jet Oscillations. The oscillation frequency of the jet is determined by taking the fast Fourier transform of instantaneous hot wire data from the exit of the nozzle at, $\eta = y/x = 0$. Figure 4 shows the variation of oscillation frequency with respect to nozzle throat width *d* for constant stagnation pressure in the plenum chamber, (ϕ=20 deg). Experiments performed at $x = 180$ mm also show that larger throat widths at a fixed communication line length induce higher oscillation frequencies. Similar trends have been observed at $y/x = 0$, $y/x = 0.05$, and $y/x = 0.3$. Increasing *d* from 1 mm to 5 mm provides a five-fold frequency increase from 15 to 75 Hz. Increasing the length of the communication line slightly reduces the oscillation frequency. For the case of increased throat width, the amount of fluid entraining into the throat area increases. Thus the ambient air enters the feedback tube sooner than the case which has a smaller throat width. If the width is too large, the pressure gradient across the jet is not strong enough to move the jet and the jet would not bend to either wall, so that no oscillation will occur. Increasing plenum chamber stagnation pressure and shorter communication lines has a tendency to increase the frequency of oscillations, Herr [12].

Axial and Lateral Mean Velocity Components. Mean velocity components have been measured by time averaging the instantaneous hot wire signal at various $\eta = y/x$ locations at $x/d = 60$ for $f = 75$ Hz. It should be noted that the data discussed from

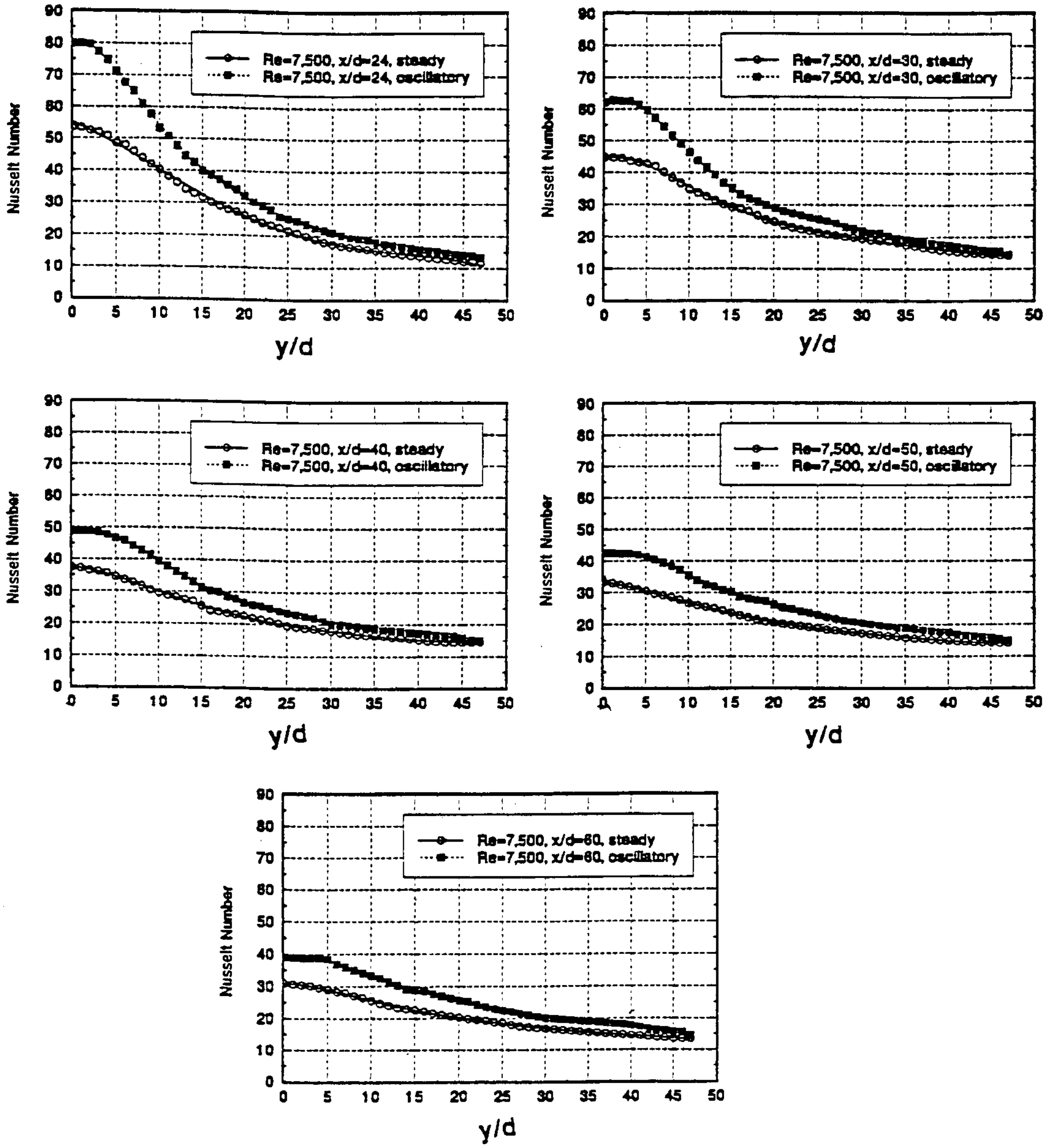

Fig. 10 Comparison of oscillating jet and stationary jet heat transfer distributions on the impingement plate, Re=7500

this point on include only the results for the nozzle that has a throat width of $d=5$ mm and a nozzle half angle of $\phi=20$ deg. The measured axial mean velocity (U/U_m) distribution of the oscillatory jet is relatively fuller than that of the stationary jet as shown in Fig. 5. This is expected because oscillation increases the spreading rate of the jet. The lateral mean velocity (V/U_m) distribution of the oscillating jet is enhanced when $0<y/x<0.14$, $(\eta=x/d=60)$. The flapping motion of the jet issued from the fluidic nozzle provides increased transport of mean kinetic energy in the lateral direction. This feature is directly related to the observed enhancements in jet half width leading to increased transport in the lateral direction, Herr [12]. The thick solid lines in Fig. 5 represents the predictions from "*the corrected similarity method*" developed by Herr and Camci [11]. "*The corrected similarity method*" is an analytical extension of the stationary turbulent jet solution with special emphasis paid to deterministic oscillations of the jet. Figure 5 shows that "*the corrected similarity method*" based prediction of mean velocities is in very good agreement with hot wire measurements where $0<y/x<0.275$. The stationary turbulent jet solution for U and V (based on a conventional similarity method) is represented by tiny dots in Fig. 5.

Additional Stresses and Heat Fluxes Due to Deterministic Oscillations. The instantaneous velocity and temperature can be decomposed into three parts, Hussain and Reynolds [21], a time averaged quantity (U_i,Θ), ensemble averaged deterministic oscillations (u_i^*,θ^*) and stochastic turbulent fluctuations (u_i,θ),

$$\begin{aligned}\tilde{u}_i&=U_i+u_i^*+u_i\\ \tilde{\theta}&=\Theta+\theta^*+\theta\end{aligned}\tag{5}$$

In an oscillatory flow, the continuity equation can be decomposed as,

$$\frac{\partial U_i}{\partial x_i}+\frac{\partial u_i}{\partial x_i}+\frac{\partial u_i}{\partial x_i}=0\tag{6}$$

Finally, the time averaged momentum equation for a flow with self-sustained oscillations is as follows,

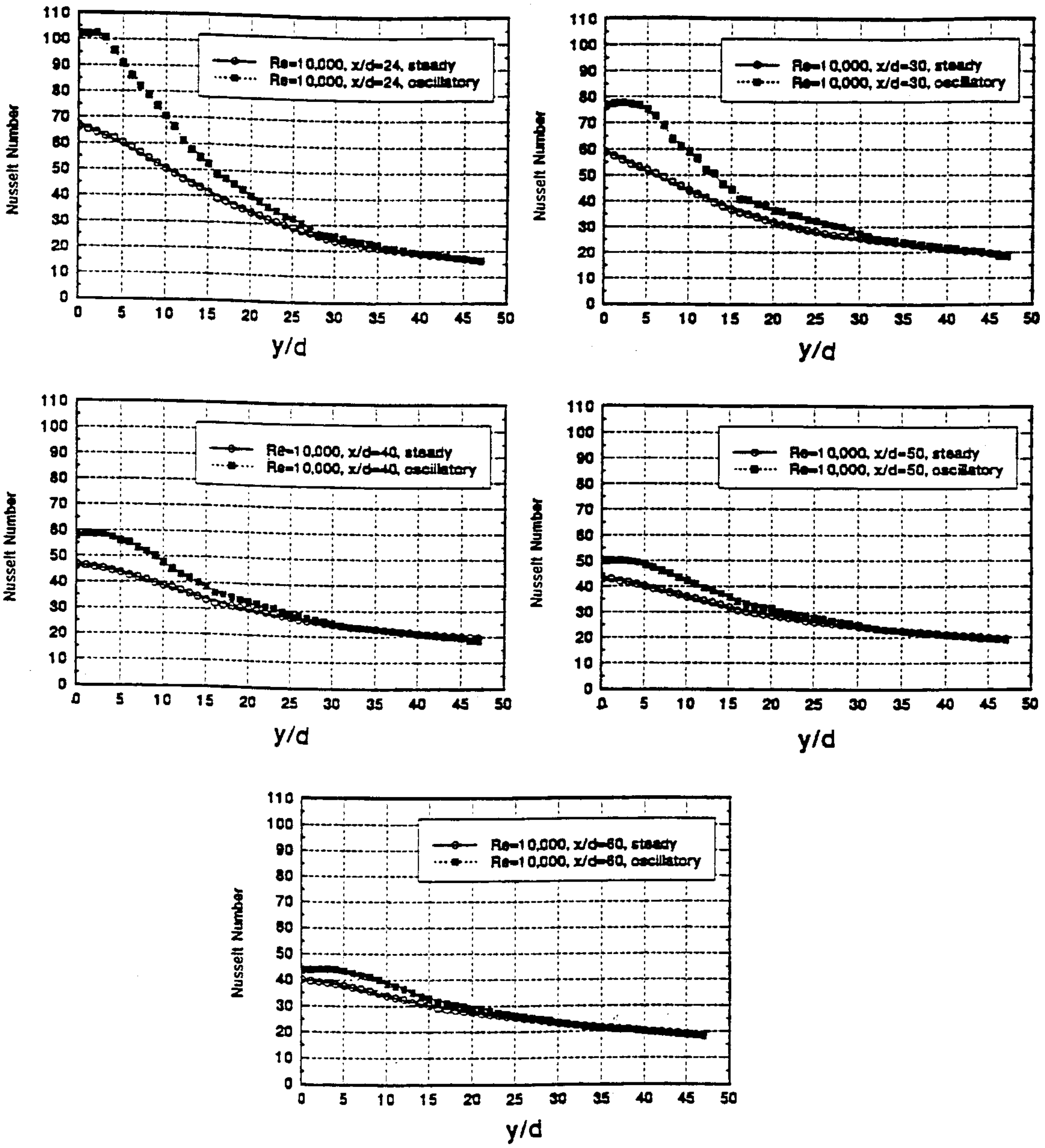

Fig. 11 Comparison of oscillating jet and stationary jet heat transfer distributions on the impingement plate, Re=10,000

$$\frac{\partial(U_iU_j)}{\partial x_j}=-\frac{1}{\rho}\frac{\partial P}{\partial x_i}+\frac{\partial}{\partial x_j}\left(\nu\frac{\partial U_i}{\partial x_j}-\overline{u_i^*u_j^*}+\overline{u_iu_j}\right) \tag{7}$$

$$\frac{\partial(U_j\theta)}{\partial x_j}=\frac{\partial}{\partial x_j}\left(\gamma\frac{\partial\theta}{\partial x_j}-\overline{u_j^*\theta^*}+\overline{u_j\theta}\right) \tag{8}$$

Equation 7 clearly shows that in addition to shear stress due to molecular viscosity, there are two additional apparent stresses termed as $-\overline{u_i^*u_j^*}$ and $-\overline{u_iu_j}$. The apparent stress terms are generated by the nonlinear inertia term (convective acceleration) that is the left hand side of the instantaneous momentum equation. Additional inertia force due to random oscillations of the turbulent field is usually termed as Reynolds stress $-\overline{u_iu_j}$. The term $-\overline{u_j^*u_j^*}$ is due to the inertia force originating from deterministic variations of the oscillating jet flow. This extra stress term is named as oscillation stress $-\overline{u_j^*u_j^*}$ throughout this study. Similar to the development leading to Eq. 7, one can obtain a time averaged thermal energy equation, Eq. 8, Herr and Camci [13]. The three terms on the right hand side of the energy equation are conduction heat flux $\gamma(\partial\theta/\partial x_j)$ due to molecular conductivity, oscillation heat flux $-\overline{u_j^*\theta^*}$ due to flapping motion of the jet and turbulent heat flux $-\overline{u_j\theta}$ due to random fluctuations of the flow field. Figure 5 also shows a comparison of the time averaged and ensemble averaged turbulent stress $\langle uv\rangle/U_m^2$ in function of η at $x/d=60$, $f=80$ Hz. Reynolds stresses due to turbulent fluctuations reach a peak around $\eta=0.10$ and diminish near the centerline and near the outer edge of the jet where $\eta>0.30$.

Heat Transfer From Stationary Impinging Jet. Stationary jet related Nusselt number distributions on the impingement plate are given in Fig. 6 as baseline distributions. Experiments at three different Reynolds numbers (7500, 10,000, and 14,000) are presented for various impingement plates to nozzle distance values ($x/d=24,30,40,50$, and 60). A strong influence of plate to nozzle distance on stagnation point heat transfer is shown in Fig. 6. Nus

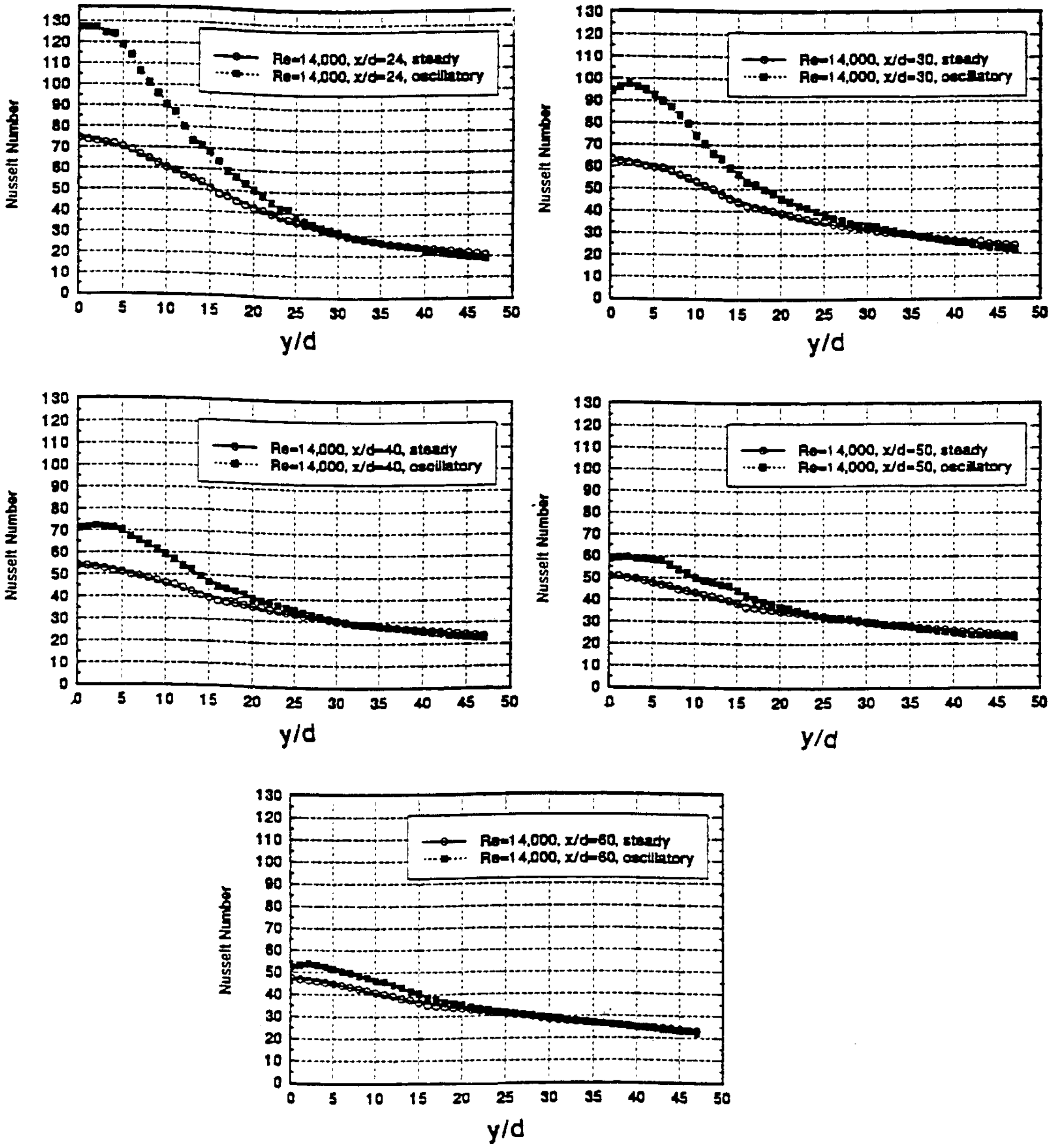

Fig. 12 Comparison of oscillating jet and stationary jet heat transfer distributions on the impingement plate, Re=14,000

selt number at the stagnation point increases from 30 to 55 when x/d is reduced from 60 to 24 at Re=7500. This trend repeats itself for Re=10,000 and 14,000. The Nusselt number depends on x/d in the near impingement region $0<y/d<20$, while in the wall jet region, the heat transfer is almost independent of x/d for all Re numbers. At the minimum x/d value of 24, the jet is predicted to be fully turbulent for all Reynolds numbers. In other words, potential core does not exist at this x/d. The heat transfer information given in Fig. 6 provide the reference stationary heat transfer distributions when oscillating jet results are compared to stationary jet. In general the local heat transfer on the impingement plate is a function of x/d, y/d, Re, and Pr. This functional dependency can be represented by a power law in the form,

$$\mathrm{Nu}=\sim\mathrm{Re}^{n}\mathrm{Pr}^{m}. \tag{9}$$

The exact form of Eq. 9 varies from study to study depending on the heat transfer configuration, flow and thermal boundary conditions, local turbulence production and unsteadiness in the flow. The molecular Prandtl number can be taken constant for air under present conditions. For the stationary impinging jet, the most representative value for n has been found to be $n=0.56$, when m is unity. At a fixed impingement plate to nozzle distance, all three heat transfer distributions for different Re values will collapse into a unique curve, if the results are plotted $\mathrm{Nu}/\mathrm{Re}^{-0.56}$ versus y/d. Figure 7 clearly demonstrates this feature for 5 different x/d values ($x/d=24,30,40,50,60$).

Heat Transfer Enhancement From Self-Oscillating Impinging Jet. The stationary jet flow can be converted into an oscillating jet flow by opening the communication lines at points A' and B' which are sealed for stationary jet experiments. The communication line diameter at A' and B' is 6 mm. The half angle for the nozzle exit section is kept constant at $\theta=20$ deg. The flow conditions inside the nozzle are identical within quoted uncertainty values for both stationary and oscillating jets, for comparison purposes.

Figure 8 shows Nusselt number distributions over the impingement plate in function of y/d at different Re and impingement plate to nozzle distance (x/d) values. When compared to the stationary jet values as presented in Fig. 6, the oscillatory jet heat transfer results are significantly enhanced as shown in Fig. 8.

Another observation is the relatively flat distributions of Nusselt number around the stagnation line of the impingement plate compared to the stationary jet distributions. The well known high heat transfer effectiveness of the stagnation region is now spread over a relatively larger area round the stagnation point via organized flapping motion of the jet, Fig. 8 $(x/d=40,50,60)$.

When shorter plate to nozzle distances $(x/d=24,30)$ are examined, one can observe that the maximum heat transfer does not occur at the exact center line $y/d=0$. Off-center peaks are visible in Fig. 9 for $x/d=24$ and 30. The stagnation line Nusselt numbers are slightly lower than the peak values. The heat transfer enhancement around the centerline point is spread over a much wider area by double peas presented in Fig. 8, especially at shorter plate to nozzle distances ($x/d=24$ and 30). This observation is consistent with the fact that the oscillating flow now sweeps through a larger interaction are on the impingement plate with enhanced thermal transport features due to imposed deterministic unsteady motion.

Current experiments suggest that the impingement plate positions where $x/d<40$ are the most effective heat transfer enhancement cases when the oscillating jet is impinged on a flat surface. Removing the Reynolds number dependency from the oscillating jet heat transfer results can be achieved by introducing the same type of functional dependency as presented in Eq. 9. For the oscillating jet, the most representative value for n has been found to be $n=0.50$ when m is taken as 1. At a fixed impingement plate to nozzle distance, all three heat transfer distributions for three different Re values again collapse into a unique curve $(\mathrm{Nu}/\mathrm{Re}^{-0.50}$ in function of $y/d)$. Figure 9 presents this feature for 5 different x/d values $(x/d=24,30,40,50,60)$.

Figures 10, 11, and 12 show significant heat transfer improvement when a stationary jet is converted into an oscillating jet at fixed Reynolds number and impingement plate to nozzle distance. for Re=7500 and $x/d=24$, the stagnation line local Nusselt number for oscillatory impinging jet is 30 percent higher than that of the stationary jet. When Reynolds number is increased to 14,000 the enhancement from oscillations is about 71 percent higher compared to stationary impinging jet, at $x/d=24$. The heat transfer enhancement almost diminishes in the outer region of the impingement plate where $y/d>25$ for all Re numbers and impingement plate to nozzle distance values. In general, the enhancements become more pronounced as the Reynolds number is gradually increased from 7500 to 14,000.

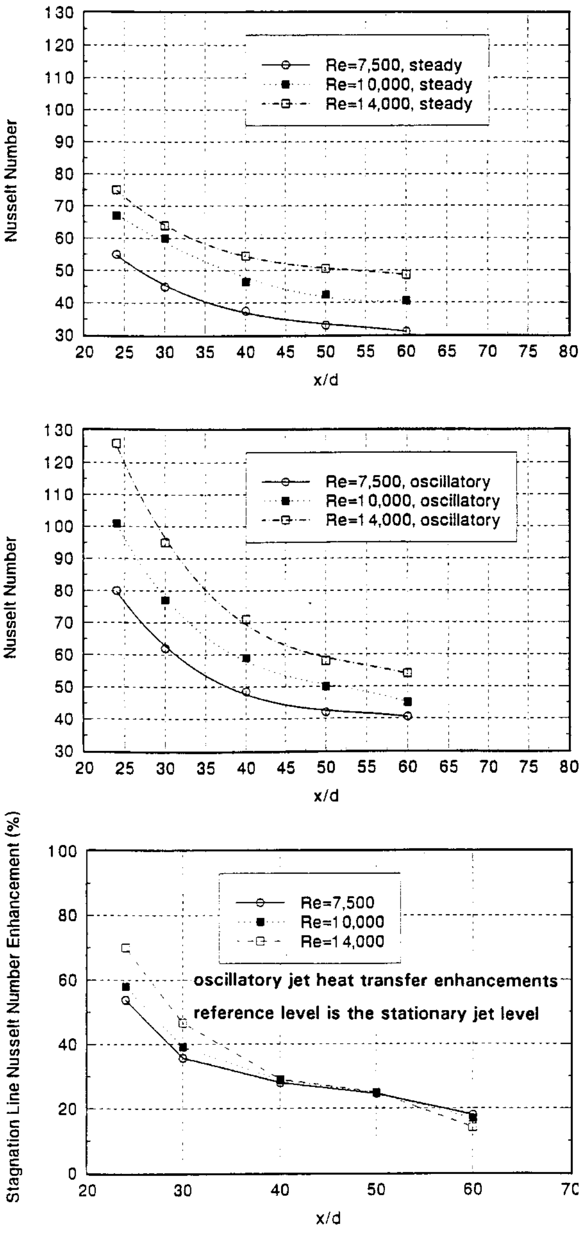

Fig. 13 Stagnation line heat transfer at various nozzle to impingement plate distances, without and with jet oscillations

Comparison of Heat Transfer Enhancements at the Stagnation Line. Local Nusselt numbers at $y/d=0$ for both the stationary jet and the oscillating jet are given in Figs. 13(*a*) and 13(*b*). For the stationary jet, at $x/d=30$, the stagnation point Nusselt number is about 20 percent less than the case for $x/d=24$ regardless of the Re number of the jet. For larger spacing, where $x/d>40$ (40,50,60), dependence of Nusselt number on x/d becomes weaker as shown in Fig. 13(*a*). At large nozzle to impingement plate distances, flow near the stagnation point is influenced from ambient air entrainment at a more significant rate compared to short x/d cases. All of the current heat transfer measurements show that Nusselt number levels at the stagnation point are drastically increased, when the stationary jet is switched into its oscillating mode, Fig. 13(*b*). The enhancement rate has a slight Re number dependency. However, x/d dependency at a given Re number is much stronger. When $x/d<40$, oscillation induced enhancements are all greater than 30 percent in reference to the stationary jet Nusselt number values. Figure 13(*c*) summarizes the relative heat transfer enhancement values in reference to the stationary jet for all Re numbers and x/d values. The minimum enhancement from oscillations has been measured as approximately 18 percent at $x/d=60$. However, if one reduces the plate to nozzle distance, significant Nusselt number enhancement values are encountered. For example at $x/d=40$ the enhancement from oscillations is about 30 percent. After this point, the enhancements become stronger for smaller plate to nozzle distances. At $x/d=24$, there is about 70 percent heat transfer augmentation on the stagnation line for Re=14,000.

The oscillation driven enhancements discussed in this paragraph may be explained by using time averaged momentum and thermal energy equations as discussed in previous paragraphs. When unsteady deterministic fluid motion governs the heat transfer process, the additional inertia forces (oscillation stresses) due to the existence of the periodic (deterministic) flow play a significant role in the conservation of linear momentum, Eq. 7. The thermal energy transfer is also influenced because of the existence of the oscillations. For the case of heat transfer, oscillation heat flux terms become as significant as conventional turbulent heat flux terms in the energy conservation statement, Eq. 8, Herr [12]. When x/d is small, the oscillation heat fluxes and stresses dominate the enhancement process, since the large amount of ambient air entrainment does not affect the thermal energy transfer process. When x/d is large, the ambient air entrainment overweighs the oscillation heat fluxes. Thus the enhancement caused by jet oscillations become almost Re number independent.

Conclusions

It is possible to convert a stationary impinging cooling jet into a self-oscillating-impinging jet by adding two communication ports at the throat section. The unsteady travel of compression and expansion waves in the communication loop can easily put a stationary planar jet into a flapping mode for more effective thermal transport enhancement.

Oscillation frequencies ranging from 20 Hz to 100 Hz are possible by adjusting the proper length and diameter of the communication line and the stagnation pressure in the nozzle plenum chamber.

A triple-decomposition technique applied to the instantaneous velocity field and temperature field clearly indicates the contributions of additional fluid stresses (oscillation stress) and thermal energy transfer due to oscillatory motion (oscillation heat flux). The flapping motion of the jet clearly improves thermal transport near the impingement plate via the imposed deterministic/periodic motion.

Oscillation of the jet increases convection and diffusion significantly, however the kinetic energy production is only slightly modified. Previous studies performed by the authors show that most of the kinetic energy is contained in the deterministic part.

For the case of oscillating-impinging-jet, the area containing the enhanced heat transfer zone on the impingement plate is enlarged effectively when compared to the stationary jet.

Oscillating jet heat transfer results are compared against stationary jet results at three different Reynolds number levels (7500, 10,000, 14,000) at various nozzle to plate distances ($x/d=24,30,40,50,60$). Significant heat transfer coefficient enhancements ranging from 20 percent to 70 percent over the stationary jet values exist because of the oscillation motion of the impinging jet.

When the jet is put into the oscillating mode, the Reynolds number dependency of oscillating jet heat transfer distribution can be removed by plotting Nu/Re$^{-0.50}$ against y/d for a prescribed x/d value. The data show that at a fixed nozzle to plate distance x/d, all three heat transfer distributions for individual Re number values collapse into a unique curve.

The current heat transfer enhancement achieved suggest that it is possible to implement the present self-oscillating-impinging-jet concept in future turbine blade internal cooling systems, on rotating disks, in electronic cooling, aircraft/helicopter de-icing systems and heat exchanger systems.

Acknowledgments

The authors would like to acknowledge the assistantship provided to Frank Herr during the execution of this project at the Turbomachinery Heat Transfer Laboratory by the Department of Aerospace Engineering, the Pennsylvania State University. Thanks are also due to Mr. George Sayers for the precision machining of Aluminum nozzles used in this study.

Nomenclature

d = nozzle throat width, see Fig. 2 (linear dimension)
f = oscillation frequency of the jet
h = convective heat transfer coefficient
H = thickness of the plexiglass impingement plate
i,j,k = summation indices
k = thermal conductivity
m,n = exponents in Nu number correlation
Nu = Nusselt number, Nu$=hd/k$
p = instantaneous pressure
P = time averaged pressure
Pr = molecular Prandtl number
q = wall heat flux rate
q = turbulent kinetic energy using u, v, w
q* = oscillation kinetic energy using u^*, v^*, w^*
Re = Reynolds number, Re$=Ud/v$, based on bulk velocity of the jet at the throat section
t = time
T = temperature
U,V,W = mean velocity components
u,v,w = velocity fluctuations due to stochastic fluctuations (turbulence)
u^*,v^*,w^* = deterministic (periodic) velocity component
$-\langle uv\rangle$ = ensemble averaged Reynolds stress, $-\langle u_iu_j\rangle$
$-\overline{uv}$ = time averaged Reynolds stress, $-\overline{u_iu_j}$
x,y,z = Cartesian coordinates
x/d = impingement plate to nozzle distance (normalized)
x = axial direction for the jet
y = lateral direction for the jet

Greek letters

ϕ = nozzle half angle at the divergent exit section
Θ = time averaged local temperature in the flow field
θ = temperature fluctuations due to stochastic fluctuations (turbulence)
θ^* = deterministic (periodic) temperature
γ = thermal diffusivity
η = similarity variable, $\eta=y/x$
μ = absolute viscosity
ν = kinematic viscosity $\nu=\mu/\rho$
ρ = density

Subscripts

char = characteristic
cond = conduction
conv = convection
gen = generated
m = centerline quantity (at $y=0$)
o = total condition
rad = radiated
t = turbulent quantity
w = wall
w,back = back side of the wall

Superscripts

$*$ = deterministic (periodic) quantity
m,n = correlation constants
$\sim$ = instantaneous quantity

References

[1] Martin, H., 1977, "Heat and Mass Transfer Between Impinging Gas Jets and Solid Surfaces," *Advances in Heat Transfer*, T. Irvine and J. P. Hartnett, eds., **13**, Academic Press, New York, pp. 1–60.
[2] Goldstein, R. J., Behbahani, A. I., and Heppelmann, K. K., 1986, "Streamwise Distribution of the Recovery Factor and the Local Heat Transfer Coefficient to an Impinging Circular Air Jet," Int. J. Heat Mass Transf., **29**(8), pp. 1227–1235.
[3] Gardon, R., and Cobonpue, J., 1962, "Impingement Cooling From a Circular Jet in a Cross Flow," *Proceedings of 2nd International Heat Transfer Conference*, pp. 719–730.
[4] Gardon, R., and Akfirat, J. C., 1965, "The Role of Turbulence in Determining the Heat Transfer Characteristics of Impinging Jets," Int. J. Heat Mass Transf., **8**, pp. 1261–1272.
[5] Goldstein, R. J., and Franchett, M. E., 1988, "Heat Transfer From a Flat Surface to an Oblique Impinging Jet," ASME J. Heat Transfer, **110**, pp. 84–90.
[6] Foss, J. F., 1979, "Measurements in a Large-Angle Oblique Jet Impingement Flow," AIAA J., **17**(8), pp. 801–802.
[7] Goldstein, R. J., Sobolik, K. A., and Seol, W. S., 1990, "Effect of Entrainment on the Heat Transfer to a Heated Circular Aid Jet Impinging on a Flat Surface," ASME J. Heat Transfer, **112**, pp. 608–611.
[8] Goldstein, R. J., and Seol, W. S., 1991, "Heat Transfer to a Row of Impinging circular Air Jets Including the Effects of Entrainment," Int. J. Heat Mass Transf., **34**(8), pp. 2133–2147.
[9] Viets, H., 1975, "Flip-Flop Jet Nozzle," AIAA J., **13**(8), pp. 1375–1379.
[10] Raman, G., Hailye, M., and Rice, E., 1993, "Flip-Flop Jet Nozzle Extended to Supersonic Flows," AIAA J., **31**(6), pp. 1028–1035.
[11] Herr, F., and Camci, C., 1994, "Validation of an Analytical Model for an Unsteady Planar Jet with Self-Sustained Oscillations," AIAA paper 94-2205.

[12] Herr, F., 1995, ''Turbulent Transport in a Planar Jet with Self-Sustained Deterministic Oscillations and the Character of Impinging Region Heat Transfer,'' Ph.D. thesis, Dept. of Aerospace Engineering, Pennsylvania State University, University Park, PA.

[13] Herr, F., and Camci, C. 1994, ''Turbulent Mixing and Transport in a Planar Jet with Self-Sustained Deterministic Oscillations,'' 1994 ASME Winter Annual Meeting, ASME AD-Vol. 40, ASME, New York.

[14] Page, R. H., Chinnock, P. S., and Seyed-Yagoobi, J., 1996, ''Self-Oscillation Enhancement of Impingement Jet Heat Transfer,'' AIAA Journal of Thermophysics, **10**(2), pp. 380–382.

[15] Azevedo, L. F. A., Webb, B. W., and Queiroz, M., 1994, ''Pulsed Air Jet Impingement Heat Transfer,'' Exp. Therm. Fluid Sci., **8**, pp. 206–213.

[16] Liu, T., and Sullivan, J. P., 1996, ''Heat Transfer and Flow Structures in an Excited Circular Impinging Jet,'' Int. J. Heat Mass Transf., **39**(17), pp. 3695–3706.

[17] Mladin, E. C., and Zumbrunnen, D. A., 1997, ''Local Convective Heat Transfer to Submerged Pulsating Jets,'' Int. J. Heat Mass Transf., **40**(14), pp. 3305–3321.

[18] Lueptow, R. W., Breuer, K. S., and Haritonidis, J. H., 1988, ''Computer-Aided Calibration of x-Probes Using a Look-up Table,'' Exp. Fluids, **6**, pp. 115–118.

[19] Wiedner, B. G., and Camci, C., 1996, ''Deterministic of Convective Heat Flux on Steady-State Heat Transfer Surfaces With Arbitrarily Specified Boundaries,'' ASME J. Heat Transfer, **118**, pp. 101–107.

[20] Kline, S. J., and McClintock, F. A., 1953, ''Describing Uncertainties in Single-Sample Experiments,'' Mech. Eng. (Am. Soc. Mech. Eng.), **75**, pp. 3–8.

[21] Hussain, A. K. M. F., and Reynolds, W. C., 1970, ''The Mechanics of an Organized Wave in Turbulent Shear Flow,'' J. Fluid Mech., **41**, pp. 241–258.

[22] Panchapakesan, N. R., and Lumley, J. L., 1993, ''Turbulence Measurements in Axisymmetric Jets of Air and Helium,'' Part 1. Air Jet,'' J. Fluid Mech., **246**, pp. 197–223.

Structure and Dynamics of Laminar Jet Micro-Slot Diffusion Flames

John Baker
e-mail: jbaker@me.ua.edu

Mark E. Calvert
Department of Mechanical Engineering,
University of Alabama,
Tuscaloosa, AL 35487-0276

David W. Murphy
Department of Mechanical Engineering,
University of Alabama at Birmingham,
Birmingham, AL 35294-4461

Results of an experimental investigation into the behavior of laminar jet diffusion flames, produced using micro-slot burner ports, are presented. Under certain conditions, the cross-sectional shape of micro-slot flames is qualitatively similar to the cross-sectional shape of circular burner port flames produced in an environment where molecular diffusion is the primary transport mechanism. An order of magnitude analysis reveals that, over the range of experimental conditions examined, the behavior of the experimentally observed micro-slot flames is not necessarily diffusion-controlled. A comparison of the experimental data with an accepted theoretical model shows that current theoretical models do not accurately predict the experimentally observed flame heights. A theoretical expression for purely diffusion-controlled micro-slot flame height is developed and compared with experimental micro-slot flame data. The region where this theoretical expression is valid is identified through an examination of the diffusion to buoyancy parameter. A qualitative discussion of micro-slot flame structure is also presented. [DOI: 10.1115/1.1482083]

Keywords: *Combustion, Flame, Gaseous, Heat Transfer, Scaling*

1 Introduction

It has long been recognized that buoyancy induced flow is one of the principal factors influencing the behavior of diffusion flames in a terrestrial environment. Unfortunately, the impact of buoyancy is so pervasive that it is difficult/impossible to experimentally isolate buoyancy from other combustion related phenomena in a terrestrial environment. Numerous investigators have examined the impact of buoyancy on diffusion flame behavior or have attempted to develop techniques for minimizing/isolating the impact of buoyancy. Davis et al. [1] proposed varying the ambient pressure, while maintaining the same fuel and oxidizer mass flow rates, to vary the impact of buoyancy. Reasoning that the effective gravitational acceleration is proportional to the square of the pressure, it was hypothesized that by reducing the ambient pressure one would be able to reduce buoyancy forces. A reduction in ambient pressure did produce shorter, broader flames but it was later shown in Dietrich et al. [2] that these flames are not dynamically similar to flames in a reduced-buoyancy environment. Using a scaling analysis based on flame height and reduced gravity experimental data, Dietrich et al. [2] proved that reducing the ambient pressure does not significantly remove buoyant convection. In the same paper, it was also indirectly shown that a diffusion flame could exist in an environment where molecular diffusion is the only transport mechanism.

Since the forces associated with buoyancy are proportional to the acceleration due to gravity, conducting experiments in a reduced, or micro-, gravity environment is an effective way of reducing/eliminating the impact of buoyancy forces. Currently the expense of conducting experiments in a microgravity environment limits access to such an environment. Even in a microgravity environment, rapid small-scale variations in acceleration, i.e., *g*-jitter, are known to affect combustion behavior. The impact of *g*-jitter on combustion related phenomena is still an area of active research [3].

Buoyancy forces are proportional to the cube of a characteristic length. Therefore if one were to decrease a diffusion flame's characteristic length to a small enough value, the flame should behave in a manner relatively unaffected by buoyancy. This type of behavior has been experimentally observed using laminar jet diffusion flames produced with circular burner ports having inner diameters of less than 1 mm [4]. In Ban et al. [4], the importance of accounting for axial diffusion in the momentum equations when describing the behavior of diffusion microflames was investigated. Recall that axial diffusion of momentum has typically been neglected in classical descriptions of jet diffusion flames [5]. Using a similarity analysis, a theoretical model was developed for laminar axisymmetric jet diffusion microflames. While the introduction of axial diffusion into the theoretical model did not significantly affect the predicted flame height, it did dramatically improve the ability of the model to predict flame shape. Note that this theoretical microflame model did not include a buoyancy force term.

Theoretical descriptions of diffusion flames, such as the classical Burke-Shumann solution [6], have been successful in describing diffusion flame behavior despite the assumption of negligible buoyancy. The success of these theoretical models has been explained by the fact that such models are compared with experimental data produced using circular burner ports. Buoyancy forces associated with a flame accelerate the fluid in the axial direction and, as a result, increase the concentration gradients in the radial direction. The increase molecular diffusion in the radial direction acts to decrease the velocity in the axial direction. For a circular burner port, these two phenomena cancel out. This is not the case for flames produced using slot burners as was shown in the seminal work of Roper [7]. For slot flames, Roper identified three regimes: the buoyancy-controlled, the transition, and the momentum-controlled regimes. In the buoyancy-controlled regime, the flame height of a slot flame was found to be proportional to the buoyant acceleration raised to the 1/3 power. As one might expect, in the momentum-controlled regime buoyancy was found to have a negligible impact on the flame height. The Froude number, defined as [7]

$$\mathrm{Fr}=\frac{(Q_F I Y_{F,\mathrm{stoic}}/bh)^2}{aL_f} \tag{1}$$

was used to determine whether a flame was buoyancy-controlled $(\mathrm{Fr}\ll 1)$, transitional $(\mathrm{Fr}\cong 1)$, or momentum-controlled $(\mathrm{Fr}\gg 1)$.

Contributed by the Heat Transfer Division for publication in the JOURNAL OF HEAT TRANSFER. Manuscript received by the Heat Transfer Division February 20, 2001; revision received March 19, 2002. Associate Editor: J. P. Gore.

Note that this definition of the Froude number is based upon the flame height and not the burner port diameter. In Eq. (1), the mean buoyant acceleration is [7]

$$a \cong 0.6g[(T_f/T_\infty)-1] \tag{2}$$

and I is the ratio of the actual initial momentum to that for uniform flow (for parabolic exit velocity $I=1.5$ and for uniform flow $I=1.0$). For momentum-controlled slot flames, the Roper's theoretical expression [7] and experimental correlation [8] are respectively given as

$$L_{f,M,\mathrm{thy}}=\frac{b\phi^2 Q_F}{hID_\infty Y_{F,\mathrm{stoic}}}\left(\frac{T_\infty}{T_F}\right)^2\left(\frac{T_f}{T_\infty}\right)^{0.33} \tag{3}$$

$$L_{f,M,\mathrm{exp}}=8.6\times 10^4\frac{b\phi^2 Q_F}{hIY_{F,\mathrm{stoic}}}\left(\frac{T_\infty}{T_F}\right)^2 \tag{4}$$

where $\phi=1/\{4\cdot inverf[1/(1+S)]\}$ and where *inverf* is the inverse error function. For buoyancy-controlled flames, the theoretical expression [7] and experimental correlation [8] are respectively given as

$$L_{f,B,\mathrm{thy}}=\left[\frac{9\phi^4 Q_F^4 T_\infty^4}{8D_\infty^2 a h^4 T_F^4}\right]^{1/3}\left(\frac{T_f}{T_\infty}\right)^{2/9} \tag{5}$$

$$L_{f,B,\mathrm{exp}}=2.0\times 10^3\left[\frac{\phi^4 Q_F^4 T_\infty^4}{a h^4 T_F^4}\right]^{1/3} \tag{6}$$

For the transition regime, the flame height is given as [7]

$$L_{f,\mathrm{trans}}=\frac{4}{9}L_{f,M}\left(\frac{L_{f,B}}{L_{f,M}}\right)^3\left\{\left[1+3.38\left(\frac{L_{f,B}}{L_{f,M}}\right)^3\right]-1\right\} \tag{7}$$

The above closed-form expressions are now the standard expressions used for predicting laminar diffusion flame heights using slot burners. It should be noted that the slot flames in Roper et al. [8] were co-flow diffusion flames, while the flames examined in this study were produced by a jet of gas burning in quiescent air. It was stated in Roper et al. [8] that the co-flow of air had no effect on flame height for the flames produced using slot burners. While more complicated theoretical descriptions of laminar diffusion flames have since been developed, slot flame behavior is still traditionally characterized as either buoyancy-controlled or momentum-controlled [9].

Laminar diffusion flames represent an archetypal combustion process that has been extensively researched and several texts have chapters devoted to the subject [10,11]. Diffusion microflames produced using circular burner ports have only recently been examined and such flames could potentially be used as a means of isolating buoyancy in a terrestrial environment. Diffusion microflames produced using slot burners have not yet been investigated. Given that the behavior of slot flames is known to be different from flames produced using circular burner ports, an examination of diffusion microflames produced using slot burners is warranted. In this paper, the behavior of laminar jet diffusion microflames produced using slot burners is examined. In §2, an expression for a purely diffusion-controlled flame is developed. To gain insight into the phenomena responsible for microflame behavior, an order of magnitude analysis was performed and the methodology of this analysis is outlined §3. The methods used to obtain the experimental data and the accuracy of the experimental data are discussed in §4 and §5, respectively. The results of the investigation are provided in §6. Conclusions as to the behavior of micro-slot flames and the effectiveness of mathematical models to predict laminar jet micro-slot diffusion flame height are given in §7.

2 Purely Diffusion-Controlled Flames

For slot burner ports, Roper [7] showed that

$$\int_0^{L_f} u_z dz=\frac{\phi^2 Q_F^2 T_f^2}{Dh^2 T_\infty^2} \tag{8}$$

Roper used Eq. (8) to develop theoretical expressions for flame height in both the buoyancy-controlled and momentum-controlled regimes. This was accomplished by defining different functions for the axial component of velocity in the two regimes. In this investigation, the axial component of velocity in a purely diffusion-controlled flame has been assumed to be given as

$$u_z=u_D=D\frac{dY_F}{dz} \tag{9}$$

Fick's law of diffusion, i.e.,

$$\frac{d}{dz}\left(\rho D\frac{dY_F}{dz}\right)=0 \tag{10}$$

was used to determine the variation of the fuel mass fraction in the axial direction. Note that axial diffusion was ignored in Roper's mathematical formulation leading to Eq. (8). Assuming a constant density and diffusion coefficient, Eq. (10) provides a linear concentration profile in the axial direction. Applying the following boundary conditions

$$Y_F|_{z=0}=1 \tag{11}$$

$$-\rho D\left.\frac{dY_F}{dz}\right|_{z=L_f}=-k''\rho Y_F|_{z=L_f} \tag{12}$$

the axial component of velocity in a purely diffusion-controlled slot flame is found to be

$$u_z=u_D=\frac{Dk''}{D-L_f k''} \tag{13}$$

Note that Eq. (12) is a statement that, at the flame height, the rate at which the fuel is consumed is equal to the rate at which it is supplied by diffusion. Implicit in Eq. (12) is also the assumption that the reaction is first-order. Substituting Eq. (13) into Eq. (8) and integrating yields the following expression for the flame height of a purely diffusion-controlled flame produced using a slot burner:

$$L_{f,D,\mathrm{thy}}=\frac{\left(\frac{\phi Q_F T_f}{hT_\infty}\right)^2}{k''D\left[1+\frac{1}{D^2}\left(\frac{\phi Q_F T_f}{hT_\infty}\right)^2\right]} \tag{14}$$

For a diffusion-controlled slot flame, the flame height is not a function of the burner port width. This behavior is similar to that for a buoyancy-controlled slot flame. Also note that Eq. (14) predicts that as the flow rate increases the flame height approaches a constant value of D/k''. As will be shown below, Eq. (14) does not accurately predict micro-slot flame height for larger values of the volumetric flow rate.

Thermal radiation has not been included in the above model. As previously noted, microflames appear to be qualitatively similar to microgravity flames. Since thermal radiation is known to be significant in microgravity flames, one may suppose that accounting for thermal radiation should also be important in predicting microflame behavior. The principal reason that thermal radiation has not been included in the above model is that the inclusion of thermal radiation, except possibly under the most severe assumptions regarding thermal radiation behavior, would have removed the possibility of developing a closed-form solution. In addition, the standoff distance in microgravity flames is greater than that for flames in a terrestrial environment [12]. For microflames, while the standoff distance is larger relative to the overall size of the flame, there is no evidence that the standoff distance increases in size for microflames. The flame heat feedback by conduction is therefore not reduced and the relative significance of thermal radiation is not increased. In addition, the luminosity of microflames does not decrease to the extent observed in microgravity flames. While no quantitative data has been collected in this study to show that the temperature of microflames is lower relative to larger flames, the luminosity of the microflames seems to imply that the flame temperature is not significantly lower. Since the magnitude of the temperature drop in microgravity flames is proportional to the ratio of the radiative heat loss to the combustion heat release [12], the observed microflame behavior seems to indicate that the relative contribution of radiative heat transfer does not increase for microflames.

Heat loss to the burner port was also not considered in the above model. The primary reason for this assumption is that in Nakamura et al. [13], the temperature of the burner port and thus the heat loss to the burner port was found to have no effect on microflame flame height for circular burner ports. Burner port temperature did affect the quenching distance and this was identified as an important consideration when formulating the flame chemistry model for use in a multidimensional computational model of microflame behavior.

3 Order of Magnitude Analysis

To estimate the relative importance of buoyancy, momentum, and axial diffusion on flame height, an order of magnitude analysis was conducted. The gradient of the kinetic energy associated with the axial flow was assumed to be equal to the buoyant acceleration plus the gradient of the kinetic energy associated with the axial flow due to molecular diffusion. This is analogous to the assumptions made in Roper [7] except for the addition of the molecular diffusion contribution. Using this assumption, the axial component of the fuel velocity is found to be

$$u_z=[u_{zo}^2+2az+u_D^2]^{1/2} \tag{15}$$

The first term on the right hand side represents the momentum contribution to the axial velocity, the second term represents the buoyant contribution, and the third term represents the molecular diffusion contribution. With regard to the molecular diffusion contribution, there are two limits to the diffusion velocity, u_D. If $k'' \ll D/L_f$, the process is rate-controlled and the magnitude of the diffusion velocity is simply k''. On the other hand, if $k'' \gg D/L_f$ the process is diffusion-controlled and the magnitude of the diffusion velocity is D/L_f. For the order of magnitude analysis, the velocity associated with molecular diffusion was assumed to be diffusion-controlled. Assuming that the momentum contribution is negligible and expanding Eq. (15) in a binomial series gives

$$u_z=(2aL_f)^{1/2}\left(1+\frac{1}{4}N_{DB}+\frac{1}{32}N_{DB}^2+\cdots\right) \tag{16}$$

where N_{DB} is the diffusion to buoyancy parameter defined as

$$N_{DB}=D^2/aL_f^3 \tag{17}$$

The diffusion to buoyancy parameter may also be recast as $N_{DB}=1/\mathrm{GrSc}^2$ where the Grashof and Schmidt numbers are respectively defined as $\mathrm{Gr}=aL_f^3/v^2$ and $\mathrm{Sc}=v/D$. If $N_{DB} \ll 1$ then the flame is buoyancy-controlled and the expressions developed by Roper, Eqs. (5) and (6), should predict the flame height. If $N_{DB} \gg 1$ then the flame is diffusion-controlled.

In a similar manner, assuming the buoyant contribution is negligible and expanding Eq. (15) in a binomial series gives

$$u_z=u_{zo}\left(1+\frac{1}{2}N_{DM}^2+\frac{1}{8}N_{DM}^4+\cdots\right) \tag{18}$$

where N_{DM} is the diffusion to momentum parameter defined as

$$N_{DM}=D/u_{zo}L_f \tag{19}$$

As noted in Roper [7], $u_{zo}=Q_F I Y_{F,\mathrm{stoic}}/bh$ and the diffusion to momentum parameter may be recast as $N_{DM}=1/IY_{F,\mathrm{stoic}}$ ReSc where the Reynolds number is defined as $\mathrm{Re}=Q_F L_F/bhv$. Note that in these definitions, it has been assumed that initial fuel temperature is the ambient temperature. If $N_{DM} \ll 1$ then the flame is momentum-controlled and the expressions developed by Roper, Eqs. (3) and (4), should predict the flame behavior. If $N_{DM} \gg 1$ then the flame is purely diffusion-controlled. It is interesting to note that the Froude number, as defined in Roper, Eq. (1), may also be recast as $\mathrm{Fr}=N_{DB}/N_{DM}^2$. An examination of the Froude number, the diffusion to buoyancy parameter, and the diffusion to momentum parameter is sufficient to determine the relative importance of the three transport mechanism for micro-slot jet diffusion flame.

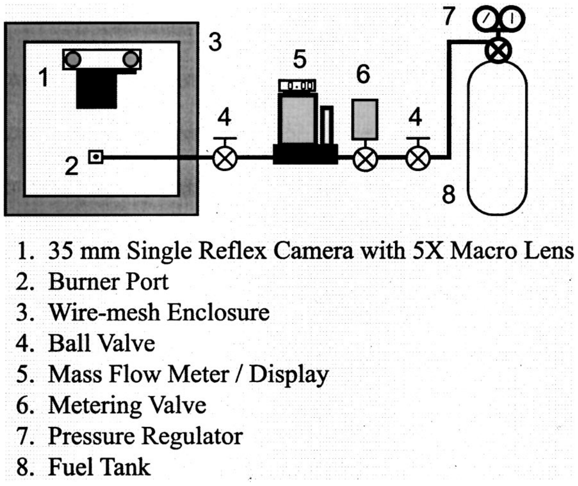

Fig. 1 A schematic diagram of the experimental test cell

4 Experimental Methods

Figure 1 is a schematic representation of the experimental test cell. As can be seen from the figure, the fuel flow rate was measured using a mass flow meter with a range of 0 to 20 ml/min and calibrated for propane. The flow rate was controlled using a metering valve. Several ball valves were placed along the length of the 1/4″ stainless steel tubing to allow portions of the system to be isolated. The burner port was surrounded by a wire screen mesh enclosure to eliminate any random air currents that may have affected flame behavior. Optical images of the flames were recorded using a 35 mm single reflex camera equipped with a 5× macro lens. The dimensions of the slot burner ports are given in Table 1 with the respective dimensions identified in Fig. 2. The slot burner ports were constructed from cylindrical brass tubing. The rectangular slots were formed near the end of the brass tubing by mechanically "pinching" the tubing. The slot width, *b*, was determined using stainless steel feeler gages of known thickness. The slots were observed under a 10× magnifier to ensure that the

Table 1 Burner port dimensions

Dimension (mm)	B1	B2	B3
b	0.254	0.762	0.102
h	3.550	3.390	3.82
t	0.260	0.260	0.260

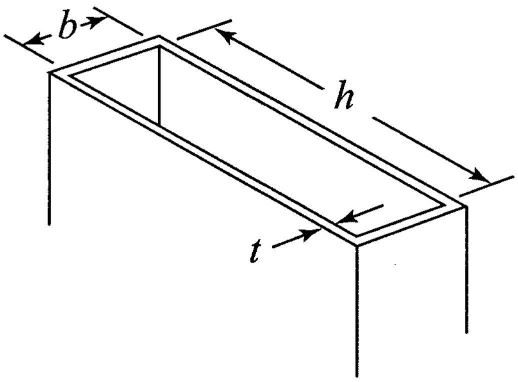

Fig. 2 A schematic diagram of the burner port

Table 3 Baseline parameters

Parameter	Magnitude
D	$1.794\times10^{-4} m^2/s$
I	1.0
k''	$0.1 m/s$
T_f	$1500 K$
T_F	$298 K$
T_∞	$298 K$
$Y_{F,stoic}$	0.06
ϕ	6.99297

slot width was uniform across the burner. The slot length, h, and the wall thickness, t, were determined using digital micrometers.

Prior to recording data, the flow rate was set to a level known to produce a flame. Once a flame was established the flow rate was decreased until the flame extinguished. The flow rate was then slightly increased to a point where the flame could be reestablished. Once the flame was reestablished, an image of the flame was recorded. The flow rate was then gradually increased and several images were recorded. The flow rate was increased and data collected until a subjective determination of the point where buoyancy forces became significant was noted. This point corresponded to the point where the flame began to assume the familiar "teardrop" shape. To ensure repeatability, this above procedure was repeated four times for a total of 33, 26, and 21 data points for burner ports B1, B2, and B3, respectively. High-resolution digital images in the form of jpeg format image files were then obtained during the processing of the photographic film. The flame height for each of the data points was determined using these files and a commercially available image analysis program. The quantitative results for flame height and shape were obtained by identifying the position of peak blue luminosity on the images. For non-sooting flames and flames where the soot does not penetrate the flame sheet, previous researchers have shown that this location also corresponds to the stoichiometric location [14].

5 Experimental Accuracy

The uncertainty of the experimental measurements was determined using the Euclidean norm of the bias error limit and the precision error limit

$$U=\sqrt{B^2+P^2} \tag{14}$$

The precision error limit and the bias error limit for each of the measured quantities is provided in Table 2. The precision and bias error limits of the volume flow rate were determined from the manufacturer's calibration data sheet. The precision error limit was taken as the reported uncertainty in the flow rate, ±1.5 percent full-scale, and the bias was taken as the average of the bias observed in the 5 point calibration data. The burner port width was measured using feeler gages of known thickness. The precision of the feeler gauges was taken as one-half the feeler gage's least count. The bias was assumed to be zero. The precision of the burner port length measurement was determined using a gage block of known width. The initial precision error limit was taken as the 95 percent confidence level of 41 measurements of the gage block using the same micrometers used to measure the burner port width. This value was found to be 0.003074 mm. Since this value was less than one-half the micrometer's least count, i.e., 0.005 mm, one-half the micrometer's least count was specified as the precision error limit. The bias was taken as the difference between the stated length for the gage block and the average value of the 41 measurements. The precision and bias error limits for the burner port length measurement will be the same as those reported for the burner port wall thickness measurement since the same micrometers were used for the wall thickness measurement. The precision error and bias limits for the flame height measurement were determined by taking 40 measurements, using the same commercially available image analysis software used to determine the flame height, of a high resolution jpeg image of a gage block of known width. The precision error limit was taken as the 95 percent confidence level of the 40 measurements of the gage block image. The bias was taken as the difference between the stated length of the gage block and the average length of the 40 measurements.

Table 2 Precision and bias

	$\pm P$	$\pm B$
Q	$0.3 ml/\text{min}$	$0.03 ml/\text{min}$
b	$0.0005 mm$	$0.00 mm$
h	$0.005 mm$	$0.00 mm$
L_F	$0.0115 mm$	$0.0194 mm$

6 Results and Discussion

Table 3 presents a listing of the baseline parameters used in the calculations. The value for the binary diffusion coefficient was calculated for a binary mixture of air and propane at a temperature of 1500 K and a pressure of 101.3 kPa, as outlined in Reid et al. [15]. The ratio of the actual initial momentum to that for uniform flow was assumed to be unity because of the geometry of the burner ports. Since the slot burner ports were formed at the end of cylindrical brass tubing, a relatively uniform velocity profile should exit at the burner port exit. The value of the reaction rate constant presented in the table represents an order of magnitude estimate. This estimate was determined by noting that since the flame is stationary and since there is a relatively small distance between the flame and the burner port, the reaction speed should be on the same order of magnitude as the velocity of the fuel leaving the burner port. For all the experimental conditions considered, the fuel flow rate was $O(10^{-8}\ \text{m}^3/\text{s})$ and the burner exit area was $O(10^{-7}\ \text{m}^2)$ and thus the reaction rate constant given in Table 3. It is recognized that the reaction rate constant is typically determined using an Arrhenius type relation. Note that the first-order reaction model used to develop the diffusion-controlled flame height expression is of questionable accuracy near the flame leading edge. Also note that the temperature near the flame leading edge may be several hundred degrees lower than the fully developed flame sheet temperature and that a significant, relative

Table 4 Range of dimensionless parameters

Burner Port	$Fr_{min}/$ Fr_{max}	$N_{DB,min}/$ $N_{DB,max}$	$N_{DM,min}/$ $N_{DM,max}$
B1	$2.46\times10^{-4}/$ 1.39×10^{-3}	$2.33\times10^{-2}/$ 8.43×10^{-1}	$4.15\times10^{0}/$ 5.28×10^{1}
B2	$2.40\times10^{-5}/$ 1.80×10^{-4}	$1.45\times10^{-2}/$ 6.47×10^{-1}	$9.00\times10^{0}/$ 1.64×10^{2}
B3	$2.15\times10^{-3}/$ 8.11×10^{-3}	$2.31\times10^{-2}/$ 1.27×10^{0}	$1.69\times10^{0}/$ 2.43×10^{2}

to the characteristic size of the flame, quenching zone exists near the burner port. Given limitations of the first-order reaction model and the temperature dependence of an Arrhenius relation, the order of magnitude estimate of the reaction rate constant should be sufficient for the analysis. The value of the flame temperature was taken to be the same as that assumed in Roper [7]. The initial fuel and the ambient temperature were both taken to be room temperature. The value for the function ϕ and the fuel mass fraction were calculated for a stoichiometric propane-air reaction.

The Froude number, Eq. (1), the diffusion to buoyancy parameter, Eq. (17), and the diffusion to momentum parameter, Eq. (19), were calculated using the above baseline data and the experimentally observed flame data. Table 4 shows the range of these three parameters for each of the burner ports. From an examination of the Froude number, it is clear that in an analysis that considers only buoyancy and momentum, the micro-slot flames are in the buoyancy-controlled regime. For micro-slot flames, the table also shows the importance of accounting for molecular diffusion. While the minimum diffusion to buoyancy parameter is $O(10^{-2})$ for all the burner ports, the maximum values indicate that buoyancy and diffusion are of comparable magnitude. From the diffusion to momentum parameters, it is clear that molecular diffusion is at least of comparable magnitude to momentum and the forces associated with molecular diffusion can be several orders of magnitude greater than those associated with momentum. From this information one may conclude that micro-slot flames, while similar to diffusion flames produced in a microgravity environment, i.e., in a purely diffusive environment, are not buoyant-free over the entire range of conditions. Over a certain range of conditions, momentum, buoyancy, and molecular diffusion contributions must be accounted for if one is to accurately predict micro-slot flame behavior. It is interesting to note that in Ban et al. [4], microflames produced using circular burner ports are characterized as convection-diffusion controlled. This conclusion was based upon a Froude number definition that employed the burner port diameter as the characteristic length. From Roper [7] and Dietrich, et al. [2], one may conclude that the flame height is a more appropriate characteristic length. An examination of the results in Ban et al. [4] shows that even if the characteristic length is taken to be the flame height and not the burner port diameter, the Froude number for the flames examined in that study range from $O(1)$ to $O(10)$. Using the previously defined regimes (transition, momentum-controlled, and buoyancy-controlled), this would indicate that the flames in Ban et al. [4] fall within the transitional to momentum-controlled regimes. These regimes have no meaning for flames produced using circular burner ports, however. As previously stated, for circular burner port geometries molecular diffusion effects tend to cancel out the effects of buoyant acceleration. Buoyancy effects would therefore play an insignificant role in the behavior of micro-flames produced using circular burner ports. The diffusion to buoyancy parameter for the flames examined in Ban et al. [4] ranged from $O(10^{-3})$ to $O(10^{-1})$ while the diffusion to momentum parameter ranged from $O(10^{-2})$ to $O(10^{-1})$. From these values, one would expect that buoyant acceleration would be more important than molecular diffusion in the microflames produced using circular burner ports. Again, the interaction between molecular diffusion and buoyancy results in buoyancy having a negligible impact on circular burner port microflame behavior and, therefore, characterizing circular burner port microflames as convection-diffusion controlled as stated in Ban et al. [4] is appropriate. In this study, the impact of buoyancy is not cancelled out by molecular diffusion and therefore one must consider buoyancy forces when characterizing the flame behavior, even for so-called microflames.

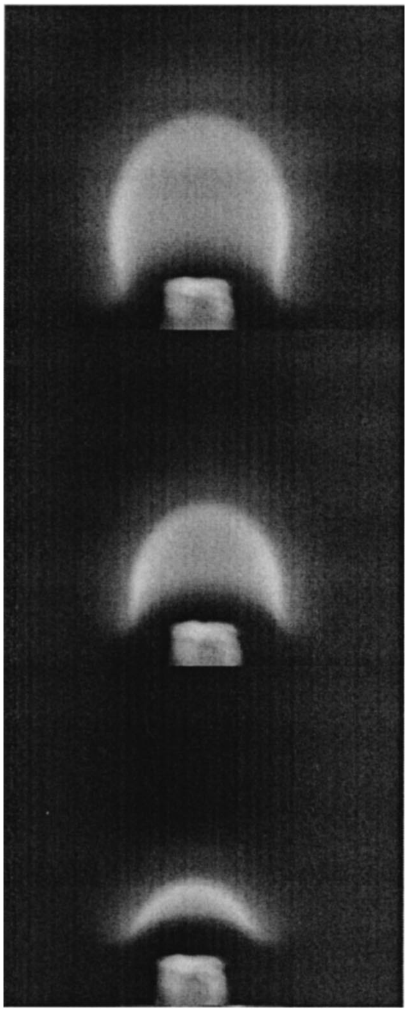

Fig. 3 Photographic images of typical micro-slot diffusion flames. Note an increasing flow rate from the bottom to the top.

Figure 3 provides three photographic images of typical microflames observed in this study. Figure 4 is a qualitative depiction of the flame shape at various flow rates for burner port B2. As for the flame height, the flame sheet was defined as the center of the blue luminescent region of the flame. At a 2.2 mL/min flow rate, the flame has a semicircular shape and a flame sheet is only observable well above the burner port exit due to quenching associated with the burner port. For flow rates of 5 and 7 mL/min, the flame continues to have a semicircular shape but the leading edge of the flame moves lower. For these flow rates, the cross sectional shape of the micro-slot flames is qualitatively the same as for circular burner port flames produced in a microgravity environment. At a flow rate of 9 mL/min, the existence of soot was first observed. At this flow rate the soot did not penetrate the flame

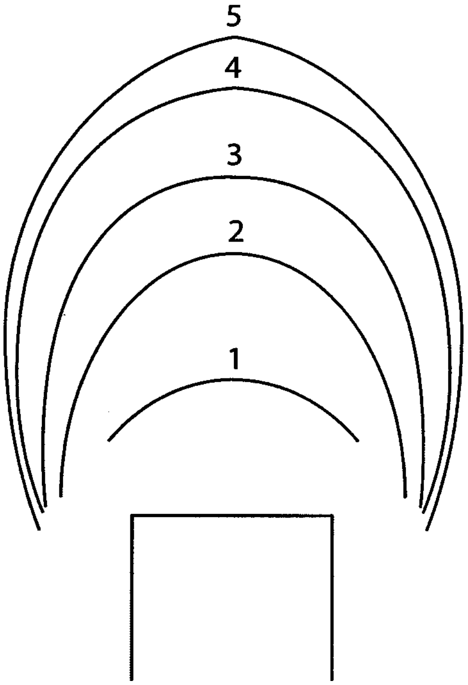

Fig. 4 Schematic representation of Burner Port B2 flame shapes: (1) 2.2 mL/min, (2) 5 mL/min, (3) 7 mL/min, (4) 9 mL/min, and (5) 10 mL/min.

sheet and the flame sheet was observed to be at the same horizontal position as the burner port exit. Soot did intersect the flame sheet at a flow rate of 10 mL/min and the flame began to assume the familiar teardrop shape associated with diffusion flames. For this flow rate, the flame height was estimated from a visual extrapolation from the jpeg image. As mentioned in §4, once the flame began to assume a teardrop shape, no additional data was recorded.

Figures 5, 6, and 7 show plots of flame height as a function of flow rate. The experimental measurement uncertainty for the flame height and the flow rate for all of these plots is respectively $U_{L_f}=\pm 2.26\times 10^{-2}$ mm and $U_{Q_F}=\pm 0.3$ mL/min. Again note that the flame height was taken to be the maximum height of the peak blue luminescent region of the flame. This point was clearly observable except for several data points corresponding to the larger flow rates. At these points soot was present in the flame. While the soot never fully penetrated the flame tip, it was difficult to clearly identify the flame sheet from the jpeg images and the flame height was visually extrapolated from the jpeg images. Also shown on these plots is Roper's [7] theoretical expression for the buoyancy-controlled flame height, Eq. (5), and the theoretical expression for a purely diffusion-controlled flame, Eq. (14). It is clear to see that the Roper's theoretical expression for flame height does not accurately predict the experimentally observed behavior, especially for larger flow rates. The reason for this may again be found in the above discussion of the dimensionless parameters. Roper's expression assumes that buoyancy is the dominant transport mechanism and for micro-slot flames this is not the case. As can also be seen from these figures, the theoretical expression for the purely diffusion-controlled flame height accurately predicts the behavior for the smaller flow rate values. As one would expect, the predicted value of the flame height using an expression for a diffusion-controlled flame is less than the experimentally observed flame height for larger flow rates. Again, this behavior can be explained by considering the physical mechanisms at work. For larger flow rates and larger flames, the mechanisms of buoyancy and momentum begin to play an increasingly important role in the behavior. While molecular diffusion may still be significant, the other mechanism must now also be considered.

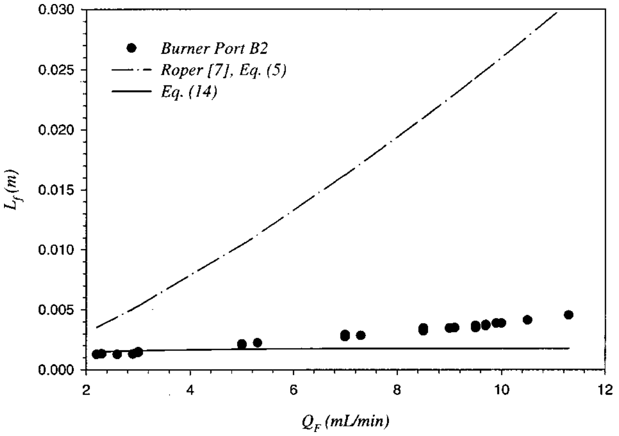

Fig. 6 Micro-slot diffusion flame height as a function of flow rate for Burner Port B2

To determine the range for which the theoretical expression for purely diffusion-controlled flame height is applicable, the theoretical value of the diffusion to buoyancy parameter, N_{DB}, was compared with the experimental value. This comparison is shown in Fig. 8 along with a line corresponding to a perfect correlation

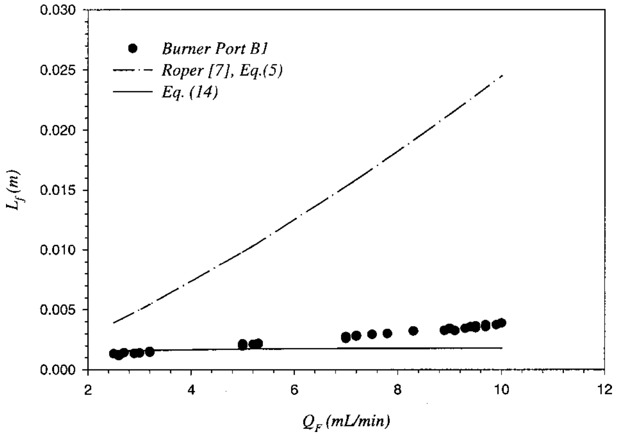

Fig. 5 Micro-slot diffusion flame height as a function of flow rate for Burner Port B1

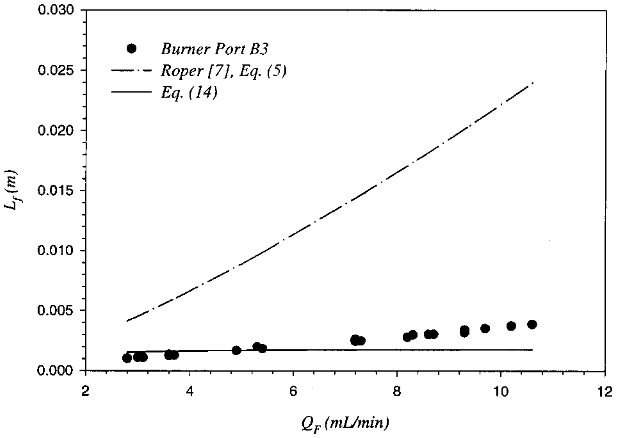

Fig. 7 Micro-slot diffusion flame height as a function of flow rate for Burner Port B3

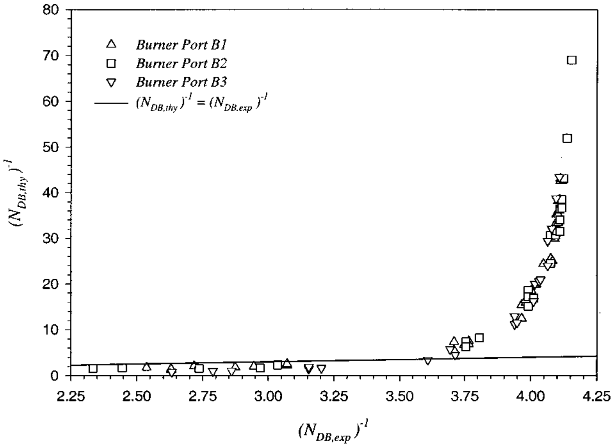

Fig. 8 Theoretical versus experimental diffusion to buoyancy parameter

between the theoretical and experimental values. The theoretical value of N_{DB} was calculated using Eq. (14) for the flame height while the experimental value was calculated using the experimentally observed flame height. It is quite clear from the figure that a regime exists outside of which Eq. (14) is valid. From the figure, for a value greater than $N_{DB}^{-1} \cong 3.75$ the theoretical expression for purely diffusion-controlled flame height should not be used. For a value less than 3.75, the theoretical expression should provide an accurate prediction of the flame height as there is a nearly one-to-one correspondence between $N_{DB,\mathrm{thy}}^{-1}$ and $N_{DB,\mathrm{exp}}^{-1}$. One may therefore conclude that care should be taken before assuming that microflames are buoyant free despite the qualitative similarities between such flames and flames produced in a reduced, or microgravity environment.

7 Summary and Conclusions

This paper has examined the nature of laminar jet micro-slot diffusion flames. Using slot burner ports with burner widths less than 1 mm across, a series of experiments was conducted and data was collected for propane-air flames. Data was collected in the form of high-resolution jpeg images and these images were analyzed to determine flame height and flame shape as a function of flow rate and burner port geometry. A theoretical expression capable of predicting the flame height for purely diffusion-controlled micro-slot flames was developed. An order of magnitude analysis was conducted to determine the relative importance of buoyancy, momentum transfer, and molecular diffusion on micro-slot flame behavior. The experimental data was compared to an existing closed-form mathematical model that has been effectively used to model diffusion flames and to the theoretical expression for purely diffusion-controlled flames. In addition to noting that to characterize micro-slot diffusion flame behavior one must examine the Froude number and either the diffusion to buoyancy or the diffusion to momentum parameter, the following conclusions may be drawn:

1. Despite the shape of micro-slot diffusion flames, the forces associated with buoyancy are not always negligible. It is hypothesized that the cross-sectional shape of laminar jet micro-slot diffusion flames may be the result of significant axial diffusion. Axial diffusion has been shown to be significant in the behavior of circular port micro-flames. A theoretical flame height expression developed using an axial velocity due solely to molecular diffusion is capable of accurately predicting micro-slot diffusion flame heights under certain conditions.
2. Previously developed closed-form mathematical expressions used to predict laminar diffusion flame height do not accurately predict the behavior of laminar jet micro-slot diffusion flames.

Given the importance of laminar diffusion flames as a model for more complex combustion processes, it is important to fully understand the behavior of such flames over a wide range of conditions. Microflames represent a flame regime that has yet to be fully explored. This investigation has identified several areas needing additional investigation and has provided the first closed-form mathematical expression capable of predicting laminar jet micro-slot diffusion flame behavior.

Acknowledgments

This work was supported by NASA Microgravity Combustion Program (Grant No. NAG3-2560) and the Alabama Space Grant Consortium. The authors would like to thank Letitia McMullin for her assistance in collecting the experimental data.

Nomenclature

a = mean buoyant acceleration
b = burner port width
B = bias error limit
D = diffusion coefficient
Fr = Froude number
g = acceleration due to gravity
Gr = Grashof number
h = burner port length
I = momentum correction factor
k'' = reaction rate constant
L_f = flame height
P = precision error limit
N_{DB} = diffusion to buoyancy parameter
N_{DM} = diffusion to momentum parameter
Q_F = fuel volume flow rate
Re = Reynolds number
S = molar stoichiometric oxidizer-fuel ratio
Sc = Schmidt number
t = burner port wall thickness
T = temperature
u = velocity
U = measurement uncertainty
Y_F = fuel mass fraction
z = coordinate direction

Greek Symbols

ν = kinematic viscosity
ϕ = function used in flame height calculation

Subscripts

B = buoyancy-controlled
D = diffusion-controlled
exp = experimental
f = flame
F = fuel
M = momentum-controlled
stoic = stoichiometric conditions
thy = theoretical
trans = transitional regime
z = coordinate direction
∞ = ambient conditions

References

[1] Davis, R. W., Moore, E. F., Santoro, R. J., and Ness, J. R., 1990, "Isolation of Buoyancy Effects in Jet Diffusion Flame Experiments," Combust. Sci. Technol., **73**, pp. 625–635.
[2] Dietrich, D. L., Ross, H. D., and T'ien, J. S., 1994, "Candle Flames in Non-Buoyant and Weakly Buoyant Atmospheres," AIAA Paper No. 94-0429.
[3] Mell, W. E., McGrattan, K. B., and Baum, H. R., 1999, "Simulation of Combustion Systems with Realistic g-Jitter," in *Fifth International Microgravity*

Combustion Workshop, May 18–20, The National Center for Microgravity Research on Fluids and Combustion, NASA Glenn Research Center.

[4] Ban, H., Venkatesh, S., and Saito, K., 1994, ''Convection-Diffusion Controlled Laminar Micro Flames,'' ASME J. Heat Transfer, **116**, pp. 954–959.

[5] Spalding, D. B., 1979, *Combustion and Mass Transfer*, Pergamon Press, New York.

[6] Burke, S. P., and Schumann, T. E. W., 1928, ''Diffusion Flames,'' Ind. Eng. Chem., **20**(10), pp. 998–1004.

[7] Roper, F. G., 1977, ''The Prediction of Laminar Jet Diffusion Flame Sizes: Part I. Theoretical Model,'' Combust. Flame, **29**, pp. 219–226.

[8] Roper, F. G., Smith, C., and Cuningham, A. C., 1977, ''The Prediction of Laminar Jet Diffusion Flame Sizes: Part II. Experimental Verification,'' Combust. Flame, **29**, pp. 227–234.

[9] Villermaux, E., and Durox, D., 1992, ''On the Physics of Diffusion Flames,'' Combust. Sci. Technol., **84**, pp. 279–294.

[10] Turns, S. R., 2000, *An Introduction to Combustion*, 2nd Ed., McGraw-Hill, New York.

[11] Williams, F. A., 1985, *Combustion Theory*, 2nd Ed., Benjamin Cummings, New York.

[12] Tien, J. S., 2000, ''The Role of Radiation on Microgravity Flames,'' 8th International Conference on Numerical Combustion, March 5–8, Amelia Island, Florida, USA.

[13] Nakamura, Y., Ban, H., Saito, K., and Takeno, T., 2000, ''Structure of Micro (Millimeter) Diffusion Flames,'' 3rd International Symposium on Scale Modeling, Sept. 10–13, Nagoya, Japan.

[14] Mitchell, R. E., Sarofim, A. F., and Clomburg, L. A., 1980, ''Experimental and Numerical Investigation of Confined Laminar Diffusion Flames,'' Combust. Flame, **37**, pp. 227–244.

[15] Reid, R. C., Prausnitz, J. M., and Poling, B. E., 1987, *The Properties of Gases and Liquids*, 4th Ed., McGraw-Hill, New York.

Achintya Mukhopadhyay[1]

Xiao Qin

Suresh K. Aggarwal
Professor
Mem. ASME
e-mail: ska@uic.edu

Ishwar K. Puri
Professor
Fellow ASME

Department of Mechanical Engineering
(MC 251)
University of Illinois at Chicago
842, West Taylor Street
Chicago, IL 60607-7022

On Extension of ''Heatline'' and ''Massline'' Concepts to Reacting Flows Through Use of Conserved Scalars

A new formulation for extending the concept of heatlines and masslines to reacting flows through use of conserved scalars has been proposed. The formulation takes into account the distinct diffusion coefficients of different species. Results have been obtained for a number of two-dimensional nonreacting and reacting free shear flows under normal and zero gravity. For nonreacting flows, total enthalpy and elemental mass fractions have been used as the transported conserved scalars. For reacting flows, mixture fractions, defined as normalized elemental mass fractions and enthalpy, have been employed. The results show this concept to be a useful tool for obtaining better insights into the global qualitative picture of scalar transport for both nonreacting and reacting flows.

[DOI: 10.1115/1.1473139]

Keywords: *Combustion, Heat Transfer, Numerical Methods, Visualization*

Introduction

Stream functions and streamlines are routinely used for visualization of flow fields in CFD analysis. As analogous concepts for visualization of convective-diffusive heat and species transport respectively, heatlines and masslines have also been used for nearly two decades. The heatlines and masslines represent non-crossed conduits for flow of heat and species respectively, and thus their shapes give a global picture of heat and species transport, in much the same way as the streamlines provide information on mass flow in single component systems. Although the concept of heat flux lines is well established in conduction heat transfer, the concept of heatline was first introduced by Kimura and Bejan [1] and its counterpart for mass transfer by Trevisan and Bejan [2]. Subsequently, this visualization technique has been used for various geometries [3,4,5,6,7]. Bejan [8] has presented a review of pre-1995 literature on heatlines and masslines. Recent advances in this field include use of heatlines for porous media [9], spherical geometries in presence of radial mass efflux [10], turbulent flows [11] and conjugate problems [12,13]. Although most of the studies utilizing heatlines and masslines have been limited to steady flows, Aggarwal and Manhapra [4,5] have extended the concept to transient heat transfer problems in cylindrical geometries to present instantaneous pictures of heat transport.

Apart from using heatlines and masslines as post-processing tools, some works have also been reported, which present improved or alternative formulations for these. Bello-Ochende [6] derived a Poisson-type equation for heat function, analogous to that used for calculating stream functions in terms of vorticity. Morega and Bejan [14,9] used similarity variables to derive closed form expressions for heatlines in forced convective boundary layers over flat plates in fluid media and fluid-saturated porous media respectively. Costa [15] followed a similar approach to develop analogous closed form expressions for natural convection from vertical flat plates for both isothermal and isoflux boundary conditions. Costa [16] applied the concept of heat and masslines to study double diffusive natural convection in square enclosures, filled with moist air. The relative importance of heat and mass diffusivities explicitly appeared in his work through Lewis number. However, for the particular fluids considered, his study was essentially limited to $\mathrm{Le} \approx 1$. Costa [17] presented a unified formulation for stream function, heat function and mass function in a form, suitable for direct incorporation into a CFD code, and solving them, utilizing the same procedures, which are used for solution of the primitive variables.

Objective

An important requirement for derivation of heat and mass functions is that the corresponding energy and species transport equations do not contain any source term. This has rendered this approach unsuitable for an important class of transport phenomena, namely, reacting flows. A survey of the existing literature also reveals that all the work reported so far have been limited to wall-bounded external and internal flows. The objective of this work is to provide a more general formulation for heat and mass functions, which would include reacting flows and would reduce to the conventional formulations for nonreacting flows. This formulation would be used to study the scalar transport in nonreacting jets and jet flames. As would be evident from the following section, the focal points of the present work are: (1) extension of the concept of heatline and massline to reacting flow through use of conserved scalar, (2) development of a formulation in terms of conserved scalar incorporating differential diffusion effects, and (3) application of this formulation to two-dimensional planar nonreacting and reacting free shear flows. We emphasize that the present formulation is intended for use as a post-processing visualization and analysis tool only. Consequently, the simulations of nonreacting and reacting flows previously developed using codes that have been thoroughly validated and discussed in earlier publications from our group [18,19] have been used to illustrate this post-processing technique.

Analysis

For reacting flows, the energy equation, expressed in terms of temperature or sensible enthalpy, contains a source term, representing heat released during combustion. Similarly, species conservation equations become non-homogeneous due to presence of terms representing production and/or destruction of the respective

---

[1] Visiting Scholar; on leave from Mechanical Engineering Department, Jadavpur University, Calcutta 700032, India

Contributed by the Heat Transfer Division for publication in the JOURNAL OF HEAT TRANSFER. Manuscript received by the Heat Transfer Division August 16, 2001; revision received February 28, 2002. Associate Editor: J. P. Gore.

species, owing to chemical reactions. However, it is possible to express the scalar transport in terms of homogeneous differential equations through use of variables, which are conserved in a chemical reaction. Such variables, termed conserved scalars, are the total enthalpy (i.e. sum of sensible enthalpy and enthalpy of reaction) of the mixture and atomic mass fractions of individual elements. Our objective in the present work is to derive the reacting flow counterparts of heat and mass functions by using these conserved scalars.

The present analysis begins with the scalar transport equations for reacting flows in coordinate-free form.

Energy Equation. The energy equation is expressed in terms of total mixture enthalpy (i.e., sum of sensible enthalpy and enthalpy of reaction) in the following form [20,21]:

$$\frac{\partial}{\partial t}(\rho h)+\nabla\cdot(\rho \mathbf{V}h)=\frac{\partial p}{\partial t}+\mathbf{V}\cdot\nabla p-\nabla\cdot\mathbf{q}+\underline{\underline{\tau}}:\ \nabla\mathbf{V}+\sum_{i=1}^{N}\rho_i\mathbf{f}_{v,\mathbf{i}}\cdot(\mathbf{V_i}-\mathbf{V}) \tag{1}$$

In the above equation, h denotes the enthalpy of the gas mixture, modeled as a mixture of ideal gases. Hence, the mixture enthalpy can be expressed as

$$h=\sum_{i=1}^{N}y_ih_i=\sum_{i=1}^{N}y_i\left[\Delta h_{f_i}+\int_{T_{\text{ref}}}^{T}C_{p_i}(T)dT\right] \tag{2}$$

Equation (1) is simplified by invoking the usual assumptions [20] for low Mach number reacting flows, namely, negligible viscous dissipation and pressure work and presence of gravity as the only body force. In addition, radiative heat transfer and Dufour effects are neglected and Fick's Law is assumed to be valid. Neglecting radiative heat loss is a reasonable assumption for many reacting flows, except for fuels with high soot forming characteristics and for conditions close to extinction. The use of Fick's Law for modeling the diffusion in a multicomponent mixture is justified by the presence of nitrogen as the dominant species in most reacting flows involving combustion of fuel in air. For such situations, it is a common practice [22] to incorporate the differential diffusion effects of the various species within the framework of Fick's Law by considering binary diffusion of each species with respect to nitrogen. With these simplifications, the energy equation has the following form:

$$\frac{\partial}{\partial t}(\rho h)+\nabla\cdot(\rho\mathbf{V}h)=\nabla\cdot\left[(k\nabla T)+\rho\sum_{i=1}^{N}D_{i-N_2}h_i\nabla y_i\right] \tag{3}$$

The above form of energy equation does not contain any source term. However, in order to express the right hand side of Eq. (3) in terms of total enthalpy, some transformations have to be carried out, which give rise to some additional source-like terms, as a result of unequal thermal and mass diffusivities ($\mathrm{Le}_i\neq 1$). Hence, for expressing the energy equation in terms of total enthalpy, the assumption of unity Lewis number is generally invoked. In our analysis, we present an alternative transformation that enables us to express the equation in terms of an effective diffusion coefficient and total mixture enthalpy, without requiring the assumption of unity Lewis number. However, we would like to note here that this transformation is possible in a straightforward manner in the present case, only because it is done as a part of post-processing. For the sake of convenience and clarity, the subsequent derivation will be carried out in two-dimensional Cartesian coordinates only. However, it can be readily extended to other systems also.

We can define species-averaged mass diffusion coefficients for use in Eq. (3) as:

$$D_x\sum_{i=1}^{N}h_i\frac{\partial y_i}{\partial x}=\sum_{i=1}^{N}D_{i-N_2}h_i\frac{\partial y_i}{\partial x} \tag{4}$$

$$\text{i.e.,}\quad D_x=\frac{\displaystyle\sum_{i=1}^{N}D_{i-N_2}h_i\frac{\partial y_i}{\partial x}}{\displaystyle\sum_{i=1}^{N}h_i\frac{\partial y_i}{\partial x}} \tag{4a}$$

A similar equation for D_y is obtained, considering the gradients in y-direction. The average values of mass diffusivities are different for diffusion fluxes in x and y-directions, due to the existence of different mass fraction gradients in the two directions.

The incorporation of Eqs. (4a) and a similar equation for D_y into Eq. (3), expressed in Cartesian coordinates, yields the following form:

$$\begin{aligned}\frac{\partial}{\partial t}(\rho h)+\frac{\partial}{\partial x}(\rho v_xh)+\frac{\partial}{\partial y}(\rho v_yh)&=\frac{\partial}{\partial x}\left(k\frac{\partial T}{\partial x}+\rho D_x\sum_{i=1}^{N}h_i\frac{\partial y_i}{\partial x}\right)\\&\quad+\frac{\partial}{\partial y}\left(k\frac{\partial T}{\partial y}+\rho D_y\sum_{i=1}^{N}h_i\frac{\partial y_i}{\partial y}\right)\end{aligned} \tag{5}$$

Using the definition of h_i (Eq. (2)), it can be shown that

$$\frac{\partial h_i}{\partial x}=C_{p_i}\frac{\partial T}{\partial x} \tag{6}$$

Multiplying the above equation by y_i and summing over all species, we obtain

$$\frac{\partial T}{\partial x}=\frac{1}{\overline{C}_p}\sum_{i=1}^{N}y_i\frac{\partial h_i}{\partial x} \tag{7}$$

Finally, $\Sigma_{i=1}^{N}h_i\partial y_i/\partial x$ can be replaced by $\partial h/\partial x-\Sigma_{i=1}^{N}y_i\partial h_i/\partial x$. Thus, we have

$$k\frac{\partial T}{\partial x}+\rho D_x\sum_{i=1}^{N}h_i\frac{\partial y_i}{\partial x}=\rho\left[\left(\frac{k}{\rho\overline{C}_p}-D_x\right)\sum_{i=1}^{N}y_i\frac{\partial h_i}{\partial x}+D_x\frac{\partial h}{\partial x}\right] \tag{8}$$

A similar equation is obtained for y-direction also.

We again define an effective diffusion coefficient in the following way:

$$D_{\text{eff},x}=\frac{\left[\left(\dfrac{k}{\rho\overline{C}_p}-D_x\right)\displaystyle\sum_{i=1}^{N}y_i\frac{\partial h_i}{\partial x}+D_x\frac{\partial h}{\partial x}\right]}{\dfrac{\partial}{\partial x}\displaystyle\sum_{i=1}^{N}y_ih_i} \tag{9}$$

Similarly we can define an effective diffusion coefficient, $D_{\text{eff},y}$ in y-direction.

Inserting the results of Eqs. (8) and (9) in Eq. (5), we obtain the energy equation in the following form:

$$\frac{\partial}{\partial t}(\rho h)+\frac{\partial}{\partial x}(\rho v_xh)+\frac{\partial}{\partial y}(\rho v_yh)=\frac{\partial}{\partial x}\left(\rho D_{\text{eff},x}\frac{\partial h}{\partial x}\right)+\frac{\partial}{\partial y}\left(\rho D_{\text{eff},y}\frac{\partial h}{\partial y}\right) \tag{10}$$

For quasi-steady flows, this simplifies to

$$\frac{\partial}{\partial x}\left(\rho v_xh-\rho D_{\text{eff},x}\frac{\partial h}{\partial x}\right)+\frac{\partial}{\partial y}\left(\rho v_yh-\rho D_{\text{eff},y}\frac{\partial h}{\partial y}\right)=0 \tag{11}$$

For single component fluids, it is clearly observed that the effective diffusivities reduce to thermal diffusivity and Eqs. (10) and (11) are equivalent to the thermal energy equation written in terms of temperature

Elemental Species Conservation Equation. Employing Fick's Law for modeling molecular diffusion of species in the multicomponent mixture in the same way as discussed in the context of the energy equation, the species conservation equation takes the following form:

$$\frac{\partial}{\partial t}(\rho y_i)+\nabla\cdot(\rho\mathbf{V}y_i)=\nabla\cdot(\rho D_{i-N_2}\nabla y_i)+\omega_i \tag{12}$$

We define elemental mass fraction, Z_j as $Z_j=\Sigma_{i=1}^{N}w_{j,i}y_i$ where $w_{j,i}=W_j\mu_{j,i}/\mathbf{M}_i$. Multiplying each species equation by $w_{j,i}$ and summing over all species we obtain

$$\frac{\partial}{\partial t}\left(\rho\sum_{i=1}^{N} y_i w_{j,i}\right)+\nabla\cdot\left(\rho\mathbf{V}\sum_{i=1}^{N} y_i w_{j,i}\right)$$
$$=\nabla\cdot\left(\sum_{i=1}^{N}\rho D_{i\text{-}N_2}w_{j,i}\nabla y_i\right)+\sum_{i=1}^{N}\omega_i w_{j,i} \tag{13}$$

From elemental mass conservation, the last term on RHS of Eq. (13) is zero. As in the case of energy equation, we again restrict our derivation to Cartesian system only for convenience. Again, as in the energy equation, we define species averaged diffusion coefficients in *x*- and *y*-directions. The equation for effective diffusivity in *x*-direction is as follows:

$$D'_{j,x}=\frac{\displaystyle\sum_{i=1}^{N}D_{i-N_2}W_{j,i}\frac{\partial y_i}{\partial x}}{\displaystyle\sum_{i=1}^{N}w_{j,i}\frac{\partial y_i}{\partial x}} \tag{14}$$

Employing Eqs. (14*a*) and a similar expression for effective diffusivity in *y*-direction ($D'_{j,y}$) in Eq. (13), the elemental mass fraction equation becomes

$$\frac{\partial}{\partial t}(\rho Z_j)+\frac{\partial}{\partial x}(\rho v_x Z_j)+\frac{\partial}{\partial y}(\rho v_y Z_j)$$
$$=\frac{\partial}{\partial x}\left(\rho D'_{j,x}\frac{\partial Z_j}{\partial x}\right)+\frac{\partial}{\partial y}\left(\rho D'_{j,y}\frac{\partial Z_j}{\partial y}\right) \tag{15}$$

For quasisteady flows, the equation becomes

$$\frac{\partial}{\partial x}\left(\rho v_x Z_j-\rho D'_{j,x}\frac{\partial Z_j}{\partial x}\right)+\frac{\partial}{\partial y}\left(\rho v_y Z_j-\rho D'_{j,y}\frac{\partial Z_j}{\partial y}\right)=0 \tag{16}$$

It may be noted here that for nonreacting flows, Eqs. (15) and (16) are equivalent to species conservation equations.

Enthalpy Functions and Elemental Mass Functions. From Eqs. (11) and (16), it is obvious that the mixture enthalpy and elemental mass fractions are conserved in a chemical reaction. Hence, their distributions are affected only by the transport mechanisms, advection and diffusion and hence, they can be considered analogous to temperature and mass fraction in nonreacting flows. Extending this analogy further, we define two additional functions, enthalpy function, H and elemental mass function, M_j as follows:

$$\frac{\partial H}{\partial y}=\rho v_x(h-h_{\text{ref}})-\rho D_{\text{eff},x}\frac{\partial h}{\partial x} \tag{17a}$$

$$-\frac{\partial H}{\partial x}=\rho v_y(h-h_{\text{ref}})-\rho D_{\text{eff},y}\frac{\partial h}{\partial y} \tag{17b}$$

$$\frac{\partial M_j}{\partial y}=\rho v_x(Z_j-Z_{j,\text{ref}})-\rho D'_{j,x}\frac{\partial Z_j}{\partial x} \tag{18a}$$

$$-\frac{\partial M_j}{\partial x}=\rho v_y(Z_j-Z_{j,\text{ref}})-\rho D'_{j,y}\frac{\partial Z_j}{\partial y} \tag{18b}$$

The contour plots of the above functions over the entire field may, similarly, be called as enthalpy lines and elemental masslines. As explained by Bejan [8], the utility of the above functions as visualization tools strongly depend on the choice of reference values. This will be further discussed in the context of our results. It should also be noted that the enthalpy lines and elemental masslines reduce to conventional heatlines and masslines for nonreacting flows.

In combustion analysis, the similitude between different flow configurations is often demonstrated by expressing the results in a conserved scalar space. For this purpose, it is customary to use suitably normalized values of conserved scalars as the independent variable. The conserved scalars are scaled in such a way that the normalized values, known as mixture fraction (ξ) range from 0 to 1 in the entire solution domain. We have also constructed mixture fraction lines, (based on mixture fractions as the transported conserved scalars) to investigate whether these lines provide us with further insights into various aspects of reacting flows, like differential diffusion of the different species. The actual definition of mixture fraction adopted by us will be detailed subsequently in connection with the specific cases considered.

Configuration

The formulation will first be used to visualize the transport phenomena in nonreacting heat and mass transfer problems. These relatively simple problems will be used to assess the capability of the present formulation to elicit useful information, about the nature of the flow. For such situations, the enthalpy lines and the elemental masslines are identical to the conventional heatlines and masslines, used in earlier studies. The nonreacting situations considered in the present work are: (*a*) hot air issuing into a cold air ambient, and (*b*) methane jet issuing into air. These cases are considered as nonreacting counterparts of a nonpremixed methane-air jet flame considered subsequently. For both nonreacting and reacting cases, we shall investigate the effect of gravity on the transport phenomena by presenting results at normal and zero gravity.

For hot air issuing into cold air stream, the hot air stream is 7.5 mm wide, issuing into a large coflow of air. Similarly, for both nonreacting and reacting cases, the methane jet is 7.5 mm wide. The hot air (or methane) jet is embedded in a 200 mm wide cold air (or air) jet for the air-into-air (or methane-into-air) case. Utilizing the symmetry of the configuration, only one half of the domain is used for the study. In the vertical direction, the domain extends to 150 mm, which was found to be large enough from earlier studies [18] for the flow field inside the domain to be unaffected by the boundary location. The governing conservation equations, boundary conditions and grid distributions are detailed in Ref. [18]. However, in all the figures we present the domain only up to an axial distance of 80 mm for clarity.

Solution Methodology

Solution of Enthalpy Function and Mass Function Equations. The solution of the conservation equations (mass, momentum, energy, and species) is detailed in Ref. [18]. The grid sensitivity and the validation of the code used for solving the transport equations have been discussed in earlier works [18,19,22]. Based on the findings of these works, all results are presented for a non-uniform grid distribution with 121 grids in *y*-direction and 61 grids in *x*-direction. Here only the procedure for solving the equations for enthalpy function and elemental mass function will be discussed. For solving Eqs. (17) and (18), the values of enthalpy function and mass function were arbitrarily set to zero at $x=0$, $y=0$. Since the differences in the values of enthalpy and mass functions at different locations are of interest, the results are unaffected by this arbitrary specification of datum. Using the values of H and M at (0,0), the values for points along the axis $(x,0)$ were computed by integration of Eqs. (17*a*) and (18*a*). Subsequently, using the values of H and M at the axial points $(x,0)$, the functions were evaluated at other points along the row (x, y) by integration of Eqs. (17*b*) and (18*b*).

Results and Discussions

Hot Air Mixing With Cold Air. In this case, no species conservation equation needs to be solved, and, hence, the transport process is completely described by enthalpy lines only. However, since only one species is present, change in enthalpy that takes place on mixing is entirely due to changes in sensible enthalpy. Consequent to our modeling all gas species as ideal gases, the sensible enthalpy is a function of temperature only. Hence, the enthalpy change directly correlates with change in temperature.

Figure 1 shows the contours of enthalpy line for a planar jet of hot air at 394 K issuing at a velocity of 0.3 m/sec into a coflowing stream of cold air at 294 K, moving with a velocity of 0.1 m/sec. The enthalpy of the cold air has been taken as the reference enthalpy for the calculation of enthalpy function (cf. Eqs. (17*a*) and (17*b*)). Such a choice of minimum value of the transported scalar as the reference quantity has been shown [8] to be most effective for visualization purpose. However, the contours presented here, correspond to a normalized enthalpy function, defined as $(H-H_{\min})/(H_{\max}-H_{\min})$. The difference in the values of enthalpy functions between two enthalpy lines gives the magnitude of the enthalpy crossing the region between the two lines. With the present normalized enthalpy functions, these values represent the fraction of the total enthalpy flow that passes between the concerned enthalpy lines. In the cases considered, the interface between the two fluid streams at the inlet to the computational domain is at $x=3.75$ mm. Figures 1(*a*) and 1(*b*) show that in presence of gravity, the enthalpy lines are much more vertical, compared to those at 0-g. The transport of enthalpy is governed both by advection and diffusion. In presence of gravity, the hot fluid is strongly accelerated in the vertical direction due to buoyancy effect. This makes the advection in vertical direction the dominant scalar transport mechanism. This is reflected in the shape of the enthalpy line also. The shapes of the streamlines clearly indicate the entrainment of the cold fluid into the hot fluid. However, since the cold fluid does not transport any net enthalpy into the mixed stream, this entrainment is not reflected in the enthalpy line profiles. On the other hand, at zero gravity, the hot stream is not accelerated as in the case of normal gravity. Consequently, the entrainment of the colder fluid is much weaker. The divergence of the enthalpy line is caused by the fact that in absence of the gravitational acceleration, diffusion effects become more important. In the present configuration, the diffusion is primarily in the transverse direction, due to a strong temperature gradient in this direction. The importance of cross-stream diffusion for the 0 g case is highlighted by the significantly greater divergence of the enthalpy lines, compared to the streamlines. On the other hand, the near-alignment of the enthalpy lines with the streamlines near the top of the domain for the 0 g case and nearly throughout the domain for the 1 g case illustrate the dominance of advection in the scalar transport at these locations.

Methane Mixing With Air. For assessing the utility of elemental mass functions and associated masslines, we first considered nonreacting coflowing streams of methane and air, both of which were at 294 K. The velocity of the methane stream at the inlet plane was 1 m/sec, while that of air was 0.2 m/sec. The masslines of elemental carbon, in this case, are identical with the masslines of methane.

Figure 2(*a*) shows the masslines, based on carbon, and enthalpy lines. It may be noted that the two streams are at identical temperatures. However, differences in the enthalpies of formation and specific heats lead to differences in enthalpies of the two species. Hence, the enthalpy transfer takes place in this case as a result of species interdiffusion. From an enthalpy transfer perspective, this mixing can, therefore, be visualized as a mixing process of two streams with different enthalpies. Since methane has a negative

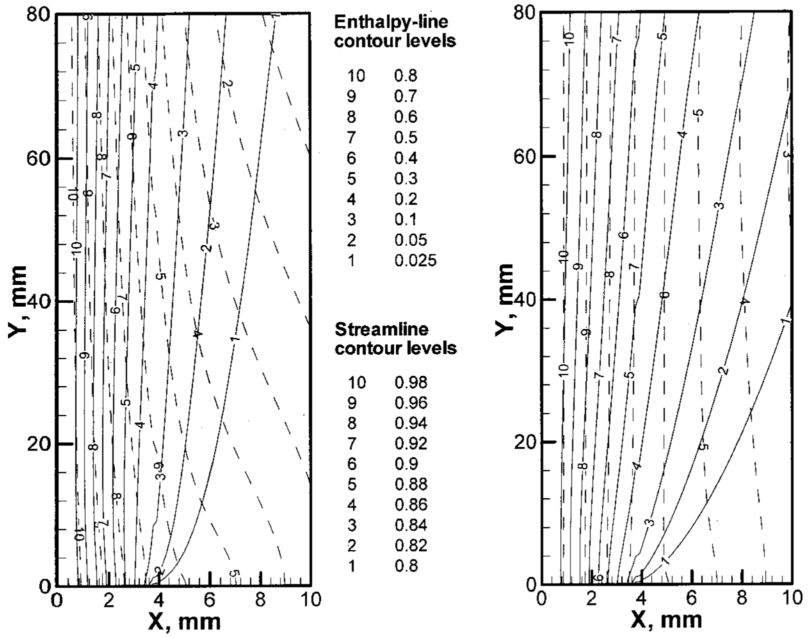

Fig. 1 Enthalpy lines and streamlines for hot air (394 K, 0.3 m/sec) flowing into cold air (294 K, 0.1 m/sec). The solid lines indicate enthalpy lines while the dashed lines indicate streamlines. The vectors correspond to enthalpy flux (*a*) normal gravity; and (*b*) Zero gravity.

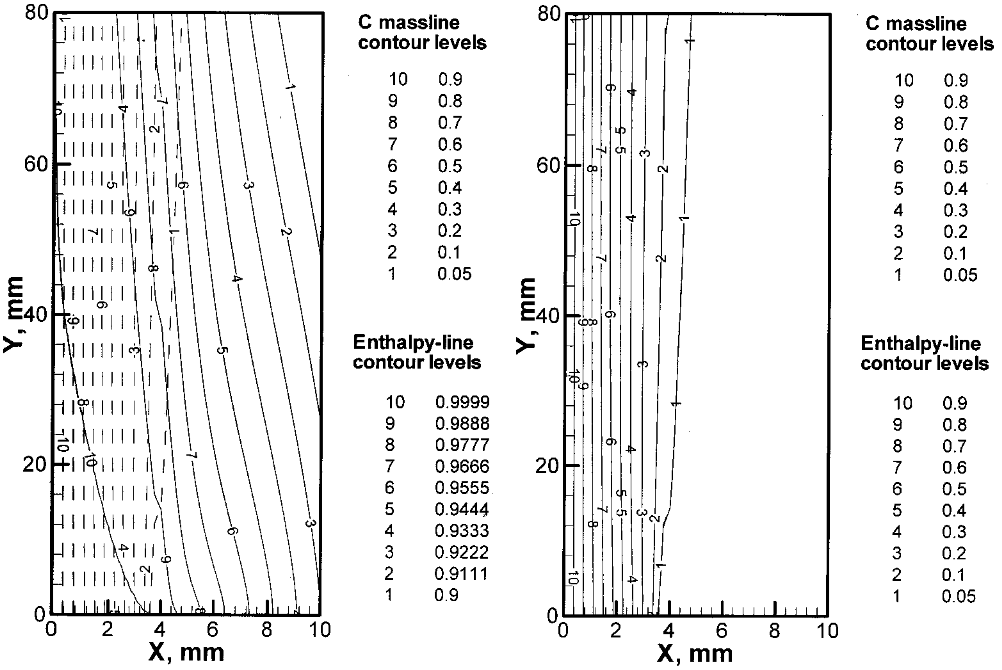

Fig. 2 (*a*) Elemental mass (carbon) lines and enthalpy lines in a planar jet consisting of methane in the inner stream (294 K, 1.0 m/sec) flowing with air (294 K, 0.2 m/sec) in the outer stream at 1-g case. The solid lines indicate enthalpy lines while the dashed lines indicate masslines; and (*b*) Mixture fraction lines based on elemental mass fraction (carbon) lines and enthalpy for the case depicted in Fig. 2(*a*). The solid lines indicate enthalpy-based lines while the dashed lines indicate carbon-based lines.

enthalpy of formation while that for air, modeled as a mixture of oxygen and nitrogen, is zero, the enthalpy transfer is from air to methane.

We have already mentioned that in reacting flows, similitude between different flow configurations is often demonstrated with the help of mixture fractions, which are conserved scalars, normalized in a suitable way. It is expected that irrespective of the choice of the particular conserved scalar used in the definition of mixture fraction, identical distributions of mixture fractions are obtained, provided the diffusion coefficients for the different scalars are identical. To test this hypothesis, two sets of mixture fractions, defined on the basis of enthalpy and mass fraction of carbon, were considered. The mixture fraction (ξ) was defined with respect to the conserved scalar as follows:

$$\xi=\frac{Z-Z_a}{Z_f-Z_a} \tag{19}$$

In the above equation, Z is a conserved scalar (enthalpy or atomic mass fraction of carbon). Substituting ξ for h in Eqs. (17*a*) and (17*b*) and for Z in Eqs. (18*a*) and (18*b*), we obtain the corresponding dimensionless forms of H and M, respectively. We call these normalized variables as *mixture fraction functions* (in analogy with enthalpy function and elemental mass function) and their contours as *mixture fraction lines*. The mixture fraction lines, thus constructed, using enthalpy and carbon mass fraction, are shown in Fig. 2(*b*). The two sets of mixture fraction lines are seen to be practically identical. This close similarity is not unexpected, considering the fact that all the species involved (N_2, O_2, and CH_4) have nearly identical thermal and mass diffusivities. Moreover, this is an advection-dominated situation and hence, differential diffusion effects are less evident.

Reacting Flows. Having assessed the capability of our formulation to illustrate the important features of scalar transport in nonreacting free shear flows, we now extend the concept to reacting flows, by investigating the scalar transport in planar laminar nonpremixed flames under both normal and zero gravity conditions. For both 0 g and 1 g cases, the fuel (methane) and air enter the computational domain at 0.3 m/sec and 294 K. The fuel stream is 7.5 mm wide. Only one half of the domain is considered due to the symmetry of the configuration. For the reacting flows, results are presented only in terms of mixture fraction lines. It may, however, be noted that for the present reacting flow model involving 24 chemical species [23], the contributions to the mixture fractions come from more than one species. Hence, unlike nonreacting flows, here, the mixture fraction is not proportional to the mass fraction of any particular species. Rather, it can be viewed as a linear combination of the mass fractions of several species. Consistent with earlier studies [24,25], gravity is found to have a destabilizing effect on the flame. Thus, while under 0-g conditions, steady flames are obtained, for same conditions under normal gravity, flames are observed to oscillate with a definite frequency.

Zero-Gravity Flame. Figures 3(*a*) and 3(*b*) show the distribution of mixture fraction lines based on elemental mass fraction of carbon and hydrogen respectively, superposed on streamlines. The contours of heat release rate which are good indicators of the flame shape and location [18] are also shown in the figure. As in the nonreacting flow situations, alignment of the mixture fraction lines with the streamlines indicates that the transport of the conserved scalar is advection-dominated. On the other hand, a divergence of the mixture fraction lines, relative to the streamlines highlights the importance of cross-stream diffusion. Since cross-stream diffusion is caused by flame curvature and hydrodynamic straining in the vicinity of the flame [26,27], the patterns of the mixture fraction lines and streamlines can provide a qualitative picture of the flame curvature and flame stretch. However, a detailed discussion on these lines is beyond the scope of the present work and will be covered in a subsequent work. The figures show that for both carbon and hydrogen the mixture fraction lines are aligned with the streamline, away from the flame. On the other

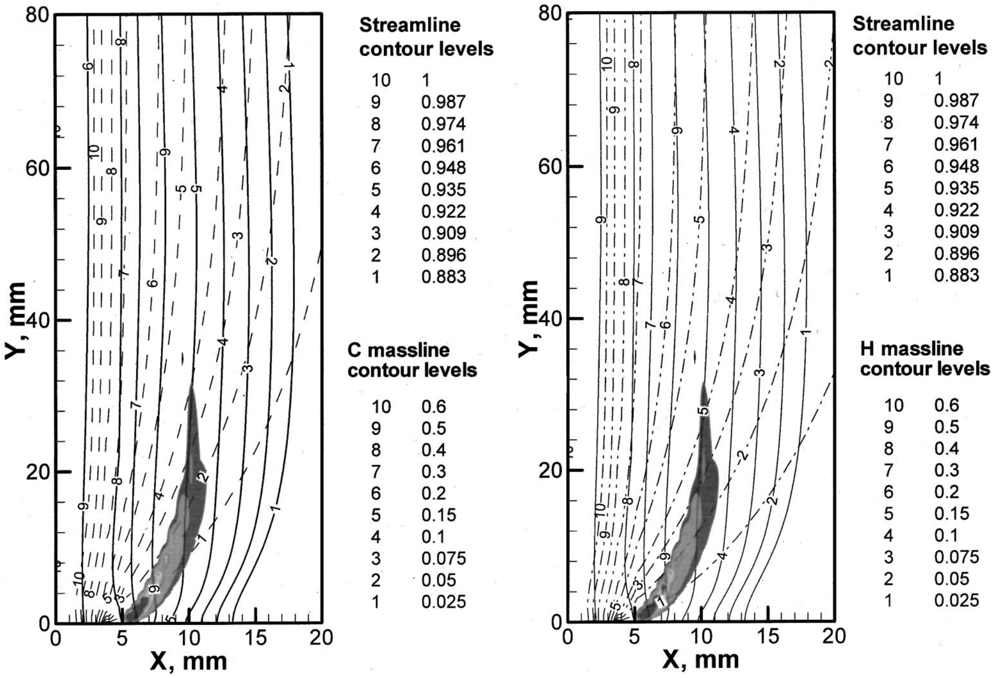

Fig. 3 Streamlines and mixture fraction lines for nonpremixed flame under zero gravity. The dashed lines indicate mixture fraction lines while the solid lines indicate streamlines (*a*) ξ based on carbon mass fraction, and (*b*) ξ based on hydrogen mass fraction. The reaction zone (nonpremixed flame) depicted in terms of the heat release rate contours is also shown.

hand, near the flame, the mixture fraction lines fan out across the streamlines, highlighting the importance of cross-stream diffusion in this region.

The species contributing to carbon and hydrogen mixture fractions are all either reactants or products of combustion. Consequently, the flame acts as a sink or source for these species, resulting in large spatial gradients in the vicinity of the flame. This makes diffusion important in the region. Although the patterns of mixture fraction lines in Figs. 3(*a*) and 3(*b*) are qualitatively similar, a more careful observation reveals a greater divergence of the hydrogen-based mixture fraction lines. This is discussed in greater detail in the context of Fig. 4.

Figure 4(*a*) compares the mixture fraction lines based on elemental mass fractions of carbon and hydrogen. A comparative study of the mixture fraction distributions, obtained from different elemental mass fractions, has been used in the past [28,29] to study the flame structure by interpreting the mixture fraction distributions in terms of the differential diffusivities of various species formed during combustion. Bilger [28] developed a formulation for differential diffusion of turbulent nonpremixed flames in terms of mixture fractions and perturbations about the equal diffusivity, adiabatic, equilibrium theory prediction. Smith et al. [29] used pulsed Raman spectroscopy to measure the temperature and concentrations in chemically reacting jets of H_2/CO_2 in air and used the measured concentration profiles to calculate the elemental mass fractions of carbon and hydrogen. They used these mixture fraction data to illustrate the differential diffusion effect between CO_2 and H_2. However, some authors [30] have objected to this approach on the ground that the mixture fraction or elemental mass fraction reflects the cumulative concentration of all the species, containing the particular element. For example, it is difficult to conclude from a mixture fraction distribution of hydrogen element, whether the leading contributor to the elemental mass fraction is water or molecular hydrogen or some radical like atomic hydrogen. Our objective is to investigate whether the mixture fraction lines, representing flux directions, provide us with additional insights into the flame structure.

Figure 4(*a*) shows that the mixture fraction lines, based on carbon and hydrogen are coincident, away from the flame. This is because of the fact that prior to initiation of the reaction, the only source for both carbon and hydrogen is the fuel. Hence, far upstream of the flame, these mixture fraction lines are essentially equivalent to methane masslines. In the vicinity of the flame and downstream, the hydrogen mass fraction show greater lateral divergence than those based on carbon. This distribution enables us to conclude that the effective mass diffusivity for hydrogen-containing species is higher than that for carbon-containing species. Since, the hydrocarbon species and many of the radicals contain both carbon and hydrogen, this distribution is a clear indicator of the relative abundance of some hydrogen-containing species with high mass diffusivities like H_2 and H. Thus, knowledge of the transport properties of the species involved in the reaction enables one to make a qualitative assessment of the flame structure (in terms of composition distribution) from inspection of the mixture fraction lines. For this purpose, these lines, being more directly related to the advective and diffusive transport of the different species, appear to be better suited than the isolines of mixture fractions.

Figure 4(*b*) shows the mixture fraction lines based on carbon and enthalpy. The distribution is again observed to be similar, although the enthalpy lines show a greater divergence. This may be due to the fact that the effective diffusivity in Eq. (17) have contributions from all the 24 species involved, including the highly mobile hydrogen-containing ones (H and H_2). This is in contrast with Fig. 2, where the enthalpy lines and mixture fraction lines are virtually identical. In the nonreacting case of Fig. 2, the only species present are CH_4, O_2, and N_2., all of which have Lewis numbers close to unity. The contrasting characteristics of the two cases illustrate the importance of differential diffusion in this visualization technique.

Normal-Gravity Flame. As already mentioned, the laminar nonpremixed flames under normal gravity conditions are found to oscillate with a definite frequency. The instantaneous temperature

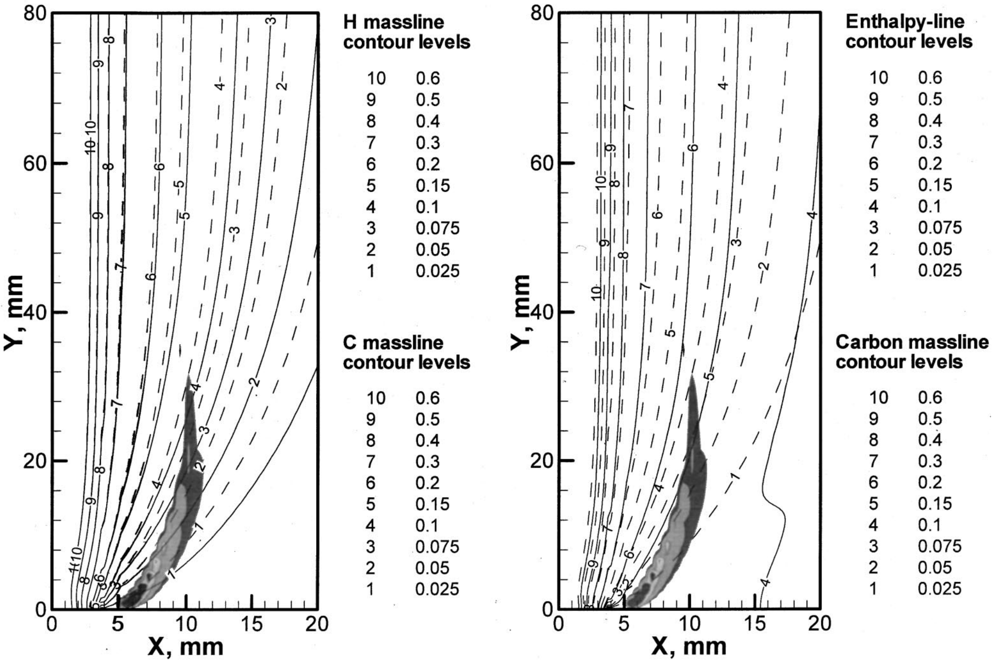

Fig. 4 (*a*) **Mixture fraction lines based on hydrogen and carbon for nonpremixed flame under zero gravity. The dashed lines indicate mixture fraction lines based on carbon while the solid lines indicate mixture fraction lines based on hydrogen. The reaction zone (nonpremixed flame) depicted in terms of the heat release rate contours is also shown; and (*b*) Mixture fraction lines based on hydrogen and enthalpy for the same. The dashed lines indicate mixture fraction lines based on carbon while the solid lines indicate mixture fraction lines based on enthalpy. The reaction zone (nonpremixed flame) depicted in terms of the heat release rate contours is also shown.**

fields in Fig. 5, obtained at different times show that the time period of this oscillation is 0.08 seconds. The temperature distribution also shows the formation of large vortical structures, which are known to cause the observed unsteadiness in the flame.

Although the concepts of enthalpy lines and masslines are based on an assumption of steady flow, Aggarwal and Manhapra [4,5] have shown in the context of transient heat transfer that these lines can reflect the instantaneous directions of heat flow in the computational domain. However, the implicit assumption is that the response time of the flow is much faster than the externally imposed time constant, such that the quasisteady assumption is valid. Considering the width of the fuel jet as the length scale and

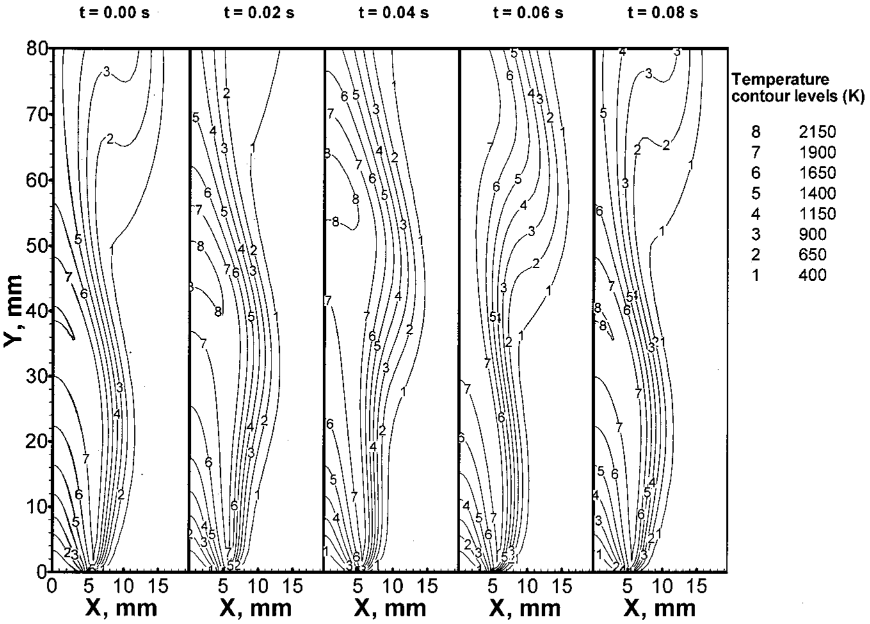

Fig. 5 Temperature contours for nonpremixed flame under normal gravity at different time instants over one period of oscillation

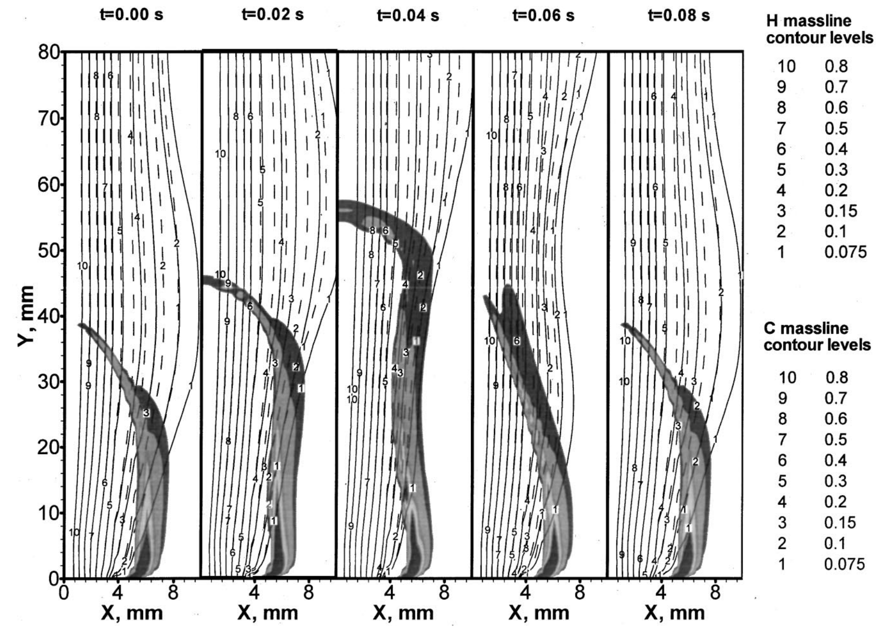

Fig. 6 Mixture fraction lines, based on elemental carbon (dashed lines) and elemental hydrogen (solid lines) for nonpremixed flame under normal gravity at different time instants over one period of oscillation

inlet velocity of the fuel as the velocity scale, we obtain a characteristic flow time of the order of 0.0125 seconds. Since we are primarily interested in the transport phenomena around the flame, situated close to the inlet, the choice of inlet conditions to determine the characteristic time is appropriate. Since the flow time thus obtained is almost one order of magnitude smaller than the time constant for the oscillation, the assumption of quasisteadiness is justified.

The mixture fraction lines, based on carbon and hydrogen elemental mass (cf. Fig. 6), give similar qualitative picture as the 0-g flame. However, the shapes of the outer mixture fraction lines also show the existence of the large vortical structures.

Conclusions

A new formulation for extending the concept of heatlines and masslines to reacting flows through use of conserved scalars has been proposed. The formulation takes into account the distinct diffusion coefficients of different species. Results have been obtained for a number of two-dimensional nonreacting and reacting free shear flows under normal and zero gravity. For nonreacting flows, total enthalpy and elemental mass fractions have been used as the transported conserved scalars. For reacting flows, mixture fractions, defined as normalized elemental mass fractions and enthalpy, have been employed. The results show this concept to be a useful tool for obtaining better insights into the global qualitative picture of scalar transport for both nonreacting and reacting flows. For nonreacting flows, flow of hot air stream into a cold air stream and that of a methane jet into an air jet have been considered. The importance of diffusive transport increases with temperature and absence of gravity. For reacting flows, the mixture fraction lines indicate the presence of strongly diffusing hydrogen-containing species in the vicinity of the flame. Results suggest that the concept of mixture fraction lines can be a useful visualization tool for characterizing the nonpremixed flame structure and examining the similitude between flames in different configurations.

Acknowledgments

This research was supported by the National Science Foundation Combustion and Plasma Systems Program through Grant No. CTS-9707000 for which Dr. Farley Fisher is the Program Director. Computations were performed on the SGI workstations at NCSA at Urbana-Champaign.

Nomenclature

C_p = specific heat (kJ/kgK)
$\overline{C_p}$ = average specific heat of mixture, $\overline{C_p}=\Sigma_{i=1}^{N} y_i C_{p_i}$ (kJ/kgK)
D = width of hot jet at inlet (m)
D_{i-N_2} = binary mass diffusion coefficient of species i in nitrogen (m^2/sec)
D_x, D_y = species-averaged mass diffusivity for enthalpy calculation (Eq. 4) (m^2/sec)
$D_{\text{eff},x}, D_{\text{eff},y}$ = effective mass diffusivity for enthalpy calculation (Eq. 9) (m^2/sec)
$D'_{j,x}, D'_{j,y}$ = species-averaged mass diffusivity for mass fraction calculation of element j (Eq. 14) (m^2/sec)
$\mathbf{f}_{v,i}$ = body force per unit volume on species i (kN/m^3)
h = enthalpy (kJ/kg)
Δh_f = enthalpy of formation (kJ/kg)
H = enthalpy function (Eq. 17) (kW/m)
k = thermal conductivity (W/mK)
$\mathbf{M}_i$ = molecular weight of species i
M_j = elemental mass function of element j (Eq. 18) (kg/m-sec)
p = pressure (kPa)
$\mathbf{q}$ = heat flux vector (kW/m^2)
Ri = Richardson number (Eq. 19) (dimensionless)
T = temperature (K)
u_j = velocity of hot jet at inlet (m/sec)
W_j = atomic weight of element j
v = velocity (m/sec)
y = species mass fraction (dimensionless)
Z = elemental mass fraction (dimensionless)

Greek Symbols

ρ = density (kg/m^3)
$\mu_{j,i}$ = number of atoms of element j in 1 molecule of species i

ω = volumetric reaction rate (kg/m^{3}sec)
ξ = mixture fraction (dimensionless)
$\underline{\underline{\tau}}$ = stress tensor

Subscript

a = air
f = fuel
i = i^{th} component
j = hot jet
max = maximum
min = minimum
ref = reference
x = x-component
y = y-component
∞ = ambient

References

[1] Kimura, S., and Bejan, A., 1983, ''The 'Heatline' Visualization of Convective Heat Transfer,'' ASME J. Heat Transfer, **105**, pp. 916–919.
[2] Trevisan, O. V., and Bejan, A., 1987, ''Combined Heat and Mass Transfer by Natural Convection in a Vertical Enclosure,'' ASME J. Heat Transfer, **109**, pp. 104–112.
[3] Littlefield, D., and Desai, P., 1988, ''Buoyant Laminar Convection in a Vertical Cylindrical Annulus,'' ASME J. Heat Transfer, **110**, pp. 814–821.
[4] Aggarwal, S. K., and Manhapra, A., 1989, ''Use of Heatlines for Unsteady Buoyancy-Driven Flow in a Cylindrical Enclosure,'' ASME J. Heat Transfer, **111**, pp. 576–578.
[5] Aggarwal, S. K., and Manhapra, A., 1989, ''Transient Natural Convection in a Cylindrical Enclosure Non-Uniformly Heated at the Top Wall,'' Numer. Heat Transfer, Part A, **15**, pp. 341–356.
[6] Bello-Ochende, F. L., 1988, ''A Heat Function Formulation for Thermal Convection in a Square Cavity,'' Int. Commun. Heat Mass Transfer, **15**, pp. 193–202.
[7] Ho, C. J., and Lin, Y. H., 1989, ''Thermal Convection of Air/Water Layers Enclosed in Horizontal Annuli With Mixed Boundary Conditions,'' Waerme- und Stoffuebertrag., **24**, pp. 211–224.
[8] Bejan, A., 1995, *Convection Heat Transfer*, 2nd ed., Wiley, New York.
[9] Morega, Al M., and Bejan, A., 1994, ''Heatline Visualization of Forced Convection in Porous Media,'' Int. J. Heat Fluid Flow, **15**, pp. 42–47.
[10] Chattopadhyay, H., and Dash, S. K., 1995, ''Numerical Visualization of Convective Heat Transfer From a Sphere—With and Without Radial Mass Efflux,'' Int. J. Numer. Methods Heat Fluid Flow, **5**, pp. 705–716.
[11] Dash, S. K., 1996, ''Heatline Visualization in Turbulent Flow,'' Int. J. Numer. Methods Heat Fluid Flow, **6**, pp. 37–46.
[12] Oh, J. Y., Ha, M. Y., and Kim, K. C., 1997, ''Numerical Study of Heat Transfer and Flow of Natural Convection in an Enclosure With a Heat-Generating Conducting Body,'' Numer. Heat Transfer, Part A, **31**, pp. 289–303.
[13] Kim, S. J., and Jang, S. P., 2001, ''Experimental and Numerical Analysis of Heat Transfer Phenomena in a Sensor Tube of a Mass Flow Controller,'' Int. J. Heat Mass Transf., **44**, pp. 1711–1724.
[14] Morega, Al M., and Bejan, A., 1993, ''Heatline Visualization of Forced Convection Laminar Boundary Layers,'' Int. J. Heat Mass Transf., **36**, pp. 3957–3966.
[15] Costa, V. A. F., 2000, ''Heatline and Massline Visualization of Laminar Natural Convection Boundary Layers Near a Vertical Wall,'' Int. J. Heat Mass Transf., **43**, pp. 3765–3774.
[16] Costa, V. A. F., 1997, ''Double Diffusive Natural Convection in a Square Enclosure With Heat and Mass Diffusive Walls,'' Int. J. Heat Mass Transf., **40**, pp. 4061–4071.
[17] Costa, V. A. F., 1999, ''Unification of the Streamline, Heatline, and Massline Methods for the Visualization of Two-Dimensional Transport Phenomena,'' Int. J. Heat Mass Transf., **42**, pp. 27–33.
[18] Shu, Z., Aggarwal, S. K., Katta, V. R., and Puri, I. K., 1997, ''Flame-Vortex Dynamics in an Inverse Partially Premixed Combustor: The Froude Number Effects,'' Combust. Flame, **111**, pp. 276–294.
[19] Aggarwal, S. K., Puri, I. K., and Qin, X., 2001, ''A Numerical and Experimental Investigation of ''Inverse'' Triple Flames,'' Phys. Fluids, **13**, pp. 265–275.
[20] Williams, F. A., 1985, *Combustion Theory*, 2nd ed., Benjamin-Cummings, Menlo Park, CA.
[21] Bird, R. B., Stewart, W. E., and Lightfoot, E. N., 1960, *Transport Phenomena*, Wiley, New York.
[22] Shu, Z., 2001, ''A Numerical Investigation of Steady and Unsteady Methane-Air Partially Premixed Flames,'' Ph.D thesis, University of Illinois at Chicago.
[23] Peters, N., and Rogg, B., eds, 1993, *Lecture Notes in Physics*, Springer-Verlag.
[24] Hoshangadi, A., Merkle, C. L., and Turns, S. R., 1990, ''Analysis of Forced Combusting Jets,'' AIAA J., **28**, pp. 1473–1480.
[25] Azzoni, R., Ratti, S., Aggarwal, S. K., and Puri, I. K., 1999, ''Gravity Effects on Triple Flames: Flame Structure and Flow Instability,'' Phys. Fluids, **11**, pp. 3449–3464.
[26] Poinsot, T., Echekki, T., and Mungal, M. G., 1992, ''A Study of the Laminar Flame tip and Implications for Premixed Turbulent Combustion,'' Combust. Sci. Technol., **81**, pp. 45–73.
[27] Echekki, T., 1997, ''A Quasi-One-Dimensional Premixed Flame Model With Cross-Stream Diffusion,'' Combust. Flame, **110**, pp. 335–350.
[28] Bilger, R. W., 1981, ''Molecular Transport Effects in Turbulent Diffusion Flames at Moderate Reynolds Number,'' AIAA J., **20**, pp. 962–970.
[29] Smith, L. L., Dibble, R. W., Talbot, L., Barlow, R. S., and Carter, C. D., 1995, ''Laser Raman Scattering Measurements of Differential Molecular Diffusion in Turbulent Nonpremixed Jet Flames of H_2/CO_2 Fuel,'' Combust. Flame, **100**, pp. 153–160.
[30] Echekki, T., and Chen, J. H., 1998, ''Structure and Propagation of Methanol-Air Triple Flames,'' Combust. Flame, **114**, pp. 231–245.